ISSN 2188-5001

MATERIALS DESIGN AND
CHARACTERIZATION LABORATORY

SUPERCOMPUTER CENTER

ACTIVITY REPORT 2018

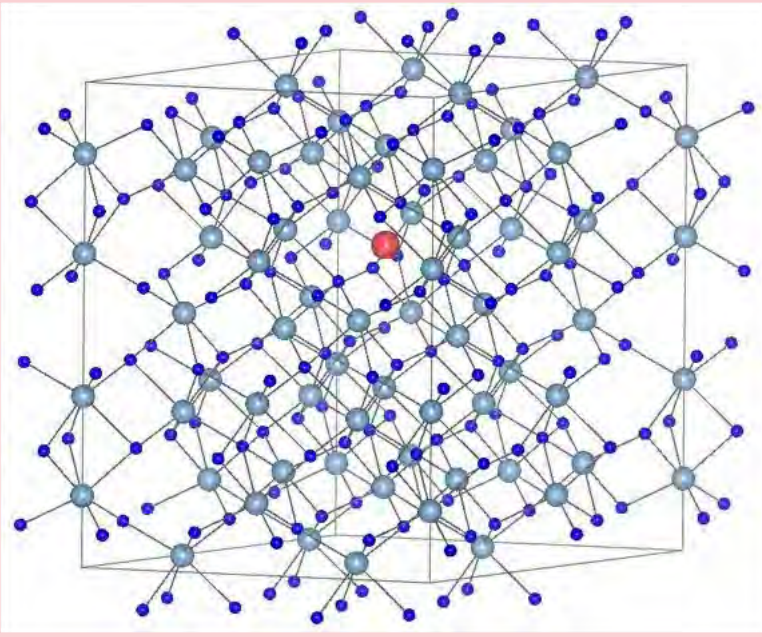

INSTITUTE FOR SOLID STATE PHYSICS
THE UNIVERSITY OF TOKYO

Materials Design and Characterization Laboratory (MDCL)

The MDCL was established as the third research facility of the Institute for Solid State Physics (ISSP) when the latter was reorganized in May 1996. Its aim is to promote material science with an emphasis on the "DSC cycle", where DSC stands for design, synthesis and characterization, three processes for developing new materials.

The MDCL consists of two sections, Materials Design (MD) section and Materials Synthesis and Characterization (MSC) section. The Supercomputer Center of the ISSP (SCC-ISSP) is placed in the MD section, while in the MSC section there are seven laboratories for joint use; Materials Synthesis Laboratory, Chemical Analysis Laboratory, X-ray Diffraction Laboratory, Electron Microscope Laboratory, Electromagnetic Measurement Laboratory, Spectroscopy Laboratory, and High-Pressure Synthesis Laboratory.

Almost all the facilities of the MDCL are open to scientists in Japan through the User Programs conducted by two steering committees of the MDCL. One is the steering committee of the SCC-ISSP, under which the Supercomputer Project Advisory Committee is placed for reviewing proposals. The other is the steering committee of the MSC facilities. More than half of the members of these committees are from the outside of ISSP.

PREFACE

The Supercomputer Center (SCC) is a part of the Materials Design and Characterization Laboratory (MDCL) of ISSP. Its mission is to serve the whole community of computational condensed-matter physics of Japan providing it with high performance computing environment. In particular, the SCC selectively promotes and supports large-scale computations. For this purpose, the SCC invites proposals for supercomputer-aided research projects and hosts the Steering Committee, as mentioned below, that evaluates the proposals.

The ISSP supercomputer system consists of two subsystems: System B, which is intended for more nodes with relatively loose connections. In July, 2015, the SCC replaced the two supercomputer subsystems (SGI Altix ICE 8400EX and NEC SX-9) to one new system (System B, SGI ICE XA/UV hybrid system). The system B consists of 1584 CPU nodes, 288 ACC nodes, and 19 FAT nodes. The CPU node has 2 CPUs (Intel Xeon). The ACC node has 2CPUs (Intel Xeon) and 2GPUs (NVIDIA Tesla K40). The FAT node has 4CPUs (Intel Xeon) and large memory (1TB). The system B has totally 2.6 PFlops theoretical peak performance.
The new system C (HPE SGI 8600) was installed in January, 2018. It consists of 252 nodes, and each node has 2 CPUs (Intel Xeon) and 192 GB of memory. The system C has totally 774 TFlops.

The hardware administration is not the only function of the SCC. Since 2015, the SCC has started “Project for advancement of software usability in materials science”. In this project, for enhancing the usability of the ISSP supercomputer system, we perform some software-advancement activities such as implementing a new function to an existing code, releasing a private code on Web, and writing manuals. Two target programs were selected in school year 2018 and developed software were released as DSQSS (proposal made by A. Masaki (RIKEN)) and RESPACK (proposal made by K. Nakamura (Kyutech)). The SCC has also started a service for porting users’ materials science software to General Purpose GPUs (GPGPU) since 2015. Two programs were selected for the GPGPU porting in school year 2018.

All staff members of university faculties or public research institutes in Japan are invited to propose research projects (called User Program). The proposals are evaluated by the Steering Committee of SCC. Pre-reviewing is done by the Supercomputer Project Advisory Committee. In school year 2018, totally 283 projects were approved. The total points applied and approved are listed on Table. 1 below. Additionally, we supported post-K and other computational materials science projects through Supercomputing Consortium for Computational Materials Science (SCCMS).

The research projects are roughly classified into the following three (the number of projects approved):

First-Principles Calculation of Materials Properties (131)
Strongly Correlated Quantum Systems (33)
Cooperative Phenomena in Complex, Macroscopic Systems (119)

All the three involve both methodology of computation and its applications. The results of the projects are reported in 'Activity Report 2018' of the SCC. Every year 3-4 projects are selected for “invited papers” and published at the beginning of the Activity Report. In the Activity Report 2018, the following three invited papers are included:

"Development of Open-Source Software mVMC and its Applications",
Takahiro MISAWA, Yuichi MOTOYAMA, and Kota IDO

"First-Principles Studies on Anomalous Electron and Spin Transport Properties in Non-Trivial Spin Textures",
Fumiyuki ISHII

"Coarse-Grained Force Field for Lipid Domain Formation Simulations”,
Sangjae SEO, and Wataru SHINODA

June 14, 2019

Naoki Kawashima
(Chairman of the steering committee, SCC, ISSP)

CONTENTS

1 OUTLINE

1.1 Supercomputer System

In SY2018, the ISSP supercomputer center provided users with System B - SGI ICE XA/UV hybrid system and System C - HPE SGI 8600 system. System B is a massively-parallel supercomputer with three types of compute nodes: 19 "Fat" nodes, 1584 "CPU" nodes, and 288 "ACC" nodes. "Fat" nodes are each comprised of four Intel Xeon E5-4627v3 CPUs (10 cores/CPU) and 1 TB of memory. "CPU" nodes have two Intel Xeon E5-2680v3 CPUs (12 cores/CPU) and 128 GB of memory. "ACC" nodes have two nVIDIA Tesla K40 GPUs in additon to two Xeon E5-2680v3 CPUs and 128 GB of memory. System B achieves 2.6 PFLOPS in theoretical peak performance with high power efficiency. The subsystem comprised of only CPU nodes ranks 61st on the November 2015 Top 500 List, which is a ranking based on total performance measured by the HPL benchmark. The subsystem of ACC nodes ranks 104th on the Top 500 List, and it also ranks 23rd on the Green 500 List, which is a ranking based on performance per watt of electrical power consumption. The compute nodes communicate to each other through FDR Infiniband. The Fat nodes are interconnected in fat tree topology, while the CPU and ACC nodes are connected in enhanced hypercube topology. System B entered official operation on Aug. 21, 2015. SY2018 was the fourth year of the operation of the current System B. System C is a massively-parallel supercomputer with 252 "CPU" nodes, which have two Intel Xeon Gold 6148 CPUs (20 cores/CPU) and 192 GB of memory. System C achieves 774 TFLOPS in theoretical peak performance. System C entered official operation in April, 2018. SY2018 was the first year of the operation of the current System C. For further details, please contact ISSP Supercomputer Center (SCC-ISSP).

[Correspondence: center@issp.u-tokyo.ac.jp]

1.2 Project Proposals

The ISSP supercomputer system provides computation resources for scientists working on condensed matter sciences in Japan. All scientific staff members (including post-docs) at universities or public research institutes in Japan can submit proposals for projects related to research activities on materials and condensed matter sciences. These proposals are peer-reviewed by the Advisory Committee members (see Sec. 1.3), and then the computation resources are allocated based on the review reports. The leader of an approved project can set up user accounts for collaborators. Other types of scientists, including graduate students, may also be added. Proposal submissions, peer-review processes, and user registration are all managed via a web system.

The computation resources are distributed in a unit called "point", determined as a function of available CPU utilization time and consumed disk resources. There were calls for six classes of research projects in SY 2018. The number of projects

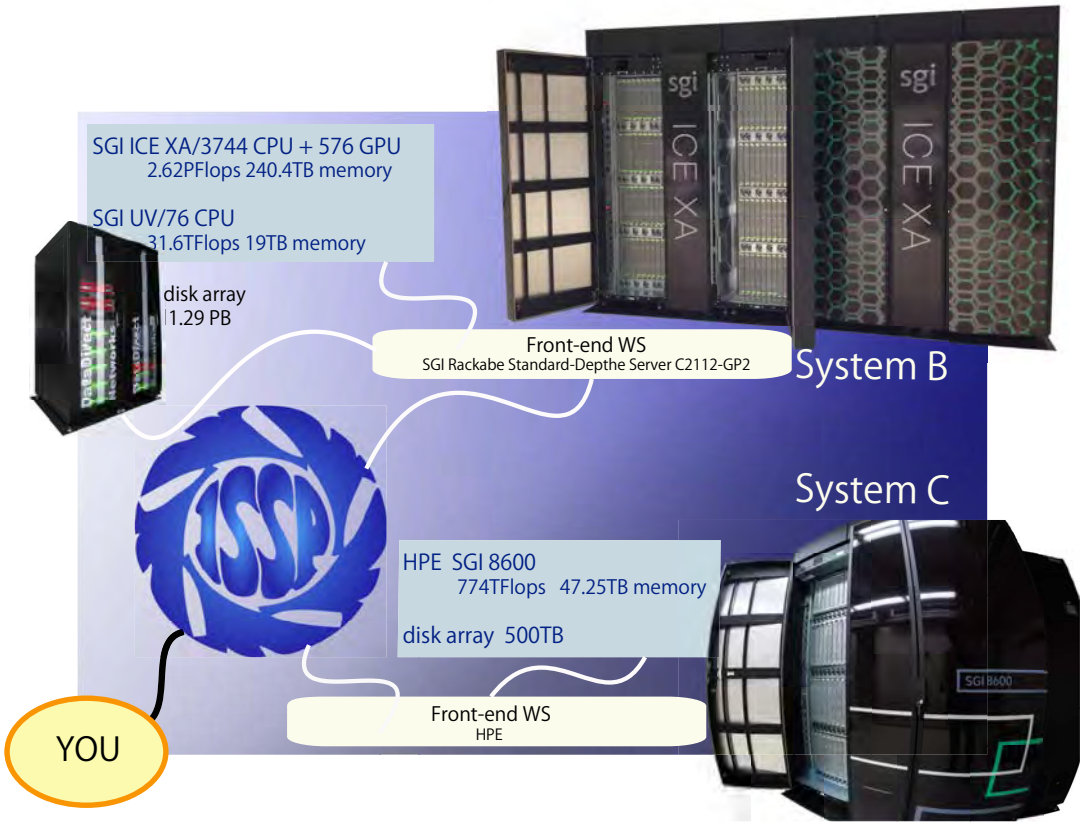

Figure 1: Supercomputer System at the SCC-ISSP

and the total number of points that were applied for and approved in this school year are listed in Table 1.

In addition, from SY 2016, ISSP Supercomputer is providing 20% of its computational resources for Supercomputing Consortium for Computational Materials Science (SCCMS), which aims at advancing parallel computations in condensed matter, molecular, and materials sciences on the 10-PFlops K Computer and the exascale post-K project. Computational resources have also been alloted to Computational Materials Design (CMD) workshops, as well as for Science Camps held in ISSP for undergraduate students.

1.3 Committees

In order to fairly manage the projects and to smoothly determine the system operation policies, the Materials Design and Characterization Laboratory (MDCL) of the ISSP has organized the Steering Committee of the MDCL and the Steering Committee of the SCC-ISSP, under which the Supercomputer Project Advisory Committee (SPAC) is formed to review proposals. The members of the committees in SY 2018 were as follows:

Table 1: Classes of research projects in SY 2018

Class	Maximum Points		Application	# of Proj.	Total points			
					Applied		Approved	
	Sys–B	Sys–C			Sys–B	Sys–C	Sys–B	Sys–C
A	100	100	any time	20	2.0k	1.0k	2.0k	1.0k
B	1k	500	twice a year	70	64.2k	3.5k	42.6k	2.9k
C	10k	2.5k	twice a year	168	1,395.3k	77.2k	620.0k	62.0k
D	10k	2.5k	any time	8	42.3k	3.0k	30.0k	2.5k
E	30k	2.5k	twice a year	17	490.0k	46.0k	279.5k	39.8k
S	–	–	twice a year	0	0	0	0	0
SCCMS				25	235.5k	19.1k	235.5k	19.1k
Total				308	2229.3k	149.7k	1209.6k	127.28k

- Class A is for trial use by new users; proposals for Class A projects are accepted throughout the year.
- Proposals for projects in Classes B (small), C (mid-size), E (large-scale), and S (exceptional) can be submitted twice a year. Approved projects in Classes A, B, C, and E continue to the end of the school year.
- In Class D, projects can be proposed on rapidly-developing studies that need to perform urgent and relatively large calculations. An approved project continues for 6 months from its approval.
- Class S is for projects that are considered extremely important for the field of condensed matter physics and requires extremely large-scale computation. The project may be carried out either by one research group or cooperatively by several investigators at different institutions. A project of this class should be applied with at least 10,000 points; there is no maximum. We require group leaders applying for Class S to give a presentation on the proposal to the Steering Committee of the SCC-ISSP. Class S projects are carried out within one year from its approval.
- Project leaders can apply for points so that the points for each system do not exceed the maximum point shown in this table.

Steering Committee of the MDCL

HIROI, Zenji	ISSP (Chair person)
KAWASHIMA, Naoki	ISSP
OZAKI, Taisuke	ISSP
NOGUCHI, Hiroshi	ISSP
UWATOKO, Yoshiya	ISSP
MORI, Hatsumi	ISSP
SUGINO, Osamu	ISSP
TOHYAMA, Takami	Tokyo Univ. of Sci.
ONO, Tomoya	Univ. of Tsukuba
YAMAURA, Jun-ichi	Tokyo Tech.
TAKAHASHI, Hiroki	Nihon Univ.
YOSHIMOTO, Yoshihide	Univ. of Tokyo
TAKEDA Mahoto	Yokohama Natl. Univ.
KIMURA, Kaoru	Univ. of Tokyo
SUZUKI, Takafumi	Univ. of Hyogo

Steering Committee of the SCC-ISSP

KAWASHIMA, Naoki	ISSP (Chair person)
NOGUCHI, Hiroshi	ISSP
OZAKI, Taisuke	ISSP
SUGINO, Osamu	ISSP
TSUNETSUGU, Hirokazu	ISSP
KATO, Takeo	ISSP
KONDO, Takeshi	ISSP
KASAMATSU, Shusuke	ISSP
WATANABE, Hiroshi	ISSP
MORITA, Satoshi	ISSP
HIGUCHI, Yuji	ISSP
NAKAJIMA, Kengo	Univ. of Tokyo
TSUNEYUKI, Shinji	Univ. of Tokyo
HATANO, Naomichi	Univ. of Tokyo
MOTOME, Yukitoshi	Univ. of Tokyo
ONO, Tomoya	Univ. of Tsukuba
TOHYAMA, Takami	Tokyo Univ. of Sci.
YOSHINO, Hajime	Osaka Univ.
SUZUKI, Takafumi	Univ. of Hyogo
YOSHIMOTO, Yoshihide	Univ. of Tokyo
OKUMURA, Hisashi	NINS-RSCS
HOSHI, Takeo	Tottori Univ.
YATA, Hiroyuki	ISSP
FUKUDA, Takaki	ISSP

Supercomputer Project Advisory Committee

KAWASHIMA, Naoki	ISSP (Chair person)
NOGUCHI, Hiroshi	ISSP
SUGINO, Osamu	ISSP
OZAKI, Taisuke	ISSP
TSUNETSUGU, Hirokazu	ISSP
KATO, Takeo	ISSP
KONDO, Takeshi	ISSP
KASAMATSU, Shusuke	ISSP
HIGUCHI, Yujihi	ISSP
WATANABE, Hiroshi	ISSP
MORITA, Satoshi	ISSP
NAKAJIMA, Kengo	Univ. of Tokyo
TSUNEYUKI, Shinji	Univ. of Tokyo
IMADA, Masatoshi	Univ. of Tokyo
HATANO, Naomichi	Univ. of Tokyo
SUZUKI, Takafumi	Univ. of Hyogo
YOSHIMOTO, Yoshihide	Univ. of Tokyo
OKUMURA, Hisashi	NINS-RSCS
HOSHI, Takeo	Tottori Univ.
ONO, Tomoya	Univ. of Tsukuba
YOSHINO, Hajime	Osaka Univ.
MOTOME, Yukitoshi	Univ. of Tokyo
TOHYAMA, Takami	Tokyo Univ. of Sci.
KITAO, Akio	Tokyo Tech.
ARITA, Ryotaro	RIKEN-CEMS
IKUHARA, Yuichi	Univ. of Tokyo
SHIBATA, Naokazu	Tohoku Univ.
AKAGI, Kazuto	Tohoku Univ.
YANASE, Yoichi	Kyoto Univ.
HATSUGAI, Yasuhiro	Univ. of Tsukuba
OKADA, Susumu	Univ. of Tsukuba
KOBAYASHI, Nobuhiko	Univ. of Tsukuba
NAKAYAMA, Takashi	Chiba Univ.
HOTTA, Takashi	Tokyo Metropolitan Univ.
MATSUKAWA, Hiroshi	Aoyama Gakuin Univ.
YAMAUCHI, Jun	Keio Univ.
HAGITA, Katsumi	National Defense Academy
KONTANI, Hiroshi	Nagoya Univ.
SAITO, Mineo	Kanazawa Univ.
KAWAKAMI, Norio	Kyoto Univ.
YUKAWA, Satoshi	Osaka Univ.
SUGA, Seiichiro	Univ. of Hyogo
TATENO, Masaru	Univ. of Hyogo
YASUDA, Chitoshi	Univ. of the Ryukyus
OGATA, Masao	Univ. of Tokyo

WATANABE, Satoshi	Univ. of Tokyo
OKAMOTO, Yuko	Nagoya Univ.
HUKUSHIMA, Koji	Univ. of Tokyo
NEMOTO, Koji	Hokkaido Univ.
YABANA, Kazuhiro	Univ. of Tsukuba
HIDA, Kazuo	Saitama Univ.
WATANABE, Kazuyuki	Tokyo Univ. of Sci.
FURUKAWA, Nobuo	Aoyama Gakuin Univ.
KUROKI, Kazuhiko	Osaka Univ.
TAKANO, Hiroshi	Keio Univ.
YASUOKA, Kenji	Keio Univ.
TANAKA, Yukio	Nagoya Univ.
MASUBUCHI, Yuichi	Nagoya Univ.
KAWAMURA, Hikaru	Osaka Univ.
KUSAKABE, Koichi	Osaka Univ.
SHIRAI, Koun	Osaka Univ.
SAKAI, Toru	JAEA
ISHIBASHI, Shoji	AIST
OTANI, Minoru	AIST
TOMITA, Yusuke	Shibaura Inst. Tech.
MIYASHITA, Seiji	Univ. of Tokyo
SHIRAISHI, Kenji	Nagoya Univ.
OGUCHI, Tamio	Osaka Univ.
KAWAKATSU, Toshihiro	Tohoku Univ.
KOBAYASHI, Kazuaki	NIMS
TATEYAMA, Yoshitaka	NIMS
KIM, Kang	Osaka Univ.
OTSUKI, Tomi	Sophia Univ.
MORIKAWA, Yoshitada	Osaka Univ.
ODA, Tatsuki	Kanazawa Univ.
TADA, Tomofumi	Tokyo Tech.
TODO, Synge	Univ. of Tokyo

1.4 Staff

The following staff members of the SCC-ISSP usually administrate the ISSP Supercomputer.

KAWASHIMA, Naoki	Professor (Chair person)
NOGUCHI, Hiroshi	Associate Professor
OZAKI, Taisuke	Professor
SUGINO, Osamu	Professor
WATANABE, Hiroshi	Research Associate
KASAMATSU, Shusuke	Research Associate
HIGUCHI, Yuji	Research Associate

MORITA, Satoshi	Research Associate
YATA, Hiroyuki	Technical Associate
FUKUDA, Takaki	Technical Associate
ARAKI, Shigeyuki	Technical Associate

2 STATISTICS (SCHOOL YEAR 2018)

2.1 System and User Statistics

In the following, we present statistics for operation time taken in the period from April 2018 to March 2019 (SY 2018). In Table 2, we show general statistics of the supercomputer system in SY 2018. The total numbers of compute nodes in System B and System C are 1891 and 252, respectively. Consumed disk points amount to about 3% of the total consumed points in System B.

In the left column of Fig. 2, availabilities, utilization rates, and consumed points in Systems B and C are plotted for each month. Throughout the school year, the utilization rates were very high, while the availability was reduced in August and September due to the OS update of System B and a lightning strike.

The user statistics are shown in the right column of Fig. 2. The horizontal axis shows the rank of the user/group arranged in the descending order of the execution time (hour×nodes). The execution time of the user/group of the first rank is the longest. The vertical axis shows the sum of the execution time up to the rank. From the saturation points of the graphs, the numbers of "active" users of Systems B and C are around 300 and 70, respectively. The maximum ranks in the graphs correspond to the number of the users/groups that submitted at least one job.

2.2 Queue and Job Statistics

Queue structures of Systems B and C in SY2018 are shown in Table 3. In System B, users can choose from three types of compute nodes; jobs submitted to queues with "cpu", "acc", and "fat" at the end of their queue names are submitted to CPU, ACC, and Fat nodes, respectively, while only CPU nodes are available in System C. See Sec. 1.1 for a description of each type of compute node. The user then has to choose the queue according to the number of nodes to use and the duration of their calculation jobs. Queue names starting with "F" are for jobs taking 24 hours or less, while those starting with "L" can run much longer up to 120 hours. More nodes are allotted to "F" queues in order to maximize the turnaround time of user jobs. The queue names starting with "i" are used for interactive debugging of user programs and the elapsed time limit is 30 minutes. The number following "F", "L", or "i" correspond to the number of nodes that can be used by one user job.

To prevent overuse of the storage, points are charged also for usage of disk quota in the three systems, as shown in Table 4. Disk points are revised often for

System B

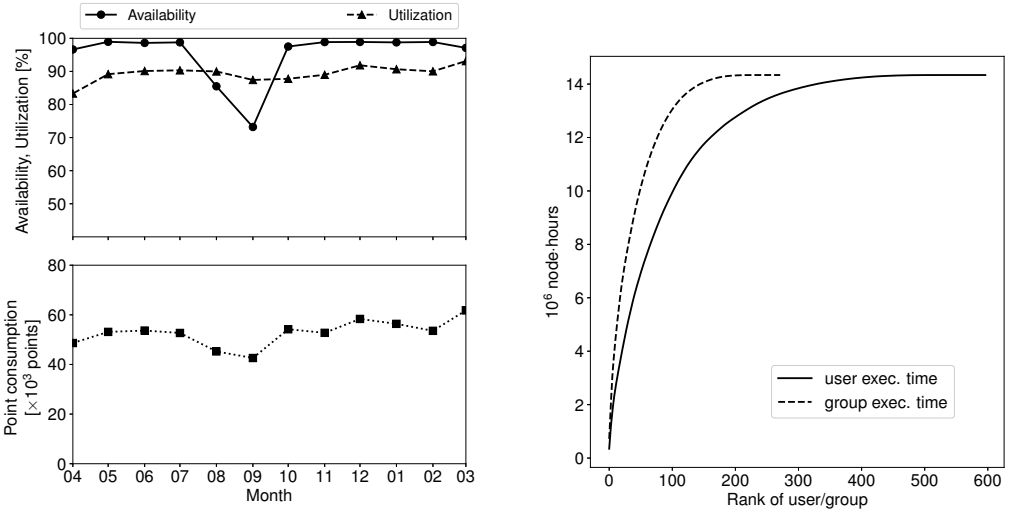

System C

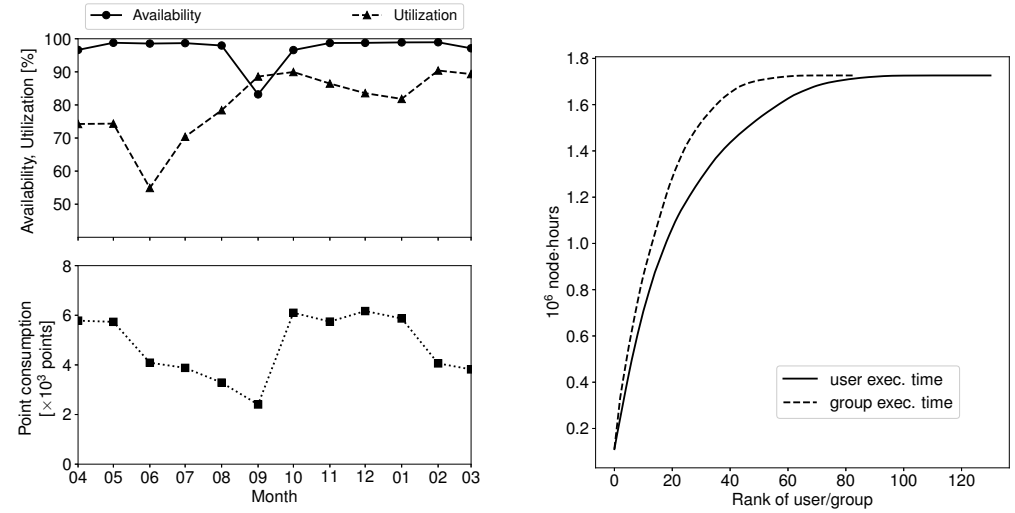

Figure 2: Left: Availabilities, utilization rates and point consumptions of each month during SY 2018. Right: User statistics. The horizontal axis shows the rank of the user/group arranged in the descending order of the execution time (hour×nodes). The vertical axis shows the sum of the execution time up to the rank.

Table 2: Overall statistics of SY 2018

	System B	System C
total service time ($\times 10^3$ node·hours)	16037	2157
number of executed jobs	728794	105
total consumed points ($\times 10^3$ point)	655	58
CPU points ($\times 10^3$ point)	633	57
disk points ($\times 10^3$ point)	22	1
total exec. time ($\times 10^3$ node·hours)	14339	1726
availability	95.14%	96.90%
utilization rate	89.40%	80.20%

optimal usage of the resources by examining usage tendencies each year.

Although we do not mention here in detail, to promote utilization of the massively parallel supercomputer, background queues for system B ("B4cpu", "B36cpu", "B144cpu", "B18acc", "B72acc", and "B2fat") and background queues for system C ("B4cpu", "B9cpu", "B36cpu") which charge no points for the jobs have also been open.

The number of jobs, average waiting time, and total execution time in each queue are shown in Table 5. In System B, a large portion of jobs have been executed in "F" queues. The largest amount of the execution time has been consumed in the large-scale "F144cpu" queue, but substantial number of jobs were run in every queue, suggesting that a wide variety of user needs are met by this queuing scheme. In most of these queues, the queue settings meet the user's tendencies in that the waiting times are on the order of the elapsed-time limit.

2.3 Project for Advancement of Software Usability in Materials Science

From School Year 2015, the supercomputer center (SCC) has started "Project for advancement of software usability in materials science". In this project, for enhancing the usability of the supercomputer system in ISSP, we perform some software-advancement activity such as implementing a new function to an existing code, releasing a private code on Web, writing manuals. Target programs are publicly offered in December and selected in the review by the Steering Committee of SCC. The projects are carried out by the software development team composed of three members in ISSP. In SY 2018, two projects were selected as listed in Table 6.

2.4 GPGPU Support Service

As noted in Sec. 1.1, ACC nodes with graphics processing units (GPU) were introduced in System B in School Year 2015. Since GPUs were introduced in the

ISSP Supercomputer center for the first time, many programs developed or utilized by users of this center have not been programmed for GPU computing. To help users take advantage of GPUs, the supercomputer center has started a service for porting users' materials science software to General Purpose GPUs (GPGPU). After a call for proposals (which will usually be in December), target programs for the next school year are selected by the Steering Committee of SCC. The porting service is carried out on each program for about two months; the coding is performed by engineers from the computer vendor supplying the ISSP supercomputer system, and ISSP staff oversee the progress of the project and manage necessary communications with the proposer. Copyrights of the resulting software basically belong to the proposers, but the supported contents might be published under agreement with the proposer. In SY 2018, two projects are selected as listed in Table 7.

Acknowledgments

The staffs would like to thank Prof. Takafumi Suzuki (now at University of Hyogo) for developing WWW-based system (SCM: SuperComputer Management System) for management of project proposals, peer-review reports by the SPAC committee, and user accounts. We also thank Ms. Reiko Iwafune for creating and maintaining a new WWW page of the ISSP Supercomputer Center.

Table 3: Queue structures in SY 2018

System–B

queue name	Elapsed time limit (hr)	# of nodes /job	# of nodes /queue	Memory limit (GB)	job points /(node·day)
F4cpu	24	1–4	216	120/node	1
L4cpu	120	1–4	108	120/node	1
F36cpu	24	5–36	288	120/node	1
L36cpu	120	5–36	144	120/node	1
F144cpu	24	37–144	1008	120/node	1
L144cpu	120	37–144	144	120/node	1
i18cpu	0.5	1–18	72	120/node	1
F18acc	24	1–18	180	120/node	2
L18acc	120	1–18	90	120/node	2
F72acc	24	19–72	72	120/node	2
i9acc	0.5	1–9	36	120/node	2
F2fat	24	1–2	17	1000/node	4
L2 fat	120	1–2	6	1000/node	4
i1fat	0.5	1	2	1000/node	4

System–C

queue name	Elapsed time limit (hr)	# of nodes /job	# of nodes /queue	Memory limit (GB)	job points /(node·day)
F4cpu	24	1–4	54	170/node	1
L4cpu	120	1–4	18	170/node	1
i4cpu	0.5	1–4	18	170/node	1
F9cpu	24	5–9	36	170/node	1
L9cpu	120	5–9	18	170/node	1
F36cpu	24	10–36	144	170/node	18(36)/(# of nodes)*
L36cpu	120	10–36	36	170/node	18(36)/(# of nodes)*

* For F/L36cpu queue, the number of occupied node increases in increments of 18 nodes.

Table 4: Disk points of Systems B and C

		point/day
System B	`/home`	$0.001 \times \theta(q - 300)$
	`/work`	$0.0001 \times \theta(q - 3000)$
System C	`/home`	$0.001 \times \theta(q - 150)$
	`/work`	$0.0001 \times \theta(q - 1500)$

* q is denoted in unit of GB.
* $\theta(x)$ is equal to the Heaviside step function $H(x)$ multiplied by x, i.e., $xH(x)$.

Table 5: Number of jobs, average waiting time, total execution time, and average number of used nodes per job in each queue.

System-B

queue	# of Jobs	Waiting Time (hour)	Exec. Time ($\times 10^3$ node·hour)	# of nodes
F4cpu	235752	7.08	1153.21	1.33
L4cpu	12538	24.93	589.27	1.61
F36cpu	21578	21.71	1366.82	11.85
L36cpu	1622	73.67	765.61	14.04
F144cpu	12275	40.80	7052.94	84.86
L144cpu	374	174.22	886.26	92.21
i18cpu	74462	0.27	110.91	8.59
F18acc	34273	6.86	645.79	2.39
L18acc	5531	22.21	535.15	2.89
F72acc	2410	40.30	246.63	64.47
i9acc	8691	0.16	6.62	5.13
F2fat	7435	23.64	79.66	1.24
L2fat	813	27.46	29.55	1.33
i1fat	4903	1.67	1.01	1.00

System-C

queue	# of Jobs	Waiting Time (hour)	Exec. Time ($\times 10^3$ node·hour)	# of nodes
F4cpu	60204	3.18	246.69	1.29
L4cpu	3992	7.17	69.96	1.29
i4cpu	19973	0.05	8.63	3.54
F9cpu	3047	26.47	123.88	7.11
L9cpu	147	31.26	46.35	7.12
F36cpu	3181	22.60	749.15	26.65
L36cpu	129	34.80	122.54	28.60

Table 6: List of Project for advancement of software usability in materials science for SY 2018.

Project Proposer	Project Name
Kazuma Nakamura Kyushu Institute of Technology	Development of first-principles electronic-structure calculation software by combining effective-model derivation code (RESPACK) and model-analysis codes (HΦ/mVMC)
Masaki Akiko RIKEN	Development of a quantum Monte Carlo Solver -DSQSS- implementing nontrivial parallelization

Table 7: List of supported software and project proposers for the GPGPU support service for SY 2018.

Project Proposer	Project Name
Hiromi Nakai Waseda Univ.	Acceleration of divide-and-conquer based density-functional tight-binding molecular dynamics method by using GPGPU
Kazuyoshi Yoshimi ISSP	GPU acceleration of matrix-vector product operations in quantum lattice model solver HΦ

Development of open-source software mVMC and its applications

Takahiro Misawa, Yuichi Motoyama, and Kota Ido
Institute for Solid State Physics, University of Tokyo
Kashiwa-no-ha, Kashiwa, Chiba 277-8581

Abstract

In this activity report, we overview open-source software mVMC (many-variable variational Monte Carlo), which can perform the variational Monte Carlo calculations with many variational parameters for a wide range of the quantum many-body systems. We also show its recent applications to the high-T_c superconductivity and the quantum spin liquid. In the first part of the report, we explain the basic properties of mVMC including the Monte Carlo sampling method, implemented wavefunctions, optimization methods (the steepest descend method and the stochastic reconfiguration method), and the recent extension to simulations in the grand canonical ensemble. As applications of mVMC, we first show the analysis of the interfaces of the cuprates. A recent experiment shows that the superconducting temperature is pinned at optimal value in the bulk compound at the interfaces of the cuprates ($La_2CuO_4/La_{2-x}Sr_xCuO_4$) irrespective of the hole doping ratio. By using mVMC, we solve an effective model for the interfaces and reproduce the anomalous pinning at the interfaces. We also clarify the origin of the pinning is the inter-layer phase separation, which dissolves inner-layer phase separation through the reconstruction of the hole densities around the interfaces. Then, we show the application of mVMC to the quantum spin liquid in the Kitaev model (Kitaev spin liquid). By using the grand canonical ensemble, we show that mVMC can reproduce the Kitaev spin liquid.

1 Introduction

Correlation effects among electrons in solids induce many intriguing phenomena such as the high-T_c superconductivity [1, 2, 3] and the exotic elementary excitations in the quantum spin liquids [4]. To reveal how and why the correlation effects induce such exotic phenomena, it is necessary to develop numerical methods that can accurately treat the correlation effects.

The variational Monte Carlo (VMC) method (for reviews see Refs. [5, 6]) is one of the promising methods for performing accurate analysis of correlated electrons. The VMC method was first used for analyzing the properties of the quantum liquids of He^4 [7] and He^3 [8]. As the optimization of many variational parameters is a difficult problem, the number of variational parameter was limited up to around ten or one hundred (10^2) for a long time. After the proposal of the stochastic optimization (SR) method [9, 10] proposed by Sorella, we can optimize more than one thousand (10^3) variational parameters. By using powerful supercomputers and the improved SR method [11], it is now possible to optimize more than several hundred thousand (10^5) variational parameters.

In the 2016 fiscal year, we have developed open-source software mVMC [12, 13, 14], which can perform the many-variable variational Monte Carlo method for a wide range of Hamiltonians of correlated fermion systems. The development of mVMC has

been supported by "Project for advancement of software usability in materials science (PASMS)" [15], which is managed by the center of the supercomputer at Institute for Solid State Physics. We note that the code of mVMC [16, 17] was originally written by Daisuke Tahara, who was a graduate student in Imada group in the University of Tokyo. Based on his code, several people including authors have improved and added new functions in mVMC.

In the past decade, mVMC has been applied to a wide range of quantum many-body systems such as the frustrated Heisenberg models [18, 19], the Hubbard models at half filling [16, 17], the doped Hubbard models [16, 20, 21, 22], and the Kondo-lattice models [23, 24]. mVMC has also been applied to more realistic Hamiltonians such as ab initio low-energy Hamiltonians for the iron-based superconductors [25, 26, 27, 28], the organic conductor [29], and the cuprates [30, 31]. As we show later, mVMC has been applied to the interfaces of cuprates (multi-layer Hubbard model) [32]. It is also possible to apply mVMC to the spin-orbit coupled systems including the Kitaev spin liquid [33, 34, 35, 36] and the systems with electron-phonon couplings [37, 38]. Furthermore, recent studies reveal that mVMC can be used for the non-equilibrium calculations [39, 40] and the finite-temperature calculations [41].

In this activity report, we briefly explain the basic properties of mVMC and its recent applications to strongly correlated electron systems. This report is organize as follows: In Sec. 2, we detail the models that can be treated by mVMC, Monte Carlo sampling method, wavefunctions implemented in mVMC, and optimization methods. We also describe the recent implementation of the grand canonical ensemble in mVMC in Sec. 2.5. In Sec. 3, we show applications of mVMC to the interfaces of the cuprates [32], and the Kitaev model [36]. Section 4 is devoted for summary and discussions.

2 Basic of mVMC

In this section, we describe the models that can be treated by mVMC, Monte Carlo sampling in the VMC method, and the wavefunctions implemented in mVMC. We detail the stochastic reconfiguration method, which enables us to optimize many variational parameters. We also explain how to perform VMC simulations in the grand canonical ensemble, which has been recently implemented in mVMC. We note that VMC simulations in the grand canonical ensemble cannot be performed in the released version, which will be available in near future.

2.1 Model

By using mVMC, users can treat the general Hamiltonians defined as

$$\mathcal{H} = \mathcal{H}_T + \mathcal{H}_I, \tag{1}$$

$$\mathcal{H}_T = -\sum_{I,J} t_{IJ} c_I^\dagger c_J, \tag{2}$$

$$\mathcal{H}_\mathcal{I} = \sum_{I,J,K,L} \mathcal{I}_{IJKL} c_I^\dagger c_J c_K^\dagger c_L, \tag{3}$$

where capital characters I, J, K, L denote the site indices including the spin degrees of freedom ($\sigma = \uparrow$ or $\downarrow$), i.e., $I = (i, \sigma)$, where i represents the ith site. Here, $c_I^\dagger$ (c_I) is the creation (annihilation) operator of an electron on site I. This Hamiltonian includes the arbitrary one-body transfers and two-body interactions in the particle-conserved systems. General one-body potential t_{IJ} represents the hopping between site I and site J. General two-body interaction $\mathcal{I}_{IJKL}$ represents the interaction which annihilates a particle at site J and a particle at site L, and creates a particle at site I and a particle at site K.

As a special case of the general Hamiltonian defined in Eq. (3), we can treat the localized spin Hamiltonian such as the Heisenberg model by prohibiting the doubly occupied sites and the vacancy sites in the Monte Carlo samplings. It is also possible to treat the Kondo-lattice model, where the localized

spins and itinerant electrons coexist. We note the spinless-fermion models can be treated by restricting Monte Carlo samplings in the fully polarized states (e.g., samplings only in $\sigma =\uparrow$ states).

Users of mVMC can perform VMC calculations by preparing one input file whose length is typically less 10 lines for the standard models such as the Hubbard model and the Heisenberg model. Details of user interfaces are shown in Ref. [14]. Tutorials for mVMC and some script files for the standard models can be found in the GitHub repository (mVMC-tutorial) [42].

2.2 Monte Carlo sampling

Here, we explain how the Markov-chain Monte Carlo sampling is used in the VMC method. In the VMC method, the expectation value of the physical quantities A is expressed by

$$\begin{aligned}\langle A\rangle &= \frac{\langle\psi|A|\psi\rangle}{\langle\psi|\psi\rangle} = \sum_x \frac{\langle\psi|A|x\rangle\langle x|\psi\rangle}{\langle\psi|\psi\rangle} \\ &= \sum_x \rho(x)\frac{\langle\psi|A|x\rangle}{\langle\psi|x\rangle}, \qquad (4)\\ \rho(x) &= \frac{|\langle x|\psi\rangle|^2}{\langle\psi|\psi\rangle}, \qquad (5)\end{aligned}$$

where $|\psi\rangle$ is a many-body wavefunction and $|x\rangle$ denotes a complete basis such as the real-space configuration.

From Eq. (4), by performing the Markov-chain Monte Carlo sampling with respect to the weight $\rho(x)$, i.e., by generating the real-space configurations according to the weight $\rho(x)$ iteratively, we can evaluate $\langle A\rangle$ as

$$\langle A\rangle \sim \frac{1}{N_{\mathrm{MC}}}\sum_x \frac{\langle\psi|A|x\rangle}{\langle\psi|x\rangle}, \qquad (6)$$

where N_{MC} is the number of Monte Carlo samplings. It should be noted that the $\rho(x)$ is obviously positive definitive and the infamous sign problem never appears in the VMC method. In mVMC, we use the Mersenne twister [43] for generating pseudo random numbers.

2.3 Wavefunction

Wavefunctions implemented in mVMC are given as

$$|\psi\rangle = \mathcal{P}\mathcal{L}|\phi_{\mathrm{Pf}}\rangle, \qquad (7)$$

where $|\phi_{\mathrm{Pf}}\rangle$ denotes the pair-product wavefunctions, $\mathcal{L}$ denotes the quantum-number projectors such as the total-spin and the momentum projections, and $\mathcal{P}$ denotes the correlation factors such as the Gutzwiller and the Jastrow factors.

Because the details of the quantum-number projectors and the correlation factors are shown in Ref. [14], in this report, we only explain the several variations of the pair-product wavefunction $|\phi_{\mathrm{Pf}}\rangle$. The general form of the pair-product wavefunction is given as

$$|\phi_{\mathrm{Pf}}\rangle = |\phi_{\mathrm{GC}}\rangle = \exp\left[\sum_{I,J} F_{IJ}c_I^\dagger c_J^\dagger\right]|0\rangle\,, \qquad (8)$$

where F_{IJ} is treated as the variational parameters. This is nothing but the generalized Bardeen-Cooper-Schrieffer (BCS) wavefunctions, which include both singlet and triplet pairings. The inner product between $|\phi_{\mathrm{GC}}\rangle$ and $|x\rangle$ is represented as the Pfaffian of a skew-symmetric matrix constructed from the pairing F_{IJ}, which is detailed in Sec. 2.5. Although it is possible to directly treat the general form of the pair-product wavefunction, there is no necessary to use $|\phi_{\mathrm{GC}}\rangle$ for particle-number conserved systems. In other words, we need to employ $|\phi_{\mathrm{GC}}\rangle$ only when the particle-number conservation is explicitly broken in target Hamiltonians.

To treat particle-number conserved systems efficiently, we often use the particle-number fixed wavefunctions defined as

$$|\phi_{\mathrm{Pf}}\rangle = |\phi_{\mathrm{SGC}}\rangle = \left[\sum_{I,J} F_{IJ}c_I^\dagger c_J^\dagger\right]^{N_{\mathrm{e}}/2}|0\rangle, \qquad (9)$$

where N_{e} is the particle number. Furthermore, for systems where the total value of S^z is fixed

to 0, we can use the anti-parallel Pfaffian wavefunction defined as

$$|\phi_{\mathrm{Pf}}\rangle = |\phi_{\mathrm{AP-Pf}}\rangle = \left[\sum_{i,j} f_{ij} c^{\dagger}_{i\uparrow} c^{\dagger}_{j\downarrow}\right]^{N_{\mathrm{e}}/2} |0\rangle. \tag{10}$$

Clearly, by employing the restriction on the total value of S^z, the number of variational parameters can be reduced. Thus, to reduce the numerical cost, it is better to impose the restrictions on the pair-product wavefunctions if it is possible.

2.4 Optimization method

The key procedure in the VMC method is how to optimize the variational parameters $\boldsymbol{\alpha}$ to lower the energy E according to the variational principle. As an optimization method, the general gradient method is often used, which is given as

$$\Delta\boldsymbol{\alpha} = \alpha_{\mathrm{new}} - \alpha_{\mathrm{old}} = -\eta X^{-1}\boldsymbol{g}, \tag{11}$$

$$g_k = \frac{\partial E}{\partial \alpha_k}, \tag{12}$$

where η is a small constant and X is matrix whose dimension is the number of variational parameters. If we choose the identity matrix as X, the optimization method is called the steepest decent (SD) method. As we show later, the SD method do not efficiently work for optimizing many variational parameters.

In the stochastic reconfiguration (SR) method [9, 10], we take X as the overlap matrix S, which is defined as

$$S_{\alpha\beta} = \langle\bar{\psi}_\alpha|\bar{\psi}_\beta\rangle, \tag{13}$$

$$|\bar{\psi}_\alpha\rangle = \frac{\partial|\bar{\psi}\rangle}{\partial\alpha}, \tag{14}$$

$$|\bar{\psi}\rangle = \frac{|\psi\rangle}{\sqrt{\langle\psi|\psi\rangle}}. \tag{15}$$

As it is mentioned in the literature [14, 39, 41, 14, 44], the SR method is nothing but the imaginary-time evolution based on the time-dependent variational principle. As we show later, the SR method works well for optimization of many-variational parameters. We note the natural gradient method [45] used in the field of the neural network is the same as the SR method (the overlap matrix is called natural gradient in the filed of the neural network).

In Fig. 1, we show the optimization processes by the SD method and the SR method by taking 4×4 Hubbard model as an example. For both the random initial state and the initial state made from the unrestricted Hartree-Fock (UHF) solutions, the SR results can reach the ground state faster than than the SD results. In our experience, for many variational parameters, the speed of the convergence by the SD method is always slower than the SR method.

2.5 Grand canonical ensemble

The present mVMC package can be applied to a wide range of quantum lattice models. However, only systems where the total number of the particles is fixed are applicable. Due to this restriction, we cannot treat Hamiltonians which does not conserve the number of the particles such as the BCS Hamiltonian.

Recently, we have implemented the new functionality to perform VMC simulations in the grand canonical ensemble (GCE). The employed mean-field part in the trial wavefunction [Eq. (7)] is the generalized BCS wavefunction *without* the particle-number projection, namely

$$|\phi\rangle = \exp\left[\sum_{I,J} f_{IJ} c^{\dagger}_I c^{\dagger}_J\right]|0\rangle\,. \tag{16}$$

Here $I = (i,\sigma)$ and the pairing f_{IJ} is treated as the variational parameters.

We generate Monte Carlo samples in the GCE by using Metropolis-Hastings algorithm. The acceptance probability $p(x\to y)$ is defined

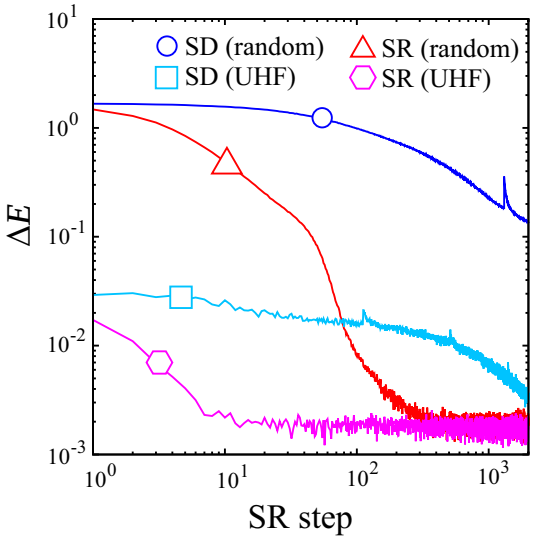

Figure 1: Optimization processes for 4×4 Hubbard model for $U = 4$ and $t = 1$ at half filling with periodic boundary conditions. The relative energy is defined as $\Delta E = (E_{\mathrm{mVMC}} - E_{\mathrm{exact}})/N_{\mathrm{s}}$, where E_{mVMC} (E_{exact}) represents the energy obtained by mVMC (exact diagonalization). N_{s} denotes the number of sites. We do not impose the sublattice structure in the variational parameters and the number of variational parameters are 266. Random (UHF) means that the initial state of the wavefunctions is prepared by random variational numbers (the UHF solution).

as

$$p(x \to y) = \min\left(1, \left|\frac{P(y)\,\langle\phi|y\rangle}{P(x)\,\langle\phi|x\rangle}\right|^2 \frac{g(x|y)}{g(y|x)}\right), \tag{17}$$

where $g(y|x)$ is the proposal distribution for proposing a new configuration y from a given one x with the total number of the particles $N_{\mathrm{e}} = 2N$. Although $g(y|x)/g(x|y) = 1$ for systems with the fixed particle number, we should be careful to consider the ratio of the proposal distributions $g(y|x)/g(x|y)$ when two particles is added or removed from the old configuration x. This is because the dimension of systems for $2N \pm 2$ is different from that for $2N$. For example, the ratio when a new configuration is generated by adding two particles is

$$\frac{g(y|x)}{g(x|y)} = \frac{(2N_s - 2N)(2N_s - (2N+1))}{(2N+2)(2N+1)}. \tag{18}$$

The inner product between the BCS wavefunction $|\phi\rangle$ and the real space configuration $|x\rangle$ for $N_{\mathrm{e}} = 2N$ is given as

$$\langle x|\phi\rangle = \mathrm{Pf}[X], \tag{19}$$

$$X_{IJ} = f_{R_I R_J} - f_{R_J R_I}, \tag{20}$$

$$|x\rangle = c^\dagger_{R_1} \cdots c^\dagger_{R_{2N}} |0\rangle\,. \tag{21}$$

Here, X is a skew symmetric matrix whose dimension is $2N$. It is worth noting that even in the GCE, the fast update techniques for calculations of Pfaffian and inverse matrices can be used when a real-space configuration is updated by adding or removing two particles. In this report, we introduce the fast update scheme when the electron configuration $|x\rangle$ is updated as $|x'\rangle = c^\dagger_{R_{2N+1}} c^\dagger_{R_{2N+2}} |x\rangle$. The skew symmetric matrix X' with the $2N+2$ dimension is described as

$$X' = \begin{pmatrix} X & B \\ -B^T & C^{-1} \end{pmatrix}, \tag{22}$$

$$B^T = -\begin{pmatrix} f_{R_1 R_{2N+1}} & \cdots & f_{R_{2N} R_{2N+1}} \\ f_{R_1 R_{2N+2}} & \cdots & f_{R_{2N} R_{2N+2}} \end{pmatrix}, \tag{23}$$

$$C^{-1} = \begin{pmatrix} 0 & f_{R_{2N+1} R_{2N+2}} \\ f_{R_{2N+2} R_{2N+1}} & 0 \end{pmatrix}. \tag{24}$$

By using the following lemma

$$\mathrm{Pf}\begin{pmatrix} A & B \\ -B^T & C^{-1} \end{pmatrix} = \mathrm{Pf}A \times \mathrm{Pf}\left(C^{-1} + B^T A^{-1} B\right), \tag{25}$$

the new Pfaffian $\mathrm{Pf}X'$ can be described as

$$\mathrm{Pf}X' = \mathrm{Pf}X \times \mathrm{Pf}D, \tag{26}$$

$$D = C^{-1} + B^T A^{-1} B. \tag{27}$$

Since $\mathrm{Pf}X$ and X^{-1} have been already known, 2×2 skew symmetric matrix D can be easily

computed and its numerical cost $\mathcal{O}(N^2)$. The inverse matrix X'^{-1} is computed as

$$X'^{-1} = \begin{pmatrix} X'^{-1}_{11} & X'^{-1}_{12} \\ X'^{-1}_{21} & X'^{-1}_{22} \end{pmatrix}, \tag{28}$$

$$X'^{-1}_{11} = X^{-1} - X^{-1}BDB^T X^{-1}, \tag{29}$$

$$X'^{-1}_{12} = -X^{-1}BD^{-1}, \tag{30}$$

$$X'^{-1}_{21} = D^{-1}B^T X^{-1}, \tag{31}$$

$$X'^{-1}_{22} = D^{-1}, \tag{32}$$

from the LDU decomposition of X' defined in Eq. (22). The numerical cost for evaluation of X'^{-1} is $\mathcal{O}(N^2)$.

3 Applications

In this section, we show applications of mVMC to the superconductivity at the interfaces of the cuprates [32] and the quantum spin liquid in the Kitaev model [36].

3.1 Application to interfaces of cuprates

In the cuprates, it is well known that the high-T_c superconductivity appears by doping carriers into the Mott insulators. Although there are many families of cuprates, it is common that the critical temperatures of superconductivity show dome-like structures as a function of the doping rates [1, 2, 3] as shown in Fig. 2(a). In other words, it is the *common sense* that the critical temperatures are optimized at the specific doping rate.

Recent experiment of the cuprates interfaces by the Božović group [46], however, challenges the common sense in the cuprates. In the experiment, they make the clean interfaces ($La_2CuO_4/La_{2-x}Sr_xCuO_4$) between the insulating mother compounds of the cuprates (La_2CuO_4) and the over-doped metallic cuprates ($La_{2-x}Sr_xCuO_4$), and they examine superconducting properties at the interfaces. Although no superconductivity appears both in the mother compound and over-doped cuprates in the bulk solid, they have found that the superconductivity appears at the interfaces of them. They also find that the superconducting temperatures do not depend on the doping rate in the metallic cuprates as is schematically shown in Fig. 2(b). Furthermore, they also show that the superconducting temperature is nearly pinned at the optimal value (T_c ∼42K) of the bulk cuprates of $La_{2-x}Sr_xCuO_4$. This pinning behavior of T_c is in a sharp contrast with the bulk system where a dome-like doping dependence of T_c has been commonly found in the doping concentration dependence.

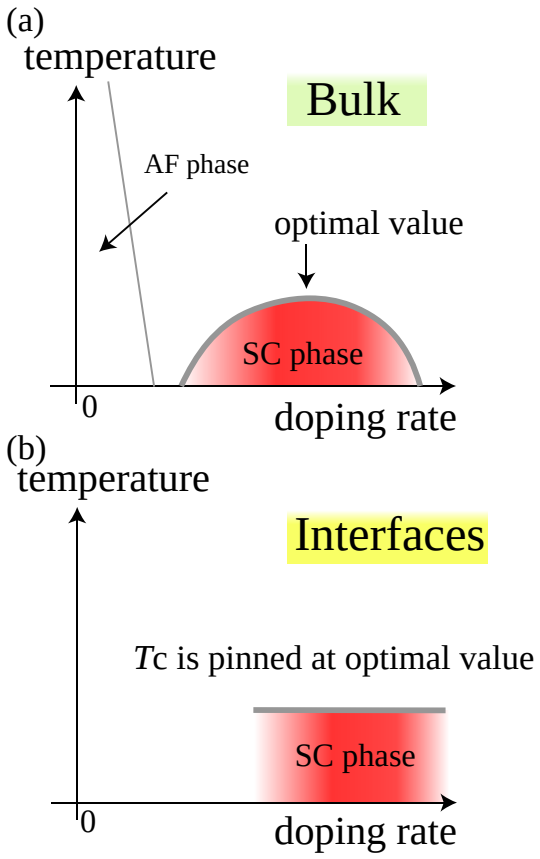

Figure 2: Schematic picture for the experimental phase diagram for (a) bulk solid of the cuprates and (b) interfaces of the cuprates. AF (SC) phase means antiferromagnetic (superconducting) phase.

To clarify the origin of the unexpected pinning of T_c observed at the interfaces of the cuprate, we analyze the multi-layer Hubbard

model [shown in Fig. 3(a)] by using mVMC, which is one of the simplest theoretical models for the interfaces. The Hamiltonian of the model is given as

$$\begin{aligned} H = &-t \sum_{\langle i,j\rangle,\sigma,\nu} (c^{\dagger}_{i\sigma\nu} c_{j\sigma\nu} + \text{h.c.}) \\ &- t_z \sum_{i,\sigma,\langle\nu,\nu'\rangle} (c^{\dagger}_{i\sigma\nu} c_{i\sigma\nu'} + \text{h.c.}) \\ &+ U \sum_{i,\nu} n_{i\uparrow\nu} n_{i\downarrow\nu} - \sum_{i,\sigma,\nu} \epsilon_{\nu} n_{i\sigma\nu}, \end{aligned} \tag{33}$$

where $c^{\dagger}_{i\sigma\nu}$ ($c_{i\sigma\nu}$) is the creation (annihilation) operator of an electron at ith site on the νth layer with spin σ and $n_{i\sigma\nu} = c^{\dagger}_{i\sigma\nu} c_{i\sigma\nu}$ is the corresponding number operator. For simplicity, we consider only the nearest-neighbor pair for the intra-layer transfer t and the inter-layer transfer t_z. In this calculation, we consider the five-layer Hubbard model ($0 \le \nu \le 4$). We employ the parameter values within the realistic constraint of the cuprate interface suggested from the experimental results and ab initio calculations, i.e., for the inter-layer transfer we take $t_z = 0.05t$ and the onsite Coulomb interaction is set to $U = 8t$. In this analysis, we set the energy unit $t = 1$ (~ 0.5 eV in the cuprates).

The layer-dependent onsite level energy is represented by ϵ_{ν}. From the experiment, it is known that the inter-layer diffusion of Sr atoms occur around the interfaces [47, 46]. To realistically mimic the inter-layer diffusion effect that makes the onsite energy level gradually change within a few layer, we employ the following layer dependent onsite energy

$$\epsilon_{\nu+1} = \epsilon_{\nu} - \Delta\epsilon \ (1 \le \nu \le 3), \tag{34}$$

where $\Delta\epsilon$ is a constant. The layer dependence of the onsite level energy is shown in Fig. 3 (b). We assume that the 0th is insulating and the other layers ($\nu \ge 1$) are metallic. To make the 0the layer insulating, we take $\epsilon_0 = \epsilon_1 + 1$.

By using mVMC, we analyze the multi-layer Hubbard model for several choices of $\Delta\epsilon$. We calculate the layer-dependent hole density

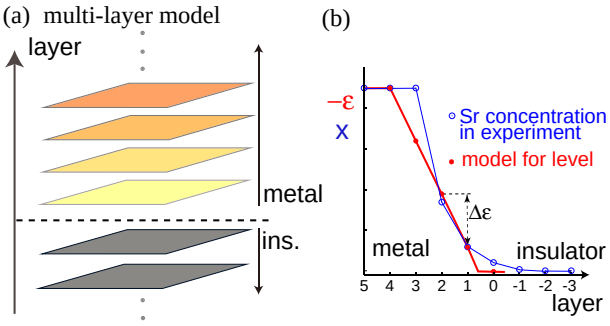

Figure 3: (a) Schematic picture of the theoretical models for the interface of cuprates. The dotted line denotes the interface between the metallic and insulating layer. The color schematically illustrates the change in the carrier concentration obtained by mVMC calculations. (b) Layer dependence of the onsite level energy employed in the multi-layer Hubbard model (red line). In the metallic phase around the interface, we assume that the onsite energy level changes linearly. From this layer-dependence of the onsite level energy, we mimic the effects of interlayer Sr diffusion observed in experiment [47]. We show the layer dependence of the Sr concentration as blue curves, which is taken from Ref. [47]

$\delta_{\nu} = 1 - N_{\nu}/N_{\rm s}$, where N_{ν} ($N_{\rm s}$) is the average electron number of the νth layer (the number of the sites in each layer). We find that the bulk hole density, $\delta_{\rm bulk} = \delta_4$, monotonically increases as a function of $\Delta\epsilon$. This result indicates that we can change the doping rate in the metallic region by controlling $\Delta\epsilon$. Thus, we can examine how the changes in the bulk hold density affect the superconducting properties at the interfaces.

To investigate the superconducting properties, we calculate the layer-dependent equal-time superconducting correlations of $d_{x^2-y^2}$-

wave symmetry defined as

$$P_\nu(\boldsymbol{r}) = \frac{1}{2N_{\rm s}} \sum_{\boldsymbol{r}_i} \Big[\langle \Delta_\nu^\dagger(\boldsymbol{r}_i) \Delta_\nu(\boldsymbol{r}_i + \boldsymbol{r}) \rangle + \text{h.c.} \Big], \tag{35}$$

$$\Delta_\nu(\boldsymbol{r}_i) = \frac{1}{\sqrt{2}} \sum_j f(\boldsymbol{r}_j - \boldsymbol{r}_i)(c_{i\uparrow\nu} c_{j\downarrow\nu} - c_{i\downarrow\nu} c_{j\uparrow\nu}), \tag{36}$$

where Δ_ν denotes the $d_{x^2-y^2}$-wave superconducting order parameter at the νth layer, $f_d(\boldsymbol{r})$ is the form factor that describes the $d_{x^2-y^2}$-wave symmetry, and $\delta_{i,j}$ denotes the Kronecker's delta and $\boldsymbol{r} = (r_x, r_y)$. To estimate the superconducting long-range order, we calculate long-range limit of $P_\nu(\boldsymbol{r})$, which is defined as

$$\bar{P}_\nu = \frac{1}{M} \sum_{2<r=|\boldsymbol{r}|<\sqrt{2}L} P_\nu(\boldsymbol{r}). \tag{37}$$

where M is the number of vectors satisfying $2 < r = |\boldsymbol{r}| < \sqrt{2}L$ (L represents the linear dimension of each layer). For sufficiently large L, this quantity converges to the square of the superconducting order parameter ($|\langle \Delta_\nu^\dagger(\boldsymbol{r}) \rangle|^2$) and we have actually shown that $\bar{P}_\nu$ allows for a practical estimate of the superconducting long-range order in Ref. [20].

In Fig. 4(a), we plot the $\delta_{\rm bulk}$ (metallic bulk density) dependence of $\bar{P}_\nu$. As a result, we find that the superconductivity mainly appears at the interface (the 1st layer [$\nu = 1$]). Furthermore, we also find that the superconducting correlations at the interface ($\bar{P}_{\nu=1}$) is nearly fixed to the constant value and we confirm that its constant value is nearly equal to the maximum value in the bulk system, i.e., single-layer Hubbard model. This result is well consistent with experimental results where $T_{\rm c}$ is pinned at the optimal value in the bulk. We note that the same superconducting order parameter at $T = 0$ naturally yields the same $T_{\rm c}$.

In the analysis for the bulk cuprates, if we simply ignore the effects of the long-range Coulomb interactions, we find that the phase separation occurs around half filling and the

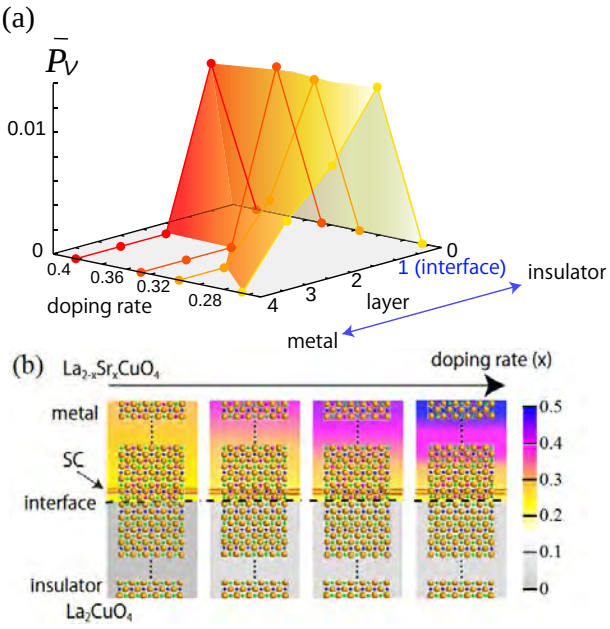

Figure 4: (a) Superconducting correlations for the multi-layer model. Superconducting correlations are pinned at constant value at the interface irrespective of the doping rate in the metallic region.(b) Schematic picture for inter-layer phase separation. The color denote the charge density. Because of the inter-layer degrees of freedom, the instability toward the phase separation in the inner layer is dissolved through the reconstruction of the charge density around the interfaces.

superconducting correlations have maximum value at the edge of the phase separation [48]. By comparing the results for the bulk system and the interfaces, we find that instability toward the phase separation existing in the bulk system is *automatically* dissolved around the interfaces by using the inter-layer degrees of freedom as is schematically shown in Fig. 4(b). In other words, the carrier density at the interfaces is always fixed at the optimal value in the bulk system through the inter-layer phase separation, which dissolves the inner-layer phase separation existing in the bulk system. This result shows that the interfaces provide an ideal tool to stabilize superconductivity without fine tuning of the doping rates.

3.2 Application to the Kitaev model

As an application in the GCE, we perform VMC simulations on the optimization of the ground state in the Kitaev model on the honeycomb lattice [49]. The Kitaev model is defined as

$$\mathcal{H} = \sum_{\gamma=x,y,z} \sum_{\langle I,J\rangle \in \gamma-\text{bond}} K_\gamma S_I^\gamma S_J^\gamma, \qquad (38)$$

where I means a site index which includes a unit-cell index i with a degree of freedom of the unit cell $\alpha \in (A, B)$, *i.e.* $I = (i, \alpha)$. Kitaev proved that the ground state of the Kiteav model can be analytically obtained and it is the quantum spin liquid. In addition, for the isotropic Kitaev model, non-Abelian anyons emerge as the elementary excitation by applying magnetic fields, which are important for the realization of the topological quantum computing. Although it seems to be artificial for the Ising interactions to have the dependence on the bond direction, it was theoretically proposed that the Kiteav interaction is dominant in strongly correlated materials with strong spin-orbit coupling [50]. Inspired from this proposal, many researchers have tried to synthesize Kitaev-like compounds and understand how the Kitaev spin liquid can stably exists.

One of the analytical ways to solve the Kitaev model is to use the Jordan-Wigner (JW) transformation. It was shown that the original spin Hamiltonian can be mapped onto the spinless BCS Hamiltonian with many-body interaction on z-bond by using the JW transformation defined as

$$S_j^+ = \prod_{k<j} (-2S_k^z)\, c_j^\dagger, \qquad (39)$$

$$S_j^z = (n_j - \frac{1}{2}), \qquad (40)$$

and its ground state can be described as the BCS wavefunction[51, 52]. The fermionized Kitaev model by the JW is represented as

$$\begin{aligned}\mathcal{H} = &\frac{J_x}{4}\sum_i (c_{iA}^\dagger - c_{iA})(c_{iB}^\dagger + c_{iB}) \\ &+ \frac{J_y}{4}\sum_i (c_{iB}^\dagger + c_{iB})(c_{i+e_1,A} - c_{i+e_1,A}^\dagger) \\ &+ \frac{J_z}{4}\sum_i (2n_{iB} - 1)(2n_{i+e_2,A} - 1) \\ &+ \mathcal{H}_{\text{boundary}}, \end{aligned} \qquad (41)$$

where e_1 and e_2 are primitive translation vectors for the honeycomb lattice. We clearly see that there are the BCS terms, $c_I^\dagger c_J^\dagger$ and $c_I c_J$, in Eq. (41). $\mathcal{H}_{\text{boundary}}$ means the boundary term which includes string operators due to the application of the JW transformation. When the system satisfies the open boundary condition, this term is banished and thus the original model defined in Eq. (38) can be exactly mapped onto the fermionized one.

Figure 5 shows the optimization process of VMC calculations in the antiferromagnetic Kitaev model by using two different basis; the original spin basis and JW fermion basis. Both are obtained by using a random initial state which has the lowest energy at the 4000 SR step in ten random states. We also perform the ED simulation by using open-source software $\mathcal{H}\Phi$[53], whose result is shown as the black thin line in Fig. 5. It is clearly seen that the JW fermion result converges to the exact ground state. On the other hand, although the energy by the conventional spin-basis wave function is gradually decreased, it does not seem to reach to the true ground state. This result indicates that the JW fermion basis is more appropriate for obtaining the Kitaev spin liquid without falling into local minima during the optimization process.

4 Summary

In this report, we first explained the basics of mVMC. We explained that mVMC can treat the general Hamiltonians with the arbitrary

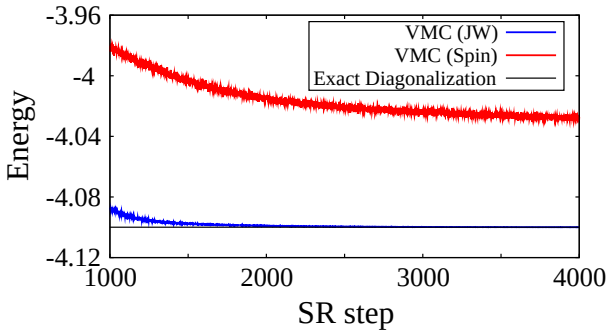

Figure 5: Optimization process in the antiferromagnetic Kitaev model for 4×3 unit cell and $J_x = J_y = J_z = 1$. Red and blue lines show the results by using Eqs. (8) and (9), respectively. Black thin line represents the energy obtained by using the exact diagonalization method.

one-body part and the arbitrary two-body interactions. We also explained the Monte Carlo sampling used in mVMC and the wavefunction implemented in mVMC. We also explained two optimization methods; the steepest descent (SD) method and the stochastic reconfiguration (SR) method. By taking the Hubbard model as an example, we showed that the speed of the optimization by the SD method is slower than that of the SR method. We also detailed the recent extension of mVMC for treating the systems without particle-number conservation

Then, we showed two recent application of mVMC. One is the application to the interfaces of the cuprates. By solving the multi-layer Hubbard model, which is an effective model for the interfaces the cuprates, we showed that the pinning of the T_c observed in the experiment can be well reproduced. We also clarified the origin of the pinning is the inter-layer phase separation. This result indicates that interfaces of the high-T_c superconductors offers an ideal platform for stabilizing optimal superconductivity without fine tuning of the doping rate.

Another application is the analysis of the Kitaev model. By performing the Jordan-Wigner transformation, it is known that the Kitaev model is exactly solved and the quantum spin liquid appears. There is, however, the anomalous part, which breaks the particle number conservation, inevitably appears. To treat the Kitaev model under the Jordan-Wigner transformation, we used mVMC with the grand canonical ensemble. As a result, mVMC with the grand canonical ensemble works well for reproducing the Kitaev spin liquid.

Acknowledgment

This work was supported by Grant-in-Aid for Building of Consortia for the Development of Human Resources in Science and Technology from the MEXT of Japan. A part of the numerical calculation of this work was performed with the supercomputer in the Institute for Solid State Physics, the University of Tokyo. We also thank the computational resources of the K computer provided by the RIKEN Advanced Institute for Computational Science through the High Performance Computing Infrastructure System Research projects (hp140215, hp150211, hp150173, and hp160201) supported by the MEXT of Japan. This work was also supported by JSPS KAKENHI (Grant Nos. 16K17746 and 16H06345), and by MEXT as a social and scientific priority issue (Creation of new functional devices and high-performance materials to support next-generation industries) to be tackled by using post-K computer. The authors acknowledge Satoshi Morita, Kazuyoshi Yoshimi, Mitsuaki Kawamura, Takahiro Ohgoe, Masatoshi Imada, and Takeo Kato for collaborations in developing mVMC. The work on the interfaces of the cuprates was done by collaboration with Yusuke Nomura, Silke Biermann, and Masatoshi Imada.

References

[1] M. Imada, A. Fujimori, Y. Tokura, Rev. Mod. Phys. **70**, 1039 (1998).

[2] P. A. Lee, N. Nagaosa, X.-G. Wen, Rev. Mod. Phys. **78**, 17 (2006).

[3] B. Keimer, S. A. Kivelson, M. R. Norman, S. Uchida, J. Zaanen, Nature **518**, 179 (2015).

[4] L. Balents, Nature **464**, 199 (2010).

[5] C. Gros, Ann. Phys. **189**, 53 (1989).

[6] F. Becca, S. Sorella, Quantum Monte Carlo approaches for correlated systems, Cambridge University Press, 2017.

[7] W. L. McMillan, Phys. Rev. **138**, A442 (1965).

[8] D. Ceperley, G. V. Chester, M. H. Kalos, Phys. Rev. B **16**, 3081 (1977).

[9] S. Sorella, Phys. Rev. B **64**, 024512 (2001).

[10] S. Sorella, M. Casula, D. Rocca, J. Chem. Phys. **127**, 014105 (2007).

[11] E. Neuscamman, C. J. Umrigar, G. K.-L. Chan, Phys. Rev. B **85**, 045103 (2012).

[12] `https://github.com/issp-center-dev/mVMC`

[13] `https://ma.issp.u-tokyo.ac.jp/en/app/518`

[14] T. Misawa, S. Morita, K. Yoshimi, M. Kawamura, Y. Motoyama, K. Ido, T. Ohgoe, M. Imada, T. Kato, Computer Physics Communications **235**, 447 (2019).

[15] `http://www.issp.u-tokyo.ac.jp/supercom/softwaredev`

[16] D. Tahara, M. Imada, J. Phys. Soc. Jpn. **77**, 114701 (2008).

[17] D. Tahara, M. Imada, J. Phys. Soc. Jpn. **77**, 093703 (2008).

[18] R. Kaneko, S. Morita, M. Imada, J. Phys. Soc. Jpn. **83**, 093707 (2014).

[19] S. Morita, R. Kaneko, M. Imada, J. Phys. Soc. Jpn. **84**, 024720 (2015).

[20] T. Misawa, M. Imada, Phys. Rev. B **90**, 115137 (2014).

[21] H.-H. Zhao, K. Ido, S. Morita, M. Imada, Phys. Rev. B **96**, 085103 (2017).

[22] K. Ido, T. Ohgoe, M. Imada, Phys. Rev. B **97**, 045138 (2018).

[23] Y. Motome, K. Nakamikawa, Y. Yamaji, M. Udagawa, Phys. Rev. Lett. **105**, 036403 (2010).

[24] T. Misawa, J. Yoshitake, Y. Motome, Phys. Rev. Lett. **110**, 246401 (2013).

[25] T. Misawa, K. Nakamura, M. Imada, J. Phys. Soc. Jpn. **80**, 023704 (2011).

[26] T. Misawa, K. Nakamura, M. Imada, Phys. Rev. Lett. **108**, 177007 (2012).

[27] T. Misawa, M. Imada, Nat. Commun. **5**, 5738 (2014).

[28] M. Hirayama, T. Misawa, T. Miyake, M. Imada, J. Phys. Soc. Jpn. **84**, 093703 (2015).

[29] H. Shinaoka, T. Misawa, K. Nakamura, M. Imada, J. Phys. Soc. Jpn. **81**, 034701 (2012).

[30] M. Hirayama, T. Misawa, T. Ohgoe, Y. Yamaji, M. Imada, arXiv:1901.00763 (2019).

[31] T. Ohgoe, M. Hirayama, T. Misawa, K. Ido, Y. Yamaji, M. Imada, arXiv:1902.00122 (2019).

[32] T. Misawa, Y. Nomura, S. Biermann, M. Imada, Sci. Adv. **2**, e1600664 (2016).

[33] Y. Yamaji, M. Imada, Phys. Rev. B **83**, 205122 (2011).

[34] M. Kurita, Y. Yamaji, S. Morita, M. Imada, Phys. Rev. B **92**, 035122 (2015).

[35] M. Kurita, Y. Yamaji, M. Imada, Phys. Rev. B **94**, 125131 (2016).

[36] K. Ido, T. Misawa, in preparation.

[37] T. Ohgoe, M. Imada, Phys. Rev. B **89**, 195139 (2014).

[38] T. Ohgoe, M. Imada, Phys. Rev. Lett. **119**, 197001 (2017).

[39] K. Ido, T. Ohgoe, M. Imada, Phys. Rev. B **92**, 245106 (2015).

[40] K. Ido, T. Ohgoe, M. Imada, Sci. Adv. **3**, e1700718 (2017).

[41] K. Takai, K. Ido, T. Misawa, Y. Yamaji, M. Imada, J. Phys. Soc. Jpn. **85**, 034601 (2016).

[42] `https://github.com/issp-center-dev/mVMC-tutorial`

[43] `http://www.math.sci.hiroshima-u.ac.jp/~m-mat/MT/SFMT`

[44] G. Carleo, F. Becca, M. Schiró, M. Fabrizio, Sci. Rep. **2**, 243 (2012).

[45] S.-I. Amari, Neural computation **10**, 251 (1998).

[46] J. Wu, O. Pelleg, G. Logvenov, A. T. Bollinger, Y.-J. Sun, G. S. Boebinger, M. Vanetić, Z. Radović, I. Božović, Nat. Mat. **12**, 877 (2013).

[47] G. Logvenov, A. Gozar, I. Božović, Science **326**, 699 (2009).

[48] T. Misawa, M. Imada, Phys. Rev. B **90**, 115137 (2014).

[49] A. Kitaev, Ann. Phys. (N. Y). **321**, 2 (2006).

[50] G. Jackeli, G. Khaliullin, Phys. Rev. Lett. **102**, 017205 (2009).

[51] X.-Y. Feng, G.-M. Zhang, T. Xiang, Phys. Rev. Lett. **98**, 087204 (2007).

[52] H.-D. Chen, Z. Nussinov, J. Phys. A Math. Theor. **41**, 075001 (2008).

[53] M. Kawamura, K. Yoshimi, T. Misawa, Y. Yamaji, S. Todo, N. Kawashima, Comput. Phys. Commun. **217**, 180 (2017).

First-principles studies on anomalous electron and spin transport properties in non-trivial spin textures

Fumiyuki ISHII

Nanomaterials Research Institute

Kanazawa University, Kakuma-machi, Kanazawa, Ishikawa 920-1192

1 Abstract

Electron spins can act as inter-converter of electricity, light, sound vibration, and heat [1]. Spin-related transport properties of materials originate in its spin structures of real and momentum space. To design spin conversion materials, we have studied anomalous Nernst effect, i.e., anomalous Hall effect induced by temperature gradient in magnetic materials [2], and Rashba effect [3] and persistent spin helix state [4] in non-magnetic materials.

We have studied the systems with special spin structures applicable to spintronics or thermoelectric conversion based on first-principles density functional calculations using OpenMX [5]. We focused on surfaces, interfaces and 2D system with peculiar spin textures such as Rashba spin textures that can lead to spin-to-charge conversion (from a spin current to a charge current), and skyrmion that can enhances Berry curvatures in momentum space.

2 First-principles methods

We have performed first-principles electronic-structure simulations based on the non-collinear density functional theory (DFT) with two-component spinor wave functions for Kohn–Sham–Bloch orbitals [8,9] using the OpenMX code [5]. We used the generalized gradient approximation with the Perdew-Burke-Ernzerhof functional to treat the exchange-correlation potential [10]. We used the fully-relativistic total angular momentum dependent norm-conserving pseudopotentials considering the spin–orbit interaction [11,12]. We extended the wave functions using a linear combination of multiple pseudoatomic orbitals [13,14].

To study anomalous Nernst effect, the Wannier90 code was used to construct maximally localized Wannier functions (MLWFs) based on the results of the DFT calculations [15]. We also simulated the transport properties based on the MLWFs using the semiclassical Boltzmann transport theory [16]. We have previously used this method successfully to study the thermoelectric properties of half-Heusler compounds with the formula CoMSb (M=Sc, Ti, V, Cr, and Mn) [17].

In the study of Rashba effect, we deduce the spin polarization in the momentum space from the momentum $\boldsymbol{k}$-dependent spin density matrix. The spin density matrices $P^{n}_{\sigma,\sigma'}(\boldsymbol{k}) = \int \psi^{*\,n}_{\sigma}(\boldsymbol{k},\boldsymbol{r})\psi^{n}_{\sigma'}(\boldsymbol{k},\boldsymbol{r})d\boldsymbol{r}$ are calculated using the spinor Bloch wavefunction, the component of

which is given by $\psi_\sigma^n(\boldsymbol{k},\boldsymbol{r})$ which is obtained from the OpenMX calculations, where σ is the spin index (↑ or ↓) and n is the band index.

3 Anomalous Nernst effect

We are interested in how to achieve much higher thermoelectric conversion efficiency by effectively manipulating electron-spin degree of freedom. As one possibility, we have been studying Berry-phase-mediated thermoelectric effects, namely the contribution of the anomalous Hall conductivity (AHC) to thermoelectric power. What we target here is the

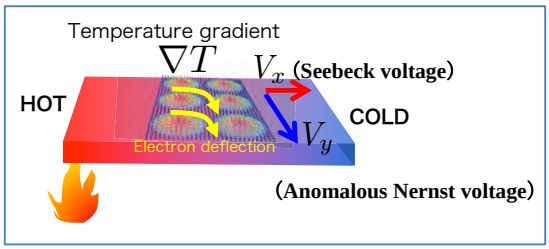

Fig. 1: Thermoelectric effect in skyrmion crystal.

anomalous Nernst effect (ANE), which is a heat-to-electricity conversion observed in magnetic materials and directly related to AHC. We discussed AHC mainly driven by an effective magnetic field, Berry curvature, induced by spin-orbit coupling and/or spin chirality.

We have so far found from computations on simple models that, in the so-called 2D Skyrmion crystal (SkX) phase, where skyrmions are crystallized in two dimensions, the crystal-momentum component of effective magnetic field gives rise to the band structure that could generate large ANE when chemical potential μ is properly tuned [6]. Fig.1 shows schematic view of thermoelectric effect (Seebeck effect and anomalous Nernst effect) in SkX. Although

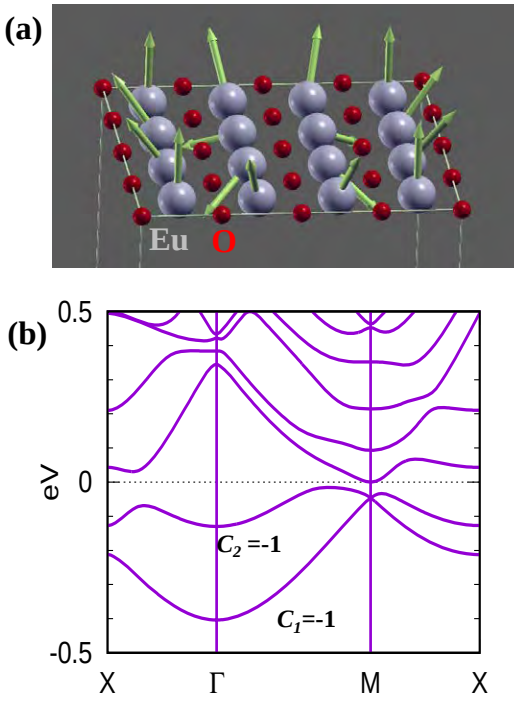

Fig. 2. (a) Calculated spin structures for skyrmion of EuO monolayer model. (b) Calculated band structure and corresponding band-by-band decomposition of Chern number.

the large ANE was most clearly confirmed in the simplest model of square SkX with single s-orbital per site, our subsequent computations on more realistic multi-orbital models of also showed possible large ANE [7].

We have performed first-principles calculations for 2D SkX of EuO monolayer (Fig. 2(a)). The charge density cutoff energy was set at 250 Rydbergs and a regular k-point mesh (20,20,1) was used for the self-consistent calculations (SCFs). A sizable transverse thermoelectric coefficient is predicted to arise in

a SkX assumed on EuO monolayer where carrier electrons are introduced upon a quantum anomalous Hall insulating phase of Chern number C_{total} = 2. This encourages future experiments to pursue such an effect.

To achieve band-by-band analysis for AHC, we have implemented the methods in OpenMX computing Berry curvature on discretized Brillouin zone [18]. The Chern number of each band C_{n} (n: band index) can be calculated by integrating the Berry curvature.

Figure 2 (b) shows the band structure of electron-doped EuO monolayer. There is a narrow band gap of about 20 meV between the valence band top and conduction band bottom. The occupied two bands with Chern number C_{total}=2 are mainly composed of Eu 5d and 6s characters. We have calculated anomalous Nernst coefficients N by using semiclassical Boltzmann transport theory with constant relaxation time, $\tau = 10$ fs. The Nernst coefficients are related to the conductivity tensor, and these relationships can be represented as shown below [7]:

$$N = \frac{N_0 - \theta_{\text{H}} S_0}{1 + \theta_{\text{H}}^2}$$

where $N_0 = \alpha_{xy}/\sigma_{xx}$, $S_0 = \alpha_{xx}/\sigma_{xx}$, $\theta_{\text{H}} = \sigma_{xy}/\sigma_{xx}$ are the pure Nernst coefficient, pure Seebeck coefficient, and Hall angle ratio, respectively. The electrical conductivity tensors were computed from

$$\sigma_{xx} = \int e^2 \tau \sum_n v_{x,n}^2(k) \left(-\frac{\partial f(\varepsilon_{n,k})}{\partial \varepsilon_k}\right) dk$$

while the AHCs were computed from

$$\sigma_{xy} = e^2 \sum_n \Omega_n^z(k)\, f(\varepsilon_{n,k}) dk.$$

The thermoelectric conductivity tensors were computed by

$$\alpha_{ij} = \frac{\text{k}_\text{B}}{e} \int \sigma_{ij}(\varepsilon) \frac{\varepsilon - \mu}{T} \left(-\frac{\partial f(\varepsilon_{n,k})}{\partial \varepsilon_k}\right) d\varepsilon$$

where $e, \tau, v_{x,n}^2(k), f, \varepsilon_{n,k}, \hbar, \Omega_n^z(k), T, \text{k}_\text{B}$ and μ are the elementary charge, relaxation time, group velocity of electrons, Fermi-Dirac distribution function, energy, reduced Planck constant, Berry curvature, temperature, Boltzmann's constant, and chemical potential, respectively.

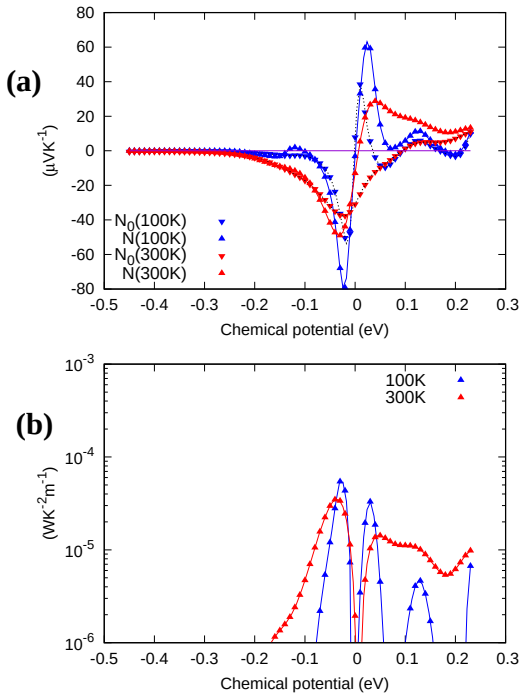

Fig. 3. (a) The chemical potential dependence of anomalous Nernst coefficients and (b) power factors. Results are shown for different values of temperature 100K and 300K. We assumed the constant relaxation time τ = 10 fs.

The calculated chemical potential dependence of Nernst coefficients N, pure Nernst coefficients

and power factor are plotted in Fig 3(a) and (b). The large anomalous Nernst coefficients up to 60 μV/K and power factor up to 70 μW/mK^2 can be obtained. Such N arises from the coexistence of large longitudinal thermoelectric coefficient and large Hall angle ratio, realized in the vicinity of a narrow band gap with Chern number C_{total} = 2. The origin of reported other materials are mainly pure Nernst effect, N_0, in metallic magnetic materials. This is the reason why the anomalous Nernst effect is smaller than Seebeck effect in general. In contrast, electron-doped EuO monolayer is narrow-gap Chern insulator. It is similar to the case that the narrow gap semiconductor shows large Seebeck effects. This demonstrates a prototype of novel class of new thermoelectric materials utilizing the nanoscale topological spin textures, motivating further studies including relevant experiments. We concluded that the SkX and narrow-gap Chern insulators could be candidate materials for thermoelectric applications.

4 Spin-to-charge conversion

In recent years, a phenomenon called spin-to-charge current (SCC) conversion that converts a spin current into a charge current is attracting much attentions [19]. There is inverse Rashba Edelstein effect (IREE) as a more efficient method than inverse spin Hall effect [20] which is one of the origins of the SCC conversion. The SCC conversion by IREE has been reported to occur at the materials interfaces with Rashba effect. The Rashba effect is an effect of resolving the spin degeneracy in a non-magnetic material whose space inversion symmetry is broken [3]. The efficiency of SCC using IREE is evaluated by the conversion factor λ_{IREE}, i.e., the ratio of the injected (resulted) spin (charge) current J_{S} (J_{C}) densities as $\lambda_{\text{IREE}} = J_{\text{C}}/J_{\text{S}}$. The λ_{IREE} is proportional to the Rashba coefficient α_{R} as $\lambda_{\text{IREE}} = \alpha_{\text{R}}\tau_{\text{S}}/\hbar$ where τ_{S} is the spin relaxation time and $\hbar$ is reduced planck constant [19].

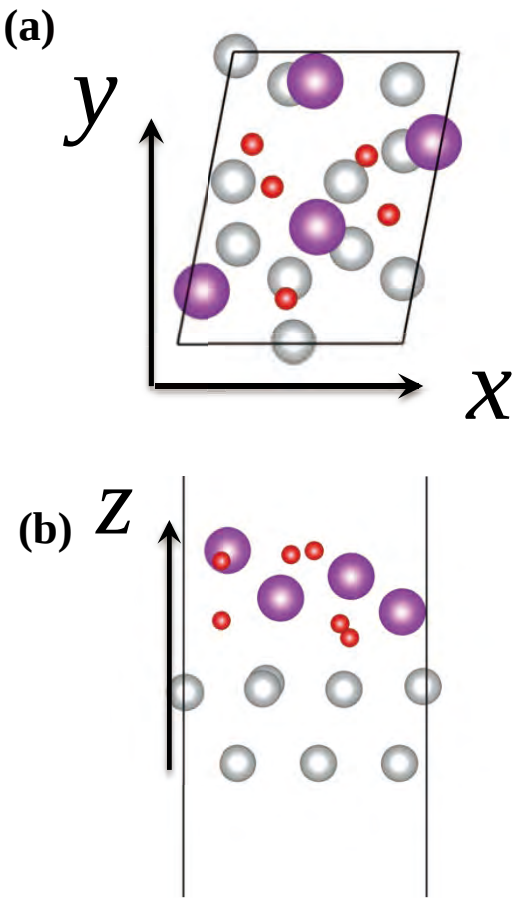

Fig. 4. Calculated model of interfaces noble metal/α-Bi_2O_3; (a) Top view; (b) side view. White, purple and red circles correspond to noble metal, Bismuth and Oxygen.

In order to improve the SCC conversion efficiency, many materials interfaces were studied such as substances with large Rashba coefficientsand long spin relaxation time.

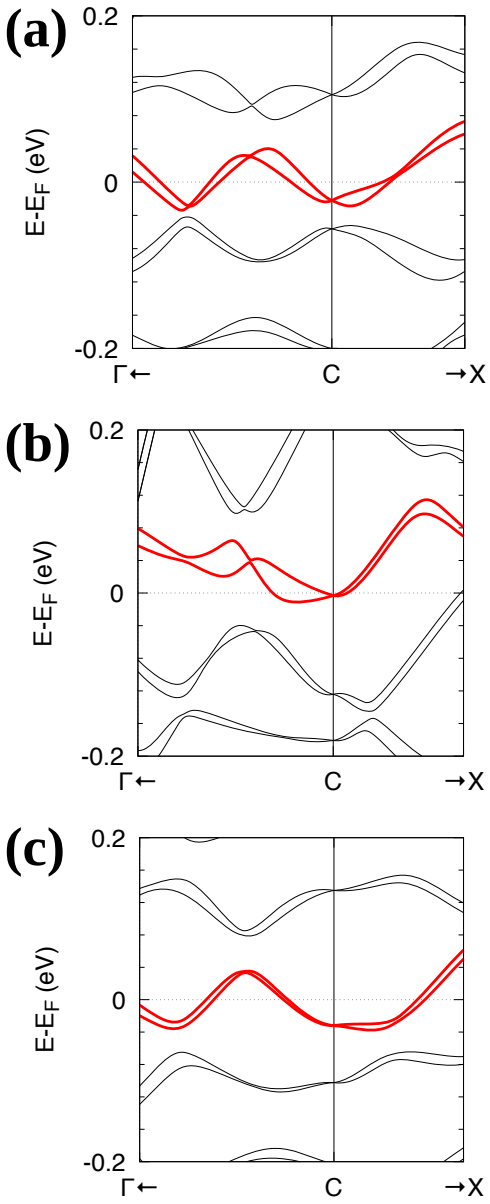

Fig. 5. Band structures for *M*(111)/α-Bi2O3. (a) *M* = Cu; (b) *M*=Ag; (c) *M*=Au. The enlarged views of the band structures around C-point are shown through each path from C-point to the point dividing CΓ or CX line internally in the ratio 1:4.

Figure 4 shows the interface model of (111) face-centered–cubic noble metal with oxide insulator α-**type** structure Bi_2O_3, *M*(111) (*M*=Cu, Ag, Au)/α-Bi_2O_3. Fig. 5(a)-(c) shows the band structure for the NM(111)/α–Bi_2O_3 systems, where the symmetry points (Γ, C, X) are those in the first Brillouin zone shown in Fig. 7(a). There is a free-electron-like band around C-point near the Fermi energy for each system, and its Rashba spin splitting is anisotropic.

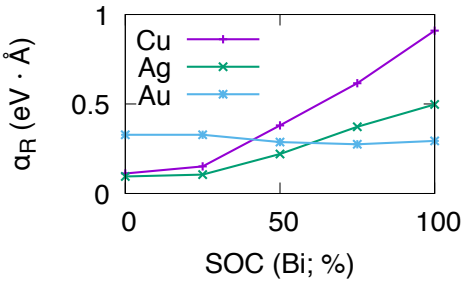

Fig. 6. Strength dependence of spin-orbit coupling (SOC) of Bi on Rashba coefficient for noble metal/α-Bi2O3.

A trend in the Rashba spin splitting is corresponding to obtained the Rashba coefficients $\boldsymbol{\alpha_R}$ as the average of the ones along CΓ and CX line around C-point. Our calculated $\boldsymbol{\alpha_R}$ are 0.91, 0.50 and 0.29 for *M* = Cu, Ag and Au, respectively, in units of eV·Å. The strength dependence of SOC in Bi on the $\boldsymbol{\alpha_R}$ is shown in Fig. 6. For *M* = Cu and Ag, the $\boldsymbol{\alpha_R}$ increases as the strength of SOC of Bi increases. When the SOC of Bi is turned off, the $\boldsymbol{\alpha_R}$ becomes zero and this indicates that the SOC of Bi is essential for occurring large $\boldsymbol{\alpha_R}$. On the other hand, for *M*

= Au, $\boldsymbol{\alpha_R}$ decreases as the strength of SOC of Bi increases. Even if there is no SOC of Bi, $\boldsymbol{\alpha_R}$ is not zero and this may be originated from the SOC of Au. In the case of *M* = Cu and Ag, α_R is more drastically changed compared to Au case. It suggests that the influence on the α_R due to noble metal is different depending on the species Cu, Ag, and Au. Fig. 7 shows the spin textures for the *M*(111)/α-Bi_2O_3 system. The anisotropic Rashba spin structures are shown for *M* = Cu (Fig. 7 (b)) and for *M* = Ag (Fig. 7 (c)), while the non-Rashba type spin structures are shown for *M* = Au (Fig. 7 (d)). Since **α**-Bi_2O_3 is monoclinic ($P2_1/c$, No. 14) and C-point is Brillouin zone-boundary, each system has no 4-fold rotational symmetry (around C-point) that makes Fermi surface and spin textures isotropic. The anisotropic Rashba spin vortices for *M* = Cu and Ag are opposite to each other (e.g. The vortex for lower energy bands shown in Fig. 7, *M* = Cu is the clockwise, while that for *M* = Ag is the anti-clockwise.), which may support experimental result [21] that the sign of α_R^{exp} in Ag(111) /Bi_2O_3 is positive while that in Cu(111) /Bi_2O_3 is negative. For *M* = Au, there are non-Rashba type spin splitting. This may be due to strong SOC of Au. On the other hand, in the experiment, a symmetric circular spin structure was observed by angle dependence results but not an anisotropic one, because the amorphous Bi_2O_3 results in a symmetric potential in x-y plane.

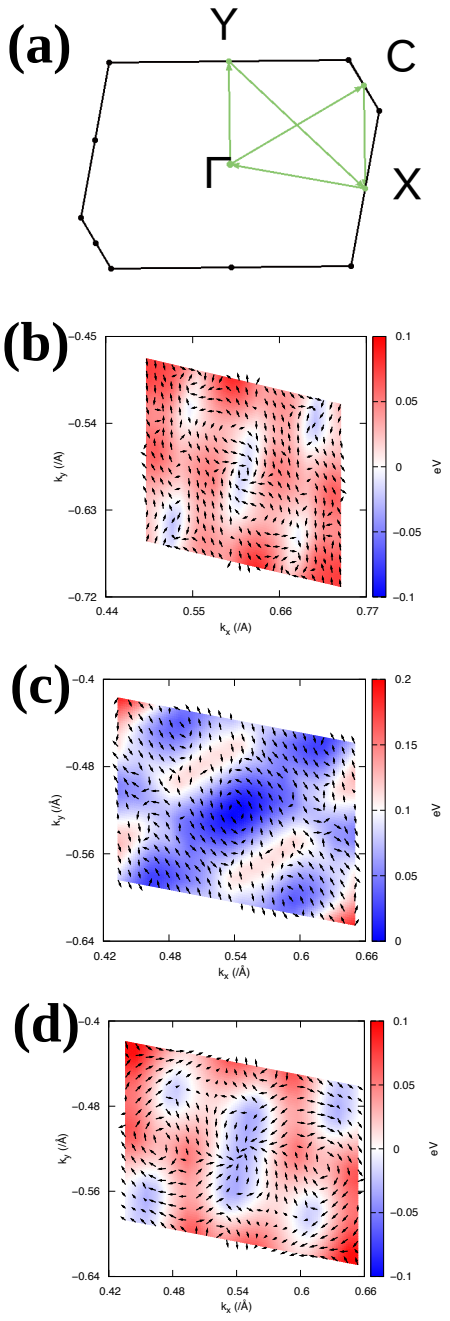

Fig. 7. (a) Schematic of the first Brillouin zone with high symmetry points. Energy dependence of spin textures of lower energy bands in fig. 5 around C point for (b) Cu(111)/α-Bi_2O_3; (c) Ag(111)/α-Bi_2O_3; (d) Au(111)/α-Bi_2O_3.

5 Summary

We have studied the systems with special spin structures applicable to spintronics or thermoelectric conversion based on first-principles density functional calculations using OpenMX [5]. We focused on surfaces, interfaces and 2D system with peculiar spin textures such as skyrmion crystals in real space that can enhances Berry curvatures in momentum space and anomalous Nernst effect. The Rashba spin textures in momentum space can lead to spin-to-charge conversion (from a spin current to a charge current). Recently, we also discussed photo-induced spin to charge conversion [22].

We also study other spin textures, non-collinear spin structures in real space for computational design for quantum spin ice [23] and collinear spin textures in momentum space, i.e., persistent spin helix states that can lead to long spin lifetime[24,25].

Acknowledgement

The author acknowledges the collaboration with H. Kotaka, Y.P. Mizuta, N. Yamaguchi, S. Minami, H. Sawahata, M. Sugita, Y. Tanaka, and M. Saito.

References

[1] Y. Otani, M. Shiraishi, A. Ohiwa, E. Saito, and S. Murakami, Nat. Phys. **13** (2017) 829.

[2] N. Nagaosa, J. Sinova, S. Onoda, A. H. MacDonald, and N.P. Ong, Rev. Mod. Phys. **82** (2010)1539.

[3] Y. A. Bychkov, and E. I. Rashba, J. Phys. C **17**(1984) 6039.

[4] B. Bernevig, J. Orenstein, and S. Zhang, Phys. Rev. Lett. **97** (2006) 236601.

[5] T. Ozaki et al., Open source package for Material eXplorer, http://www.openmx-square.org

[6] Y.P. Mizuta and F. Ishii, Sci. Rep. **6** (2016) 28076.

[7] Y.P. Mizuta, H. Sawahata, F. Ishii, Phys. Rev. B **98** (2018) 205125.

[8] U. von Barth and L. Hedin, J. Phys. C **5** (1972) 1629.

[9] J. Kübler, K. H. Höck, J. Sticht, and A. R. Williams, J. Phys. F **18** (1988) 469.

[10] J. P. Perdew, K. Burke, and M. Ernzerhof, Phys. Rev. Lett. **77** (1996) 3865.

[11] I. Morrison, D. M. Bylander, and L. Kleinman, Phys. Rev. B **47** (1993) 6728.

[12] G. Theurich and N. A. Hill, Phys. Rev. B **64** (2001) 073106.

[13] T. Ozaki, Phys. Rev. B **67** (2003) 155108.

[14] T. Ozaki and H. Kino, Phys. Rev. B **69** (2004) 195113.

[15] A. A. Mostofi, J. R. Yates, G. Pizzi, Y.-S. Lee, I. Souza, D. Vanderbilt, and N. Marzari, Comput. Phys. Commun. **185** (2014) 2309.

[16] G. Pizzi, D. Volja, B. Kozinsky, M. Fornari, and N. Marzari, Comput. Phys. Commun. **185** (2014) 422.

[17] S. Minami, F. Ishii, Y.P. Mizuta, and M. Saito, Appl. Phys. Lett. **113** (2018) 032403.

[18] T. Fukui, Y. Hatsugai, H. Suzuki, J. Phys. Soc. Jpn., **74** (2005) 1674.

[19] R. J. Sánchez, L. Vila, G. Desfonds, S. Gambarelli, J. Attané, D. J. Teresa, C. Magén, and A. Fert, Nat. Commun. **4** (2013) 2944.

[20] V. M. Edelstein, Solid. State. Commun. **73** (1990) 233.

[21]H. Tsai, S. Karube, K. Kondou, N. Yamaguchi, F. Ishii, Y. Otani, Sci. Rep. **8** (2018) 5564.

[22] J. Puebla, F. Auvray, N. Yamaguchi, M. Xu, S.Z. Bisri, Y. Iwasa, F. Ishii, and Y. Otani, Phys. Rev. Lett. **122** (2019) 256401.

[23] S. Onoda and F. Ishii, Phys. Rev. Lett. **122** (2019) 067201.

[24] M. A. Absor, F. Ishii, H. Kotaka, nd M. Saito, App. Phys. Express **8** (2015) 073006.

[25] N. Yamaguchi and F. Ishii, App. Phys. Express **10** (2017) 123003.

Coarse-Grained Force Field for Lipid Domain Formation Simulations

Sangjae Seo, and Wataru Shinoda
Department of Materials Chemistry, Nagoya University,
Furo-cho, Chikusa-ku, Nagoya, 464-8603

1. Introduction

During the last decades, the structure of cellular membrane has gained lots of attentions due to its biological importance [1]. Especially, the functions and existence of lipid raft in the plasma membrane have been intensively studied by experiments, theories, and computer simulations. The lipid raft model suggests that the biological membrane is not homogeneous, rather separated into liquid ordered (L_o) and disordered (L_d) domains mostly due to the different affinity of cholesterol (Chol) between saturated and unsaturated lipids. Experimentally, the fluorescent microscopes have revealed the existence of lipid raft in the model vesicles, which have simple compositions [2, 3]. However, despite of the enormous effort to reveal the structure of lipid raft *in vivo*, our knowledge is still limited due to its size and dynamic nature. In this regard, molecular dynamics (MD) simulation has been extensively exploited to study the membrane structure. MD simulation gives insightful information in atomic resolutions by numerically solving the Newton's equation of motion for atoms. The forces acting on each particle are calculated based upon the force field (FF), which contains a set of parameters of empirical potential function. Since the accuracy of the MD simulation results rely on the quality of FF, it is of great importance to develop accurate FF. Recent all-atom (AA) FFs, which are generally fitted to the quantum mechanical data, provides accurate structural properties of lipids [4, 5]. However, because AA FF requires expensive computational costs, it is not eligible to investigate the phase separation of lipid membrane. Coarse-grained (CG) FFs exploit less detailed description of atoms. Several heavy atoms are mapped into one single bead, so that it can easily reduce the number of interactions. In this report, we will shortly introduce the available CG FFs, and our recent development of CG FF for the purpose of phase separation simulation.

1.1. Coarse-grained force fields

MARTINI is one of the most successful CG FF for the simulation of biomolecules [6, 7]. Generally, four heavy atoms are represented by a single CG site. MARTINI FF has fixed number of CG sites, and the interactions between CG sites were determined by the reproduction of partitioning free energies. Since the available CG bead types are predefined, such as polar, nonpolar, apolar, and charged, user can readily create a CG model of new molecule without any further parameterization process. However, due to the fixed number of CG bead types and constrained σ value (*i.e.*, σ=0.47 nm) of Lennard-Jones (LJ) interaction, the accuracy is not always guaranteed.

Iterative Boltzmann inversion (IBI) method derives the CG interactions from the structural data retrieved from the fine grained model [8]. The radial distribution function (RDF) obtained from the AA MD simulation is targeted. RDF is converted into the interaction potential by Boltzmann inversion, and iteratively updating trial potential, finally the tabulated potential for interaction is determined. Although IBI is a systematic way to determine the parameters, because IBI only accounts for the structural aspect, the thermodynamic properties are poorly

described.

Shinoda-DeVane-Klein (SDK) model was designed to accurately predict the interfacial properties [9, 10]. The parameters were optimized against the thermodynamic properties, and SDK model can accurately reproduce the membrane properties. However, the previous cholesterol model developed in the SDK was not successful to show the phase separation of lipid mixtures in the same condition to the experiment [11]. In this study, we developed a new CG FF, coined SPICA FF, which can accurately predict the phase behavior, in the spirit of SDK model [12].

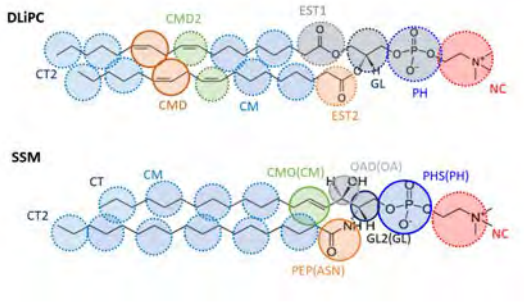

Fig. 1: CG Mapping of DLiPC and SM lipid. Solid circle indicates the new bead developed in this study and dashed circles are taken from SDK model. The name of bead type in the parenthesis is the similar bead taken from the SDK model.

2. Methods

2.1. Modeling and parameterization

SPICA FF was developed as an extension of SDK model. We added new lipid types; sphingomyelin (SM) and polyunsaturated lipids, and optimized the Chol parameters to accurately reproduce the structural properties. CG mapping scheme and resolution followed that of the SDK model. Three to four heavy atoms of lipid molecules were mapped into CG beads. Figure 1 depicts the CG mapping of SM and DLiPC. Functional groups, such as hydroxyl group, and amino group, were mapped into one CG bead.

SPICA FF exploits the same functional form of the potential functions used in the SDK model. The bonded interactions are defined as,

$$U_{\text{bonded}} = \sum_{\text{bond}} k_b (r_{ij} - r_0)^2 + \sum_{\text{angle}} k_\theta (\theta_{ijk} - \theta_0)^2 + \sum_{\text{dihed}} k_\phi \left[1 + \cos\left(n\phi_{ijkl} - d\right)\right] \quad (1)$$

For the angle parameter, in order to avoid angle collapse, additional Lennard-Jones (LJ) type interaction is sometimes added.

$$U_{1-3}^{\text{correct}} = \sum_{1-3} \left[U_{nb}\left(r_{ij}\right) - U_{nb}\left(r_{\min}\right)\right] \quad \text{for} \quad r_{ij} < r_{\min} \quad (2)$$

We determined the parameters of bonded interaction by fitting to the distribution obtained from the AA MD simulation. The non-bonded interaction is defined as;

$$U_{nb}(r_{ij}) = \begin{cases} \frac{3\sqrt{3}}{2}\varepsilon_{ij}\left[\left(\frac{\sigma_{ij}}{r_{ij}}\right)^{12} - \left(\frac{\sigma_{ij}}{r_{ij}}\right)^{4}\right] & \text{for the pairs involving water} \\ \frac{27}{4}\varepsilon_{ij}\left[\left(\frac{\sigma_{ij}}{r_{ij}}\right)^{9} - \left(\frac{\sigma_{ij}}{r_{ij}}\right)^{6}\right] & \text{for any other pairs} \end{cases} \quad (3)$$

Basically, the non-bonded interactions were determined to satisfy surface tension and density of analogue molecules. For the cross interactions (between different bead types), the σ values were easily determined by the Lorentz-Berthelot rule, $\sigma_{ij} = \frac{\sigma_{ii} + \sigma_{jj}}{2}$. However, fitting to such thermodynamic properties could not decide most of ε values of cross interactions because it does not follow the conventional combination rule. Thus, for lipid molecules, the remaining

cross interactions were optimized by targeting membrane properties, such as membrane area, thickness, area compressibility modulus. Moreover, for the optimization of Chol model, in order to make Chols correctly partition in the mixture systems, 2D RDF was also considered. Namely, we calculated 2D RDF of Chol-lipid in lipid membranes for a series of different concentration of Chol from AA MD simulations, which were used as reference data for the optimization of CG parameters.

Since there was no systematic way to determine the parameters that simultaneously satisfy the membrane properties, we explored the parameters by random searching. To reflect the chemical interaction, we multiplied the scaling value, *k*, to the conventional combination rule, $\varepsilon_{ij} = k\sqrt{\varepsilon_{ii}\varepsilon_{jj}}$, and created a huge number of parameter sets, which have various scaling values for each interaction. Then, we chose the best parameter set, which most accurately reproduce all the target membrane properties.

2.2. Molecular dynamics simulation

We conducted both AA and CG MD simulations. AA MD simulations were conducted using NAMD package with the CHARMM36 FF [4] to produce the reference data. The AA MD simulations were run for 1 μs at 323K and 1atm controlled by Langevin dynamics and Nosé-Hoover Langevin piston, respectively. CG MD simulations were conducted using LAMMPS for 500 ns to calculate the membrane properties. Nosé-Hoover thermostat and Parrinello-Rahman barostat were used to maintain the temperature and pressure at 323K and 1atm, respectively. For ternary mixture systems, the temperature was set at 298K, which is the same condition as the experiments.

The initial structures were prepared by the CHARMM-GUI [13]. In case of ternary mixtures, the small patches created by CHARMM-GUI were duplicated to generate large membrane.

2.3. Analyses

We measured the various membrane properties to assess the SPICA FF. Area per lipid was measured by dividing the simulation box size by the number of lipids. The thickness of membrane was defined as the average phosphate-phosphate distance. The area compressibility was calculated by

$$K_A = \frac{k_B T \langle A \rangle}{N \sigma^2_{\langle A \rangle}} \tag{4}$$

where $< A >$ and $\sigma^2_{<A>}$ are the average surface area and the dispersion, respectively. The segmental order parameter was calculated by

$$S_{ZZ} = \frac{\left\langle 3\cos^2\theta - 1 \right\rangle}{2} \tag{5}$$

where θ is the angle between membrane normal and the vector connecting consecutive hydrophobic tail beads.

For the phase separation simulation, we quantified the degrees of phase separation by the contact ratio, which is defined as

$$\Phi_C = \frac{N_{chol-sat}}{N_{chol-sat} + N_{chol-unsat}} \tag{6}$$

where $N_{x\text{-}y}$ is the number of contacts between *x*-lipid type and *y*-lipid type. We counted the number of contacts in the shared edged from the Voronoi tessellation.

3. Results and Discussion

3.1. Membrane properties

We evaluated the quality of SPICA FF by comparing the membrane properties to the AA simulations and experimental results. Table. 1 lists calculated membrane properties of area, thickness, and area compressibility. The membrane properties of unitary membrane show good agreement with AA MD result.

Lipid	SA/lipid [Å^2]		Thickness [Å]		K_A [mN/m]	
	AA	CG	AA	CG	AA	CG
SSM	54.4	57.2	43.1	41.4	440	460
PSM	55.4	56.8	40.7	39.6	350	460
DLiPC	70.2	71.3	36.9	36.9	263	357

Table 1: Calculated membrane properties of unitary membranes. Errors of SA/lipid and thickness are less than ±1%, and K_A is less than 10%.

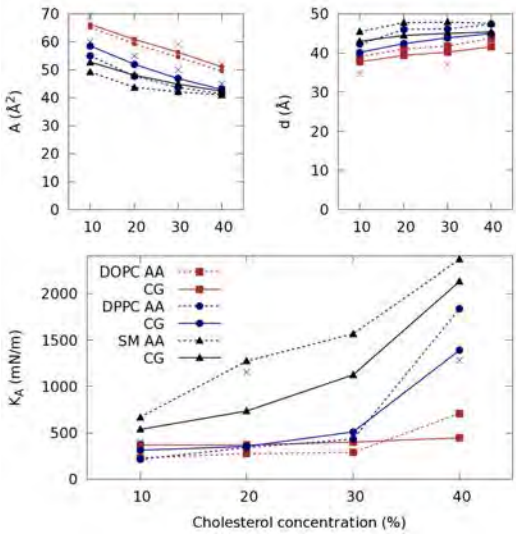

Fig. 2: Membrane properties containing Chol.

Figure 2 displays the membrane properties of binary mixtures containing various Chols contents. Similar to the unitary systems, the results of CG MD simulations of binary mixtures are well agreed with the AA MD simulation results. The condensing effect and ordering effects, which are evidenced by the smaller area and larger thickness in the higher Chol concentration, are well reproduced by the SPICA force field.

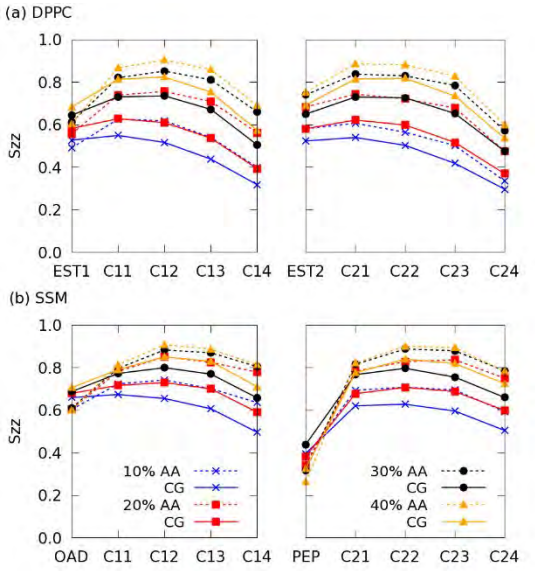

Fig. 3: Order parameters of membranes containing Chol.

The order parameter of CHARMM FF was extensively evaluated by comparing to the experimental values, and it has been shown that CHARMM can accurately reproduce the S_{CD} value [4]. Since we cannot directly evaluate the S_{CD} value from CG MD, we calculated the CGed segmental order parameter, S_{ZZ}, (Eq.(5)) instead, and compared between AA and CG MD simulations. As shown in Fig. 3, although *Szz* values of CG MD simulation are slightly lower than that of AA MD simulation, the overall agreement is still satisfactory and the *Szz* variation as a function of chol concentration is also reproduced. The ordering effect of Chol is

clearly shown by higher order parameters in the higher Chol concentrations.

We also paid extra attentions to the Chol distribution. We plot the 2D RDF and compared with AA MD simulation result (Fig. 4). In case of DOPC membrane, the RDF plots of Chol almost coincide with AA simulation result. The locations and height of each peak are well reproduced by SPICA FF.

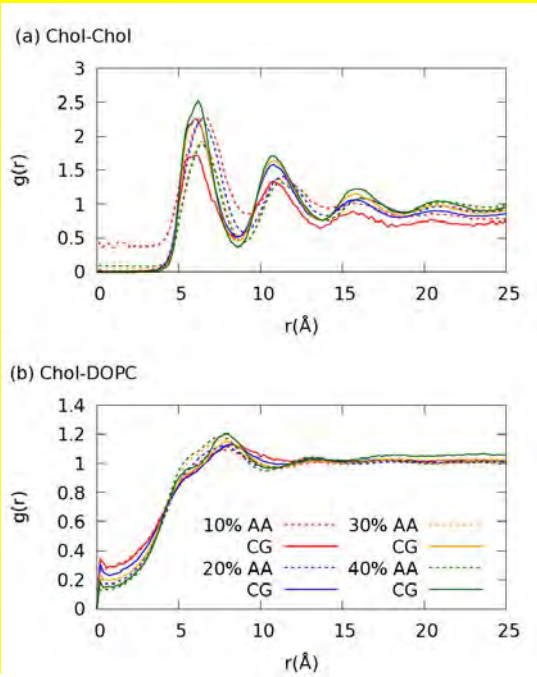

Fig. 4: 2D RDFs of each pair in DOPC membrane containing Chol. (a) Pair of Chol-Chol, and (b) Chol-DOPC

In addition to the 2D RDF, we also checked the Chol distribution with respect to the Chol faces. Chol has two faces; α-face is a flat surface, and β-face is a rough surface containing protruded methyl group. Due to the asymmetric structure of Chol, it has been known that the Chol distribution shows three-fold symmetry. Figure 5 shows the in-plane Chol distribution with respect to the reference orientation of Chol. First, the highlights correspond to the peaks in the 2D RDF curves. In case of AA MD simulation, one can observe the three hot spots pointed by the red arrows, which indicates the three-fold symmetry. Although the Chol model of SPICA failed to reproduce 3-faces, the overall distribution on α-face and β-face is still well reproduced.

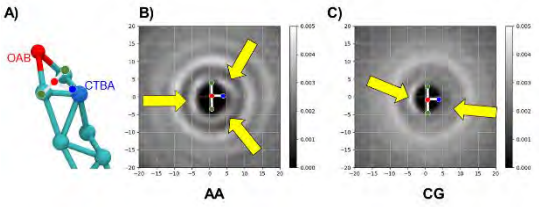

Fig. 5: In-plane probability distribution of Chols. (a) Schematic description of the orientation. (b-c) Arrows indicate the three-, and two-fold symmetry.

3.2. Phase separation simulation

One of the main goals of the development of the SPICA FF was to accurately reproduce the phase behavior in the ternary mixture. As mentioned above, the stronger interaction between Chols and saturated lipids leads to the phase separation of L_o and L_d domains. First, we evaluated the chemical potential of Chol in different lipid membranes. One Chol molecule in the lipid bilayer was pulled from the equilibrium position to the water region, and the required free energy was calculated by the adaptive biasing force method [14]. As Fig 6 depicts, the free energy difference between in the lipid bilayer and water region. Smaller free energy difference at higher Chol concentration indicates that Chols prefer the higher concentrations regardless of the lipid type. In addition, Chol shows preferred interaction with saturated lipid, such as SSM and DPPC. The chemical potential difference between DOPC and saturated lipid suggests that Chol prefers to stay in the saturated lipid domain

and the trend is accelerated as increasing Chol concentration, which leads to the phase separation.

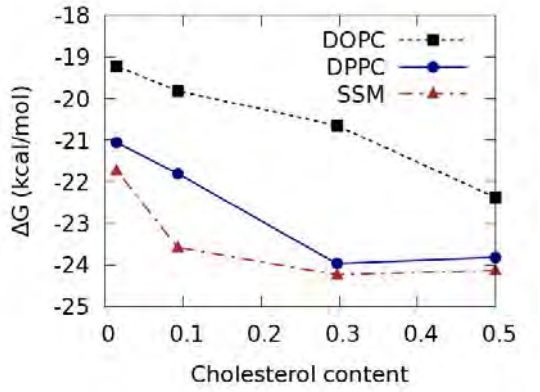

Fig. 6: Chemical potential of Chols in different lipid membrane.

We simulated the ternary mixture of DOPC, DPPC and Chol (DPPC-DOPC-CHOL) in 1:1:1 ratio. This composition extensively investigated by the fluorescent experiments has been shown macroscopic phase separations. However, the MARTINI FF has failed to obtain the phase separation of this mixture. We have carried out a CG-MD simulation of the DPPC-DOPC-CHOL mixture for 4 μs and succeeded in showing a phase separation. As shown in Fig. 7, the membrane was phase separated into L_o region enriched with DPPC and Chol, and L_d region mostly consisted with DOPC. The contact ratio increased up to 0.8, which clearly indicated the enrichment of Chols in the DPPC region.

We also tested the polyunsaturated lipid for the phase separation. The CG MD simulation of the mixture of DPPC, DLiPC, and Chol (DPPC-DLiPC-Chol) was conducted for 4 μs. Similar to the membrane of DPPC-DOPC-CHOL, DPPC-DLiPC-Chol membrane was also phase separated. Interestingly, the membrane showed anti-registered (phase asymmetric) domain separation. We speculated that the large hydrophobic mismatch leads to the anti-registration. The average thickness of L_o

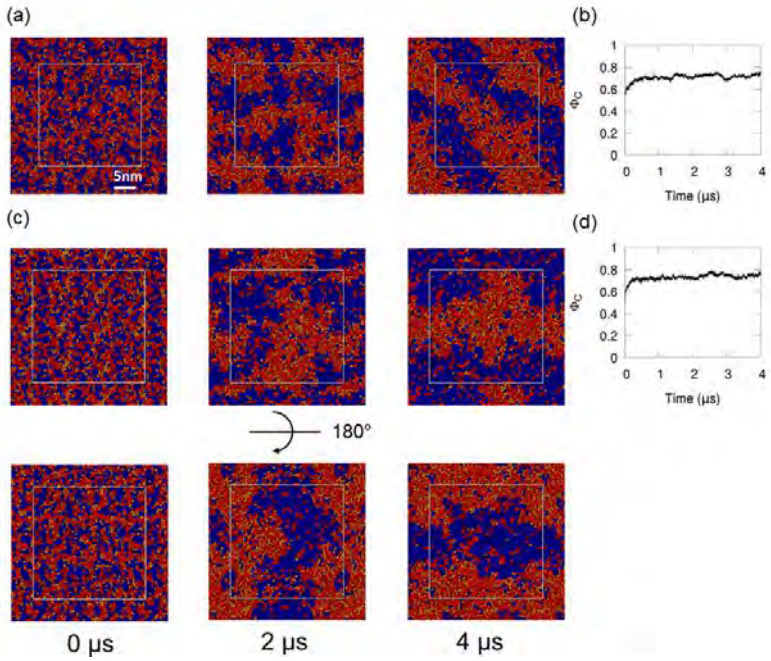

Fig. 7: Snapshots of phase separation in the course of simulation. (a-b) DPPC-DOPC-Chol, (c-d) DPPC-DLiPC-Chol.

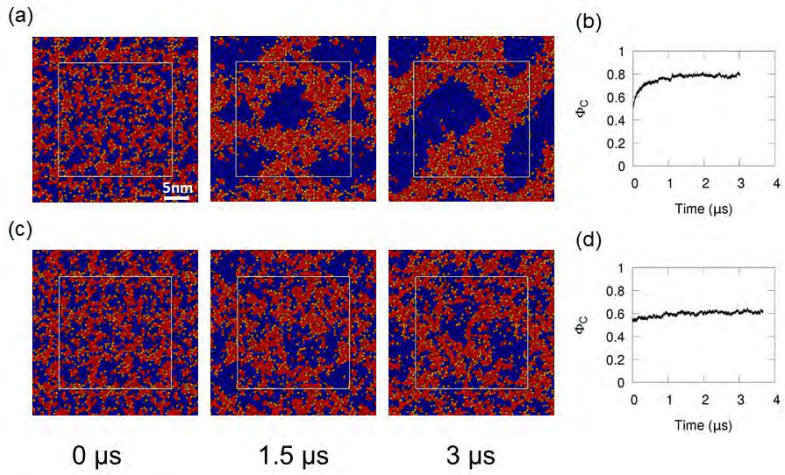

Fig. 8: Snapshots of phase separation in the course of simulation. (a-b) SSM-DOPC-Chol, (c-d) SSM-POPC-Chol.

domains enriched with DPPC and Chol increases up to 44 Å, whereas, L_d domains, mostly consisting DLiPC is only about 37 Å. Thus, the large hydrophobic mismatch between L_o and L_d domain may give rise to the anti-registration to minimize the hydrophobic mismatch energy.

Since SM lipids are generally accepted as the main lipid type induces the phase separation in the plasma membrane, we also run the CG MD simulation of the mixture of SSM, DOPC, and Chol (SSM-DOPC-CHOL). Experimentally, it already has shown that the ternary mixture of SSM-DOPC-CHOL shows the macroscopic phase separation [2]. Figure 8 displays the phase behavior in the course of the simulation. Similar to experimental results, the mixture showed phase separations after 4 μs. The contact ratio increased up to 0.8. Also, it has been experimentally shown that the replacement of DOPC to POPC leads to the conversion from macroscopic phase separation to microscopic phase separation [2]. We could observe the same phenomenon. As shown in Fig 8, in case of SSM-POPC-CHOL, the domain size after the phase separation is much reduced and the membrane shows ambiguous domain boundaries. It was also confirmed in the contact ratio plot. Although the contact ratio slight rises at the initial step of phase separation, the value was saturated at ~0.6. This clearly indicates the disruption of domains because of the replacement of unsaturated lipid.

4. Conclusion

Accurate prediction of phase separation using CG MD simulation is important to understand underlying mechanism of lipid raft formation. In this research, we developed a new coarse-grained force field, called SPICA, which can accurately reproduce the membrane properties and phase behavior. The parameters were fitted against the membrane area, thickness, and area compressibility modulus. More importantly, the Chol model was highly optimized against RDF, so that the Chol partitioning in the mixture was accurately calculated. Then, we ran a series of CG MD simulations of the ternary mixtures consisting saturated lipid, unsaturated lipid, and Chol. The phase behavior observed from the CG

MD simulation was consistent with experimental result. Interestingly, we found that the significant hydrophobic mismatch gives rise to the anti-registration. We expect that the SPICA FF developed in this research will enable us to understand the lipid raft and membrane structure. The FF parameters are provided on the official website, http://spica-ff.org/. An extension of SPICA FF for proteins are now underway. We are going to publish the FF in near future.

References

[1] K. Simons and E. Ikonen, Nature, **387** (1997) 569-572.

[2] S.L. Veatch and S.L. Keller, Biophys. J., **85** (2003) 3074-3083.

[3] T. Baumgart, S.T. Hess, and W.W. Webb, Nature, **425** (2003) 821-824.

[4] J.B. Klauda, et al., J. Phys. Chem. B, **114** (2010) 7830-7843.

[5] J.P.M. Jämbeck and A.P. Lyubartsev, J. Chem. Theory Comput., **9** (2012) 774-784.

[6] S.J. Marrink, et al., J. Phys. Chem. B, **111** (2007) 7812-7824.

[7] M.N. Melo, H.I. Ingólfsson, and S.J. Marrink, J. Chem. Phys., **143** (2015).

[8] D. Reith, M. Pütz, and F. Müller-Plathe, J. Comput. Chem., **24** (2003) 1624-1636.

[9] W. Shinoda, R. DeVane, and M.L. Klein, Mol. Simul., **33** (2007) 27-36.

[10] W. Shinoda, R. DeVane, and M.L. Klein, J. Phys. Chem. B, **114** (2010) 6836-6849.

[11] C.M. MacDermaid, et al., J. Chem. Phys., **143** (2015).

[12] S. Seo and W. Shinoda, J. Chem. Theory Comput., **15** (2018) 762-774.

[13] J. Lee, et al., J. Chem. Theory Comput., **12** (2015) 405-413.

[14] E. Darve, D. Rodríguez-Gómez, and A. Pohorille, J. Chem. Phys., **128** (2008).

3.2 First-Principles Calculation of Material Properties

Mechanisms of Semiconductor Interface Formation and its Electronic Properties based on Quantum Theory

Atsushi Oshiyama

Institute of Materials and Systems for Sustainability, Nagoya University

Furo-cho, Chikusa-ku, Nagoya 464-8601

In the fiscal year of 2018, on the basis of the density-functional theory we have clarified 1) an elementary process of the decomposition of ammonia and the incorporation of nitrogen into GaN network during the epitaxial growth of GaN [1,2], 2) the structure of carbon-related carrier traps at the SiC/SiO2 MOSFET interface[3], and 3) the reason for the improvement of the SiC/SiO2 interface using phosphorus [4,5]. In the following, I will explain the first issue.

Mechanisms of GaN MOVPE: NHx reactions on the growing surface

GaN is a principal material for optoelectronic devices and also emerging in power electronics. This is obviously due to its wide band gap and robustness. To endorse its superiority as power devices, however, growth of high-quality GaN films is an inevitable requirement and the clarification of atom-scale mechanisms of the growth of the GaN films is highly demanded. Metal Organic Vapor Phase Epitaxy (MOVPE) with trimethylgallium (TMG) and ammonia (NH3) as gas sources is regarded as the most suitable technique of growing GaN films. Many experimental and theoretical efforts have revealed that TMG is decomposed in the gas phase and the growing surface is generally Ga rich. Knowledge of the decomposition and incorporation of NH3 is, however, extremely poor. We have performed first-principle total-energy electronic-structure calculations that clarify reaction pathways and corresponding energy barriers for the decomposition of NH3 and the N incorporation on the growing GaN surface. On the contrary to a prevailed picture in the past, we find that the reaction is catalyzed by the presence of the surface [1,2].

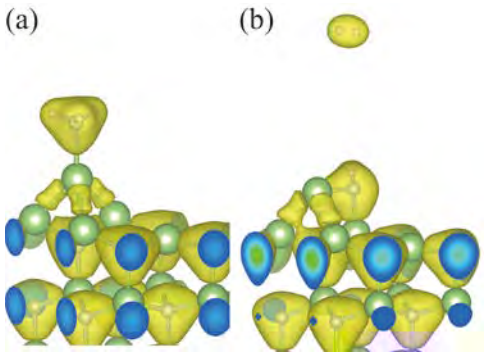

Fig. 1: The initial (a) and the final (b) atomic structures of the decomposition reaction of NH$_3$. Large and small balls depict Ga and N atoms, respectively. The electron density in each structure is shown as yellow iso-value surface. Adsorbed NH3, surrounded by upper yellow surface in (a), is decomposed and the -Ga-N(H)-Ga- unit is formed in the subsurface region with an H$_2$ being desorbed (b).

We start with the identification of the growing surface. Preparing the (0001) bare surface, we have examined stable adsorption configurations for Ga atom as well as for other

molecular species. We have found that the most stable configuration for the additional Ga atom is so-called T4 configuration in which the Ga atom is adsorbed on the site above the second-layer N atom. This surface has been indeed shown to be thermodynamically stable below 1500 K under whole range of V/III ratio in MOVPE. We then examine the adsorption configuration of an NH3 molecule on the Ga-adatom surface. We have found that the NH3 is adsorbed on the top of the Ga-adatom site. The calculated electron density shows the formation of the bond between the Ga adatom and the N atom in NH$_3$. It is also found that the Ga-Ga back bond is relatively weak as is evidenced by the less accumulation of the electron density [Fig. 1 (a)].

This Ga-Ga bond is a candidate for the N attacking site during the MOVPE. Hence we have explored reaction pathways for the NH$_3$ to be decomposed. We have found that the reaction, [NH3 on GaN] $\rightarrow$ [NH in GaN] + [H2 in gas phase], takes place. The initial and the final atomic structures in this reaction are shown in Figs. 1 (a) and (b), respectively. In the final structure, N in NH3 intervenes in the weak Ga-Ga back bond, forming the network of - Ga adatom - N(H) - Ga -. The N atom has been incorporated in GaN bond network after this reaction. The calculated energy profile along the reaction is shown in Fig.2. The energy barrier for the reaction is calculated to be 0.63 eV, being surprisingly small even though the Ga-Ga bond is destructed in this reaction. Further exploration of the reactions for H2 desorption leads to a reaction channel toward the incorporated N surrounded by four Ga atoms with the energy barrier of 2 eV. This barrier is overcome by the free-energy gain for the H2 molecule in the gas phase: The hydrogen chemical potential at 1300 K in the gas phase is evaluated to be -2.1 eV, considering translation, vibration and rotation motions of H2.

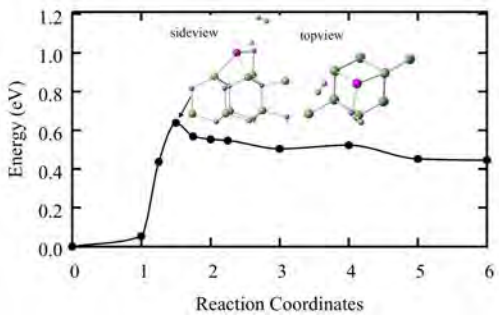

Fig. 2: Calculated energy profile for the reaction of the NH3 decomposition and the NH incorporation (see text and Fig. 1) on the Ga-rich GaN(0001) growing surface. The transition-state geometry is also shown.

Related Publications

[1] K. M. Bui, J.-I. Iwata, Y. Kangawa, K. Shiraishi, Y. Shigeta, and A. Oshiyama, J. Phys. Chem. C **122**, 24665 (2018).

[2] K. M. Bui, J.-I. Iwata, Y. Kangawa, K. Shiraishi, Y. Shigeta, and A. Oshiyama, J. Cryst. Growth **507**, 421 (2019)

[3] Y.-i. Matsushita and A. Oshiyama, Jpn. J. Appl. Phys. **57**, 125701 (2018).

[4] T. Kobayashi, Y.-i. Matsushita, T. Okuda, T. Kimoto and A. Oshiyama, Appl. Phys. Exp. **11**, 121301 (2018).

[5] T. Kobayashi, Y.-i. Matsushita, T. Kimoto and A. Oshiyama, Jpn. J. Appl. Phys. **58**, 011001 (2019).

Analyses on atomic, magnetic, and electronic structures in high-performance spintronics materials

Tatsuki ODA[1,2], Nurul IKHSAN[2], Tomosato KANAGAWA[2], Indra PARDEDE[2], Daiki YOSHIKAWA[2], Marleni WIRMAS[2], Hasan Al RASYID[2], Masao OBATA[1,2]

[1]*Institute of Science and Engineering, Kanazawa University, Kanazawa, Ishikawa 920-1192*

[2]*Graduate School of Natural Science and Technology, Kanazawa University, Kanazawa, Ishikawa, 920-1192*

We studied the several topics involved with this project; implementation of new approach on the magnetic anisotropy originating from spin dipole-dipole interaction and application to thin films. We also investigated the thickness dependence of magnetic anisotropy in Cr/Fe(x)/MgO.

Spin dipole-dipole interaction

We implemented the magnetic dipole interaction (MDI) in a first-principles planewave-basis electronic structure calculation based on spin density functional theory [1]. This implementation, employing the two-dimensional Ewald summation, enables us to obtain the total magnetic anisotropy energy of slab materials with contributions originating from both spin-orbit and spin dipole-dipole couplings on the same footing. The implementation was demonstrated using an iron square lattice. The result indicates that the magnetic anisotropy of the MDI is much less than that obtained from the atomic spin moment model due to the prolate quadrupole component of the spin magnetic moment density. This new approach allows us to take a self-consist treatment among the magnetic dipole field caused by the spin density and the exchange field originating from the exchange interaction. In this work, the implementation was performed in two dimensional system, however, the evaluation of spin dipole-dipole interaction can be extended to three dimensional system without any difficulty.

Application to thin films

The new implemented method was used to evaluate the shape magnetic anisotropy for the thin films of ferromagnetic and antiferromagnetic slabs as demonstration [2]. We found that in the ferromagnetic slab with Fe/MgO interfaces, the quadrupole component of atomic spin density suppresses the shape magnetic anisotropy energy in addition to the conventional suppression appearing as magnetic surface. In the antiferromagnetic MnPt slab, which has a perpendicular favor originating from the crystalline magnetic dipole interaction, a surface effect of the Mn

edge appears as an enhancement. This shape anisotropy was found to be comparable to those of the anisotropy originating from the spin-orbit interaction with different sign. Thus whole anisotropy of system may almost cancel out in MnPt system.

Interface systems of Cr/Fe(*x*)/MgO (x=1-9)

Electronic structure and magnetic anisotropy energy (MAE) of Cr buffered Fe/MgO interface were investigated in terms of thickness dependence by means of a fully relativistic density functional approach [3]. The electronic structure indicated that the interface state gets occupied unlike a typical rigid band picture as the number of Fe layers decreases, leading large perpendicular aniso-tropies in the oscillating behavior for its thickness dependence. The maximum of the MAE originating from spin-orbit interaction (SOI) reaches to 2 mJ/m^2. It is found that the saddle point nature and dispersionless at the Fermi level may be an origin of its large perpendicular magnetic anisotropy. To evaluate the MAE from SOI, the in-plane shape magnetic anisotropy from magnetic dipole interaction (MDI) was estimated. The calculated MAE from MDI required a suppression in the calculated total magnetization for realizing a fair agreement with an experimental MAE. With using a rescaled magnetization it was found that a possible perpendicular anisotropy may appear in the thickness range of experimental data.

Fermi level smearing effect

Effects of the Fermi level smearing introducing temperature dependence of energy-band occupation numbers were investigated in terms of magnetic anisotropy by using a density functional theory [4]. In a perpendicular magnetization film Fe(0.7nm) /MgO, the magnetocrystalline anisotropy shows a decrease with respect to the smearing temperature; $0.4mJ/m^2$ from 10.5K to 527K. This reduction is not negligible and is expected to be partially compensated by a reduction in the shape magnetic anisotropy, assuming reasonable values of the Curie temperature and saturated magnetic moment. The resulting temperature dependences in the total perpendicular magnetic anisotropy energy is in agreement with those of available experimental data semi-quanti-tatively.

References

[1] T. Oda and M. Obata: J. Phys. Soc. Jpn. **87** (2018) 064803.

[2] I. Pardede *et al.*: IEEE Trans. Magn. **55** (2018) 1300104.

[3] N. Ikhsan *et al.*: The Sci. Rep. Kanazawa Univ. **62** (2018) 23.

[4] N. Ikhsan *et al.*: The Sci. Rep. Kanazawa Univ. **62** (2018) 37.

Analyses on magnetic and electronic structures in high-performance spintronics materials

Tatsuki ODA[1,2], Indra PARDEDE[2] , Daiki YOSHIKAWA[2], Tomosato KANAGAWA[2], , Nurul IKHSAN[2], Hasan Al RASYID[2], Masao OBATA[2]

[1]*Institute of Science and Engineering, Kanazawa University, Kanazawa, Ishikawa 920-1192*

[2]*Graduate School of Natural Science and Technology, Kanazawa University, Kanazawa, Ishikawa, 920-1192*

We studied the magnetic anisotropy and its electric field (EF) effect in the thin film related with spintronic devices. We obtained a sign change in electric field control perpendicular magnetic anisotropy energy at Fe/MgO interface. EF control on magnetic anisotropy energy (MAE) in the system which contains Fe/MgO interface with Cr underlayer was performed by means of first-principles electronic structure calculations. An opposite sign in EF coefficient γ was observed by introducing Fe/Cr intermixing. This intermixing leads to a substantial rearrangement in the electronic structure due to proximity effects of Fe and Cr. The origin of such an opposite sign in γ was discussed along the modulation of occupied and unoccupied *d*-band near the Fermi level. By introducing strain effect, the enhancements of MAE and γ were achieved with the maximum absolute values, 2.43 mJ/m^2 and 170 fJ/Vm respectively. The present result provides a new possible degree of freedom for the EF control in MAE as the underlayer configuration.

We systematically investigated EF effect in Fe/MgO interface systems with Cr underlayer by introducing the interchange of Cr and Fe layers. Our model using slab system, vacuum (0.79nm)/Cr(6ML)/Fe(1ML)/Cr(1ML)/Fe(3 ML)/MgO (5ML)/vacuum (0.79 nm) (system A) and vacuum(0.79nm)/Cr(5ML)/Fe (1ML) /Cr(1ML)/Fe(1ML)/Cr(1ML)/Fe (2ML)/MgO (5ML)/vacuum(0.79nm)(system B). The magnetic anisotropy energy (MAE) was calculated from the total energy difference between in-plane magnetization ([100]) and out-of-plane magnetization ([001]), MAE = E[100]-E[001]. To apply an EF, we used the effective screening medium (ESM) method. To obtain the EF inside the MgO layer, we took into account the dielectric constant (9.8 for MgO).

The MAE for system A and B in zero EF are 1.28 mJ/m^2 and 1.48 mJ/m^2, respectively. These values were largely enhanced, compared to the system which consists of Cr(6ML)/Fe (4ML)/MgO(5ML)(MAE = 0.59 mJ/m^2 without introduce Fe/Cr intermixing). In addition, this

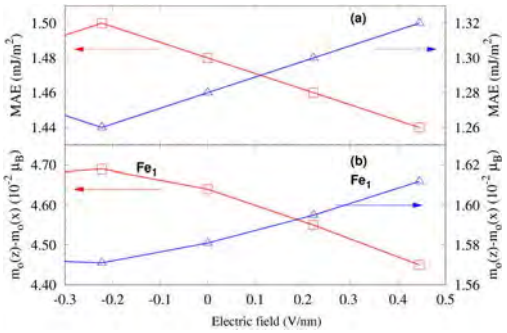

Fig. 1. (a)Electric field effect in MAE and (b) anisotropy of orbital magnetic moment for system A (triangle) and system B (square).

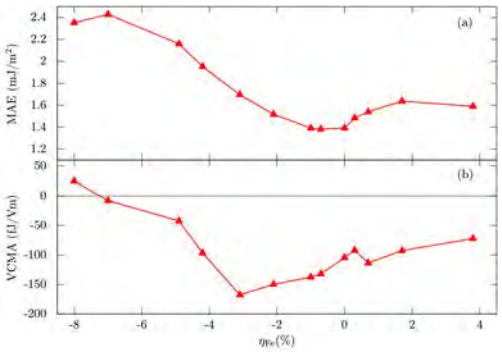

Fig. 2. Strain dependence of (a) MAE and (b) EF effect (VCMA) in Cr/Fe /MgO slab.

PMA value is comparable to the experimental result [2] after subtracting the shape anisotropy contribution, $K_d t$=0.690mJ/m^2. $K_d t$ is estimated by using continuum model, $K_d t\ t_{Fe} = -\mu_0 M_s^2/2$, where μ_0 is the permeability of vacuum and M_s is saturation magnetization. In this estimation, we used M_s=0.0785 memu/cm^2 extracted from experimental data for t_{Fe}=0.56nm(1ML～0.14 nm)[2].

We calculated MAE as strain dependence for system B, as shown in Fig. 2(a). In this work, the variation of strain is taken in the range of -8.0% to 3.8% for the ratio with respect to Fe lattice constant (2.87Å). As a result, MAE increases with increasing tensile strain (increase in lattice constant) and increasing compressive strain (reduce in lattice constant) with the maximum value of 2.43 mJ/m^2. This MAE is strongly related to the spin-orbit-couplings of *d*-orbital component on the interface Fe, especially those of eigen-states near the Fermi level.

Furthermore, the electric field (EF) coefficient (γ) as strain dependence is shown in Fig. 2(b). The maximum absolute value of γ is 170 fJ/Vm at η_{Fe}=-3.1%. This larger value can be related to a large amount of *d*-orbital states around the Fermi level.

References

[1] I. Pardede *et al.*: IEEE Trans. Magn. **55** (2018) 1700104.

[2] T. Nozaki *et al.*, Phys. Rev. Appl. 5, (2016) 044006.

Functional property of electrodes

OSAMU SUGINO
Institute for Solid State Physics,
The University of Tokyo, Kashiwa-no-ha, Kashiwa, Chiba 277-8581

The water splitting and the fuel-cell reactions occurring on the electrode have recently become an important target of modern surface/interface science. Those reactions are known to occur efficiently catalyzed by platinum but novel class of catalysts such as TiO_2 has attracted attention because of technological importance; however, the reason why TiO_2 should play a role as electrocatalyst is not well known. As a step towards the understanding, we applied a thermodynamic approach to the oxygen reduction reaction (ORR), which has been successfully used to explain why existing electrocatalysts are far from ideal. The approach says that at least one of the elementary steps for ORR is an uphill reaction almost unexceptionally; this happens because adsorption energy of O_2H is linearly dependent on that of OH for most existing catalysts. This phenomenological rule implies that those adsorption energies cannot be modified independently of each other to satisfy the ideal condition by changing the catalyst materials. *In addition*, the adsorption energies follow a universal line that does not cross the point of ideal catalyst.

Our first-principles calculation, however, shows that the adsorption energies do not strictly follow a linear relationship on a rutile and brookite TiO_2 surfaces when a surface Ti atom is doped with various transition metals [1]. That is, there is significant fluctuation in the $E_{ads}(O_2H)$-$E_{ads}(OH)$ plot, where E_{ads} means the adsorption energy. It is also found that the adsorption energies approach much closer to the ideal point when doped with some transition metals.

The results of the calculation indicate that the universal relationship is exceptionally violated on TiO_2. They also indicate that, when there is a way to stabilize the dopants at a complex interface although they are not so stable on our model surface that is atomically flat, the dopants may strongly enhance the ORR. We conjecture that such reaction environment may be provided in some part of the real catalyst; we are planning to make it sure by performing an ab initio Monte Carlo simulation.

References

[1] Y. Yamamoto, S. Kasamatsu, and O. Sugino, *submitted*.

Theoretical Analyses on Various Properties Concerning Nanodevices

Satoshi WATANABE
Department of Materials Engineering, the University of Tokyo
7-3-1 Hongo, Bunkyo-ku, Tokyo, 113-8656

1 Introduction

Recently, possibilities of novel nanoscale information and energy devices have been explored with various materials and operation mechanisms. This requires deeper understanding on material properites at nanoscale. Considering this situation, we have been performing atomic/electronic level simulations (mainly based on density functional theory (DFT)), taking various nanostructures as target systems. In the followings, some of our results in the fiscal year 2018 are described.

2 Neural network potentials for ion diffusion under electric fields

Motivated by a recent proposal of novel memory device using Au (or Ni)/amorphous Li_3PO_4/Li heterostructure [1], we have been examining Li ion diffusion behavior in amorphous Li_3PO_4. To facilitate this study, we constructed high-dimientional neural network (HDNN) potentials for efficient prediction of ion diffusion behaviors [2]. Since the ion behaviors under applied electric fields is crucial in the switching in the proposed device, it is desirable to extend the HDNN potential method so that it can take account of applied electric fields. For this purpose, we have developed NN to predict Born effective charge.

The training data are Born effective charges evaluated with density functional purterbation theory for various atomic arrangements obtained via *ab initio* molecular dynamics (MD) simulations starting from the γ-$Li_{12}P_4O_{16}$ structure (at 2000 K with a constant volume). The root mean square errors of the Born effective charge evaluated with the developed NN are 0.065 (e/atom) and 0.069 (e/atom) for the training and test data. We have also developed a MD code, where the forces acting on respective atoms are expressed as the sum of the forces calculated with the previously developed HDNN potential [2] and the force changes due to an applied electric field estimated using the present NN for the Born effective charge. To check the validity of this MD code is in progress.

3 Phonon-related properties of GaN

GaN is promising for power semiconductor device, blue light emitting diode (LED), etc. In such applications, phonon plays important roles, for example, in thermal management in power semiconductor device and emission efficiency in LED. Quantitative evaluation of such phonon-related properties is still a challenging task. Therefore, we have been studying such properties of GaN using DFT-based simulations. Here, we discuss 1) phonon band structures and thermal transport properties and 2) scattering rates due to electron-phonon interaction.

For the thermal transport, the evaluation of themal conductivities using DFT has become possible recently. However, it is computationally very demanding, which hinders the application of this approach to systems with

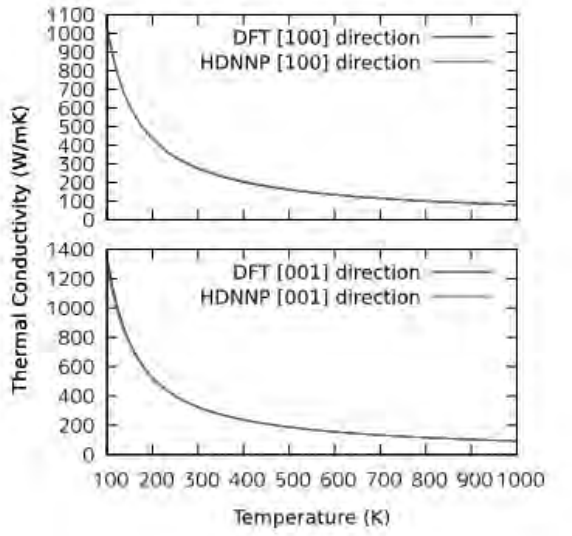

Figure 1: Temperature dependence of thermal conductivities of perfect wurtzite GaN crystal in (a) [100] and (b) [001] directions. Dark and light curves denote the results calculated using DFT and HDNN potential, respectively [3].

defects. So we have applied the HDNN potential techniques mentioned in the previous section to this problem. We have found that the HDNN potentials constructued our previous procedure [2] cannot provide sufficient accuracy of prediction of forces, while training the HDNN potential with forces can achieve good agreement with DFT results on phonon band structures and thermal conductivities of GaN as seen in the temperature dependence of thermal conductivities evaluated using the anharmonic lattice dynamics method (Fig. 1) [3].

For the electron-phonon interaction, we have examined the electron-phonon scattering rates from first principles using the density functional perturbation theory and maximally localized Wannier function. In doing so, we adopted EPW package [4, 5]. We have found that the scattering rates depend on the carrier wave number strongly. In addition, we have found that the applied strain changes the energy and wave number of carriers that suffer strong scattering from phonon.

4 Magnetism of adsorbed atoms and molecules on solid surfaces

The control of the perpendicular magnetic anisotropy (PMA) at the surface/interface of ferromagnetic metals is essentially important in novel magnetic devices based on the magnetic tunnel junctions. Since the interfacial PMA is sensitive to the electronic states at the surface/interface and these states are affected by adsorption of atoms and molecules, we started *ab initio* analysis of magnetism of adsorbed atoms and molecules on solid surfaces.

In the case of the PMA in an Fe(001) surface covered by Co-phthalocyanine (CoPc) molecule, as a preliminary results, we have found that the PMA is enhanced up to 18% by CoPc adsorption, which is in good agreement with experimental results. In the case of tramsition metal atoms on transition metal dichalcogenides, we have found that the stable adsorption sites changes with the applied strain, and magnetic moment of the adsorbed transition metal atom changes drastically in some combination of adsorbed atom species and transition metal dichalcogenides substrates.

References

[1] I. Sugiyama, R. Shimizu, T. Suzuki, K. Yamamoto, H. Kawasoko, S. Shiraki, and T. Hitosugi: APL Mater. **5** (2017) 046105.

[2] W. Li, Y. Ando, E. Minamitani, and S. Watanabe: J. Chem. Phys. **147** (2017) 214106.

[3] M. Ogura: Master thesis, the University of Tokyo (2019).

[4] F. Giustino, M. L. Cohen, and S. G. Louie: Phys. Rev. B **76** (2007), 165108.

[5] S. Poncé et al.: Comput. Phys. Commun. 209 (2016) 116.

First-Principles Study of Excited Electron, Positron and Atom Dynamics and Optical Responses of Nanostructures

Kazuyuki WATANABE, Yasumitsu SUZUKI,
Yoshihiro UEDA, Kazuki UCHIDA
Department of Physics, Tokyo University of Science
1-3 Kagurazaka, Shinjuku-ku, Tokyo 162-8601

In this project we investigated the following four topics on the basis of time-dependent density functional theory (TDDFT). 1) Secondary-electron emission from multi-layer graphene (MLG), 2) Multicomponent TDDFT for coupled electron-positron dynamics, 3) Finite temperature effects on laser-assisted field evaporation from a Si surface, and 4) Excitonic signature in dielectric functions of two-dimensional atomic layered materials.

1) *Secondary-electron emission (SEE) from MLG* [1]:

We calculated the amount of secondary electrons (NSE) emitted from MLG using real-time TDDFT simulations, and found its dependence on the layer number (L) of MLG and the incident energy of the electron wave packet (WP). NSE tends to converge to a certain value with increasing L, which is more conspicuous for a low-incident energy ($\sim$200 eV) electron WP than for a high-incident energy electron WP ($\sim$800 eV). The convergence stems from the attenuation of the incident electron WP upon scattering by each graphene layer. The attenuation was found to be proportional to the total number of excited electrons, which strongly depends on the incident energy. Our study enables the direct evaluation of NSE for layered and bulk materials and also provides useful insight into SEE from surfaces covered with layered materials. The simulations have been conducted by our home-made TDDFT code, KENS. Parallelized calculations have been performed using System B.

2) *Multicomponent density functional theory for coupled electron positron dynamics* [2]:

We have developed time-dependent multicomponent density functional theory (TD-MCDFT) for coupled electron-positron systems. The TD-MCDFT is a first-principles method that treats both the electron and positron dynamics quantum mechanically. The TD-MCDFT was applied to LiH under a laser field. There was no simple relationship between the laser energy and the positron detachment probability, which indicates a complex coupling between electronic and positronic motion. We found that the attached positron significantly suppresses laser-induced electronic excitations, which suggests the possibility that the absorption spectrum and excited-state nuclear dynamics may also be changed. There are more promising applications of the theory, such as application to the positron migration in the bulk of the material to reveal how it is trapped in a defect or surface, and positron scattering by materials. These are basic processes in positron beam experiments, and the TD-MCDFT methodology developed this time will be valuable for the study of fundamental positron physics. The simulations have been conducted by our home-made code, TiMESS. Parallelized calculations have been performed using System B.

3)*Finite temperature effects on laser-assisted field evaporation from a Si surface* [3]:

We investigated finite temperature effects on laser-assisted field evaporation from a Si surface using real-time TDDFT. We focused on finite electron and lattice temperatures, both of which were characterized on different time scales. The results indicate that dangling bonds at clean surfaces support thermal excitation under finite electron temperature conditions. It was also determined that thermal excitation induces electron transfer from the surface to the interior of the Si bulk under an electrostatic field, resulting in ionization of the surface atoms. The finite electron temperature effect on evaporation dynamics was found to be negligible. Increases in the finite lattice temperature, however, apparently induce atomic motion both parallel and perpendicular to the surface, thus appreciably enhancing the evaporation rate under electrostatic and laser fields. The present TDDFT simulations provide theoretical support for finite temperature effects during laser-assisted field evaporation, and this method can be applied to various non-equilibrium thermal phenomena, such as laser ablation. The simulations have been conducted by our homemade TDDFT code, KENS. Parallelized calculations have been performed using System B.

4) *Excitonic signature in dielectric functions of two-dimensional atomic layered materials* :

We first calculated the dielectric function of bi-layer hexagonal boron nitride by many-body pertubation theory (MBPT) and found the excitonic signature that depends on its stacking type. We next calculate the dielectric functions of these systems by TDDFT with the meta GGA exchange-correlation potential and the bootstrap kernel and found the structures that are qualitativey similar to those by MBPT. Our study has shown the validity of TDDFT approach for the analysis of optical properties of complex two-dimensional atomic layered materials for which the MBPT method needs an extremely long simulation time. All MBPT calculations and TDDFT calculations have been conduced using EXCITING (http://exciting-code.org/) and ELK (http://elk.sourceforge.net/) code, respectively. Parallelized calculations have been performed using System B.

References

[1] Y. Ueda, Y. Suzuki, and K. Watanabe, Appl. Phys. Express **11**, 105101 (2018).

[2] Y. Suzuki, S. Hagiwara and K. Watanabe, Phys. Rev. Lett. **121**, 133001 (2018).

[3] K. Uchida, Y. Suzuki and K. Watanabe, submitted.

Reduction of Rare Metals in Formic Acid Decomposition Catalysts and Oxygen Storage Materials

Yuji KUNISADA

Center for Advanced Research of Energy and Materials, Faculty of Engineering, Hokkaido University, Sapporo, Hokkaido 060-8628

We investigated the catalyst atom adsorption and diffusion properties on non-metal element doped graphene and MXene supports with the aid of the first principles calculation based on the density functional theory (DFT). We also investigated the corresponding catalytic activity. In addition, we investigated oxygen sorption properties of substituted brownmillerite oxides.

At first, we investigated adsorption and diffusion properties of Cu atoms on non-metal element doped graphene and MXene. We also investigated the catalytic activity using a theoretical volcano plot reported in previous study.[1] We performed the total energy and electronic structure calculations using The Vienna Ab initio simulation package (VASP). We installed parallelized VASP with Intel® MPI Library and Intel® Math Kernel Library. We found that the adsorption energies and diffusion activation barriers of Cu atoms increase by non-metal element doping into graphene lattice. From the adsorption energy of intermediates, we estimated the reaction activities. However, a single Cu atom catalyst shows low activity because of its strong intermediate adsorption. This trend is also observed in the case of a MXene supported Cu atom.

We also investigated the oxygen sorption properties of Sr_2AlMnO_5 and Sr_2AlMnO_5.[2] We revealed that Sr substitution decreases the operating temperature, which indicates that the heteroatom substitution can control the operating temperature.

We also studied the plasmonic properties of an Ag nanoparticle dimer using Discrete Dipole approximation for Electron Energy Loss Spectroscopy (DDEELS). From comparison between simulated and experimental EELS spectra, we revealed that multipolar plasmon is observed in the EELS experiment.[3]

References

[1] J. S. Yoo, F. A.-Pedersen, J. K. Nørskov, F. Studt: ACS Catal. 4 (2014) 1226.

[2] Y. Kunisada, G. Saito, K. Hayami, T. Nomura, N. Sakaguchi: Surf. Inter. Anal. 51 (2019) 65.

[3] N. Sakaguchi, S. Matsumoto, Y. Kunisada, M. Ueda: J. Phys. Chem. C 123 (2019) 6735.

Development of first-principles electronic-structure and transport calculation method based on real-space finite-difference approach

Tomoya ONO
Center for Computational Sciences, University of Tsukuba
Tennodai, Tsukuba, Ibaraki 305-8577

SiC has attracted considerable attention owing to its excellent physical properties, such as its high thermal conductivity, high breakdown strength, and large band gap. Among the numerous polymorphs of SiC, 4H-SiC has been recognized as the most promising candidate for power electronics devices. However, unlike Si MOSFETs, SiC MOSFETs have unacceptably low carrier mobility. One of the origins of the low carrier mobility is the generation of a large number of interface defects at SiC/SiO_2 interface. Although several experimental studies reported that carrier mobility increases when interface defect density is reduced by NO annealing after thermal oxidation, the carrier mobility is still much lower than that of SiC bulk and it has not been clarified role of N atoms at the interface yet. To improve the carrier mobility of SiC MOSFETs, it is important to understand and control the electronic structure of the SiC/SiO_2 interface after the annealing. In this study, we carried out density functional theory calculations to examine the atomic and electronic structures of the $SiC(0001)/SiO_2$ interface after annealing.

It is not straightforward to characterize the atomic structure of the $SiC(0001)/SiO_2$ interface because SiO_2 at the SiC/SiO_2 interface is mainly amorphous. Here, we assumed that crystalline structures exist locally at the SiC/SiO_2 interface and employed the most possible candidate for the interface atomic structures reported in Ref. 1. Moreover, two types of atomic layers, h and k, with respect to the stacking orientation of 4H-SiC appear at the 4H-SiC(0001) surface. The effect of the two types of the interface structure was also investigated. The first-principles calculations were performed by RSPACE code.[2]

As for the atomic structures after the NO annealing, it is reported that the N atoms accumulate at the interface.[3] However, there still remain many discussions, whether N atoms exist in the SiO_2 or the SiC substrate. We assumed that the N atoms accumulate in the SiC substrate. For the comparison of the stability of the (oxy)nitrized SiC structure on SiC(0001) surface, we calculated the lattice constant of the (oxy)nitrized SiC by removing the Si atom and replacing the C atoms by the N atoms. It is well known that there are two types of atomic layers in 4H-SiC bulk, h and k. To imitate the atomic layers just below the interface and minimize the unfavorable effect of SiC part on the lattice constant, 2H- and 3C-SiCs were employed. Table 1 shows lattice constants of the (oxy)nitrized SiC, indicating that the lattice constant mismatch of the (oxy)nitrized SiC to SiC(0001) is small.

The computational models for the interfaces, in which N and O atoms are inserted, are shown in Fig. 1. The areal density of N atoms is 1.6×10^{15} (cm^{-2}), which agrees well with experimental result obtained by secondary ion mass spectrometry and atom probe

Table 1: Lattice constants of (oxy)nitrized structure of SiC (in Å).

	3C			2H		
Polymorph	Structure	a	c	Structure	a	c
SiC	Si_9C_9	3.07	7.54	Si_6C_6	3.07	4.92
Nitrized	$(SiC)_5Si_3N_4$	3.01	7.23	$(SiC)_2Si_3N_4$	2.98	4.87
Oxynitrized	$(SiC)_4Si_4N_4O_2$	3.07	7.39	$(SiC)Si_4N_4O_2$	3.01	4.82

Table 2: Formation energy of (oxy)nitrized structure of SiC [in eV/SiC(0001)-3x1]. The zero of energy is the formation energies of h type interfaces.

	Interface		Bulk	
	h	k	h	k
Nitrized	0.00	+0.38	+0.64	+1.02
Oxynitrized	0.00	+0.40	+1.13	+1.65

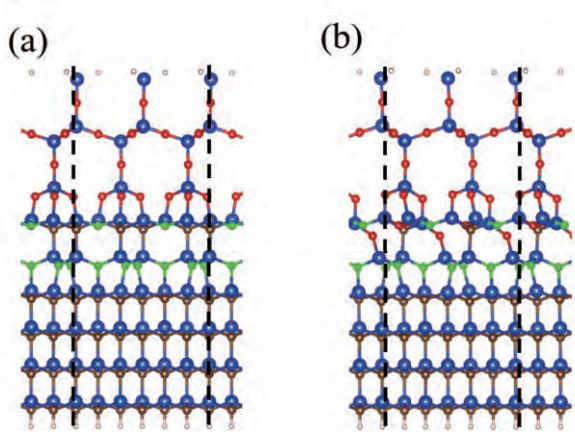

Figure 1: Computational models for (a) nitridized and (b) oxynitrized interfaces. Large (blue), small middle light (brown), and small dark (red) balls are Si, C, and O atoms, respectively. The vertical broken lines represent the boundary of the supercell.

field ion microscope.[3] Table 2 shows the formation energy of the interface, in which the minus of the formation energy means that the (oxy)nitrization occurs preferentially by the annealing. When we compare the (oxy)nitrized structures just below the interface and that in the bulk, the formation energy at the interface is smaller than that in the bulk, indicating that the N atoms introduced by the annealing accumulate just below the interface. Moreover, the previous theoretical calculations reported that the difference in the formation energies between the h and k type SiC/SiO_2 interfaces is comparable ($\sim$ 20meV/SiC(0001)-3x1).[4] The formation energy of the k type nitrized interface is much smaller than that of the h type nitrized interface. Because the variation of the conduction band edge due to the coexistence of the h and k type SiC/SiO_2 interfaces causes the scattering,[5] we can conclude that the NO annealing improves the carrier mobility by preferentially generating the h type nitrized interface.

References

[1] T. Ono *et al.*, Phys. Rev. B **96** (2017) 115311.

[2] K. Hirose, T. Ono, Y. Fujimoto, and S. Tsukamoto: First Principles Calculations in Real-Space Formalism (Imperial College, London, 2005).

[3] K. Yamada *et al.*, The 78th JSAP Autumn Meeting (2017) 5a-A203-3.

[4] C.J. Kirkham and T. Ono, J. Phys. Soc. Jpn. **85** (2016) 024701.

[5] S. Iwase, C.J. Kirkham and T. Ono, Phys. Rev. B **95** (2017) 041302(R).

Study on the Temperature Induced Stability of Defects on Rutile TiO_2(110) surfaces

Kenji YASUOKA

Department of Mechanical Engineering,

Keio University, Kohoku, Yokohama, Kanagawa 223-8522

TiO_2, a wide-gap semiconductor, have attracted considerable attention due to its potential applications as solar cell, photocatalysts and biocompatible materials.[1] There are three major polymorphs of TiO_2, rutile, anatase, and brookite. In particular, rutile TiO_2 (110) surface is known to be thermodynamically most stable surface and have been studied intensively as a model surface. Upon surface reaction on this surface, defects are known to take an important role,[2] however its microscopic property remains largely unknown.

In this study, we have approached this problem using first-principles molecular dynamics (MD) of interface between defective surface and water. By using this method, we were explicitly able to treat the dynamics of water and their chemical reaction with the TiO_2 (110) surface. This calculation was performed with multi-leveled parallelism on multiple computer nodes by taking advantages of the node-node data transmission technology such as the "enhanced hypercube" topology and 4× FDR InfiniBand 2× used in the System B.

As a result, bond formation between water molecule and surface Ti defect were observed. This result suggests that stability of Ti defect on the surface is stabilized by forming a bond. Since behavior of water is expected to depend largely on temperature, it can be anticipated that this mechanism is largely temperature dependent. This result is also in agreement with the experimental reporting by Wendt et al. [2], where they suggested importance of Ti defect at near-surface regions. The stabilization mechanism in this study may contribute to modifying theoretical estimate of surface defect concentration. It must be noted however, due to heavy computational cost, complete sampling of phase space is not taken yet. Thus, further calculation and statistical analysis is required to draw a final conclusion.

References

[1] U. Diebold: Surf. Sci. Rep. **48** (2003) 53.

[2] S. Wendt, P. T. Sprunger, E. Lira, G. K. H. Madsen, Z. Li, J. Ø. Hansen, J. Matthiesen, A. Blekinge-Rasmussen, E. Lægsgaard, B. Hammer and F. Besenbacher: Science **320** (2008) 1755.

Interaction between osmolytes in water revealed by ab initio molecular dynamics simulation

Tatsuhiko OHTO

Graduate School of Engineering Science,

Osaka University, 1-3 Machikaneyama, Toyonaka, Osaka 560-8531

Trimethylamine N-oxide (TMAO) and urea (shown in Fig. 1), which are small organic molecules solvated in water, coexist in cells of marine animals to control the osmotic pressure. TMAO stabilizes protein structure, whereas urea destabilizes it. But, the mechanism of cancellation of the effects due to TMAO and urea is not clear. In this work, we have identified how TMAO and urea interact in water by ab initio molecular dynamics (AIMD) simulation. We show that the interaction between both osmolytes is favored by hydrophobic association from the potential of mean force (PMF) shown in Fig. 2.

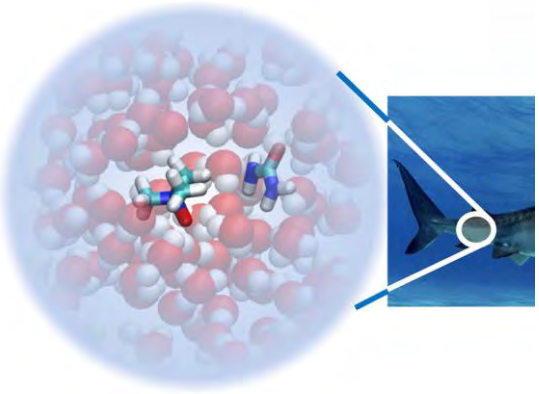

Fig. 1: Structures of the SAM-water interface and the snapshot.

Because one of the reviewers suggested that a simulation with a hybrid functional is necessary, we did it with revPBE0-D3 using the resource of the class D. Thanks to the additional calculations, the paper was published[1], although the data is not shown in the main text due to the short trajectory.

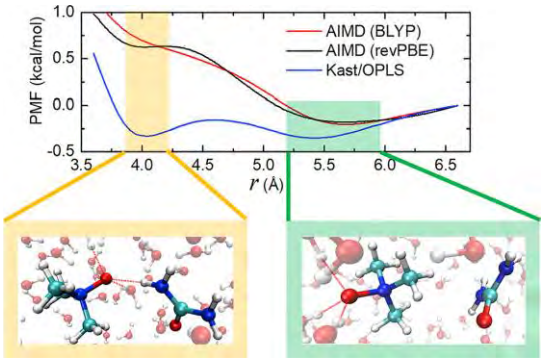

Fig. 2: PMF calculated with BLYP-D3, revPBE-D3, and a classical force field.

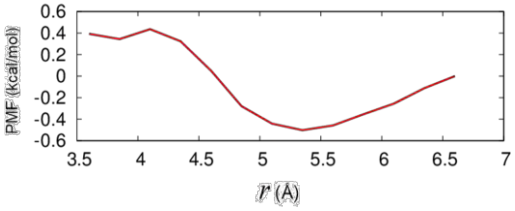

Fig. 3: PMF calculated with revPBE0-D3.

References

[1] W. J. Xie et al. Chem **4**, 2615 (2018).

First-principles molecular dynamics simulation of the interface between water and a supramolecular self-assembled monolayer

Tatsuhiko OHTO

Graduate School of Engineering Science,

Osaka University, 1-3 Machikaneyama, Toyonaka, Osaka 560-8531

Ab initio molecular dynamics (AIMD) simulation is a powerful tool to describe heterogeneous systems such as the water/solid interface. Although AIMD is computationally expensive, it describes electronic states beyond classical force fields,[1] which is important for interfaces.

We have simulated sum-frequency generation (SFG) spectra at the self-assembled monolayer (SAM)-water interface, shown in Fig. 1, using AIMD simulations. The SFG response of the N-H, C-H stretch is the key to understand the orientation and conformation of the SAM. In particular, the hydrogen bond network between melamine and barbituric acid can be detected from the sign of the N-H stretch resonses, if the stretch frequencies are well separated. We employed CP2K code [2], based on the Gaussian plane wave (GPW) method. About 20 ps of trajectory could be accumulated. We will continue running the AIMD and analyze the results after completing the AIMD simulations.

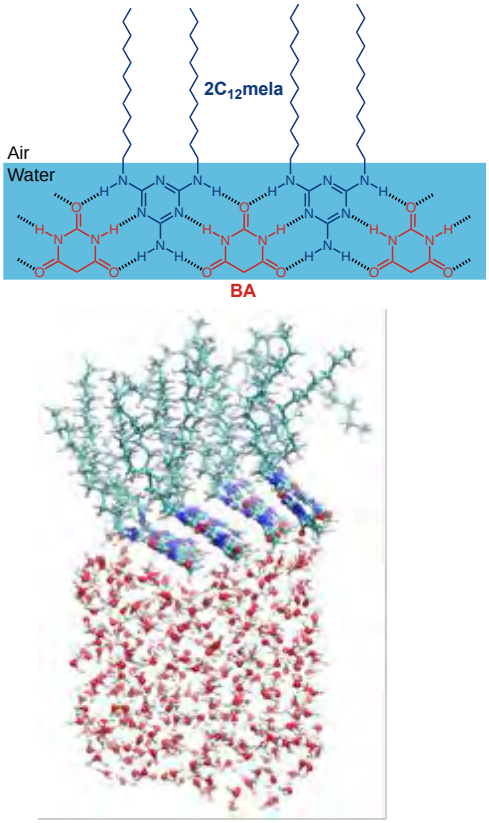

Fig. 1: Structures of the SAM-water interface and the snapshot.

References

[1] T. Ohto et al. Phys. Chem. Chem. Phys. **19**, 6909 (2017).

[2] The CP2K developers group, http://cp2k.berlios.de/

Ab initio molecular dynamics simulation of doped-graphene/water interfaces

Tatsuhiko OHTO

Graduate School of Engineering Science,

Osaka University, 1-3 Machikaneyama, Toyonaka, Osaka 560-8531

Ab initio molecular dynamics (AIMD) simulation is a powerful tool to describe heterogeneous systems such as the water/solid interface. Although AIMD is computationally expensive, it describes electronic states beyond classical force fields,[1] which is important for interfaces.

We have simulated sum-frequency generation (SFG) spectra of isotopically diluted water at the water-graphene and water-hexagonal boron-nitride (hBN) sheet interfaces, using ab initio molecular dynamics simulations. The simulations themselves were performed using ISSP several years ago and recently the paper was published.[2] A sharp 'dangling' O-D peak around ~2640 cm-1 appearing in both simulated SFG spectra evidences that both graphene and hBN are hydrophobic. The dangling O-D peak is 10 cm^{-1} red-shifted at the water-hBN interface relative to the peak at the water-graphene interfaces. This frequency difference manifests a stronger O-D…N intermolecular interaction between water and hBN than a O-D…C interaction between water and graphene.

To modify the hydrophobic interaction, we calculated doped-graphene water interfaces using the CP2K code [3]. We prepared 2 % B-doped, 2 % N-doped and 10 % N-doped graphene sheets. We tried to accumulate the 80 ps trajectory for each system and completed 80 % of AIMD runs. We will continue running the AIMD and analyze the results after completing the AIMD simulations.

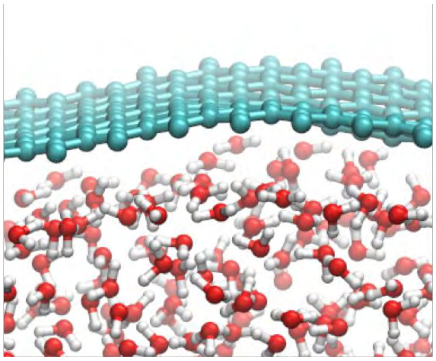

Fig. 1: Structures of the graphene-water interface.

References

[1] T. Ohto et al. Phys. Chem. Chem. Phys. **19**, 6909 (2017).

[2] T. Ohto et al. Phys. Chem. Chem. Phys. **20**, 12979 (2018)

[3] The CP2K developers group, http://cp2k.berlios.de/

Solid State Quantum Chemical Analysis of Fluorinated Polymer Electret

Seonwoo KIM, and Yuji SUZUKI

Department of Mechanical Engineering

The University of Tokyo, Hongo, Bunkyo-ku, Tokyo 113-8656

Electret is a dielectric with quasi-permanent charges. The electrons/ions trapped in the electret material can independently form electrostatic field more than tens of years. In recent years, a vibration-driven electret energy harvester that efficiently converts ambient vibration into electricity gathers much attention as a power source for low-power electronics. In order to improve the harvester's performance, it is essential to develop a new electret material with high surface potential and long-term charge stability.

An amorphous polymer electret CYTOP (AGC Inc.) has desirable characteristics for energy harvesting (low dielectric constant, hydrophobicity, high thermal stability, etc.). Performance of CYTOP as electret is dependent on its end-group, even the number of fluorinated repeat unit is much larger than that of the end-group. Figure 1. shows

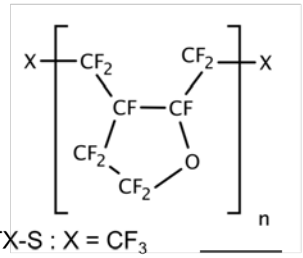

CTX-S : X = CF_3
CTX-A : X = COOH
CTX-M : X = CONH-C_3H_6-Si(OC_2H_5)$_3$

Fig. 1. Chemical structure of CYTOP series.

three kind of CYTOP series with different end-group. In recent study, we adopted long-range-corrected density functional theory (LC-DFT) analysis to calculate electron affinity (EA) of CYTOP series [1]. Calculated EA made qualitative agreement with material's performance as electret (surface potential, thermal stability of trapped charge). Yet, calculated EA was found to have considerable overestimation tendency, because the analysis is only performed for a free molecule in vacuum state, which is different from real solid polymeric system.

In this study, the authors aim to analyze real electron affinity of CYTOP electret. Solid state quantum chemical analysis is performed, acknowledging morphological diversity and influence of molecules surrounding the trap site to LC-DFT calculation.

Firstly, amorphous CYTOP system is prepared with molecular dynamic (MD) simulation. MD force field parameters are fitted with reference quantum mechanical (QM) calculation results, in order to make mimic QM behavior. Each system is made of 89 CTX-S hexamers and 1 CTX-X (X=S, A, M) hexamer to reflect ratio of end-group and repeat unit in real CYTOP. The system is firstly

mixed randomly at 1,000 K to form 1,000 identical random geometry, and then slowly cooled down to 300 K to create morphology of electron-trapped CYTOP system. The energy of molecule is calculated considering three terms; the first is QM term which we can obtain from CAM-B3LYP/6-31+G(d,p) level energy calculation. The second term is electrostatic energy shift. Wavefunctions obtained from QM calculation are converted to multipoles of rank 1-4 using multipole analysis package GDMA [2]. Influence of surrounding molecule to the charge trapping site is acknowledged by calculating multipole-multipole interaction between molecules. The third term is the multipole induction. Multipoles calculated in the second term influence each other thus correction term should be introduced. With these terms in hand, one can calculate solid state energy of a molecule at certain electronic state. Electron affinity is calculated while comparing molecular energy at neutral (0) and negatively-charged (-1) state. Normalized histogram is obtained from 1,000 identical cases, and portraited as density of state (DoS). Figure 2. shows result of solid state electron affinity analysis. Obtained DoS makes gaussian-like distribution. The medians of distribution are, 3.41 eV (CTX-S), 3.94 eV (CTX-A), and 4.56 eV (CTX-M). The electron affinity of CTX-S makes agreement with EA measured by LEIPS (3.6 eV) within error range [1], implying that the present method reflects real amorphous polymer electret system well.

The calculation is performed with SGI ICE XA ISSP system B, using quantum mechanical simulation package NWChem [3], molecular dynamic simulation package GROMACS [4], and solid state analysis package VOTCA-CTP [5]. Every calculation is held with 1 node (24 CPUs). In case of CYTOP hexamers, the calculation cost was approximately 150 CPU hours for QM calculation, 100 CPU hours for MD simulation, 5 CPU hours for multipole analysis and solid state analysis. In total, 765,000 CPU hours are used for analysis of CTX-S, CTX-A, and CTX-M.

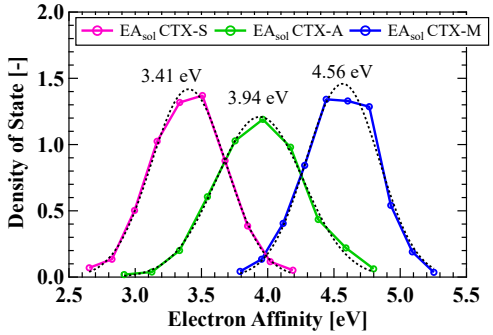

Fig. 2. Solid state electron affinity of CYTOP series.

This work was partially supported by JST CREST Grant Number JPMJCR15Q3.

References

[1] S. Kim et al., Sci. Technol. Adv. Mater., **19**, (2018), 486-494.

[2] A. J. Stone, J. Chem. Theory Comput., **1** (2005) 1128-1132.

[3] M. Valiev et al., Comput. Phys. Commun. **181**, (2010) 147.

[4] S. Pronk et al., Bioinformatics, **29**, (2013) 845-854.

[5] V. Rulhe et al., J. Chem. Thery Comput., **7**, (2011), 3335-3345.

First-principles calculation for muon and positron experiments of wide gap semiconductors

Mineo SAITO

Institute of Science and Technology, Kanazawa University

Kakuma, Kanazawa, 920-1192 Japan

The muon spin resonance is an effective tool to determine the dynamics of hydrogen in semiconductors since muonium bears similarities to hydrogen. Recently, application of this technique to wide gap semiconductors attract scientific interests. To confirm the reliability of density functional theory calculations, we study bond-centered muonium in silicon since this system has been intensively studied but there are still unresolved problems. In this study, we carry out a reliable calculation and quantitatively reproduce the experimental Fermi contact interaction constants (FCIC); the deviation is only 4 %. We find that a large size of supercell is necessary to obtain reliable results. We clarify that the spin density is negative at the muon site whereas it is positive at the nearest Si sites (Fig. 1). The negative spin density at the muon site is found to induce the negative FCIC.

Spin polarized positron annihilation technique detected some spin polarized vacancies in semiconductors. We systematically study the magnetic properties of vacancies in BN, AlN, GaN, BeO, ZnO, ZnS, and CdS by using the spin-polarized density functional theory. The magnetic moments in all nitride semiconductors are 3 μB whereas the other systems have the magnetic moments of 2 μB. In the case of GaN, we find that the real-space distribution of the majority spin density is narrower than that of the minority spin density, predicting that the positron-electron pair mometum density of the majority spin is broader than that of the minority spin.

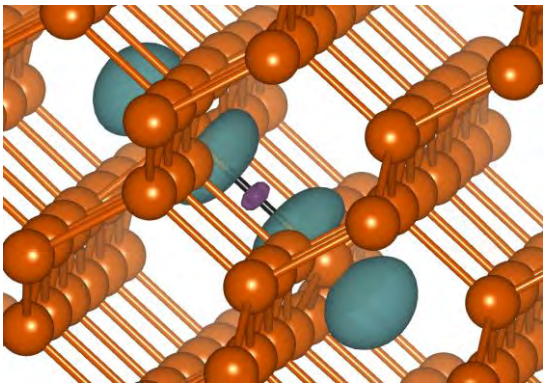

.Fig. 1

Development and application of first-principles simulation methods: from structure prediction to superconductivity

Shinji TSUNEYUKI

Department of Physics, School of Science,

The University of Tokyo, 7-3-1 Hongo, Bunkyo-Ku, Tokyo 113-0033

Institute for Solid State Physics,

The University of Tokyo, Kashiwa-no-ha, Kashiwa, Chiba 277-8581

We are developing and applying post-processes of first-principles simulations based on density functional theory (DFT) to tackle with structure prediction, superconductivity and dynamical phenomena in condensed matter. I summarize important achievements in FY2018 in the below.

(i) Data assimilation for crystal structure prediction

Theoretical prediction of unknown crystal structure has been a hard and longstanding problem in science since the number of possible structures increases rapidly with the number of atoms and elements in the unit cell. The problem is especially severe when we use first-principles simulations that require large computational cost even for one-shot calculation.

In this project, we are developing a method of structure prediction supported by experimental data. The method is designed to utilize powder diffraction data whose range of diffraction angle is limited by experimental setup or whose quality is insufficient for Rietveld analysis just like ultra-high-pressure experiments. In this method, instead of finding the global minimum of the multi-dimensional potential energy surface $E(\mathbf{R})$ as a function of the atomic positions $\mathbf{R}$, we define the effective potential $F(\mathbf{R})$ by the sum of $E(\mathbf{R})$ and a penalty function which increases when the simulated diffraction pattern deviates from the experimental one:

$$F(\mathbf{R}) = E(\mathbf{R}) + \alpha N D[I_{\mathrm{obs}}, I_{\mathrm{calc}}(\mathbf{R})].$$

Here, D is a function of experimental data I_{obs} and the calculated data $I_{\mathrm{calc}}(\mathbf{R})$. N is the number of atoms in the simulation cell and α is a control parameter. There are various possibilities for the mathematical expression of D, but in this project, we use crystallinity [1] or correlation coefficient.

In FY2018, we made a program that utilizes DFT for the calculation of $E(\mathbf{R})$ and realized simulated annealing with $F(\mathbf{R})$. We used the program to find structures of H_3S at ultra-high pressure and Y_2CH_3 successfully [2].

(ii) Spin fluctuation effect in superconducting DFT

Recently an extension method has been proposed that incorporates the effect of spin

fluctuation into the superconducting transition temperature calculation method based on the superconducting DFT (SCDFT) (Essenberger et al., 2014). We applied the method to non-magnetic iron at high-pressure and clarified that the energy dependence of the spin-fluctuation-mediated interaction can raise the transition temperature through the retardation effect.

(iii) Multiscale simulation of non-thermal ablation of metals

Laser processing is used in a wide range of applications. It is widely known that we have to use a laser with a pulse width of femtoseconds to perform metal microfabrication, but the physical mechanism is not well understood. Many differences between experimental and theoretical calculations have also been reported. Therefore, the optimum laser irradiation conditions at the time of laser processing often rely on empirical rules, and it is difficult to determine from simulation or theory. Our goal is to elucidate the physical mechanism of metal microfabrication.

Based on the results of finite-temperature DFT calculations, we have proposed an electronic entropy induced mechanism for the laser ablation that the entropy of electrons excited under non-equilibrium conditions plays a dominant role [3]. In FY2018, to discuss the validity of our mechanism, we made a multi-scale simulation method based on the two-temperature model, where we simulate the electronic temperature with finite difference method and the atomic motion with molecular dynamics. For this method, we made an interatomic potential model that depends on the electron temperature and formulated the equations of atomic motion so that the simulation satisfies the energy conservation law. With this method, we simulated laser ablation of Copper with changing laser fluence and successfully found atomic emission at low fluence, spallation and so-called phase explosion at high fluence [4].

References

[1] N. Tsujimoto, D. Adachi, R. Akashi, S. Todo and S. Tsuneyuki, Phys. Rev. Materials 2, 053801 (2018).

[2] N. Tsujimoto, Ph.D. Thesis, The University of Toyo (2019).

[3] Y. Tanaka and S. Tsuneyuki, App. Phys. Exp. 11, 046701 (2018) (Spotlights 2018).

[4] Y. Tanaka, Ph.D. Thesis, The University of Toyo (2019).

Analyses on self-organization processes using dissimilarity sampling

Yasuteru SHIGETA

Center for Computational Sciences,

University of Tsukuba, Tsukuba, Ibaraki, 305-8577

Self-organization is a phenomenon in which well-designed molecules spontaneously gather to produce unique structures and is a common process in nature and has great potential for providing a confined nanospace for molecular recognition, transfer, reaction, and catalysis. In particular, it is one of the essential elementary processes in the formation of structures of biological molecules, such as double helix DNAs and tertiary/quaternary structures of proteins, a membrane by the self-assembly of lipid bilayers, the formation of amyloid fibers, and so on. The molecular self-assembly in biological systems plays a crucial role in the function of cells. In order to design and synthesize a new molecular nanoarchitecture, understanding the formation mechanisms is quite essential.

Hiraoka *et al.* developed a hexameric aggregate, nanocube, assembled from gear-shaped amphiphiles (GSAs) **1** in a solvophobic environment. However, the formation process of $\mathbf{1}_6$ has not been completely explored yet. Generally, it is very difficult to elucidate self-assembly processes by conventional molecular dynamics (MD) simulations. Instead, we used a dissimilarity sampling method [2] for investigating the dissociation process of $\mathbf{1}_6$ into 6 monomers. Figure 1 shows the representative structures from pentamer to dimer [3]. Judging from the dissociation processes we suggested the formation process and important structures. Once a stable trimer, $\mathbf{1}_3$, is formed, it creates a hydrophobic core to absorb hydrophobic guest molecules in the space in contact with three HMEs. These guest molecules further stabilize $\mathbf{1}_3$ and might accelerate the formation of the nano- cube, because more non-covalent interactions strengthen the stability not only of $\mathbf{1}_6$, but also of other oligomeric structures, especially $\mathbf{1}_2$ or $\mathbf{1}_5$. Conversely, a hydrophobic molecule of suitable size, say two tribromomesitilenes, serves as a nucleation core to form a quite stable nanocube.

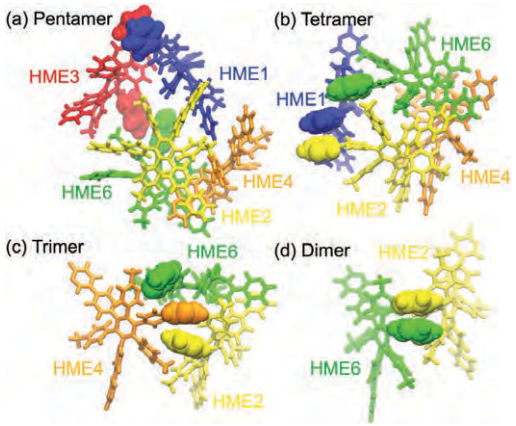

Figure 1 Structures of *n*-mers (n = 2 to 5)

References

[1] S. Hiraoka, K. Harano, M. Shiro and M. Shionoya, J. Am. Chem. Soc. **130** (2008), 14368–14369.

[2] R. Harada, T. Mashiko, M. Tachikawa, S. Hiraoka, Y. Shigeta: Phys. Chem. Chem. Phys. **20** (2018) 9115.

Optical properties of six isomers of a carbon nanocage

Yoshifumi NOGUCHI

Department of Applied Chemistry and Biochemical Engineering, Graduate School of Engineering, Shizuoka University, Johoku 3-5-1, Hamamatsu, Shizuoka 432-8561, Japan

In 2014, a carbon nanocage ($C_{96}H_{80}$), which corresponds to the joint part of a branched carbon nanotube, was successfully synthesized and its optical properties were measured in solution [1]. However, because benzene rings connected through a single C-C bond can rotate each other, the external experimental and environmental conditions can easily reverse the order of stability of the energetically close six isomers; thus, isomers have not yet been identified through the measured the UV-vis absorption spectra in the solution.

In this study, we applied the first-principles GW+Bethe-Salpeter method based on the many-body perturbation theory and attempted to identify the isomers through a comparison between the simulated and experimentally measured UV-vis absorption spectra. In our simulation, we used an original first-principles program, in which employs an all-electron mixed basis approach. With this program, the GW+Bethe-Salpeter calculation for a 176 atoms system can be completed within 3 days, when 288 INTEL XEON processors (or 3456 CPU cores) and total 18 TB memory on a system B supercomputer are used.

The experimental UV-vis absorption spectra were measured in the solution at a finite temperature [1] and the theoretical spectra were simulated for the most stable (labeled as D2) and most unstable (labeled as T) isomers in vacuum at zero temperature [2]. The peak top position is 3.92 eV for the experimental spectrum, 4.02 eV for D2, and 3.93 eV for T. Although both isomers are in a good agreement with the experimental results, the most unstable isomer, T, is clearly better than D2. In addition, the other spectral parameters such as the height of the second peak and the peak width show better results for T. The results of this study suggest that the T isomer is more strongly stabilized by the external experimental conditions such as by the solvation effect.

References

[1] K. Mitsui, Y. Segawa, and K. Itami: J. Am. Chem. Soc., **136** 16452 (2014).

[2] Y. Noguchi, D. Hirose, and O. Sugino: Eur. Phys. J. B. **91** 125 (2018).

Direct coupling of replica exchange Monte Carlo method with first-principles calculations for thermodynamic sampling of configurational disorder in solids

Shusuke KASAMATSU

Academic Assembly, Yamagata University

1-4-12 Kojirakawa, Yamagata-shi, Yamagata 990-8560

Metal and oxide alloy systems have varying degrees of disorder which determine the physical properties of those systems. To simulate such disorder, a natural approach may be to combine first-principles calculations based on density functional theory (DFT) with Metropolis Monte Carlo sampling. However, due to the high computational cost of DFT calculations, many previous works have relied on lightweight models fitted to density functional calculations. Due to the difficulty in obtaining reliable *and* lightweight models, this approach has seen limited use in many-component systems. Thus, in this project, we decided to reexamine the feasibility of bypassing the use of fitted models through efficient use of cluster supercomputers.

To we decided to rely on the replica exchange Monte Carlo (RXMC) method [1]. The Figure shows our computational scheme. There are N_{repl} Metropolis samplers running in parallel. Each of the samplers spawns parallel DFT processes (we used VASP [2]) to perform local structural relaxation and energy calculation at every Metropolis step. We benchmarked the scheme on the calculation of the degree of cation disorder in $MgAl_2O_4$ and found that it is efficient enough to perform sampling without resorting to fitting models [3]. In other words, we showed that it is now possible to sample configurational disorder in solid state systems directly from first principles through a combination of parallel sampling algorithms and state-of-the-art supercomputers,

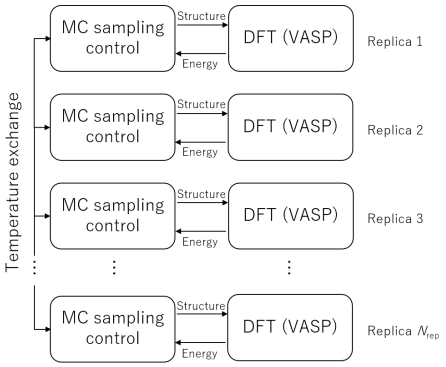

Fig. :. Our RXMC-DFT sampling scheme.

References

[1] K. Hukushima and K. Nemoto: J. Phys. Soc. Jpn. **65** (1996) 1604.

[2] G. Kresse and J. Furthmueller: Phys. Rev. B **54** (1996) 11169.

[3] S. Kasamatsu and O. Sugino: J. Phys.: Condens. Matter **31** (2019) 085901.

First-principles quantitative approach to the interplay of charge and spin fluctuations in superconductors

Ryosuke AKASHI
Department of Physics, University of Tokyo
Hongo, Bunkyo-ku, Tokyo 133-0033

In this project, we investigated the interplay of the dynamical charge and spin fluctuation effects in the superconductors. Many superconductors are classified as "conventional", where the electronic pairing is dominated by the mechanism mediated by the phonon exchange between the electrons. In such systems, the effects of the electron-electron Coulomb interaction is secondary, but still have quantitative impact on the superconducting T_c. The screened static Coulomb interaction strongly suppresses the pairing. On the other hand, the dynamical fluctuations of charge and spin degrees of freedom, which also originates from the Coulomb interaction, can affect the pairing via more complex mechanisms. In the uniform electron gas, the former is expected to enhance the pairing (plasmon mechanism [1, 2]), whereas the latter, which is presumably uniform ferromagnetic fluctuation induced by the exchange effect, suppress the phonon-induced singlet pairing [3]. But for non-uniform realistic cases the situation is thought to be more complicated.

Recently, there has been progress in the first-principles calculation method for superconductors. The density functional theory for superconductors (SCDFT [4, 5]) has been extended to include the charge [2] and spin fluctuation [6] effects. This enables us to elucidate the abovementioned complicated interplay of the fluctuation effects in real superconductors from first principles.

We addressed the superconducting phase in iron emerging under pressure. Although the elemental iron is ferromagnetic metal, at pressure of several ten GPa, its crystal structure changes into the hcp one, the magnetic order vanishes and superconductivity occurs with $T_c \simeq 3\ K$ [8]. This superconducting phase is obviously on the verge of the magnetic transition point and coexistent with strong spin fluctuation and its role on the superconducting phenomenon should be non-trivial.

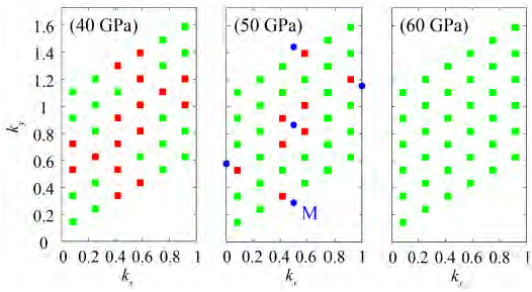

FIG. 1. **q**-point grid in the primitive hcp Brillouin zone on the $q_z = 0$ plane. Red points indicate where the sign change of the eigenvalues of D (see Eq. (2)) occurs, whereas at the green points D is positive definite. The sign change represent the strong spin fluctuation with wavenumber $\mathbf{q} = M$

According to the SCDFT, the superconducting order parameter at temperature T is determined by the following gap equation

$$\Delta_{n\mathbf{k}} = -\mathcal{Z}_{n\mathbf{k}}\Delta_{n\mathbf{k}} - \frac{1}{2}\sum_{n\mathbf{k}} \mathcal{K}_{n\mathbf{k}n'\mathbf{k}'} \frac{\tanh\frac{\beta E_{n'\mathbf{k}'}}{2}}{E_{n'\mathbf{k}'}} \Delta_{n'\mathbf{k}'}. \tag{1}$$

Δ is the order parameter and $n\mathbf{k}$ labels the Kohn-Sham band index and crystal wavenumber, respectively. $E_{n\mathbf{k}} = \sqrt{\xi_{n\mathbf{k}}^2 + \Delta_{n\mathbf{k}}^2}$ and β is the inverse temperature. The gap equation kernels $\mathcal{Z}$, $\mathcal{K}$ have been formulated so that the mass-renormalization and pairing effects mediated by the phonons and electron-electron Coulomb interactions, and can be

evaluated with the output of the normal-state Kohn-Sham equation and phonon properties obtained with the density functional perturbation theory [5–7]. We examined the spin fluctuation effects on the superconducting phase by evaluating the T_c with the gap equation using the formulas of $\mathcal{Z}$ and $\mathcal{K}$ with and without the spin fluctuation.

First, in a certain pressure range, we found numerical divergence of the kernels. To clarify its origin, we analyzed the dynamical spin susceptibility χ calculated with the following formula in the plane-wave basis $\{\exp[i\mathbf{G}\cdot\mathbf{r}]\}$

$$\sum_{\mathbf{G}_2}\left[\delta_{\mathbf{G}\mathbf{G}_2}-\sum_{\mathbf{G}_1}\chi^{\mathrm{KS}}_{\mathbf{G}\mathbf{G}_1}(\mathbf{q},i\omega_n)I^{\mathrm{xc}}_{\mathbf{G}_1\mathbf{G}_2}\right]\chi_{\mathbf{G}_2\mathbf{G}'}(\mathbf{q},i\omega_n) = \chi^{\mathrm{KS}}_{\mathbf{G}\mathbf{G}'}(\mathbf{q},i\omega_n),$$

where χ^{KS} denotes the independent particle polarizability calculated with the Kohn-Sham states. This formula is abbreviated by the matrix representation

$$D\chi = \chi^{\mathrm{KS}}. \tag{2}$$

The divergence of χ occurs when any eigenvalues of D changes from positive to negative through zero. We found that this sign change occurs with $\omega_n = 0$ around a certain $\mathbf{q}$ point in the Brillouin Zone as shown in Fig. 1. This divergence is thought to be an artifact originating from the approximate formula Eq. (2), but at least indicates large spin fluctuation with the corresponding wavenumber. We hence limited the calculation with the spin fluctuation to the high pressure regime where D is positive definite.

The calculated superconducting T_c with and without the spin fluctuation is shown in Fig. 2. First we note that in the pressure regime where the superconducting phase is experimentally observed ($\lesssim$ 30 GPa), the calculation yields the ferromagnetic phase as the ground state (in the pressure region indicated by "FM" with an arrow), at odds with the experiment. We then assume that the generalized gradient approximation (GGA [9]) for

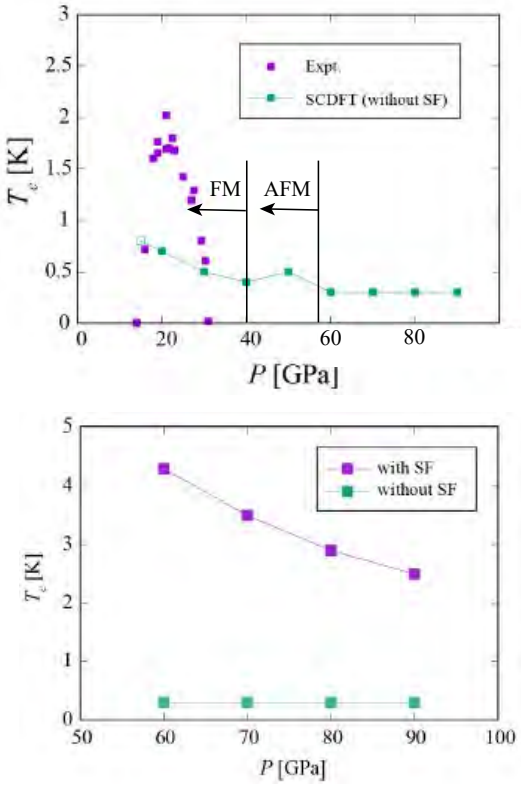

FIG. 2. Calculated and experimentally observed T_cs of Fe under pressure. (upper) Experimental values and the calculated results without the spin fluctuation (SF) effect. The arrows indicate the pressure regions where ferromagnetic phase is stabilized and antiferromagnetic fluctuation diverges numerically. (lower) The calculated results with and without the SF effect.

the exchange correlation functional tends to overestimate the stability of the magnetic order. The calculated T_c without the spin fluctuation effect shows little pressure dependence as shown in the left panel. On the other hand, with the spin fluctuation effect, T_c shows a decreasing trend with increasing the pressure. This could corresponds to the right half of the dome-like dependence observed experimentally. Interestingly, the spin fluctuation enhances the T_c, which cannot be explained with the simplistic uniform electron gas picture mentioned above. This result suggests a novel superconducting mechanism could be possible where the spin fluctuation is the main driving force of the superconducting pairing in the

compressed iron.

The above results have been published as a dissertation [10]. The first-principles electronic structure calculations were done with the plane-wave basis code package QUANTUM ESPRESSO (5.1)(Ref. [11]). The phonon and electron-phonon properties were calculated with the PHonon program in this package, which is based on the density functional perturbation theory [12]. The Brillouin-Zone integration for the metallic systems were done with the optimized tetrahedron method [13]. The GGA-PBE [9] exchange-correlation potential was used. Parallel calculation was performed with respect to **k** points (*-npool* option) as implemented in *ph.x* code. The calculations were mainly done in System B.

[1] Y. Takada, J. Phys. Soc. Jpn. **45**, 786 (1978).

[2] R. Akashi and R. Arita, Phys. Rev. Lett. **111**, 057006 (2013).

[3] N. F. Berk and J. R. Schrieffer, Phys. Rev. Lett. **17**, 433 (1966).

[4] M. Lüders, M. A. L. Marques, N. N. Lathiotakis, A. Floris, G. Profeta, L. Fast, A. Continenza, S. Massidda, and E. K. U. Gross, Phys. Rev. B **72**, 024545 (2005).

[5] M. A. L. Marques, M. Lüders, N. N. Lathiotakis, G. Profeta, A. Floris, L. Fast, A. Continenza, E. K. U. Gross, and S. Massidda, Phys. Rev. B **72**, 024546 (2005).

[6] F. Essenberger, A. Sanna, A. Linscheid, F. Tandetzky, G. Profeta, P. Cudazzo, and E. K. U.Gross. Phys.Rev. B, **90** 214504 (2014).

[7] R. Akashi, M. Kawamura, S. Tsuneyuki, Y. Nomura, and R. Arita, Phys. Rev. B **91**, 224513 (2015)

[8] K. Shimizu, T. Kimura, S. Furomoto, K. Takeda, K. Kontani, Y. Onuki, and K. Amaya, Nature **412**, 316EP (2001).

[9] J. P. Perdew, K. Burke, and M. Ernzerhof, Phys. Rev. Lett. **77**, 3865 (1996).

[10] Y. Hizume, Master thesis "Theoretical study on the effect of spin-fluctuation in superconductivity in iron under high pressure" (Department of Physics, The University of Tokyo, 2019).

[11] P. Giannozzi *et al*, J. Phys.: Condens. Matter **21**, 395502 (2009); http://www.quantum-espresso.org/.

[12] S. Baroni, S. de Gironcoli, A. Dal Corso, and P. Giannozzi, Rev. Mod. Phys. **73**, 515 (2001).

[13] M. Kawamura, Y. Gohda, and S. Tsuneyuki, Phys. Rev. B **89**, 094515 (2014).

First-principles study of ionization and diffusion of metal atoms at metal/solid interfaces in electric fields: toward semiconductor and organic substrates

Takashi NAKAYAMA
Department of Physics, Chiba University
1-33 Yayoi, Inage, Chiba 263-8522

Metal/solid interfaces are essential structures for various electronic/optical devices. During the fabrication and operation of devices, however, a variety of defects are often generated, particularly from their interfaces in electric fields, which produces various carrier traps and promotes the degradation of devices. However, there are little theoretical works on defect formations around metal/solid interfaces. In this works, we studied the formations of various point defects, such as interstitial metal atoms, atom vacancies, and impurity dopants, around metal/solid interfaces in electric fields using first-principles calculations.

To simulate the interfaces, we adopt (2×2)–(4×4) metal/solid repeated-slab models made of 4 ML metal atoms and 16 ML inorganic/organic solids. The formation energy of a point defect was calculated as a function of the distance from the interface by the standard first-principles method in the density functional theory. We employ a primitive method to produce an electric field perpendicular to the interface by simply removing electrons from the present slab system. All atom positions are optimized for all interfaces.

Figs. 1(a)-1(c) show the formation energies of C-vacancy, P-dopant, and Al-dopant defects in SiC layers around Au/2H-SiC interfaces, respectively, as a function of the distance from the interface, for various values of electric fields. The formation energies of point defects gradually increase with increasing the distance from the interface in the case without an electric field, which is a general trend observed for point defects around metal/solid interfaces. The most remarkable feature is that, with increasing the electric field, the formation

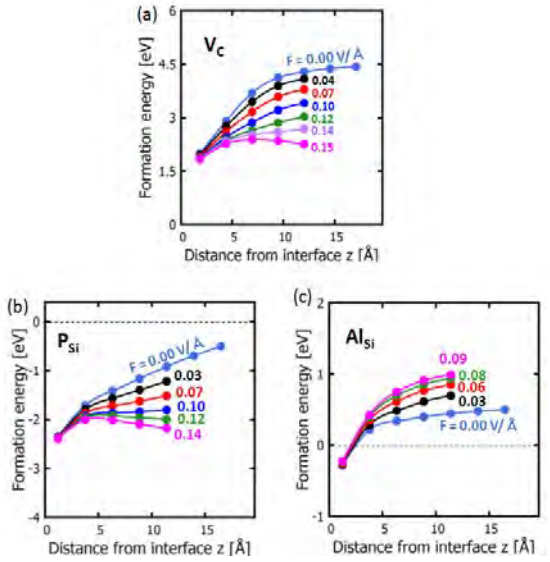

Fig.1. Calculated formation energies of (a) C-vacancy, (b) P dopant, and (c) Al dopant as a function of the distance z of a defect from the Au/2H-SiC interface. The cases with various electric fields (F = 0-0.15 V/Å) are shown in different colors.

energies in inner 2H-SiC layers decrease for the former two defects, while it increases for the latter defect. We also studied various point defects and found that formation of anion vacancies and donor-type dopants is easy, while the formation of acceptor-type dopants becomes difficult around the metal/solid interfaces when the positive voltage is applied to the metal electrode.

To understand the variation of formation energy, we show the ionization charges of C-vacancy in Fig. 2(a), as a function of the distance from the interface. We can clearly see that the ionization charge increases with increasing the electric field. This variation is explained by considering the capacitor model shown in Fig. 2(b). When the C vacancy is produced in 2H-SiC layers, the electron-

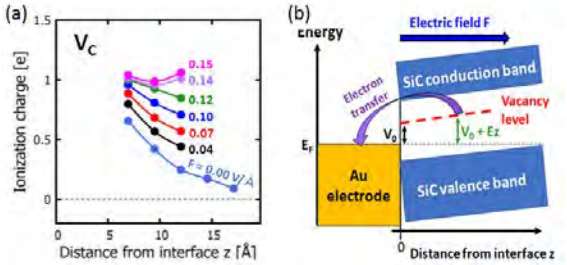

Fig.2. (a) Calculated ionization charge of C-vacancy as a function of the distance from the Au/2H-SiC interface for various values of electric fields (F = 0-0.15 V/Å). (b) Schematic picture to explain the electron transfer between electronic state of defect and metal electrode around metal/solid interface in electric field, for the cases of C-vacancy.

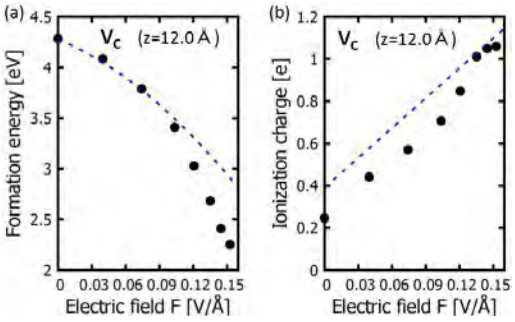

Fig.3. (a) Calculated formation energy and (b) ionization charge of C-vacancy at z = 12 Å around the Au/2H-SiC interface, as a function of the electric field. Dots are obtained by the first-principles calculation, while blue dashed lines are by the capacitor model.

occupied vacancy state appears in the band gap of 2H-SiC. Since the Fermi energy of Au electrode E_F is located below this state, the electron transfer q occurs from the vacancy state to the Au layers as shown by the arrow in Fig. 2(b). By considering the energy gain and loss by this electron transfer, we obtain the formation energy and ionization charge of C-vacancy as $E_{form}(F, z) = E_0 - \varepsilon SF^2 z/2 - \varepsilon SFV_0 - \varepsilon SV_0^2/2z$ and $q = \varepsilon SF + \varepsilon SV_0/z$, where E_0 is the formation energy in bulk SiC, F the electric field, z the distance from the interface, S the effectice area of ionization charge, V_o the energy position of vacancy state, and ε the dielectric constant of SiC.

Figures 3(a) and 3(b) show the variations of the formation energy and ionization charge of C vacancy at the fixed z = 12Å position. We can see that such variations are well explained by the present capacitor model. In this way, the electron transfer between defect and metal electrode is the key to understand the variation of defect formation energies around the metal interface in electric field.

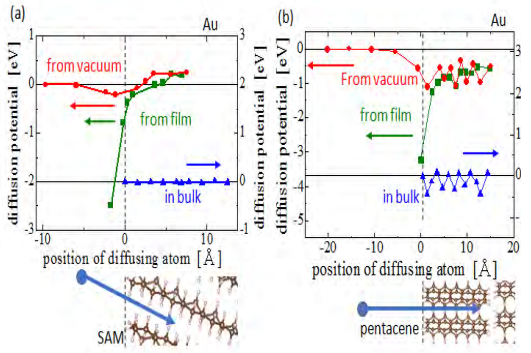

Fig.4. Calculated diffusion potentials for Au metal atom in (a) SAM and (b) pentacene solids, as a function of metal- atom position. Lower pictures display the corresponding position.

Then, we consider the cases of metal/organic solid interfaces. Figures 4(a) and 4(b) show the diffusion potentials of Au atom around Au/SAM and Au/pentacene interfaces. In the case of SAM, metal atom easily penetrates and diffuses in solids reflecting the weak interaction between metal atom and molecules. In case of pentacene, on the other hand, since the interaction between metal atom and molecules is attractive and strong, metal atom actively enters into solids and is tightly bonded to molecules. The difference in metal-atom behavior comes from the difference in electronic structure between SAM and pentacene, which are respectively σ- and π-orbital molecular systems.

All these calculations were performed using the xTAPP, VASP, and pspwf codes. In order to realize the calculations for the present interface systems in electric fields, because the system is made of a large number of atoms (300-1000 atoms), the advanced computing facility having multi-task and higher-speed CPU (more than 64 cores × 2.5GHz), larger-size memory (around 128GB), and larger-size strange (more than 1 TB) is indispensable. These conditions are realized only by the ISSP supercomputing systems.

Redox-driven spin transition in layered battery materials

Atsuo YAMADA

Department of Chemical System Engineering,

The University of Tokyo, Bunkyo-ku, Hongo, Tokyo 113-8656

Electronic spin plays a crucial role in determining the physical and chemical properties of transition-metal compounds. In battery ceramics electrode materials containing transition-metals *M*, it is likely that *M* exhibits a hitherto unreported redox-driven spin transition (RDST), which might considerably influence the operating potential of the electrodes.

In the present study, we have discovered an existence of RDST occurring for the Co^{3+}/Co^{2+} redox couple in layered transition-metal oxides using density functional theory calculations, leading to a colossal potential hysteresis (> 1 V) between the cathodic (low spin (LS) Co^{3+} to LS Co^{2+}) and anodic (high spin (HS) Co^{2+} to HS Co^{3+}) reactions.

All the calculations are performed using Vienna Ab-initio simulation package (VASP). The projector-augmented-wave (PAW) method and a plane-wave basis set with a kinetic energy cutoff of 550 eV were used. We applied GGA+U where values of U_{eff} = 3.9, 4.0, 3.4, 6.0 eV were used for the *d* electrons of Mn, Fe, Co, and Ni atoms, respectively.

Our work points to the considerable influence of the spin-state variance on their battery performance. In a practical sense, redox-driven spin transitions cause a large voltage hysteresis and a large loss in energy efficiency. Thus, Co^{3+}/Co^{2+} should be used with care as the redox couples in battery electrodes.

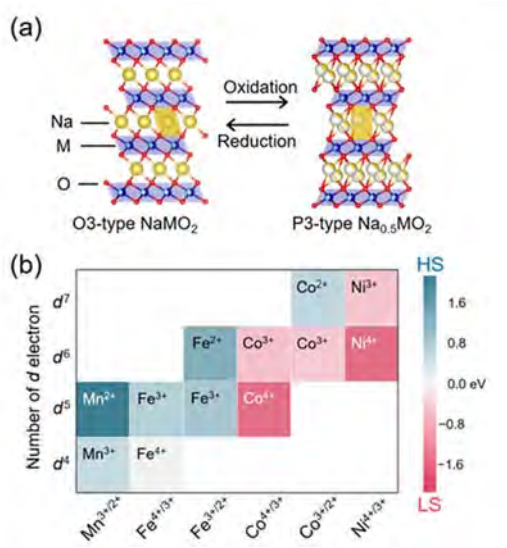

Fig. 1: (a) Schematic illustration of Na_xMO_2 upon Na^+ (de)intercalation. (b) Stable spin states of M''^{n+} in $Na_xTi_{0.5}M'_{0.5}O_2$ and $Na_xAl_{0.5}M'_{0.5}O_2$.[1]

References

[1] Eriko Watanabe, Masashi Okubo, Atsuo Yamada et al, *Chem. Mater*., **31** (2019) 2358.

[2] Eriko Watanabe, Yuki Yamada, Masashi Okubo, Atsuo Yamada et al, *Chem. Rec*., **19** (2019)

First-Principles DFT Calculations for Topological-Insulator Multilayers

Kunihiko YAMAUCHI
ISIR-SANKEN, Osaka University, Ibaraki, Osaka 567-0047

Based on *Ab-initio* approach, we have theoretically designed heterostructure of various tetradymite-type topological insulators. A three-dimensional topological insulator exhibits the non-trivial quantum states which can be characterized by the insulating bulk states and the spin-polarized metallic surface states. The latter is known to have a Dirac cone dispersion and show the helical spin structure, as having an appealing potential for future spintronics device applications. Although the highly insulating bulk state and the tunable Dirac cone in the bulk band gap are desired for the applications, many of topological insulators have been found to be metallic due to the existence of impurities and/or structural disorder.

In order to tune the Dirac points energy, we control the artificial multilayer composed of Bi_2Se_3-related topological quintuple layers. Band-structure calculations are performed by using a projector augmented wave method implemented in Vienna Ab initio Simulation Package (VASP) code with generalized gradient approximation. After the crystal structure was fully optimized, the spin-orbit coupling was included self-consistently. MPI parallelization was performed over bands and plane wave coefficients using $16 \sim 96$ cores in system B.

After we tested several combinations of hetero-structural slabs, some successful results are obtained as shown in Fig. 1. Here the Dirac point is located exactly at the middle of the band gap at the $\overline{\Gamma}$ point, while the bulk band structure keeps rather large band gap. In order to understand the shift of the surface-state energy, the work function of slab structure was evaluated. It reveals that the surface energy is determined by the difference in work function between surface and bulk materials. Our finding provides a way to obtain the ideal Dirac cone state in artificial multilayers of topological insulator that is appealing for the future spintronics applications.

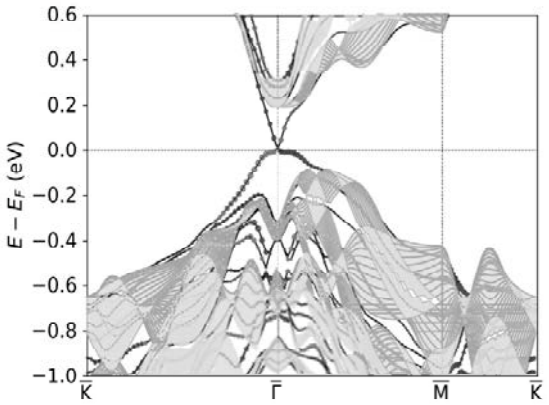

Figure 1: Calculated bandstructure of a multilayer slab which consist of ternary tetradymite topological insulators. The spin-polarized surface states are indicated by open and filled circles. The bulk band projection is also shown.

References

[1] T. Kosaka, K. Yamauchi, and T. Oguchi: in preparation.

Large scale ab initio calculations on the fundamental processes of solar energy convergence devices and on designing principles for new materials

Koichi YAMASHITA

Department of Chemical System Engineering, School of Engineering,

The University of Tokyo, 7-3-1, Hongo, Bunkyo-ku, Tokyo 113-8656

1. Defect structures and anion orderings on perovskite photocatalysts for water-splitting

Water-splitting photocatalysts are expected as hydrogen production devices using sunlight, but, its energy-conversion efficiency is still low for practical use. Recent studies have reported that the defects and anion orderings improve the physical properties of semiconductors. Therefore, we investigated the defects or anion orderings.

Defective perovskite oxides $Sr_{1-x}NbO_3$ have recently been reported as water-splitting photocatalysts. Its band structure is metallic, but it can split water into oxygen or hydrogen by specific sacrificial reagents, and the carrier mobility is expected to be high. In this work, we performed density functional theory (DFT) calculation to identify the bands and *k*-points that can absorb light nearby experimental optical gap, which suggested that the Fermi level is shifted due to the formation of Sr defects and O vacancies, the optical gap is changed, and the absorption of light can be controlled by the defect amount. Besides, the defect dependence of the optical gap suggests that Sr defects and O vacancies may coincide. [1]

The band gaps of certain perovskite oxynitrides are suitable for water-splitting under visible light irradiation. However, due to the myriad of anion orderings, traditional DFT calculations can only investigate some of them. In this work, we combined DFT calculations with machine learning to rapidly predict the large size anion ordering of $BaNbO_2N$, which can oxidize water under light irradiation up to 740 nm. The machine learning model was trained to predict the energy and band gap obtained by DFT calculation from the anion ordering. Our method has reduced more than 99.99% of the calculation cost of predicting total energy using only DFT calculation. Besides, by using the Metropolis method, we were able to predict the stable anion configuration of a large supercell, which is difficult to calculate using DFT calculations. This work demonstrates a means of predicting the properties of functional materials based on more realistic elemental ordering with a reasonable computational load. [2]

2. Device-Scale Simulations of Organic Photovoltaics for Performance Improvement

Organic photovoltaics, OPVs, are promising energy harvesting devices, but their power conversion efficiencies are lower than traditional silicon ones. Morphology—the degree of phase

separation and miscibility of the organic semiconductors—is a key factor for performance improvement since it strongly affects exciton dissociation and charge collection. Bulk heterojunction, BHJ, morphologies are widely adapted because of both of nanoscale phase separation (~10 nm) and bicontinuous transport pathways. There are many experimental techniques to observe morphologies; especially, conductive atomic force microscopy (C-AFM), a contact-mode variant of AFM, offers high-resolution (from a few to dozens of nanometers) examination of components under the probe tip. It is, however, challenging to experimentally obtain three-dimensional high-resolution information about morphologies.

In this work, C-AFM of BHJ morphologies was simulated by dynamic Monte Carlo algorithm [3] to obtain three-dimensional information from two-dimensional images. The system was ITO/P3HT:PCBM/Al as a model since it has been well studied. The device scale (50^3nm^3, 1-nm grid) morphologies were generated by Metropolis Monte Carlo of reptation [3]. Charge injection, hopping, recombination, and extraction were stochastically simulated. We analytically solved Laplace equation of a bispherical coordinate system to obtain the electric potential arising from the applied voltage and the difference of Fermi levels of the electrodes. Simulations were performed for all the probe points, *i.e.* lattices on the surface, and the currents were evaluated.

The cross-sections of morphologies and hole injection current are shown in Fig. 1 Hole injection current ranges from a few picoamperes to a few hundreds of picoamperes when a probed lattice was donor, which agrees with experiments. On the other hand, electron injection current was low (0.02 pA at maximum) due to high injection barrier and low potential gain, resulting in no charge recombination. Morphologies with smaller interfacial areas tended to show higher current because of their favorable transport pathways.

In this work, only a few morphologies were examined as model cases. This simulation is viable for high throughput computations, which will enable to predict three-dimensional morphologies from experimental C-AFM images with such technique as machine learning.

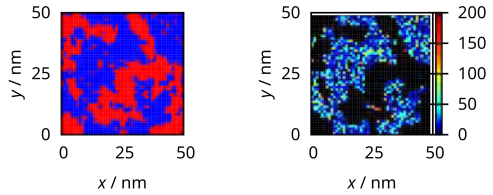

Fig. 1: (left) A cross-section and (right) a simulated C-AFM image (hole injection current divided by pA) of a BHJ morphology. Blue and red lattices represent donor and acceptor, respectively.

References

[1] M. Kaneko, K. Mishima, and K. Yamashita: J. Photochem. Photobiol. A: Chem. **375** (2019) 175–180.

[2] M. Kaneko, M. Fujii, T. Hisatomi, K. Yamashita, and K. Domen: J. Energy Chem. **36** (2019) 7–14.

[3] E. Kawashima, M. Fujii, and K. Yamashita: Phys. Chem. Chem. Phys. **18** (2016) 26456–2646.

Singular atomic structure and its electronic property in oxide material

Kazutoshi INOUE[1],Mitsuhiro SAITO[2], and Yuichi IKUHARA[1,2,*]
[1] *Advanced Institute for Materials Research, Tohoku University, Sendai, Miyagi, 980-8577*
[2] *Institute of Engineering Innovation, The University of Tokyo, Yayoi, Tokyo, 113-8656*

We found a formation of singular atomic structures in MgO thin films around grain boundaries and grain-boundary triple junctions through a combination of scanning transmission electron microscopy (STEM) and first-principles calculations [1]. The atomic arrangements possess a two-dimensional random arrangement of one-dimensionally ordered atomic columns which is different from the known solid states — crystal, quasicrystal and amorphous. The structure is referred to as the "one-dimensionally (1D) ordered crystal" which can be a metastable phase in a confined region. They consist of the structural units that are similar to the ones found in coherent grain boundaries.

The MgO thin film was deposited on metallic thin films by RF-magnetron sputtering in high vacuum at room temperature. STEM observations were carried out with a 200kV STEM with a sub-Å resolution. Atomic models were constructed from STEM images. Then, density-functional theory calculations were carried out using Vienna Ab-initio Simulation Package (VASP) within projector augmented wave scheme with an energy cut-off of 500 eV. We applied the generalized gradient approximation of Perdew, Bucke, and Ernzerhof to address exchange-correlation functional. Sampling of the irreducible Brillion Zone (BZ) was performed with a regular Monkhorst-Pack grid of Gamma centered 9×9×9 and 13×13×13 k-points for the 1D ordered crystal and the MgO bulk, respectively. Full relations of all atoms were itinerated under the conjugate gradient algorithm until the magnitude of Hellmann-Feynman force on each atom converged to less than 0.03 eV/Å. Total energy was calculated using the linear tetrahedron method with Blöchl correction.

To obtain accurate electronic properties for the 1D ordered crystal and its bulk counterpart, the hybrid HSE06 functional was adopted to determine the electronic density of states (DOS). A set of Gamma-centered 5×5×7 k-points and a Gaussian smearing scheme with a converged width of 0.05 eV for integrating BZ were applied. The energy tolerance was converged less than 10^{-5} eV. The HSE06 gives a much more accurate prediction of the band gap of 6.5 eV for the bulk MgO. The total DOS indicates a significantly reduced band gap of 3.0 eV for the 1D ordered crystal which is obviously smaller than that of the bulk MgO.

To confirm the theoretical predictions, we also measured the band gaps using low-loss electron energy loss spectroscopy (EELS) with a monochromated STEM. The band gaps of the 1D ordered crystal and the bulk MgO are measured to be 3.2 eV and 7.4 eV, respectively, in a good agreement with the theoretical prediction. These results suggest that the MgO 1D ordered crystal should be a wide-band-gap semiconductor.

The discovery of the 1D ordered crystals is of fundamental scientific interest and will encourage more efforts for exploring the potential applications.

References

[1] D. Yin, C. Chen, M. Saito, K. Inoue, Y. Ikuhara: Nat. Mat., 18 (2019) 19-23.

Large-scale device-material research by massively parallel electronic structure calculation and data science

Takeo Hoshi

Department of Applied Mathematics and Physics, Tottori University,

4-101 Koyama-Minami, Tottori 680-8550, Japan.

The present project was carried out for the joint research between electronic structure calculations and data science. Related mathematical studies and software development were also carried out. The main collaborators are Yusaku Yamamoto (U. Elec. Comm.), Koji Hukushima (U. Tokyo), Takatoshi Fujita (IMS), Hiroyuki Matsui (Yamagata U.), Toshio Hyodo and Ayahiko Ichimiya (KEK).

The large-scale electronic-state and transport calculations were carried out for flexible organic devices. As a main achievement, principal component analysis (PCA) was carried out so as to analyze large-scale electronic state calculation data for exploration of organic polymer device materials [1-3]. The method is given by the dimensional reduction of electronic wavefunctions, since the original data size is huge. The reduction is realized, when the participation ratio of wavefunctions, a measure of quantum localization, is chosen as the descriptor. The computation was carried out for electronic states for 40,000 samples of disordered organic polymers with 1,200 atoms by our large-scale electronic state calculation code ELSES (http://www.elses.jp/) on the K computer. As results, the polymer samples are classified into four groups correctly and the physical meaning of the principal components is clarified. The present method is general and forms a rigorous foundation of the data-driven material science. Numerical methods for large-scale electronic state calculations were developed for efficient contour integral [4], intermediate eigenpair computation [5], middleware for parallel eigenvalue computation with the performance prediction function by Bayesian inference [6]. In addition, preliminary researchs were carried out for large-scale exiton calculation of organic interface [7] and large-scale electronic state calculation of disordered pentacene thin film [8], the development of data analysis on positron diffraction experiment [9].

As mathematical studies, we developed a new preconditioner for the CG method which combines the block red-black ordering with relaxed modified incomplete Cholesky factorization. Numerical experiments on a multicore processor shows that the preconditioner is both effective and scalable [10]. We also developed a new algorithm for the nonlinear eigenvalue problem based on signed singular values [11].

References

[1] T. Hoshi, H. Imachi, K. Oohira, Y. Abe, and K. Hukushima, ‘Principal component analysis with electronic wavefunctions for exploration of organic polymer device materials’, International Meeting on High-Dimensional Data-Driven Science , Kyoto, 10-13. Sep. 2017

[2] T. Hoshi, H. Imachi, Y. Abe, K. Oohira, K. Hukusima, ‘Principal component analysis with large-scale electronic state calculation for ultra-flexible device materials’, Waseda U., 18th SIAM Conference on Parallel Processing for Scientific Computing (SIAM-PP18), 7-10, Mar. 2018.

[3] (Award) T. Hoshi, ‘Organic-device material research based on 100-nano-meter electronic structure calculation and data science’, Excellent achievement award of HPCI projects, 2. Nov., 2017.

[4] H. Kohashi, K. Sugita, M. Sugihara and T. Hoshi, ‘Efficient methods for computing integrals in electronic structure calculations’, JSIAM Letters 9, pp. 81-84 (2017)

[5] D. Lee, T. Hoshi, T. Sogabe, Y. Miyatake, S.-L. Zhang, ‘Solution of the k-th eigenvalue problem in large-scale electronic structure calculations’, submitted; Preprint (http://arxiv.org/abs/1710.05134).

[6] T. Hoshi, T. Fukumoto, T. Fukaya, Y. Yamamoto, ‘Analysis and prediction of the performance in generalized eigenvalue solvers on Oakforest-PACS’, International Workshop on Eigenvalue Problems: Algorithms; Software and Applications, in Petascale Computing (EPASA2018), 5-6, Mar. 2018.

[7] MD K. ALAM, T. Fujita, T. Hoshi, ‘Excited-state calculation for large size C60/Pentacene interface based on the fragment molecular orbital method’, Meeting of The Japan Society of Applied Physics, Hakata, 5-8, Sep 2017.

[8] T. Hoshi, Y. Abe, A. Kuwata, K. Kakuda, T. Fujita, H. Matsui, 'Large-scale electronic state calculation in disordered pentacene thin film', Meeting of The Japan Society of Applied Physics, Waseda U., 17-20, Mar. 2018 (Japanese)

[9] T. Hoshi, K. Tanaka, I. Mochizuki, T. Hyodo, A. Ichimiya, Y. Nakanishi, K. Hukushima, ‘Development of data analysis software for positron diffraction’, 2nd Workshop on Positron Diffraction, organized by T. Hyodo and T. Hoshi, KEK Tsukuba, 30. Mar. 2018. (Japanese)

[10] A. Shioya and Y. Yamamoto, 'The danger of combining block red–black ordering with modified incomplete factorizations and its remedy by perturbation or relaxation', Jpn. J. Ind. Appl. Math., 35, pp 195-216 (2018).

[11] K. Ooi, Y. Mizuno, T. Sogabe, Y. Yamamoto and S.-L. Zhang, 'Solution of a nonlinear eigenvalue problem using signed singular values', East Asian J. Appl. Math. 7, pp. 799 - 809 (2018).

DFT sampling studies on interfacial properties of batteries and catalysts

Yoshitaka TATEYAMA

Center for Green Research on Energy and Environmental Materials (GREEN), National Institute for Materials Science (NIMS), 1-1 Namiki, Tsukuba, Ibaraki 305-0044; Elements Strategy Initiative for Catalysts & Batteries (ESICB), Kyoto University, Goryo-Ohara, Nishikyo-ku 615-8245.

We are working on (1) developments of theoretical, computational and data-driven techniques [1-3] as well as (2) understanding of surface and interface reactions, essential in the energy and environmental technologies such as battery and catalyst [1,4]. Recently, we have developed some multiscale techniques involving the DFT-level calculations.

In this report, we introduce a study via DFT-based surface microkinetics simulations of NO + CO reaction on Rh surface, which is widely used as a model reaction on the NO_x reduction by the three-way catalyst [1]. Though there are many DFT microkinetics studies, inclusion of surface reactions and development of automated protocol were still very rare.

We assumed that the catalysis cycle consists of the following elementary reaction steps; NO dissociation, N_2O formation, N_2 formation, and CO_2 formation. The adsorption energies, reaction energies, and activation energies were all evaluated with the DFT calculations. For the exchange-correlation interaction, the RPBE functional was used. All the DFT calculations were done by VASP 5.4. The microkinetic analysis was carried out with the DFT-calculated energetics.

In Figure 1, the reaction rates of NO consumption, N_2O formation, N_2 formation and CO_2 formation were plotted with respect to temperature (T). The results show that the N_2O formation is faster than the N_2 formation at low T, while the opposite behavior is observed at high T. This agrees with the experiments in which N_2O and N_2 were reported as the main product at low and high T regions, respectively. The surface coverage, shown in Figure 1 (right), shows good correspondence with change of the reaction rate: At T = 300 - 400 K, the NO dissociation takes place and thus the surface NO is consumed while N and O coverage increases. At T = 500 – 600 K, the surface O is consumed because of the CO2 formation and at higher T range the surface N decreases as the N2 formation occurs. The surface coverage changes strongly suggest that accumulation of the N species on the surface is crucial for N + N → N_2 reaction to take place.

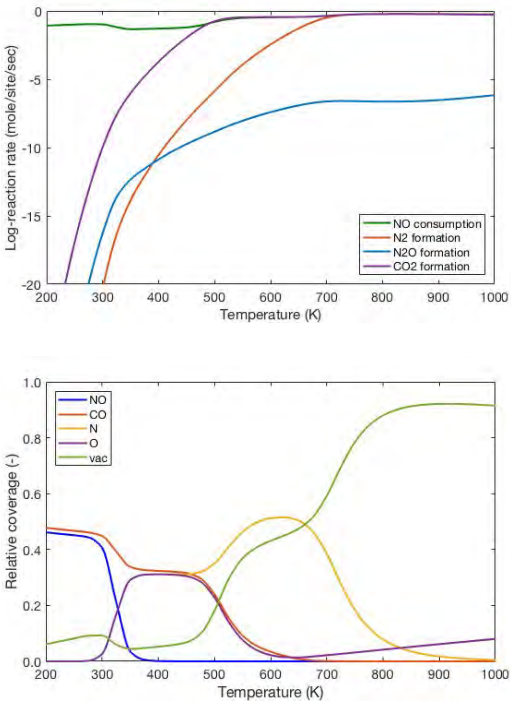

Figure 1: (upper panel) The reaction rates of four elementary reaction steps in the NO + CO reaction and their changes with respect to the temperature. (lower panel) the change in the surface coverages of reaction intermediates as the function of the temperature.

References

[1] A. Ishikawa, Y. Tateyama: J. Phys. Chem. C **122** (2018) 17378-17388.

[2] R. Jalem, M. Nakayama, Y. Noda, T. Le, I. Takeuchi, Y. Tateyama, H. Yamazaki: Sci. Tech. Adv. Mater. **19** (2018) 231-242.

[3] K. Sodeyama, Y. Igarashi, T. Nakayama, Y. Tateyama, M. Okada: Phys. Chem. Chem. Phys. **20** (2018) 22585-22591.

[4] L. Szabova, M. F. Camellone, F. N. Ribeiro, V. Matolin, Y. Tateyama, S. Fabris: J. Phys. Chem. C 122 (2018) 27507-27515.

First-principles study of quantum transport in nanostructures

NOBUHIKO KOBAYASHI
Institute of Applied Physics, University of Tsukuba
1-1-1 Tennodai Tsukuba Ibaraki 305-8573

1 Introduction

The aim of this project is to reveal and predict charge, heat and spin transport in materials from first-principles. Theoretical studies on transport properties are indispensable for the recent developments of high-performance electronic devices. Quantum nature is essential in nanoscale systems, and atomistic analysis based on detailed electronic states calculations are indispensable to discuss the transport property. In order to investigate transport properties, we have developed the nonequilibrium Green's function (NEGF) method, and the O(N) time dependent wave-packet diffusion (TD-WPD) method on the basis of the density functional theory (DFT). Using these methods, we have investigated charge, head and spin transport properties of materials. [1, 2]

2 O(N) TD-WPD method and application to organic semiconductors

Organic semiconductors have attracted much attention for their applications to flexible, printable, lightweight, and low-cost electronic devices. They are crystals that are assemblies of π-conjugated molecules weakly bonded by van der Waals interactions, and single crystallization has been achieved, enhancing the mobility. It is expected that the mechanism of carrier transport in organic semiconductors can be elucidated and that materials exhibiting high mobility can be developed by novel molecular synthesis.

We developed the O(N) TD-WPD method for the quantum transport calculation of huge systems of up to 100 million atoms a decade ago.We calculated the conductance and the mobility of the system with micron-order lengths at room temperature at the atomistic levels. Using this method we can study the transport properties from diffusive to ballistic regimes including the effect of realistic electron-phonon scattering, and determine the mean free path and relaxation time from an atomistic viewpoint. We performed DFT calculations of electronic structures and interactions between molecules of single-crystal organic semiconductors including the effect of the van der Waals interaction, and applied the TD-WPD method to the analysis of transport properties of the organic semiconductors.

We analyzed the transport properties of various organic semiconductors, and confirmed that the calculated mobilities and their temperature dependences are quantitatively in good agreement with those obtained in experiments.The essence of the requirements to quantitatively evaluate mobility is employing the proper computation method of diffusion coefficient defined using the velocity correlation function. Moreover, quantitatively accurate evaluations of both two-dimensional transfer-integral networks based on DFT and effects of dynamic disorder induced by all phonon modes on the electronic states are also required. Since our methodology enables quantitative prediction of the transport properties of various soft materials using first-principles calculations, our method becomes a powerful tool when developing new materials. [3]

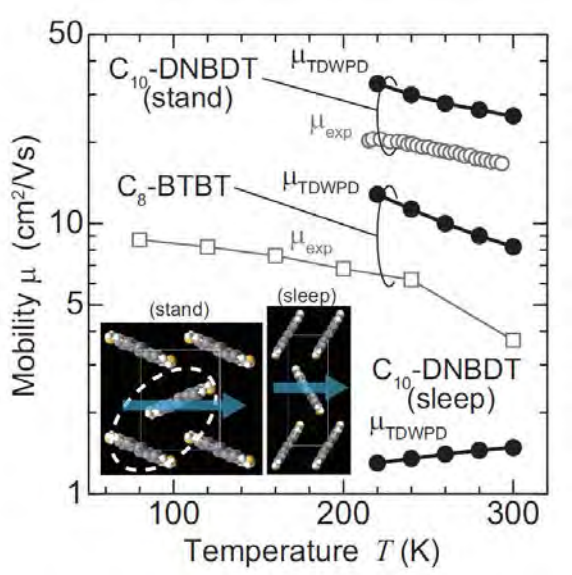

Figure 1: Mobility of C10-DNBDT (sleep), C10-DNBDT(stand) and C8-BTBT are shown by solid circles. The two different crystal structures of the C10-DNBDT polymorphs are shown in the insets. The mobilities are calculated along the column direction shown by the arrow. The experimental data points for C10-DNBDT (stand) and C8-BTBT are shown by circles and squares.

3 NEGF method and application to thermoelectricity

We have developed an efficient numerical calculation code for the ab-initio electron transport based on the DFT and NEGF formalism. We have applied the method to analyses of thermoelectricity of magnetic semiconductors.

Thermoelectric materials have attracted considerable attention from viewpoints not only of materials science but also of applications for energy harvesting by waste heat, and intensive works have been devoted to enhance conversion efficiency from thermal energy into electricity. The efficiency is expressed as a function of the figure of merit $ZT = \sigma S^2 T/\kappa$, where σ, S, κ and T are the electrical conductivity, the Seebeck coefficient, the thermal conductivity and the temperature, respectively, and the thermoelectric power factor is written as σS^2. Enhancement of thermoelectric efficiency is not an easy task since the Seebeck coefficient, the electrical conductivity, and the thermal conductivity are not independent of each other. There is the trade-off between σ and S, and materials with high electric conductivity tend to have high thermal conductivity.

We analyze the thermoelectric properties of a magnetic semiconductor by NEGF-DFT. The electronic transport properties, Seebeck coefficient, and the figures of merit are estimated for doped systems and thin films. We theoretically demonstrate the enhancement in the figure of merit by doping, which is in agreement with experimental work, and show further enhancement by the optimized doping.[4, 5]

References

[1] N. Kobayashi, H. Ishii, K. Hirose, Jpn. J. Appl. Phys. 57, 08NA01 (2018).

[2] N. Kobayashi, H. Ishii, K. Hirose, in *3D Local Structure and Functionality Design of Materials* eds H. Daimon, Y. C. Sasaki (World Scientific, 2018) p133.

[3] H. Ishii, J. Inoue, N. Kobayashi, K. Hirose, Phys. Rev. B 98, 235422 (2018).

[4] H.Takaki, K.Kobayashi, M.Shimono, N.Kobayashi, K.Hirose, N.Tsujii, T.Mori, Materials Today Physics 3 85e92 (2017).

[5] H.Takaki, K.Kobayashi, M.Shimono, N.Kobayashi, K.Hirose, N.Tsujii, T.Mori, Jpn. J. Appl. Phys. (2019) in press.

van der Waals density functional theory study of molecular adsorption on metal surfaces

Ikutaro HAMADA

Department of Precision Science and Technology, Graduate School of Engineering, Osaka University, 2-1 Yamada-Oka, Suita, Osaka 565-0871

Molecular adsorption on the electrode surface is one of the important building blocks in diverse devices relevant to energy harvesting and storage, such as fuel cell, solar cell, and secondary battery, to name only a few. The accurate description of the molecular adsorption is challenging in the conventional density functional theory based on the local density and generalized gradient approximations (GGA), because they cannot capture the dynamic and nonlocal nature of the van der Waals interaction, crucial in the molecule-surface interaction. In this work, we use rev-vdW-DF2[1], an offspring of the van der Waals density functional (vdW-DF)[2], which has been show to describe the molecular adsorption on solid surfaces accurately.

All the calculations were performed using STATE[3], our in-house plane-wave pseudopotential code. We used an efficient algorithm[4] of the self-consistent vdW-DF.

In this work, we studied small water clusters on a Cu(110) surface, to investigate the origin of the formation of one-dimensional water chain made from pentagon. We constructed water clusters one by one, starting from monomer to octamer. Overall, the structures obtained with vdW-DF are similar to those obtained in previous studies using GGA with slightly larger adsorption energies. We found that the water pentamer is stable, and hexamer is slightly less stable than the pentagon based cluster (i.e., pentamer plus additional water molecule). For octamer, we found that the pentagon based structure is also stable. We concluded that the pentagon based structure is formed as a result of a delicate balance between hydrogen bonding between water molecules and the interaction between water molecule and substrate.

References

[1] I. Hamada: Phys. Rev. B **89** (2014) 121103(R)

[2] M. Dion et al.: Phys. Rev Lett. **92** (2014) 246401.

[3] Y. Morikawa, H. Ishii, and K. Seki: Phys. Rev. B. **64** (2004) 041403.

[5] J. Wu and F. Gygi: J. Chem. Phys **136** (2012) 224107.

[6] A. Shiotari and Y. Sugimoto: Nat. Commun. 8 (2017) 14313.

Rashba effects in surface-Bi nanostructures

Yoshihiro GOHDA
Department of Materials Science and Engineering, Tokyo Institute of Technology
J1-3, Nagatsuta-cho 4259, Midori-ku, Yokohama 226-8502, Japan

Systems exhibiting the Rashba effect is of fundamental importance due to their characteristic spin textures. The Rashba effect is possible not only in two-dimensional surface structures, but also in one-dimensional surface nanostructures. As a possible candidate for technological applications, spin-filtering exploiting the Rashba effect is promising, which is caused by band structures with opposite spin directions at the Fermi energy for the positive and negative electron momenta with each other. Even though such a band structure is proposed using an application of the magnetic field [1], it has not been realized yet without an external magnetic field. As a constituent element of the one-dimensional nanostructure, Bi is expected to be promising because of large spin-orbit coupling coming from its large atomic number.

In this study, we investigated a new one-dimensional Rashba system, Bi-adsorbed In atomic chains, using first-principles calculations [2]. First-principles calculations were performed on the basis of density functional theory with the generalized gradient approximation by the OpenMX code [3]. One of the most stable structures in the system shows unconventional spin textures, which is the reversal of the spin polarization direction in Rashba bands. This band structure is caused by a gap-opening due to the avoided-crossing of two Rashba bands. We have confirmed using a group-theoretical analysis that four relevant Rashba bands are classified into two irreducible representations as in Fig. 1 (a). The avoided-crossing is caused by the hybridization of two Rashba bands belonging to the same irreducible representation. The schematic representation of this hybridization is shown in Fig. 1 (b). Together with the shift of the Fermi level within the gap, our results suggest a new spin-filtering mechanism through atomic chains. In addition, our mechanism has a great advantage; previous spin-filtering mechanisms require the external magnetic field [1], whereas ours does not need the magnetic field. This feature is suitable for spintronic applications.

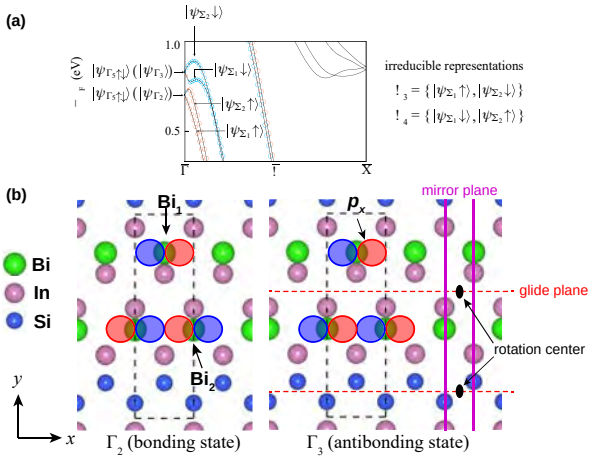

Figure 1: (a) Spin-polarization components parallel to the y axis as open circles with the band dispersion. The classification of the four Rashba bands into the irreducible representations are also shown. (b) Schematic illustrations of the hybridization together with the symmetry elements. The drawn orbitals represent p_x orbitals of Bi.

[1] C. H. L. Quay *et al.*, Nature Phys. **6**, 336 (2010).
[2] T. Tanaka and Y. Gohda, Phys. Rev. B **98**, 241409(R) (2018)
[3] T. Ozaki, Phys. Rev. B. **67**, 155108 (2003).

Study on Removal Mechanism in Catalyst-Referred Etching of Single Crystalline SiC with Pure Water

Pho Van BUI, Daisetsu TOH, Kouji INAGAKI, Yoshitada MORIKAWA

Graduate School of Engineering,

Osaka University, 2-1 Yamada-oka, Suita, Osaka 565-0871

Polishing is an extremely important technique used in the finishing processes for optical and semiconductor surfaces and determines the performance of the final products. To produce a smooth surface without introducing any crystallographically damaged surface, the only pure chemical etching method is desired. Recently, catalyst-referred etching (CARE) method using Pt catalyst and water (as an etchant) has been proposed [1-3]. CARE can planarize SiC and various crystalline semiconductor materials to atomically smooth surfaces. However, the removal rate (RR) was sufficiently slow for crystalline materials (to be lower than several tens of nm/h) [4]. Our recent studies indicate that the etching via CARE is hydrolysis reaction, in which the catalyst assists water dissociation and stabilization of hypervalent states, an increasing rate of the reaction, as seen in Fig. 1 [5].

The research is carried out to clarify the catalytic mechanism by finding new catalysts having suitable binding energy with OH using first-principles calculations.

Reaction heats for the below reaction were previously calculated over the most close-packed surface of a number of metals at a quarter monolayer coverage [6].

$$H_2O + * \rightarrow HO^* + {}^1/_2 H_2$$

where H_2O and H_2 are in the gas phase and * denotes a site on the surface. The positive value means that the final state is less stable, i.e. the binding energy with OH is weak and vice versa. The results are summarized in Fig. 2.

Until now, Pt was selected as a catalyst because of its corrosion resistance and stability. However, the RR can be improved by using a new catalyst with higher catalytic activity. I have

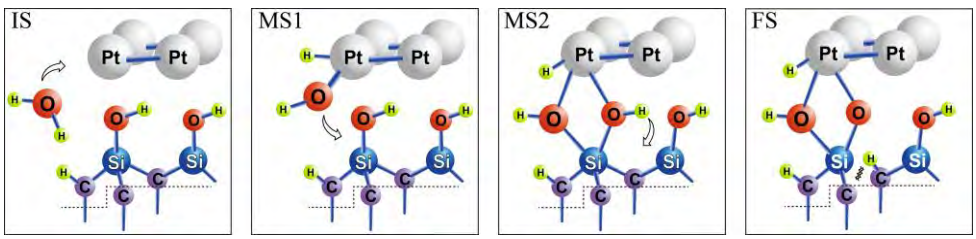

Fig. 1: Mechanistic reaction pathway of SiC in water using a Pt catalyst.

tested the performance of CARE using some catalysts and found that the RRs using a Ni and Ru are ca. 3 and 6 times higher than that using a Pt, respectively [6]. Our experimental results agreed well with the calculated results showing that Ni and Ru have higher binding energy with OH compared to Pt, promoting the water dissociation (Fig. 2).

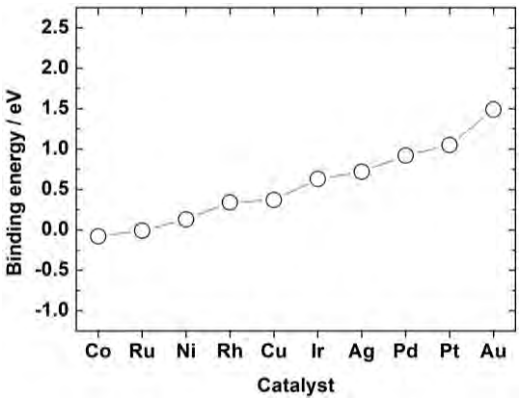

Fig. 2: M─OH binding energies on some metal surfaces.

Due to the high stability under ambient conditions and high RR, we investigate the interaction of water on the Ru surface by using massive parallel computer simulations. The adsorption energy and activation barrier of water on Ru are calculated and shown in Fig. 3.

The calculated results showed that the water dissociation capability of Ru is quite good. Additionally, we employ the Ru surface as a catalyst for SiC removal. The method and model are described elsewhere [5]. The calculated results revealed the catalytic mechanism of Ru is similar to that of a Pt catalyst.

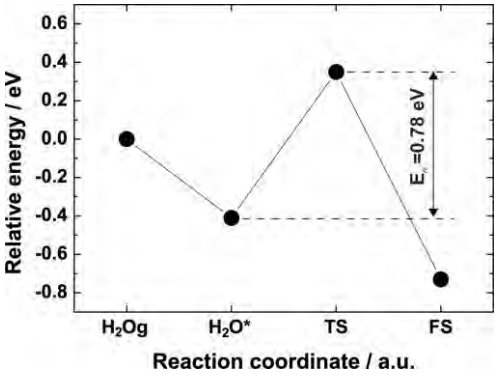

Fig. 3: Adsorption energy and activation barrier of Ru, where H_2Og, H_2O*, TS, and FS is the isolated, molecularly adsorbed, transition and final/dissociated states.

References

[1] H. Hara Y. Sano, H. Murata, K. Arima, A. Kubota, K. Yagi, J. Murata, and K. Yamauchi: J. Electron. Mater. **35** (2006) L11.

[2] T. Okamoto, Y. Sano, K. Tachibana, K. Arima, A. N. Hattori, K. Yagi, J. Murata, S. Sadakuni, and K. Yamauchi: J. Nanosci. Nanotech. **11** (2011) 2928.

[3] H. Hara, Y. Sano, K. Arima, K. Yagi, J. Murata, A. Kubota, H. Mimura, K. Yamauchi: J. Sci. Technol. Adv. Mater. **8** (2007) 162.

[4] A. Isohashi, P. V. Bui, D. Toh, S. Matsuyama, Y. Sano, K. Inagaki, Y. Morikawa, and K. Yamauchi: Appl. Phys. Lett. **110** (2017) 201601.

[5] P. V. Bui, D. Toh, A. Isohashi, S. Matsuyama, K. Inagaki, Y. Sano, K. Yamauchi, and Y. Morikawa: Jpn. J. Appl. Phys. **57** (2018) 055703.

[6] J. K. Nørskov, J. Rossmeisl, A. Logadottir, and L. Lindqvist: J. Phys. Chem. B **108** (2004) 17886.

[7] P. V. Bui, D. Toh, S. Matsuyama, Y. Sano, K. Yamauchi: euspen conference proceeding (2019).

Bronsted Acidity on Oxide Surface Induced by Neutralization of Lewis Acid Sites by Molecules

Ryuhei Sato and Shu Yamaguchi

Department of Materials Engineering,

The University of Tokyo, Bunkyo-ku, Hongo, Tokyo 113-0032

Proton activity on oxide surface is paid considerable attention for the application to catalysts like sulfated zirconia for strong solid acid and Cu/ZnO for methanol synthesis. Since these catalysts utilize the reactions with local proton and electron migration, the acid-base and Red-Ox property on the surface strongly influence on their efficiency. However, in conventional methods like titration and electrophoretic measurement, acid-base property on the surface is only evaluated macroscopically without considering the difference of acidity between the sites on the surface. In addition, the mechanism about the emergence of Brønsted acidity on Lewis acid-base sites like metal and oxide ion sites on oxide surface by molecular adsorption is still unclear. Therefore, we cannot evaluate the change in acidity on the surface by the adsorption of reactants and products during reactions, which makes it difficult to design the new strong solid acid and solid base with surface modification and predict the catalytic efficiency of metal/oxide catalysts. Under such circumstance, here, we studied the adsorption of acid-base molecules and subsequent emergence of Brønsted acidity and discuss the relationship between this Brønsted acidity and strength of adsorption to develop a new approach to evaluate p*K*a from adsorption energy.

Adsorption reaction of H_2O, HCOOH, CH_3OH, H_2S, CH_3SH, and HCSSH on cubic ZrO_2 (110) surface is analyzed by *ab initio* molecular dynamic (AIMD) simulation. Also, for HCOOH, CH_3OH, and H_2S adsorbed surface, subsequent hydration reaction is also analyzed. All the simulations were performed by home-made code written by F. Shimojo et al. [1]. The GGA/PBE functional and PAW method were employed with L4cpu and L36cpu queues.

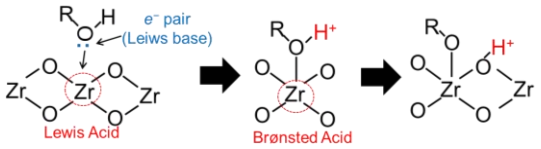

Figure 1. Schematic image of adsorption and subsequent deprotonation of acid-base molecules on ZrO_2 surface.

From the observation of adsorption reaction of these acid-base molecules, it is found that there is a common mechanism about adsorption and subsequent emergence of Brønsted acidity. That is, these molecules as a Lewis base

neutralize the metal ion sites (strong Lewis acid) by the adsorption, subsequently dissociate protons, and work as Brønsted acid (Fig. 1). Therefore, it is considered that p*K*a for chemisorbed molecules could be determined from adsorption energy, since the strength of O(S)-H bond is inversely proportional to that of Zr-O(S) bond to reduce the number of atomic bonding around O(S) atom.

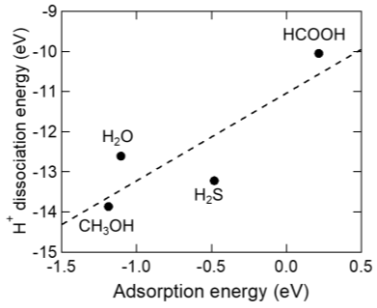

Figure 2. H^+ dissociation energy vs adsorption energy of single molecule on ZrO_2 (110) surface calculated from the total energy difference of DFT simulation.

Figure 2 shows the relationship between H^+ dissociation energy and adsorption energy of single acid-base molecule on bare cubic ZrO_2 (110) surface. As shown in this figure, there is a linear relationship between H^+ dissociation energy and adsorption energy, implying that p*K*a could be determined from adsorption energy. Actually this kinds of p*K*a evaluation is already shown in molecular system [2], where the linear relationship between p*K*a for adducts of Lewis acid and Brønsted base molecules (i.e. NH_3 and H_2O) and strength of Lewis acidity of combined Lewis acid molecules is already shown from simple DFT calculation. However, the problem of p*K*a estimation of adsorbate on oxide surface is the strong solvation effect and the interaction between adsorbates. Therefore, to extract the parameter to discuss the relationship between deprotonation and adsorption property of molecules, the change in electronic states of atoms during hydration reactions of theses adsorbates is analyzed. Density of states (DOS) analysis shows the electronic states of Zr ion sites do not change before and after the adsorption and H^+ dissociation. In addition, by comparing the DOS of H atom in these molecules and that of O(S)-H bond, it is found that H atom does not have electrons and electrons are localized in O(S)-H bond. Therefore, it is considered that by analyzing the change in electronic states of O(S) atom in adsorbates and bonds around it, the deprotonation and adsorption property with solvation effect and interaction between adsorbates could be discussed. However, it is also found that the projection function to decompose the total energy into the energy of each atom has non-negligible error to discuss the chemical reaction. Therefore, to find the way to overcome this error induced by projection function will be the next challenge to develop the method to evaluate p*K*a from adsorption energy.

References

[1] F. Shimojo, R.K. Kalia, A. Nakano, P. Vashishta, *Comp. Phys. Comm.* **140** (2001) 303.

[2] A. P. Lathem, Z. M. Heiden, *Dalton Trans.* **46** (2017) 5976.

First-Principles Molecular-Dynamics Study of Structural and Electronic Properties of Covalent Liquids and Glasses under Pressure

Fuyuki SHIMOJO, Akihide KOURA, Hiroyuki KUMAZOE, Kho UJIHARA

Institute for Solid State Physics,

Department of Physics, Kumamoto University, Kumamoto 860-8555

The investigation of the dynamic properties of molten materials under pressure is important from perspectives of geophysics as well as fundamental liquid-state science. A remarkable feature in the pressure dependence of the diffusivity of covalent liquids, such as liquid boron oxide and liquid zinc chloride, is that while the two diffusion coefficients of elements are almost the same at relatively low pressures, the difference between them increases with pressure after they exhibit a maximum [1], i.e., the dynamic asymmetry appears.

Our calculations of liquid magnesium forsterite Mg_2SiO_4 also shows a noticeable pressure dependence of the dynamic properties. Figure 1 shows the self-diffusion coefficients of elements as a function of pressure. Being different from other covalent liquids, the dynamic asymmetry is seen at pressures below 5 GPa; the three self-diffusion coefficients are largely different from each other. With increasing pressure, the self-diffusion coefficient of magnesium approaches that of oxygen, and they have almost the same values with similar pressure dependence above approximately 15 GPa. The self-diffusion coefficient of silicon is lower than those of other elements in the whole range of pressure investigated in this study. It is important to consider the microscopic origin of this anomalous pressure dependence of the diffusivity in connection with the change from low- to high-coordinated structures.

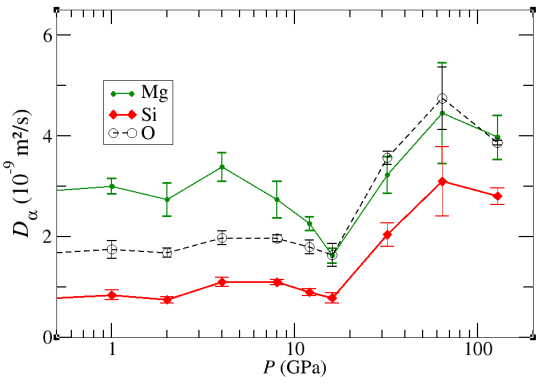

Fig. 1: Pressure dependence of self-diffusion coefficients of elements in liquid Mg_2SiO_4.

References

[1] A. Koura, S. Ohmura and F. Shimojo, J. Chem. Phys. **138**, 134504 (2013); A. Koura and F. Shimojo, Phys. Status Solidi B **255**, 1800103 (2018)

First principles calculations and development of graph analysis method for magnetic alloys and amorphous grain boundary phases in permanent magnets

Asako TERASAWA
Department of Materials Science and Engineering, Tokyo Institute of Technology
J1-3, Nagatsuta-cho 4259, Midori-ku, Yokohama 226-8502, Japan

Improvement of Nd-Fe-B magnets without heavy rare earth elements is one of the topics of increasing importance in the applied physics and materials science. The key for high-coercivity Nd-Fe-B magnets lies in the Nd-rich grain boundary (GB) phases [1]. However, the details of structural and magnetic properties of those GB phases are not clarified yet. Some experiments revealed the relationship between the crystallinity of GB phases and the relative angles between the interfaces and the c-plane of neighboring grains [2], which indicates the complexity of the physics in grain boundary phases in Nd-Fe-B magnets.

Considering these backgrounds, we targeted the amorphous grain boundary phase for a computational study of magnetism in Nd-based permanent magnets. The problem of amorphous grain boundary phases involves two important topics; the origin of the difference in crystallinity of grain boundary phases depending on the composition ratio and the magnetism of grain boundary phases depending on the composition ratio and the local structures.

To tackle these problems, we performed coupled analyses of structure and magnetism of Nd-Fe amorphous alloys having different composition ratios. To simulate the grain boundary phase, we created a model of amorphous Nd-Fe alloy containing 54 atoms computationally on the basis of density functional theory (DFT). For the DFT calculations, we adopte OpenMX [3] code. For the systems created, we performed structural analyses using the Delaunay [4] and Gabriel graphs [5]. It was shown by the comparison of radial distribution functions (RDFs) that the Gabriel graphs depict the nearest neighbor networks in amorphous Nd-Fe alloys well. We also examined the 2D histogram of coordination numbers statistically from the MD simulation results, as well as the angular distribution functions between two adjacent edges in the Gabriel graphs. It was shown that the extent of short-range order becomes weak at the Nd composition ratio of 41 %, which is close to the Nd composition of amorphous grain boundary phase observed in the experiment [2]. We published these results in Journal of Chemical Physics [6].

Even though the structural properties of amorphous grain boundary phases started to unveil by such efforts, investigation of their magnetic properties is still a difficult problem, because it is difficult to determine the spin alignment of such a complicated structure. To solve this problem, we implemented the Liechtenstein formula to calculate exchange coupling constants from the output of OpenMX. We derived the explicit form of Liechtenstein formula on the non-orthogonal local orbital basis with Green's function formalism. We adopted the finite pole approximation [7] of Fermi function

for fast computation of energy integral.

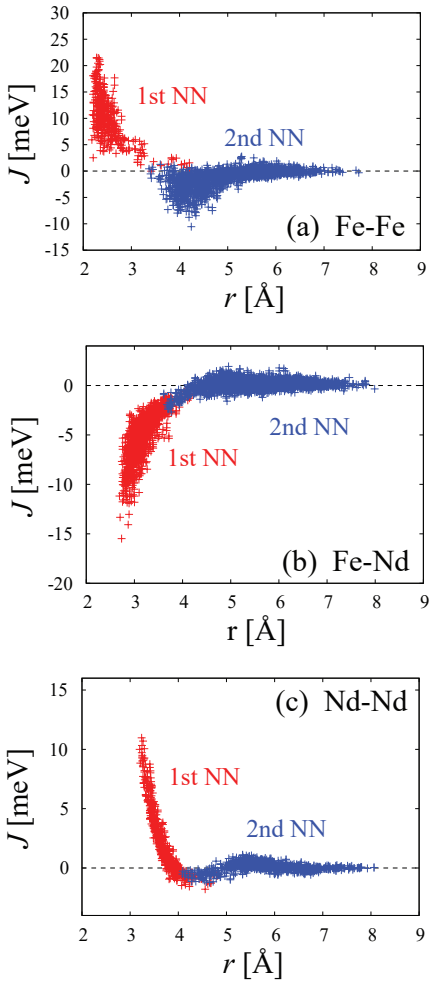

Figure 1: Exchange coupling constants in Nd-Fe amorphous alloys of Nd composition ratio at 41%, for element pair component of (a) Fe-Fe, (b) Fe-Nd, and (c) Nd-Nd. (Color online)

Using this formula, we calculated the exchange coupling constants between two atoms in the Nd-Fe amorphous using Liechtenstein method [4]. We obtained strong distance dependences and fluctuations of exchange coupling constants J_{ij} (see Fig. 1). The distance dependence curves of J deform gradually depending Nd composition ratio. These features indicate that the exchange couplings do not only depend on atomic species and distance between two atoms, but also for surrounding environment.

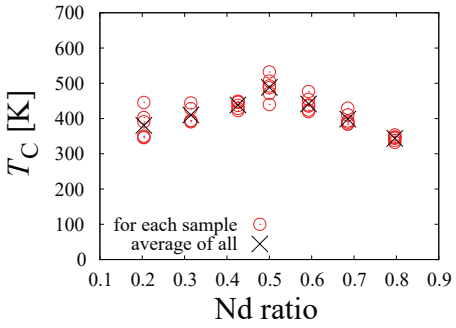

Figure 2: The Curie temperature as a function of Nd composition ratio for independent 6 samples.

It is also possible to calculate the Curie temperature from all the non-negligible J_{ij} in the whole system under the mean field approximation. Figure 2 shows the Curie temperature as a function of Nd composition ratio. As seen in Figure 2, the Curie temperature reaches maximum at around the Nd composition ratio of 50%.

Calculations and interpretations of magnetism of amorphous materials had been a big challenge for materials science for many decades, and our approach can open up a new perspective to the amorphous magnetism.

References

[1] K. Hono *et al.*, Scripta Mater. **67**, 530 – 535 (2012).

[2] T. T. Sasaki *et al.*, Acta Mater. **115**, 269 (2016).

[3] T. Ozaki, Phys. Rev. B **67**, 155108 (2003).

[4] B. Delaunay, Bulletin de l'Acad é mie des Sciences de l'URSS. **6**, 793 – 800 (1934).

[5] K. R. Gabriel *et al.*, Society of Systematic Biologists, **18**, 259 – 270 (1969).

[6] A. Terasawa and Y. Gohda, J. Chem. Phys. **149**, 154502 (2018)

[7] T. Ozaki, Phys. Rev. B **75**, 035123 (2007).

First-principles study on the nanoscale physics of $Nd_2Fe_{14}B$

Yasutomi TATETSU

Meio University, Biimata, Nago, Okinawa 905-8585

In 1970's, Re_2Fe_{17}, where Re represents rare earth elements, could be considered as permanent magnets. However, the Curie temperature (T_c = 330K) was not high enough for permanent magnets. B was introduced into Re_2Fe_{17} by Sagawa [1], who is the inventor of Nd-Fe-B sintered magnets, in order to increase the magnetic properties, for example, magnetic moment, magnetization, Curie temperature, etc. of Re_2Fe_{17}. This led to creating $Nd_2Fe_{14}B$ known as the main phase of Nd-Fe-B sintered magnets. However, the role of B in $Nd_2Fe_{14}B$ was not clearly studied from nanoscale physics.

We systematically studied the effects of B in $Nd_2Fe_{14}B$ on the magnetic properties and electronic states through first-principles calculations [2]. We used OpenMX [3] mainly on System B for the present study. In order to understand how B changes the magnetic moment and magnetization of $Nd_2Fe_{14}B$, we calculated these two physical quantities of $Nd_2Fe_{14}B$, $Nd_2Fe_{14}B_0$ and Nd_2Fe_{14}. $Nd_2Fe_{14}B_0$ has the same lattice parameters and the atomic positions of $Nd_2Fe_{14}B$, but B is not present in it. Nd_2Fe_{14} is a hypothetical material and its lattice parameters and atomic positions are optimized, therefore, these are not the same as $Nd_2Fe_{14}B$. We find that B does not increase the magnetic moment and magnetization of $Nd_2Fe_{14}B$. We check the stability of $Nd_2Fe_{14}X$ (X = B, C, N, O, F) by comparing the formation energies of $Nd_2Fe_{17}X$. We find that the formation energies of $Nd_2Fe_{14}B$ or $Nd_2Fe_{14}C$ become negative relative to that of $Nd_2Fe_{17}B$ or $Nd_2Fe_{17}C$ (see Fig.1). Our calculation result is in good agreement with the experimental fact that $Nd_2Fe_{14}B$ and $Nd_2Fe_{14}C$ stably exist. The main role of B in $Nd_2Fe_{14}B$ is not to increase the magnetic properties but stabilizes the structure of $Nd_2Fe_{14}B$ itself.

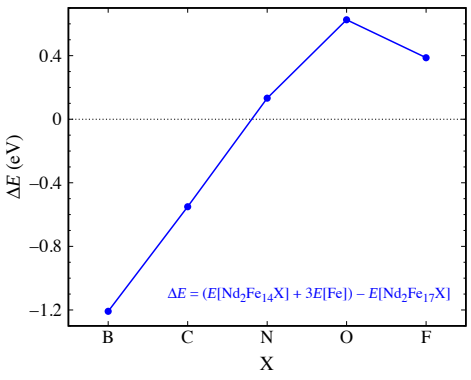

Figure 1. The formation energy of $Nd_2Fe_{14}X$.

References

[1] M. Sagawa *et al.*, J. Appl. Phys. **55**, 2083 (1984).

[2] Y. Tatetsu *et al.*, Phys. Rev. Mater. **2**, 0744100 (2018).

[3] http://www.openmx-square.org

Development of ab initio many-body perturbation calculation software RESPACK and its applications to Ta_2NiS_5 and Ta_2NiSe_5

Kazuma NAKAMURA
Quantum Physics Section, Kyushu Institute of Technology
1-1 Sensui-cho, Tobata, Kitakyushu, Fukuoka, 804-8550

As progress of this year, I have released a new version of the software RESPACK [1] for many-body perturbation calculation and effective low-energy model derivation. RESPACK is possible to calculate the maximally localized Wannier function, response function with random phase approximation and related optical properties, and frequency-dependent electronic interaction parameters, etc, and the new version includes the GW calculation. RESPACK supports *ab initio* band calculation codes using norm conserving pseudopotentials plus plane wave basis set, and officially supports xTAPP [2] and Quantum ESPRESSO [3] packages. An automatic generation script from these band-calculation output to input files for RESPACK is prepared. An input file for specifying calculation conditions is designed pursuing simplicity and is given in a namelist format. RESPACK has a wide application including simple metals, semiconductors, $3d/4d$ transition-metal compounds, organic and aromatic compounds, etc. It supports OpenMP/MPI and intel/GNU compiler environments. The new version also includes utility such as interfaces to model-analysis solvers mVMC [4] and $\mathcal{H}\Phi$ [5]; users can automatically obtain these inputs via RESPACK.

In this report, as a RESPACK application, I present results for an *ab initio* GW calculation of transition-metal chalcogenides Ta_2NiS_5 and Ta_2NiSe_5 which are actively studied as a possible candidate of excitonic insulators. Using an *ab initio* GW calculation, we studied low-energy electronic structures, especially for the band gap. These materials have a layered structure stacked loosely by a weak van der Waals interaction, and in each layer, Ni single chains and Ta double chains are running along the a axis of the lattice to form a quasi-onedimensional (1D) chain structure. The observed resistivity shows a semiconducting behavior over a wide temperature range with a quasi-1D anisotropic electron conduction at high temperatures. The experimental band gaps at room temperature are estimated as nearly 0.13 and 0.36 eV for the sulfide and selenide, respectively [6]. The crystal structure is body-centered orthorhombic (a=3.415 $\mathring{A}$, b=12.146 $\mathring{A}$, c=15.097 $\mathring{A}$ for Ta_2NiS_5 and a=3.496 $\mathring{A}$, b=15.829 $\mathring{A}$, c=15.641 $\mathring{A}$ for Ta_2NiSe_5) and contains 16 atoms in the body-centered unit cell. We calculate density functional band structure, maximally localized Wannier functions, dielectric properties, and GW spectral functions to understand the low-energy properties of these compounds.

Density-functional calculations were performed with xTAPP with plane-wave basis sets, where we employed norm-conserving pseudopotentials and the generalized gradient approximation (GGA) for the exchange-correlation potential. Maximally localized Wannier functions were used for the interpola-

tion of the self-energy. The experimental structure obtained by an X-ray measurement at room temperature was adopted in the calculations [6]. The cutoff energies in the wave function and the charge densities are 196 and 784 Ry, respectively, and a 7×7×3 k-point sampling was employed. The cutoff for the polarization function was set to 4 Ry, and 100 bands were considered. Nickel pseudopotential was constructed under the semicore configuration $(3s)^2(3p)^6(3d)^9$ by employing the cutoff radius 0.8 bohr. It should be noted that in the GW calculation of $3d$ transition-metal compounds, it is very important in quantitative accuracy to use a pseudopotential parametrized for the semicore configuration.

Figure 1(a) compare the calculated GW spectral function with the density-functional GGA bands (white solid curve) of Ta_2NiS_5. The GW spectra give clear gap in contrast to the GGA ones being the metallic band structure. We also show in Fig. 1(b) the comparison of the GW (green curve) with GGA (red curve) density of states. The GW gap is estimated as nearly 2 eV.

Figure 2 displays the results of Ta_2NiSe_5. The view of the figure is the same as that of Fig. 1. Our calculated GGA band structure is in a good agreement with the past results [7]. The GW band gap is near 1 eV and appreciablly smaller than the sulfide. In the case of insulators, it would be necessary to solve the Bethe-Salpeter equation for a more quantitative argument for the band gap, which is an important issue for the future study.

For code developments of RESPACK, I acknowledge Yoshihide Yoshimoto, Yoshiro Nohara, Yusuke Nomura, Terumasa Tadano, Mitsuaki Kawamura, and Maxime Charlebois. For making interface with mVMC and $\mathcal{H}\Phi$, I thank to Takahiro Misawa, Kazuyoshi Yoshimi, and Yuichi Motoyama. I also thank to Shinji Watanabe for useful discussions about transition-metal chalcogenide.

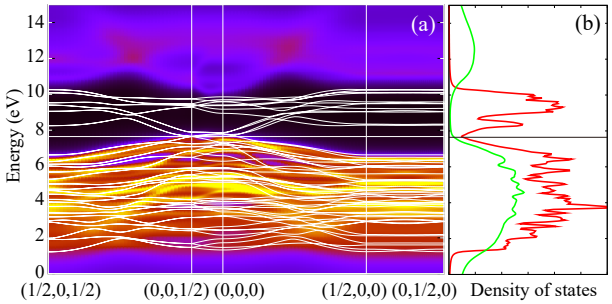

Figure 1: (Color online) (a) Calculated GW spectral function of Ta_2NiS_5, where the GGA bands are superposed with white solid curves. (b) Comparison between the GW (green) and GGA (red) density of states.

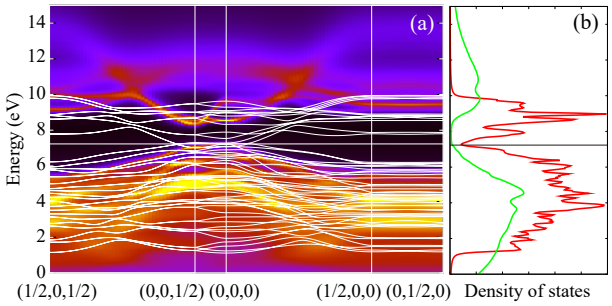

Figure 2: (Color online) (a) Calculated GW spectral function of Ta_2NiSe_5, where the GGA bands are superposed with white solid curves. (b) Comparison between the GW (green) and GGA (red) density of states.

References

[1] https://sites.google.com/view/kazuma7k6r

[2] http://xtapp.cp.is.s.u-tokyo.ac.jp/

[3] http://www.quantum-espresso.org/

[4] https://github.com/issp-center-dev/mVMC

[5] http://issp-center-dev.github.io/HPhi/index.html

[6] S. A. Sunshine, J. A. Ibers, Inorg. Chem.,**24**, 3611 (1985).

[7] T. Kaneko, T. Toriyama, T. Konishi, Y. Ohta1, Phys. Rev. B **87**, 035121 (2013).

Analysis of Thermoelectric Properties of Clathrate Compounds with Ab Initio Calculations

Masato OHNISHI

Department of Mechanical Engineering, The University of Tokyo

7-3-1 Hongo, Bunkyo, 113-8656

Clathrate compounds are promising candidates for thermoelectric materials in terms of the "electron-crystal phonon-glass" concept. Because of strong anharmonic potential of guest atoms in cage structures of type-I clathrates, guest phonon modes lead to strong phonon scattering. Recently, first-principles simulations of phonon properties of a clathrate have been first demonstrated with using self-consistent phonon (SCP) theory that can include temperature-dependent 4th-order anharmonic interatomic force constants (IFCs) into harmonic IFCs [1]. In this study, we reveal unusual anharmonic effects of phonons by comparing phonon properties of type-I $Ba_8Ga_{16}X_{30}$ (X = Si, Ge, Sn; BGX) as shown in Fig. 1 with first-principles simulations. Figure 2 shows that imaginary (negative) frequencies appeared without including the anharmonicity can be rifted up to positive values with using the SCP method. We have succeeded, for the first time, to calculate temperature-dependent thermal conductivities of BGSn with first-principles approach, which has the minimum thermal conductivity among the reported values of clathrates. Because the selection of atoms composing cage structures, namely Si, Ge, or Sn, manipulates strength of the anharmonicity, we have clearly observed effects of anharmonicity of phonons in clathrates. For example, we have observed an unusual effect of grain boundaries on phonon transport in BGSn; polycrystallization decreases a thermal conductivity of BGSn more at higher temperature.

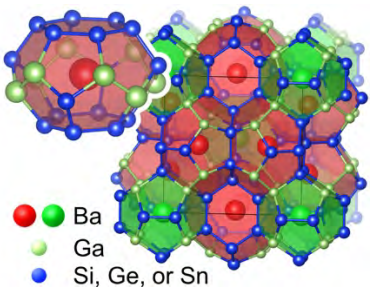

Fig. 1. Type-I $Ba_8Ga_{16}Sn_{30}$ clathrate.

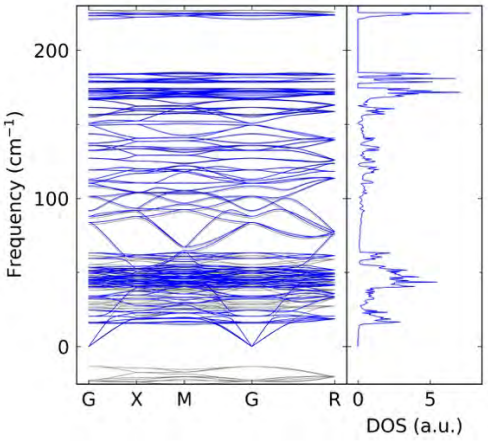

Fig. 2. Phonon dispersion and density of states of type-I BGSn. Blue and grey lines show results, respectively, with and without considering quartic anharmonicity.

References

[1] T. Tadano and S. Tsuneyuki, Phys. Rev. Lett. **120**, 105901 (2018).

Ab initio studies toward functional nanomaterials based on abundant elements

Tetsuya TAKETSUGU
Faculty of Science, Hokkaido University
N10W8, Sapporo, Hokkaido 060-0810

Ab initio studies on various nano materials are crucial to understand and design new functional materials with abundant elements for reducing costs and dependences on precious metals used in many important aspects in our daily lives and therefore toward sustainable society. Heterogeneous catalysts used in automotive gas exhausts control, water gas shifts, fuel cells, as well as combustive decomposition of ammonia rely mostly on the expensive and rare metals such as Pt, Rh, Pd, or Ru. Platinum and palladium are also used for hydrogen based energy strategies. Due to their high cost and limited amounts, to reduce or even replace these metals is emergent issues in industry. To that end, we perform density functional theoretical (DFT) computations under the periodic boundary conditions together with projector augmented wave method with VASP using ISSP supercomputers to gain chemical insights to understand the chemical mechanisms in conventional catalysts as well as to design novel catalysts with abundant elements.

Also important aspect of function of nanomaterials is in its excited states. To utilize electronically excited molecules as a functional materials, the interaction between light and matter should be studied as well as its dynamical behavior. To this end, we studied electronic excitations in real-time using SALMON, which allows us to study a direct electron dynamics and molecular dynamics following the induced electron movements under the framework of the time dependent density functional theory solved in real-time and real-space algorithm.

Concerning the catalysis, NO and NH_3 decompositions are studied [1-3]. As a preliminary step, we mostly utilized cluster models for these reaction pathway searches. Cu, Ag, and Au are used for NO decomposition and Cu, Ni, and Ru are used for NH_3 adsorption and decompositions. The cluster calculations showed that Cu is a good candidate for abundant catalysts for these reactions. For the surface calculations, we are performing DFT calculations on surfaces under the periodic boundary conditions using VASP, using several surface faces.

On the studying excited states of a molecule, we tested real-time electron dynamics calculations using benzene molecule. We have confirmed from many test calculations that for an accurate and reliable results, a real-space mesh of 0.25 Å and time step of 1 as is required. Parallel calculations using MPI and OpenMP are also tested and it turned out that the balanced combination of these two types of parallelization gives better performance, though the balance depends on the system size, i.e., the number of electrons and atoms.

References [1] T. Iwasa, et al., J. Phys. Chem. A, 123, 210-217 (2019). [2] S. Kiritoshi, T. Iwasa, K. Araki, Y. Kawabata, T. Taketsugu, S. Hinokuma, and M. Machida, RSC Advances, 8 41491-41498 (2018). [3] S. Hinokuma, K. Araki, T. Iwasa, S. Kiritoshi, Y. Kawabata, T. Taketsugu, and M. Machida, Catal. Commun., 123, 64-68 (2019).

Development of new structural search method and search for new functional materials

Masaaki GESHI

Institute for NanoScience Design,

Osaka University, Machikaneyama, Toyonaka, Osaka 560-8531

We propose an efficient structure search method by using first-principles calculation based on a random search method. What is most costly is calculation of structural optimization. Therefore, we have to reduce the number of first-principles calculations itself. To realize this, we propose a method to perform the structural optimization only on structures selected by enthalpy values calculated by one self-consistent field (SCF) calculation. To do this correctly and effectively, we propose One-Shot Enthalpy used Random Structure Searching (OSE-RSS) method.

The basic concept of the OSE-RSS method is as follows. In a potential energy surface (PES), we can consider physically true that *a certain structure near the ground state must reach the ground state except for a case that a potential energy surface is abnormal*. We cannot prove or guarantee that a certain structure reaches to the ground state after performing the structural optimization. However, the above sentence is considered true, at least physically.

The described idea is explained in Fig. 1. The enthalpy values of the randomly generated initial structures are distributed on the enthalpy surface.

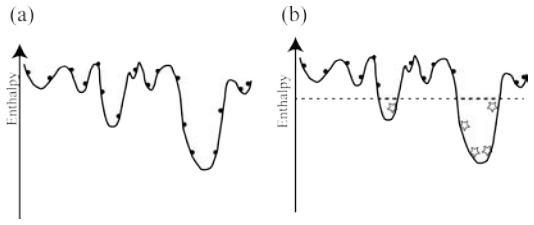

Fig.1 The concept of the OSE-RSS method. (a) The normal RSS method and (b) the OSE-RSS method. The black solid circles and open stars also mean the enthalpy of the generated initial structures. The latter is lower than a given criteria.

In the normal RSS method, all enthalpy values of the randomly generated structures are calculated after performing the full structural optimization as shown in Fig. 1(a). However, in the OSE-RSS method, the full structural optimization is performed only for the selected structures with lower enthalpy values as shown in Fig. 1(b).

This method can significantly reduce the computational cost. We apply this method to Si and H2S and some materials, and demonstrate the usefulness of this method.

Elucidation of the surface of supported metal catalyst in an electric field

Yasushi Sekine

Sekine Laboratory, Applied Chemistry,

Waseda University, Okubo, Shinjuku, Tokyo 169-8555

We have studied ammonia synthesis using the electric field. Our findings from an earlier study suggested that proton conducting support surface promotes N_2 dissociation in the electric field [1], [2]. In general, N_2 directly dissociates into nitrogen atom over an active metal. In the electric field, however, the H^+ over support reacts with N_2 over active metals, and N_2H is formed. The novel reaction path in the electric field suggests that factors which determines ammonia synthesis rate will be different from the general ones. Therefore, we focused on the optimization of active metals for ammonia synthesis in the electric field [3].

First, the N_2H formation energies for active metals (Ru, Fe, Co, Ni. Pd, Pt) were considered using DFT calculations. We used super computer for this calculation. As a calculation package, VASP-5.4.1 was used, and various models were calculated at the same time. Results suggested that Fe and Ni are suitable for N_2H formation. Based on the findings, ammonia synthesis tests were conducted. Results revealed that, Fe and Ni based catalysts exhibited higher activity than Ru, which is the best metal for the conventional ammonia synthesis using heterogenous catalysts. Investigating the correlation between the calculated N_2H formation energy and experimental ammonia synthesis rate, we found out the ammonia synthesis rate in the electric field is well scaled by N_2H formation energy over active metals as shown in Fig.1

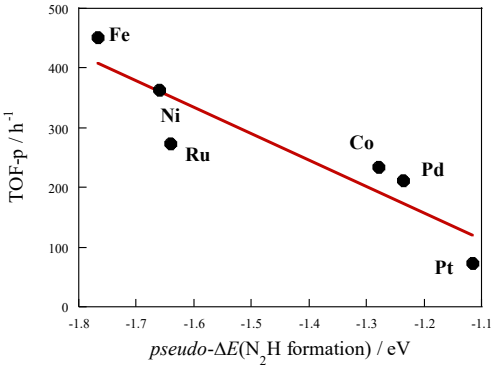

Fig. 1. Correlation between ammonia synthesis rate (TOF-p) and calculated N_2H formation energy (pseudo-ΔE(N_2H formation)).

References

[1] R. Manabe *et al*, *Chem. Sci.,* **8**, (2017) 5434-5439.

[2] K. Murakami *et al, Catal. Today*, **303**, (2018) 271-275.

[3] K. Murakami *et al, Catal Today, in press*.

Reduction of Rare Metals in Fuel Cell Catalysts and Hydrogen Permeable Membrane

Norihito Sakaguchi

Center for Advanced Research of Energy and Materials, Faculty of Engineering, Hokkaido University, Sapporo, Hokkaido 060-8628

We investigated the catalyst atom adsorption and diffusion properties on non-metal element doped graphene and hydrogen dissolution and diffusion properties in the interfaces of ceramic materials, with the aid of the first principles calculation based on the density functional theory (DFT).

At first, we investigated adsorption and diffusion properties of Pt atoms on non-metal element doped graphene. This year, we focused on the surrounding gas effect on adsorption and diffusion properties of Pt atoms. In order to model the operating environment of fuel cells, we consider the H, H_2, O, O_2, OH as the surrounding gas. We performed the total energy and electronic structure calculations using The Vienna Ab initio simulation package (VASP). We installed parallelized VASP with Intel® MPI Library and Intel® Math Kernel Library. We found that the adsorption energies and diffusion activation barriers of Pt atoms on non-metal element doped graphene decrease by surrounding gas adsorption. This is because the strong covalent bonds between Pt atom and adsorbates form using electron contributing weak covalent bonds between Pt and atoms and non-metal element doped graphene. However, In the cases of O-, Si, P-doped and monovacant graphene, the adsorption energies and diffusion activation barriers are still lager than 1 eV. Therefore, we concluded that the these dopants in graphene can prevent the detachment and surface diffusion of Pt atoms.[1]

We also investigated the hydrogen dissolution and diffusion properties in the interfaces of TiN. We found that the interface of TiN grains realizes high hydrogen permeability. We also studied hydrogen absorption properties in ceramic materials[2] and optical properties of doped ceramic materials using DFT calculations. [3]

References

[1] S. Hasegawa, Y. Kunisada, N. Sakaguchi: ACS Omega 4 (2019) 6573.

[2] T. Watanabe, Y. Kunisada, N. Sakaguchi: ChemPhysChem in press.

[3] G. Saito, Y. Kunisada, T. Watanabe, X. Yi, T. Nomura, N. Sakaguchi, T. Akiyama: J. Am. Ceram. Soc. 102 (2019) 524.

Ab initio molecular dynamics study of static structure of glasses

Akihide KOURA
Student Affairs Department,
Kumamoto University, Kurokami, Chuo-ku, Kumamoto, 860-8555

We have investigated the static structure of amorphous materials under pressure based on *ab initio* molecular dynamics (AIMD) simulations. In this year, we especially focused on the amorphous Mg-Zn-Y and V_2O_5 alloys.

On the V_2O_5 glass, we have focused on not only the static structure but also the diffusion mechanism, because experimental studies suggest O atoms are desorbed from the V_2O_5 glass, then the composition may become V_2O_{5-x}. However, the desorption mechanism is still unclear. In order to clarify the mechanism, AIMD simulations were carried out. In this study, the generalized gradient approximation was used for the exchange-correlation energy. The dispersion correction by Grimme and the Hubbard correction were also employed. We used a 168-atom system in a cubic supercell. At first, we obtained the bulk amorphous state by cooling from 4000 to 300 K.

In order to make the surface, the supercell size was elongated and the final configuration of the amorphous V_2O_5 was set at the center of the cell as a slab. It was expected that an O_2 molecule desorbed because an O-O bond appeared as soon as starting calculation. However, O_2 molecule desorption from the slab did not occur at 300 K. In order to enhance the desorption, the temperature of system was increased gradually up to 1700 K, however, the slab become widely spread in whole cell as a bulk system without O_2 desorption. To avoid this change, a larger system which has enough vacuum is required.

We also studied the static structure of amorphous Mg-Zn-Y alloy. Although the main component of the alloy is Mg atoms, fragments of $L1_2$-type Zn_6Y_8 cluster exist in the amorphous state. These fragments contribute the stability and toughening of alloy because of the strong bonds.

In our calculation processes, F4 queue was mainly used during all calculation processes with using 96 cores. This number of cores is more useful to submit jobs comparing with using larger number of cores. When we used 384 or 576 cores to run a job using more big system, our queuing time become rather long. Therefore, in order to have enough calculation time stably, we had to choose suitable number of cores.

In this year, three studies [1-3] with using ISSP supercomputer were published.

References

[1] A. Koura and F. Shimojo, *Phys. Status Solidi* B **255** (2018) 1800103.
[2] S. Hosokawa, *et al.*, *J. Alloys Compd.* **762** (2018) 797.
[3] M. Inui, *et al*, *Phys. Rev.* B **97** (2018) 174203.

Prediction of properties of organic ferroelectrics and piezoelectrics by first-principles calculation

Shoji ISHIBASHI
Research Center for Computational Design of Advanced Functional Materials (CD-FMat), National Institute of Advanced Industrial Science and Technology (AIST)
Tsukuba, Ibaraki 305-8565

Organic ferroelectrics and piezoelectrics are promising materials since they contain neither toxic nor rare elements. Recently, we observed the transition from an antiferroelectric (AFE) phase to a ferroelectric (FE) phase under a strong electric field on squaric acid (SQA) and proposed two possible FE phases (FE-α and FE-β) with their molecular arrangements and space groups [1]. The experimentally observed FE phase is thought to be the FE-α phase. On the other hand, the FE-β phase has not yet been experimentally confirmed.

In the present study, by computationally applying a static electric field [2], we simulate the AFE-to-FE transitions in SQA [3]. The calculations are performed using the computational code QMAS. As for the exchange-correlation functional, to reproduce the lattice parameters accurately, the rVV10 functional [4] is used.

Depending on the direction of the electric field, two different metastable ferroelectric (and piezoelectric) phases have been found. One of them corresponds to the experimentally confirmed FE-α phase, whereas the other corresponds to the FE-β phase. The spontaneous polarization values of the phases are 14.5 and 20.5 μC/cm^2, respectively. They are relatively high among those of the existing organic ferroelectrics. Their crystal structures are obtained as a function of the electric field. Significant converse piezoelectric effects are observed for both the phases as shown in Fig. 1 ($\sim$10 pm/V).

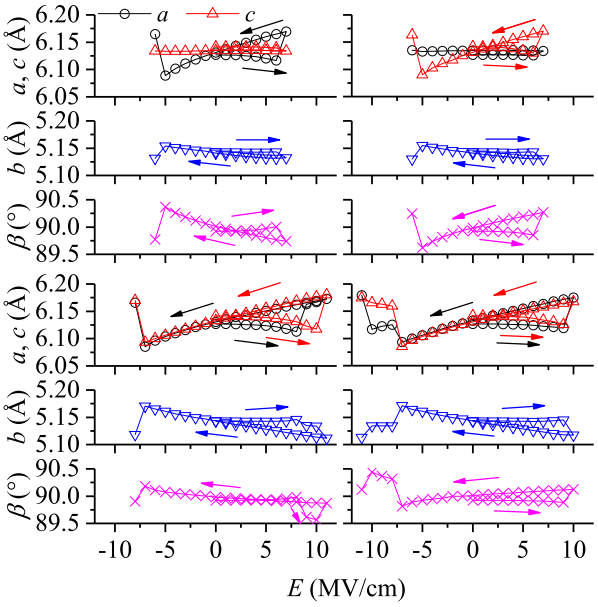

Figure 1: Variation in lattice parameters under electric field. $\boldsymbol{E} \parallel$ (upper left) $\boldsymbol{x}$, (upper right) $\boldsymbol{z}$, (lower left) $\boldsymbol{x}+\boldsymbol{z}$, and (lower right) $\boldsymbol{x}-\boldsymbol{z}$.

References

[1] S. Horiuchi, R. Kumai, and S. Ishibashi: Chem. Sci. **9** (2018) 425.

[2] I. Souza, J. Iñiguez, and D. Vanderbilt: Phys. Rev. Lett. **89** (2002) 117602.

[3] S. Ishibashi, S. Horiuchi, and R. Kumai:Phys. Rev. B **97** (2018) 184102.

[4] R. Sabatini, T. Gorni, and S. de Gironcoli: Phys. Rev. B **87** (2013) 041108(R).

Topological Analysis and Order Parameter of the System

Kazuto AKAGI

AIMR, Tohoku University, Katahira, Aoba-ku, Sendai, Miyagi 980-8577

We have studied nano-crystallization in highly supercooled Ti-based liquids by MD simulations and experimental measurements [1]. The growth of nano-crystals in MD trajectories can be detected by a conventional CNA (common neighbor analysis), but it was still difficult to see change in structures during the incubation period before the nucleation. This year, we introduced topological data analysis (TDA) based on persistent homology to evaluate local order in the system quantitatively.

Four systems ($Ti_{75}Ni_{25}$, $Ti_{67}Ni_{33}$, $Ti_{55}Ni_{45}$ and $Ti_{50}Ni_{50}$; 51,200 atoms) × 25 different configurations were annealed at 3,000 K for 100 ps, cooled down to 950 K during 200 ps and held at 950 K for 3,000 ps with NPT ensemble using LAMMPS with EAM[2]. "HomCloud" package [3] was used to generate a series of alpha complex from each atomic configuration and calculate persistent homology. The system was divided into 24×24×24 overlapped cells to evaluate the local order, and "HomCloud" parallelized to treat massive objects was performed on 6 nodes of System B.

The output from "HomCloud" gives the structural information on 1-dim. holes (ring structure) or 2-dim. holes (cavity) as a "persistence diagram (PD)" recording *birth* and *death* timing of each hole. Since the growth of *bcc* structure was commonly observed in the PD, we performed MD calculation of a $Ti_{50}Ni_{50}$ system with *bcc* structure at 950K to prepare a reference PD. An order-parameter was designed as inner-product between a sample PD and the reference PD via appropriate vectorization. Using this order-parameter, we obtained novel findings such as "increase of *precursor* structure before nucleation" and "correlation with local potential energy (Figure)" to make further statistical analyses.

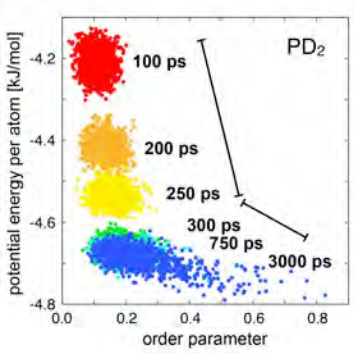

Fig. Change in ordering mode detected by TDA

References

[1] Z. Wang, C. L. Chen, S. V. Ketov, K. Akagi, A. A. Tsarkov, Y. Ikuhara, and D. V. Louzguine-Luzgin, Materials & Design **156** (2018) 504.

[2] L. Ward, A. Agrawal, K.M. Flores and W. Windl, https://arxiv.org/abs/1209.0619 .

[3] HomCloud, https://www.wpi-aimr.tohoku.ac.jp/hiraoka_labo/homcloud/

Developments of new materials using materials informatics

Tomoki YAMASHITA
Research and Services Division of Materials Data and Integrated System (MaDIS), National Institute for Materials Science (NIMS)
1-2-1 Sengen, Tsukuba, Ibaraki 305-0047

We have developed a crystal structure prediction method based on Bayesian optimization [1] and published a crystal structure prediction tool, CrySPY as an open source software [2]. CrySPY is interfaced with VASP[3], Quantum ESPRESSO[4], soiap[5], and LAMMPS code for structure optimization. Crystal structure prediction with Bayesian optimization can efficiently select the most stable structure from a large number of candidate structures with a lower number of searching trials using a machine learning technique. In the field of crystal structure prediction, there is a very popular algorithm, evolutionary algorithm [6, 7, 8]. Evolutionary algorithm is one of the structure generation methods, while Bayesian optimization is classified into a selection-type algorithm The key point here is that a selection-type algorithm is not exclusive with evolutionary algorithm.

First we have implemented evolutionary algorithm into our CrySPY code, and carried out test simulations using VASP, Quantum ESPRESSO, and soiap. Then we compared searching efficiency among RS, EA, and BO in the small system of Si16. In each algorithm, a hundred structures were searched. A hundred structures were selected from randomly generated five hundred structures particularly in BO. The success rates to find the most stable structure were 60%, 60%, and 50% for RS, EA, and BO, respectively. The importance of random generation is found compared with evolutionary operations even in EA. RS could be the most efficient for small systems. For the system of Si32, the success rates were 40%, 70%, and 40% for RS, EA, and BO, respectively. When the system becomes complicated, the efficiency of random structure generation gets worse. EA is a better algorithm for structure generation in large systems.

References

[1] T. Yamashita, N. Sato, H. Kino, T. Miyake, K. Tsuda, and T. Oguchi, Phys. Rev. Materials **2**, 013803 (2018).

[2] https://github.com/Tomoki-YAMASHITA/CrySPY.

[3] G. Kresse and J. Furthmüller, Phys. Rev. B **54**, 11169 (1996).

[4] P. Giannozzi et al., J.Phys.:Condens.Matter **21**, 395502 (2009).

[5] https://github.com/nbsato/soiap.

[6] A. R. Oganov and C. W. Glass, J. Chem. Phys. **124**, art. 244704 (2006).

[7] A. R. Oganov, A. O. Lyakhov and M. Valle, Acc. Chem. Res. **44**, 227 (2011).

[8] A. O. Lyakhov, A. R. Oganov, H. T. Stokes, and Q. Zhu, Comp. Phys. Comm. **184**, 1172 (2013).

Development of an efficient electron-transport simulator for atomic-layered materials

Yoshiyuki EGAMI
Division of Applied Physics, Faculty of Engineering, Hokkaido University
Kita 13, Nishi 8, Kita-ku, Sapporo, Hokkaido 060-8628

Recently, due to the improvement of computing power and the diffusion of massively parallel computers, obstacles for performing calculations with large computational costs, such as numerical simulation of large-scale models and pursuit of computational accuracy using first-principles calculations, are reduced. However, in order to use limited computer resources effectively, it is essential to develop an algorithm with low computational costs.

In the electron-transport property calculations for nanoscale materials suspended semi-infinite electrodes, the self-energy matrices in the electrodes are required. The computational cost for obtaining the self-energy matrices are generally proportional to the cube of the electrode length of the lateral direction perpendicular to the transport direction. This prevent us to perform the transport calculations for two-dimensional systems with a large surface. So far, I developed first-principles electron-transport property simulators[1, 2, 3] based on the real-space finite-difference approach[4], and clarified the transport properties of nanoscale materials[5, 6].

In this subject, the procedure for preparing the self-energy matrices was improved to carry out the transport property calculations of a large-scale system with low calculation cost without deterioration of calculation accuracy. In the procedure, the self-energy matrices of the large electrode unit cell, where the primitive unit cell is repeated in the directions parallel to the electrode surface, can be accurately reproduced from those of the small primitive unit cell without accuracy deterioration.

For demonstration of the proposed method, electron transport properties of a fluorinated graphene were examined, where graphene surface is terminated by fluorine atoms. We discussed the controllability of transport properties by chemical modification, and clarified the influence of the density and the structural symmetry of adatoms on the transport properties. In particular, the changes in transmission due to the difference in the structural symmetry are so small that it is difficult to observe them if the self-energy matrices cannot be calculated accurately. The procedure can accurately and efficiently evaluate such slight changes that may be buried in numerical errors. These works have been performed on System B and System C.

References

[1] Y. Egami, K. Hirose and T. Ono: Phys. Rev. E **82**, 56706 (2010).
[2] Y. Egami and K. Hirose: JPS Conf. Proc. **1**, 016012 (2014).
[3] Y. Egami, S. Iwase, S. Tsukamoto, T. Ono and K. Hirose: Phys. Rev. E **92**, 033301 (2015).
[4] K. Hirose *et al.*: *First-Principles Calculations in Real-Space Formalism*, (Imperial College Press, London, 2005).
[5] Y. Egami and H. Akera: Physica E **88** (2017) 212.
[6] Y. Egami and M. Taniguchi: Jpn. J. App. Phys. **57** (2018) 021601.

Ab-initio simulations of high-order harmonic generation from crystalline solids

Yasushi SHINOHARA

Photon Science Center,

The University of Tokyo, Hongo, Bunkyo-ku, Tokyo 113-8656

State-of-the-art coherent light sources allow us to induce nonequilibrium electron dynamics beyond the perturbative regime [1]. One of the simplest phenomena in the photo-induced electron dynamics is high-order harmonic generation (HHG), photon emission peaked at multiple photon energies of driving field frequency. Intensity distribution and angle dependence of the emitted HHG spectra are expected to have information on electronic structures of materials.

We have developed an *ab-initio* theoretical framework to describe electron real-time dynamics for crystalline solids [2]. The theoretical framework is based on electronic structures derived by density-functional-theory (DFT). The DFT calculation is performed by Elk FP-LAPW code [3]. Eigenvalues and momentum operator matrix elements based on local-density approximation are taken from Elk output files. We perform real-time evolution of a quantum system with the eigenvalues and matrix elements under applied vector potential because we employ the velocity gauge for electron-light interaction. We have already applied our code to HHG from GaSe and compared it with experimental results [2].

This year, we work on theoretical development and its application related to relaxation, and another application of our codes.

When photon energy is close to the band gap of materials, intense HHG yield above band gap is realized. Interband contribution to the yield is expected to be stronger for this situation because induced dipole due to electron-hole excitation can generate photon for this photon energy range. Fast relaxation for interband density-matrix is reported to realize well-peaked spectra on the multiple photon energies rather than a broad spectral feature. The relaxation was defined by field-free Hamiltonian. A way to introduce the relaxation depends on whether gauge we choose, the length- or the velocity-gauge, apart from the choice of the actual equation of motion. We employ a length-gauge-based-relaxation formula [4], while we use the velocity-gauge for the equation motion. This formula is derived via a gauge transformation from the length-gauge equation of motion with the relaxation term. The transformed equation motion has a physically natural interpretation that the relaxation happens only for components of instantaneous

eigenfunction meaning no-relaxation for the adiabatically evolved system. This formula is installed in our previous code. Simulations with the relaxation are performed to GaSe but higher driving photon frequency than previous investigations. In addition to the relaxation role in the HHG that peaked structure, our simulation shows fast relaxation leads to expected crystal symmetry of HHG spectra which is consistent with experimental results [4].

We apply our framework, without the relaxation, to HHG from perovskite CsPbCl3 compared with experimental results [6]. The total yield of HHG spectra is dominated by the intraband contribution from our simulation. We perform further decomposition of the intraband contribution to each band contribution. Our results show the most prominent part is from valence top bands rather than conduction bands.

References

[1] F. Krausz and M. Ivanov, Rev. Mod. Phys. **81** (2009) 163.

[2] K. Kaneshima, Y. Shinohara, K. Takeuchi, N. Ishii, K. Imasaka, T. Kaji, S. Ashihara, K.L. Ishikawa, and J. Itatani, Phys. Rev. Lett. **120** (2018) 243903.

[3] http:/elk.sourcefourge.net

[4] Y. Shinohara, in preparation.

[4] K. Imasaka, T. Kaji, Y. Shinohara, K.L. Ishikawa, S. Ashihara, in preparation.

[6] Hideki Hirori, Peiyu Xia, Yasushi Shinohara, Tomohito Otobe, Yasuyuki Sanari, Hirokazu Tahara, Nobuhisa Ishi, Jiro Itatani, Kenichi L. Ishikawa, Tomoko Aharen, Masashi Ozaki, Atsushi Wakamiya, Yoshihiko Kanemitsu, APL Materials **7**, 041107 (2019).

Thickness dependence of strain in β-$FeSi_2$(100) nano-sheet

Ken HATTORI
Graduate School of Science and Technology, Nara Institute of Science and Technology
Takayama, Ikoma, Nara 630-0192

Using in-plane two-dimensional (2D) X-ray diffraction (XRD), author's group has been studied the strain of β-$FeSi_2$(100) nano-films on Si(001) [1] prepared in ultra-high vacuum. The thickness of the film was approximately 1.5 nm, corresponding three quintuple layers (QL). Here unity QL has stacking layers of Si (8 atoms in a b-c unit)/Fe (2)/Fe (2)/Si (8)/Fe (4) with a Si (8) bottom layer, as shown in Fig. 1 [2].

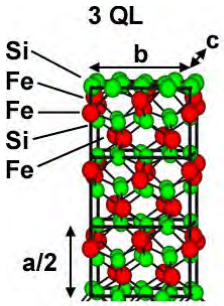

Figure 1: A model of β-$FeSi_2$(100) with 3 QL in thickness. 1 QL corresponds to half of lattice constant a.

Since the lattice mismatch of β-$FeSi_2$(100) to Si(001) is +1.4% in the b axis and +2.0% in the c axis, we expect the compressive strain of -1.4% and -2.0% of β-$FeSi_2$ from the bulk lattice constants b (7.791 Å in experiment) and c (7.833 Å), respectively, when the complete epitaxial growth. 2D XRD peak-fitting analyses for β-$FeSi_2$ diffraction spots indicated, however, that the strain were 0.0% and -0.3%, respectively. High-resolution transmission electron microscopy (HR-TEM) also showed uncompressed β-$FeSi_2$. This implies that the interaction of β-$FeSi_2$ to Si substrate is weak, and that β-$FeSi_2$ acts as a strain-free and free-standing nano-film. This is a quite curious behavour of the nano film; the film is not epitaxially grown.

In addition, the XRD results also indicate anisotropic strain between b and c (0.0% and -0.3%), which implies the deformation of the rectangular unit (7.79 Å× 7.83 Å) to square-like unit (7.79 Å× 7.81 Å) in the nano film. In order to confirm the deformation behavour, we calculated strain of free-standing β-$FeSi_2$(100) as a function of thickness using Simulation Tool for Atom TEchnology (STATE)-Senri [3] under the super computing system in the institute for solid state physics.

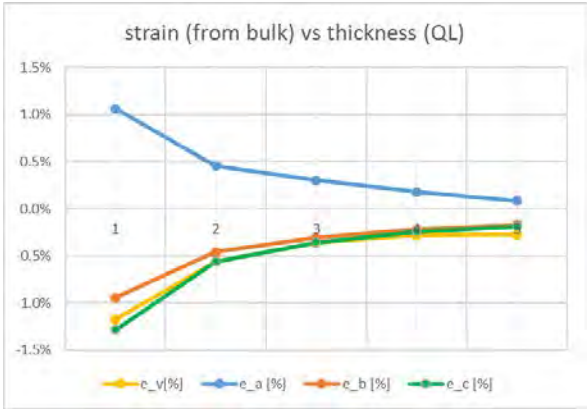

Figure 2: Strain of a (blue), b (brown), c (green) axes, and volume (yellow) from the bulk values in the free-standing β-$FeSi_2$(100), as a function of thickness (QL unit).

The models with 1, 2, 3, 4, and 5 QLs have total 32, 56, 80, 104, and 128 atoms with slabs of 5.0, 10.0, 14.9, 19.9, and 24.8 Å and vacuums of 5.6, 11.2, 16.9, 22.5, and 28.2 Å, respectively. The 4×4×1 k-point mesh was used. The total energy was calculated as a function of in-plane lattice constants b and c, where the bottom Si atoms were fixed to positions proportional to the calculated bulk positions. The strain in b and c directions, and also a direction from

the bulk values were estimated from the lattice constants satisfying the energy minimum.

Figure 2 shows the strain of a, b, and c axes as a function of thickness. The strain of b and c decrease and of a increase with decreasing thickness. This implies shrinking in-plane lattice constants and expanding out-of-plane lattice constant in the complete free-standing nano-films. In addition, we notice that strain of c is more compressed than strain of b. This tendency supports our XRD results

The authors thank Profs. Morikawa, Hamada, and Inagaki in Osaka University, and Prof. Yanagisawa in Ryukyu University for their great support in STATE-Senri calculations.

References

[1] S. Takemoto, K. Hattori, et al., (unpublished).

[2] O. Romanyuk, K. Hattori, M. Someta, and H. Daimon, Phys. Rev. B **90** (2014) 155305.

[3] Y. Morikawa, Phys. Rev. B **63** (2001) 033405, and references therein.

Theoretical Study of Industrial Enzyme and Drug Target Protein using the Forth Revolution

Yuta Yamamoto[1], Shogo Nakano[2], Vladimir Sladek and Hiroaki Tokiwa[1]

[1]Rikkyo University, 3-34-1 Nishi-Ikebukuro, Toshima, Tokyo 171-8501

[2]University of Shizuoka, 52-1 Yada, Suruga-ku, Shizuoka 422-8526

In order to improve stability and bioactivity of the target industrial enzyme, we could rationally design artificial enzyme proteins based on the expansion of protein sequence databases, such as full-consensus design (FCD) and ancestral-sequence reconstruction (ASR). Artificial enzyme with enhanced activity levels compared with native ones can potentially be generated by such methods, but successful design is rare because preparing a sequence library by curating the database and selecting a method is difficult. Utilizing a curated library prepared by reducing conservation energies, we successfully designed several artificial l-threonine 3-dehydrogenases (SDR-TDH) with higher activity levels than native SDR-TDH, FcTDH-N1, and AncTDH, using FCD and ASR, respectively.[1] Structural molecular dynamics (MD) simulations and *ab initio* quantum chemical calculations using the fragment molecular orbital (FMO) method for the SDR-TDHs systems revealed that only the flexibility at specific regions was changed, suggesting that multiple mutations introduced in the artificial SDR-TDHs altered their flexibility and thereby affected their enzymatic properties. Benchmark analysis of the SDR-TDHs indicated that both FCD and ASR can generate highly functional proteins if a curated library is prepared appropriately.

We, furthermore, develop the 3D-visualization of interaction energies in protein system (3D-VIEP) method; the toolkit AnalysisFMO, which should enable a more efficient and convenient workflow with FMO data generated by quantum-chemical packages such as GAMESS, PAICS, and ABINIT-MP programs for the theoretical evaluation of activity of a pharmaceutical candidate complied with certain expectations. [2]

Reference

[1] S. Nakano, T. Motoyama, Y. Miyashita, Y. Ishizuka, N. Matsuo, H. Tokiwa, S. Shinoda, Y. Asano, S. Ito, *Biochemistry,* **57(26),** 3722-3732 (2018) DOI: 10.1021/acs.biochem.8b0033.

[2] T. Tokiwa, S. Nakano, Y. Yamamoto, T. Ishikawa, S. Ito, V. Sladek , K. Fukuzawa, Y. Mochizuki, H. Tokiwa, F. Misaizu, Y. Shigeta, *J. Chem. Inf. Model.,* **59 (1)**, 25–30 (2019) DOI: 10.1021/acs.jcim.8b00649.

Theoretical Design of Energy Harvesting and Storage Device Materials by First-Principles Calculations

Hiroyoshi MOMIDA, Motoyuki HAMAGUCHI, Hiroshi KATSUMOTO
Institute of Scientific and Industrial Research, Osaka University
8-1 Mihogaoka, Ibaraki, Osaka 567-0047

By using the first-principles calculations, we have investigated piezoelectric properties of wurtzite materials as the energy harvesting device materials and electrode properties of transition metal oxide materials for the lithium-ion secondary batteries as the energy storage device materials. The calculations are done using HiLAPW and Quantum Espresso codes.

Piezoelectricity of nano-structures of wurtzite materials: The wurtzite materials can have piezoelectric properties because of the lack of inversion symmetry [1]. Recently, nano-structured ZnO have been attracted great interest because of their high piezoelectric performance. In this study, we have studied the piezoelectric properties of nano-film and nano-tube structures of wurtzite ZnO by means of the first-principles calculations. In the nano-film structure of ZnO(0001), we find that the significant thickness dependence of atomic structures. The wurtzite-type atomic structures are kept for thicker films, but the flatter atomic structures are more stable for thinner films. We also perform the first-principles calculations for ZnO [0001] nano-tubes with $\{10\bar{1}0\}$ facet. The calculated result shows that the ZnO nano-tubes with small diameter can have higher piezoelectric properties compared with the bulk values.

Electrode properties of Li-ion secondary battery materials: The so-called cation-disordered rock-salt structure materials including Li_2MTiO_4 (M = transition-metal elements) have been expected to be a candidate cathode material for future Li-ion secondary batteries [2]. Recently, it has been experimentally reported that the battery performance of Li_2MnTiO_4 can be improved by increasing the composition ratio of Li as to be $Li_{2+2x}Mn_{1-x}Ti_{1-x}O_4$ ($x \sim 0.2$). To clarify microscopic origin of the improvement, we have performed the first-principles calculations of $Li_{2+2x}Mn_{1-x}Ti_{1-x}O_4$ models with several excess amounts of Li (x) ranging from 0 to 0.5. From the energy analyses, we evaluate the theoretical voltage-capacity profiles of the materials, showing that the calculated voltage values are consistent with the experimental values. The calculated electronic structures show that the redox reactions of Mn are the primary mechanism for the battery reactions especially in the early discharge process, and that the redox reactions of O becomes important in the latter discharge reaction process. We have also studied material properties of SnS anode materials for Na-ion batteries [3].

References

[1] H. Momida and T. Oguchi: Appl. Phys. Express **11** (2018) 041201/1-4.

[2] M. Hamaguchi, H. Momida, and T. Oguchi: J. Phys. Soc. Jpn. **87** (2018) 044805/1-8.

[3] H. Kotaka, H. Momida, A. Kitajou, S. Okada, and T. Oguchi: J. Comput. Chem. Jpn. **18** (2019) 78-83.

First-principles Thermodynamics and Statistical Mechanics Simulations of Catalytic Reactions at Solid Surfaces

T. N. PHAM, S. A. Wella, S. E. M. PUTRA, F. MUTTAQIEN, K. INAGAKI, Y. HAMAMOTO, I. HAMADA, and Y. MORIKAWA
Department of Precision Science and Technolgy, Graduate School of Engineering, Osaka University, 2-1 Yamada-oka Suita, Osaka 565-0871

In this project, we have studied atomic geometries, electronic properties and chemical reactions at surfaces and interfaces, especially, we focused on etching processes of SiC in water using Pt catalysts [1], dopants in semiconductors [2], NO dissociation by hydrogen bonding on Cu(110) [3], metal-insulator transition at $LaNiO_3$ thin-films on $SrTiO_3$ substrate [4], bonding states of single-atom Pt at graphene edges [5], the origin of the change in the absorption spectra upon oxidation and reduction in Ru-complexes [6], and formic acid adsorption on Cu(111) [7]. In the present report, we discuss the enhancement of the NO dissociation by hydrogen bonding[3].

Nitric oxide (NO) emission from the exhaustive gas of combustion process has caused negative impacts on the environment, e.g, acid rain, photochemical smog, and ozone depletion. Therefore, NO reduction to harmless substances is an important task to mitigate the environmental pollution. The catalysts of expensive precious metals such as Pt, Rh, and Pd are often employed to remove NO as well as CO and unburned hydrocarbon gases simultaneously from the exhaust gas. However, the practice requires that the catalysts must be abundant, low cost, and high catalytic activity. Among various alternative materials, copper-based catalysts are very promising owing to their excellent performances for the NO reduction.

As essential steps for the NO reduction, the NO adsorption and dissociation to N and O on the copper surfaces have been intensively studied by both experiment and theory. On low-index Cu surfaces, i.e., Cu(100), Cu(110), and Cu(111), NO is molecularly adsorbed at rather low temperature followed by formations of dimeric $(NO)_2$ and N_2O species with further gas exposure. Recently, Shiotari and coworkers experimentally studied the NO adsorption and dissociation on the Cu(110) surface at low-coverage region using scanning tunneling microscopy (STM), reflection absorption infrared spectroscopy, and electron energy loss spectroscopy [8].

Herein we present a DFT calculation to clarify the role of water molecules and the mechanism of the hydrogen bonding induced NO dissociation on the Cu(110) surface.

The calculations were carried out by using the simulation tool for atom technology (STATE) package [9, 10]. The Vanderbilt ' s ultrasoft pseudopotentials were used to describe the electron-ion interactions. Wave functions and argumented charge density were expanded by a plane wave basis-set with cutoff energies of 36 and 400 Ry, respectively. In this study, we compared results obtained by the Perdew-Burke-Ernzerhof (PBE) generalized gradient approximation (GGA) exchange-correlation functional to those obtained by van der Waals density functionals (vdW-DFs),

which take into account the dispersion interaction. We used vdW-DF1, optB86b-vdW, and rev-vdW-DF2[11] functionals as implemented in the STATE code[10].

After optimizing possible initial NO/Cu(110) configurations, we obtained two types of favorable adsorption configurations: (1) an upright NO in which N binds to the surface (N*O) and (2) a side-on NO connecting two short-bridge sites (N*O*) along [001] direction. The van der Waals corrected functionals such as rev-vdW-DF2 and optB86b-vdW successfully reproduce the side-on configuration of adsorbed NO, which is an important precursor for the NO dissociation. The NO dissociation without water requires an activation energy of 0.76 eV. We find that hydrogen bonds efficiently reduce the activation energy of NO dissociation down to 0.34 eV and 0.27 eV with a water dimer and two water dimers near N*O*, respectively. Our study reveals the promotion effect of the water molecules is only dominant when one of the water molecules in a water dimer donates a hydrogen bond to O of side-on NO (see Fig. reffig:fig1. The N-O bond is weakened as the results of the enhanced back donation by the hydrogen bond between the water dimer and side-on NO. Our present results provide a physical insight of the role of hydrogen bonds from water, which may be helpful to practical applications of copper surface in NO reduction as well as the design of novel catalysts for this purpose.

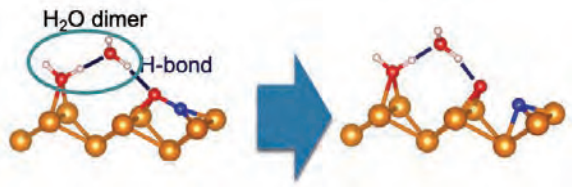

Figure 1: Hydrogen-bond enhanced N-O dissociation on Cu(110).

References

[1] P. V. Bui, D. Toh, A. Isohashi, S. Matsuyama, K. Inagaki, Y. Sano, K. Yamauchi, and Y. Morikawa: Jpn. J. Appl. Phys. **57** (2018) 055703.

[2] Y. Takano, N. Kobayashi, and Y. Morikawa: J. Phys. Soc. Jpn. **87** (2018) 061013.

[3] T. N. Pham, M. Sugiyama, F. Muttaqien, S. E. M. Putra, K. Inagaki, D. N. Son, Y. Hamamoto, I. Hamada, and Y. Morikawa: J. Phys. Chem. C **122** (2018) 11814.

[4] H. D. Nguyen, B. T. Cong, and Y. Morikawa: J. Phys. Soc. Jpn. **87** (2018) 114704.

[5] S. A. Wella, Y. Hamamoto, Suprijadi, Y. Morikawa, and I. Hamada: Nanoscale Adv. **1** (2019) 1165.

[6] S. S. Tan, S. Yanagisawa, K. Inagaki, M. B. Kassim and Y. Morikawa: Phys. Chem. Chem. Phys. **21** (2019) 7973.

[7] S. E. M. Putra, F. Muttaqien, Y. Hamamoto, K. Inagaki, I. Hamada, and Y. Morikawa: J. Chem. Phys. **150** (2019) 154707.

[8] A. Shiotari, T. Mitsui, H. Okuyama, S. Hatta, T. Aruga, T. Koitaya, and J. Yoshinobu: J. Chem. Phys. **140** (2014) 214706.

[9] Y. Morikawa: Phys. Rev. B **51** (1995) 14802.

[10] Y. Hamamoto, I. Hamada, K. Inagaki, Y. Morikawa: Phys. Rev. B **93** (2016) 245440.

[11] I. Hamada: Phys. Rev. B **89** (2014) 121103.

Analysis on atomic and magnetic structure in magnetic molecular complex, crystal and interface and investigation of electron correlation effect

Masao OBATA[1,2], Mega CHRISTIVANA[2], and Hasan Al RASYID[2]

Institute of Science and Engineering, Kanazawa University, Kanazawa, Ishikawa 920-1192

Graduate School of Natural Science and Technology, Kanazawa University, Kanazawa, Ishikawa, 920-1192

We have investigated the weak-bound magnetic material systems such as magnetic molecular crystal and two-dimensional layered material. They have received a lot of attention due to their unique physical properties such as its magnetization and crystal structure which could be controllable by external field. However, the current density functional theory (DFT)-based first-principles approach are not suitable for investigating these material accurately due to omission of some physical interactions, e.g. van der Waals (vdW) interaction and magnetic dipole-dipole (MDI) energy. Therefore, we developed computational method to evaluate these contributions.

1) MDI energy estimation of magnetic crystal

We have developed computational approach to employ MDI energy, which is one origin of magnetic anisotropy and diamagnetic field. It may be calculated with using spatial spin density $\mathbf{m}(\mathbf{r}) = (m_x, m_y, m_z)$ obtained from DFT calculation as follows:

$$E_{\mathrm{MDI}} = \sum_{\alpha\beta} \iint d\mathbf{r} d\mathbf{r}' m_\alpha(\mathbf{r}) f(\mathbf{r}-\mathbf{r}') m_\beta(\mathbf{r}'),$$

where $\mathrm{f}(\mathbf{r}) = \frac{1}{8c^2}\frac{r^2\delta_{\alpha\beta}-3r_\alpha r_\beta}{r^5}$ and c is speed of light in Hartree unit. We applied this approach to antiferromagnetic molecular crystal (monoclinic crystal solid oxygen α phase: α-O_2). The obtained magnetic anisotropy energy of α -O_2 shows that the b-direction of monoclinic structure is the easy axis of molecular spin moment [1], supporting the experimental result.

2) Implementation and application of vdW-DF approach with non-collinear magnetism

We extended vdW-DF [2] — which is able to estimate nonlocal correlation energy without empirical parameter — to non-collinear magnetism. As a demonstration, we applied it to a triangle magnetic lattice of β-phase solid oxygen. Our method could predict crystal structure more accurately compared to a standard generalized gradient approximation.

References

[1] M. Obata et al., AIP Adv. **8**, 10149 (2018).

[2] M. Dion et al., Phys. Rev. Lett. **92**, 246401 (2004).

First-Principles Study on Hydrogen Adsorption and Desorption of Germanene

M. ARAIDAI[1,2,3], M. KUROSAWA[2,3], A. OHTA[2,3], and K. SHIRAISHI[1,2]

[1]*Institute of Materials and Systems for Sustainability,*
[2]*Graduate School of Engineering,*
[3]*Institute for Advanced Research,*
Nagoya University, Furo-cho, Chikusa-ku, Nagoya, Aichi 464-8601

Two-dimensional crystals consisting of group IV element heavier than carbon, such as silicene, germanene, and stanene, are supreme thin-film materials. They have been theoretically predicted to possess high carrier mobility and some intriguing functions such as band-gap control and topological insulator [1,2]. They have been recently synthesized on metallic substrates [3-6]. However, it has been reported that the electronic state of silicene on a metallic substrate are dramatically modified by the strong interactions with the surface atoms [7,8]. On the other hand, a hydrogenation of $CaSi_2$ [9] or $CaGe_2$ [10] crystal is one of the most promising methods to fabricate single layer Si or Ge crystal. A hydrogenated silicene (silicane) or germanene (germanane) crystal can be obtained by the hydrogenation and we can easily exfoliate the free-standing one from the crystal. In this study, we theoretically investigate whether hydrogen atoms can be desorbed from the germanane by controlling hydrogen atmosphere; that is, a free-standing germanene can be created from a germanane.

To discuss the hydrogen adsorption and desorption property of germanane, we calculate the free energies of reactant and products. The difference ΔG determines the direction of this reaction. If ΔG is negative, germanene is created. If positive, germanane is created. The free energy consists of two parts: contributions of electrons and lattice vibration. We used VASP code [11] to calculate the electronic contributions and ALAMODE code [12] to calculate the vibrational contributions.

Figure 1 shows the phase diagram for germanene formation. The horizontal axis is temperature, and the vertical axis is hydrogen pressure. The color contour indicates ΔG. We can see that the boundary between positive and negative regions is the left upper corner of the diagram. We observe from Fig. 1 that ΔG is negative over a wide area. Therefore, germanene can be created from germanane at ordinary temperatures and pressures. On the other hand, we have found that silicene cannot be created from silicane at ordinary temperatures and pressures.

References

[1] K. Takeda and K. Shiraishi, Phys. Rev. B **50**, 14916 (1994). [2] M. Ezawa, New J. Phys. **14**, 033003 (2013). [3] A. Fleurence, et al., Phys. Rev. Lett. **108**, 245501 (2012). [4] P. Vogt, et al., Phys. Rev. Lett. **108**, 155501 (2012). [5] L. Li, et al., Adv. Mat. **26**, 4820 (2014). [6] F.-F. Zhu, et al., Nat. Mater. **14**, 1020 (2015). [7] Z.-X. Guo, et al., J. Phys. Soc. Jpn. **82**, 063714 (2013). [8] M. X. Chen and M. Weinert, Nano Lett. **14**, 5189 (2014). [9] H. Nakano and T. Ikuno, Appl. Phys. Rev. **3**, 040803 (2016). [10] E. Bianco, et al., ACS Nano **7**, 4414 (2013). [11] G. Kresse and D. Joubert, Phys. Rev. B **59**, 1758 (1999). [12] T. Tadano, et al., J. Phys.: Condens. Matter **26**, 225402 (2014).

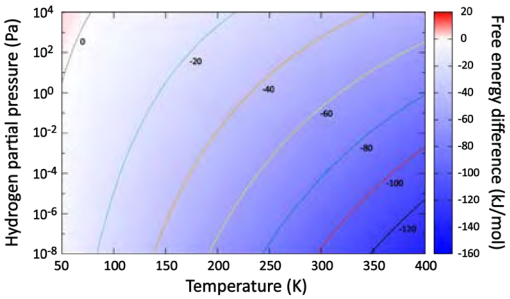

Fig. 1: Phase diagram on hydrogen adsorption and desorption of germanene.

Ab initio Molecular Dynamics Simulation of Sustained Chemical Reaction Processes in Deep-sea Hydrothermal Vents

Kohei Shimamura

Graduate School of System Informatics,

Kobe University, 1-1 Rokkodai, Nada-ku, Kobe 657-8501

We have investigated ocean impact events of meteorites during late heavy bombardment period lasting about 3.8 billion years ago by *ab initio* molecular dynamics (AIMD) simulation based on density functional theory (DFT). The impact energy and the reductive action of metallic iron contained in the meteorites would have resulted in a large amount of reductive molecules on a global scale, providing an environment that was easy to maintain life activity. We therefore have investigated the reaction processes in which reductive carbon source molecules were produced from carbon dioxides by imitating oceanic collision of the iron bearing-meteorites, where hydrocarbons and carboxylic acids were produced and their production processes were clarified in detail at the atomistic level [1].

However, it is questionable whether the impact events were directly involved in the birth of life although the events may have changed the ancient Earth's environment to reductive one. This is because the events cannot supply reductive molecules continuously. For this reason, we have focused on the alkaline deep-sea hydrothermal vent environment. In this environment, a reducing agents such as hydrogen are constantly supplied, and a sustained chemical reaction system can be constructed on the precipitated film-like or vesicle-like iron sulfides. We have simulated this environment and have already confirmed by simulation that a carboxylic acid was produced from a carbon dioxide on the sulfide surface. However, due to the large calculation cost of AIMD, it was not possible to make the calculation system large enough to confirm the sustained chemical reaction.

In order to achieve our goal, we need to employ lower computational cost methods that can represent chemical reactions. Therefore, we attempt to solve this problem by using two methods, that is, molecular dynamics simulation using density functional tight binding (DFTB) and an empirical interatomic potential based on and artificial neural network (ANN).

Reference

[1] K. Shimamura, F. Shimojo, A. Nakano, and S. Tanaka: J. Comp. Chem. **40**, 349 (2019).

Modulation of phonon modes originate from impurities in GaN

Masato Oda

Department of Applied Physics,

Wakayama University, 930, Sakaedani, Wakayama, 640-8510

GaN is one of the most important materials in devices such as light-emitting diodes (LEDs) and laser diodes. However, defects in the GaN structure may result in degradation in the active regions of such devices. Yet, it remains unknown how these defects originate. Thus, we quantitatively investigated the electron–phonon interactions that occur around Ga vacancies (V_{Ga}) in GaN by carrying out first-principles calculations.

We show that, the conditions required for the phonon-kick mechanism in the neutral state [1] are also valid in the positively charged state [2]. Moreover, the defect reactions via the phonon-kick mechanism are likely to occur around V_{Ga} due to the higher-amplitude localized modes, which should cause N atoms to migrate toward the V_{Ga} and form a N_{Ga}–V_N complex defect.

These findings are an important contribution to our basic knowledge of the origin of defects in GaN and have practical applications in the development of light-emitting diodes and transistors that offer longer lifetimes and higher efficiencies.

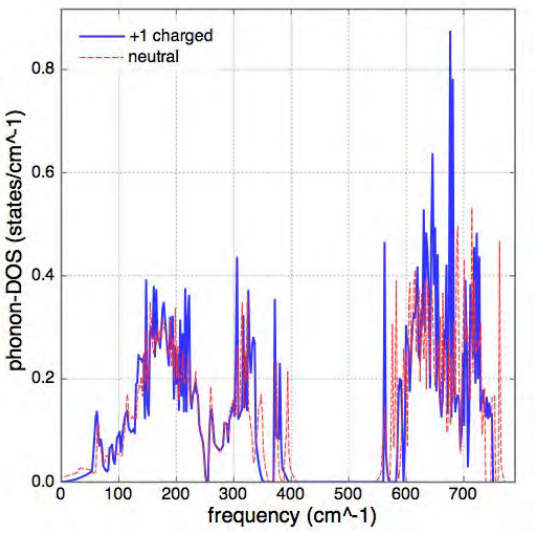

Fig. 1 Phonon DOS of V_{Ga} in GaN in the positively charged and the neutral states.

References

[1]T. Tsujio, M. Oda, and Y. Shinozuka: Jpn. J. Appl. Phys. 56, 091001 (2017).

[2]M. Oda: Jpn. J. Appl. Phys., in press

Vibrational properties of crystalline organic semiconductors from first-principles

Susumu Yanagisawa
Department of Physics and Earth Sciences, Faculty of Science, University of the Ryukyus
1 Senbaru, Nishihara, Okinawa 903-0213

These years, impacts of the crystal geometry and configuration between neighboring molecules upon electronic properties of organic semiconductor crystals have been demonstrated[1], and the importance of accurately describing the van der Waals (vdW) interaction in molecular solids from first-principles has been realized. Thanks to the development of reliable vdW-inclusive methods, prediction of crystal geometries of organic crystals in quantitative agreement with experiments is becoming possible. The author has theoretically demonstrated subtle interplay between the crystal geometries and the intermolecular transfer integrals[2]. Description of the vdW interaction between the molecular adsorbate and the metal substrate clarified the impact of the slight molecular geometry relaxation upon the interface electronic structure[3].

First-principles calculations have been used for gaining insights into not only the electronic properties at low temperature, but also those at room temperature. However, such approaches may not be valid in case of organic crystals, whose structural configurations or conformations can be significantly fluctuated, depending on the ambient temperature. In such cases, the electron-phonon coupling effect upon the electronic band structure at finite temperature may be non-negligible[4]. In this study, to gain insights into the electron-phonon coupling and resulting modification of the crystalline band structure of organic semiconductor crystals from first-principles, we conducted calculation of phonon dispersion of some typical organic semiconductor crystals such as naphthalene and rubrene.

To calculate the phonon dispersion, we employed the Quantum Espresso v6.3[5]. To obtain as accurate force constants and phonon frequencies as possible, we set tight convergence thresholds on total energy, force, and pressure, and for self-consistency during crystal geometry optimization. Optimized norm-conserving Vanderbilt (ONCV) pseudopotentials[6] were used, and the plane wave cutoff energy was 240 Ry. The dynamical matrices were treated within the density functional perturbation theory (DFPT)[7], as implemented in the Quantum Espresso program. The $\mathbf{q}$-point set within the Brillouin zone at which the second-order energy is calculated was 4×4×4 (2×2×2) for naphthalene (rubrene). Throughout the calculation, a variant of the vdW density functional[8, 9, 10] was used. The lattice constants of the equilibrium structures obtained were in agreement with experiments measured at low temperature, with the mean absolute deviation from the experimental values being within 1 %. All the calculations were done on system B of the supercomputer center in ISSP, and the number of cores used in the flat MPI calculation ranged from 384 to 576.

As a test case, the phonon dispersion of crystalline naphthalene was calculated (see Figure 1). The calculated phonon dispersion curve is characterized by the phonon modes

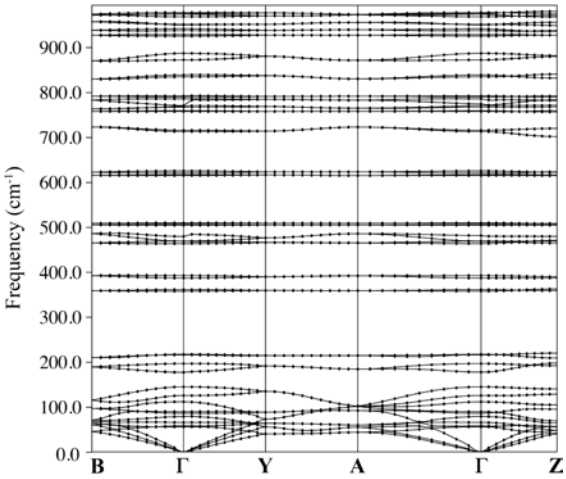

Figure 1: Calculated phonon dispersion curve of crystalline naphthalene

Table 1: Phonon frequencies at Γ point of crystalline rubrene. Units are cm^{-1}.

modes	frequency
B_{1u}	$20.6i$
B_{3u}	20.0
B_{2u}	36.8
B_{1u}	42.8
B_{3g}	43.6
B_{1g}	45.3

whose frequencies are below 150 cm^{-1}, that are dominated by the intermolecular vibrational modes. The dispersion curve is in agreement with the previous result obtained with similar level of theory, and in fair agreement with experiments[11]. In case of rubrene, however, as shown in Table 1, one of the phonon frequencies became an imaginary frequency. The erroneously imaginary phonon frequency may come from accumulation of the numerical errors in the calculated forces. The three lowest phonon frequencies corresponding to lattice translation should be zero due to the acoustic sum rule. There may some room for improvement on the numerical treatment for imposing the acoustic sum rule[12], and further test is in progress.

The author would like to thank Ikutaro Hamada for providing me with theoretical crystal geometries which can be used as initial geometries of the calculation and for advice on the phonon calculation.

References

[1] J.-L. Brédas, J. P. Calbert, D. A. da Silva Filho, and J. Cornil, Proc. Natl. Acad. Sci. U. S. A. **99** (2002) 5804.

[2] S. Yanagisawa, K. Yamauchi, T. Inaoka, T. Oguchi, and I. Hamada, Phys. Rev. B **90** (2014) 245141.

[3] K. Yonezawa, S. Yanagisawa, and S. Kera, in preparation for publication.

[4] S. Ciuchi, R. C. Hatch, H. Höchst, C. Faber, X. Blase, and S. Fratini, Phys. Rev. Lett. **108** (2012) 256401.

[5] P. Giannozzi et al., J. Phys. Condens. Matter **21** (2009) 395502; P. Giannozzi et al., J. Phys. Condens. Matter **29** (2017) 465901.

[6] D. R. Hamann, Phys. Rev. B **88** (2013) 085117.

[7] S. Baroni, S. de Gironcoli, A. Dal Corso, and P. Giannozzi, Rev. Mod. Phys. **73** (2001) 515.

[8] I. Hamada, Phys. Rev. B **89** (2014) 121103(R).

[9] T. Thonhauser et al., Phys. Rev. Lett. **115** (2015) 136402; T. Thonhauser et al., Phys. Rev. B **76** (2007) 125112.

[10] R. Sabatini et al., J. Phys.: Condens. Matter **24** (2012) 424209.

[11] F. Brown-Altvater, T. Rangel and J. B. Neaton, Phys. Rev. B **93** (2016) 195206.

[12] X. Gonze and C. Lee, Phys. Rev. B **55** (1997) 10355.

Magnetic properties of Fe/Pd(001) bilayer affected by quantum-well states in Pd layer

Kousuke Mochihara[1], Hiroyuki Kageshima[2], and Tetsuya Sato[1]

1Department of Applied Physics and Physico-Informatics, Keio University, 3-14-1 Hiyoshi, Kohoku-ku, Yokohama 223-0061, Japan

2Interdisciplinary Graduate School of Science and Engineering, Shimane University, 1060 Nishikawatsu-cho, Matsue 690-8504, Japan

It is known that at interface between 3d transition metal and (Pd, Pt), strong magnetic anisotropy is generated. We found experimentally that the magnetic anisotropy and magnetic moment of Fe/Pd depend on the thickness of Pd layer [1]. In order to clarify the magnetization change, we performed first-principles calculation using the PHASE/ 0 program.

We used the pseudopotential method and LDAPW92 to the exchange and correlation interactions. A slab of vacuum (two monolayers) /Fe (three monolayers) /Pd (N monolayers) /vacuum (three monolayers), 59 × 59 × 1 k-points, and 36Ry of cut-off energy were used.

We calculated lattice constant which obtains the lowest energy. Using the obtained lattice constant, we calculated Pd layer thickness dependency of the magnetic moment of Fe / Pd slab. As a result, magnetic moment of Fe/Pd changed in oscillatory manner with Pd 6 MLs period, which was in agreement with the experiment. It is known that quantum well states formed in Pd layer changes the electronic state near the Fermi energy in a 6 MLs period [2]. The change of the electronic state based on the Pd quantum well states is considered to be the cause of the change of magnetic moment of Fe/Pd.

We also calculated the energy difference between when the magnetic moment was directed in the out-of-plane direction and when it was directed in the in-plane direction. The energy difference changed depending on Pd layer thickness. In order to investigate the mechanism, electronic band dispersions were calculated. As a result the electronic state near Fermi energy changes depending on the thickness of Pd layer. The magnetic anisotropy is considered to have changed because they depend on electronic states near the Fermi energy.

References

[1] K. Mochihara *et al.*: ICM2018, Moscone center, San Francisco (2018)

[2] S. Sakuragi *et al.*: Phys. Rev. B **97**, 214421 (2018)

Effects of light elements on transport properties of liquid Fe alloy under ultrahigh pressure condition : ab initio molecular-dynamics simulations

Satoshi OHMURA

Research Center for Condensed Matter Physics / Department of Environmental and Civil Engineering

Hiroshima Institute of Technology, Saeki-ku, Hiroshima, 731-5143

We have studied effects of light elements on transport properties of liquid Fe alloy under ultrahigh pressure conditions using ab initio molecular-dynamics simulations. Liquid Fe is a main component of earth's outer core. However, light element (LE) such as hydrogen, carbon, oxygen, silicon and sulfur are expected to be also present in the core. The LE are known to have a strong influence on structural and transport properties of liquid iron under high pressure. However, there are still many uncertainties as to the influence of these LE. Under this circumstance, we have performed ab initio molecular-dynamics simulations for liquid Fe with H, C, O, S and Si at various concentrations from 0 to 30 at% under high presssure. The simulation clarified that H, C and O which are relatively lighter element compared with Si and S are incorporated into the liquid interstitially while Si and S are "substitutional" -type impurities for liquid Fe. In terms of transport property, "substitutional"-type light elements such as Si and S have more influence on electrical conductivity than "interstitial"-type light elements such as H, C and O.

In addition to liquid FeS mixture, we have investigated the structural properties of liquid S (single material). The static structures of liquid S under high pressure obtained by our simulation indicate the existence of a covalent-like interaction even in the metallic state and the covalent-like interaction gradually decreases with increasing pressure. By analyzing the static structure factor, it is found that the covalent-like interaction still remains at approximately 200 GPa, and liquid S has a simple liquid structure at 320 GPa and higher pressures. These results indicate that the covalent-like interaction disappears at a pressure between 200 and 320 GPa [1].

References

[1] S. Ohmura and F. Shimojo, J. Phys. Condens. Matter **31,** (2019) 215101.

Theoretical analysis of dynamical effects of nanographene

Koichi KUSAKABE
Graduate School of Engineering Science, Osaka University
1-3 Machikaneyama, Toyonaka, Osaka 560-8531

1. Switching of edge states at an armchair graphene edge

Introduction of a coherent TO-phonon mode at the armchair edge can cause deformation of the atomic arrangement in the graphene. This mode induces an edge state (Fig. 1) around the Dirac point. Realization of coherent-phonon-induced edge states is within an experimentally feasible condition,[1] which are dynamically induced edge states at the a_{11} arm-chair edge different from the static edge states at a_{21} edges by chemical modification.[2]

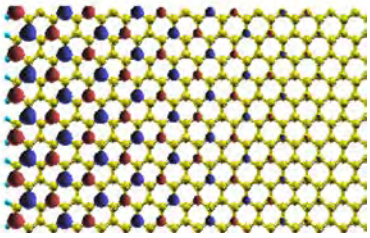

Figure 1: An armchair edge state.

2. Magnetically controlled gap at the Dirac cone in Ni/graphene/Ni

When a local Ni/graphene/Ni sandwiched structure is in the ground state having the anti-parallel configuration of spin moments in the upper and lower Ni slabs, the spin-dependent potential causes gap opening of the Dirac cone by the broken chiral symmetry for each of spin components. Since switching to the parallel configuration recovers the symmetry, closed Dirac cones appear. Using this function, we proposed a magnetically controlled Dirac cone for spin-electronic applications.[3]

3. Simulation of excited TNT molecules

The electron transfer among TNT molecules can cause the weakened CH bonds as well as rotational motion of nitro groups. The explored adiabatic potential surfaces are tested for possible correlation effects when the local short-range correlation is added by the U term. Although the effect is not big, we have proposed relevance of an electron correlation effect promoting localization of catalytic electrons for the enhanced oxidative dehydrogenation promoting production of nanographene.

4. Development of simulation tools

Owing to the correlation-induced redistribution of holes in multi-layer cuprates,[4] relevance of the correlation effecte for the multi-layer cuprate superconductors is shown using a TPSC approach.[5] In this respect, development of self-consistent simulation tools are under development, where a unified picture by the super processes can be a solution.[6]

Acknowledgement

This work was partly supported by KAKENHI (Nos. 16H00914 and 18K03456).

References

[1] K. Kusakabe, *et al.* J. Phys. Soc. Jpn. 87, 084716 (2018). [2] M. Ziatdinov, *et al.* Phys. Chem. Chem. Phys. **19**, 5145-5154 (2017). [3] Y. Wicaksono, *et al.* CARBON, **143**, 828-836 (2018). [4] K. Nishiguchi, *et al.* J. Phys. Soc. Jpn. **86**, 084707 (2017) . [5] K. Nishiguchi, *et al.* Phys. Rev. B. **98**,174508 (2018). [6] S. Teranishi, *et al.* J. Phys. Soc. Jpn. **87**, 114701 (2018).

Exploration of surface reactions on model real catalyst

Wataru MIZUKAMI
Department of Advaced Matrerials Science and Engineering, Fackulty of Engineering Sciences Kyushu University, 6-1 Kasuga Park, Fukuoka, 816-8580, Japan

This year, we studied two chemical reactions on inorganic surfaces using density functional theory (DFT) utilizing parallel computational resources of ISSP's supercomputer system: Alkylation of Ziegler–Natta catalyst; diffusion of an organic semiconductor molecule 3,4,9,10-perylene-tetracarboxylic-dianhydride (PTCDA) on Ge(001) surface. We used the Vienna Ab initio Simulation Package (VASP) version 5.4.4 for DFT calculations. Transition states of those reactions were located using the nudged elastic band (NEB), climbing-image NEB and dimer method successively.

The first system, Ziegler–Natta catalyst, was based on titanium chlorides supported by $MgCl_2$. It has been industrially widely used for olefin polymerization. Despite its popularity and long history, its detailed reaction mechanisms have not been fully understood yet owing to the difficulty in studying chemical reactions of inhomogeneous catalyst. We studied the alkylation process, which occurs prior to polymerization process and activates titanium chlorides on $MgCl_2$ surface. The reaction profiles of the process were computed for $TiCl_n$ on $MgCl_2(100)$ surface. Our calculations validated that not a single but two alkyl aluminum molecules are involved in the alkylation process and form a transition state with a titanium chloride. Additionally, it was found that the consideration of dispersion interactions is vital to estimate reaction energies for this system; DFT calculations with dispersion corrections indicated that the reaction is exothermic, while it is endothermic without the corrections.

Secondly, we studied the diffusion process of PTCDA on the Ge(001) surface. Organic-inorganic hybrid semiconductors have attracted attention as future electronic materials. It is, therefore, important to know the basic properties of interfaces between organic and inorganic semiconductors. PTCDA is an organic molecule and n-type organic semiconductor, while germanium is a well-known inorganic semiconductor; PTCDA on Germanium can be looked as a model system to investigate interfaces of organic-inorganic semiconductors. Recently, STM experiments observed that PTCDAs on Ge(001) take only a single configuration and they can order on a semiconductor surface at high temperatures[1, 2] The estimated activation energy was larger than 30kcal/mol. Such a high activation barrier explains why the self-ordering of chemisorbed PTCDA occurs only at high temperatures.

References

[1] P. Kocan, Y. Yoshimoto, K. Yagyu, H. Tochihara, T. Suzuki, J. Chem. Phys. C 121, 3320-3326 (2017).

[2] P. Kocan, B. Piczyrak, L. Jurczyszyn, Y. Yoshimoto, K. Yagyu, H. Tochihara, T. Suzuki, Phys. Chem. Chem. Phys. *in press.*

van der Waals density functional study of organic-metal interfaces

Yuji HAMAMOTO

Department of Precision Science and Technology, Graduate School of Engineering, Osaka University, Yamada-oka, Suita, Osaka 565-0871

Atomic force microscopy (AFM) [1] is a powerful experimental technique that does not only to visualize the structure of molecules adsorbed on solid surfaces with high resolution, but also enables real-time imaging of chemical reactions of surface-adsorbed molecules. Recently, Shiotari and coworkers have demonstrated that a polycyclic aromatic hydrocarbon adsorbed on the copper (100) surface undergoes an unprecedented dehydrogenation reaction with mechanical stimuli from the AFM tip. While almost all the details of the reaction path have been elucidated by the AFM measurements, the molecular structure of a non-planar intermediate state remains unidentified, since the application of AFM imaging is limited to planar structures.

The purpose of the present study is to fill in the gap in the mechano-chemical reaction path using the van der Waals density functional method [3] as implemented in the STATE code [4-6]. As a starting point of the reaction path analysis, we here investigate the adsorption structures of the initial and final molecules of the reaction referred to as DAPh and DAPyr, respectively. To determine the adsorption

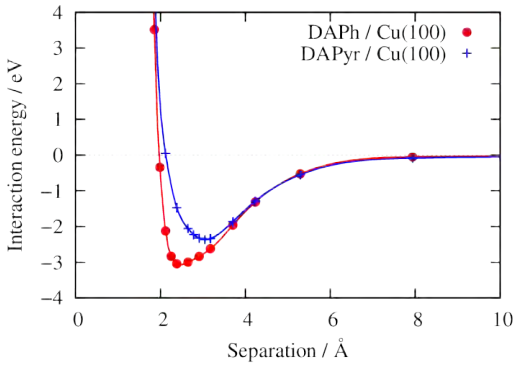

Fig. 1: Interaction energy between planar DAPh and DAPyr molecules and the Cu(100) surface.

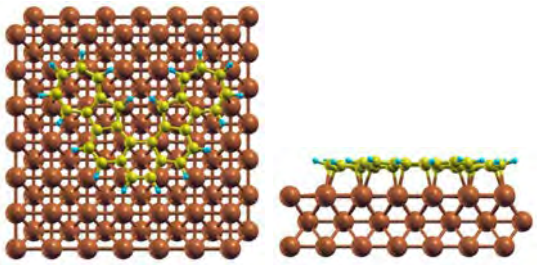

Fig. 2: Relaxed adsorption structure of a DAPh molecule on the Cu(100) surface.

structures, we first calculate interaction energies between planar DAPh and DAPyr molecules on the Cu(100) surface plotted as a function of the molecule-surface separation as shown in Fig. 1. We further relax the structure near the bottom of each energy curve, and depict the relaxed structure of e.g. DAPh/Cu(100) in Fig. 2, which reveals that the DAPh molecule is slightly

distorted and weakly chemisorbed on the surface. The analysis of the reaction path between these two adsorption structures is left to future calculations.

References

[1] L. Gross, F. Mohn, N. Moll, P. Liljeroth, and Gerhard Meyer, Science **325**, 1110 (2009).

[2] A. Shiotari, T. Nakae, K. Iwata, S. Mori, T. Okujima, H. Uno, H. Sakaguchi and Y. Sugimoto, Nat. Commun. **8**, 16089 (2017).

[3] M. Dion, H. Rydberg, E. Schröder, D. C. Langreth, and B. I. Lundqvist, Phys. Rev. Lett. **92**, 246401 (2004).

[4] Y. Morikawa, K. Iwata, and K. Terakura, Appl. Surf. Sci. **169-170**, 11 (2001).

[5] Y. Hamamoto, K. Inagaki, I. Hamada and Y. Morikawa, Phys. Rev. B **93**, 245440 (2016).

[6] S. A. Wella, H. Sawada, N. Kawaguchi, F. Muttaqien, K. Inagaki, I. Hamada, Y. Morikawa, and Y. Hamamoto, Phys. Rev. Materials **1**, 061001(R) (2017).

First-principles study of electronic properties of graphene layers

Yoshitaka FUJIMOTO
Depertment of Physics, Tokyo Institute of Technology
Oh-okayama, Meguro, Tokyo 152-8551

Graphene is an attractive sensing device material for gas sensors owing to its unique and excellent properties such as large surface-to-volume ratio, strong sensitivity, and high carrier mobility at room temperatures.

Here, we report atomic geometries, energetics, and electronic transport properties of various gas molecules including environmentally polluting and toxic gas molecules (NO, NO_2, CO, CO_2, O_2, and N_2) adsorbed on the B-doped and N-doped graphenes and examine the possibilities of sensor applications of doped graphene for detecting toxic molecules [1, 2].

Table 1 shows the adsorption energies and the distances between the doped graphene and the adsorbed molecules for various gas molecules adsorbed on the B-doped and the N-doped graphenes. For B-doped graphene, only NO and NO_2 molecules can bind chemically with short distances and large adsorption energies, while the remaining four molecules are not chemically but physically adsorbed with relatively long distances and small adsorption energies. For N-doped graphene, all six types of molecules are not chemically adsorbed. It is thus found that the B-doped graphene can chemically bind with only NO and NO_2 molecules in air.

The adsorptions of NO and NO_2 molecules could change the electrical conductances of the graphene. Therefore, the variation of the transport properties could be detected and would be utilized for sensor applications. We here examine the electron transport properties of the graphenes with and without NO and NO_2 molecules. The conductances of the undoped graphene show a linear dispersion as in the experimental observations. For the B-doped graphene, electrons are scattered by the B-atom impurity in graphene, which reduces the conductances ($\sim$ 30 %) compared with those of pristine graphene at the energy $E =$ 0.5 eV. For the NO_2 molecule adsorbed on the B-doped graphene, the conductances decrease by $\sim$ 40 %. For the adsorption of the NO molecule on the B-doped graphene, the conductances reduce by $\sim$ 50 %. For the energy $E =$ – 0.5 eV, the conductance of the B-doped graphene without any adsorbates decreases by $\sim$ 30 % compared with that of the pristine graphene, and its reduction rate is almost the same as that at the energy $E = 0.5$ eV. The conductance for the adsorption of the NO_2 molecule decreases by above 50 %, while for the adsorption of the NO molecule, the reduction of the conductance occurs by $\sim$ 35 %. The adsorptions of molecules could change the conductances of the graphenes, and the variation of the conductances depends on the types of the adsorbates. The variation of the con-

Table 1: Adsorption energy E_a (eV) and distance d (Å) between molecule and B(N) atom for each gas molecules adsorbed on B(N)-doped graphene.

	B-doped		N-doped	
	E_a	d	E_a	d
NO	-1.23	2.15	-0.35	2.62
NO_2	-1.16	1.59	-0.74	2.66
CO	-0.12	2.89	-0.14	2.94
CO_2	-0.03	2.84	-0.11	2.73
O_2	-0.20	1.83	-0.32	2.69
N_2	-0.27	2.93	-0.30	2.87

ductances induced by the adsorptions of NO and NO_2 molecules could be useful for sensor applications.

In summary, we have studied the adsorption effects of the various molecules including environmentally polluting gases on the B-doped and the N-doped graphenes using first-principles density-functional calculations. Only the NO and NO_2 molecules can chemically bind on the B-doped graphene. The adsorptions of NO and NO_2 molecules could change the conductances of the graphene, and the variation of such electrical signals induced by molecular adsorptions could be detected by using sensor devices such as field-effect transistors and so on.

References

[1] Y. Fujimoto and S. Saito, Chem. Phys. **478**, 55 (2016).

[2] Y. Fujimoto and S. Saito, Jpn. J. Appl. Phys. **58**, 015005 (2019).

Theoretical analysis of catalytic surface reaction with proton conductors

Fumiya Murase, Junichiro Otomo

Department of Environment Systems, Graduate School of Frontier Science,

The University of Tokyo, Kashiwa-no-ha, Kashiwa, Chiba 277-8581

Ammonia has attracted interest as an energy career for the storage and transport of renewable energies. Recently, electrochemical ammonia synthesis using proton conducting electrolysis cell have been studied. The rate-determining step of Ammonia synthesis were found to be N_2 dissociation. N_2 dissociation are assumed to be contributed by back-donation of electrons.

In this study, to clarify the mechanism of N_2 dissociation in electrochemical ammonia synthesis using proton conducting electrolysis cells, we investigated the effect of adsorption of N_2 on metal surfaces. We used Fe and Ru slab models as catalysts. The calculated models are shown in Fig.1. Each slab consists of 12 atomic layers and there is a vacuum region between the slabs of length over 15 Å. In the models, N_2 was far enough from metal surfaces and adsorbed on Fe (110) or Ru (1110) facets.

The calculations in this work were conducted by the density functional theory (DFT) using the Vienna ab initio simulation package (VASP) 5.3.3. [1]. Core-valence effects were included with the projector -augmented wave (PAW) method [2] with plane waves up to a cut-off energy of 500 eV.

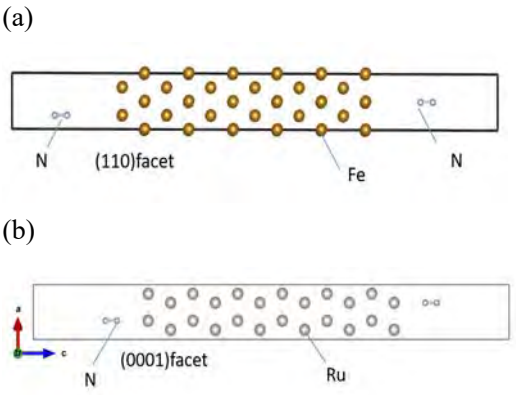

Fig. 1: Structure of calculated slab models

Partial densities of states (pDOS) were calculated to clarify the effect of N_2 adsorption on N_2 dissociation. Fig.2 shows pDOS of N_2 and Ru, and Fig.3 shows pDOS of N_2 and Fe. Both figures suggest that peaks of antibonding orbitals from N 2p broaden and small peaks appear where $E\text{-}E_f$ is under 0 eV when N_2 is absorbed on a metal surface. The results suggest a back-donation of electrons from d-orbitals to unoccupied N 2p. It is assumed that occupied orbitals under 0 eV have an effect on N_2 dissociation.

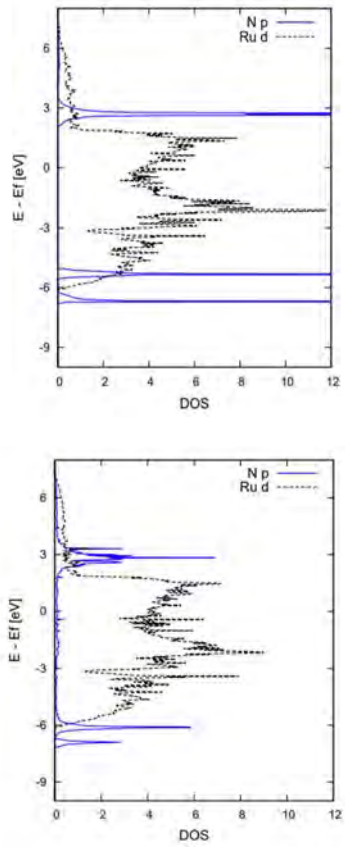

Fig.2: Partial densities of states of the N_2 and Ru (above: N_2 molecule, below: N_2 adsorbed on the on-top)

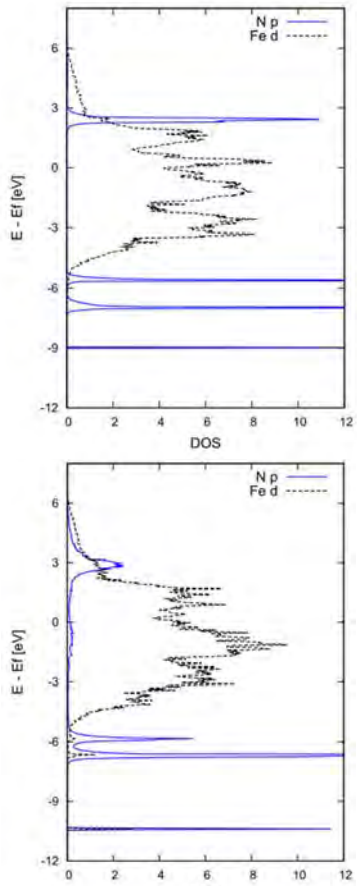

Fig.3: Partial densities of states of N_2 and Fe (above: N_2 molecule, below: N_2 adsorbed on the on-top)

In the future plan, electric field on ammonia synthesis will be investigated. In addition, not only N_2 dissociation but also H association mechanism will be examined Furthermore, to study the reaction path, we will use the nudged elastic band (NEB) [3].

References

[1] Kresse, G. and Hafner, J.: Phys. Rev. B. **43** (1993) 558-561.

[2] Bl¨ochl, P :Phys. Rev. B. **50** (1994) 17953

[3]Henkelman, G.:J. Chem. Phys., **113 (22) (2000)** 9901-99

Ab-initio Metaheuristics for Functional Design of Nanocarbon

Kenji TSURUTA, Keiichi MITANI, Kyosuke SATO, Md. Abdullah Al ASAD, and Satoshi OHMURA[a]

Graduate School of Natural Science and Technology, Okayama University, Okayama 700-8530
[a] Department of Civil and Environmental Engineering, Hiroshima Institute of Technology, Hiroshima 731-5193

Materials design/development often requires extra-long human effort to find optimum condition for targeted properties. Recently various metaheuristic algorithms have been proposed and utilized vastly to identify optimum structures/processes in complex matters such as protein structures, drug designs, multi-element composition of functional materials, and chemical reaction processes. Many of these are based on the objectives to minimize modeled by empirical interactions and/or reaction rates. There are, however, only a few examples [1] where the methodology has been developed from first principles and applied successfully to predicting transport properties of materials.

In the present work, we have developed a metaheuristic optimization algorithm (MOA) combined with an *ab-initio* evaluation of diffusion paths and their energy barriers for an atom to migrate in a given environment [2]. Using this methodology, we searched for optimum doping conditions for inserting a lithium atom into edges of layered nano-graphenes. This optimization search provides computational prediction of charge/discharge performance of Li ion battery with nano-carbon based anodes.

Our combined approach consists of two data/operation streams in the computation; the MOA loop on the "master node", and the *ab-initio* calculation task on the "*ab-initio* cluster". We employ the genetic algorithm (GA) as a MOA and the energy barrier for the Li insertion is estimated with the Nudged Elastic Band (NEB) method with the Density-Functional-Theory (DFT). The *ab-initio* NEB calculation estimates a minimum-energy path of Li atom for a given set of parameters (species, number, and positions of dopant, the initial and the final state of Li atom insertion) selected by the MOA (GA).

In the GA search, we started with setting the parameter range as follows: Dopant species, the maximum number of dopants, the number of substitutional sites are N, 7, 20 respectively. After eleven iterations, the energy deviation was converged within 0.2 eV. It has thus been predicted that substitutional doping of two N atoms into graphitic sites is the most optimum conditions for Li insertion, followed by two pyridinic doping as the second minimum. Figure 1 illustrates the predicted insertion path under the two graphitic doping condition. The detailed path depicted in the figure implies that Li atom is likely migrating through a window between two N dopants with an energy barrier of 0.14 eV as predicted by the NEB result [2]. A preliminary experiment for a half-cell anode of LIB indicated that the effect of N doping into nanocarbon-based anode [3] could indeed improve a rapid charging property.

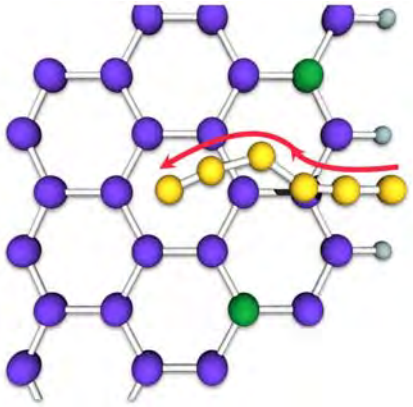

Fig. 1: The insertion path of Li in the GA predicted most optimum doping conditions.

References

[1] A. Supady, V. Blum, and C. Baldauf, *J. Chem. Inf. Model* **55**, 2338 (2015).

[2] K. Tsuruta, K. Mitani, Md.A.A. Asad, Y. Nishina, K. Gotoh, and A. Ishikawa, *Mater. Sci. Forum* **941**, 2356 (2018).

[3] Y. Nishina in *Molecular Technology, Volume 4: Synthesis Innovation 2019*, p.31 (2019).

The Elucidation of Reaction Mechanism of Polyalcohol Dehydration in High Temperature Water with Metadynamics Calculations

Chang Yong Lik[1], Takehiko Sasaki[1], Motoyuki Shiga[2]

1 Department of Complexity Science and Engineering, Graduate School of Frontier Sciences, The University of Tokyo, Kashiwa-no-ha, Kashiwa, Chiba 277-8561

2 Center for Computational Science and E-Systems, Japan Atomic Energy Agency 148-4 Kashiwanoha Campus, 178-4 Wakashiba, Kashiwa, Chiba, 277-0871

1 Introduction

Recently, high-temperature water (HTW) is recognized as a reaction medium in green chemistry. The dehydration reaction of 1,2,5-pentanetriol (PTO) to tetrahydrofurfuryl alcohol (THFA) and 3-hydroxytetrahydropyran (3-HTHP) in HTW with pressurized CO_2 was reported by Yamaguchi et al. [1]. In order to elucidate these reaction mechanisms we conducted Metadynamics calculations corresponding to the experimental conditions. The free energy surface (FES) analysis was carried out to study the reaction mechanism behind the dehydration

Fig. 1: The dehydration of PTO.

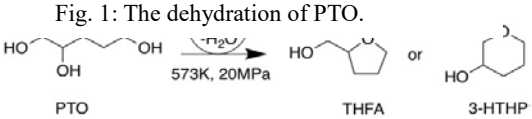

process, and compare it with the previous experimental study [1].

The dehydration reaction pathways of PTO are labeled as 5PTO2, 5PTO5, 6PTO1 and 6PTO5 as shown in Figure 2.

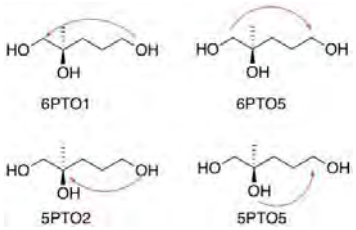

Fig. 2: The dehydration reaction pathways of PTO.

2 Method

By using PIMD[2] (Metadynamics software) developed by one of the coauthor M. Shiga associated with DFTB3 [3] or VASP [4], we analyzed the Free Energy Surfaces by Metadynamics and examined the dehydration reaction to obtain the energy barrier of the transition state from the free energy analysis and estimate the number of calculation steps and required time for the reaction to happen.

In Metadynamics, the FES of the system is sampled based on the reaction coordinates (Collective Variables: CV) of the system, then a positive Gaussian function potential was added to the actual FES to bias the reaction. The definition of CV is shown in Figure 3.

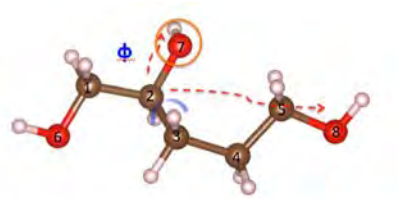

Fig. 3: The definition of CV [5PTO2]: Dihedral angle Φ (C2-07&C3-C4), the difference in bond length r (d=r_{28}-r_{27},) coordination number n_2 (the number of hydrogen attached to O7).

3 RESULTS and DISCUSSION

The free energy of (R)-PTO was calculated with Metadynamics by adding a Gaussian function potential of height=100 K and width={Φ = 12.0 °, r = 0.20, n = 0.066}. 6PTO1, 6PTO5 via S_N2 yielded 3-HTHP, while 5PTO2, 5PTO5 via S_N2 yielded THFA. Typical FES results are shown in Fig. 4. The free energy of each reaction pathway was calculated with DFTB and VASP. The free energy barrier of THFA was lower than that of 3-HTHP. This is in line with the experimental results whereby THFA and 3-HTHP are the main and by-products respectively. MTD simulations have provided insights on the mechanism behind the PTO dehydration reaction. It is understood from the free energy profile obtained from MTD simulations that the proton-assisted S_N2 process is the dominant mechanism. No minima are found in the protonated region ($n \approx 2.0$) before the C-O bond exchange on the free energy profile of all reaction pathways, therefore the protonation of hydroxyl group and the C-O bond exchange has to occur in a single step.

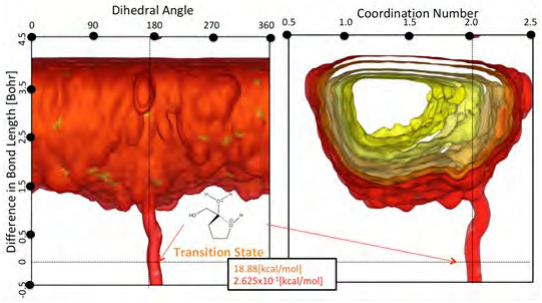

Fig. 4. Free energy surface of 5PTO2 reaction pathway

As the proton-assisted S_N2 process is seen in this study and the previous work [1] this reaction mechanism is believed to be common in polyalcohol dehydration in HTW under acidic condition. The proton is passed around in a network of hydrogen bond network between the water molecules or between the water molecules and polyalcohol. The acidicity of HTW facilitates the protonation of the hydroxyl group essential for the reaction. This explains why the polyalcohol dehydration is accelerated with the presence of carbon dioxide in HTW. These results are published recently [5].

References

[1]A. Yamaguchi, N. Hiyoshi, O. Sato, K.K. Bando, M. Shirai, Green Chem., 2009, 11, 48-52.

[2]PIMD.https://ccse.jaea.go.jp/ja/download/pimd/index.jp.html.

[3]Density Functional Theory based Tight Binding. https://www.dkb.org.

[4]VASP. https://www.vasp.at/.

[5]Y.L. Chang, T. Sasaki, J. Ribas-Arino, M. Machida, M. Shiga, J. Phys. Chem. B 123 (2019) 1662.

Density functional calculations of the catalytic site of fuel cell and photocatalyst

Kazume NISHIDATE
Faculty of Science and Engineering, Iwate University
Ueda 4-3-5, Morioka, Iwate 020-8551

A proton exchange membrane fuel cell (PEMFC) is an energy device in which chemical energy is directly converted into electric energy through the oxygen reduction reaction (ORR). This reaction offers a promising technology to develop efficient and clean power sources for electric vehicles. However, the most effective catalysts currently used for the ORR are platinum group metals (PGM) and their scarcity and expensiveness have been main obstacles to large-scale commercialization. Therefore, it is very important to develop inexpensive and yet efficient non-PGM catalysts for the mass production of fuel cell devices. Meanwhile, a pioneering work [1] has been reported on the ORR activity of Fe(Co)-N4 macrocyclic molecule adsorbed on carbon materials. Ever since this discovery, a class of Metal-Nitrogen-Carbon (M-N-C) ORR active sites have been extensively studied. Although the energetics have been analyzed in these studies, electronic structure and electron transfer dynamics during the ORR have not been clarified.

We have studied the ORR of FeN_4 embeded in graphene (Gr) and carbon nanotube (CNT) with the first-principles DFT calculations using Vienna Ab initio Simulation Package (VASP). [2] We evaluate the electron transfer between an O_2 molecule and the FeN_4 catalytic site, where O_2 was adsorbed on Fe with end-on bent geometory. Two carbon systems are considered. The first is the 5×5 Gr sheet which forms a 12.3 Å $\times$ 12.3 Å equilateral parallelogram. The second is the (10, 0) CNT which is put in a standing position on 20 Å $\times$ 20 Å square plane. The CNT unit is stacked three times in the axial direction and its dimension corresponds to 12.8 Å. The diameter of CNT is 7.9 Å. Cyclic boundary conditions are imposed on Gr as well as on CNT supercells. Throughout the calculations, an O_2 molecule is easily adsorbed on the top of the Fe with the end-on bent atomic configuration. On adsorbing hydrogen atoms, a H_2O molecule is formed and is immediately desorbed from the surface. The overall electronic configurations of the FeN_4 center in Gr during the ORR is essentially the same as those in CNT, demonstrating an universal nature of the reaction mechanism. However, we also found a difference in atomic structure in the ORR. The height of Fe on Gr increases up to 0.344 Å during the ORR while the Fe height on CNT is only 0.217 Å due to the mechanical surface tension, which also affects the energy landscape of ORR. After the ORR, the FeN_4 centers on Gr and CNT recover their initial in-plane configurations and are capable of subsequent ORR.

References

[1] R. Jasinski: Nature **201** (1964) 1212.

[2] S. Aoyama, J. Kaiwa, P. Chantngarm, S. Tanibayashi, H. Saito, M. Hasegawa, and K. Nishidate: AIP Advances **8** (2018) 115113 (9 pages).

Study on physical properties of structural elementary excitations of semiconductor surfaces and interfaces

Hiroyuki KAGESHIMA
Graduate School of Natural Science and Technology, Shimane University
1060 Nishi-Kawatsucho, Matsue, Shimane 690-8504

Our project has been focused on the physical properties of structural elementary excitations of semiconductor surface and interfaces. We have performed two topics in this year. One is physical properties of vacancies in two-dimensional material MoS_2 [1]. The other is physical properties of SiO interstitials in SiO_2 at the interface with Si [2, 3, 4]. The calculations were performed based on the first-principles calculation. Program package VASP was employed.

In the first topic, we focus on the supporting effect on vacancy formation in monolayer MoS_2. Vacancy formation is generally more suppressed for the supported cases than the freestanding case in non-negatively-charged conditions. These are the results of difference in charging of vacancies. We can thus propose that MoS_2 should be processed in the S-rich and non-negatively-charged conditions to prevent the formation of vacancies. We can also propose that the choice of supporting substrate is important to process MoS_2 to obtain better quality electronic devices.

In the second topic, we focus on the pressure effect on SiO_2 with SiO interstitials. It is know that the SiO interstitials are injected into the oxide when the Si is thermally oxidized. In addition, for the Si pillar oxidation, it is known that a large compressive pressure as high as 5 GPa is induced in oxide. We therefore study the pressure effect on the dynamical property of SiO_2 with SiO interstitials. Analyzing calculated results, we found that the Si dynamical property is enhanced by the pressure at 3000 K, while it is slightly diminished at 6000 K. This indicates that Si dynamical property is more enhanced by the pressure at the experimental oxidation temperature such as 1000 K. We also fit the pressure dependence of Si diffusion coefficients by the Lorentz type function of pressure (at 3000 K) or parabolic function (at 6000 K). Then we evaluate the activation volume as the function of SiO density. The results show that the activation volume is negative in low SiO density, but its absolute value decreases with the SiO density. This suggests that the SiO interstitials suppress the pressure effects on Si dynamical property.

References

[1] S. Urasaki and H. Kageshima, Jpn. J. Appl. Phys. **57** (2018) 125202.

[2] Y. Yajima, K. Shiraishi, T. Endoh, and H. Kageshima, Jpn. J. Appl. Phys. **57** (2018) 06KD01.

[3] Y. Yajima, K. Shiraishi, T. Endoh, and H. Kageshima, 2018 International Conference on Solid State Devices and Materials (SSDM2018), Tokyo, Japan, PS-1-04 (2018).

[4] Y. Yajima, K. Shiraishi, T. Endoh, and H. Kageshima, 14th International Conference on Atomically Controlled Surfaces, Interfaces, and Nanostructures (ACSIN-14), Sendai, Japan, 22P118 (2018).

Ab Initio Band Structure Calculation of InSb Using VASP

Hiroki FUJISHIRO

Department of Applied Electronics,

Tokyo University of Science, Niijuku, Katsushika, Tokyo 125-8585

High electron mobility transistors (HEMTs) are one of the most promising devices for future terahertz electronics. InSb is suitable for use in the channel layer of high-speed HEMTs since InSb has the lightest electron effective mass in III-V semiconductors. However, there are no lattice-matched barrier materials for InSb channel HEMTs. As a result, InSb channel is compressively strained in HEMTs. On the other hand, Monte Carlo (MC) simulations are the powerful tool to predict performance of HEMTs. For MC simulations, accurate band parameters are strongly required. In this work, we carried out ab initio band structure calculations of unstrained and compressively strained InSb using Vienna Ab initio Simulation Package (VASP) based on the method in the local density approximation to obtain band parameters.

As for the band parameters of InSb, several papers have already been published [1, 2]. Table 1 summarizes the band parameters of InSb. In our previous work [2], we calculated the unstrained and the strained band structures of InSb by the empirical pseudopotential method. We could not obtain the values of the band gap energy E_g. To overcome this problem, we carried out the band structure calculations of unstrained and compressively strained InSb using VASP. In Table 1, our present calculation results are also shown. We obtained the E_g of 0.34 and 0.48 eV for unstrained (0%) and compressively strained (-1.32%) InSb, respectively. The E_g value in this work is larger than that in [1]. The electron effective mass in the Γ valley m_Γ^* is almost same as the values in the previous papers [1, 2]. The increase in the value of m_Γ^* was observed for the -1.32% compressively strained InSb, which is the same as our previous result [2].

Using the obtained band structures, we'll carry out more rigorous MC simulations of InSb channel HEMTs.

References

[1] H. Rodilla, T. González, D. Pardo, and J. Mateos: J. Appl. Phys. **105** (2009) 113705.

[2] H. Nishino, Kawahira, F. Machida, S. Hara, and H. I. Fujishiro: Proc. 22nd Int. Conf. on IPRM (2010) p. 156.

Table 1 Several band parameters of InSb.

	0% [1]	0% (Pseudopotential) [2]	-1.32% (Pseudopotential) [2]	0% (VASP) [This work]	-1.32% (VASP) [This work]
E_g(eV)	0.18	—	—	0.34	0.48
m_Γ^*	0.014	0.016	0.022	0.015	0.022
m_L^*	0.22	0.18	0.18	0.052	0.051
m_X^*	0.13	0.38	0.38	0.065	0.066
$E_{\Gamma-L}$(eV)	0.76	1.04	1.00	1.04	1.06
$E_{\Gamma-X}$(eV)	0.46	1.57	1.48	2.64	2.69

Calculations of Phonon Properties in Oxides, and of Dielectric Functions in Halides

Takayuki MAKINO

Department of Electric and Electronics Engineering,

University of Fukui, Bunkyo Fukui, Fukui 910-8557

I tried the phonon calculations for oxides by using "phonopy" to obtain its dispersion and density of states. Supercells with displacements are needed to be created for the calculations of phonon dispersion and/or their density of states. Number of the created configurations is dependent on the symmetry of the relevant crystal (see, for example, Table 1). In other words, a number of *ab-initio* supercell calculations have to be executed to obtain force on atoms, though they are binary materials (N_{atom}=2). Due to the abovementioned situations, I have not completed the tasks. Despite this fact, I have already successfully created a force constants file for one of these oxides. The related postprocess will be performed sequentially, because this package can be executed even under Linux-based personal computers.

material	symmetry	configuration	N_{typ}	N_{atom}
A	Pnma	40	40	2
B	Pnma	40	40	2
C	Pnma	60	40	2

I also tried dielectric function calculations for halide-based mixed crystals. Because the dielectric function cannot be directly converted from the spectral distribution of the density of states, so I tried to calculate them by using "RESPACK". I was able to finally master how to convert the self-consistent field calculation results from "Quantum ESPRESSO" to "RESPACK" formats by communicating with the staffs. The validity and comparison with our experimental data of the partially obtained results are being checked currently.

Acknowledgments

I am indebted to kind suggestions and customization of the program from the RESPACK staffs (Professor K. Nakamura *et al*.).

References

[1] K. Nakamura *et al*.: Phys. Rev. B **74** (2006) 235113.

[2] L. Chaput, A. Togo, I. Tanaka, and G. Hug, Phys. Rev. B, **84** (2011) 094302.

Magnetic properties of rare earth mixed crystal magnet materials

H. Akai
Institute for Solid State Physics, University of Tokyo
Kashiwa-no-ha, Kashiwa, Chiba 277-8581

The purpose of the present study is to develop a system that can generate permanent magnet materials databases in the multi-dimensional composition spaces by using first-principles electronic structure calculation. Given a structure and a set of components, e.g., $Sm(Fe_{1-x}Co_x)_{12}(N_{1-y}S_y)$, we typically need calculations for 100∼1000 different systems. Since these systems are compositionally disordered, usual band structure calculation is not suitable for realistic simulations. An efficient way to handle this problem is to use the KKR-CPA method, which can take a configurational average of such disordered systems rather accurately. Unfortunately, the full-potential scheme is not implemented in the present version of KKR-CPA used now[1] (full-potential KKR-CPA codes exist but they do not suit the present purpose because of their heavy computational demands). On the other hand, the pseudo-potential codes can calculate the ordered system quite efficiently although their accuracy has to be checked from time to time through comparisons with the results obtained by other more reliable method such as full-potential KKR and WIEN2k. Considering the above, one of the practical ways to take is to combine KKR-CPA and pseudo-potential codes: use pseudo-potential codes for the end points (i.e., ordered alloys) of composition space and use KKR-CPA to interpolate all the remaining region of the space. A computational system "HOFMAN" constructed under such a strategy is now running.

An example of the usage of HOFMAN system is seen in Fig. 1, where a new alloy system $Sm(Fe_{1-x}Co_x)_{12}(N_{1-y}S_y)$ is examined.

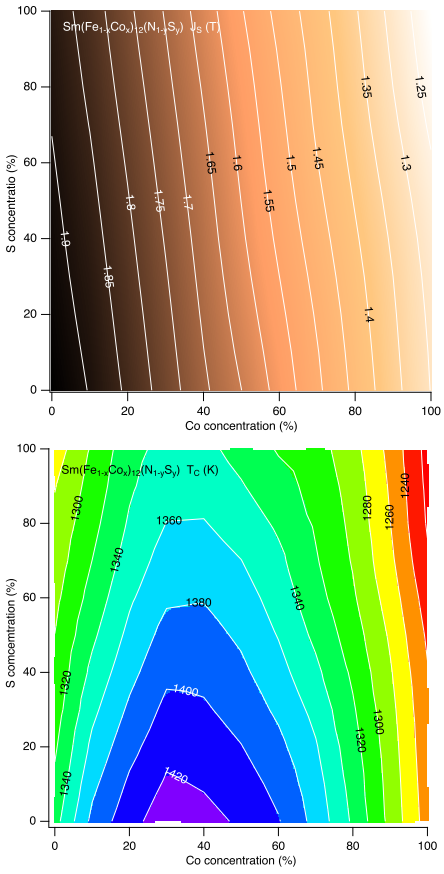

Figure 1: Magnetization (T) (top) and T_C (K) (bottom) of $Sm(Fe_{1-x}Co_x)_{12}(N_{1-y}S_y)$.

References

[1] H. Akai, AkaiKKR, `http://kkr.issp.u-tokyo.ac.jp/` (2002).

Ab initio inspection on doping effects on rare-earth permanent magnets

Munehisa Matsumoto (Akai Group)
Institute for Solid State Physics, University of Tokyo
Kashiwa-no-ha, Kashiwa, Chiba 277-8581

April 26, 2019

We have been exploring possibilities to improve rare-earth permanent magnets (REPM's) on the basis of fundamental understanding for the intrinsic electronic structure. The champion magnet, Nd-Fe-B ternary alloy, is made of the main-phase compound $Nd_2Fe_{14}B$. Its excellent magnetic properties at room temperature are traded off with a drawback with poor high-temperature performance. The possible directions for improving the intrinsic properties of REPM's include raising the Curie temperature and/or enhancing the temperature resistance of magnetic properties.

A standard way to raise the Curie temperature is to make an alloy with Co. Thus it is important to understand how Co-doping works in $Nd_2Fe_{14}B$. Even though some experimental observation on the site preference of doped elements in $Nd_2Fe_{14}B$, it is only in recent days that *ab initio* investigations on $Nd_2Fe_{14}B$ have been in major trends. This is partly because the large unit cell of $Nd_2Fe_{14}B$ with 4 formula units or 68 atoms is demanding in terms of computational resource. Also this practical problem comes on top of the fundamental problem in dealing with $4f$ electrons. At the core of our calculations are open-source package for *ab initio* electronic structure calculations, AkaiKKR [1] and OpenMX [2]. With these the instrinsic properties of doped $Nd_2Fe_{14}B$ can be addressed in a reasonable time on System B. Continuous exploration of the compositinal space is done on the basis of coherent potential approximation using AkaiKKR. Effect of discrete replacement of host atoms by dopant atoms is investigated by OpenMX. Part of our recent results on Co-doped $Nd_2Fe_{14}B$ where one Co atoms replaces one Fe atom out of the possible 56 atomic sites in the unit cell of $Nd_2Fe_{14}B$ is shown in Fig. 1 for the mixing energy which is defined as follows.

$$\begin{aligned}\Delta E_{\rm mix} &= U[{\rm Nd_2(Fe_{1-x}Co_x)_{14}B}] \\ &\quad -(1-x)U[{\rm Nd_2Fe_{14}B}] \\ &\quad -xU[{\rm Nd_2Co_{14}B}]\end{aligned}$$

Here $U[M]$ is the calculated energy for a given material M. It is clearly shown that doped

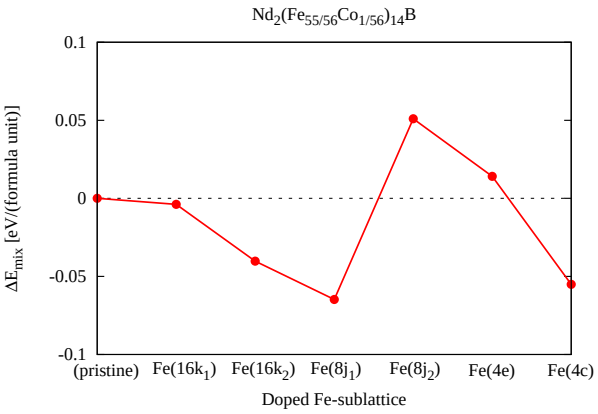

Figure 1: Calculated mixing energy of Co and $Nd_2Fe_{14}B$.

Co prefers Fe($8j_1$) sublattice among the six

sublattices in the host $Nd_2Fe_{14}B$ [3]. Remarkably the numerically observed trend is consistent with past experimental claims in that Co prefers Fe($8j_1$) and avoids Fe($8j_2$). It also can be shown that this particular preference originates in the magnetic exchange couplings between the host Fe and dopant atoms. Such fundamental understanding should pave the way toward the improvement of intrinsic properties avoiding unnecessary tradeoff's between various desired properties to make a good REPM.

References

[1] H. Akai: `http://kkr.issp.u-tokyo.ac.jp/jp/`. See also `https://ma.issp.u-tokyo.ac.jp/app/113`.

[2] T. Ozaki *et al*: `http://www.openmx-square.org/`. See also `https://ma.issp.u-tokyo.ac.jp/app/594`.

[3] M. Matsumoto, preprint (arXiv: 1812.10945)

Electronic structure and superconductivity based on a first-principles approach

Hiroaki IKEDA
Department of Physics, Ritsumeikan University
Kusatsu, Shiga 525-8577

Our aim is to develop the first-principles band structure calculations and understand the pairing mechanism of unconventional superconductivity in the strongly correlated electron systems. This year, we studied the following topics using Class B; material design of new high-T_c superconductors and the quasiparticle self-consistent GW (QSGW) band structure in the iron-based superconductors.

First of all, we tried material design of hydride superconductors using USPEX code after high-T_c H_3S. We performed it for some binary and ternary compounds of hydrogen. Obviously, it is difficult that the space group keeps high symmetry in ternary compounds under high pressure. This may be disadvantageous to realize high-T_c superconductors. On the other hands, in binary hydrides, 260K superconductivity in LaH_x was realized [1]. This motivated us to calculate superconductivity in YbH_x, since atomic configuration of Yb atom is fully-occupied f^{14} while that of La atom is fully-empty f^0. Figure 1 shows enthalpy of formation in YbH_x. We can see that YbH_2 is the most stable, but there are some metastable structures, YbH_6 etc, under high pressure. Then we calculated the electron-phonon coupling constant λ in these structures. Finally, we found that YbH_6 indicates $T_c \sim 50$K at 200GPa. Suppression of T_c, as compared with LaH_x, comes from the fact that Yb f orbitals are hybridized with ligand hydrogens, and phononic modes of ligand hydrogen are suppressed.

Next, we performed the QSGW calculations

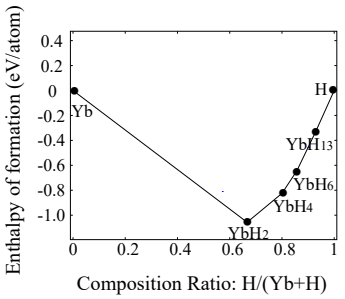

Figure 1: Enthalpy of formation at 200GPa in Yb-H system.

in a variety of iron-based superconductors. As well-known, the LDA/GGA calculations in the iron-based superconductors describe overall features of the electronic structure. However, size, curvature, and orbital characters of Fermi surfaces are significantly deviated from the experimental observations. This is a serious problem in understanding the superconducting pairing mechanism. As the iron-based superconductors are semi-metallic, this problem can have a similar aspect to the fact that the LDA/GGA cannot well describe the band gap of semiconductors. Here, we applied the QSGW method, which well explains the band gap in semiconductors. We found that the QSGW approach can improve the band structures. A part of this work was used in the dHvA analysis of FeS in [2].

References

[1] M. Somayazulu *et al.*, Phys. Rev. Lett. **122**, 027001 (2019).

[2] T. Terashima *et al.*, Phys. Rev. B **99**, 134501 (2019).

Development and control of spin texture by band engineering using quantum-well state

Shunsuke SAKURAGI
Institute for Solid State Physics, University of Tokyo
Kashiwa-no-ha, Kashiwa, Chiba 277-8581

We have studied a magnetism induced by quantum-well states using density functional theoretical calculation. This year, we focused on a mechanism by which the magnetism of Pd(100) ultrathin film, which shows ferromagnetism induced by quantum-well states, can be controlled by tailoring the Pd/stacking layer interface electronic states (i.e., scattering phase shift of the quantum-well states) [1].

For the experimental observation of the control of magnetism in metals using an external field, thin films with a few monolayers are generally used because of the screening effect. Although previous research showed the effect of the change in the Fermi energy and polarization of the orbital character of the electrons by applying the electronic field, the standpoint of tuning the quantum size effect which was occurred by nano-scaling of the materials was not well discussed. Our present study was focused on quantum-well induced ferromagnetism, which appeared after forming the ultrathin film. Using DFT calculation with PHASE/0 code [2], we clearly show the possibility of paramagnetic to ferromagnetic switching by modifying the interface electronic states of the quantum-wells. Our present discovery opens up a new way to control magnetism by tuning the size effect.

Generally, the quantum-well states, which is the origin of the ferromagnetism in Pd(100) ultrathin films, are described in a one-dimensional quantum-well model containing the phase shift, which is the effect of the electron scattering at the interfaces of wells. First, we expand the function of the phase shift from the real space to momentum space dependency. This theory means that controlling the shape of quantum-well band dispersion will be artificially achieved by modifying the interface electronic states. For the appearance of ferromagnetism, making a flat band at the Fermi energy is important, and we clearly show that stacking of the fcc *d*-electron transition metal layer on Pd quantum-wells makes a flat band, from the DFT calculation based on this theory. We expect that the control of magnetism predicted in our present theory will be experimentally observable in a system of a stacking layer/Pd ultrathin film on a piezo substrate. This can modify the layer spacing (i.e., tune the hybridizing of the wave functions at the interfaces of the wells), and the nonmagnetic to ferromagnetic switching using the multilayer nano film system should be easily achieved.

References

[1] Shunsuke Sakuragi, Hiroyuki Kageshima, and Tetsuya Sato : submitted to Phys. Rev. B.

[2] https://azuma.nims.go.jp/software/phase

Study of interaction between radiation damage and interstitial atom

Kazuhito Ohsawa

Institute for Applied Mechanics,

Kyushu University, Kasuga-koen, Kasuga, Fukuoka 816-8580

Introduction

The study of hydrogen (H) isotope retention in tungsten (W) are important issue in the field of fusion reactor because W is one of the plausible plasma facing materials (PFMs). Usually, H seldom dissolve in W. However, H atoms are trapped in the vacancy-type lattice defects created under the irradiation circumstance. Actually, a large amount of retention of deuterium (D) was observed in the irradiation damage zone of W specimen. In particular, tritium (T) retention in the PFM is one of the serious problem associated with fusion reactor because T is radioisotope whose half-life is 12 years. H atom trapping in monovacancy in W have been reported in some previous works. Therefore, we investigated the H atom trapping in divacancy in W in the present work.

Simulation method

The binding energies of H atoms to the divacancy and stable configurations of the H atoms in it were calculated in terms of first-principle calculations based on density functional theory. We used the Vienna ab-initio simulation package (VASP). Then, a large simulation cell, containing 6x6x6 bcc lattice (432 atoms), were used in order to reduce the effects of periodic boundary condition imposed on the simulation cell.

Results

First, we examined the stable configuration of the divacancy in W. The divacancy in the first nearest neighbor configuration is the most stable structure. Second, we investigated stable structures of H atoms in the divacancy, as shown in Fig. 1. The H atoms are located in the vicinity of the octahedral interstitial sites (O-sites). There are 12 O-sites next to the divacancy. Then, six are located in the center of the divacancy where two monovacancies are in contact with each other. The other six O-sites are located outside of the center. H atoms preferentially occupy O-sites in the center of the divacancy. All H atoms occupy O-sites in the center of the divacancy in the case of k=2, and 4, where k is the total number of H atoms trapped in the divacancy. However, repulsive interactions usually act among H atoms in metals. So, H atoms gradually occupy the outside O-sites, as

the number of H atoms in the divacancy increases. Actually, two H atoms occupy outside O-sites in the case of k=6, even though all O-sites in the center are not occupied by H atoms.

Binging energies of H atoms trapped in the vacancy-type lattice defects, i.e., monovacancy and divacancy, in W are presented in Fig.2 as a function of the number of H atoms. A maximum of 12 H atoms can be accommodated in the monovacancy. While, 18 H atoms can be accommodated in the divacancy at least.

Discussion

We consider how to determine the stable structures of H atoms in the divacancy. There are two kinds of O-sites next to the divacancy. Therefore, the attractive interactions to an H are different by the types. Besides, the mutual repulsion acts among H atoms. As a result, the stable structures of H atoms are determined by the balance of the attractive and repulsive interactions.

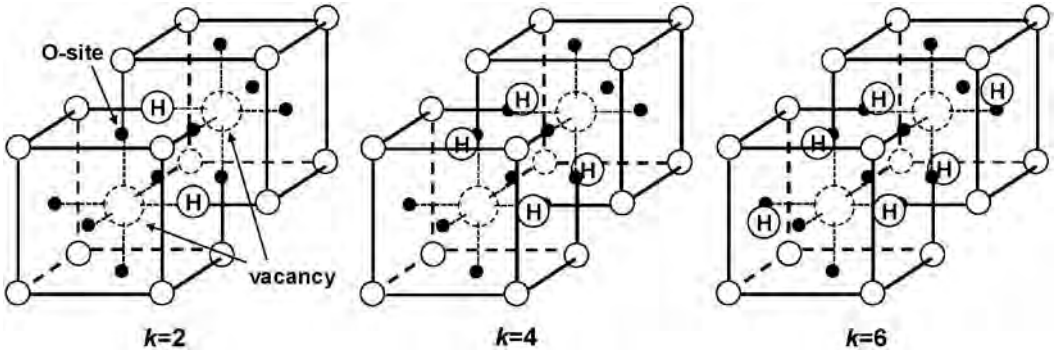

Fig. 1: Schematic view of stable configurations of H atoms trapped in divacancy in W. Number of H atoms is k. They are located close to O-sites.

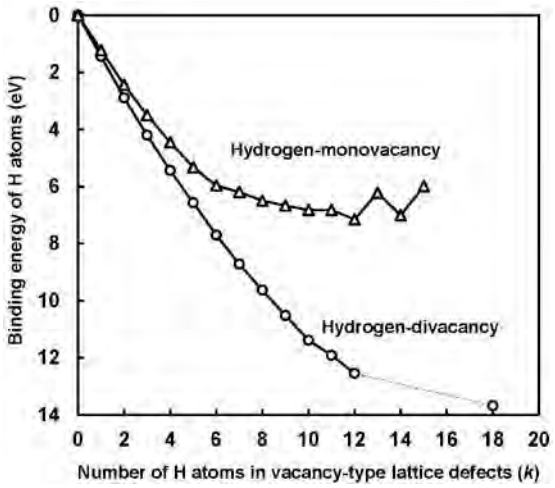

Fig. 2: Binding energy of H atoms to mono or divacancy in W.

Theoretical Study on the Aggregation-Induced Emission

Norifumi YAMAMOTO

Department of Applied Chemistry,

Chiba Institute of Technology, 2-17-1 Tsudanuma, Narashino, Chiba 275-0016

In this project, the mechanism of aggregation-induced emission (AIE) of tetraphenylethylene (TPE) was studied theoretically.

The TPE has been known to exhibit the AIE, which is non-emissive in dilute solutions but becomes highly emissive in solid or aggregates [1]. In this study, the AIE of TPE was investigated by using *ab initio* electronic structure calculations, together with molecular dynamics (MD) simulations.

In order to elucidate the characteristics of the potential energy profiles for the photochemical processes of TPE, the minimum energy paths for the photo isomerization reaction of TPE in an isolated phase were investigated using *ab initio* electronic structure calculations. The spin-flip approach within the time-dependent density functional theory (SF-TDDFT) method was used to compute the potential energies and analytical gradients for the electronic ground (S_0) and first excited (S_1) states of the molecule. All electronic structure calculations of CN-MBE presented herein were performed using the GAMESS program.

The results of SF-TDDFT calculations showed that the potential energies of TPE for electronic ground (S_0) and first excited (S_1) states are degenerated at a conformation with the twist angle of 90° around its ethylenic C=C bond, which can lead the fluorescence quenching of TPE molecule in dilute solutions.

The free-energy profile of the photo isomerization of TPE in condensed phase was computed using MD simulations based on an empirical force field representation. All MD simulations of TPE presented herein were carried out using the GROMACS 2016.3 program.

The results of MD simulations revealed that TPE tends to assemble in close contact, where the ethylenic C=C bond rotation is markedly restricted in aggregates, preventing the fluorescence quenching via the S_0/S_1 conical intersection; TPE in THF solution, however, proceeds a barrierless non-radiative transition. These results gave a clear picture of the AIE mechanism of TPE, which is agree with that of a cyanostilbene derivative [2].

References

[1] Hong, Y.; Lam, J. W. Y.; Tang, B. Z., *Chem. Soc. Rev*., Vol. 40, pp. 5361−5388 (2011).

[2] Yamamoto, N., *J. Phys. Chem. C*, Vol. 122, pp. 12434−12440 (2018).

Development of the determination technique of model parameters based on the accurate ab-initio quantum simulation

Hirofumi SAKAKIBARA

Department of Applied Mathematics and Physics,

Tottori University, Koyama-cho Minami, Tottori city, Tottori 680-8552

It is not so easy to treat strongly-correlated electrons only by first-principles calculation. Thus we often derive a low-energy from first-principles calculations. If the model describes strong correlations in some model calculations, it can be said that such strong correlation effect my be described in a (quasi-)first-principles method.

Especially for magnetism, metal-insulator transition, and superconductivity, single-band or multi-band Hubbard models are often adopted. In such Hubbard models, on-site electron interaction U is an essential parameter. Therefore, we have constructed a new method to determine U, named model-mapped RPA (mRPA) [1].

In the previous annual report, we have developed our mRPA code so as to be applicable to multi-orbital cases [2]. Then we obtained the model parameter of two single-layered cuprates La_2CuO_4 (T_c~40K) and $HgBa_2CuO_4$ (T_c ~100K). Then we assume two-orbital Hubbard model consisting of the $d_{x^2-y^2}$ orbital and the d_{z^2} orbital [2,3]. The two-orbital model fully derived from first-principles calculation explains the experimental difference of T_c in fluctuation-exchange approximation [4].

We also compare the results of mRPA and constrained RPA (cRPA) [5]. We found that the U of the $d_{x^2-y^2}$ orbital is larger in La_2CuO_4 than $HgBa_2CuO_4$ in cRPA, while smaller in La_2CuO_4 than $HgBa_2CuO_4$ in mRPA [4]. This result does not mean that our mRPA code does not work well.

To confirm this point, we applied mRPA to $SrVO_3$. $SrVO_3$ is a famous benchmark material, in which the energy-bands are almost separated between the model space and the outside of the model space. Here the model space is spanned by the maximally localized Wannier functions. Separated band structure is desirable condition because the model space is well defined. Then we obtained U=3.12 eV in cRPA and U=2.85 eV in mRPA. It seems that these two methods agree with each other. This result means that mRPA code may work well.

Contrary to $SrVO_3$, the band structure of the model space is not separated from the outside of the model space in the two cuprates. Namely, the model space is more ill-defined in cuprates

than $SrVO_3$. From the comparison between $SrVO_3$ and two cuprates, we can imagine that the well-definedness of the model spaces may affect methodological dependence of the Hubbard *U*. The detailed explanation of the dependence is shown in our recent paper [4]. In this annual report, we only give the conclusion that the projection method [7] adopted in cRPA may give rise to the dependence, where the projection method is used to define the model space.

In mRPA, such a projection method is not needed. In mRPA, we match the effective interaction obtained from first-principles and model calculations. Namely, we perform both of first-principles calculation and model calculation to determined *U* so that the both effective interactions become identical. Then the determination process is unique in mRPA. This is one of the advantages of mRPA.

For $SrVO_3$, we also obtained an extended Hubbard models consisting of not only the on-site interaction but also the nearest-neighbor site interaction *V*. We found *U* becomes larger (*U*=3.29 eV) when we consider an extended Hubbard model [4]. This is because that *V* weakens the local part of the effective interaction and thus *U* should become larger to maintain the value of local term of the effective interaction, which is determined independently of the model we consider. Since this conclusion may be general for metallic system, we will investigate further materials on this point of view.

References

[1] H. Sakakibara *et al*: J. Phys. Soc. Jpn. **86,** 044714 (2017).

[2] H. Sakakibara *et al.,* Phys. Rev. Lett. **105** 057003 (2010).

[3] H. Sakakibara *et al*, Phys. Rev. B **89**, 224505 (2014).

[4] H. Sakakibara and T. Kotani, arXiv:1812.03731 (2018).

[5] F. Aryasetiawan, M. Imada, A. Georges, G. Kotliar, S. Biermann, and A. I. Lichtenstein, Phys. Rev. B **70**, 195105 (2004).

[6] E. Sasioglu, in Lecture Notes of the 45th IFF Spring School "Computing Solids-Models ab initio methods and supercomputing" (Forschungszentrum Julich, 2014).

First-principles study on positron states in d0 ferromagnetics and at solid surfaces

Satoshi HAGIWARA

National Institutes for Quantum and Radiological Science and Technology,

1233, Watanuki-machi, Takasaki, Gunma, 370-1292, Japan

In this work, we studied the following two topics: 1) the positron state in the Ga vacancy in GaGdN, 2) developing the theory of positronium formation using realistic material surface. These works are collaboration with experimental group.

1) the positron state in the Ga vacancy in GaGdN: A spin-dependent positron annihilation spectroscopy is a powerful tool for investigating defect induced ferromagnetism, because positron is easily trapped by vacancy type defect and annihilates with electrons around the positron. In this respect, positron annihilation parameters provide information on electronic and magnetic states around vacancy type defects [1]. A previous study has reported that the Gd-doped GaN generates huge magnetization at room temperature (~4000μ_B). Afterwards, GGA+U study suggested that this huge magnetization is caused by Ga vacancy [2]. However, there are no reports on direct observation of defect induced magnetism of GaGdN. For this reason, we carried out the TCDFT calculation for spin-polarized positron annihilation parameters. The TCDFT calculation is performed using ABINIT code [3]. We found that differential magnetic doppler spectrum depends on the spin-density around the Ga vacancy.

2) developing the theory of positronium formation using realistic material surface: A positronium (Ps) is a bound state between an electron and a positron like a hydrogen atom. Ps formation is caused in positron re-emission process and is allowed outside of the metal surfaces, because Ps formation is prohibited inside of metal due to strong electron screening effect to a positron [4]. We found that the theoretical spectra including interaction between Ps and surface remaining hole [5] show in good agreement with experiment.

References

[1] F. Tuomisto and I. Makkonen, Rev. Mod. Phys. **85**, 1583 (2013).

[2] Y. Gohda and A. Oshiyama, Phys. Rev. B **78**, 161201(R) (2008).

[3] X. Gonze et al., Comput. Phys. Commun. **205**, 106 (2016).

[4] C. Hugenschmidt, Surf. Sci. Rep. **71**, 547 (2016).

[5] A. Ishii, Surf. Sci. **209**, 1 (1989).

First-Principles Molecular Dynamics Study on Structural Properties of Fayalite Fe_2SiO_4 under High-Pressure

Masaaki MISAWA

Faculty of Science and Engineering, Kyushu Sangyo University, Fukuoka 813-8503

Fayalite (Fe_2SiO_4), the iron-rich end member of olivine ($Mg_xFe_{2-x}SiO_4$), undergoes crystal-to-amorphous structural transformation under high-pressure (~40 GPa) at room temperature. Based on an in-situ infrared spectroscopy [1], it is explained that the pressure-induced amorphization is triggered by the deformation of tetrahedral SiO_4 structural units in the crystalline phase into octahedral SiO_6, distorted octahedral SiO_6 or pyramidal SiO_5 units. However, it is not clear that the distribution of those structural units and what kind of atom is the network former/modifier in the amorphous phase.

To investigate the detailed structural properties of pressure-amorphous fayalite, we have carried out first-principles molecular dynamics simulations for the amorphization process of fayalite. The electronic states were calculated using projector augmented-wave method within the framework of density functional theory, in which the generalized gradient approximation was used for the exchange-correlation energy. In order to represent the electronic states of localized d-orbitals in Fe atoms, spin-polarization was taken into account and DFT+U method was employed. First the pressure was increased from ambient pressure to 300 GPa to create the pressure-amorphous fayalite, and then return to ambient pressure to compare with experimental results. All of simulations are performed at room temperature.

As a result of the simulations, we confirm that massive structural change occurs and disordered structure was obtained at high pressure. In the obtained structure, both of pyramidal SiO_5 and octahedral SiO_6 units exist and those SiO_x units form corner-shared network structure at 40 GPa. On the other hand, at ambient pressure, most of Si atoms revert to tetrahedral SiO_4 units and Si-O network structure was disconnected. These disconnected SiO_x units form only monomer or dimer, which show good agreement with experimental prediction of the forsterite glass structure [2].

References

[1] Q. Williams, E. Knittle, R. Reichlin, S. Martin and R. Jeanloz: J. Geophys. Res. **95** (1990) 21549.

[2] S. Kohara, K. Suzuya, K. Takeuchi, C.-K. Loong, M. Grimsditch, J. K. R. Weber, J.A. Tangeman, and T. S. Key: Science **303** (2004) 1649.

Theoretical Design of Novel Magneto-Electric Oxides

Masayuki TOYODA
Department of Physics, Tokyo Institute of Technology
Ookayama, Meguro-ku, Tokyo 152-8551

Magneto-electric materials have promising potential for technological innovations, owing to their cross correlation between magnetism and electricity. A novel family of oxides represented by $Ba(TiO)Cu_4(PO_4)_4$[1] exhibit quadrupole-type alignment of localized $S = 1/2$ spin moments, which gives rise to the magneto-eletric responses[2].

In this study, we performed systematic survey of the electronic structures and magnetic properties of $A(TiO)Cu_4(PO_4)_4$ (A = Ba, Sr, and Pb) based on the density-functional theory. The computations have been done by using the ISSP supercomputer system B.

For all the oxides, the ground state is found to be antiferromagnetic (AFM) with the quadrupole-type alignment of the spin moments, which is the characteristic feature of this family. However, from the evaluation of the magnetic exchange interaction J, we found that the inter-layer interaction varies upon the replacement of the A ion. For the case of A = Ba and Sr, the inter-layer interaction is AFM and, therefore, the materials show antiferroelectricity (AFE), which gives no macroscopic polarization. On the other hand, for the case of A = Pb, the interaction is ferromagnetic (FM) and the materials exhibits ferroelectric (FE) polarization.

From the analysis of the charge density distribution (Fig. 1), it is found that FM inter-layer interaction in $Pb(TiO)Cu_4(PO_4)_4$ is mediated by the Pb-s states that has broader distribution than the other counterparts. Based on this insight, we also found that A = Sn can be yet another magneto-electric oxide that shows AFM and FE ordering.

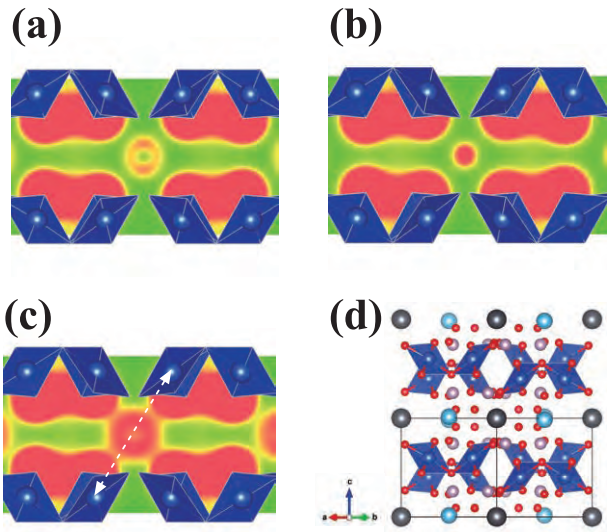

Figure 1: Partial electronic charge density distribution of the valence band states in (a) $Ba(TiO)Cu_4(PO_4)_4$, (b) $Sr(TiO)Cu_4(PO_4)_4$, and (c) $Pb(TiO)Cu_4(PO_4)_4$ projected on (110) plane. The crystal structure viewed from [110] direction is also shown in panel (d).

References

[1] K. Kimura, M. Toyoda et al., Nat. Commun. **7**, 13039 (2016).

[2] K.T. Delaney, M¡. Mostovoy, and N.A. Spaldin, Phys. Rev. Lett. **102**, 157203 (2009).

[3] K. Kimura, M. Toyoda, P. Babkevich, K. Yamauchi, M. Sera, V. Nassif, H. M. R øønnow, and T. Kimura, Phys. Rev. B **97**, 134418 (2018).

Electronics structures of newly crystallized large aromatic organic semiconductors

Toshihiro Shimada, Ichiro Yamane, Nobuhiko Sakai, Takahiro Tamura, Wei Liu, Meiqi Zhang, Takashi Yanase, Taro Nagahama

Division of Applied Chemistry, Faculty of Engineering,

Hokkaido University, Kita 13 Nishi 8, Kita-ku, Sapporo, 060-8628 Japan

We are studying synthesis reactions and properties of solid state materials, including new carbon materials[1], organic semiconductors[2], and nanostructures. We use computer to calculate electronic band structure and stability of various materials.

This year, we focused on electronic band structure of new organic semiconductor crystals which we have recently developed the method to make single crystals. The structure of the molecule (Benzo[i]benzo[6',7']quinoxalino [2',3':9,10]phenanthro[4,5-abc]phenazine; BBQPP in the following) is shown in Fig. 1. We grew single crystals of this and other molecules and determined the crystal structures by using x-ray diffraction.

Fig. 1: BBQPP

Using ISSP supercomputer, we calculated the band structure of BBQPP based on the atomic positions determined from x-ray diffraction. The calculation was carried out using the Vienna Ab initio simulation package[3] which is based on DFT, plane waves and pseudopotentials. Our calculation was performed with the projector augmented wave method and the exchange-correlation energy treated using the PBE functional[4] based on the generalized gradient approximation. The cutoff energy was 400 eV. The result is shown in Fig. 2. Strong one dimensional character of the electronic structure was noticed.

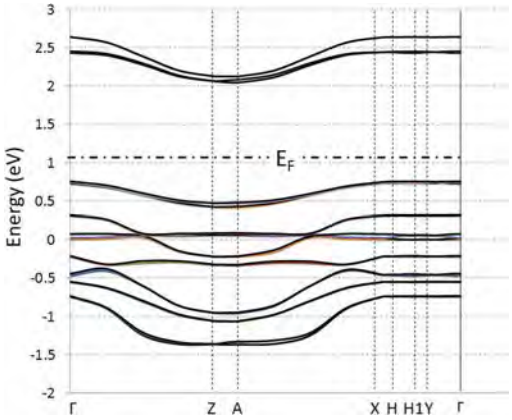

Fig.2: Band structure of BBQPP

References

[1] I. Yamane et al., Jpn.J. Appl.Phys. 58, SBBG13 (2019).

[2] N. Sakai et al., ibid, SBBG08 (2019).

[3] G. Kresse J. Furthmüller, Phys. Rev. B54,11169 (1996).

[4] J. P. Perdew, K. Burke, M. Ernzerhof, Phys. Rev. Lett. 77, 3865 (1996).

Elucidation of electronic states of caged compounds in aqueous solution

Miyabi HIYAMA
Graduate School of Science and Technology, Gunma University,
Tenjin-cho, Kiryu, Gunma 376-8515

Caged-luciferins are known as the compounds which can generate luciferin by UV photolytic reaction as shown in Figure 1.They are expected to be powerful tool in spectroscopic studies for catalytic reaction such as firefly bioluminescence.

A new caged-luciferin designed in Akiyama group of ISSP was synthesized and its molecular structure was identified with NMR[1]. When we use this caged-luciferin for spectroscopic studies, we need the detail of electronic states of this molecule in aqueous solutions. In this year, we invested the electronic structures of this caged-luciferin in aqueous solution by DFT calculations.

The polarized continuum model was used for the description of water solute molecules. All calculations were performed using the GAUSSIAN09 [2] program on system B of Super Computer Center in ISSP.

It was found that there are forty equilibrium structures for the caged-lucifein in aqueous solution and these structures are classified in terms of characteristics in their configurations[3, 4] .

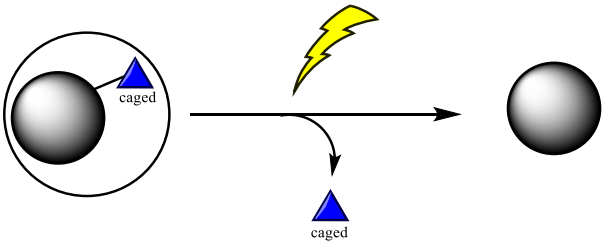

Figure 1: Conceptual diagram for Cage-luciferin

References

[1] Kurata et al. , J. Photochem. Photobiol. B, **189** (2018) 81.

[2] Gaussian 09, Revision D.01, M. J. Frisch et al.

[3] Usukura et al. The 12th Annual meeting of Japan Society for Molecular Science.

[4] Hiyama, Symposium for reaction Path Search 2018.

Calculation of oxide surface properties for catalyst informatics

Yoyo HINUMA

Center for Frontier Science

Chiba University, 1-33 Yayoicho, Inage, Chiba, Chiba 263-8522

Surface point defects of metal oxides, for instance O vacancies, have a dominant effect on heterogeneous catalysis. The Mars-Van Krevelen mechanism is one of the most frequently encountered catalytic process. In one example, O vacancies on a metal oxide catalyst surface act as reaction sites. The energy required to remove O from a surface, which is denoted as the surface O vacancy formation energy (E_{Ovac}), can be used to rationalize and predict catalytic performance in such a catalytic process. Calculation of E_{Ovac} requires a slab-and-vacuum model with sufficient spacing between O vacancies, hence some estimation of E_{Ovac} from less costly calculations, such as slab-and-vacuum model calculations with minimum cell size and even bulk calculations, will be effective in screening materials for a given purpose.

A total of 33 binary oxide surfaces of insulating and semiconducting oxides was evaluated using the automated nonstoichiometric and nonpolar slab-and-model generation algorithm by Hinuma et al. [1,2]. A good correlation was found between E_{Ovac} and band gap, bulk formation energy, and electron affinity was found. Moreover, the relation between subsequent small molecule (O_2, NO, CO, CO_2, and H_2) for 16 surfaces were assessed. The adsorption mode was strongly governed by E_{Ovac}, where a large E_{Ovac} benefits side-on adsorption for NO and CO as well as dissociative adsorption for energy showed CO_2 and H_2. Furthermore, the side-on and dissociative adsorption energy is linearly dependent on E_{Ovac}. [3]

These findings serve as the basis for more efficient catalyst design because E_{Ovac} was found to influence the stability of O vacancies and the adsorption mode, which in turn can be estimated to some extent using cheaply obtained physical quantities, namely band gap, bulk formation energy, and electron affinity.

References

[1] Y. Hinuma et al.: Comp. Mater. Sci. 113 (2016) 221.

[2] Y. Hinuma et al.: Phys. Rev. Mater. 2 (2018) 124603.

[3] Y. Hinuma et al.: J. Phys. Chem. C. 122 (2018) 29435.

Search and realization of novel electronic properties of solid surfaces and interfaces and of small particles

Takeshi INAOKA
Department of Physics and Earth Sciences, Faculty of Science, University of the Ryukyus, 1 Senbaru, Nishihara, Okinawa 903-0213

We describe two of those subjects which we addressed this year.

Graphene is a very popular single-layer structure of carbon (C) atoms arranged in a hexagonal lattice. However, we consider that there might be different monolayer structures of C atoms. Last year, we presented another stable structure which is composed of tetragonal and octagonal patterns. It was found that the electron system is a semi-metal which is characterized by the electron pocket around the $\bar{\mathrm{M}}$ point and the hole pocket around the $\bar{\Gamma}$ point. This year, we proposed a similar stable structure which is constituted of tetragonal, hexagonal, and octagonal patterns.

In scanning tunneling microscopy (STM) light emission spectra of Ni(110)-(2x1)-O surface appear stepwise structures due to oxygen (O) atom vibration parallel to the surface [1]. These structures are considered to originate from the change in the local density of states (LDOS) below the STM tip owing to the vibration [1]. From this standpoint, we started first-principles calculations of this system at higher levels than in previous works.

We employed the program package 'Vienna Ab initio Simulation Package' (VASP) [2,3] on systems B and C.

(1) Proposal of a novel single-layer structure of carbon atoms [4]

By means of first-principles calculations with the generalized gradient approximation (GGA), we investigated a C monolayer structure shown in Fig. 1. We optimized the in-plane structure including the primitive unit cell size. Then, we checked the stability of this structure to the plane-normal atom displacement. It was found that the cohesive energy per C atom evaluated by separating the crystal into isolated atoms is comparable to that of graphene, and that the in-plane structure is stable.

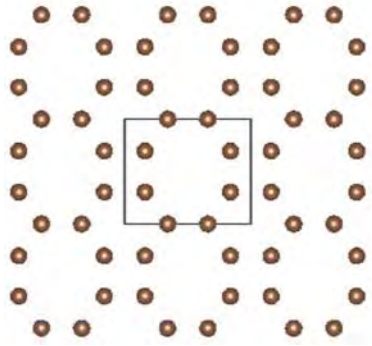

Fig. 1 Proposed monolayer structure of C atoms

The energy contour map of the twelfth band showed that there exists a hole pocket around the $\bar{\mathrm{X}}$ point which extends toward the $\bar{\Gamma}$ point. On the other hand, the energy contour map of the thirteenth band indicated that there lies an electron pocket around the $\bar{\mathrm{M}}$ point that spreads toward the Y point. These pockets compensating each other asserts that this crystal is semi-metal with large electron or hole density estimated to be 1.4×10^{14} cm^{-2}. From the electron density distribution, we realized that the twelfth and thirteenth bands are formed by hybridization of plane-normal p orbitals of C atoms. Each band has its own hybridizing character.

(2) Electronic structure of Ni(110)-(2x1) O surface [5]

To examine how the O atom displacement in phonon vibration changes the LDOS, we started first-principles calculation of this system.

Previously, first-principles calculations were performed for O-adsorbed Ni surfaces. However, slabs of several atomic

layers were treated because of limitations of computer performance at that time. In the present work, we intend to identify sufficient slab thickness to represent semi-infinite substrate by using slabs of several tens of atomic layers.

Figure 2 exhibits the optimized slab structure of 11 Ni atom layers with an adsorbed O atom at each surface. We assume the missing-row reconstructed O p(2x1)/Ni(110) surface. Figure 3 displays the orbital-projected density of states (pDOS) for p_x orbital of the O atom (full curves) and for d_{xy} orbital of the topmost Ni atom (dotted curves). The black and red lines are for majority and minority spins, respectively. The p_x pDOS of the O atom for each spin shows a peak near the Fermi level E_F, which accords with a peak of the d_{xy} pDOS of the Ni atom. This peak-energy agreement is considered to indicate the bonding of the p_x state of the O atom and the d_{xy} state of the Ni atom. At the next stage, we will investigate the peak shift of the p_x pDOS of the O atom in surface phonon vibration.

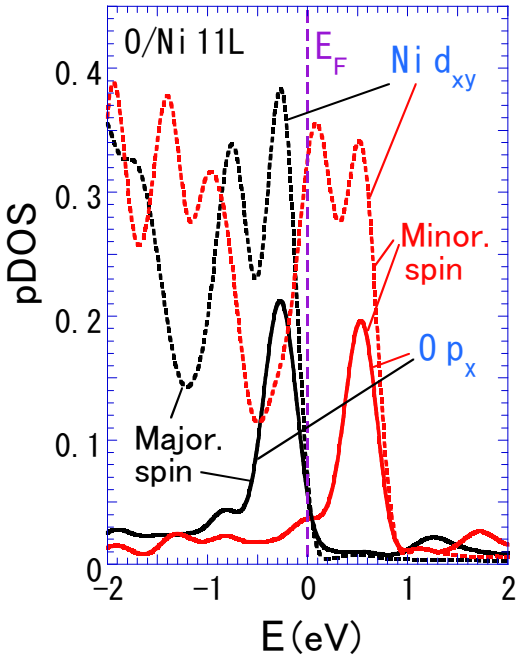

Fig. 3 Orbital-projected density of states of the adsorbed O atom and the surface Ni atom. For details, see the text.

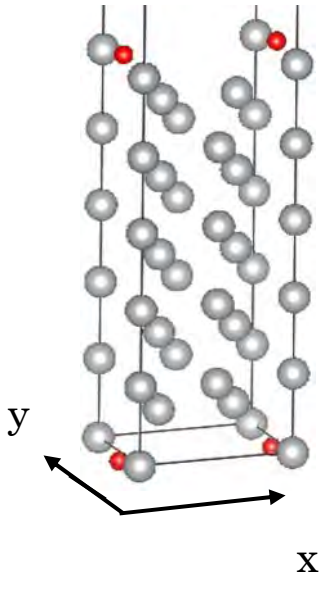

Fig. 2 Optimized slab structure of O p(2x1) Ni(110) surface. The slab is composed of 11 Ni atom layers and an adsorbed O atom at each surface.

References

[1] Y. Uehara, T. Inaoka, T. Nishio, and S. Katano, J. Appl. Phys. **123** (2018) 224302 (8 pages).
[2] G. Kresse and J. Hafner: Phys. Rev. B **47** (1993) 558-561.
[3] G. Kresse and J. Furthmüller: Comput. Mat. Sci. **6** (1996) 15-50.
[4] T. Inaoka and Y. Nakaema, to be prepared.
[5] T. Inaoka and Y. Uehara, to be prepared.

Chemical doping of nano-structured PbS

Ken-ichi SHUDO
Fac. of Sci/Eng., Yokohama National University
Tokiwadai 79-5, Hodogaya-ku Yokohama 240-8501

Galium oxide family are wide-gap semiconductors, and their optical features, tunable by impurity dope, are expected to be useful for many applications. In order to analyze our experimental data of photo-absorption/luminescence a ected by the impurities in Ga_2O_3 [1], electronic states of ϵ- and κ-Ga_2O_3 with Co dope were calculated using the VASP code [2] based on rst principles theory.

Calculations were done for a single unit cell through supercells sized to 8 4 4, with/without Co dope as an impurity atom. The calculation was typically done in one or four computer-nodes, in *hybrid* parallelism (8 MPI 3 openMP par node, typically). We began with the optimization without the impurity. The lattice constants were xed at the obtained optimized dimension, and a Ga atom was then replaced by Ge. As expected from the small lattice constant of **b** and **c** direction, 1 1 2 or 1 2 1 supercell of Ga_2O_3 gave instable results, suggesting necessity of careful conformation of the impurity to avoid the Co-Co interaction at high density of the impurity.

The results in density functional theory (DFT) gave Co-induced states in the band gap (see the main panel of Figure 1). They are not satisfactory in that the calculated band gap did not agree with the experimental data, as often seen in DFT. Thus we concluded some modi - cation should be introduced, such as empirical methods namely DFT+U or non-local external potential (NLEP) [3]. However, the tendency of bandgap increase/decrease in the calculated results (inset of Fig.1) was in good agreement with out experimental results.

At the same time, we performed preliminary calculation of impurity states in PbS crystal, and detailed analysis of spin-polarization of monolayer lm of metal organic framework (MOF) started as an ISSP project (H29-Cb-0009) from 2018.

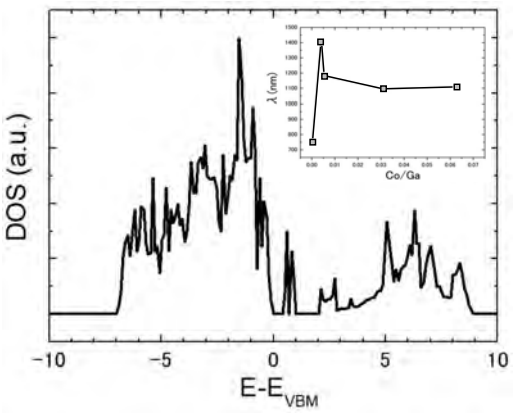

Figure 1: Calculated density of electronic states with a Co atoms in a 8 4 4 ϵ-Ga_2O_3 supercell. Inset: band-gap to varied density of the Co impurity.

References

[1] K. Mukai, A. Tsuno, K. Shudo, and H. Otani: Jap. j. Appl. Phys. **58**, SBBK05 (2019).

[2] G. Kresse: Phys. Rev.**B 59**, 1758–1775 (1999); see also `https://www.vasp.at`

[3] S. Lany, H. Raebiger, and A. Zunger: Phys. Rev. B 77, 241201 (2008).

First-principles Study of Defects of Magnesium Alloys

Daisuke Matsunaka

Department of Mechanical Systems Engineering,

Shinshu University, 4-17-1 Wakasato, Nagano 380-8553

Magnesium (Mg) has been of increasingly interest from the engineering viewpoint, because of its low density and relatively high specific strength. Despite intensive research efforts, there remain various problems to be overcome; low ductility and low toughness at room temperature. As polycrystalline magnesium materials are applied for the engineering use, it is important to elucidate grain boundary properties. We have performed molecular dynamics analyses of symmetric tilt gran boundaries for [0001], [10-10], and [1-210] rotation axes using three types of interatomic potentials. The gran boundary energy vary for misorientation and there are energy cusp misorientations corresponding to twin boundaries for [10-10], and [1-210] rotation axes. On the other hand, for [0001], the misorientation dependence of grain boundary energy is relatively simple. These results imply that the anisotropy of hcp structure is reflected in the symmetric tilt grain boundaries.

In Mg alloys with rare earth elements, the addition in solid solution causes a significant increase in ductility. It is an important issue to elucidate effects of an alloying element on each deformation mode such as deformation twinnings and non-basal slips. First-principles calculations give us valuable information of alloying elements. Development of interatomic potentials for alloys which can describe the first-principles results is necessary for atomistic simulations of deformation in Mg alloys. In this study, we tried to develop an interatomic potential for Mg alloy in terms of artificial neural network framework, based on first-principles results. As learning data, we calculated crystal structures such as fcc and bcc as well hcp and their deformed models and defective models, in which the number of atoms are relatively small. We have successfully implemented the developed potential into large-scale molecular dynamics simulations.

References

[1] D. Matsunaka and K. Kawahara: Proc. 4th Multi-scale Mater. Mech. Symp. (2019) P20.

[2] K. Oboso, Y. Fujioka, S. Yoshioka, and D. Matsunaka: Conf. Proc. Jpn. Soc. Comp. Eng. Sci. **24** (2019) A-03-04.

Calculation of Catalyst Electronic Structures for Catalyst Informatics

Takashi TOYAO

Institute for Catalysis,

Hokkaido University, N-21, W-10, Sapporo 001-0021,

Machine learning (ML) methods have gained much attention among the molecular and materials science communities for use in the prediction of various kinds of physical and chemical properties. ML methods could serve as a fast and high-precision alternative to the first-principles modelling. Several successful examples are already available for predictions and discoveries of organic chemistry reactions including ones that use homogeneous catalysts. However, targets of ML predictions for heterogeneous catalysis have been limited. Our group has been trying to contribute to establishing "Catalysis Informatics" by utilizing ML [1-2].

Here, we have calculated adsorption energies of CH_4 related species, namely CH_3, CH_2, CH, C, and H on the Cu-based alloys by using density functional theory (DFT), as shown in Figure 1 and 2. These DFT-calculated adsorption energies of CH_3, CH_2, CH, C, and H on Cu-based alloys will be used for ML predictions, and furthermore, for utilization of CH_4.

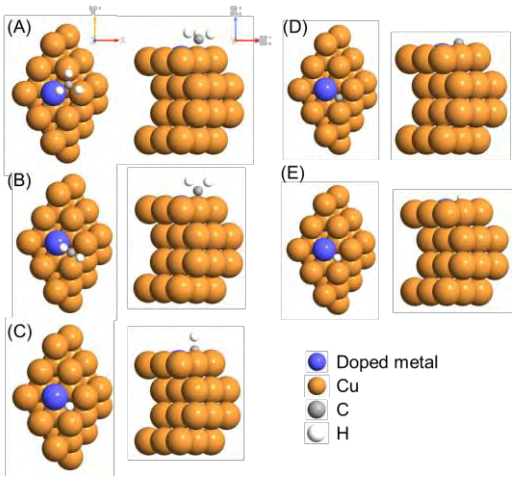

Figure 1. Adsorption models for (A) CH_3, (B) CH_2, (C) CH, (D) C, and (E) H on Cu-based alloys. Color code: gray: C; white: H; brown: Cu; blue: doped metal atoms.

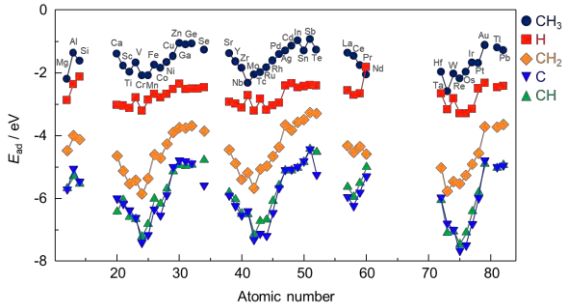

Figure 2. DFT-calculated adsorption energies of CH_3, CH_2, CH, C, and H on the Cu-based alloys.

References

[1] I. Takigawa, K. Shimizu, K. Tsuda, S. Takakusagi, RSC Advances, **2016**, *6*, 52587-52595.

[2] T. Toyao, K. Suzuki, S. Kikuchi, S. Takakusagi, K. Shimizu, I. Takigawa, The Journal of Physical Chemistry C, **2018**, *122*, 8315–8326

Structural study on surface reconstruction and solvent effects of nanoparticles

Akira YOKO

WPI – Advanced Institute for Materials Research (WPI-AIMR), Tohoku University

2-1-1 Katahira, Aoba-ku, Sendai 980-8577, Japan

Nanoparticle structures have been investigated because the nanoparticle structure is different from that of the bulk crystal. Surface reconstruction takes an important role in nanoparticle structure.

We have investigated nanoparticle structure of perovskite oxides, which have different surface energies depending on the composition [1]. The difference in particle size observed in experiments using supercritical water could be explained by the difference in calculated surface energies. Surface energies of nanoclusters are different from that of bulk surface calculated with slab model, and the calculation of nanoclusters was essential.

This year, calculation of interface energies of nanoclusters considering the effects of the solvent. The implicit solvent model which consider the effects of dielectric constant was applied. Calculations were conducted via VASPsol code with clusters consisting of 40 atoms. The dielectric constant of supercritical water was used (e.g., 5.9 for 400 °C, 30 MPa). Dielectric medium stabilized metal oxide nanoclusters resulting in the decrease in interface energy compared to the surface energy in the vacuum. Interestingly, the dielectric medium affects nanocluster structures.

The effects of dielectric constant on nanoparticle structure were also investigated using $BaTiO_3$ as a model. The tetragonality defined as the ratio of the lattice of c-axis and a-axis was evaluated changing dielectric constant. As a result, the tetragonality of $BaTiO_3$ decreased with an increase in dielectric constant as shown in Figure 1. The previous experimental study elucidated that cubic and tetragonal $BaTiO_3$ formed at high and low water density conditions, respectively. The calculated results in this study could explain the tendency. Larger scale calculation would be required to elucidate this phenomenon.

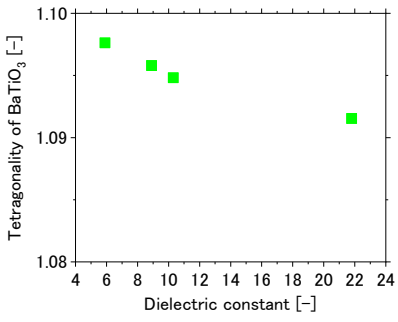

Fig. 1: Tetragonality of $BaTiO_3$ in dielectric medium.

References

[1] A. Yoko: J. Phys. Chem. C. **122(42)** (2018) 24350.

First-principles study on the structural stability of long-period stacking ordered structure in Fe based shape memory alloys

Takao Tsumuraya
Kumamoto University
2-39-1 Kurokami, Kumamoto 860-8555, Japan

Fe-Mn-Si based alloys is known to exhibit a shape-memory effect associated with deformation-induced martensitic transformation from face-centered cubic (fcc) γ-austenite to hexagonal closed packed (hcp) ϵ-Martensitic phase [1, 2]. Among them, Fe-15Mn-10Cr-8Ni-4Si (mass%) alloy appeared to have outstanding properties of low-cycle fatigue lives and is practically used in a seismic damping component of architectural constructions [3]. Recently, under cyclic push-pull loading of the Fe-Mn-Si-based alloys, a new phase different from ϵ phase was found by TEM. The new phase shows electron diffraction spots at the 1/3 position of the 10-11 spots of the ϵ phase, which suggests the existence of a long-period stacking ordered (LPSO) structure.

In 1963, Lysak and Nikolin also discovered a new phase which is different from ϵ phase during heating and cooling cycles of Fe-Mn-C alloys using the x-ray diffraction measurements [4, 5]. This new phase is called ϵ' phase. Later, a similar phase was found by Oka *et al* using transmission electron microscopy (TEM). The ϵ phase is formed by stacking faults from fcc structure where $a/\sqrt{6}$ partial dislocation occurs every two layers on (111) plane of fcc structure which is parallel to (0001) plane of hcp structure. This type of dislocation is called Shockley's partial dislocation. However, such a long time, actual stacking sequence of the ϵ' (LPSO) phase and the relative stability with γ and ϵ phases still remain unclear.

To understand the actual stacking pattern of the LPSO like structure and relative stability with γ and ϵ phases, we study phase stability and magnetic properties of pure Fe with 4H (dhcp), $6H_1$, $6H_2$, and 10H structures, together with 2H (hcp) and 3R (fcc) structures using first-principles density-functional theory (DFT) calculations within a generalized gradient approximation (GGA) (Fig. 1). The Kohn-Sham equation is solved by all-electron full-potential linearized augmented plane wave (FLAPW) method [6]. It is clearly shown that $6H_2$ is the most stable structure. Therefore, we conclude that the LPSO phase adopts the $6H_2$ structure. We also claried the origin of structural stabilities from electronic structure point of view.

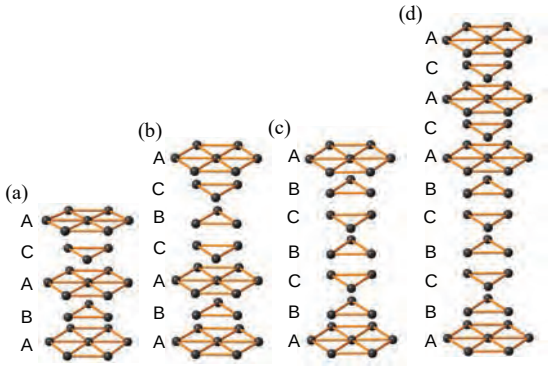

Figure 1: Candidates of long-period stacking ordered structure of Fe, (a) dhcp (4H), (b) $6H_1$, (c) $6H_2$, and (d) 10H.

References

[1] A. Sato, Y. Yamaji, and T. Mori, Acta Metall. **34**, 287 (1986).

[2] K. Ogawa and S. Kajiwara, Mater. Trans. **34**, 1169 (1993).

[3] T. Sawaguchi, P. Sahu, T. Kikuchi, K. Ogawa, S. Kajiwara, A. Kushibe, M. Higashino, and T. Ogawa, Scripta Mater **54**, 1885 (2006).

[4] L. I. Lysak and B. I. Nikolin, Martensitic phase with a mul- tilayer structure, Dokl. Akad. Nauk SSSR **153**, 812 (1963).

[5] Z. Nishiyama, Martensitic transformation, (London Aca- demic Press, 1978).

[6] E. Wimmer, H. Krakauer, M. Weinert, and A. J. Freeman, Phys. Rev. B **24**, 864 (1981).

Study on Electronic Properties in New Nanoscale Surfaces and Interfaces

Katsuyoshi KOBAYASHI
Department of Physics, Ochanomizu University
2-1-1 Otsuka, Bunkyo-ku, Tokyo 112-8610

In 2018 we have developed a method of calculation for spin and angle resolved photoelectron spectroscopy (SARPES). We have previously developed a new calculation method of SARPES [1]. In this method we used results of repeated-slab calculations with plane wave basis for the final states in photo-excitation. This was done because program packages for density functional calculations using plane wave basis are readily available, and the calculation of momentum matrix elements is easy. One point to consider is the boundary condition of final state wave functions in vacuum regions. We formed out-going plane-wave states in vacuum regions for final states by linear combination of repeated-slab states. This method was applied to the Bi(111) surface. Calculated results reproduced experimental ones [2]. A problem in the previous calculation is that the final states used for evaluating the matrix elements of photo-excitation are not the out-going states but time-reversed LEED states [3]. In 2018 we developed a method of forming the time-reversed LEED states using the results of repeated-slab calculations.

We performed density-functional calculations using the VASP program package to obtain self-consistent electron ground states. Bulk Bloch states of the excited states above vacuum levels were formed by linear combination of the wave functions given by the repeated-slab calculations. The time-reversed LEED states were made by eliminating the backward propagating Bloch states from the repeated-slab states. Matrix elements of photo-excitation were calculated using the time-reversed LEED states for final states. This method was applied to the Bi(111) surface. Figure 1 shows calculated results of spin expectation values. The difference between the results of the out-going states [1] and the time-reversed LEED states is small. Calculated results reproduce experimental results [2].

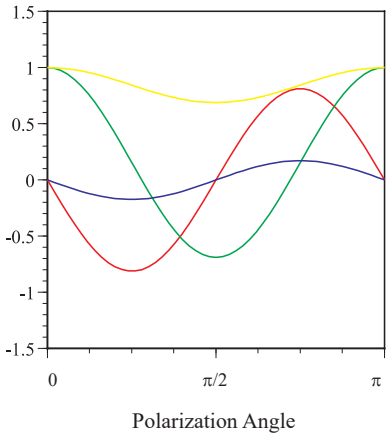

Figure 1: Spin expectation values calculated as a function of polarization angle of incident light. Red, green, and blue lines are x, y, and z components of spin expectation values. Yellow lines show intensity of photo-electrons.

References

[1] K. Kobayashi *et al.*: Phys. Rev. B **95** (2017) 205436.

[2] K. Yaji *et al.*: Nat. Commun. **8** (2017) 14588.

[3] I. Adawi : Phys. Rev. **134** (1964) A788.

Coherent phonon spectroscopy of atomic layer materials

Ahmad Ridwan Tresna Nugraha

Department of Physics, Graduate School of Science

Tohoku University, 6-3 Aramaki-Aza-Aoba, Aoba-ku, Sendai, Miyagi 980-8578

Ultrashort (femtosecond) laser pulses applied to a solid-state material with duration less than a phonon period (~20-200 fs) in the material may generate lattice oscillations coherently, known as coherent phonons. Excitations of coherent phonons are necessary to utilize the phonon modes as a basic component in phononic devices. In particular, we have to look for some materials that could host several coherent phonon modes.

Atomic layer materials, such as transition metal dichalcogenides (TMDs) and their hetero-structures, could be a good candidate for hosting the coherent phonons due to the presence of few-THz phonon modes that do not require sub-fs laser to excite them (50-fs laser is sufficient). A typical setup to excite and observe coherent phonons is shown in Fig. 1, in which the pump-probe technique is utilized.

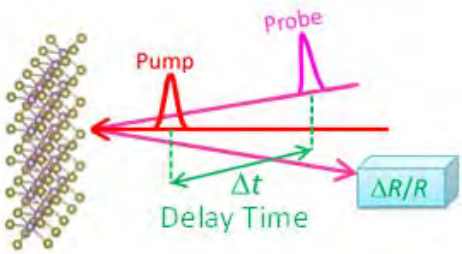

Fig. 1: Coherent phonon spectroscopy through ultrafast pump-probe technique.

In the pump-probe spectroscopy, an important physical quantity that can be measured is the change in either differential resistance ($\Delta R/R$) or different transmittance ($\Delta T/T$) as a function of delay time (Δt) between the pump and probe laser. The emergence of these quantities reflects the generation of coherent phonons because it is expected that there will be no macroscopic optical responses unless the lattices oscillate coherently. The changes in the optical quantities further indicate that the energy band of the materials might be modulated.

Therefore, to analyze the coherent phonon generation from the theoretical point of view, what we need to do firstly is to calculate the electronic band structure and phonon dispersion of the material under consideration. We can then modify the atom position in the material following the possible atomic displacement due to the coherent phonon oscillations. While such a calculation was possible without using supercomputer for some materials like carbon nanotubes that have a sophisticated tight-binding approximation [1,2], supercomputer is required to calculate band structure and phonon dispersion for most of TMDs.

In this 2018 fiscal year, we submitted several jobs in ISSP supercomputer system B to calculate the band structures and phonon dispersions of some atomic layer materials by considering displacement due to coherent phonon oscillations. An example given here is modulation of the band gap in monolayer MoS_2 by the oscillation of longitudinal acoustic (LA) phonon mode. The result is shown in Fig. 2.

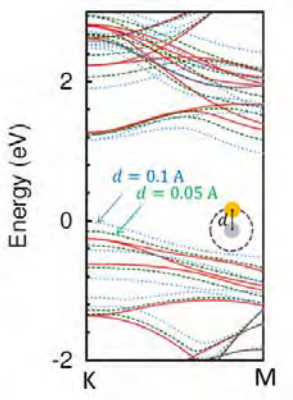

Fig. 2: Band gap modulation in monolayer MoS_2 by displacement *d* of the atoms due to the LA phonon.

In the particular calculation of MoS_2, we artificially exaggerate the amplitude of LA phonon oscillation as large as 0.1 angstrom to 0.05 angstrom so that we can see the effect of the phonon oscillation on the band structure of MoS_2 (Fig. 2). The ongoing work now is to calculate the absorption coefficient by this band gap modulation because the differential reflectance or differential transmittance is proportional to the change of absorption coefficient at different band structures [4].

References

[1] A. R. T. Nugraha et al.: Phys. Rev. B **84**, (2011) 174302.

[2] A. R. T. Nugraha et al.: Phys. Rev. B **91**, (2015) 045406.

[3] A. R. T. Nugraha et al.: J. Phys. Condens. Matter **29** (2017) 055302 .

[4] A. R. T. Nugraha et al.: *unpublished*.

First-principles meta-dynamics analysis of Catalyst Referred Etching method (reaction of water molecule on Ga_2O_3 surface)

Kouji INAGAKI

Graduate School of Engineering, Osaka University

Yamadaoka 2-1, Suita, Osaka 565-0871

Ga_2O_3 has been attracting attention as novel wide-bandgap material for power electronic and efficient optical devices, since recently an efficient crystal fabrication technic for the material has been developed. We studied interaction properties between water molecule and Ga_2O_3 sur-face, which plays crucial role in the most of fabrication processes for electronic devices such as polishing or chemical cleaning using water solvent in the polishing fluid or the chemicals. Water adsorption on Ga_2O_3 (100) surface which surface is the most stable has been already studied [1] with the purpose of analysis of catalytic properties of water split-ting on the surface. In the device fabrication field, unstable (010) surface is important because it is the crystal growth surface with fast growth rate. Here, we report molecular and dis-sociative adsorption of water molecule on Ga_2O_3 (010) surface as the first step of analyzing surface damage induced by etching or oxidation of the surface. We used STATE-senri code for first-principles calculations. The adsorption energies calculated as 0.79eV and 0.98 eV for molecular and dissociation, respectively. Only in the dissociative adsorp-tion case, Ga atom at the adsorption site shows a substantial magnitude of displacement ~0.5 Å as shown in Fig. 1. This indicates that once water molecule adsorbs on Ga_2O_3 surface, it become dissociated and impose a strain to the Ga atom. This indicates the initial stage of surface etching or oxidation.

References

[1] V.M.Bermudez, et.al.: Chem. Phys. 323 193 (2006).

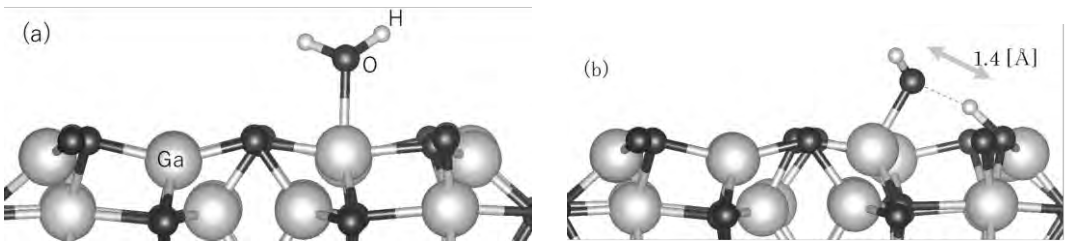

Fig. 1: Atomic configuration of H_2O molecule on Ga_2O_3 (010) surface. Molecular adsorption (a). Dissociative adsorption (b).

3.3 Strongly Correlated Quantum Systems

Mechanism of pseudogap and superconductivity with low-energy fermionic excitations in high-T_c cuprates

Masatoshi IMADA

Department of Applied Physics, The University of Tokyo,

Hongo 7-3-1, Bunkyo-ku, Tokyo 113-8656

Recent progress in accuracy of numerical simulations has enabled much more precise determination of the ground states of the strongly correlated systems than before. Thanks to the progress, it has recently been elucidated how the *d*-wave superconducting and stripe states are severely competing in the simple Hubbard models by using combined variational Monte Carlo, tensor network and Lanczos methods [1,2] consistently with other methods. It has revealed that the ground states of most part of carrier doped Mott insulator in the Hubbard model are various periodicity of stripe states.

On the other hand, *ab initio* Hamiltonian of carrier doped $HgBa_2CuO_4$ recently derived without any adjustable parameters beyond model studies [3,4] by applying multi-scale *ab initio* scheme for correlated electrons (MACE) has been studied by applying the same improved numerical method [5], where the competition of stripe and superconductivity well reproduces the experimental phase diagram. More concretely, a high-T_c cuprate superconductor $HgBa_2CuO_{4+}$ has been studied by solving an *ab initio* low-energy effective Hamiltonian. Its ground-state phase diagram reproduces experiments including Mott gap, antiferromagnetic ordered moment in the mother material and superconducting phase extended in a wide range of hole density, which severely competes with a period-4 charge ordered state near $\delta \sim 0.1$ as is observed by recent X-ray scattering measurements. Crucial role of off-site interactions on the amplitude and stability of the superconductivity is revealed. Furthermore, we find that the enhancement of superconductivity is well correlated with that of charge fluctuations rather than spin fluctuations.

Based on the superconductivity reproduced by the numerics, we have also studied the superconducting mechanism in more depth. An experimental long-standing puzzle was the featureless structure in the spectral function indicated by the angle resolved photoemission spectroscopy (ARPES) spectra, in contrast to the case of conventional strong-coupling BCS superconductors in the history. We have shown before how the puzzle has been solved with the help of quantum-cluster studies of dynamical mean-field theory (DMFT) of the Hubbard model, where the featureless structure is a consequence of the cancellation of the prominent peaks in both of the normal anomalous part of self-energies [6,7].

We have recently examined this problem from a completely independent machine learning studies purely based on the ARPES data [8]. Recent progress of machine-learning techniques opens possibilities of exposing physical quantities hidden in direct measurements only from available experimental data combined with nonlinear regression analyses. The Boltzmann-machine method has been applied to the angle-resolved photoemission spectroscopy spectra of cuprate superconductors. The result shows that prominent peak structures exist both in normal and anomalous self-energies, but they cancel in the total self-energy making the structure apparently invisible, while the peaks make dominant contributions to superconducting gap, hence providing a decisive testimony for the origin of superconductivity. This is consistent with the former DMFT studies of the Hubbard model. The present achievement opens avenues for innovative machine-learning spectroscopy method. An emergent dark fermion theory has also been discussed in detail in connection to the peak structure revealed above [9].

We have further formulated a method of deriving effective low-energy Hamiltonian for nonperiodic systems such as interfaces for strongly correlated electron systems by extending MACE to make challenging studies of lattice relaxation around the interface possible. We have applied the formalism to copper-oxide high T_c superconductors in an example of the interface between overdoped $La_{2-x}Sr_xCuO_4$ and Mott insulating La_2CuO_4 recently realized experimentally [10]. We show that the parameters of the two-orbital *Eg* Hamiltonian derived for the $La_2CuO_4/La_{1:55}Sr_{0:45}CuO_4$ superlattice differ considerably from those for the bulk La_2CuO_4, particularly significant in the partially-screened Coulomb parameters and the level difference between the d_{x2-y2} and d_{z2} orbitals, ΔE. Here, the lattice relaxation on the E_g Hamiltonian has been examined from first principles. We find that the CuO_6 octahedra distort after the relaxation as a consequence of the Madelung potential difference between the insulator and metal sides, by which the layer dependence of the hopping and Coulomb parameters becomes more gradual than the unrelaxed case. Furthermore, the structure relaxation dramatically changes the ΔE value and the occupation number at the interface. This study not only evidences the importance of the ionic relaxation around interfaces but also provides a set of layer-dependent parameters of the *ab initio Eg* Hamiltonian, which is expected to provide further insight into the interfacial superconductivity when solved with low-energy solvers.

This is a combined report for E project “Mechanism of pseudogap and superconductivity with low-energy fermionic excitations in high-T_c cuprates”, D project “Highly accurate analysis of an effective Hamiltonian for high-T_c cuprates by the many-variable variational Monte Carlo method combined with tensor network”, and shared project for post-K project “Applications of highly accurate lattice model solvers with

tensor network and machine learning for mechanisms of superconductivity".
and "Emergent phenomena from combined strong electron correlation and electron-Phonon coupling"

This series of work has been done in collaboration with M. Hirayama, T. Ohgoe, K. Ido, A.S. Darmawan, Y. Nomura, Y. Yamaji, T. Misawa, T. Tadano, T. J. Suzuki, T. Yoshida, A. Fujimori, S. Sakai, and M. Civelli,. The calculations were performed on computers at the Supercomputer Center, ISSP, Univ. of Tokyo. The work is also supported by JSPS Kakenhi 16H06345, the RIKEN Center for Computational Science under the HPCI project (hp170263 and hp180170) and the MEXT HPCI Strategic Programs, CDMSI. This project has used the software HPhi and mVMC.

References

[1] Kota Ido, Takahiro Ohgoe, and Masatoshi Imada, Phys. Rev. B. **97**, 045138 (2018).

[2] Andrew S. Darmawan, Yusuke Nomura, Youhei Yamaji, and Masatoshi Imada, Phys. Rev. B **98**, 205132 (2018).

[3] Motoaki Hirayama, Youhei Yamaji, Takahiro Misawa, and Masatoshi Imada, Phys. Rev. B **98**, 134501 (2018).

[4] Motoaki Hirayama, Takahiro Misawa, Takahiro Ohgoe, Youhei Yamaji, and Masatoshi Imada, arXiv:1901.00763.

[5] Takahiro Ohgoe, Motoaki Hirayama, Takahiro Misawa, Kota Ido, Youhei Yamaji, and Masatoshi Imada, arXiv:1902.00122.

[6] Shiro Sakai, Marcello Civelli, and Masatoshi Imada, Phys. Rev. Lett. **116**, 057003 (2016).

[7] Shiro Sakai, Marcello Civelli, and Masatoshi Imada, Phys. Rev. B. **94**, 115130 (2016).

[8] Youhei Yamaji, Teppei Yoshida, Atsushi Fujimori, Masatoshi Imada, arXiv:1903.08060.

[9] Masatoshi Imada and Takafumi J. Suzuki, J. Phys. Soc. Jpn. **88**, 024701 (2019).

[10] Terumasa Tadano, Yusuke Nomura, Masatoshi Imada, arXiv:1902.03743.

Study on frustrated quantum spin systems using machine-learning solvers

Yusuke NOMURA and Masatoshi IMADA

Department of Applied Physics

The University of Tokyo, Hongo, 7-3-1, Bunkyo-ku, Tokyo 113-8656

Frustrated spin systems may host spin liquid ground states. Once the spin liquid states are realized, we can expect several intriguing behaviors such as fractionalized excitation. Therefore, possibility of realizing spin liquid states is investigated intensively from both experiment and theory.

One of the candidate Hamiltonians for realizing spin liquid is J_1-J_2 Heisenberg model on the two-dimensional square lattice, where the next nearest neighbor exchange J_2 competes with the nearest neighbor exchange J_1, with geometrical frustration. Despite much numerical effort, the controversy on the ground state of the square-lattice J_1-J_2 Heisenberg model has not been settled yet.

In the present study, we introduce very accurate variational wave functions utilizing machine learning techniques to investigate the ground state of J_1-J_2 Heisenberg model. The variational wave function is constructed by combining the restricted Boltzmann machine (RBM) and the pair-product (PP) states. The RBM is a type of artificial neural networks, allowing for a flexible and unbiased description of a wide variety of quantum states [1]. The PP wave function or geminal wave function used in conventional wave-function methods properly describes nonlocal entanglement, helping machine learning to learn many-body ground states efficiently. The combined wave function has been shown to give highly accurate results [2].

Using the accurate RBM+PP wave function, we investigate the possible spin liquid in the J_1-J_2 Heisenberg model. In particular, we focus on the correlation ratio and level crossing. The correlation ratio is based on the ratio between the peak value of structure factor in the momentum space and the value at the neighboring momentum, and is a very sensitive probe for the phase transition [3]. The level crossing of the excited states is also useful in detecting the phase transition [4]. Our numerical results of the correlation ratio and level crossing both suggest a spin liquid ground state for a finite range of J_2 around $J_2/J_1 = 0.5$. The spin liquid in this model is shown to be gapless, in which both the singlet and triplet sectors become gapless.

References

[1] G. Carleo and M. Troyer, Science **355**, 602

(2017).

[2] Y. Nomura, A. S. Darmawan, Y. Yamaji, and M. Imada, Phys. Rev. B **96**, 205152 (2017).

[3] R. K. Kaul, Phys. Rev. Lett. **115**, 157202 (2015).

[4] L. Wang and A. W. Sandvik, Phys. Rev. Lett. **121**, 107202 (2018).

Theoretical and numerical study on novel quantum phenomena in spin-orbit coupled materials

Yukitoshi MOTOME

Department of Applied Physics,

The University of Tokyo, Bunkyo, Tokyo 113-8656

We have theoretically studied a variety of intriguing phenomena in correlated electron systems with strong spin-orbit coupling. During this fiscal year, we have been making substantial progress on the following topics (project numbers: H30-Ca-0064 and H30-Cb-0014). We have also devoted our efforts to a closely related topic on the Kitaev-type quantum spin liquids (project number: H30-D-0005). We summarize the main achievements for each topic below.

(i) *Magnetielectric effect*: We have performed a systematic study of the magnetic phase diagrams and magnetoelectric responses for a simple model that we constructed for a family of compounds composed of low-symmetric square cupola of Cu S=1/2 spins. We compared our theoretical results and the experimental data in collaboration with the experimental groups [1,2]. We have also studied a magnetoelectric effect in a heterostructure of band insulator and ferromagnet [3].

(ii) *Nonreciprocal transport*: We have unveiled nonreciprocal spin Seebeck responses in antiferromagnets on noncentrosymmetric lattices [4]. We have also elucidated a nonreciprocal spin transport in monoaxial chiral magnets, which would be useful as a spin-current diode in spintronics devices [5].

(iii) *Materials design by ab initio calculations*: Based on *ab initio* band calculations and model constructions, we have developed a generic theory for the e_g-orbital systems on a honeycomb structure. We found a plethora of peculiar band crossings, such as multiple Dirac nodes, semi-Dirac nodes, quadratic band crossings, and line nodes [6]. We have also proposed new candidate materials of *f*-electron systems for the Kitaev quantum spin liquids [7].

(iv) *Magnetic vortices and skyrmions*: We have clarified that both Neel- and Bloch-type magnetic vortices can appear in spin-orbit coupled metals, by using an effective spin model [8]. We extended the study to itinerant electron models and found interesting magnetic textures by a large-scale simulation [9]. We have also clarified the effect of magnetic anisotropy on the magnetic skyrmions with a high topological number of two [10].

(v) *Kitaev quantum spin liquids*: By using the Majorana mean-field theory, we have found successive phase transitions in the

antiferromagnetic Kitaev model while increasing an external magnetic field, where the Majorana fermionic states change their topology in the reciprocal space [11]. Also, upon our theoretical results obtained thus far, we have collaborated with several experimental groups for identifying the signatures of Majorana excitations in the Kitaev magnets: thermal Hall effect [12] and its half-quantization [13], Raman scattering [14], and nuclear quadrupole and magnetic resonances [15]. We have published a second article of our review on this topic [16].

References

[1] Y. Kato, K. Kimura, A. Miyake, M. Tokunaga, A. Matsuo, K. Kindo, M. Akaki, M. Hagiwara, S. Kimura, T. Kimura, and Y. Motome: Phys. Rev. B **99** (2019) 024415.

[2] K. Kimura, Y. Kato, K. Yamauchi, A. Miyake, M. Tokunaga, A. Matsuo, K. Kindo, M. Akaki, M. Hagiwara, S. Kimura, M. Toyoda, Y. Motome, and T. Kimura: Phys. Rev. Mat. **2** (2018) 104415, *Editors' Suggestion*.

[3] K. N. Okada, Y. Kato, and, Y. Motome, preprint (arXiv:1902.04204), accepted for the publication in Phys Rev. B.

[4] R. Takashima, Y. Shiomi, and Y. Motome: Phys. Rev. B **98** (2018) 020401(R).

[5] S. Okumura, H. Ishizuka, Y. Kato, J. Ohe, and Y. Motome, preprint (arXiv:1903.12358).

[6] Y. Sugita and Y. Motome, Phys. Rev. B **99** (2019) 041101(R).

[7] S.-H. Jang, R. Sano, Y. Kato, and Y. Motome, preprint (arXiv:1807.01443).

[8] S. Hayami and Y. Motome: Phys. Rev. Lett. **121** (2018) 137202, *selected as Cover image*.

[9] K. N. Okada, Y. Kato, and Y. Motome: Phys. Rev. B **98** (2018) 224406.

[10] S. Hayami and Y. Motome: Phys. Rev. B **99** (2019) 094420.

[11] J. Nasu, Y. Kato, Y. Kamiya, and Y. Motome: Phys. Rev. B **98** (2018) 060416(R).

[12] Y. Kasahara, K. Sugii, T. Ohnishi, M. Shimozawa, M. Yamashita, N. Kurita, H. Tanaka, J. Nasu, Y. Motome, T. Shibauchi, and Y. Matsuda, Phys. Rev. Lett. **120** (2018) 217205.

[13] Y. Kasahara, T. Ohnishi, Y. Mizukami, O. Tanaka, S. Ma, K. Sugii, N. Kurita, H. Tanaka, J. Nasu, Y. Motome, T. Shibauchi, and Y. Matsuda, Nature **559** (2018) 227.

[14] Y. Wang, G. B. Osterhoudt, Y. Tian, P. Lampen-Kelley, A. Banerjee, T. Goldstein, J. Yan, J. Knolle, J. Nasu, Y. Motome, S. Nagler, D. Mandrus, and K. S. Burch, preprint (arXiv:1809.07782).

[15] Y. Nagai, T. Jinno, Y. Yoshitake, J. Nasu, Y. Motome, M. Itoh, and Y. Shimizu, preprint (arXiv:1810.05379).

[16] 求 幸年, 那須 譲治: 固体物理 **53** (2018) 305.

Numerical studies on fractional excitations in strongly correlated electron systems

Youhei YAMAJI
Department of Applied Physics, the University of Tokyo
Hongo, Bunkyo-ku, Tokyo 113-8656

Fractionalized excitations have been actively studied in strongly correlated electron systems over the last several decades. The exploration of the fractionalized particles initiated by the discovery of the fractional quantum Hall effect has flourished and led to findings of exactly solvable many-body quantum systems such as the Kitaev model [1], which has been proposed to capture low-energy spin degrees of freedom in honeycomb networks of heavy transition metal ions typified by an iridium oxide Na_2IrO_3 and α-$RuCl_3$ [2].

Although these *relativistic* Mott insulators, Na_2IrO_3 and α-$RuCl_3$, exhibit spontaneous time-reversal symmetry breakings at low temperatures, their finite-temperature behaviors have been explained by assuming fractionalized Majorana excitations. The most characteristic signature of the fractionalization is the continuous spin excitation spectrum of α-$RuCl_3$ [3], in addition to the recent observation of the quantized thermal Hall effect [4].

Estimates of exchange couplings among ruthenium ions in α-$RuCl_3$ by using the density functional theory reveal that the dominant couplings are the Kitaev interaction and off-diagonal symmetric exchange coupling [5]. The off-diagonal symmetric coupling among $S = 1/2$ quantum spins on the honeycomb lattice is given by the following hamiltonian called the Γ model,

$$\hat{H} = \sum_{\gamma=x,y,z} \sum_{\langle i,j\rangle\in\gamma} \Gamma(\hat{S}_i^\alpha \hat{S}_j^\beta + \hat{S}_i^\beta \hat{S}_j^\alpha) \qquad (1)$$

where couplings for the nearest-neighbor bonds depend on the bond direction $\gamma = x, y, z$, (α, β, γ) is a permutation of (x, y, z), and Γ is the coupling constant and set as $\Gamma = 1$. To clarify the origin of the continuum in α-$RuCl_3$ and possible fractionalization, we examine spin dynamics dominated by the Γ model.

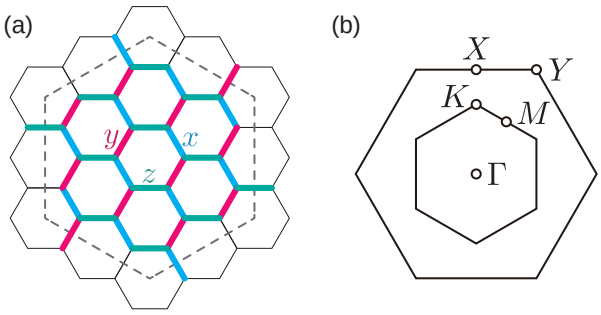

Figure 1: (a) 24 site cluster used in the present report. (b) Brillouin zone and high symmetry points of honeycomb lattices.

By applying the finite-temperature shifted Krylov subspace method [6], we simulate the exact dynamical spin structure factor $S(Q, \omega)$ of the Γ model for a 24 site cluster (see Fig. 1 (a)). At moderate temperatures $T = 0.5$, $S(Q, \omega)$ shows continuum, while suppression of low-energy spectral weight around the Γ and X points, as shown in Fig. 2 (a).

The continuum is interpreted as a combination of relaxational dynamics due to nearly degenerated exponentially degenerated low-energy states [7], which is also valid for the Kitaev model. As temperatures are lowered, the degeneracy is lifted and spin gaps seem to open as shown in Fig. 2 (b), (c), and (d), which

also resembles the spin gap opening in the Kitaev model.

The continuous spectra from the common origin in the Kitaev and Γ model indicates the existence of the fractionalized excitations even in the Γ model [7]. Further examination of the thermal Hall effect is desirable to elucidate the fractionalization.

References

[1] A. Kitaev: Ann. Phys. **321** (2006) 2.

[2] G. Jackeli and G. Khaliullin: Phys. Rev. Lett. **102** (2009) 017205.

[3] A. Banerjee, *et al.*: Science **356** (2017) 1055.

[4] Y. Kasahara, *et al.*: Nature **559** (2018) 227.

[5] For example, H.-S. Kim and H.-Y. Kee: Phys. Rev. B 93 (2016) 155143.

[6] Y. Yamaji, T. Suzuki, and M. Kawamura: arXiv:1802.02854.

[7] A. M. Samarakoon, G. Wachtel, Y. Yamaji, D. A. Tennant, C. D. Batista, and Y. B. Kim: Phys. Rev. B **98** (2018) 045121.

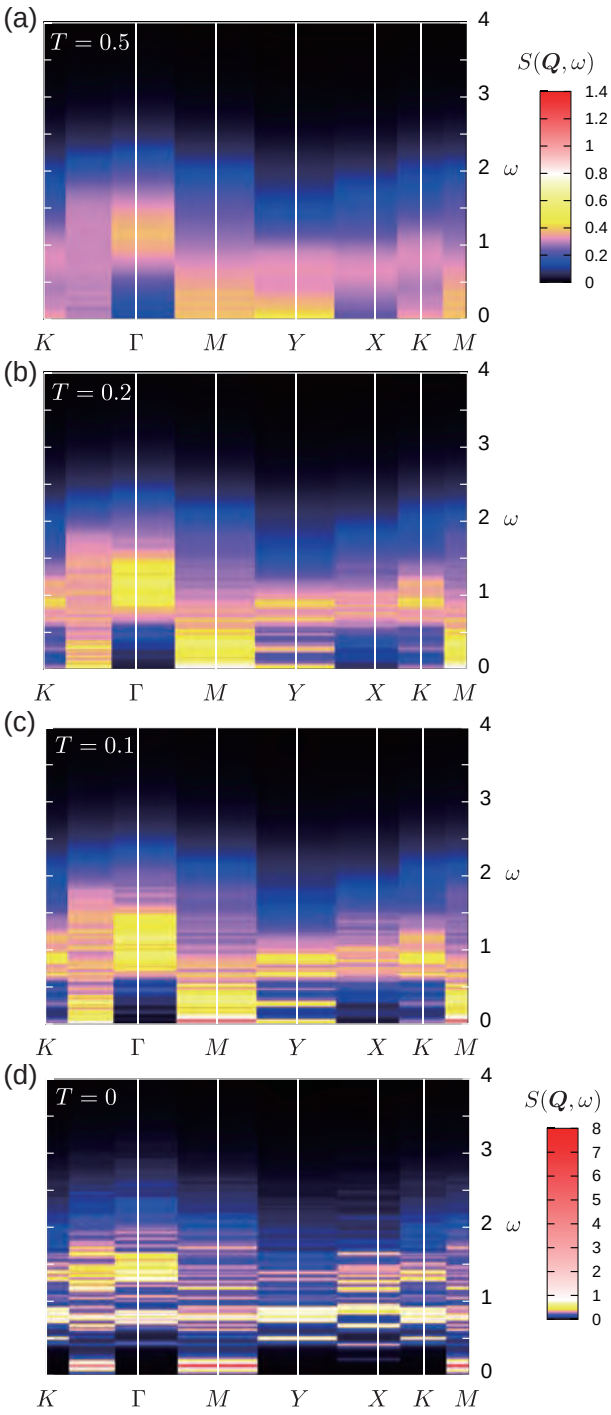

Figure 2: Finite-temperature $S(Q,\omega)$ along a path connecting high symmetry points defined in Fig. 1 (b), at $T = 0.5$ (a), $T = 0.2$ (b), $T = 0.1$ (c), and $S(Q,\omega)$ at $T = 0$ (d).

Study of magnetism and topological phase formation in strongly correlated quantum systems

Norio KAWAKAMI

Department of Physics,

Kyoto University, Kitashirakawa, Sakyo-ku, Kyoto 606-8502

We have studied strongly correlated quantum systems with focus on magnetism and topological phase formation.

(1) We have first explored topological states with magnetic order in heavy-fermion systems having a mirror symmetry. While in the absence of spatial symmetry topological phases cannot exist in two-dimensional (2D) antiferromagnetic phases, we have elucidated that in the presence of a mirror symmetry a topological phase emerges, and have explicitly shown this for a 2D periodic Anderson model. In the ferromagnetic phase around quarter filling, a half-metallic state with a spin-selective gap appears with properties characterized by a Chern number. [1]

(2) The observation of quantum oscillations in topological Kondo insulators SmB_6 and YbB_{12} is a recent puzzling experimental discovery. Quantum oscillations observed in the resistivity and the magnetization are usually explained by the existence of the Fermi surface. However, the Kondo insulators do not have a Fermi surface and thus should not show quantum oscillations. By performing real-space dynamical mean field calculations for topological Kondo insulators in a magnetic field, we have explored this problem. To include the effects of vector potential we need to enlarge the unit cell of the material to the magnetic unit cell consisting of 80-120 atoms.

We have clearly shown that the interplay between correlations and topology leads to observable quantum oscillations without the necessity of a Fermi surface. Particularly, we have shown that correlations strongly enhance the amplitude of quantum oscillations. The enhancement originates thereby in the renormalization of the band structure and finite lifetime of quasiparticles in the Landau levels away from the Fermi energy. We believe that this scenario can explain the observation of quantum oscillations in the magnetic torque for SmB_6 as well as oscillations in the resistivity and the magnetic torque of YbB_{12}. [2]

(3) Recent experiments indicate that, contrary to the long-standing belief, $CeCu_2Si_2$ is a heavy-fermion superconductor with a fully gapped s-wave superconducting state which may be caused by an on-site attractive pairing interaction. Motivated by this finding, we have investigated the competition between

superconductivity, charge-ordering, magnetic-ordering, and the Kondo effect in a heavy fermion s-wave superconductor described by a Kondo lattice model with an attractive on-site Hubbard interaction. At half filling, we have found an intriguing phase where the magnetic ordering of f-electrons lifts the degeneracy between the charge density wave (CDW) state and the superconducting state, leading to a strong suppression of superconductivity. In addition, the system may also become a half metal in this parameter regime. Away from half filling, the CDWs vanish and are replaced by superconductivity combined with incommensurate SDWs up to moderate Kondo couplings to the f-electrons. We have shown that both CDWs as well as superconductivity enhance magnetic ordering due to the suppression of Kondo screening. [3]

(4) It is known that the topological Kondo insulator SmB_6 becomes A-type anti-ferromagnetic under pressure. It is therefore not only an interesting theoretical question to analyze the phase diagram and the impact of magnetic states on the topological properties, but has also a direct impact on experiments. Using real-space dynamical mean field theory combined with numerical renormalization group for a three-dimensional topological Kondo insulator, we have found a wide ferromagnetic phase and an A-type anti-ferromagnetic phase. As has been studied in the topologically trivial Kondo lattice model, the ferromagnetic state exhibits a gap for one spin-direction, while the other spin direction becomes metallic. As in the previous study, we have found a gap for one spin direction in the topological Kondo insulator. Furthermore, because of the mirror symmetry, topological surface states are protected in the ferromagnetic state for the gapped spin direction. We have shown that the magnetic polarization deforms the surface Dirac cones, which can appear as surface Fermi arcs in the magnetic state. For the A-type antiferromagnetic state, we have found similar features in the spectrum, although the gap closes in this magnetic state, and thus the topological protection does not work. We believe that these results can be used to understand existing experiments and demonstrate new interesting experiments for SmB_6 under pressure. [4]

We note that Real-space DMFT maps the lattice on independent quantum impurity models, which must be solved self-consistently. Because all impurities can be solved parallel, the ISSP supercomputer can be efficiently used.

References

[1] K. Kimura, T. Yoshida, and N. Kawakami, J. Phys. Soc. Jpn. **87** (2018) 084705.

[2] R. Peters, T. Yoshida, and N. Kawakami, arXiv:1901.05099.

[3] B. Lechtenberg, R. Peters, and N. Kawakami, Phys. Rev. B **98** (2018) 195111.

[4] R. Peters, T. Yoshida, and N. Kawakami, Phys. Rev. B **98** (2018) 075104.

Numerical Studies on the Role of the Incipient Band Played in Multiband Superconductivity

KAZUHIKO KUROKI
Department of Physics, Osaka University
1-1 Machikaneyama, Toyonaka, Osaka, 560-0043, Japan

We have been theoretically persuing ideal situation for superconductivity in multiband systems. In ref.[1], we proposed that high-T_c superconductivity is possible in Hubbard-type systems (with the on-site U) having wide and narrow bands, where light effective mass and strong pairing interaction is realized when the Fermi level sits in the vicinity of, but does not intersect, the narrow band, namely, the incipient narrow band. The two-leg Hubbard ladder with diagonal hoppings, a model for the ladder-type cuprates, was studied as a system in which such a situation is realized, where a possible occurrence of high T_c superconductivity was suggested. More recently, we extended our study to various quasi-one-dimensional systems, and showed the that the incipient band mechanism of high T_c superconductivity works in a wide range of systems.[2].

In 2018 fiscal year, we have extended the study to two dimensional (2D) systems. A simplest extension of the two-leg ladder Hubbard model to two dimensions is the bilayer square lattice Hubbard model, where two Hubbard models on a square lattice are coupled by vertical hoppings t_r along with diagonal hoppings t'. Here, t' controls the band width of the narrow band, while t_r controls the relative energy between the two bands. We adopted the fluctuation exchange approximation, and invesigated a large parameter space of (t_r, t', n, U), where n is the band filling and U is the on-site Hubbard interaction. Simultaneously, we also performed similar calculation for the two-leg ladder Hubbard model, and made a comparison between the two models. In both cases, superconductivity is found to be strongly enhanced when the Fermi level sits close to the narrow band edge, namely, when the narrow band is incipient. The maximum T_c is expected to be about the same between the two. On the other hand, the parameter regime where T_c remains high is wider in the quasi 1D case. We have also studied bilayer models using triangular and honeycomb lattices, and found results similar to those for the square lattice. We have further extended our study to other multiband models, such as the checkerboard lattice, Lieb lattice, and Mielke lattice, and also to three dimensional lattices, where somewhat different results were obtained. We plan to publish the details of these results in the near future. Variational Monte Carlo study on the two-leg ladder and bilayer square lattices using the mVMC code is also underway.

The above mentioned study is based on purely theoretical models, and their relevance to actual materials is of great interest. In the past years, we have shown that a ladder-like electronic structure is hidden in the 3-2-7 Ruddlesden-Popper compounds, and proposed a possible occurrence of superconductivity in those materials.[3] In 2018 fiscal year, we started two other projects regarding actual materials. One is based on the cuprate ladder compounds, where we study the lattice deformation effects, and the other is based on a vanadium oxyhydride, where ladder-like electronic structure is realized. These studies are now underway.

As for the oxyhydrides, it is also important to understand how the hydrogen atoms affect the electron-electron interaction compared to that in the oxides. In 2018 fiscal year, we constructed low energy effective models for vanadium oxyhydrides $Sr_{n+1}V_nO_{2n+1}H_n$ ($n = 1$ and ∞),[4] where we evaluated the effective interaction using constrained RPA. The band structure was calculated using the Quantum ESPRESSO code, and the Wannier functions and the effective interactions were obtained using the RESPACK code. As low energy effective models, we consider the t_{2g} model, in which only the t_{2g} orbitals are explicitly considered, and the d model, where all the d orbitals are considered. We find that in the former model, the effective electron-electron interaction is strongly screened because the e_g bands are strongly entangled with the t_{2g} bands. On the other hand, in the latter model, the effective interaction is strong, due to the large separation between the d and the anion bands.

[1] K. Kuroki, T. Higashida, and R. Arita, Phys. Rev. B **72**, 212509 (2005).
[2] K. Matsumoto, D. Ogura, and K. Kuroki, Phys. Rev. B **97**, 014516 (2018).
[3] D. Ogura, H. Aoki, and K. Kuroki, Phys. Rev. B **96**, 184513 (2017).
[4] M. Ochi and K. Kuroki, Phys. Rev. B **99**, 155143 (2019).

Competition between superconductivity and orbital order emerging in strongly correlated electron

Akihisa Koga
Department of Physics, Tokyo Institute of Technology, Meguro, Tokyo 152-8551

Strongly correlated electron systems with multiorbitals have attracted much interest since they exhibit a variety of remarkable phenomena such as, *e.g.*, colossal magnetoresistance in manganites, or exotic superconductivity in ruthenates and iron pnictides. In these compounds, charge, spin, and orbital degrees of freedom are strongly coupled with each other, leading to the emergence of novel ordered states. A special class of multiorbital systems are the fullerene-based solids, which show an unconventional form of superconductivity in the vicinity of the Mott insulating state. In these compounds, triply degenerate electronic orbitals in fullerene molecules couple with vibration modes, resulting in a strong renormalization of the local interactions. The static interorbital interactions effectively become larger than the intraorbital interactions and a sign-inverted (antiferromagnetic) Hund coupling is realized. This negative Hund coupling is expected to play an essential role in stabilizing the unconventional superconductivity in these compounds, which stimulates further investigations on multiorbital systems.

Motivated by this, we have considered the three-orbital Hubbard model by applying dynamical-mean field theory. We have found in the phase diagram (see Fig. 1) the existence of spontaneously orbital-selective Mott and orbital-selective superconducting states [1], which may be relevant for understanding the low temperature properties of the fullerene-based solids. We have also considered translational symmetry breaking state in the three-orbital system [2]. An exotic criticality of the phase transition appears between the metallic and charge density wave (CDW) phases, where the CDW order parameter does not exhibit a conventional mean-field-like square root behavior. We have elucidated, using the Landau theory, that the CDW state is accompanied by the antiferro-orbital (AFO) order and the critical behavior is described by two order parameters, where the AFO order parameter is the primary order parameter and the CDW the secondary one.

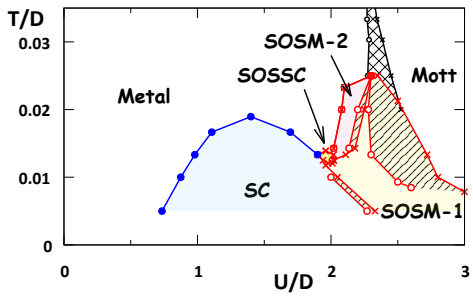

Figure 1: Phase diagram of the three orbital Hubbard model.

[C class 8000 (System B); 1450 (System C)]

References

[1] K. Ishigaki, J. Nasu, A. Koga, S. Hoshino, and P. Werner, Phys. Rev. B **98**, 235120 (2018).

[2] K. Ishigaki, J. Nasu, A. Koga, S. Hoshino, and P. Werner, Phys. Rev. B **99**, 085131 (2019).

Anomalous phenomena induced for correlated topological systems

Tsuneya Yoshida

Department of Physics,

1-1-1 Tennodai, Tsukuba, Ibaraki, JAPAN 305-8571

A variety of topological phenomena have been reported recently. In particular, for correlated systems, interplay between topology and correlations yields a rich physics. This report summarizes our recent studies with special emphasis on the following two points: (i) non-Hermitian phenomena in correlated systems; (ii) new topological states induced by interactions.

Let us start with our results obtained from non-Hermitian perspective on correlated systems. Our analysis based on the dynamical mean-field theory with the numerical renormalization group method have elucidated that correlated systems in equilibrium shows exceptional points in the single-particle spectrum [1]. We further have analyzed the non-Hermitian phenomenon by focusing on the interplay between exceptional points and symmetry. Our DMFT analysis has elucidated that the chiral symmetry of the honeycomb lattice induces a novel non-Hermitian degeneracies in the bulk which we call symmetry-protected exceptional rings[2]. Our

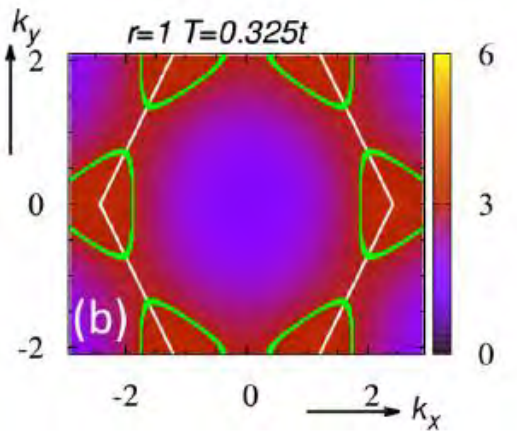

Fig.1 momentum resolved spectral weight in

scenario of the symmetry protection is quite degeneracies emerge for other symmetry classes and arbitrary dimensions.

Another aim of our studies is to reveal new topological phenomena induced by the interactions. Motivated by the recent experimental achievement, we have analyzed correlation effects on the topological pump for one-dimensional Rice-Mele model. Our DMRG analysis elucidates the jump of the polarization splits with maintaining the Chern number. This results indicates that the split of the jump is the signal of topological Mott behaviors for the

topological pump[3]. We also have discovered new topological states induced by reflection symmetry and Coulomb interactions, topological mirror Kondo metals [4,5]. In addition, we have proposed an experimental setup for cold atoms allowing us to observe the reduction of topological classification Z to Z_4[6].

References

[1] T. Yoshida, R. Peters, and N. Kawakami, Phys. Rev. B **98** (2018) 035141.

[2] T. Yoshida, R. Peters, N. Kawakami, and Y. Hatsugai, Phys. Rev. B **99** (2019) 121101.

[3] M. Nakagawa T. Yoshida, R. Peters, and N. Kawakami, Phys. Rev. B **98** (2018) 115147.

[4] R. Peters, T. Yoshida, and N. Kawakami, Phys. Rev. B **98** (2018) 075104.

[5] K. Kimura, T. Yoshida, and N. Kawakami, J. Phys. Soc. Jpn. **87**, (2018) 084705.

[6] T. Yoshida, I. Danshita, R. Peters, and N. Kawakami, Phys. Rev. Lett. **121** (2018) 025301.

Effect of magnetic anisotropy on skyrmion crystal in the Kondo lattice model

Satoru Hayami
Department of Physics, Hokkaido University, Sapporo, 060-0810

Noncollinear and noncoplanar magnetic orderings have drawn considerable interest in condensed matter physics. A noncollinear magnetic order shows the vector chirality defined by a vector product of spins and a noncoplanar magnetic order shows the scalar chirality defined by a triple scalar product of spins. Among them, the spin scalar chirality has recently attracted much interest, since it leads to an emergent electromagnetic field for electrons through the spin Berry phase mechanism [1, 2, 3]. Skyrmion crystals are one of the fundamental examples to possess such a scalar chirality degree of freedom [4].

Recently, several theoretical studies show that such a skyrmion crystal is stabilized even in the Kondo lattice model in centrosymmetric systems [5, 6, 7]. For instance, it is found that a skyrmion crystal with a high topological number of two is realized at zero magnetic field in the Kondo lattice model on a triangular lattice [8, 9]. Moreover, this skyrmion crystal phase shows phase transitions with successive changes of the topological number $2 \to 1 \to 0$ with an increase of a magnetic field. Meanwhile, such a skyrmion crystal with the topological number of two has yet to be found in experiments. Thus, it is useful to examine how the skyrmion crystal with the topological number of two in itinerant magnets is robust against perturbations, such as magnetic anisotropy, in order to search for an optimal condition for its stabilization.

In this project, we investigate the effect of a single-ion anisotropy on the skyrmion crystal phase in itinerant magnets. We examine how the spin structures in the skyrmion crystal phase are modulated and how these topological phases are robust against introducing easy-axis and easy-plane anisotropy [10]. To this end, we consider the Kondo lattice model including the single-ion anisotropy and external magnetic field on the triangular lattice. The Kondo lattice Hamiltonian is given by

$$\begin{aligned}\mathcal{H} = & - \sum_{i,j,\sigma} t_{ij} c^{\dagger}_{i\sigma} c_{j\sigma} + J \sum_{i} \mathbf{s}_i \cdot \mathbf{S}_i \\ & - A \sum_{i} (S^z_i)^2 - \sum_{i} \mathbf{H} \cdot \mathbf{S}_i, \end{aligned} \tag{1}$$

where $c^{\dagger}_{i\sigma}$ ($c_{i\sigma}$) is a creation (annihilation) operator of an itinerant electron at site i and spin σ. The first term represents the kinetic energy of itinerant electrons. We consider hopping elements between nearest-neighbor sites, $t_{ij} = t_1 = 1$, and third-neighbor sites, $t_{ij} = t_3 = -0.85$. The second term represents the onsite exchange coupling between itinerant electron spins $\mathbf{s}_i = (1/2) \sum_{\sigma,\sigma'} c^{\dagger}_{i\sigma} \boldsymbol{\sigma}_{\sigma\sigma'} c_{i\sigma'}$ and localized spins $\mathbf{S}_i$ with a coupling constant J, where $\boldsymbol{\sigma} = (\sigma^x, \sigma^y, \sigma^z)$ is the vector of Pauli matrices. We consider $\mathbf{S}_i$ as a classical spin with fixed length $|\mathbf{S}_i| = 1$. The third and fourth terms represent the easy-axis ($A > 0$) or easy-plane ($A < 0$) anisotropy and the Zeeman coupling to an external magnetic field along the z direction, which are taken into account only for the localized spins for simplicity. We set the chemical potential $\mu = -3.5$.

We investigate the ground-state phase diagram of the Kondo lattice model in Eq. (1) on the triangular lattice by performing large-

scale Langevin dynamics simulations enabled by the kernel polynomial method (KPM-LD), which enables us to calculate for large system sizes [11, 12]. Our simulation is done at zero temperature from random spin configurations for a 96^2-site cluster of the triangular lattice with periodic boundary conditions in both directions. In the KPM-LD simulations, we expand the density of states by up to 2000th order of the Chebyshev polynomials with 16^2 random vectors and we use a projected Heun scheme for 1000-5000 steps with the time interval $\Delta\tau = 2$.

As a result, we find that the spin textures on the skyrmion crystal phase with the topological number of two at zero field are deformed so as to consist of the magnetic vortices in the xy spin component and the sinusoidal wave in the z spin component [10]. In addition, we show that the skyrmion crystal phase shows a topological phase transition into the single-Q collinear in the z spin component (double-Q noncoplanar) state under easy-axis (easy-plane) anisotropy. We also show that the skyrmion crystals with the topological number of two and one show different behaviors in an applied magnetic field in the presence of single-ion anisotropy. The stable magnetic field range of the skyrmion crystal with the topological number of two is rather insensitive to the single-ion anisotropy, while the stable magnetic field region of the skyrmion crystal with the topological number of one is considerably extended (reduced) by the easy-axis (easy-plane) anisotropy, which is similar to the skyrmion crystals found in frustrated magnets. Our result indicates that the unconventional skyrmion crystal with the topological number of two in itinerant magnets is expected to be found in materials with a relatively small spin-charge coupling compared to the bandwidth and small magnetic anisotropy.

References

[1] D. Loss and P. M. Goldbart, Phys. Rev. B **45**, 13544 (1992).

[2] J. Ye, Y. B. Kim, A. J. Millis, B. I. Shraiman, P. Majumdar, and Z. Tešanović, Phys. Rev. Lett. **83**, 3737 (1999).

[3] K. Ohgushi, S. Murakami, and N. Nagaosa, Phys. Rev. B **62**, R6065(R) (2000).

[4] N. Nagaosa and Y. Tokura, Nat. Nanotechnol. **8**, 899 (2013).

[5] I. Martin and C. D. Batista, Phys. Rev. Lett. **101**, 156402 (2008).

[6] Y. Akagi and Y. Motome, J. Phys. Soc. Jpn. **79**, 083711 (2010).

[7] R. Shindou and N. Nagaosa, Phys. Rev. Lett. **87**, 116801 (2001).

[8] R. Ozawa, S. Hayami, and Y. Motome, Phys. Rev. Lett. **118**, 147205 (2017).

[9] S. Hayami, R. Ozawa, and Y. Motome, Phys. Rev. B **95**, 224424 (2017).

[10] S. Hayami and Y. Motome, Phys. Rev. B **99**, 094420 (2019).

[11] K. Barros and Y. Kato, Phys. Rev. B **88**, 235101 (2013).

[12] A. Weiße, G. Wellein, A. Alvermann, and H. Fehske, Rev. Mod. Phys. **78**, 275 (2006).

Development of powerful numerical methods for strongly-correlated systems

Yusuke NOMURA

Department of Applied Physics,

The University of Tokyo, Hongo, 7-3-1, Bunkyo-ku, Tokyo 113-8656

Developing powerful numerical methods for solving strongly-correlated Hamiltonians is a great challenge in condensed matter physics. In this fiscal year, we focus on the development of i) multi-orbital TRILEX (triply irreducible local expansion) and ii) machine learning solvers for electron-phonon coupled systems.

i) Development of multi-orbital TRILEX

TRILEX is a method which can interpolate weak-coupling and strong-coupling approaches of Green's function method [1]. In the TRILEX, we calculate the local irreducible vertex, which is usually neglected in the weak-coupling approach. In the weakly-correlated region, the vertex is almost frequency independent and the TRILEX methods reproduces spin-fluctuation and GW methods. At the same time, the TRILEX can capture Mott physics: strong frequency dependence of the local vertex induces Mott transition.

So far, the TRILEX has been applied to single-band model. In the present study, we extend the TRILEX to multi-orbital models. In multi-orbital systems, we calculate the vertex for not only charge/spin channel but also orbital channel. Then, we can investigate the competition/interplay among charge, spin, and orbital degrees of freedom. We perform benchmark calculations using $SrVO_3$, a typical strongly correlated metal. In future, we are planning to perform calculations for iron-based superconductors.

ii) Machine learning solvers for electron-phonon coupled systems

Recently, variational wave function written in terms of restricted Boltzmann machine (RBM) has been introduced to represent ground states of quantum spin Hamiltonians [2]. The RBM wave function has been shown to be able to represent ground states of spin Hamiltonians in high accuracy [2]. We extend this machine learning scheme to the electron-phonon coupled systems.

In the wave functions used so far for electron-coupled systems, the correlation between electrons and phonons are taken into account only by correlation factors [3,4]. In the present study, we first prepare entangled vibronic wave functions and more sophisticated correlations between electrons and phonons are taken into account by the RBM. Compared to the wave function proposed in Ref. [3], the improved

wave function substantially improve the accuracy of the ground state energy of one-dimensional Holstein model.

References

[1] T. Ayral and O. Parcollet, Phys. Rev. B **92**, 115109 (2015).

[2] G. Carleo and M. Troyer, Science **355**, 602 (2017).

[3] T. Ohgoe and M. Imada, Phys. Rev. B **89**, 195139 (2014).

[4] S. Karakuzu et al., Phys. Rev. B **96**, 205145 (2017)

Multi-channel Kondo effect in rare-earth systems

Takashi HOTTA
Department of Physics, Tokyo Metropolitan University
1-1 Minami-Osawa, Hachioji, Tokyo 192-0397

In this research, we have analyzed a seven-orbital impurity Anderson model hybridized with Γ_8 conduction electrons by employing a numerical renormalization group (NRG) technique. The model Hamiltonian is given by

$$\begin{aligned} H &= \sum_{\mathbf{k},\mu,\tau} \varepsilon_{\mathbf{k}} c^\dagger_{\mathbf{k}\mu\tau} c_{\mathbf{k}\mu\tau} + \sum_{\mathbf{k},\mu,\tau} V(c^\dagger_{\mathbf{k}\mu\tau} f_{a\mu\tau} + \text{h.c.}) \\ &+ \sum_{j,\mu,\tau} (\lambda_j + B_{j,\mu} + E_f) f^\dagger_{j\mu\tau} f_{j\mu\tau} \\ &+ \sum_{j_1\sim j_4} \sum_{\mu_1\sim\mu_4} \sum_{\tau_1\sim\tau_4} I^{j_1 j_2, j_3 j_4}_{\mu_1\tau_1\mu_2\tau_2,\mu_3\tau_3\mu_4\tau_4} \\ &\times f^\dagger_{j_1\mu_1\tau_1} f^\dagger_{j_2\mu_2\tau_2} f_{j_3\mu_3\tau_3} f_{j_4\mu_4\tau_4}, \end{aligned} \tag{1}$$

where $\varepsilon_{\mathbf{k}}$ is the dispersion of a Γ_8 conduction electron with wave vector $\mathbf{k}$, $c_{\mathbf{k}\mu\tau}$ denotes the annihilation operator of a Γ_8 conduction electron, μ distinguishes the cubic irreducible representation, Γ_8 states are distinguished by $\mu = \alpha$ and β, while Γ_7 and Γ_6 states are labeled by $\mu = \gamma$ and δ, respectively, τ is the pseudo-spin which distinguishes the degeneracy concerning the time-reversal symmetry, $f_{j\mu\tau}$ indicates the annihilation operator of a localized f electron in the bases of (j, μ, τ), j is the total angular momentum, $j = 5/2$ and $7/2$ are denoted by "a" and "b", respectively, and V is the hybridization between conduction and localized electrons. In the present case, we consider the hybridization between Γ_8 conduction electrons and the Γ_8 quartet of $j = 5/2$.

Concerning the local f-electron terms of Eq. (1), $\lambda_a = -2\lambda$, $\lambda_b = (3/2)\lambda$, λ is the spin-orbit coupling of f electron, $B_{j,\mu}$ denotes the crystalline electric field (CEF) potential energy, E_f indicate the f-electron level, and I denotes the Coulomb interactions between f electrons. The Coulomb interaction I is expressed with the use of four Slater-Condon parameters, F^0, F^2, F^4, and F^6. Although the Slater-Condon parameters of a material should be determined from experimental results, here we simply set the ratio as $F^0/10 = F^2/5 = F^4/3 = F^6 = U$, where U is the Hund rule interaction among f orbitals. The CEF potentials for f electrons from ligand ions are given in the table of Hutchings for the angular momentum $\ell = 3$. For a cubic structure with $O_{\rm h}$ symmetry, CEF parameters are expressed by two CEF parameters, B^0_4 and B^0_6.

As U denotes the magnitude of the Hund rule interaction among f orbitals, it is reasonable to set $U = 1$ eV. The magnitude of λ varies between 0.077 and 0.36 eV depending on the type of lanthanide ions. In the following, B^0_4 and B^0_6 are treated as parameters. To control the local f-electron number n, we appropriately adjust the value of E_f.

In this study, we analyze the model by employing the NRG method. We introduce a cut-off Λ for the logarithmic discretization of the conduction band. Owing to the limitation of computer resources, we keep M low-energy states. Here, we use $\Lambda = 5$ and $M = 4,000$. In the following calculations, the energy unit is D, which is a half of the conduction band width. Namely, we set $D = U = 1$ eV in this calculation. In the NRG calculation, the temperature T is defined as $T = \Lambda^{-(N-1)/2}$ in the present energy unit, where N is the number of renormalization steps.

In our previous research, we have investigated the two-channel Kondo effect for the

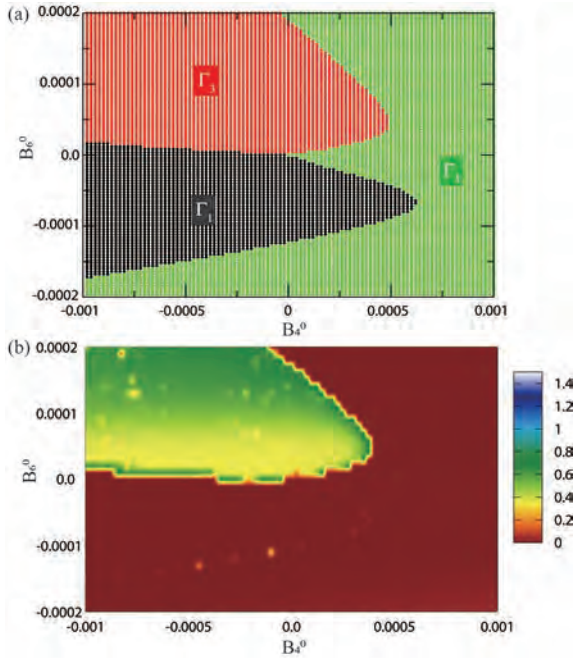

Figure 1: (a) Local CEF ground-state phase diagram for $n = 4$. (b) Contour color map of the entropy on (B_4^0, B_6^0) plane for $V = 0.87$ and $T = 5.12 \times 10^{-7}$.

case of $n = 2$, corresponding to Pr^{3+} ion [1]. We have reconfirmed the emergence of the quadrupole two-channel Kondo effect, as first remarked by Cox, when there appears the local Γ_3 ground state. We have also considered the case of $n = 3$, corresponding to Nd^{3+} ion [2]. For the case of $n = 3$ with the local Γ_6 ground state, we have discovered the magnetic two-channel Kondo effect.

Next we consider the case of $n = 4$, corresponding to Pm^{3+} ion. Although promethium has no stable isotopes, it is rather adequate to consider Np^{3+} or Pu^{3+} ion with $5f^4$ configuration. Here we show the results for $n = 4$. In Fig. 1(a), we depict local CEF ground-state phase diagram on the plane of B_4^0 and B_6^0. The region with Γ_3 ground state is widely observed for $B_6^0 > 0$.

In Fig. 1(b), we show the contour color map of the entropy for $V = 0.87$ and $T = 5.12 \times 10^{-7}$. To visualize precisely the behavior of entropy, we define the color of the entropy between 0 and 1.5, as shown in the right color bar. We immediately notice that a region with an entropy of $0.5 \log 2$ (yellow region) almost corresponds to that of the Γ_3 ground state in comparison with Fig. 1(a). Note that for large B_6^0, the color becomes green, but when we decrease the temperature, we find the entropy of $0.5 \log 2$ even for large B_6^0. The results strongly suggest the emergence of quadrupole two-channel Kondo effect for the case of $n = 4$.

Note that in the region of $B_6^0 < 0$, we observe some blurry yellow spots along the boundary region between Γ_1 singlet and Γ_5 triplet local ground states. These denote the quantum critical points, which are generally known to appear between the local CEF and Kondo singlet states.

As for the mechanism of quadrupole two-channel Kondo effect for the case of $n = 4$, we deduce that it is essentially the same as that for the case of $n = 2$ on the basis of a j-j coupling scheme. When we accommodate four electrons in the $j = 5/2$ sextet, we immediately notice that it just denotes the configuration of two holes in the sextet. Namely, the electron-hole relation on the basis of the j-j coupling scheme should be a key issue to understand the two-channel Kondo effect emerging from rare-earth ions. For the case of heavy rare-earth ions corresponding to $n = 8 \sim 12$, we believe that the present idea will be also effective. This point will be discussed in future elsewhere [3].

References

[1] T. Hotta, Physica B **536C**, 203-210 (2018).

[2] T. Hotta, J. Phys. Soc. Jpn. **86**, 083704 (2017).

[3] D. Matsui and T. Hotta, in preparation.

First-principles calculation and dynamical mean-field theory for superconductivity in multi-band systems

Yoshiaki Ōno
Department of Physics, Niigata University
Ikarashi, Nishi-ku, Niigata, 950-2181

Recently, the ternary chalcogenide Ta_2NiSe_5 has received renewed attention as a strong candidate for the excitonic insulator (EI) which is characterized by the condensation of excitons and has been argued for about half a century. The resistivity indicates a narrow gap semiconductor with a quasi one-dimensional (1-D) structure where a Ni chain and adjacent two Ta chains construct the 1-D three chain. A second-order structural transition from the orthorhombic to monoclinic phase occurs at a critical temperature T_S=328 K, below which a remarkable flattening of the valence band top is observed in the ARPES experiment without any sign of the magnetic and density-wave-type order. Several theoretical studies have revealed that the transition is well accounted for by the excitonic condensation from a normal semiconductor (orthorhombic) to the EI (monoclinic) from a mean-field analysis for the 1-D three-chain Hubbard model and from a variational cluster approximation for the extended Falicov-Kimball model. Recent optical measurements are also consistent with the EI phase below T_S.

When the pressure is applied for Ta_2NiSe_5, T_S is suppressed and the system changes from semiconducting to semimetallic both above and below T_S, and then, T_S finally becomes zero at a critical pressure $P_c \sim 8$GPa, around which the superconductivity is observed. Then, we have recently investigated the 1-D three-chain Hubbard model also in the semimetallic case and have found that the difference of the band degeneracy, the two-fold degenerate conduction bands and the nondegenerate valence band, inevitably causes the imbalance of each Fermi wavenumber and results in a remarkable excitonic state characterized by the condensation of excitons with finite center-of-mass momentum q, the so-called Fulde-Ferrell-Larkin-Ovchinnikov (FFLO) excitonic state[1, 2], as previously discussed in the electron-hole bilayer systems with density imbalance. More recently, a realistic quasi 1-D three-chain Hubbard model has also been studied and a detailed excitonic phase diagram including the FFLO state has been obtained[3].

As the superconductivity is observed near the excitonic phase in Ta_2NiSe_5, the excitonic fluctuation is considered to be a key ingredient for the pairing mechanism as early discussed by Little for quasi 1-D organic superconductors but has not been discussed for Ta_2NiSe_5 so far. Then, we investigte the excitonic fluctuation and its mediated superconductivity in Ta_2NiSe_5 on the basis of the quasi 1-D three-chain Hubbard model[4] where the FFLO excitonic order is found to take place in the semimetallic case[3]. In the semimetallic case where two conduction (c) bands and one valence (f) band cross the Fermi level, the c-f Coulomb interaction drives the instability towards the Fulde-Ferrell-Larkin-Ovchinnikov (FFLO) excitonic order characterized by the condensation of excitons with finite center-of-mass momentum corresponding to the nesting between the c and

f Fermi surfaces. Near the instability, the largely enhanced excitonic fluctuations mediate the c-f interband Cooper pairs with finite center-of-mass momentum resulting in the FFLO superconductivity[4], which is expected to be realized in the semimetallic Ta_2NiSe_5 under high pressure.

References

[1] T. Yamada, K. Domon, and Y. Ōno, J. Phys. Soc. Jpn. **85**, 053703 (2016).

[2] K. Domon, T. Yamada, and Y. Ōno, J. Phys. Soc. Jpn. **85**, 065005 (2016).

[3] K. Domon, T. Yamada, and Y. Ōno, J. Phys. Soc. Jpn. **87**, 054701 (2018).

[4] T. Yamada, K. Domon, and Y. Ōno, J. Phys. Soc. Jpn. in press.

Superconductivity and magnetic properties of the Hubbard model

Atsushi Yamada
Department of Physics, Chiba University
Chiba 263-8522, Japana, Chiba 277-8581

The interplay of electron correlations, low dimensionality, and frustrated magnetic interactions lead to a rich variety of phenomena. For example, a spin liquid state, which is a purely non-magnetic Mott insulator without spontaneously broken spatial or spin symmetry, has attracted a lot of interest. This state is realized in geometrically frustrated systems like the charge organic transfer salts κ-(BEDT-TTF)$_2$X[1] and Cs_2CuCl_4.[2] A simple theoretical model of these compounds is the Hubbard model on the an-isotropic triangular lattice, and spin liquid state is in fact found in this model.[3] A spin liquid could arise also in the intermediate coupling region of strongly correlated systems between a semimetal and ordered state, because in this case a correlation-driven insulating gap might open before the system becomes ordered. This possibility might be realized in the half-filled Hubbard model on the honeycomb lattice.

We have studied the magnetic and metal-to-insulator transitions in the half-filled Hubbard model on the honeycomb lattice by variational cluster approximation using 10-site and 16-site clusters as a reference system.[5] Our method uses an exact diagonalization of the Hubbard model defined on these clusters and parts of numerical calculations were done using the computer facilities of the ISSP.Our results agree with recent large scale Quantum Monte Carlo simulations.[4] We are currently improving our program to study superconductivity.

References

[1] Y. Shimizu, K. Miyagawa, K. Kanoda, M. Maesato, and G. Saito, Phys. Rev. Lett. **91**, 107001 (2003); Y. Kurosaki, Y. Shimizu, K. Miyagawa, K. Kanoda, and G. Saito, Phys. Rev. Lett. **95**, 177001 (2005).

[2] R. Coldea, D.A. Tennant, A.M. Tsvelik, and Z. Tylczynski, Phys. Rev. Lett. **86**, 1335 (2001); R. Coldea, D.A. Tennant, and Z. Tylczynski, Phys. Rev. Lett. **68**, 134424 (2003).

[3] T. Yoshioka, A. Koga, and N. Kawakami, Phys. Rev. Lett. **103**, 036401 (2009); P. Sahebsara and D. Sénéchal, Phys. Rev. Lett. **100**, 136402 (2008); L.F. Tocchio, H. Feldner, F. Becca, R. Valenti, and C. Gros, Phys. Rev. B **87**, 035143 (2013); A. Yamada, Phys. Rev. B **89**, 195108 (2014); L.F. Tocchio, C. Gros, R. Valentí, F. Becca, Phys. Rev. B **89**, 235107 (2014); A. Yamada, Phys. Rev. B **90**, 235138 (2014).

[4] S. Sorella, Y. Otsuka, and S. Yunoki, Sci. Rep. **2**, 992 (2012); F. F. Assaad and I. F. Herbut, Phys. Rev. X **3**, 031010 (2013); F. Parisen Toldin, M. Hohenadler, F. F. Assaad, and I. F. Herbut, Phys. Rev. B **91**, 165108 (2015).

[5] A. Yamada, Int. J. Mod. Phys. B **30**, 1650158 (2016).

Numerical approach to unconventional electronic orderings in strongly correlated systems

Shintaro HOSHINO
Department of Physics, Saitama University, Saitama 338-8570, Japan

In A_3C_{60}, three electrons are doped onto each fullerene molecule from intercalated alkaline metals denoted by A [1, 2]. In the metallic compounds, the molecular t_{1u} orbitals form three half-filled narrow bands, and the electronic correlations are strong. Even though the symmetry of the pairing state is s-wave, the superconductivity is different from that of conventional BCS superconductors. Furthermore, fullerides exhibit a superconducting dome in the vicinity of a Mott insulating phase, which is a characteristic feature for the strongly-correlated superconductors. An important ingredient in the superconducting mechanism is an effectively sign-reversed Hund's coupling. This antiferromagnetic Hund's coupling favors the low-spin ($S = 1/2$) state, which has doubly occupied orbitals and can act as a seed for superconductivity.

Recent experiments have revealed the existence of a highly anomalous metallic state near the Mott transition [3]. When the electrons are localized in the Mott phase, the electron-phonon coupling leads to a deformation of the fullerene molecule. On the other hand, in the conventional metallic regime, the molecules exhibit a nearly spherical shape. In the regime between the Mott phase and weak-coupling metal, a deformation of the fullerene molecules has been detected with the metallic property [called Jahn-Teller metal (JTM)].

We have studied the three-orbital Hubbard model with antiferromagnetic Hund's coupling [4], by using the dynamical mean-field theory combined with continuous-time quantum Monte Carlo (DMFT+CTQMC) [5]. This study proposed that the JTM may be interpreted as a spontaneous orbital-selective Mott (SOSM) state, in which the localized and itinerant electrons coexist, explaining the basic properties of the JTM. The large-scale parallelized calculation using the supercomputer in ISSP is very efficient for DMFT+CTQMC since the method is based on the Monte Carlo sampling. Recently, the technique is effectively used to further clarifying the various ordered phases in the three-orbital Hubbard model [6, 7]. We are also performing the calculation using the realistic band structure in Ref. [8], to investigate the quantitative properties in fullerides. This theoretical study will enable us to compare the obtained molecular-orbital properties with experiments directly.

References

[1] M. Capone *et al.*, Rev. Mod. Phys. 81, 943 (2009).

[2] Y. Nomura *et al.*, J. Phys.: Condens. Matter 28, 153001 (2016).

[3] R.H. Zadik *et al.*, Sci. Adv. **1**, e1500059 (2015).

[4] S. Hoshino and P. Werner, Phys. Rev. Lett. **118**, 177002 (2017).

[5] E. Gull *et al.*, Rev. Mod. Phys. **83**, 349 (2011).

[6] K. Ishigaki *et al.*, Phys. Rev. B **98**, 235120 (2018).

[7] K. Ishigaki *et al.*, Phys. Rev. B **99**, 085131 (2019).

[8] Y. Nomura, K. Nakamura and R. Arita, Phys. Rev. B **85**, 155452 (2012).

First-principles calculations of $5d$ pyrochlore oxides

Hiroshi Shinaoka
Department of Physics, Saitama University, Saitama 338-8570

We focused on the pyrochlore oxides $Cd_2Re_2O_7$ using massive parallel computer simulations. $Cd_2Re_2O_7$ has been attracting much attention because the compound hosts a variety of phases at ambient pressure and high pressures including multipole ordered states [1, 2].

First, we constructed a tight-binding model for the t_{2g} manifold in terms of maximally localized Wannier functions (MLWF). The calculations were done for the lattice constant of $a = 10.226$ Å and the internal parameter of $x(O_1) = 0.318$. We used the open-source DFT package Quantum ESPRESSO and Wannier90. Figure 1 compares the LDA (local density approximation) band structure and the fit by Wannier functions, where one can see a good agreement for the t_{2g} band near the Fermi level. The computed LDA band structure is consistent with that obtained in a previous study [3].

We analyzed the structure of the tight-binding Hamiltonian in real space. Figure 2 shows how their absolute values decay with respect to distance. A conventional face-centered cubic unit cell of the crystal structure is also shown. Although they decay roughly exponentially, we found two pronounced peaks around $r/a = \sqrt{2}/4$ and $3\sqrt{2}/4$. A closer look indicates that they correspond to hopping along one-dimensional chains shown in Fig. 2. A similar structure was found for a related compound $Cd_2Os_2O_7$.

We estimated the strength of the trigonal crystal field Δ and the spin-orbit coupling ζ in the t_{2g} manifold. We used the same notation as employed in a previous study [4]. The results are summarized in Table I. As reference data, we estimated the parameters for $Cd_2Os_2O_7$ and obtained values consistent with the previous study [5]. The values of Δ and ζ for $Cd_2Re_2O_7$ are close to those for $Cd_2Os_2O_7$. The trigonal crystal field and the spin-orbit coupling are comparable in strength.

We are planning to analyze the strongly correlated aspects of the compound using the open-source software `DCore` [6], which was developed in Project for advancement of software usability in materials science [7] in the fiscal year of 2017.

This study was done in collaboration with N. Chikano, Y. Nomura, J. Otsuki, K. Yoshimi.

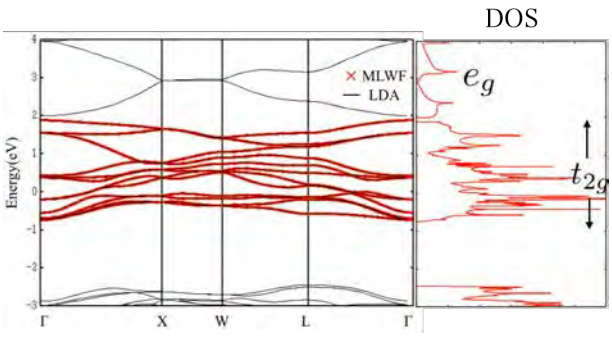

Figure 1: LDA band structure of $Cd_2Re_2O_7$.

References

[1] J. W. Harter, Z. Y. Zhao, J.-Q. Yan *et al.*, Science **356**, 295 (2017).

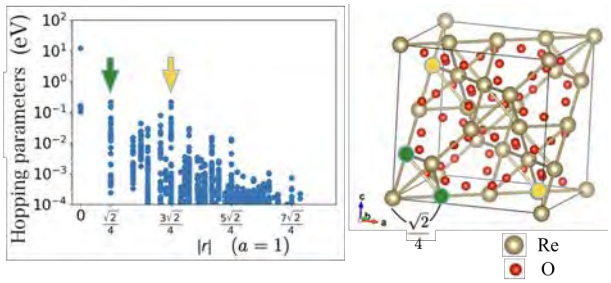

Figure 2: Analysis of elements of the hopping matrix.

	($5d^2$)	($5d^3$)	
	$Cd_2Re_2O_7$	$Cd_2Os_2O_7$	$Cd_2Os_2O_7$※
λ[eV]	0.31	0.34	0.33
Δ[eV]	0.23	0.18	0.19
$x(O(1))$	0.318	0.319	

※ A. Uehara, H. Shinaoka, Y. Motome, Physics Procedia **75**, 495-502 (2015).

Table 1: Estimated values of the spin-orbit coupling λ and the trigonal crystal field Δ.

[2] Z Hiroi, J Yamaura, T C. Kobayashi *et al.*, JPSJ **87**, 024702 (2018) and references therein.

[3] H. Harima, J. Phys. Chem. Solids **63**, 1035 (2002).

[4] H. Shinaoka, Y. Motome, T. Miyake, and S. Ishibashi, PRB **88**, 174422 (2013).

[5] A. Uehara, H. Shinaoka, Y. Motome, Physics Procedia **75**, 495 (2015).

[6] `https://github.com/issp-center-dev/DCore`

[7] `http://www.issp.u-tokyo.ac.jp/supercom/softwaredev`

Spin glass transition at finite temperature in the two dimensional transverse Ising model

Chisa Hotta
Department of Basic Science, University of Tokyo
Meguro-ku, Komaba, Tokyo 153-8902

We studied the quantum transverse Ising model on a triangular lattice with quenched bond randomness using the ISSP supercomputer system. Our Hamiltonian is given as

$$H = \sum_{\langle i,j \rangle} J_{ij}\sigma_i^z\sigma_j^z + \sum_{i=1}^{N} \Gamma\sigma_i^x, \qquad (1)$$

where σ_i^α ($\alpha = x, y, z$) is the Pauli operator on site-i, J_{ij} is the random Ising interaction with $\bar{J_{ij}} = 1$, and Γ is the transverse field. The degree of randomness R is defined as the half width of the distribution of J_{ij}.

The difficulty of obtaining reliable results in the disordered system is already well known in the long history of the classical spin glass[1]. In classical Edwards Anderson models, the spin glass transition is studied by the spin glass susceptibility and the replica overlap,

$$\chi_{\rm SG} = \frac{1}{N}\sum_{i,j=1}^{N} \langle\sigma_i^z\sigma_j^z\rangle^2, \qquad (2)$$

$$q_{\alpha\beta} = \sum_i \sigma_{i;\alpha}^z\sigma_{i;\beta}^z/N, \qquad (3)$$

where $\langle\cdots\rangle$ represents an average first over Monte Carlo timestep for each sample and then over samples of different random distributions, and the relation, $\chi_{\rm SG} = N\langle q_{\alpha\beta}\rangle^2$, holds. The glass transition T_c is determined by the binder analysis, and the finite size scaling analysis on $\chi_{\rm QSG} = L^{2-\eta}\tilde{\chi}((T - Tc)L^{1/\nu})$ demonstrates the existence of the spin glass phase[2]. However, whether there exists a finite temperature spin glass phase had been the subject of intense controversy from the 1970s. We partially follow this standard analysis, while finding after all that our spin glass cannot be simply understood within the numerical framework which worked to detect the conventional spin glass.

We performed the continuous imaginary time quantum Monte Carlo calculation to the $L \times L$ lattices with $L = 36, 48, 60$. We find that there occurs a Berezinskii-Kosterlitz-Thouless (BKT) transition at around $k_BT_{\rm BKT}/J = 0.2-0.4$. Below that temperature, the antiferromagnetic correlation develops, and the introduction of the randomness gives rise to the spin glass transition at $k_BT_{\rm sg}/J \sim 0.05 - 0.1$. The transition is detected by the Replica symmetry breaking(RSB); the L dependent behavior of the replica overlap distribution $P(q)$ shows the emergent peaks at both $q = 0$ and $q \neq 0$ indicating the two-step RSB.

By further analyzing the $\chi_{\rm SG}$, we found a particular peak structure developing at around $T_{\rm sg}$. This peak sustains even after subtracting the classical $\chi_{\rm SG}$ we obtained parallelly by setting $\Gamma = 0$. We thus consider that there is a quantum mechanical contribution to $\chi_{\rm SG}$ particular to this model. Our spin glass phase protected by the BKT phase, and disappears together with the BKT phase for $R > 0.15 - 0.2$. The work is in collaboration with Kazumasa Ueda and Masatoshi Imada in preparation.

References

[1] L. Binder and A. P. Young: Rev. Mod. Phys. **58** (1986).

[2] N. Kawashima and A. P. Young: Phys. Rev. B **53** (1996) R484 .

Photoinduced nonequilibrium dynamics in correlated electron systems

Sumio Ishihara
Department of Physics, Tohoku University

Opto-spintronics in correlated magnets

Ultrafast optical control of magnetism has attracted much interest in the recent years, accompanied by rapid progress in laser light technologies. We analyze the double exchange (DE) model defined by

$$H = \sum_{ijs} h_{ij} c_{is}^{\dagger} c_{js} - \frac{J}{S} \sum_{iss'} S_i \cdot \sigma_{ss'} c_{is}^{\dagger} c_{is'}, \quad (1)$$

where $c_{is}^{\dagger}(c_{is})$ is a creation (annihilation) operator of a conduction electron with spin s $(= \uparrow, \downarrow)$ at site i, S_i is a localized-spin operator with magnitude S, and σ^{α} $(\alpha = x, y, z)$ are the Pauli matrices. The first term represents the hopping of the conduction electrons with the transfer integral h_{ij}, and the second term represents the Hund coupling between the conduction electrons and the localized spins with the coupling constant J (> 0). It was shown that an initial ferromagnetic (FM) metal state is changed to an almost perfect antiferromagnetic (AFM) state by photoirradiation [1], which is in sharp contrast to the naive DE scenario in equilibrium states. In this theme, we study furthermore this issue.

1) In order to elucidate the microscopic mechanism that drives the FM state into the AFM state, we study the magnetic structure in a cw field by using the Floquet Green function [2]. We show that a magnon dispersion is softened and forms a dip at momentum $q = (\pi, \pi)$ by the photoirradiation, which indicates that the AFM instability develops at finite threshold intensity. An nonequilibrium electron distribution plays an essential role to induce the instability. We show that an interband-excitation peak and Floquet side peaks appear in the transient and steady states.

2) We study the topological spin textures in the photoinduced nonequilibrium state in a metallic magnetic system [3]. We focus on the transient spin structure described by the DE model from the initial FM state to the AFM ordered state. We find emergence of the topological spin texture in the photoinduced transient state through the calculation of the real-space spin configuration, the Pontryagin index, and the scalar chirality. This observation is reproduced by analyzing the thermalization spin dynamics after chemical-potential quench in a large cluster.

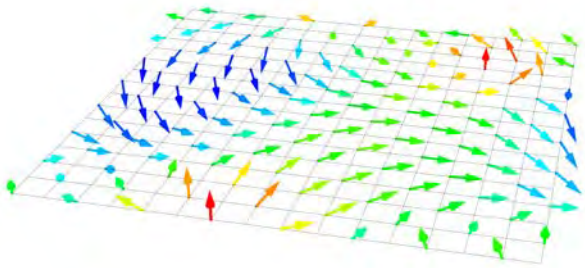

Figure 1: Snapshots of the localized spin configurations in a sublattice [3].

Complexed quantum dynamics in strongly interacting systems

Excitonic insulator (EI) has been proposed more than a half century ago in semiconductors and semimetals, has been studied intensively in the theoretical and experimental sides. When the attractive Coulomb inter-

action between electrons and holes overcomes the gap energy, the electron-hole pairs, i.e. excitons, are produced spontaneously to gain the system energy. Owing to the recent great progresses of the experimental technique, the study of the EI state is revived. Some examples materials are 1T-$TiSe_2$ and $TaNiSe_5$. A major problem of the research subjects is how to identify the EI state and transition. A new direct route to identify the EI state in experiments is required to progress this research field.

In this theme, we study the optical responses in EI states [4]. We adopt the two-orbital Hubbard model with finite energy difference between the orbitals defined by

$$\begin{aligned} H &= \Delta \sum_{i\sigma}(n_{ia\sigma} - n_{ib\sigma}) + \sum_{\langle ij\rangle\alpha\sigma} t_\alpha c^\dagger_{i\alpha\sigma} c_{j\alpha\sigma} \\ &+ \sum_i (U \sum_\alpha n_{i\alpha\uparrow} n_{i\alpha\downarrow} + U' n_{ia} n_{ib}) \\ &+ J \sum_{i\sigma\sigma'} c^\dagger_{ia\sigma} c^\dagger_{ib\sigma'} c_{ia\sigma'} c_{ib\sigma} \\ &+ I \sum_{i\alpha} c^\dagger_{i\alpha\uparrow} c^\dagger_{i\alpha\downarrow} c_{i\bar{\alpha}\downarrow} c_{i\bar{\alpha}\uparrow}, \end{aligned} \tag{2}$$

where $c_{i\alpha\sigma}$ is an annihilation operator of an electron with spin $\sigma(=\uparrow,\downarrow)$ and the orbital $\alpha(=a,b)$ at site i, and $n_{i\alpha\sigma} = c^\dagger_{i\alpha\sigma} c_{i\alpha\sigma}$ is the particle number operator. This model is analyzed by utilizing the variational cluster approach. The optical conductivity spectra are formulated in the two-particle Greens function, in which the vertex corrections are taken into account. The finite temperature phase diagram and the one-particle excitation spectra are obtained by considering the EI phase, the high-spin(HS) AFM phase and the low-spin (LS) and HS (HS/LS) ordered phase.

A unique peak structure appears in the EI state, energy of which is of the order of the intra-site inter-obital Coulomb interaction. This is due to the hybridization between the two orbitals, which is opened in the EI phase. The peak intensity almost follows the EI order parameter as shown in Fig. 2. We propose that this peak is available to identify the EI state.

These researches have been performed with collaboration with A. Ono, H. Li, M. Naka and J. Ohtsuki. The numerical calculations in these works have been done using the facilities of the Supercomputer Center, the Institute for Solid State Physics, the University of Tokyo.

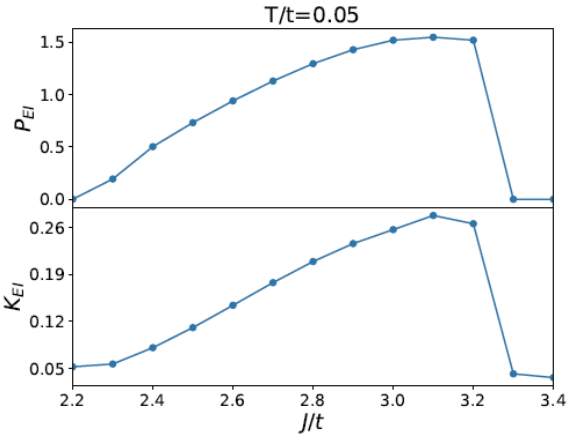

Figure 2: EI peak intensity and the EI order parameters as function of the Hund coupling parameter [4].

References

[1] A. Ono and S. Ishihara: Phys. Rev. Lett. **119**, 207202 (2017).

[2] A. Ono and S. Ishihara: Phys. Rev. B **98**, 214408 (2018).

[3] A. Ono, S. Ishihara: J. Phys. Soc. Jpn. **88**, 023703 (2019) .

[4] H. Li, J. Otsuki, M. Naka and S. Ishihara (unpublished).

Optimization variational Monte Carlo study of strongly correlated electron systems

Takashi YANAGISAWA
Electronics and Photonics Research Institute
National Institute of Advanced Industrial Science and Technology (AIST)
AIST Central 2, 1-1-1 Umezono, Tsukuba 305-8568

We have investigated the ground-state properties of the two-dimensional Hubbard model and the d-p model by using the optimized variational Monte Carlo method[1, 3, 4]. We performed parallel computation in Monte Carlo calculations. In order to reduce statistical errors, we carried out 100 $\sim$ 200 parallel calculations. Parallel computing is very helpful to reduce Monte Carlo statistical errors.

We used the wave function of an $\exp(-\lambda K) - P_G$-type wave function. This wave function is very excellent in the sense that the ground-state energy is lowered greatly and the ground-state energy is lower than that evaluated by any other wave functions[3]. We can improve the wave function systematically by multiplying by operators P_G and $e^{-\lambda K}$ many times.

We show the condensation energy as a function of the hole doping rate x in Fig. 1[4]. The calculations were performed on a 10×10 lattice with $U/t = 18$ and $t' = 0$. There are three phases: the antiferromagnetic insulator state (AFI), the coexistent state of antiferromagnetism and superconductivity (AF+SC) and the d-wave superconducting state (SC). Near half-filling for approximately $0 \leq x < 0.06$, the ground state is an AF insulator. The coexistent state exists for $0.06 < x < 0.09$. When the doping rate is as large as $x > 0.09$, the ground state is d-wave superconducting state. High-temperature superconductivity will occur in the SC phase in this figure. The reason why the AFI phase exists near $x = 0$ is due to the instability toward the phase separation. In the phase-separated state, the doped holes are not conductive.

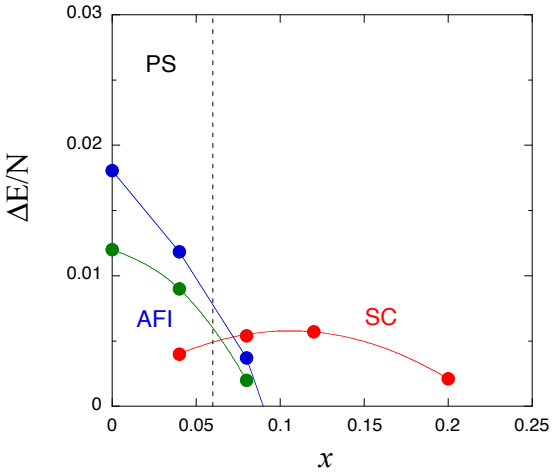

Figure 1: The condensation energy per site as a function of the hole density $x = 1 - n_e$ on a 10×10 lattice, where the wave function is $\psi_\lambda = \psi^{(2)}$. We set $t' = 0$ and $U/t = 18$. We used the wave function $\psi^{(4)}$ for the lower AF curve. In the region where $x \leq 0.06$, the ground state is an insulator due to the instability toward the phase separation.

References

[1] T. Yanagisawa et al., J. Phys. Soc. Jpn. 67, 3867 (1998).

[2] T. Yanagisawa, Phys. Rev. B75, 224503 (2007) (arXiv: 0707.1929).

[3] T. Yanagisawa, J. Phys. Soc. Jpn. 85, 114707 (2016).

[4] T. Yanagisawa, J. Phys. Soc. Jpn. 88, 054702 (2019).

Drawing phase diagram from many-variable variational wave functions with machine learning

Yuichi Motoyama
Institute for Solid State Physics, University of Tokyo
Kashiwa-no-ha, Kashiwa, Chiba 277-8581

Recently, machine learning (ML) techniques are applied for drawing a phase diagram, because this is a kind of classification problems or clustering problems, where machine learning techniques are widely used. For example [1], a well trained model (e.g., a neural network) can tell whether a spin configuration of the Ising model is generated from the ferromagnetic phase (the ordered phase) or the paramegnetic phase (the disordered phase.) For another example [2], performing the principal components analysis method, in other words, the singular value decomposition of spin configurations can detect the phase transition point. The former is an example of a supervised training and the latter is an example of an unsupervised training. For the both cases, no specific order parameters such as the spontaneous magnetization are explicitly supposed, but the machine learning models automatically extract some features to represent each phase. In the ML methods, therefore, we become free from finding the order parameter. Unfortunately, another problem appears – how to choose the input of the ML model. For the classical spin systems such as the Ising model, several studies have shown that a spin configuration can be used as an input of a ML model. It should be noted that for some models the way to represent a spin configuration is not unique, and the accuracy of the ML model sometimes depends on the representation. The XY model, for example, the state of one spin, a vector $\vec{\sigma}$, can be represented by the angle θ between $\vec{sigma}$ and the x axis or the components of $\vec{\sigma}$, say, $(\cos\theta, \sin\theta)$. In the present author's experience, the latter representation seems to be better than the former. For strongly correlated systems, on the other hand, the general input has not yet appeared. One of reasons is that there are no methods for obtaining the ground state of an arbitrary system, in other words, each method has own advantages and disadvantages.

In this study, we tried to generate inputs of ML models by using the variational Monte Carlo (VMC) method [3, 4]. The VMC method is one of the powerful methods for obtaining the ground state of strongly correlated systems, which can deal with larger system than the exact diagnonalization method and is free from the infamous sign problem breaking the path-integral Monte Carlo method down. In the VMC method, we prepare some form of the wavefunction $|\psi(\alpha)\rangle$ with some parameters α, which is called as a variational wavefunction or a trial wavefunction. From the variational principle, we can find the wavefunction of the ground state by tuning α to minimize the energy of the wavefunction $|\psi(\alpha)\rangle$. The expectation value of an arbitrary physical quantity A with respect to $|\psi\rangle$ is rigorously written as the following;

$$\begin{aligned}\langle A\rangle_\psi &= \frac{\langle\psi|A|\psi\rangle}{\langle\psi|\psi\rangle} = \frac{\sum_x \langle\psi|x\rangle\langle x|A|\psi\rangle}{\langle\psi|\psi\rangle} \\ &= \sum_x \frac{|\langle\psi|x\rangle|^2}{\langle\psi|\psi\rangle}\frac{\langle x|A|\psi\rangle}{\langle x|\psi\rangle}\end{aligned} \tag{1}$$

where $|x\rangle$ is some handy wavefunction which

forms a complete system. In the VMC method, we perform the Markov chain Monte Carlo method for generating $|x\rangle$ with the weight function $\rho(x) \equiv |\langle\psi|x\rangle|^2 \,/\, \langle\psi|\psi\rangle$ in order to take the summation over x. For quantum lattice models such as the Fermion-Hubbard model and the Heisenberg model, we can adopt the Fock states of electrons for $|x\rangle$. In this study, we investigated whether $|x\rangle$ can be used as an input of ML model or not by using the transverse field Ising chain as demonstration. $|x\rangle$ plays the same role as that of spin configurations in the classical systems where a configuration x appears with the probability $p(x) = \exp(-\beta E(x))$. This corresponding is an advantage of our choice. We modified and used a program package implementing the many-variables VMC, `mVMC` [4, 5].

References

[1] J. Carrasquilla and R. G. Melko, nat. phys. **13**, 431 (2017).

[2] L. Wang, Phys. Rev. B **94**, 195105 (2016).

[3] C. Gros, Ann. Phys. **189**, 53 (1989).

[4] T. Misawa, *et al.*, Comp. Phys. Comm. **235**, 447 (2019).

[5] `https://github.com/issp-center-dev/mVMC`.

Two competing superconducing phases in κ-type molecular conductors

Hiroshi WATANABE
Waseda Institute for Advanced Study, Waseda University
1-6-1 Nishi Waseda, Shinjuku-ku, Tokyo 169-8050

The family of quasi two-dimensional molecular conductors κ-(BEDT-TTF)$_2$X has been extensively studied as a typical example of strongly correlated electron system. Depending on the monovalent anion X, they show various quantum phases such as antiferromagnetic and spin-liquid dimer-Mott insulators, and superconductivity (SC) [1]. Owing to the similarities in the experimental phase diagrams, κ-(BEDT-TTF)$_2$X system is often compared with high-T_c cuprates, which exhibit Mott metal-insulator transition and SC [2]. Recently, carrier doping in κ-(BEDT-TTF)$_2$X has been realized using electric-double-layer transistor [3], and the direct comparison with cuprates becomes possible. The experimental result shows the electron-hole doping asymmetry, reminiscent of the high-T_c cuprates.

Here, we theoretically study the doping effect in κ-(BEDT-TTF)$_2$X [4]. We consider a four-band extended Hubbard model including onsite (U) and intersite Coulomb interactions (V_{ij}) with κ-type geometry with the largest hopping integral t_{b_1} as an energy unit. The ground state properties are studied with the variational Monte Carlo (VMC) method. The Gutzwiller-Jastrow type wave function is used for the VMC trial wave function. The system sizes for calculation are from 288 (2×12×12) to 1152 (2×24×24).

In the ground-state phase diagram, there appear various competing phases and a significant electron-hole doping asymmetry is observed [4]. Here, we focus on the change of the most favored gap symmetry of SC. Figure 1 shows the ground-state phase diagram in a $n_{\rm hole}$-U/t_{b_1} space. Only the SC phases are considered and other ordered phases are ignored. The largest intersite Coulomb interaction is fixed at V_{b_1}/U=0.5. For the hole-doped side, the d_{xy}-wave symmetry, which has similarities with high-T_c cuprates, is favored. On the other hand, for the undoped and electron-doped side, the extended-s+$d_{x^2-y^2}$-wave symmetry [5, 6, 7] is favored. The change of the symmetry of SC is attributed to the degree of frustration that is controlled by carrier doping. This is a new perspective to κ-(BEDT-TTF)$_2$X, which can also be applied to other frustrated systems in general.

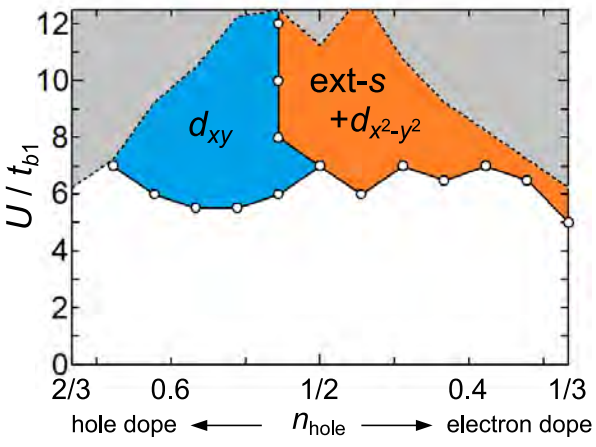

Figure 1: Ground-state phase diagram of the extended Hubbard model for κ-(BEDT-TTF)$_2$X. Only the superconducting phases are considered.

References

[1] K. Kanoda: J. Phys. Soc. Jpn. **75** (2006) 051007.

[2] R. H. McKenzie: Science **278** (1997) 820.

[3] Y. Kawasugi et al., Nat. Commun. **7** (2016) 12356.

[4] H. Watanabe, H. Seo, and S. Yunoki: submitted, arXiv: 1811.09035.

[5] K. Kuroki, T. Kimura, R. Arita, Y. Tanaka, and Y. Matsuda: Phys. Rev. B **65** (2002) 100516(R).

[6] D. Guterding, M. Altmeyer, H. O. Jeschke, and R. Valentí, Phys. Rev. B **94** (2016) 024515.

[7] H. Watanabe, H. Seo, and S. Yunoki: J. Phys. Soc. Jpn. **86** (2017) 033703.

3.4 Cooperative Phenomena in Complex Macroscopic Systems

Tensor-Network Representation of Gapless Kitaev Spin Liquids[1]

Naoki KAWASHIMA
Institute for Solid State Physics, University of Tokyo
Kashiwa-no-ha, Kashiwa, Chiba 277-8581

While the tensor network (TN) representation is recently used as the variational ansatz for various quantum many-body problems, it is also useful in capturing essence of novel quantum states, with the AKLT state as a well-known example. The Kitaev honeycomb model (KHM) is an exactly soluble model which exhibits gapless and gapped KSL ground states with fractionalized excitations. Recent successful realizations of Kitaev materials triggered a burst of theoretical investigations on it. In the present work, we propose a compact TN representation for KHM. Our variational wave function has the form $|\psi_n\rangle \equiv P_{\rm LG} R_{\rm DG}(\phi_n)$ $R_{\rm DG}(\phi_{n-1}) \cdots R_{\rm DG}(\phi_1)|(111)\rangle$ where $|(111)\rangle$ is the state where all spins are aligned to the (111) direction. The two operators $P_{\rm LG}$ and $R_{\rm DG}$ are essential in constructing the series of ansatze. The first one, $P_{\rm LG}$, is the 'loop-gas operator', which is defined as the sum of all TN operators (TPOs), each corresponding to a loop gas configuration. The second operator $R_{\rm DG}(\phi)$ is defined in a similar fashion, i.e., the sum of all TPOs corresponding to dimer-gas configurations. The parameter ϕ is such that $\tan\phi$ is the fugasity of the dimers.

The zero-th order ansatz ϕ_0, which is just a 'loop-gas state',

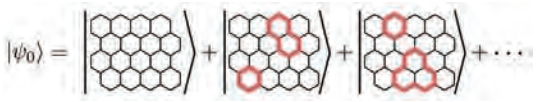

It has a remarkable feature that it is exactly identical to the classical loop-gas model. Therefore, without numerical calculation, we can say that it belongs to the Ising universality class. By optimizing $|\psi_1\rangle$, we can achieve much more accurate estimate (0.2% relative error in energy). Since the state is not exactly solvable any more, we must verify its critical properties. Our calculation shows, with more than 2 digit accuracy, that ψ_1 have the same critical properties regardless of the value of ϕ_1. Going to the even higher order approximation, ϕ_2, we can obtain very accurate result (0.007% error). From these results, we strongly believe

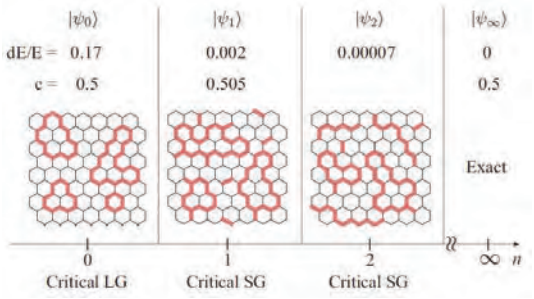

Figure 1: Comparison among the k-th order ansatze. While all belong to the same universality class, the energy converges quickly to the exact ground state energy of KHM.

that the present series of ansatze quickly converge to the exact ground state of the KHM (Fig.1), while retaining the essential properties of the KHM from the beginning ϕ_0.

[1] This report is based on H.-Y. Lee (ISSP), R. Kaneko (ISSP), T. Okubo (U. Tokyo) and N. Kawashima (ISSP), arXiv:1901.05786

Molecular Dynamics Simulation of a Kármán-Vortex Cavitation

Yuta ASANO, Hiroshi WATANABE, and Hiroshi NOGUCHI
Institute for Solid State Physics, University of Tokyo
Kashiwa-no-ha, Kashiwa, Chiba 277-8581

Cavitation is a flow phenomenon which is accompanied by a formation and growth of bubbles generated by a local pressure reduction by a high flow rate in a liquid [1]. The elucidation of the mechanism is very important in engineering fields because the cavitation causes various influences on fluid machinery. However, the mechanism of the cavitation inception remains unclear due to the difficulty to discuss the dynamics of microscopic bubble nuclei in a macroscopic flow field.

Therefore, in order to elucidate the mechanism of the cavitation from the molecular scale, we performed a molecular dynamics (MD) simulation of the Kármán-vortex cavitation using ISSP supercomputer.

In the present study, we investigated the cavitation effects on the Kármán vortex behind a circular cylinder by an MD simulation. To generate a multiphase flow, the interaction between fluid particles is employed by the Lennard-Jones (LJ) potential. The circular cylinder is modeled by a set of LJ particles whose positions are fixed on the surface of the cylinder. The computational cell is subjected to the periodic boundary condition. The temperature and the velocity in the downstream region of the cylinder are controlled by the Langevin thermostat [2]. In this way, uniform fluid can be re-introduced from the upstream side of the cylinder through the periodic boundary.

The top panel in Fig. 1 shows a snapshot of the density field at $T \simeq 1.4T_c$ (T_c: critical temperature). White color indicates a gas phase. The bubbles generated near the cylinder are caught into the Kármán vortex. Furthermore, at this temperature, it is also found that the bubbles are generated periodically in conjunction with the shedding period of the Kármán vortex. The bottom panel in Fig. 1 is a snapshot of the density field of a single-phase flow generated by using the Weeks-Chandler-Andersen potential for the interparticle interaction between fluid particles.

In order to investigate the influence of cavitation on the shedding frequency of Kármán vortex, the Strouhal number St is estimated. In the case of Fig. 1, $St \simeq 0.2$ is obtained both multiphase and single-phase flows. However, in the case of the multiphase flow, the oscillation of the lifting force caused

by vortex shedding disappear with decreasing temperature. This is because the generation of bubbles inhibits the formation of vortices and the vortex formation length significantly increases. On the other hand, in the case of single-phase flow, such a change does not occur because the decreasing temperature only causes a slight reduction in the viscosity. Therefore, we conclude that the cavitation inhibits the formation of the Kármán vortex.

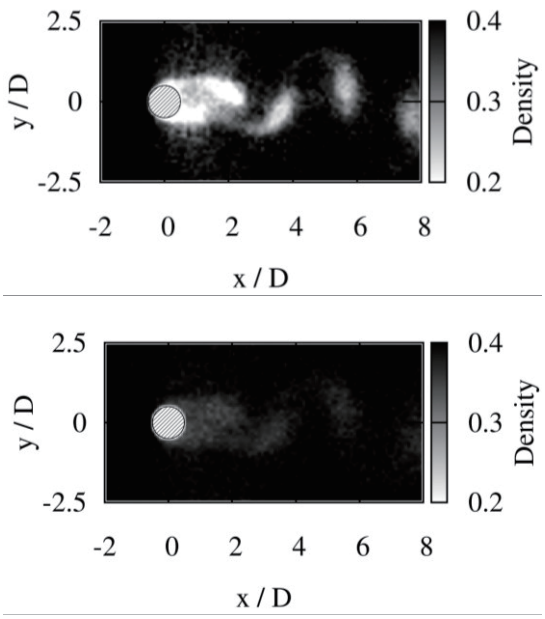

Figure 1: Snapshot of the density field of Lennard-Jones fluid (top) and Weeks—Chandler—Andersen fluid (bottom) at $T \simeq 1.4T_c$. The shaded area represents a cylinder of diameter D.

References

[1] R. E. A. Arndt: Annu. Rev. Fluid Mech. **34** (2002) 143.

[2] Y. Asano, H. Watanabe, and H. Noguchi, J. Chem. Phys. **148** (2018) 144901.

Spin and chiral orderings of the three-dimensional Heisenberg spin glass

Hikaru Kawamura and Takumi Ogawa

Graduate School of Science, Osaka University, Toyonaka 560-0043

The nature of the ordering of the three-dimensional isotropic Heisenberg spin glass (SG), a typical model of the so-called canonical SG, has been studied for years. Main issue has been whether the model exhibits the spin-chirality decoupling, i.e., exhibits two separate transitions, each associated with the glass ordering of the spin and of the chirality, $T_{SG} < T_{CG}$ [1]. The numerical situation, however, remains controversial: Some groups claimed $T_{SG} < T_{CG}$ [2], while some others $T_{SG} = T_{CG}$.

In this year`s project, we study the spin and chiral orderings of the 3D Heisenberg SG model with the nearest-neighbor random Gaussian coupling by extensive Monte Carlo simulations, to shed further light to the controversy. Larger system sizes up to $L=48$ (L the linear size) are studied both for periodic and open boundary conditions, and several independent physical quantities are computed including the correlation-length ratio and the Binder ratio are measured both for the spin and for the chirality, all of which are combined to give better estimates of T_{SG} and T_{CG} with higher precision than the preceding works. Indeed, we succeed in obtaining estimates of T_{SG} and T_{CG} as $T_{SG} = 0.130 \pm 0.001$ and $T_{CG} = 0.143 \pm 0.001$, with significantly less error bars than the previous works. The extrapolation of the finite-L data to $L=\infty$ is shown in the figure both for the spin and the chirality. The result gives a strong numerical support to the spin-chirality decoupling. The chiral-glass exponents are estimated to be $\nu_{CG}=1.39$ and $\eta_{CG}=0.43$, which supports the chirality scenario.

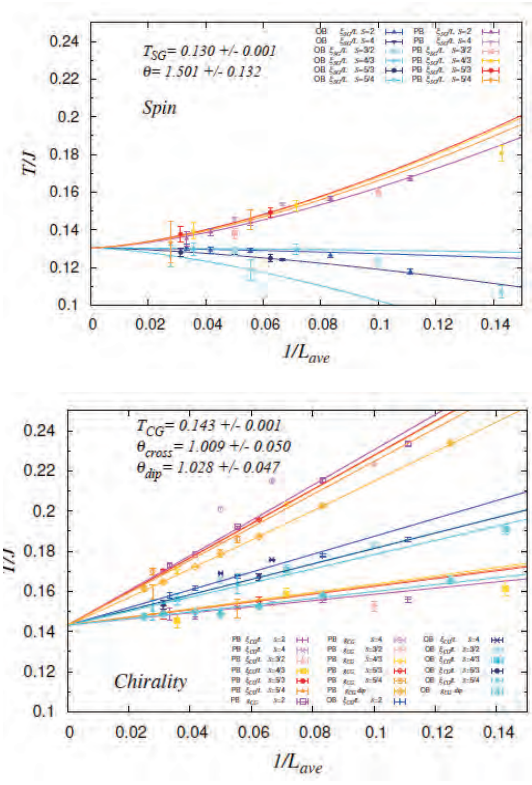

[1] H. Kawamura, Phys. Rev. Lett. **68**, 3785 (1992).

[2] D.X. Viet and H. Kawamura, Phy.s Rev. Lett. **102**, 027202 (2009).

Nature of the high-speed rupture of the two-dimensional Burridge-Knopoff model of earthquakes

Hikaru Kawamura, Koji Yoshimura and Shingo Kakui

Graduate School of Science, Osaka University, Toyonaka, Osaka 560-0043

Statistical physical study of earthquakes is often based on simplified models of various levels of simplification [1]. One of the standard models widely employed in statistical physical study of earthquakes might be the Burridge-Knopoff (BK) spring-block model. In the BK model, an earthquake fault is simulated by an assembly of blocks which is subject to the frictional force. More or less "realistic" friction law now standard in seismology might be the rate-and-state dependent friction (RSF) law. Then, it would be highly interesting to clarify the properties of the BK model obeying the RSF law. Though the statistical properties of the 1D BK model under the RSF law have been studied by the present authors' group [2], they have been limited so far to the 1D model. Under such circumstances, it is desirable to investigate the properties of the 2D BK model. In this year's project, we have tried such simulations on the 2D BK model under the RSF law, by concentrating on the high-speed rupture of main shocks [3].

The model consists of a 2D array of $N=L*L$ blocks which are subject to a RSF force. An obvious difference of the 2D model from the 1D counterpart might be its geometrical aspect. In fact, the 2D model exhibits in its stationary state a sequence of earthquake-like events of various sizes, among which very large events turn out to exhibit characteristic features. To illustrate this, we show in the above figure the way of the rupture propagation for a typical large event for $L=500$ system as color plots of the block sliding velocity. Indeed, the way of the rupture propagation is highly asymmetric and irregular in shape, a characteristic of the 2D system. For further details, please refer to ref. [3].

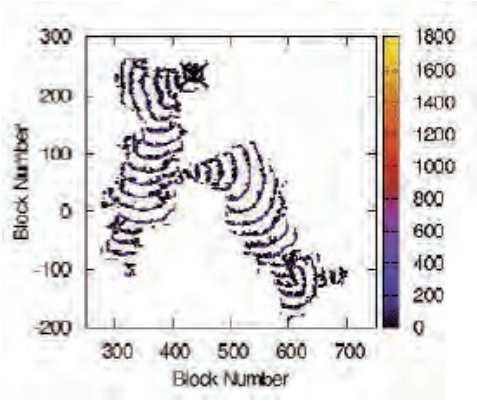

[1] For review, see, H. Kawamura, T. Hatano, N. Kato, S. Biswas and B.K. Chakrabarti, Rev. Mod. Phys. **84**, 839 (2012).

[2] H. Kawamura et al, Phys. Rev. E **95**, 04212 (2017).

[3] H. Kawamura et al, Phil. Trans. R. Soc. A **377** 20170391 (2018).

Numerical analysis of non-equilibrium dynamics of polymeric liquid and solid

Takahiro MURASHIMA

Department of Physics, Tohoku University,

6-3, Aramaki-Aza-Aoba, Aoba-Ku, Sendai, Miyagi 980-8578

We have developed two codes [1,2] implemented to massively parallel code, LAMMPS [3]. The one is for elongational flow successful in molecular dynamics simulation [1]. The other is multiscale simulation code coupling finite element method and molecular dynamics simulation [2].

Elongational flow was difficult on molecular dynamics simulation because the simulation box was collapsed within a finite simulation time. We can avoid this collapse if we set the initial simulation box not parallel to elongational direction. We have succeeded in obtaining the elongational viscosities on molecular dynamics simulation. The details are found in Ref [1].

Multiscale simulation coupling macroscopic continuum simulation and molecular dynamics simulation was difficult because the general deformation or strain was not dealt within the conventional technique on molecular dynamics simulation. The general strain can be decomposed to a rotation tensor and a stretch tensor by using QR decomposition. Using this technique, we have succeeded in coupling finite element method and molecular dynamics simulation and investigated a uniaxial loading of polymeric solid. The details are found in Ref [2].

References

[1] T. Murashima, K. Hagita, T. Kawakatsu: J. Soc. Rheol. Jpn. **46** (2018) 207.

[2] T. Murashima, S. Urata, S. Li: arXiv: 1902.09171.

[3] S. Plimpton: J. Comp. Phys. **117** (1995) 1.

How to conserve angular-momentum in discretization of Navier-Stokes equation for viscous fluids

Hiroshi NOGUCHI
Institute for Solid State Physics, University of Tokyo, Kashiwa, Chiba 277-8581

Although the Navier-Stokes equation (NSE) is derived under angular-momentum conservation (AMC), numerical simulation methods often lack it. We revealed how AMC is lost in the discretization of Navier-Stokes equation and how to recover it [1].

In conventional viscous fluids that do conserve angular momentum, the stress is expressed by a symmetric tensor: $\boldsymbol{\sigma} = -P\mathbf{I} + \eta(\nabla\mathbf{v} + (\nabla\mathbf{v})^{\mathrm{T}}) + \lambda(\nabla\cdot\mathbf{v})\mathbf{I}$. NSE is derived from this stress and $\rho D\mathbf{v}/Dt = \nabla\boldsymbol{\sigma}$:

$$\rho\frac{D\mathbf{v}}{Dt} = -\nabla P + \eta\nabla^2\mathbf{v} + (\eta+\lambda)\nabla(\nabla\cdot\mathbf{v}), \quad (1)$$

where D/Dt is the Lagrangian derivative. The second term in the shear stress, $\eta(\nabla\mathbf{v})^{\mathrm{T}}$, and compression stress, $\lambda(\nabla\cdot\mathbf{v})\mathbf{I}$, degenerately gives the last term in NSE. When the second shear stress is removed, it still results in the same equation if the coefficient is adjusted as $\lambda^{(-)} = \eta + \lambda$. Thus, the NSE can be obtained in the absence of AMC: *i.e.*, NSE by itself does not guarantee AMC. The AMC violation is caused by the implementation of these degenerated viscous terms.

We clarified how AMC is lost using Lagrangian finite volume method (LFVM). The velocity evolution of a FVM cell of volume V_i is given by

$$M_i\frac{D\mathbf{v}_i}{Dt} = \int_{V_i}\nabla\boldsymbol{\sigma}\,dV = \int_{S_i}\boldsymbol{\sigma}\hat{\mathbf{n}}\,dS \quad (2)$$

$$= \int_{S_i} -P\hat{\mathbf{n}} + \eta(\hat{\mathbf{n}}\cdot\nabla)\mathbf{v}_i + \eta\nabla v_{\mathrm{n}} + \lambda(\nabla\cdot\mathbf{v})\hat{\mathbf{n}}\,dS, \quad (3)$$

where $v_{\mathrm{n}} = \mathbf{v}\cdot\hat{\mathbf{n}}$ is the velocity normal to the interface. The momenta of the neighboring cells are transported via the stress on the interface surface between the cells. On the other hand, the integration of NSE using the divergence theorem can give a velocity evolution that DOES NOT conserve the angular momentum:

$$M_i\frac{D\mathbf{v}_i}{Dt} = \int_{S_i} -P\hat{\mathbf{n}} + \eta(\hat{\mathbf{n}}\cdot\nabla)\mathbf{v}_i + (\eta+\lambda)(\nabla\cdot\mathbf{v})\hat{\mathbf{n}}\,dS. \quad (4)$$

Because the third term in Eq. (3) is missing, the stress is asymmetric. To maintain AMC, the degenerated terms must be separately integrated in accordance with their stress origins. This relation holds in the other discretized NSE methods such as smoothed particle hydrodynamics.

The violation causes artificial rotations in multi-component fluids with different viscosities, although correct velocity evolutions are obtained for single-component fluids in the case that the boundary condition is given by the velocity. At the interface between two fluids or with a mobile solid object, AMC must be satisfied, whereas AMC can be neglected in bulk fluids. We also clarified that the condition for constant fluid rotation as a rigid body in a container rotating at a constant speed is not the AMC of the stresses, but the invariance of the viscous forces under a global rotation. To confirm our theory, we simulated the circular laminar flows of single- and binary-component fluids using two-dimensional LFVM. The results show excellent agreement with the analytical predictions for fluids with and without AMC.

References

[1] H. Noguchi: Phys. Rev. E **99**, 023307 (2019).

Designing Thermal Functional Materials via Materials Informatics

Junichiro SHIOMI

Department of Mechanical Engineering, The University of Tokyo

7-3-1 Hongo, Bunkyo, 113-8656

Heat transport plays an important role in thermal management applications. However, it is challenging to design the detail thermal functional materials due to various degrees of freedom. Materials informatics (MI), which has been considered as the fourth paradigm of science in addition to theory, simulation, and experiment, is now a promising way to accelerate the discovery and design of materials with desired thermal property.

This year we have successfully realized the wavelength-selective thermal emitter with ultra-narrow band based on aperiodic multilayer metamaterials designed by Bayesian optimization, as shown in Fig. 1. This is the first time to demonstrate the possibility of using simple multilayer structure for extremely high Q-factor.

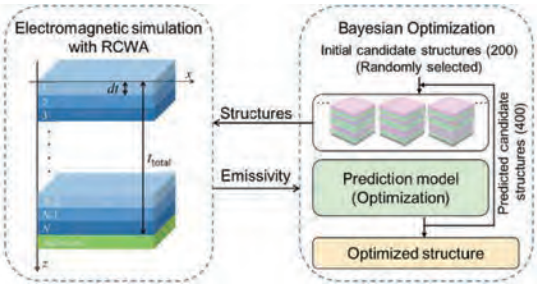

Figure 1: Schematics of Bayesian optimization for thermal radiation design.

The general optimization process can be easily understood from Fig. 1. After learning from the initial randomly-chosen training data, predictive thermal radiation property distribution can be estimated. Then it suggests new candidate structures which have high possibility to be high thermal radiation property. Those selected candidate structures were further evaluated by accurate calculation and added in training data for Bayesian optimization. After several iterations, the optimal structure can be identified. As shown in Figure 2 (a), the peaks for designed optimal structures were targeted 5, 6, 7 μm with high Q-factor of 217, 273 and 233.

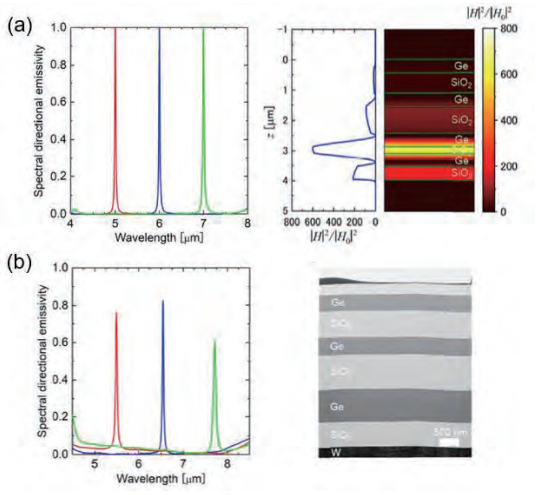

Figure 2: Thermal emitter design by Bayesian optimization, (a) Simulation, and (b) experiment.

For experimental structures show in Fig. 2 (b), a slight red shift for the targeted wavelength was observed and the amplitude for peak emissivity values were 0.76, 0.83 and 0.61 μm respectively with Q-factor of 132, 188, and 109 because the layer thicknesses of the actual fabricated samples somewhat deviated from the designed optimal case. Still, the obtained Q-factor 188 is very high and is the best experimental value among the multilayered metamaterials reported so far.

Besides the thermal radiation design, we also applied Monte Carlo tree search (MCTS) to optimize the interfacial Si-Ge roughness [2-4] for heat transport as shown in Fig. 3 (a). During the optimization, we divide the design region to 10 tree layers, the thickness of each layer is 5.43 Å, and each node in the tree has four child (0, 1, 2, 3), this gives the total number of candidates of 1048576.

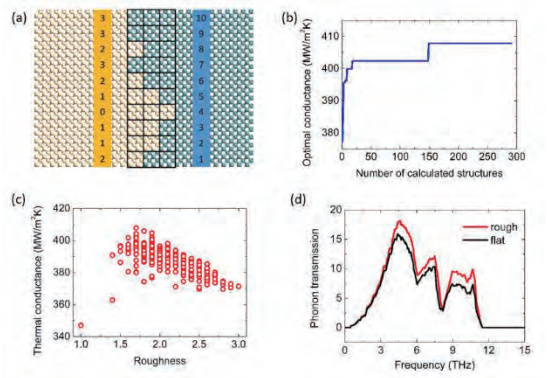

Figure 3: Interfacial roughness design by Monte Carlo tree search

As shown in Fig. 3 (b), within around 300 structures calculation, the interfacial thermal conductance quickly increases from 377 $MWm^{-2}K^{-1}$ to 408 $MWm^{-2}K^{-1}$. Figure 3 (c) shows the interfacial thermal conductance versus the roughness. The result indicates that the maximum interfacial thermal conductance appears in the middle value of interfacial roughness, which is not intuitive. By comparing the phonon transmission of the optimal and flat interface shown in Fig. 3 (d), we can find that the transmission in the middle frequency range from 4 to 10 THz is obviously enhanced.

In summary, (1) we have demonstrated the possibility of using simple multilayer structure for extremely high Q-factor based on Bayesian optimization, (2) we have designed non-intuitive rough interfacial structure to enhance heat transport via Monte Carlo tree search.

References

[1] A. Sakurai, K. Yada, T. Simomura, S. Ju, M. Kashiwagi, H. Okada, T. Nagao, K. Tsuda, J. Shiomi, ACS Central Science 5, 319, 2019.

[2] S. Ju, T. M. Dieb, K. Tsuda, J. Shiomi, Optimizing interface/surface roughness for thermal transport. NIPS 2018 Workshop: Machine Learning for Molecules and Materials, Montréal, Canada, 2018.

[3] T. M. Dieb, S. Ju, J. Shiomi, K. Tsuda, Monte Carlo tree search for materials design and discovery, MRS Communications, accepted, 2019.

[4] S. Ju, J. Shiomi, Nanoscale and Microscale Thermophysical Engineering **23**, 157-172, 2019.

Control of Phonon and Electron Transport Properties Using Mechanical Strain

Junichiro SHIOMI

Department of Mechanical Engineering, The University of Tokyo

7-3-1 Hongo, Bunkyo, 113-8656

A recent advance of nanotechnology allows us to design materials in nanoscale. When the length scale of nanostructures in materials reaches in the order of phonon wavelength, wave nature is expected to dominate their thermal transport properties. Despite many attempts to observe such coherent wave nature of phonons in experiments, very few studies have been reported the observation of coherent phonons except for at low temperature (< 10 K) or low frequency (< 1 THz) because phonons easily lose their phase information during scattering processes. Recently, Kodama *et al*. [1] have revealed that thermal conductivity of carbon nanotubes (CNTs) decreases by ≈ 60% and peak temperature of temperature dependent thermal conductivity decreases by ≈ 50 K due to encapsulation of fullerenes (top of Fig. 1). These results indicate that the encapsulated fullerenes act not as simple phonon scatterers like impurities but modulate phonon dispersion of outer single-walled CNTs (SWNTs). In this study, we show that fullerene encapsulation modulates coherent wave nature of outer SWNTs due to the periodic radial expansion. The radial expansion leads to softening and hardening of axial and radial modes, respectively, that should be caused by variation of force constants due to the induced strain. Moreover, the periodic strain leads to zone-folding effect and hybridization effect of phonon modes in outer SWNT and encapsulated fullerenes as shown in the closeup of Fig. 1. Our simulations reveal that the encapsulation-induced periodic strain makes an artificial superlattice of CNTs, which provides a new concept of tuning of microscopic thermal transport and strain-thermal engineering.

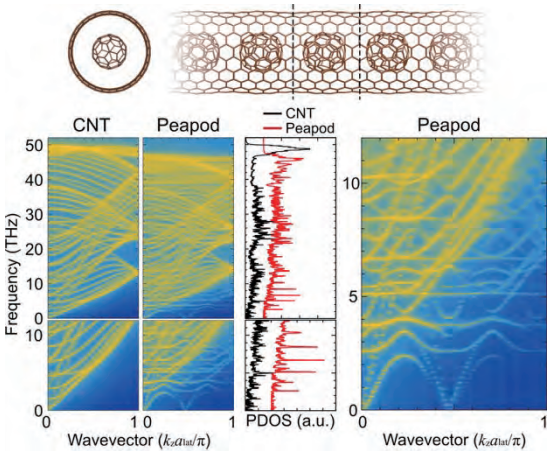

Fig. 1. Strain-induced zone-folding effects of carbon nanotubes (CNTs). [1,2] Periodicity of C_{60} fullerenes correspond to approximately four primitive unit cells of a SWNT. Bottom panels show spectral energy density and density of states (DOS) of a (10, 10) single-walled CNT (SWNT) and a C_{60}@(10, 10)SWNT peapod. k_z and a_{lat} are wavevector along the axis direction and the length of the primitive unit cell of the SWNT, respectively.

References

[1] T. Kodama, M. Ohnishi, W. Park, T. Shiga, J. Park, T. Shimada, H. Shinohara, J. Shiomi, and K. E. Goodson, Nat. Mater. **16**, 892 (2017).

[2] M. Ohnishi, T. Shiga, and J. Shiomi, Phys. Rev. B **95**, 155405 (2017).

Thermal Conduction Analysis of Cellulose Nanofibers by Molecular Dynamics

Junichiro SHIOMI

Department of Mechanical Engineering,

The University of Tokyo, 7-3-1 Hongo, Bunkyoku, 113-8656

The control of thermal energy is essential in advancing technology and preserving the environment. Cellulose nanomaterial thermal insulators have been shown to be superior to commonly-used thermal insulation materials such as silica in terms of affinity for environment and human body and thermal insulation performance. In order to get insight into the knowledge on heat conduction in cellulose nanomaterials, we have performed non-equilibrium molecular dynamics simulations for cellulose nanocrystal (CNC) and cellulose single-chain. Reedbush, Tsubame and Sekirei were used to conduct the simulations using LAMMPS and an in-house code to conduct the analysis on the thermal conductivity.

We found that thermal conductivities of CNC and cellulose single-chain range from 1.62 to 3.78 W/mK with increasing fiber lengths and the thermal conductivity of bulk CNC is calculated to be around 4.50 W/mK. Quasi-ballistic phonon transport in CNC is revealed and it suggests that shortening the length of CNC can lead to further reduction of the thermal conductivity.

The maximum length calculated in this study was only 30nm and this needs to extended to micron scale to be applied in industry, so further computational resources will be required.

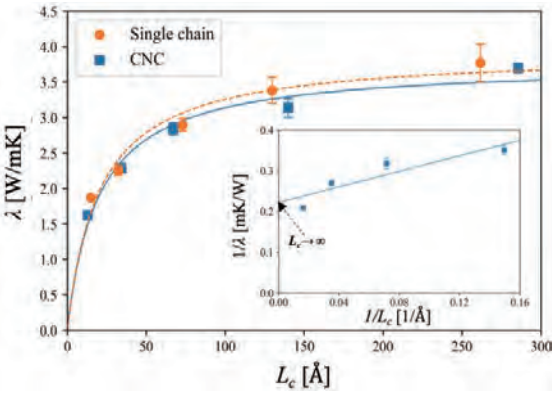

Fig. 1 Thermal conductivities of CNC and cellulose single chains as a function of the conduction region length. The inset shows extrapolation of thermal conductivity to infinite conduction-region length assuming the inverse proportionality.

Achievements

[1] M. Obori, D. Suh, S. Yamasaki, T. Kodama, T. Saito, A. Isogai, J. Shiomi: Phys. Rev. Appl. **11** (2019) 024044.

[2] M. Furuta, Bachelor's thesis (2019) the University of Tokyo.

Dynamics of fractional excitations in quantum spin liquid

Masafumi UDAGAWA
Gakushuin University
Mejiro, Toshima-ku, 171-8588

An experimental identification of quantum spin liquid (QSL) has been a central issue of condensed matter physics for decades. Since the QSL state is featureless in terms of local observables in its ground state, the excitations give the only possible route to its experimental identification. Accordingly, it is of crucial importance to clarify the nature of elementary excitations in this phase.

In this project, we focused on the two theoretical models of the QSL. One is Kitaev's honeycomb model. This model is an exactly solvable two dimensional model with QSL ground state. The Kitaev's spin liquid supports two species of fractional excitations: fermion and Vison. The dynamics of these excitations affects the observable dynamical response of this QSL. To clarify the dynamical response, we first developed an analytical solution of dynamical spin correlation for each sector of Vison configuration. By combining this solution with classical Monte Carlo method, we could obtain a solid theoretical scheme that allows an access to dynamical magnetic response at arbitrary temperatures. The advantage of this scheme is that a direct access to real-frequency representation is possible, without analytical continuation. In this project, we applied this scheme to the impurity problem, and obtained an anomalous zero-energy resonance due to the complex excitation of Vison and fermion [1].

As a second model, we also addressed the quantum spin ice model. This model is famous for its fractional excitations called magnetic monopole [2]. The nature of quantum magnetic monopole remains unclear. While they are expected to dominate the thermodynamic and transport properties of the system, the understanding of their basic properties, such as dispersion relations, is not well established. In this project, we combined degenerate first-order perturbation theory and exact diagonalization to obtain the excitation spectrum of quantum spin ice. The coupling to background spin ice manifold complicates the problem, and enlarge the Hilbert space even in a sector with small number of monopoles. We first made the breadth first search to set up Hilbert space of the two-monopole sector which satisfies the 2-in 2-out rule in all the tetrahedra except for those with monopoles. We then diagonalize the Hamiltonian on a lattice with 32 spins and obtain the two-monopole density of states. The obtained energy spectrum shows interesting phenomenon of dimensional transmutation, which leads to a steep "one-dimensional" Van-Hove singularity. This singularity is observable as a band-edge discontinuity in the inelastic neutron scattering.

References

[1] M. Udagawa: Phys. Rev. B **98** (2018) 220404(R)-1-5.

[2] M. Udagawa and R. Moessner: Phys. Rev. Lett. **122** (2019) 117201-1-6.

Quantized excitation spectra by confinement in quasi one-dimensional S=1 spin chains

Takafumi SUZUKI
Institute for Solid State Physics,
University of Hyogo, Shosha, Himeji, Hyogo 670-0083

In a pioneering study for the S=1/2 ferromagnetic (FM) Ising spin chain in weak transverse and longitudinal magnetic fields, it has been clarified that the excitation continuum shows the quantization by confinement of spinons [1]. The low energy excitation of the S=1/2 FM Ising spin chain is described by domain wall excitation that is achieved by flipping the spins of arbitrary length. The end of each domain wall carries ΔS=1/2 spinons and these spinons travel in the chain by the transverse field, which composes the excitation continuum. When the longitudinal field is further applied, it works as the linear potential for the flipped spins. Thus, the longitudinal field works as the confinement potential between the two spinons. This confinement potential causes the quantized excitation spectra whose excitation energies are well explained by the negative zeros of the Airy function (NZAF) [1]. The quasi-one-dimensional (Q1D) antiferromagnetic (AF) S=1/2 spin chains also have a chance to show the similar quantization. Shiba has argued [2] that the quantized spectra also appear in the Q1D AF Ising-like XXZ spin chains when the interchain interaction is very weak. In the Q1D Ising-like XXZ spin chains, the weak interchain interaction induces the staggered field in the spin chain at a low temperature. When the spinon-excitation continuum exists in the low-lying excitation, the staggered field works as the confinement potential between the spinons and causes the quantized spectra. In recent inelastic neutron scattering measurements on the Q1D S=1/2 spin chain compounds, $CoNb_2O_6$[3] and $(Ba/Sr)Co_2V_2O_8$[4,5], the quantized spectra explained by NZAF have been observed. The former and latter compounds are described by the FM Ising spin-chain model and the AF Ising-like XXZ spin-chain model, respectively.

In this project, we have investigated the possibility of the quantized spectra in the Q1D AF S=1 spin chains with the single-ion anisotropy by using infinite-time-evolving-block-decimation method. The Hamiltonian is written as

$$H = \sum_i [J\boldsymbol{S}_i \cdot \boldsymbol{S}_{i+1} + DS_i^{z2} + (-1)^i hS_i^z], \quad (1)$$

where $J > 0$. The last term of the Hamiltonian (1) denotes the staggered field originating from the weak interchain interaction. We have applied the real-time evolutions for the obtained ground-state wave function of the Hamiltonian (1) and calculated the dynamical spin-structure factor (DSF) via Fourier transformation of the dynamical spin-spin correlation function.

In the low-energy excitation of the AF S=1 spin chain, the multi magnon excitation appears. We have found that the magnon excitation continuum is quantized when the single-ion anisotropy is negatively large [6]. We discuss the origin of the quantization of the magnon excitation continuum below. In the following discussions, we suppose the bipartite system. In the bipartite system, all sites are classified into the two sublattice. First, we rotate the spin axis 180 degrees around the S^x axis for all spins in the sublattice B. The Hamiltonian is mapped onto $H=H_0+H_1$, where $H_0=\Sigma[-JS_i^zS_{i+1}^z+DS_i^{z2}-hS_i^z]$ and $H_1=\Sigma[S_i^+S_{i+1}^+-S_i^-S_{i+1}^-]$. Note that the staggered field is mapped onto the uniform longitudinal field. When the single-ion anisotropy is negatively large, the ground state of H_0 is given by the fully polarized state, ψ_0=|...+++++...> (or |...-----...>), where "+", "-" and "0" denote the site carrying S^z=1, -1, and 0, respectively. The low-lying excitation in the transverse component of the DSF is described by the dynamics of the excited state whose initial state is $\psi'=S^y\psi_0 \propto S^-\psi_0$ =|...++0++...>. Thus, this initial state is interpreted as an one magnon state. Next, we apply H_1 to the S^z=0 site in ψ'. The S^z =0 site shifts to the nearest-neighbor site with creating the S^z=-1 site,

namely ψ' ~ |...++-0+...>. By applying H_1 to the S^z=0 site repeatedly, the domain comprising the S^z=-1 sites develops and it results in the excitation continuum. We further apply the staggered field *h*, it works as the linear potential for ψ' ~ |...+-----0+...>. Therefore, the excitation continuum shows the quantized by the staggered field. For the longitudinal component, the similar discussion can be applied. In the longitudinal component of the DSF, the low-lying excitation is described by the two-magnon excitation, ψ''=|...++00++...>. When we apply H_1 to the S^z=0 site, the S^z=0 site moves to the nearest-neighbor site creating the Sz=-1 site. By applying H_1 to the S^z=0 site repeatedly, the domain-wall excitation ψ''=|...+0-----0+...> emerges. This domain-wall excitation constructs the excitation continuum. When the staggered field *h* is applied, it also works as the linear potential for ψ'' and the excitation continuum is quantized. From the numerical results, we have confirmed that the excitation continuum is quantized by the weak staggered field, and the quantized excitation energies are well explained by NZAF for $D << 0$[6].

We have also investigated the DSF of the FM S=1 Ising spin chain and argued whether the ΔS=2 excitation continuum in the system shows the quantization or not [7]. We have found that in the DSF the domain-wall excitation carrying ΔS=2, which is expressed as the superposition of ψ ~ |...++----++...>, can appear below the isolated mode by single magnon excitation. This excitation continuum is also quantized by the weak longitudinal fields [7]. The obtained results indicate that several S=1 compounds have a potential to show the quantized spectra below the Neel temperature.

References

[1] B. M. McCoy and T. –T. Wu, Phys. Rev. B 18, 1259 (1978).
[2] H. Shiba, Prog. Theor. Phys. 64, 466 (1980).
[3] R. Coldea, et al., Science 327, 177 (2010).
[4] B. Grenier, et al., Phys. Rev. Lett. 114, 017201 (2015) .
[5] Q. Faure, et al., Nat. Phys. 14, 716 (2018).
[6] T. Suzuki and S. Suga, Phys. Rev. B
[7] T. Suzuki and S. Suga, accepted in J. Phys. Soc. Jpn.

Numerical Study on Quantum Phase Transitions of the Spin Tubes

Tôru SAKAI[1,2,3], Hiroki NAKANO[1,2], and Tokuro SHIMOKAWA[4],
[1]*Graduate School of Material Science, University of Hyogo, Kouto, Kamigori, Hyogo 678-1297, Japan*
[2]*Research Center for New Functional Materials, University of Hyogo, Kouto, Kamigori, Hyogo 678-1297, Japan*
[3]*Synchrotron Radiation Research Center, Kansai Photon Science Institute, Quantum Beam Science Research Directorate, National Institute for Quantum and Radiological Science and Technology (QST) SPring-8, Kouto, Sayo, Hyogo 679-5148, Japan*
[4]*Okinawa Institute of Science and Technology Graduate University, Onna, Okinawa 904-0945, Japan*

Frustrated quantum spin systems have attracted a lot of interest in the field of strongly correlated electron systems. The $S = 1/2$ threeleg spin tube [1] has the spin gap because of the frustration, while the three-leg spin ladder is gapless. In the previous work using the numerical exact diagonalization of finite clusters and the finite-size scaling analysis indicated that the lattice distortion of the three-spin unit from the equilateral triangle to the isosceles one gives rise to the quantum phase transition from the spin gap phase to the gapless one [2]. One of the candidate materials of the $S = 1/2$ three-leg spin tube is the compound $[(CuCl_2tachH)_3Cl]Cl_2$ [3, 4]. However, this material has a twisted three-leg structure. Thus it would be useful to investigate the effect of the same lattice distortion on the twisted three-leg spin tube. In this paper, the lattice distortion to the isosceles triangle of the $S = 1/2$ twisted three-leg spin tube is investigated by the numerical exact diagonalization of finite clusters and the finite-size scaling analysis. As a result it is found that a quantum phase transition from the spin gap phase to the gapless Tomonaga-Luttinger liquid phase with respect to the lattice distortion. The ground state phase diagram is also presented [5].

References

[1] T. Sakai, M. Sato, K. Okamoto, K. Okunishi, and C. Itoi, J. Phys.: Condens. Matter, 22, 403201 (2010).

[2] T. Sakai, M. Sato, K. Okunishi, Y. Otsuka, K.Okamoto, and C. Itoi, Phys.Rev. B, 78, 184415 (2008).

[3] J. Schnack, H. Nojiri, P. Koegerler, G. J. T. Cooper, and L. Cronin, Phys. Rev. B 70, 174429 (2004).

[4] J. -B. Fouet, A. Laeuchli, S. Pilgram, R. M. Noack, and F. Mila, Phys. Rev. B, 73, 014409 (2006).

[5] Y. Tachibana, Y. Ueno, T. Zenda, K. Okamoto and T. Sakai, in preparation.

Numerical Diagonalization Study on the Quantum Spin Liquid in Frustrated Spin Systems

Tôru SAKAI[1,2,3], Hiroki NAKANO[1,2], and Tokuro SHIMOKAWA[4],
[1]*Graduate School of Material Science, University of Hyogo, Kouto, Kamigori, Hyogo 678-1297, Japan*
[2]*Research Center for New Functional Materials, University of Hyogo, Kouto, Kamigori, Hyogo 678-1297, Japan*
[3]*Synchrotron Radiation Research Center, Kansai Photon Science Institute, Quantum Beam Science Research Directorate, National Institute for Quantum and Radiological Science and Technology (QST) SPring-8, Kouto, Sayo, Hyogo 679-5148, Japan*
[4]*Okinawa Institute of Science and Technology Graduate University, Onna, Okinawa 904-0945, Japan*

The spin nematic phase, which is a kind of multipole phases, has attracted a lot of interest in the field of the strongly correlated electron systems, as well as the quantum spin liquid phase. Using the numerical exact diagonalization, the density matrix renormalization group (DMRG) calculation, and the finite-size scaling analysis, it is found that some spin nematic and spin liquid phases are induced by external magnetic field in the anisotropic and/or frustrated quantum spin systems. In our previous work [1], it was found that a field-induced nematic phase appears at some critical field in the anisotropic spin ladder and the mixed spin chain. The nematic phase is characterized by the power-law decay in the correlation function of the second-order spin moment. In addition at some higher critical field a quantum phase transition can occur to the conventional field-induced Tomonaga-Luttinger liquid. Several typical magnetization curves calculated by DMRG are presented. Recently the field-induced nematic phase was observed on the frustrated spin ladder system [2]. So we study on a frustrated spin ladder system [3], using the numerical diagonalization and DMRG. As a result, it is found that several exotic quantum phases, including the spin-nematic liquid phase. We also report some exact eigenstates of the present model and present several interesting phase diagrams [4]. Our recent numerical diagonalization study [5] on the $S = 1$ spin ladder system with the easyaxis single-ion anisotropy suggested that the field-induced nematic Tomonag-Luttinger liquid (TLL) phase appears. In addition another spin nematic liquid phases were predicted in the three-leg ladder system with the ring exchange interaction [6].

References

[1] T. Sakai, T. Tonegawa and K. Okamoto, Physica Status Solidi B 247, 583 (2010) .

[2] N. Buttgen, K. Nawa, T. Fujita, M. Hagiwara, P. Kuhns, A. Prokofiev, A. P. Reyes, L. E. Svistov, K. Yoshimura, and M. Takigawa, Phys. Rev B 90, 134401 (2014) .

[3] T. Hikihara, T. Tonegawa, K. Okamoto and T. Sakai, J. Phys. Soc. Jpn. 86, 054709 (2017).

[4] T. Tonegawa, T. Hikihara, K. Okamoto, S. C. Furuya, and T. Sakai, J. Phys. So. Jpn. 87, 104002 (2018).

[5] R. Yamanokuchi, K. Okamoto and T. Sakai, to appear in Proceedings of Inter-

national Conference on Megagauss Magnetic Field Generation and Related Topics (2018).

[6] Y. Tachibana, K. Okamoto and T. Sakai, in preparation.

Nonequilibrium relaxation analysis for the antiferromagnetic triangular Heisenberg model in a uniform field

Y. Ozeki and K. Murayama

Graduate School of Informatics and Engineering, The University of Electro-Communications

The antiferromagnetic (AF) triangular Heisenberg model in a uniform field is investigated by means of the nonequilibrium relaxation (NER) method [1]. The magnetic field h is applied along the z-axis. When the magnetic field is absent, it has been pointed out that a topological phase called the Z_2 vortex phase, which is a Kosterlitz-Thouless (KT) phase of vector chirality, appears [2]. In the case of non-zero field, the system shows two different symmetries, the Z_3 symmetry associated with the three sub-lattice on triangular lattice and the $O(2)$ symmetry around the direction of the applied field. The phase diagram has been obtained previously by the equilibrium Monte Carlo simulation [3], in which a coplanar phase called the Y phase, a colinear phase along the z-axis called the up-up-down phase and a non-colinear phase called the cant phase appear from low field to high field in low temperature regime. The slow dynamics due to the low dimensionality and the frustrations make it difficult to equilibrate the system around the transition point, and some problems have remained unsolved.

We study the system by the use of the NER method, and clarify the order parameters and an appropriate initial states for each phase and each boundary of phases. Preliminary calculations show the validity for these choice. Here, we report the result for high field regime where the (non-colinear) cant phase appears in low temperatures. In the previous work [3], it was concluded that the Z_3 symmetry breaks with a second order transition and a topological transition occurs due to the $O(2)$ symmetry, where the transition points are coincide with each other. In contrast to this result, we obtain a different picture on the phase transition; we observe that the $O(2)$ symmetry also breaks with a second order transition, and the finite order for this symmetry exists in the cant phase. While it has been well-known by so-called the Mermin-Wagner theorem that there is no long-range order with continuous symmetry-breaking in 2D continuous spin systems, rigorously speaking, a strict condition is necessary for the order parameter on the contribution to the Hamiltonian, which is not satisfied in the present case. Thus, the theorem can not be applied.

The Hamiltonian we consider is

$$\mathcal{H} = |J| \sum_{\langle ij \rangle} \mathbf{S}_i \cdot \mathbf{S}_j - h \sum_i S_i^z,$$

where summation for $\langle ij \rangle$ is taken over all nearest-neighboring sites on a triangular lattice. In the present study, we investigate for $h/|J| = 5$ case. The initial state of relaxation is prepared as the ground state for $h/|J| = 5$ which can be obtained exactly. We estimate the relaxation of order parameters ψ_{ABC} for the Z_3 symmetry and m_y for the $O(2)$ symmetry; m_y is the projection of the xy component on the the initial state and detects the symmetry-breaking for $O(2)$ along the z-axis.

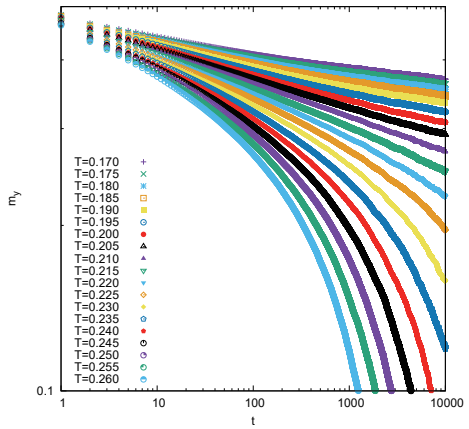

Figure 1: Relaxation of m_y for several temperatures.

Calculations are carried out on 1142×1143 triangular lattice with a skew boundary condition up to an observation time of 10^4 Monte Carlo steps (MCSs). About 40 samples are taken for statistical averaging. The estimations for m_y are plotted in Fig. 1. Using the improved dynamical scaling

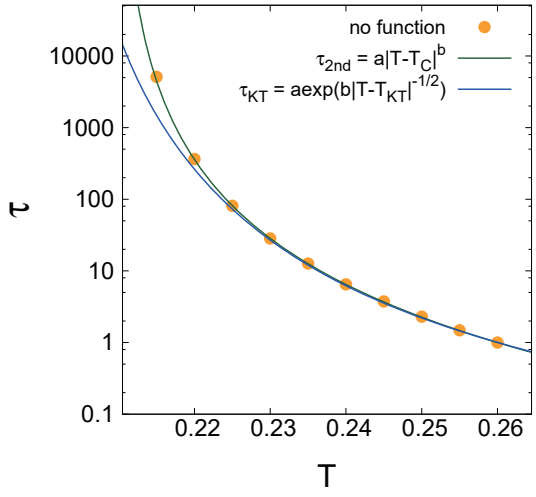

Figure 2: Comparison of estimated relaxation time.

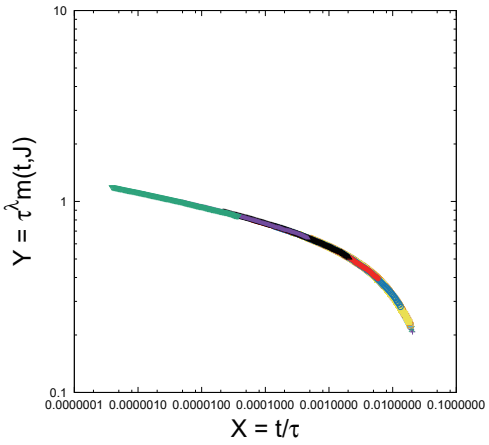

Figure 3: Scaling plot fore the high temperature regime $T \geq 0.215$.

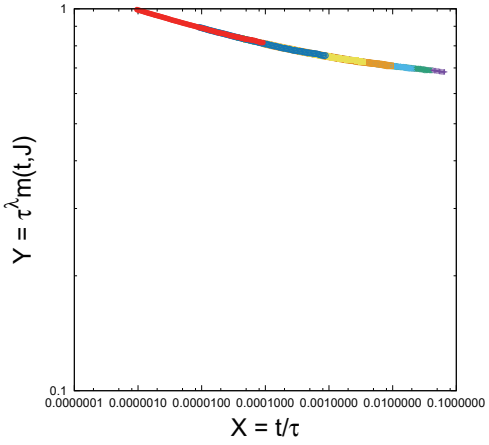

Figure 4: Scaling plot fore the low temperature regime $T \leq 0.200$.

analysis for the NER data [4], we analyze the dynamical scaling form,

$$m_y(t,T) = \tau(T)^{-\lambda} F[t/\tau(t)],$$

where T is the temperature measured in a unit of $|J|/k_{\rm B}$, $\tau(T)$ is the relaxation time, λ is a dynamical critical exponent, and t is the MCSs. We concentrate on the behavior of m_y. The result of $\psi_{\rm ABC}$ by dynamical scaling shows the second order transition consistent with the previous work [3].

Three types of scaling are performed for the data in higher temperature regime; assuming the second order transition with $\tau = a|T-T_{\rm c}|^{-b}$, assuming the KT transition with $\tau = a\exp\left[b/\sqrt{T-T_{\rm c}}\right]$, and no assumption for τ in which the estimated $\tau(T)$'s are more reliable than those obtained with an assumption. In Fig. 2, we plot the result for comparison of τ. It is shown that the second order transition is more favorable than the KT transition, which indicates that the $O(2)$ symmetry is broken and there might be a finite order for it. Thus, we analyze the data assuming the second order transition with $\tau = a|T-T_{\rm c}|^b$ for high temperature regime and low temperature one separately. The resulting scaling plots are shown in Figs. 3-4, with the estimated transition temperature $T_{\rm c} \sim 0.212$, which is consistent with the scaling analysis for $\psi_{\rm ABC}$ and that obtained in [3]. It is noted that, in Fig. 4, the upward trend of the scaling function reveals a finite ordering which indicates the break down of the $O(2)$ symmetry in two dimensional continuous system. While it has been well-known by so-called the Mermin-Wagner theorem that there is no long-range order with continuous symmetry-breaking in 2D continuous spin systems, rigorously speaking, a strict condition is necessary for the order parameter on the contribution to the Hamiltonian, which is not satisfied in the present case. Farther investigations are necessary to settle these problems.

References

[1] Y. Ozeki and N. Ito, J. Phys.: Math. Theor. **40** R149 (2007).

[2] H. Kawamura and S. Miyashita, J. Phys. Soc. Jpn. **53** 4138 (1984); H. Kawamura, et. al., J. Phys. Soc. Jpn. **79** 023701 (2010).

[3] L.Sebra, T. Momoi, P.Sindzingre, and N. Shannon, Phys. Rev. B**84** 214418 (2011)

[4] Y. Echinaka and Y. Ozeki, Phys. Rev. E**94** 043312 (2016); Y. Ozeki, A. Matsuda and Y. Echinaka, Phys. Rev. E**99** 012116 (2019).

Manipulation of quantum state by external fields

Seiji Miyashita
Department of Physics, University of Tokyo
Hongo, Bunkyo-ku, Tokyo, 113-0033

We studied the optical Bistability which is a discontinuous change of output light from a cavity as a function of strength of input. To investigate this phenomenon, we study the Tavis-Cummings model which represents a system of microcavity including atoms (or spins) with discrete energy levels contacting individual thermal bath. We have developed a highly parallelized code to study time evolution of the density matrix by a quantum master equation[1]. And we study the properties of bistability from a view point of an eigenvalue problem of time evolution operator. From the size dependence of photon density as a function of the strength of the driving force ξ, we determined the point of the first order phase transition point in the bistable region.

It is known that there are two types of regions of the steady state of such system[2]. In the low photon region, the photon and atoms strongly couple and the hybridization of both degree of freedom plays an important role, while in the high photon region, the photon plays as the classical electromagnetic field. So far, the optical bistability has been studied as a transition between the low and high photon region. In particular, in the present work, we studied the case where the photon-density in the cavity is low. We found that the transmission spectrum of detuning frequency behaves differently from the conventional case.

Moreover, we characterized the bistability by the size dependence of the relaxation time. The relaxation time is calculated from the second eigenvalue of the time evolution function. We found that the relaxation time increases exponentially with the size. We also find that it decrease inversely proportional to the sweeping rate of ξ (Fig. 1).

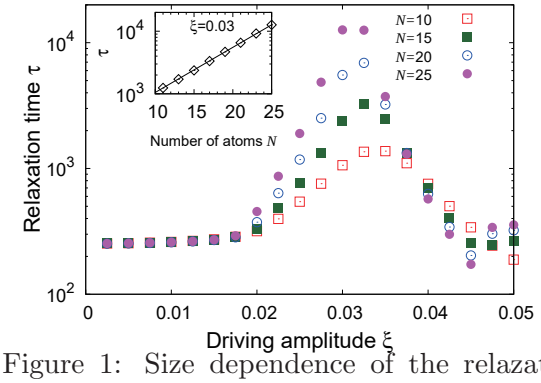

Figure 1: Size dependence of the relazation time in the bistable region of the optical bisatability

We also studied characterization of the effective spin ($S = 1/2$) induced by impurities in the so-called gapped spin chains by making use of the matrix product state (MPS). We first studied AKLT model as a prototype and found a characteristic response to the external field, and then we studied the bond-alternating Heisenberg antiferromagnetic chain (BAHAF) with MPS. We successfully constructed MPS and studied the precision of the MPS as a function of bond-dimension of the matrix [3].

References

[1] Tatsuhiko Shirai, Synge Todo, Hans de Raedt, and Seiji Miyashita, Phys. Rev. A **98**, 043802 (2018).

[2] S. Miyashita, et al.J. Phys. B Atomic Mol and Opt Phys 45, 124010 (2012).

[3] H. Nakano, Master thesis (University of Tokyo 2019)

Oligomerization process of full-length amyloid-beta peptides studied by molecular dynamics simulations

Satoru G. Itoh and Hisashi Okumura

Research Center for Computational Science,

Institute for Molecular Science, Okazaki, Aichi 444-8585

Many proteins aggregate at higher concentrations and form spherical substances called oligomers and acicular substances called amyloid fibrils. These protein aggregates cause more than 40 kinds of diseases. For example, aggregates of amyloid-β (Aβ) peptides cause Alzheimer's disease, and α-synuclein aggregates lead to Parkinson's disease. To overcome these diseases, it is essential to understand the formation mechanism of the protein oligomers and amyloid fibrils. For this purpose, we have been performing several molecular dynamics (MD) simulations of the oligomers and amyloid fibrils: We have so far revealed (a) the aggregation mechanism of Aβ fragments [1, 2], (b) conformations of full-length Aβ peptides at a hydrophilic/ hydrophobic interface [3], (c) structural difference between two ends of the Aβ amyloid fibril [4], and (d) disruption process of the Aβ amyloid fibril by a supersonic wave [5].

As for the aggregation of Aβ, we have so far mainly dealt with relatively simple systems such as Aβ fragments (i.e. not full length) in pure solvent. However, we are now trying more realistic systems with the full-length Aβ peptides. Aβ has two types, Aβ 40 (40 residues) and Aβ 42 (42 residues), which differ in the number of amino acids in the C-terminal region. It is known that the oligomerization and amyloid formation speed of Aβ42 are faster than those of Aβ40, but it is not clear why such a difference occurs. Initial formation of amyloid fibrils in the brains of Alzheimer's disease patients is thought to be caused by aggregation of Aβ42 rather than Aβ40. We performed a Hamiltonian replica-permutation MD simulation, the method of which was developed by our group, on each of the Aβ 40 dimer and Aβ 42 dimer systems. In this fiscal year, we extended the simulations to 1 μs per replica.

As a result, we observed the aggregation process as shown in Fig. 1. and found that Aβ42 forms intermolecular β-sheet more than Aβ40. We also found that this difference is caused by the fact that Aβ42 tends to form a β-hairpin more easily and a stable intermolecular β-sheet is formed between this β-hairpin and another Aβ42.

Fig. 1: Aggregation process of Aβ42 peptides.

References

[1] S. G. Itoh and H. Okumura: J. Phys. Chem. B **118** (2014) 11428.

[2] S. G. Itoh and H. Okumura: J. Comput. Chem. **120** (2016) 6555.

[3] S. G. Itoh, M. Yagi-Utsumi, K. Kato, and H. Okumura: J. Phys. Chem. B **123** (2019) 160.

[4] H. Okumura and S. G. Itoh: Sci. Rep. **6** (2016) 28422.

[5] H. Okumura and S. G. Itoh: J. Am. Chem. Soc. **136** (2014) 10549.

Doping effect on electronic structure and superconductivity in two-dimensional layered materials

Harald O. Jeschke
Research Institute for Interdisciplinary Science, Okayama University
Kita-ku, Okayama, Okayama 700-8530

Iron based superconductors are among the most intensively studied class of materials of the past decade. Significant insight into unconventional superconductivity was precipitated by the discovery of the first large family of high temperature superconductors since the discovery of the cuprates. At present, FeSe which belongs to the iron chalcogenide class of materials is at the forefront of theoretical and experimental efforts. In particular, the exceptionally large nematic region, the peculiar magnetism and the strong sensitivity to pressure are hot topics in this field. Among iron chalcogenide superconductors, lithium intercalated iron selenide, $Li_x(C_3N_2H_{10})_{0.37}FeSe$ is attracting interest [1]. In this material, it was reported experimentally [3] that the superconducting critical temperature T_c increases up to $T_c = 46$K ($x = 0.37$) and decreases when the doping level x is increased. This study suggests that increasing x changes the electronic structure dramatically, and the superconductivity changes.

We have investigated changes in electronic structure and superconductivity in lithium intercalated iron selenide, $Li_x(C_3N_2H_{10})_{0.37}FeSe$ under pressure and under doping. We perform density functional theory calculations using structural information from experiments, and we use spin fluctuation theory calculations to investigate superconductivity driven by spin fluctuation.

DFT calculations reveal that Lifshitz transitons occur as a function of x where a Fermi pocket disappears and appears around the Γ point in the unfolded Brillouin zone (Figure. 1). Furthermore, we construct five band tight binding models including the iron 3d orbitals, and clarified that these Lifshitz transitions leads to the enhancement of T_c as a function of x [4].

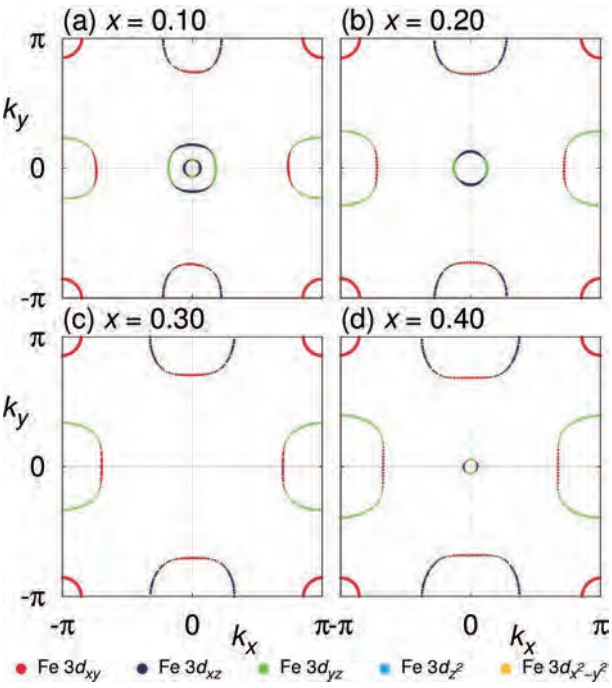

Figure 1: Change of Fermi surface in $Li_x(C_3N_2H_{10})_{0.37}FeSe$. The two hole pockets around Γ point disappears ((a), (b) and (c)). As increasing x more, one of them reappears (d).

References

[1] D. Guterding, *et al.*, Phys. Rev. **B** 91, 041112(R) (2015)

[2] M. Shimizu *et al.*, Phys. Rev. Lett. **121** (2018) 137001.

[3] R. J. Sun *et al.*, Phys. Rev. B **98** (2018) 214508.

[4] M. Shimizu *et al.*, in preparation.

Statistical-mechanical study for chiral magnets

Koji Hukushima
Department of Basic Science, University of Tokyo
3-8-1 Komaba, Meguro-ku, Tokyo 153-8902

In recent years, spin textures such as magnetic skyrmions or chiral solitons were observed in chiral magnets governed by antisymmetric Dzyaloshinskii-Moriya (DM) interactions. In magnetic systems, skyrmions were proposed theoretically as local spin vortices that are characterized by a topological charge. These fascinating topological excitations have since been extensively studied in experiments and through theoretical models.

In this project, we have numerically studied phase transitions of skyrmions in a two-dimensional chiral Heisenberg system using massively parallelized Monte Carlo simulations with a dedicated algorithm that avoids the difficulty of relaxation to equilibrium due to the long skyrmion lifetime. Our analysis relies on the analogy of the skyrmion system with interacting particle models in two dimensions. Two-dimensional particle systems, in the absence of a periodic substrate, cannot crystallize at finite temperature, that is, develop long-range positional order, but they can form a solid with algebraically decaying positional correlation functions and long-range orientational order.

At low temperature, two-dimensional chiral magnets in a magnetic field have many skyrmions as thermodynamically stable objects. In order to compute correlation functions of skyrmions at long distance, it is necessary to simulate very large systems of a two-dimensional chiral magnet. However, due to the low symmetry of chiral magnets, Monte Carlo simulation with local algorithms suffers from slow relaxation at low temperature. Our Monte Carlo method is based on modified heat-bath and over-relaxation algorithms. With the help of the local nature of both algorithms, their implementation on GPUs is rather easy to simulate the system with a checkerboard decomposition.

Each skyrmion is composed of Heisenberg spins on a discrete square lattice. Then, we assigned it a real-valued position using a local mask and compute high-quality spatial correlation functions at the fixed number of skyrmions[1]. This allows us to map the Heisenberg spin model to a model of interacting particles and to determine positional and orientational correlation functions, in analogy to what is done for two-dimensional particle systems.

At zero temperature we confirm that the ground state of the system is a triangular skyrmion crystal state with long-range positional order with locally triangular order minimally disturbed to accommodate the substrate potential. This state is incommensurate with the substrate at all densities. We find that commensurate square-shaped skyrmion crystals have higher energy than triangular crystals, even in the very dilute limit near the transition field at zero temperature.

At finite temperature, however, the ordered skyrmion state is a locally triangular "floating" solid, and it has long-range orientational correlations yet only quasi-long-range positional correlations. This solid nature of the low-temperature phase, characteristic of two-dimensional systems, is nontrivial in our system, which has discrete translational symmetry. The coupling potential affects the melting of the low-temperature skyrmion-solid state. As predicted by the KTHNY theory, we find that the skyrmion solid melts without an intermediate hexatic phase with a quasi-long-range orientational correlation.

[1] Y. Nishikawa, W. Krauth, K. Hukushima: Phys. Rev. B**99**, 064435 (2019).

Topological Order and Quantum Dynamics in Quantum Many-body Systems

Synge Todo
Department of Physics, University of Tokyo, Tokyo 113-0033, Japan
Institute for Solid State Physics, University of Tokyo, Kashiwa, 277-8581, Japan

We have developed various novel quantum Monte Carlo methods for quantum many-body systems with strong entanglement. For calculating the entanglement entropy of quantum spin systems, an efficient quantum Monte Carlo method has been developed. The entanglement entropy is one of the important indices that characterize quantum correlations and the topological order in quantum many-body systems. Our method works directly at absolutely zero temperature, and thus it is completely free from systematic errors coming from extrapolation to the zero temperature limit unlike the previous methods.

We have improved the path integral Monte Carlo method in continuous space. By using the event-chain Monte Carlo method and introducing special type of cuts in the world line configurations, we have achieved an efficient Monte Carlo update that breaks the detailed balance condition and can work in the canonical ensemble. We have applied this algorithm to a system of Bosons, and demonstrated that the convergence of distribution is much faster than the conventional method, and the time complexity with respect to the Trotter number is improved greatly.

We also have developed a nonlocal-update quantum Monte Carlo method for quantum dimer models on general lattices. Although there is no negative sign problem in the Hamiltonian of the quantum dimer models, Monte Carlo simulations had been very difficult due to the strong geometric restriction on the arrangement of dimers. By developing a method that can transition between different topological sectors, it becomes possible to discuss the phase diagram at finite temperatures in addition to absolute zero.

On the other hand, numerical methods based on the tensor network representation have been focused recently as they requires less computational cost than the exponentially expensive exact diagonalization. Representative methods include TRG and HOTRG. So far, the tensor network methods have been used mainly for uniform systems. We have extended HOTRG using projectors instead of isometries for non-uniform systems, and apply it to the Ising model with bond dilution. We have confirmed that the method using projectors converges much faster than the conventional one.

Spins coupled with photon degrees of freedom in the cavity exhibit a non-equilibrium phase transition with bistability in the number of photons. We have performed simulation based on the quantum master equations, and from the eigenvalues and eigenstates of the time evolution operator, we discussed the correspondence to the first order phase transition in the equilibrium system [1]. We also have calculated the hysteresis loop under the periodic modulation of laser intensity, from the viewpoint of the Floquet operator, and clarify that a dynamical phase transition phenomenon appears with respect to the period of modulation.

References

[1] T. Shirai, S. Todo, H. de Raedt, S. Miyashita, Phys. Rev. A **98**, 043802 (2018).

Novel phases in honeycomb lattice Kitaev materials

Tsuyoshi OKUBO
Department of Physics, The University of Tokyo
7-3-1 Hongo, Bunkyo-ku, Tokyo 133-0033

Recently, magnetic compounds with the strong spin-orbit interaction have attracted great interest. In several compounds, including Na_2IrO_3 and α-$RuCl_3$, the dominant magnetic interaction is induced by the strong spin-orbit coupling and it is considered to be the Kitaev interaction which is an Ising like anisotropic interaction with different spin component depending on the bonds. It is known that when there is only the Kitaev interaction (Kitaev model), the ground state of the $S = 1/2$ Kitaev model on the honeycomb lattice is a quantum spin liquid [1]. On the other hand, real compounds contain other interactions such as the Heisenberg interaction, further neighbor interactions, or the off-diagonal Γ interaction, which induce magnetic long range orders in these compounds at low temperature.

In order to clarify the nature of there Kitaev materials, we numerically calculate the ground states of the models with the Kitaev interaction and other interactions by means of a tensor network method. We represent the ground state wave function as a network of small tensors, and optimize each tensor element so that the energy expectation value becomes smaller. One of the most important aspect of such tensor network method is that by choosing proper tensor network structures, we can express the wave function of infinitely large systems by assuming a translational symmetry. We use the infinite tensor product states (iTPS), which is also called as the infinite projected entangled-pair states (iPEPS), as our tensor network states.

In this year, we mainly investigated the Kitaev-Gamma model where an off-diagonal interaction, the Γ term, exists in addition to the Kitaev interaction [2, 3]. The Hamiltonian of the model is given by

$$\mathcal{H} = \sum_{\gamma \in x,y,z} \mathcal{H}_\gamma, \tag{1}$$

and on z-bond,

$$\mathcal{H}_z = \sum_{\langle i,j \rangle_z} [K S_i^z S_j^z + \Gamma (S_i^x S_j^y + S_i^y S_j^x)]. \tag{2}$$

This model is considered to be an effective model for α-$RuCl_3$. In order to investigate the effect of the Γ term to the Kitaev spin liquid accurately, firstly we constructed a very accurate iTPS representation of the Kitaev spin liquid [4]. In the previous studies in the vicinity of Kitaev spin liquid, there was a serious difficulty for optimization of iTPS; it was not easy to obtain accurate Kitaev spin liquid wave function when we used random initial tensors. However, by using our iTPS representation of Kitaev spin liquid as the initial state, we obtained accurately optimized Kitaev spin liquid state even if away from the pure Kitaev model. Based on this technique we estimated that the Kitaev spin liquid state becomes unstable for $\Gamma/|K| \gtrsim 0.04$ for negative K, and, instead, a state which spontaneously breaks the lattice rotational symmetry is stabilized. This phase transition seems to be inconsistent with the previous numerical results by the exact diagonalization (ED) [2] or by the infinite density matrix renormalization group (iDMRG) [3]; they concluded that the Kitaev spin liquid state was stable for $\Gamma/|K| < \infty$.

In order to clarify this discrepancy, we might need further calculations with a larger tensor size and more sophisticated optimization techniques.

References

[1] A. Kitaev: Ann. Phys. **321** (2006) 2.

[2] A. Catuneanu, Y. Yamaji, G. Wachtel, H.-Y. Kee, and Y. B. Kim: npj Quantum Materials, **3**, (2018) 23.

[3] M. Gohlke, G. Wachtel, Y. Yamaji, F. Pollmann, and Y. B. Kim: Phys. Rev. B **97** (2018) 075126.

[4] H.-Y. Lee, R. Kaneko, T. Okubo, and N. Kawashima, arXiv:1901.05786.

Scaling theories of random topological and non topological systems

TOMI OHTSUKI[1]
TOHRU KAWARABAYASHI[2]
KEITH SLEVIN[3]
KOJI KOBAYASHI[4]
1) Dept. Phys., Sophia University, Chiyoda-ku, Tokyo 102-8554, Japan
2) Dept. Phys., Toho University, Miyama 2-2-1, Funabashi 274-8510, Japan
3) Dept. Phys., Osaka University, Toyonaka, Osaka 560-0043, Japan
4) IMR, Tohoku University, Sendai 980-8577, Japan

Recent discoveries of Weyl semimetal (WSM) have inspired extensive research of these novel topological materials. Here we have studied the effects of disorder on WSM. Based on the renormalization group analysis, we have proposed the scaling theory near the multicritical point of WSM-CI-Metal, and have verified the scaling behavior numerically [1]. We have shown that the Anderson localized phase appears between CI-Metal, while the transition is direct for WSM-Metal and CI-WSM. We have also discussed novel scaling behavior of CI-WSM transition [2].

We have also studied the Anderson transition using massively parallel supercomputing. The most precise estimations of the critical exponent for the Anderson transition have been made using the transfer matrix method. This method involves the simulation of extremely long quasi one-dimensional systems, and is inherently serial and is not well suited to modern massively parallel supercomputers. We show that this problem can be avoided by generating random sets of orthogonal initial vectors with an appropriate stationary probability distribution. We have applied this method to the Anderson transition in the three-dimensional orthogonal universality class and been able to increase the largest $L \times L$ cross section simulated from $L = 24$ (New J. Physics, **16**, 015012 (2014)) to $L = 64$ here. This permits an estimation of the critical exponent with improved precision and without the necessity of introducing an irrelevant scaling variable. In addition, this approach is better suited to simulations with correlated random potentials such as is needed in quantum Hall or cold atom systems [3]. In addition, we have calculated the distribution of Kondo temperature at the Anderson transition from the local density of states obtained by kernel polynomial method.

References

1. X. Luo, B. Xu, T. Ohtsuki, R. Shindou: Physical Reivew B **97**, 045129 (2018).
2. X. Luo, T. Ohtsuki, R. Shindou: Physical Review B **98**, 020201(R)(2018).
3. K. Slevin, T. Ohtsuki: Journal of the Physical Society of Japan **87**, 094703 (2018).

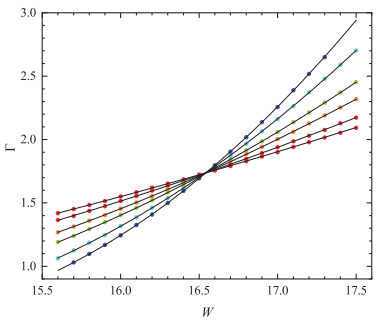

Figure 1: The estimates of normalized Lyapunov exponent $\Gamma = \langle \tilde{\gamma}_N \rangle L$ for width L =12, 16, 24, 32, 48 and 64 for various disorders W together with the finite size scaling fit (solid lines). The error bars of the numerical data are smaller than the symbol size. Taken from [3].

Data-integration approach to optimize a ferromagnet for rare-earth permanent magnets

Munehisa Matsumoto
Institute for Solid State Physics, University of Tokyo
Kashiwa-no-ha, Kashiwa, Chiba 277-8581

April 26, 2019

Permanent magnets are expected to make a significant part of the key materials in the upcoming decades in order to provide a sustainable solution to the energy problem. We are developing methods to propose a good candidate as a magnetic material for a given utility such as characterized by a typical temperature range for practical applications. Even though the champion rare-earth permanent magnet (REPM) made of Nd-Fe-B ternary alloys has been dominating the market in the past few decades, it is by no means straightforward to pin-point what would be the best material in a given situation for demands. Addition of Dy had been the solution for traction motors in hybrid cars where sufficiently strong magnetic properties at high-temperatures up to 450K are indispensable, but various instabilities in the supply of heavy rare earth elements including Dy pushed us to look for alternative chemical compositions in the past decade. Valence-fluctuating Ce can be of potential use in controlling the magnetic properties toward a desirable direction by fine-tuning the $4f$-electron states around or slightly below the Fermi level. Here we report about a recent case study [1] to demonstrate how a best candidate within the La-Ce-Fe-B quaternary alloy can be identified on the basis of *ab initio* data sets and a practical data integration approach, making an application-oriented optimization framework.

The description of REPM's involves multiple physics, starting with the microscopic electronic structure on the basis of quantum mechanics to the classical electrodynamics that govern the macroscopic magnetization dynamics. Bridging widely different scales is hardly doable at present, partly due to the lack of good numerical methodology to deal with too demanding computational costs that grow exponentially with respect to the length scale, and more fundamentally due to the lack of our understanding concerning how the microscopic electronic structure is coarse-grained through the particular microstructure of metallic materials to yield the macroscopic and off-equilibrium properties.

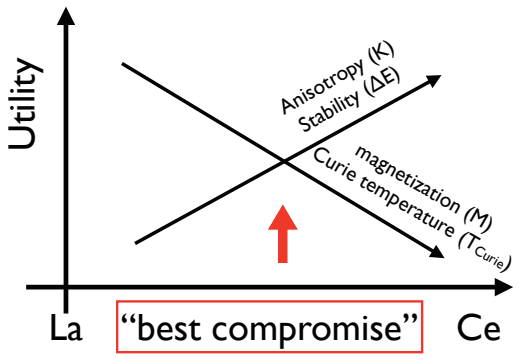

Figure 1: The overall optimization for $(La,Ce)_2Fe_{14}B$.

We calculated all of the relevant intrinsic properties of the ferromagnets $R_2Fe_{14}B$

(R=rare earth), that make the main phase of the champion REPM. Open-source package for *ab initio* electronic structure calculations, AkaiKKR [2] and OpenMX [3] are used. Magnetization M, uni-axial magnetic anisotropy energy K, Curie temperature T_{Curie}, and the formation energy ΔE as an indicator of the structure stability are calculated by appropriately combining AkaiKKR and OpenMX on the chemical composition space that is multi-dimensional in general. We focus on the cross section therein for $(La_{1-x}Ce_x)_2Fe_{14}B$ [4]. A utility function is defined for each of the observables referring to the intrinsic properties of the champion magnet compound, $Nd_2Fe_{14}B$, and integrated to assess the overall utility of the compound $(La_{1-x}Ce_x)_2Fe_{14}B$ as a function of x. The setup of the optimization problem is schematically shown in Fig. 1 While Ce-rich compounds come with better magnetic anisotropy and structure stability, La-rich compounds exceeds in Curie temperature and magnetization.

Depending on how the high-temperature edge of practical applications are given, the optimal point on the Ce-concentration axis is shifted. Interestingly, when the application temperature range spanning up to 450K is assumed, we identified that the optimal point falls on the range around 70% of Ce, in a semi-quantitative agreement with the recent technological achievement in the development of a La-Ce-based permanent magnet [5].

In this study, multiple-scale physics in REPM's and external demands on them have been incorporated in a simple-minded data model. While the fundamental developments to bridge over multiple scales are still in progress, thus constructed data models may help in providing a working phenomenology to which more fundamental theory is compared.

Construction of a more comprehensive data model will be presented elsewhere [6].

References

[1] M. Matsumoto. M. Ito, N. Sakuma, M. Yano, T. Shoji, H. Akai: preprint (arXiv:1901.10119).

[2] H. Akai: `ttp://kkr.issp.u-tokyo.ac.jp/jp/}.Seealso{\url`ttps://ma.issp.u-tokyo.ac.jp/app/113.

[3] T. Ozaki *et al*: `ttp://www.openmx-square.org/}.Seealso{\url`ttps://ma.issp.u-tokyo.ac.jp/app/594.

[4] C. V. Colin, M. Ito, M. Yano, N. M. Dempsey, E. Suard, and D. Givord: Appl. Phys. Lett. **108** (2016) 242415.

[5] T. Shoji *et al.*: Journal of Society of Automotive Engineers of Japan (2018) **72**, 102 (in Japanese); See also `https://newsroom.toyota.co.jp/en/corporate/21139684.html`

[6] Y. Harashima *et al*, in preparation.

Efficient Sampling Simulation of the Soft Modes Significantly Contribute to Protein Properties

Kazuhiro TAKEMURA, Duy TRAN, Hiroaki HATA, Kenichiro TAKABA, Ai SHINOBU, and Akio KITAO

School of Life Science and Technology, Tokyo Institute of Technology

Ookayama, Meguro, Tokyo 152-8550

Last year, we reported a simple but efficient and accurate method to generate protein-ligand complex structures, called Concentrated ligand Docking (ColDock)[1], which successfully predicted several protein-ligand complex structures. This year, we report that ColDock is also successful in observing the effects of amino acid mutations on protein-ligand complex bindings and reproducing binding pose of bulky ligands.

Proteins exert their function by interacting with other proteins or ligands. Accurate prediction of protein-protein/ligand complex structures is a key to understanding the protein function. We proposed ColDock as an efficient but accurate method to generate protein-ligand complex structures using molecular dynamics (MD) simulations at relatively high ligand concentrations. The procedure of ColDock for a given protein-ligand pair is as follows: (i) Multiple ligands are distributed randomly around the protein at relatively high concentration (~100 mM); (ii) Multiple short (100 ns) independent MD simulations are conducted. To prevent ligand aggregations which might be caused by high concentration, extra repulsive forces are applied between the ligands; (iii) The ligands in contact with the protein are selected; (iv) The selected ligands are clustered according to a root-mean-square-deviation of ligand (L-RMSD). The ligand poses are predicted as the representative poses of populated clusters.

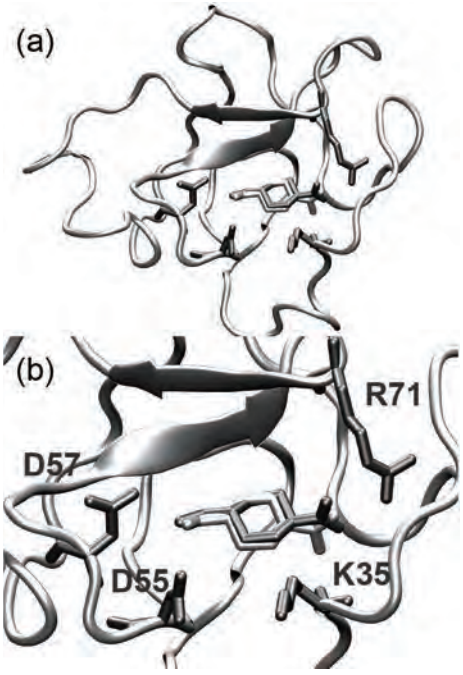

Fig. 1 Predicted (gray) and crystal (white) structures of human plasminogen kringle 4 with AMH. Effects of mutations on the labeled residues were examined.

We examined the effects of amino acid mutations on the complex of plasminogen kringle 4 with transaminomethyl-cyclohexanoic acid (AMH, Fig.1) using ColDock. An experimental study[2] showed that the D55N and R71Q mutations decrease the binding affinity, whereas K35I increases the binding affinity, and no binding was observed in D57N. We observed ligand bindings to all mutants including D57N, for which the binding was not detected experimentally. Consistent with this, only a single unbinding event among all the 50 MD simulations was observed in D57N. ColDock accurately predicted the ligand pose using the wild type (L-RMSD: 1.2 Å. Fig. 1). The populations of the first cluster were 32, 55, 25, 27, and 10 % for WT, K35I, D55N, D57N, and R71Q, respectively. The reported binding free energies of WT, K35I, D55N, and R71Q are −6.53, −6.96, −5.05, and −4.93 kcal/mol, respectively. Thus the simulated population anticorrelated very well with the reported binding free energies. Results indicated that ColDock can investigate the effects of mutations on ligand bindings.

We also examined FK506 binding to FKBP as a more difficult challenge of docking to a bulky ligand. Considering flexibility and size of the ligand, we introduced four interaction sites in each ligand molecule, and successfully prevented aggregation of FK506. In addition, we performed twenty independent 200-ns MD simulations for this target. FK506 molecules entered the binding site in 9 out of 20 simulations. We detected three largely populated clusters in the binding site. Three representative structures reproduced fraction of native contacts very well (> 0.87), and the second-ranked pose showed the lowest L-RMSD (1.2 Å, Fig. 2) among them. Although only one out of twenty trajectories reached to the pose very similar to the crystal structure, the population of the cluster was relatively high due to the stability of the pose. The results imply that ColDock can be also used for the docking of bulky ligands.

Fig. 2 Predicted (black) and crystal (white) structures of FK506 to FKBP

References

[1] K. Takemura, C. Sato & A. Kitao. J Phys Chem B 122, 7191-7200 (2018).

[2] J.H. Graversen, B.W. Sigurskjold, H.C. Thogersen, M. Etzerodt, Biochemistry, 39, 7414-9 (2000).

Multiple-Q states of the frustrated Heisenberg model on the honeycomb lattice

TOKURO SHIMOKAWA[1] and HIKARU KAWAMURA[2]
[1]*Okinawa Institute of Science and Technology Graduate University, Onna, Okinawa, 904-0495, Japan*
[2]*Department of Earth and Space Science, Graduate School of Science, Osaka University, Toyonaka, Osaka 560-0043, Japan*

Motivated by a theoretical study by Okubo *et al* [1] of the possible realization of the triple-q skyrmion-lattice state in the J_1-J_2 or J_1-J_3 triangular-lattice Heisenberg model, we here investigate the ordering properties in the J_1-J_2 classical honeycomb-lattice Heisenberg model under magnetic field.

The Hamiltonian of the honeycomb-lattice Heisenberg model is given by,

$$\begin{aligned}\mathcal{H} = &- J_1 \sum_{\langle i,j \rangle} \mathbf{S}_i \cdot \mathbf{S}_j - J_2 \sum_{\langle\langle i,j \rangle\rangle} \mathbf{S}_i \cdot \mathbf{S}_j \\ &- H \sum_i S_i^z, \end{aligned} \tag{1}$$

where $\mathbf{S}_i = (S_i^x, S_i^y, S_i^z)$ is the classical Heisenberg spin with the fixed length of $|\mathbf{S}_i| = 1$ located at the i-th site on the honeycomb lattice, $J_1 < 0$ and $J_2 < 0$ represent the antiferromagnetic NN and NNN interactions, while the $\sum_{\langle i,j \rangle}$ and $\sum_{\langle\langle i,j \rangle\rangle}$ are taken over the NN and NNN pairs J_1 and J_2, respectively.

This model has been known that the ground state of the model in zero field exhibits, for $J_2/J_1 > 1/6$, a single-q helical order with an incommensurate wavevector with an infinite ring-like degeneracy in the q-space, while, for $J_2/J_1 \leq 1/6$, the standard two-sublattice antiferromagnetic order [2]. Finite-temperature ordering properties in zero field have also been investigated by Okumura *et al* [3], and then only a single-q helical ordered state has been found as an quasi-long ranged ordered state. The in-field ordering process of the present honeycomb-lattice model is a remaining big issue since the interplay between macroscopic degeneracy in the ground state and fluctuations might lead to a intriguing behavior.

We investigate the in-field ordering properties of the model paying attention to the possible appearance of exotic multiple-q states with focusing on the parameter region, $1/6 < J_2/J_1 < 0.5$. We are successful in finding various exotic multiple-q states by means of extensive monte carlo (MC) methods after careful treatment of large finite-size dependences owing to the strong incommensurability. We have summarized our results in two papers.[4, 5]

Our results are obtained by using CPU node of system B. Our MC code is executed in parallel by using both OpenMP and MPI techniques.

References

[1] T. Okubo, S. Chung, and H. Kawamura, Phys. Rev. Lett. **108**, 017206 (2012).

[2] S. Katsura, T. Ide, and T. Morita: J. Stat. Phys. **42**, 381 (1986).

[3] S. Okumura, H. Kawamura, T. Okubo, and Y. Motome, J. Phys. Soc. Jpn. **79**, 114705 (2010).

[4] T. Shimokawa, and H. Kawamura, arXiv:1810.02951.

[5] T. Shimokawa, T. Okubo, and H. Kawamura, arXiv:1902.01582.

Bold Diagrammatic Monte Carlo Studies on the Unitary Fermi Gas

Takahiro OHGOE

Department of Applied Physics,

The University of Tokyo, Hongo, Bunkyo-ku, Tokyo 113-8656

Feynman diagrams are powerful tools for studying various fields of physics. Still, the analysis usually involves approximations, because only some types of diagrams or low-order diagrams are considered there. However, the Monte Carlo method for unbiased sampling of Feynman diagrams has been recently developed [1]. On the other hand, the diagrammatic series sometimes have zero radius of convergence. The question is whether it is still possible to make accurate predictions by summing up Feynman diagrams.

Here we report high-precision results obtained by the bold-line diagrammatic Monte Carlo method for the unitary Fermi gas with zero convergence radius [2]. We derive the large-order asymptotic behavior of the diagrammatic series, and we give mathematical arguments and numerical evidence for the resummability of the series by a specifically designed conformal-Borel method that incorporates the large-order behavior. Combining this new resummation method with diagrammatic Monte Carlo evaluation up to order 9, we obtain new results for the equation of state, which agree with the ultracold-atom experimental data, except for the 4-th virial coefficient for which our data point to the theoretically conjectured value. Furthermore, We obtained our accurate results of Tan's contact [3].

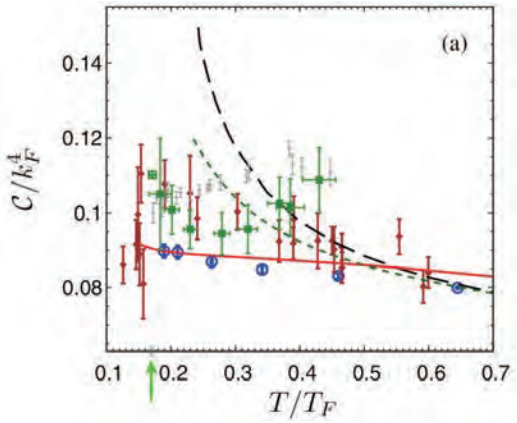

Figure 1: Tan's contact obtained by several methods. Open Circles represent our results.

References

[1] K. Van Houcke, F. Werner, T. Ohgoe, N.V. Prokof'ev and B. V. Svistunov: Phys. Rev. B **99** (2019) 035140

[2] R. Rossi, T. Ohgoe, K. Van Houcke, and F. Werner: Phys. Rev. Lett. **121** (2018) 130405

[3] R. Rossi, T. Ohgoe, E. Kozik, N. Prokof'ev and B. Svistunov, K. Van Houcke, and F. Werner: Phys. Rev. Lett. **121** (2018) 130406

Numerical study on low-energy states of quantum spin systems

Hiroki NAKANO
Graduate School of Material Science, University of Hyogo
3-2-1 Kouto, Kamigori-cho, Ako-gun, Hyogo 678-1297, Japan

It is well known that physical quantities for many-body problems are di cult to estimate precisely; in condensed matter physics, in particular, such many-body problems very often appear. Quantum spin systems are belonging to such many-body problems. To study the systems, therefore, numerical approaches have widely been employed as e ective ones. A lot of computational studies have been carried out and contributed much to our deeper understanding of the target systems.

For quantum spin systems, nowadays, three methods are often used; the numerical diagonalizations, the quantum Monte Carlo (QMC) simulations, and the density matrix renormalization group (DMRG) calculations. Each of them has merits and demerits at the same time. In the QMC simulations, large systems are handled irrespective of their spatial dimensions although the negative sign problem occurs and prevents us from obtaining precise evaluations when the systems include frustrations. The DMRG method is very powerful when a target system is one-dimensional irrespective of the presence of frustrations while this method is still under development for the cases when the spatial dimension of a target system is larger than one. The numerical diagonalization method is applicable irrespective of the presence of frustrations and the spatial dimension; however, this method also has a serious weak point. Namely, this method can treat only very small system sizes. To overcome this disadvantage as much as possible, we successfully developed a hybrid-type parallelized code of Lanczos diagonalization[1]. If we use this Lanczos-diagonalization code that we developed, we can treat various large systems that have not been previously treated yet within this method. So, we examine various quantum spin systems by this method as a primary approach.

In the project in 2018, we tackled three systems. The rst one is the $S = 1/2$ Heisenberg antiferromagnet on the kagome lattice[2]. We examine the magnetization process of this system from our result of a 45-site cluster. This study is the rst one reporting the magnetization process of a spin-1/2 Heisenberg antiferromagnet in the entire range of the magnetization for a 45-site system on an arbitrary lattice structure. From the analysis based on the 45-site result and the ones for systems smaller than the 45-site cluster, it is suggested that the magnetization plateau at the one-ninth height of the saturation does not open in the thermodynamic limit.

The second one is the $S = 2$ Heisenberg antiferromagnet in one dimension[3]. We attempt a precise estimation of the Haldane gap of this system. This system was studied in Ref. [1] where systems up to 16 sites were treated. Due to the situation that the maximum of the treated system sizes was small, a multistep convergence-acceleration procedure was not able to be carried out. Reference [3] successfully treat clusters of 18 and 20 sites additionally. Particularly, the result of the 20-site system has been obtained in a“ Large-scale HPC Challenge ” Project of the Joint Center for Advanced High Performance Computing. The obtained data sequence of the $S = 2$ nite-size spin excitation under the twisted boundary condition successfully give a more precise estimate for the $S = 2$ Haldane gap through the multistep convergence-acceleration proce-

dure.

The third one is the $S = 1/2$ Heisenberg antiferromagnet on the orthogonal-dimer lattice. This system is also called the Shastry-Sutherland model, which includes antiferromagnetic interaction forming the square lattice (J_2) and antiferromagnetic interaction at orthogonal-dimer pairs (J_1). It is well known that this system shows the mathematically exact dimer ground state when J_2/J_1 is small. This model shows, on the other hand, that the Néel-ordered ground state appears in the region of large J_2/J_1. It was pointed out that the plaquette-singlet phase exists in an intermediate region. Reference [4] reports numerical-diagonalization results for 36-site and 40-site clusters that have not been examined yet. Our calculations clearly capture the edge of the dimer phase and the edge of the Néel-ordered phase. Our calculations suggest at the same time that there appears a new boundary which is di erent from the two phase boundaries.

We also carried out calculations for other di erent systems with frustration and studied them in various viewpoints[5, 6, 7, 8, 9, 10]. Our studies contribute to our understandings of the various antiferromagnets and the nontrivial e ect of frustration in magnetic materials.

References

[1] H. Nakano and A. Terai: J. Phys. Soc. Jpn. **78** (2009) 014003.

[2] H. Nakano and T. Sakai: J. Phys. Soc. Jpn. **87** (2018) 063706(1-5)

[3] H. Nakano and T. Sakai: J. Phys. Soc. Jpn. **87** (2018) 105002(1-2)

[4] H. Nakano and T. Sakai: J. Phys. Soc. Jpn. **87** (2018) 123702(1-5)

[5] Y. Fukumoto, Y. Yokoyama, and H. Nakano: J. Phys. Soc. Jpn. **87** (2018) 124710(1-6)

[6] Y. Hasegawa, H. Nakano, and T. Sakai: Phys. Rev. B **98** (2018) 014404(1-9)

[7] T. Sakai and H. Nakano: AIP Adv. **8** (2018) 101408(1-5)

[8] T. Sakai and H. Nakano: Physica B **536** (2018) 85-88

[9] A. Shimada, T. Sakai, H. Nakano, and K. Yoshimura: J. Phys.: Conf. Series **969** (2018) 012126(1-6)

[10] T. Sakai and H. Nakano: J. Phys.: Conf. Series **969** (2018) 012127(1-6)

Microscopic calculation of the flux-flow Hall effect based on the augmented quasiclassical equations

Takafumi KITA
Department of Physics, Hokkaido University
Sapporo, 060-0810

Superconductors exhibit many interesting phenomena distinct from normal states, such as the sign change of the flux-flow Hall coefficient as a function of temperature or magnetic field. It has been pointed out that this sign change is closely related to the charge accumulated around the vortex core region. We have studied this vortex-core charging microscopically, including the mechanism of charge accumulation.

It has been elucidated that the vortex-core charging is caused by three forces: (i) the Lorentz force that acts on supercurrent, (ii) pair-potential-gradient (PPG) force, and (iii) the pressure difference arising from the slope in the density of states. London first included the Lorentz force in his phenomenological equations of superconductivity [1], and predicted emergence of net charge due to the Hall effect whenever supercurrent flows. The PPG force was first discussed by Kopnin [2]. In recent years, microscopic studies on flux-flow Hall effect has been carried out based on the augmented quasiclassical equations in the Keldysh formalism with the Lorentz and PPG forces [3]. The pressure difference arising from the slope in the density of states was first proposed by Khomskii and Freimuth [4]. Despite all these studies, the vortex-charging had not been fully understood microscopically. This is because all the force terms for describing charging are missing from the standard Eilenberger equations, which are also called quasiclassical equations of superconductivity and have been used extensively to study superconductors in a magnetic field microscopically. Very recently, we have derived augmented quasiclassical equations that incorporate all the terms responsible for charging. Using it, we have studied charging of a single vortex in three-dimensional s-wave superconductors. However, the magnetic field dependence of the vortex-charging in the Abrikosov lattice has not been fully calculated. Therefore, we calculated the magnetic field dependence of the vortex-core charging in two-dimensional s-wave superconductors due to the Lorentz and PPG forces by using the augmented quasiclassical equations in the Matsubara formalism. The force caused from the slope in the density of states is absent for this case with the cylindrical Fermi surface.

The charge caused by the Lorentz force has a strong field dependence with a peak and can be enhanced substantially from the value of an isolated vortex [6]. On the other hand, the charge caused by the PPG force decreases as the field is increased and may change its sign(Figure 1). The parameters of this system are the coherence length ξ_0, magnetic penetration depth λ_0, Thomas–Fermi screening length $\lambda_{\rm TF}$, and quasiclassical parameter δ. Figure 1 show the spatial variation of the charge density around vortex core at $\lambda_0 = 5\xi_0$, $\delta = 0.1\xi_0$, $\lambda_{\rm TF} = \delta$, temperature $T = 0.2T_{\rm c}$, and average flux density $\bar{B} = 0.88B_{\rm c2}$, where $T_{\rm c}$ is critical temperature and $B_{\rm c2}$ is upper critical field, respectively. We unveiled that the vortex charging due to the PPG force cancels the one due

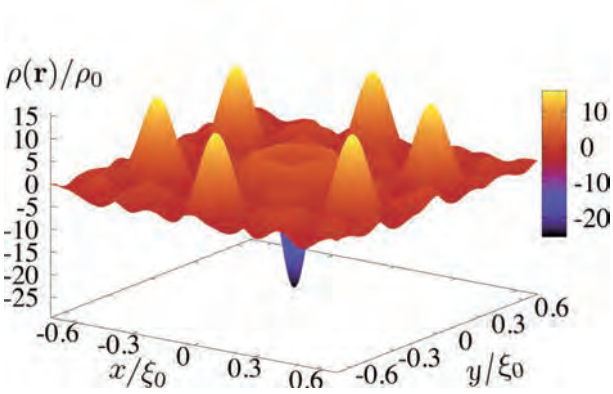

Figure 1: Vortex-charge density $\rho(\mathbf{r})/\rho_0$ in the region $-0.6\xi_0 \leq x/y \leq 0.6\xi_0$ for $\bar{B} = 0.88B_{c2}$ at $T = 0.2T_c$.

to the Lorentz force except at low magnetic field region.

In summary, we have numerically studied the magnetic field dependence of the vortex-core charging caused by the Lorentz and PPG forces in the Abrikosov lattice. The sign of the vortex-core charge due to the PPG force may change as a function of magnetic field. In the near future, we are planning to calculate transport phenomena such as the flux-flow Hall effect and non-reciprocal effect in type-II superconductors.

References

[1] F. London, *Superfluids* (Dover, New York, 1961), Vol. 1, p. 56.

[2] N. B. Kopnin, J. Low Temp. Phys. **97** (1994) 157.

[3] E. Arahata and Y. Kato, J. Low. Temp. Phys. **175** (2014) 364.

[4] D. I. Khomskii and F. V. Kusmartsev, Phys. Rev. B **46** (1992) 14245.

[5] H. Ueki, M. Ohuchi, and T. Kita, J. Phys. Soc. Jpn. **87** (2018) 044704.

[6] W. Kohno, H. Ueki, and T. Kita, J. Phys. Soc. Jpn. **85** (2016) 083705.

Analysis of Many-Body Effects in Bose–Einstein Condensate

Takafumi KITA
Department of Physics, Hokkaido University
Sapporo, Hokkaido, 060-0810

In the Bose–Einstein condensate (BEC), the 3/2-body correlations, which are the two-body processes of the exchanging one particle between condensate and non-condensate, are the sources of the many-body effects. However, it is difficult to incorporate these correlations since they are omitted in the mean-field approximation by Wick's decomposition. In recent years, we constructed the variational wave function for the ground state of the weakly interacting bosons and found that the 3/2-body correlations give a contribution comparable to the mean-field energy toward lowering the ground state energy.[1, 2, 3] Thus, it is expected that the many-body effects change the properties of the BEC system even in the weak-coupling region.

We have developed the variational approach at finite temperatures, which does not depend on the specific form of Hamiltonians, to investigate the contributions of the many-body effects in equilibrium states.[4] We apply this formalism to the weak-coupling Bose–Einstein condensed phase and incorporate the 3/2-body correlations. Unlike the zero temperature formalism, we have to introduce the Matsubara Green's function for Bogoliubov's quasiparticles to evaluate the basic expectations of them. Besides, the self-consistent equations contain some functions with multivariable functions, so that it is necessary to deal with multiple loops for numerical calculations. For those reasons, we need to use the supercomputer in ISSP to perform parallel computing.

Numerical calculations were performed for the contact interaction model $U_k = U = 4\pi a_U/m$, where m is a mass of bosons. We have to introduce a cutoff wavenumber $k_{\rm c}$ to remove the ultraviolet divergence inherent in the potential. We choose $k_{\rm c}$ so that $k_{\rm c}a_U \ll 1$ is satisfied. The units of energy and wavenumber of this system are defined by $\varepsilon_U \equiv U\bar{n}$, $k_U \equiv \sqrt{2m\varepsilon_U}$, where $\bar{n}$ is a particle number density. We take the coupling constant so that $a_U^3\bar{n} \ll 1$ is satisfied corresponding to the dilute ultracold atomic gases. We solved the self-consistent equations in the low temperature region $0 < T < T_{\rm c0}/2$ ($T_{\rm c0}$ is the critical temperature for an ideal system), and compared the results with those of the self-consistent mean-field theory, i.e., Hartree–Fock–Bogoliubov (HFB) approximation.

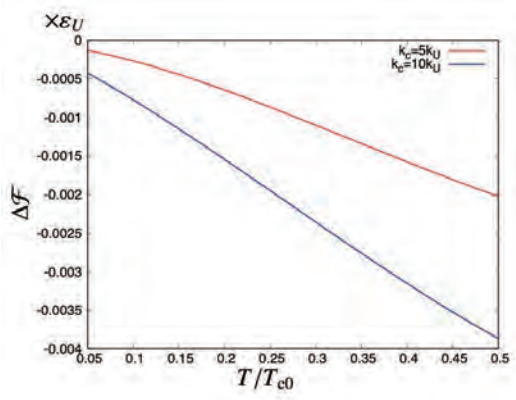

Figure 1: Free energy differences per a particle $\Delta\mathcal{F}$ as functions of T for $a_U^3\bar{n} = 10^{-6}$.

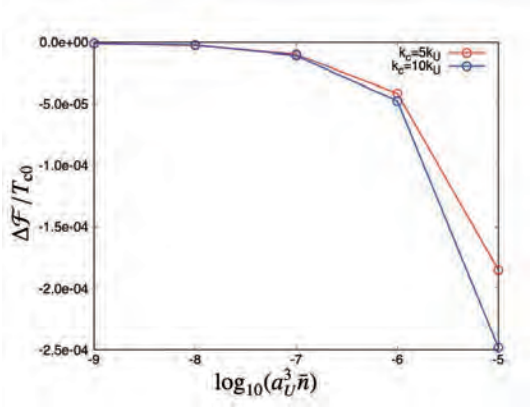

Figure 2: $\Delta\mathcal{F}$ as functions of $\log_{10}(a_U^3\bar{n})$ for $T = 0.3T_{c0}$.

Figure 1 shows the temperature dependence of the free energy. $\Delta\mathcal{F}$ is defined as the difference from the free energy of the HFB approximation. It turns out that the free energy of this system are lowered by the 3/2-body correlations as well as the zero temperature system. We also found that the contribution of the 3/2-body correlations increase with temperature and similar behavior also appears in the coupling constant dependence, as shown Figure 2. Therefore, the 3/2-body correlations should be incorporated self-consistently to investigate the thermodynamic properties even in collisionless regime.

Since the 3/2-body correlations give a finite contribution to the self-energy of the Bogoliubov's quasiparticles, it may be expected the qualitative changing the single-particle excitation as discussed in the zero temperature formalism.[1] Indeed, it turns out that the 3/2-body correlations are mainly contributed in the long wavelength region.

References

[1] T. Kita: J. Phys. Soc. Jpn. **86** (2017) 044003.

[2] W. Kohno, A. Kirikoshi, and T. Kita: J. Phys. Soc. Jpn. **87** (2018) 034002.

[3] W. Kohno, A. Kirikoshi, and T. Kita: J. Phys. Soc. Jpn. **87** (2018) 124004.

[4] A. Kirikoshi, W. Kohno, and T. Kita: J. Phys. Soc. Jpn., in press.

Dynamical DMRG study of spin dynamics in frustrated quantum spin systems

Takami TOHYAMA
Department of Applied Physics, Tokyo University of Science, Tokyo 125-8585

Two-dimensional frustrated quantum spin systems give rise to novel quantum states such as quantum spin liquids and valence bond crystal states owing to the influence of quantum fluctuation and frustration. One of possible systems will be those that have kagome-type structures. Very recently, a spin-1/2 quantum spin compound with square-kagome lattice (SKL), $Cu_6AlBiO_4(SO_4)_5$·KCl, was synthesized [1]. From the crystal structure of this compound, we naturally expect three nonequivalent exchange interactions as shown in Fig. 1. This model will provide a good starting point for studying this compound. The magnetic properties of SKL with the three nonequivalent exchange interactions have not been studied theoretically except for magnetization plateaus [2]. Therefore, it is necessary to investigate magnetic excitations on the SKL for the sake of forthcoming comparison with inelastic neutron scattering experiments.

In this project, we examine magnetic properties of the spin-1/2 Heisenberg model on SKL given by $H = \sum_{\langle i,j \rangle} J_{i,j} \mathbf{S}_i \cdot \mathbf{S}_j$, where $\mathbf{S}_i$ is the spin-$\frac{1}{2}$ operator at site i, $\langle i,j \rangle$ runs over the nearest-neighbor spin pairs, $J_{i,j}$ corresponds to one of J_1, J_2, and J_3 shown in Fig. 1.

Firstly, we theoretically calculate magnetic susceptibility and magnetization curve by finite-temperature Lanczos method and density-matrix renormalization group (DMRG), and compare them with experimental data in $Cu_6AlBiO_4(SO_4)_5$·KCl. We obtain a possible set of exchange interactions that can reproduce their experimental data:

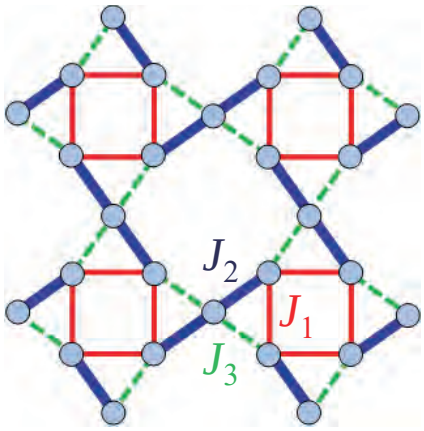

Figure 1: Square-kagome lattice with three nonequivalent exchange interactions.

$J_1 = 135$ K, $J_2 = 162$ K, and $J_3 = 115$ K.

Next we calculate dynamical spin structure factor defined by

$$S(\mathbf{q},\omega) = -\frac{1}{\pi N}\mathrm{Im}\,\langle 0|\, S^z_{-\mathbf{q}} \frac{1}{\omega - H + E_0 + i\eta} S^z_{\mathbf{q}}\,|0\rangle\,,$$

where $\mathbf{q}$ is the momentum in the extended Brillouin zone, $|0\rangle$ is the ground state with energy E_0, η is a broadening factor, and $S^z_{\mathbf{q}} = N^{-1/2}\sum_i e^{i\mathbf{q}\cdot\mathbf{R}_i} S^z_i$ with $\mathbf{R}_i$ being the position of spin i and S^z_i being the z component of $\mathbf{S}_i$. We use dynamical DMRG method for the SKL with system size $N = 48$ in the periodic boundary condition [3]. In our dynamical DMRG, the correction vector is expanded by the Legendre polynomial with a Gaussian averaging [4] and the broadening factor η is replaced by the width of the Gaussian, for which we set 0.1 in units of J_1. The number of states kept in

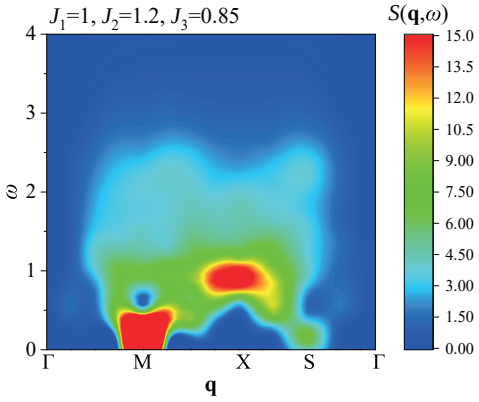

Figure 2: $S(\mathbf{q}, \omega)$ of spin-1/2 SKL Heisenberg model. J_1 is taken to be the unit of energy. The intensity in the contour map is truncated by 15.00 as shown in the intensity bar. The maximum value of intensity is 102 at the M point with $\omega = 0.15$.

the dynamical DMRG is $m = 6000$, leading to truncation error less than 1×10^{-3}.

Figure 2 shows $S(\mathbf{q}, \omega)$ along the symmetric momentum lines. The low-energy excitations less than $\omega = 0.5$ are mainly located at the M point, which indicates the presence of antiferromagnetic order in the present parameter set. However, the high-energy excitations above $\omega = 0.5$ are not given by a simple spin-wave form, but exhibit strong intensity at the X point followed by broad structure extending up to $\omega = 2$. These high-energy features may come from competing interactions giving rise to magnetic frustration. The change of intensity distribution in the momentum space between $\omega = 0.4$ and $\omega = 1$ is clearly seen in Fig. 3.

A recent preliminary result of inelastic neutron scattering experiment on polycrystalline sample of $Cu_6AlBiO_4(SO_4)_5 \cdot KCl$ reported low-energy excitations whose position does not correspond to the M point [1]. This inconsistent behavior between theory and experiment may require another parameter set of exchange interactions. This will be solved

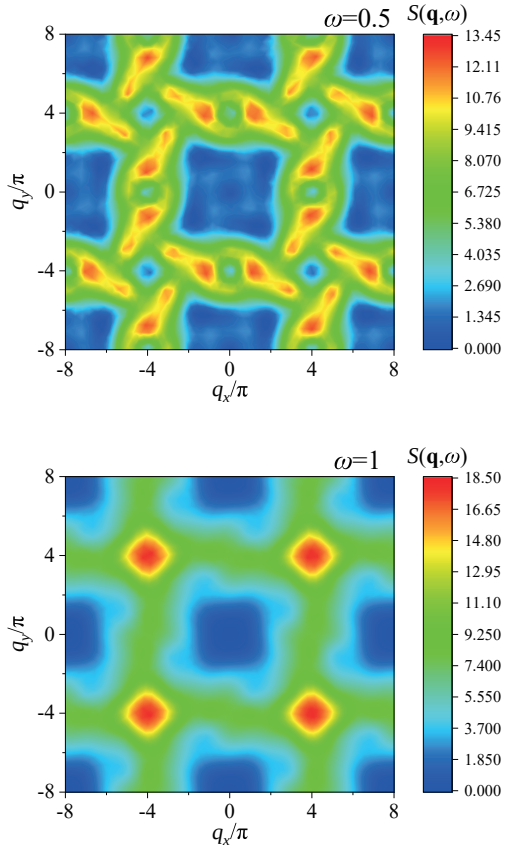

Figure 3: Intensity map of $S(\mathbf{q}, \omega)$ in the extended Brillouin zone at $\omega = 0.5$ (upper panel) and $\omega = 1$ (lower panel).

in the near future.

References

[1] M. Fujihala, K. Morita, S. Mitsuda, T. Tohyama *et al.*: unpublished.

[2] K. Morita and T. Tohyama: J. Phys. Soc. Jpn. **87** (2018) 043704.

[3] K. Morita and T. Tohyama: unpublished.

[4] S. Sota and T. Tohyama: Phys. Rev. B **82** (2010) 195130.

Numerical study of phase transition in non-equilibrium systems

Kenji HARADA
Graduate School of Informatics, Kyoto University, Kyoto 606-8501, Japan

We can define the phase of a macroscopic system out of equilibrium based on physical order parameters on a non-equilibrium steady-state distribution. The phase transition is confirmed theoretically and experimentally in many studies. However, we have little understanding of the informational aspect of a macroscopic non-equilibrium system. Recently, Wood *et al.* [1] analytically calculate the statistical Rényi entropy of the asymmetric exclusion process (ASEP). The phase boundary defined by the behavior of the Rényi entropy agrees with the conventional phase boundary of ASEP for three non-equilibrium phases. It shows the potential power of informational quantities. However, computation of the entropy is technically difficult; no method is known for the Monte Carlo simulation of a non-equilibrium system. Therefore, the knowledge about the informational aspect of a non-equilibrium system is limited than that of an equilibrium system.

In this study, overcoming the technical difficulty by the tensor network method, we will focus on the informational aspect of a $(1+1)$-dimensional directed percolation (DP) through the Rényi entropy and the entanglement entropy. If we regard a percolating direction of objects as a time direction, the $(d+1)$-dimensional DP corresponds to the d-dimensional reaction-diffusion process. There are generally two phases in a reaction-diffusion process; the active phase with finite density of objects and the inactive phase with zero density in the long-time limit, called the "absorbing" state. As shown in many numerical studies for DP[2], the transition between the active phase and the inactive phase is critical, and the concept of the universality is also extended as the DP universality class. Because of the extreme simplicity, the universality class is expected to be ubiquitous[3].

Using a tensor network scheme, we numerically calculate the time evolution of state probability distribution of DP. We find a universal relaxation of Rényi entropy at the absorbing phase transition point and a new singularity in the active phase where the second-order Rényi entropy has a cusp and the dynamical behavior of entanglement entropy changes from asymptotically-complete disentanglement to finite entanglement. We confirm that the absorbing state, though its occurrence is exponentially rare in the active phase, is responsible for these phenomena. This interpretation provides us with a unified understanding of time-evolution of the Rényi entropy at the critical point as well as in the active phase.

[1] A. J. Wood, R. A. Blythe, and M. R. Evans, *Journal of Physics A: Mathematical and Theoretical*, **50**, 475005(2017).

[2] M. Henkel, H. Hinrichsen, and S. Lübeck, *Non-Equilibrium Phase Transitions. Volume 1: Absorbing Phase Transitions*, volume 1. Springer, 2008.

[3] K.A. Takeuchi, M. Kuroda, H. Chaté, and M. Sano, *Physical Review Letters*, **99**, 234503 (2007).

Numerical studies of topological phases and bulk-edge correspondence

Y. Hatsugai
Department of Physics, University of Tsukuba
1-1-1 Tennodai, Tsukuba 305-8571, Ibaraki, Japan

As for the topological phases, the bulk is usually hidden in a sense that the system without boundaries is characterized by the absence of low energy excitation. Still the phase is topologically non trivial implies that there is some toplogical quantity that is associated with the bulk. The Chern number of the bulk and the Berry phases are typical examples. They are, however, mostly invisible experimentally except the case of the quantum Hall effects. Experimentally observables of the topological phases are boundary states and/or impurities states, as generic edge states, reflecting special feature of the bulk. This is the bulk-edge correspondence[1]. It universal validity is established in various systems from the quantum Hall effects to toplogical mechanics.

In relation to the bulk-edge correspondence, we have performed several numerical studies.

As for a typical example of the classical mechanics in 3D, we have considered "mechanical diamond" as a spring mass model in 3D. The Weyl points in the mechanical dispersion are discussed in relation to the breakdown of the chiral symmetry and the mechanical Fermi-arc as mechanical edge states are demonstrated[2]. Fractionally quantized Berry phases are defined and numerically calculated for 1 D quantum spins with Z_N symmetry. Numerical advantages to determine the phase boundary is clearly demonstrated[3]. (See Fig.1)). To reduce numerical resources, the pseudopotential is deduced from a lattice model and the manybody Chern numbers are calculated when there exists an internal degree of freedom. Then the Chern number matrices are evaluated and discussed in relation to the effective theory[4]. When the system is sufficiently large, the system should be insensible to the boundary condition. It implies the integration to define a manybody Chern number is not necessary. We have numerically demonstrated it using a large scale manybody diagonalization[5]. (See Fig.2)). One of the recent hot topics in topological phases is a higher order topological phases. In relation to it, we have performed a machine learning studies[6]. Here characteristic edge states are essential in image recognition. Another new area of topological phases is non-hermitian extension of the system. It raises interesting problem. We have demonstrated a crucial role of the symmetry using numerical calculations.[7]

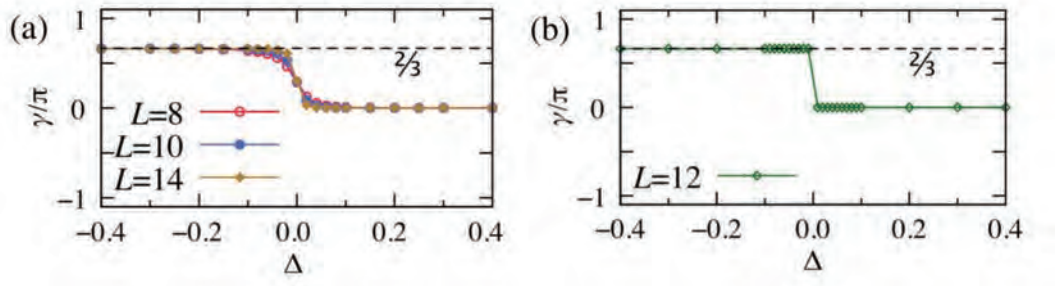

Figure 1: (a):The Berry phase for several system sizes by a usual integration path for Z_3 quantum spins. (b):The quantized Berry phase by an integration path along the high symmetric lines in the synthetic Brillouin zone. [3].

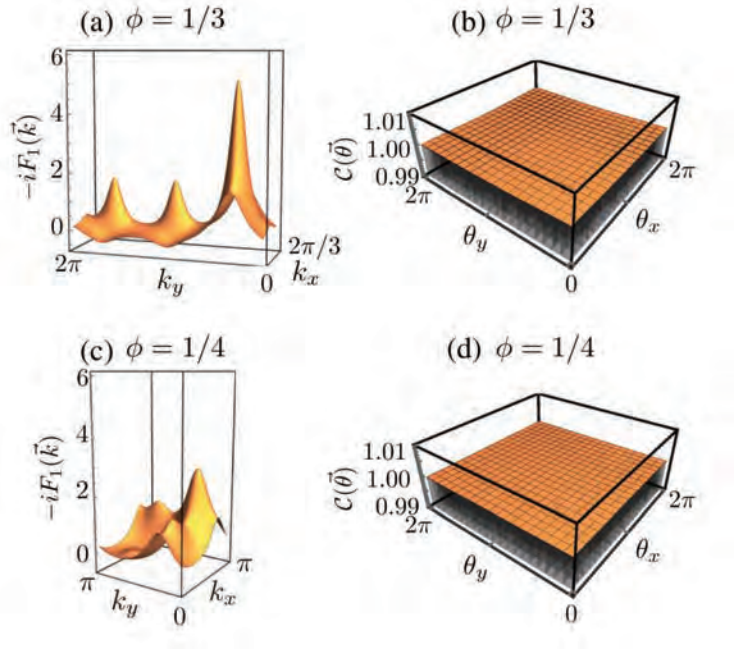

Figure 2: Single-particle Berry curvature (a), (c) and the one-plaquette Chern number (b)(d). The magnetic unit cell is (a): 3×1 and (c): 2×2. The system size is 24×24 for (b) and (d). The flux per plaquette is $\phi = 1/3$ for (a),(b) and $1/4$ for (c), (d). [5].

References

[1] Y. Hatsugai, "Chern Number and Edge States in the Integer Quantum Hall effect", Phys. Rev. Lett. 71, 3697 (1993).

[2] Y. Takahashi, T. Kariyado and Y. Hatsugai, "Weyl points of mechanical diamond", Phys. Rev. B 99, 024102 (2019).

[3] Toshikaze Kariyado, Takahiro Morimoto, and Yasuhiro Hatsugai, "Z_N Berry Phases in Symmetry Protected Topological Phases", Phys. Rev. Lett. 120, 247203 (1-5) (2018).

[4] K. Kudo and Y. Hatsugai, "Fractional Quantum Hall Effect in n = 0 Landau Band of Graphene with Chern Number Matrix", J. Phys. Soc. Jpn. 87, 063701 (1-5) (2018).

[5] Koji Kudo, Haruki Watanabe, Toshikaze Kariyado, and Yasuhiro Hatsugai, "Many-Body Chern Number without Integration", Phys. Rev. Lett. 122, 146601 (1-5) (2019), (Editors' Suggestion).

[6] H. Araki, T. Mizoguchi and Y. Hatsugai, "Phase diagram of a disordered higher-order topological insulator: A machine learning study", Phys. Rev. B 99, 085406 (1-8) (2018).

[7] Tsuneya Yoshida, Robert Peters, Norio Kawakami, and Yasuhiro Hatsugai, "Symmetry-protected exceptional rings in two-dimensional correlated systems with chiral symmetry", Phys. Rev. B 99, 121101(R)(1-5) (2019). a

Assembly process and mechanical properties of crystalline polymers by largescale coarse-grained molecular dynamics simulation

Yuji HIGUCHI
Institute for Solid State Physics, University of Tokyo
Kashiwa-no-ha, Kashiwa, Chiba 277-8581

We have studied deformation and fracture processes of polyethylene [1, 2] and double-network gels [3] using coarse-grained molecular dynamics simulations. This year, assembly process and mechanical properties of crystalline polymers were studied. For the improvement of the mechanical properties, to reveal the role of molecular structures on the stress transmitting processes during the stretching is essential. Thus, two different models of the lamellar structure consisting of amorphous and crystalline layers are stretched by large-scale coarse-grained molecular dynamics simulations on System B.

First, the lamellar structure consisting of 4×10^6 monomers is prepared. To reveal the role of molecular structures, tie chain rich and entanglement rich models are successfully constructed, where tie chains and entanglements connect solid crystalline layers in amorphous layers. Figure 1(a) shows the deformation and fracture processes in entanglement rich model. During the stretching simulations, tie chains and entanglements indeed transmit the stress. At low strain, the roles of these molecular structures are similar. At void generation, the tie chains are more important because of the rapid relaxation of the entanglements. On the other hand, entanglements delay void generation and its growth (Fig. 1(b)). Thus, the stress transmitting processes in the lamellar structure of crystalline polymers at the molecular level are successfully revealed.

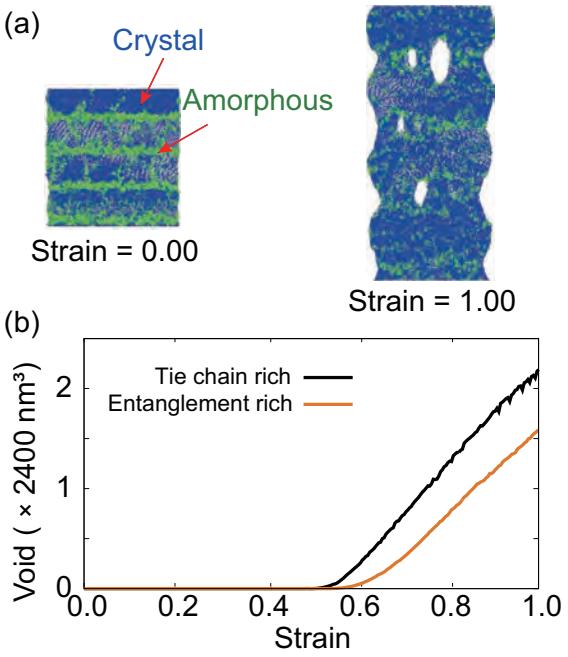

Figure 1: The deformation and fracture processes of the lamellar structure. (a) Cross-sectional snapshots in entanglement rich model. (b) Void generation and growth processes for two different models.

References

[1] Y. Higuchi and M. Kubo: Macromolecules **50** (2017) 3690.

[2] Y. Higuchi: Polym. J. **50** (2018) 579.

[3] Y. Higuchi, K. Saito, T. Sakai, J. P. Gong, and M. Kubo: Macromolecules **51** (2018) 3075.

Probable microscopic pathway of GeI_4's liquid–liquid transition

Kazuhiro Fuchizaki and Hiroki Naruta
Department of Physics, Ehime University, Matsuyama 790-8577
Takahiro Sakagami
Material Group Technology Center, AGC Techno Glass Co., Ltd., Shizuoka 421-0302

Stanley and Teixeira pioneered in 1980 that the thermodynamic anomalies in water are ascribable to the phenomena associated with a percolation transition of hydrogen bonds [1]. The nature of liquid–liquid transitions (LLTs) has been elucidated on thermodynamic basis [2]. However, to our knowledge, there has been no quantitative discussion on a microscopic basis. In particular, a relation between a liquid-liquid transition and a percolation transition has remained unanswered after the Stanley–Teixeira work.

Recently, we have shown that liquid GeI_4 undergoes a pressure-induced crossover from the low-pressure to high-pressure liquid state [3]. Here, we examine a possible microscopic pathway of the crossover by conducting an isothermal–isobaric molecular dynamics simulation. We prepared three sizes of a system consisting of 216, 1000, and 2744 molecules to allow a finite-size scaling analysis. The model employed was composed of rigid tetrahedral molecules interacting via iodine centers connected by Lennard-Jones (LJ) interaction. The LJ parameters were adjusted to reproduce the density at ambient conditions and the melting curve [4]. The deviation of the model's melting curve from the real one amounts to 40% at 1 GPa [4]. The molecular configurations generated for a 2744-system by the simulation were also used as initial inputs to a reverse Monte Carlo (RMC) analysis [5] of the experimental structure factor.

A polymerization scenario of the LLT of GeI_4 [6]

We define a physical bond between the nearest intermolecular iodine sites satisfying the conditions of forming the metallic I_2 bond. We then focus on the formation of molecular clusters in dynamic networks of the bonds. The clusters, which are mainly formed by molecules whose nearest pairs are in edge-to-edge, face-to-edge, and vertex-to-edge orientations, grow as pressure increases.

We could quantify the growth of clusters in an N-molecule system in terms of the percolation probability P and the mean cluster size S as functions of pressure p. We then evaluated the onset of percolation $\bar{p}$, which was observed below 1 GPa, and the width Δ of the transition region. We assumed the following system-size dependences for $\bar{p}$ and Δ: $\bar{p} - p_c \sim \Delta \sim N^{-1/\nu'}$, which allowed us to estimate the threshold pressure p_c in an infinite system. The scaling hypothesis indeed worked to give $p_c = 0.85(1)$ GPa and the exponent $\nu' = 4.2$. When the finite-size effects are taken into consideration, i.e., the correlation length $\xi \sim |p - p_c|^{-\nu'}$ is replaced by N, both P and $SN^{-\gamma'/\nu'}$ (with $\gamma'/\nu' \simeq 0.57$) could be consistently expressed by the universal functions of $z = (p - p_c)N^{1/\nu'}$.

We do not consider that the threshold pressure is located near the extension of the boundary between the two liquid phases is not a coincidence. We thus speculate that the liquid–

liquid crossover of GeI_4 is brought about by percolation of molecular networks.

The same microscopic scenario may apply to the LLT of liquid SnI_4, which offers similar polyamorphism. However, possible heterogeneity induced in the system before the transition would make the environment around molecules less random. A kind of bootstrap mechanism thus introduced could be reflected in the discontinuous nature of the LLT of SnI_4 if the percolation transition occurs below the liquid–liquid critical-point temperature.

Pressure-induced local symmetry breaking upon LLT of GeI_4 and SnI_4 [7]

Pressure-induced structural change in liquid SnI_4 and GeI_4 was known to be reflected in a shift of the broad peak at $\sim$ 7.5 $Å^{-1}$ of the structure factor (SF) toward lower wavenumbers [8, 3]. That is, the intramolecular Sn–I or Ge–I bond length seemed to be elongated upon compression as has been confirmed by the peak shift in the radial distribution functions [8, 3], Fourier inverted from the SFs. This curious "elongation" of the bond length has remained unresolved although we have used this aspect to judge whether the LLT occurs.

Applying the RMC method to infer the microscopic structure of liquid SnI_4 and GeI_4 offered an opportunity to address this issue. The RMC result suggested that both SnI_4 and GeI_4 molecules seem to be squashed in one direction upon compression. This speculation was confirmed by comparing the symmetry-adapted intramolecular SF, whose mathematically exact expression is obtainable, with the experimental SF.

The reduction of molecular symmetry from T_d to C_{3v} of GeI_4 molecules starts at such a low pressure as 1.5 GPa in the crossover region upon compression. We speculate that the symmetry lowering might be a precursor to the LLT because the interaction between molecules with lower symmetry can give rise to a potential function characterized by *two-length* scales [9]. The pressure-induced symmetry lowering of SnI_4 may occur in a narrow pressure range just below the LLT pressure of 1.5 GPa. The range is so narrow that the lowering could not be detected in our measurements carried out at rough pressure intervals [8]. However, the prior lowering of local symmetry is strongly expected considering a remarkable similarity in polyamorphic nature between SnI_4 and GeI_4. A local structural probe such as XAFS will be effective to confirm this prediction.

We have thus far used the model consisting of rigid molecules to discuss not only thermodynamic but also structural properties of liquid SnI_4 and GeI_4. The latter study made us realize the significance of molecular deformation on an LLT. We are now developing a new model in which molecules are deformable.

References

[1] H. E. Stanley and J. Teixeira, J. Chem. Phys. **73**, 3404 (1980).

[2] M. A. Anisimov *et al.*, Phys. Rev. X **8**, 011004 (2018).

[3] K. Fuchizaki *et al.*, J. Phys.: Condens. Matter **30**, 045401 (2018).

[4] K. Fuchizaki and Y. Asano, J. Phys. Soc. Jpn. **84**, 064601 (2015).

[5] R. L. McGreevy, J. Phys.: Condens. Matter **13**, R877 (2001).

[6] K. Fuchizaki *et al.*, J. Phys.: Condens. Matter **31**, 225101 (2019).

[7] K. Fuchizaki *et al.*, J. Chem. Phys. **150**, 114501 (2019).

[8] K. Fuchizaki *et al.*, J. Chem. Phys. **130**, 121101 (2009).

[9] E. A. Jagla, J. Chem. Phys. **111**, 8980 (1999).

Coarse grained MD simulation for fracture and reinforcement of polymer materials

Katsumi HAGITA

Department of Applied Physics,

National Defense Academy, Hashirimizu, Yokosuka, Kanagawa 239-8686

We have studied polymer materials through coarse grained MD simulations for their fracture and reinforcement. We focused on the following three subjects.

1) Fractures of polymer materials such as polyethylene including scission of main chains. Understanding of molecular mechanism and model development using various simulations.

2) Relationships between reinforcement and structure, and fracture and structure through coarse grained (CG) MD simulations.

3) Reinforcements and fractures of filler-filled rubber materials through CGMD simulations.

Especially, this year, we focused on the following research topics.

a) Crystallizations of polyethylene (PE) [1,2]. Comparison between ring and linear melts [1]. Structure formation of a quenched single polyethylene chain [2] to compare force fields.

b) Nanovoids (early fractures) in elongated polymer networks with crosslink [3] and with crosslink and nanoparticles [4].

c) Two-dimensional scattering patterns (2DSPs) in CGMD simulations. [3-9]

d) Reinforcements of filler-filled polymer materials. [3-6, 10]

e) Developments of simulation methods of coarse-grained models [11-13]

f) Visualization methods of material systems [14,15]

Regarding the subject 1), crystallization-behaviors of PE chains were studied through the topic a) in order to obtain a crystallized structure quickly. For PE, we found that united atom (UA) model with Deriding force fields provided acceleration of the crystallization process due to distribution of torsional angles [1,2]. Here, UA model can be regarded as a coarse-grained model of all-atomic simulations. LAMMPS was used for massive parallel simulations. We also investigated ReaxFF simulations using LAMMPS for continuing works from initial structure created by UAMD. Here, ReaxFF can be regarded as a coarse-grained model of DFT calculations.

Concerning the subject 2), 2DSPs originated from structure were investigated for the cases of phase-separation of ABA block copolymer [7] and nanovoids of crosslinked polymers [3] under stretching. For these topics, LAMMPS was used for massive parallel simulations. The analysis code to compute 2DSPs was developed

from scratch. As forthcoming works, studies of machine/deep learning for relationship between 2DPSs and stress-strain curves are in progress.

On the subject 3), CGMD simulations of polymer materials filled with nanoparticles [4, 6, 8] and clay (disc) [5]. Behaviors of 2DSPS were examined. For these topics, LAMMPS was used for massive parallel simulations. In addition, SMP parallelized version of OCTA/cognac was used for continuing researches. The analysis code to compute 2DSPs was developed from scratch. Moreover, particle-mesh version of two-dimensional pattern reverse Monte Carlo modeling was developed, modelling from 2DSPs of NPs in gels by CGMD simulations [8] were compared with reference NP-structure, and several verifications of actual experimental were carried.

Acknowledgement

These works were partially supported by JSPS KAKENHI, Japan, grant no.: JP18H04494. For these works, computing resources by the “Joint Usage/Research Center for Interdisciplinary Large-scale Information Infrastructures” and “High Performance Computing Infrastructure” were also contributed.

References

[1] K. Hagita, S. Fujiwara and N. Iwaoka: J. Chem. Phys. **4** (2019) 3990-3999.

[2] K. Hagita, S. Fujiwara and N. Iwaoka: AIP Advances **8** (2018) 115108.

[3] K. Hagita: Polymer **147** (2018) 247-259.

[4] K. Hagita Polymer (2019) in press.

[5] K. Hagita, Y. Shudo and M. Shibayama: Polymer **154** (2018) 62-79.

[6] K. Hagita Polymer **160** (2019) 65-72.

[7] K. Hagita, T. Tominaga, K. Akutagawa and H. Jinnai: Soft Matter **15** (2019) 926-936.

[8] K. Hagita: Polymer **166** (2019) 155-168.

[9] K. Hagita, T. Murashima and N. Iwaoka: Polymers **10** (2018) 1224.

[10] K. Hagita, T. Higuchi and H. Jinnai: Scientific reports **8** (2018) 5877.

[11] N. Iwaoka, K. Hagita and H. Takano: J. Chem. Phys. **149** (2018) 114901.

[12] K. Hagita and Y. Senda: J. Phys. Soc. Jpn., **87** (2018) 114803.

[13] T. Murashima, K. Hagita and T. Kawakatsu: J. Soc. Rheol. Jpn. (Nihon Reoroji Gakkaishi) **46** (2018) 207-220.

[14] K. Hagita, S. Matsumoto and K. Ohta: ACS Omega **4** (2019) 3990-3999.

[15] K. Hagita, Y. Kawazoe and M. Ogino: AIP Advances **9** (2019) 035001.

Large-Scale Molecular Dynamics Simulation Study on the Crystallization Mechanism of Water Including Air Molecules

Hiroki NADA

National Institute of Advanced Industrial Science and Technology (AIST),

16-1 Onogawa, Tsukuba, Ibaraki 305-8569

Studies on the crystallization mechanism of water including air molecules are important in connection with such issues as the formation of snow and ice crystals in nature. Molecular dynamics (MD) simulations are helpful tools to analyze the crystallization mechanism for real materials at the molecular level.

This study focused on the crystallization of water including air molecules in the upper region of troposphere, where metastable cubic ice (Ic) crystals are formed [1]. Since growth shapes of real Ic crystals are covered with {111} planes, an MD simulation was performed for an interface between an {111} plane of cubic ice and water including N_2 molecules. A modified six-site model was used to estimate the interaction between a pair of water molecules [2]. The potential of N_2 molecules was estimated using a model proposed by Murthy et al. [3].

The simulation indicated the growth of ice at the interface. Interestingly, the grown ice contained partly the structure of hexagonal ice (see arrows in Fig. 1). To infer whether the grown ice structure was affected by N_2 molecules, an MD simulation was also performed for the interface between an Ic {111} plane and pure water. This additional simulation did not show the hexagonal ice structure in the grown ice at the interface.

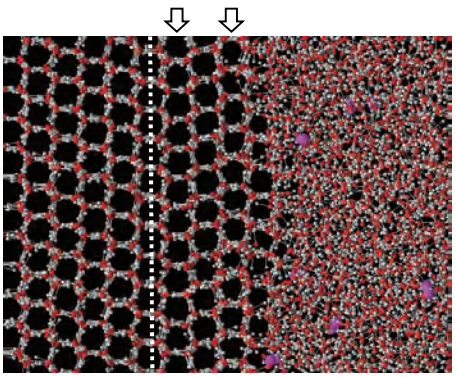

Fig. 1: Snapshots of water and N_2 molecules near the interface during growth. N atoms are represented by large pink spheres. The dashed line shows the initial position of the interface. Parts of the grown ice marked by arrows indicate the formation of hexagonal ice structure.

References

[1] T. Takahashi and T. Kobayashi: J. Cryst. Growth **64** (1983) 593.

[2] H. Nada, J. Chem. Phys. **145** (2016) 244706.

[3] C. S. Murthy, K. Singer, M. L. Klein, and I. R. McDonald, Mol. Phys. **41** (1980) 1387.

Analysis of Formation Mechanism of Calcium Phosphate Crystal by Large-Scale Molecular Dynamics Simulation Combined with Metadynamics Method

Hiroki NADA

National Institute of Advanced Industrial Science and Technology (AIST),

16-1 Onogawa, Tsukuba, Ibaraki 305-8569

Predicting crystal structures and their atomic-scale crystallization mechanisms for a multicomponent system, which has not yet been examined experimentally, using computer simulations largely contributes to the development of functional materials. Molecular dynamics (MD) simulations are helpful tools to analyze crystallization mechanisms at the atomic level. However, it is quite difficult to search for crystal structures that can be formed in a complicated multicomponent system using MD simulations, because the timescale of MD simulations is much shorter than that of crystallization in real systems.

Metadynamics (MTD [1]) is an enhanced sampling simulation method in which the transition of a system between different states is accelerated by increasing the probability of reaching high-energy states. The MTD method affords a free energy landscape that represents the thermodynamic stabilities of all possible structures of a system. Thus, if the MTD method is combined with an MD simulation, the thermodynamic stabilities of all possible crystal structures can be determined definitively, even if the simulation run is not very long.

In this study, an MD simulation combined with the MTD method was used to investigate the crystallization mechanism of calcium phosphates, which have been used for biomaterials. The simulation was performed for amorphous calcium phosphate (ACP), because the crystallization of calcium phosphates frequently occurs from ACP. Simulation results implied that the formation of metastable octa calcium phosphates (OCP) is kinetically preferable rather than the formation of hydroxy apatite (HAP). The results are qualitatively consistent with experimental observations reported so far.

References

[1] A. Laio and M. Parrinello: Proc. Natl. Acad. Sci. USA **99** (2002) 12562.

Construction of coarse-graining spin model and analysis of the coercivity

Taichi Hinokihara

Institute for Solid State Physics,

The University of Tokyo, Kashiwa-no-ha, Kashiwa, Chiba 277-8581

We have studied an atomistic scale classical spin model to analyze the coercivity of magnet. The coercivity depends on various features from microscopic properties, such as exchange couplings, to macroscopic properties, such as demagnetization field induced from the dipole-dipole interactions. Thus, it is one of the challenging problems to evaluate coercivity [1].

This year, we first focused on the construction of a new coarse-graining method that can treat temperature fluctuations. The micromagnetic model, which is frequently used to evaluate the coercivity, is only valid for the zero-temperature simulation. However, since the coercivity relates to the magnetization reversal process, which occurs stochastically, the new coarse-graining method that can take into account the thermal fluctuations are essential. We constructed the coarse-graining model by using the concept of the block spin transformation. As a result, we confirmed that our model well reproduces the domain-wall width and magnetizations.

Second, we constructed a new efficient method that can simulate spin dynamics with long-range interactions [2]. We implemented the stochastic cut-off (SCO) method into the time quantified Monte Carlo (TQMC) method. The new method, which we call TQMC+SCO method, can simulate the spin dynamics efficiently even in the case of the amorphous-like systems. In the case of three-dimensional systems, the computational time for the time step is proportional to $O(\beta N \ln N)$.

References

[1] S. Miyashita, et. al.: Scripta Materialia **154** (2018) 259.

[2] T. Hinokihara, Y. Okuyama, M. Sasaki, and S. Miyashita: arXiv: 1811.00237

Study on Complex Systems by Generalized-Ensemble Algorithms

Takuya HAYASHI, Daiki MATSUBARA, and Yuko OKAMOTO

Department of Physics, Graduate School of Science, Nagoya University

Furo-Cho, Chikusa-ku, Nagoya, Aichi 464-8602

Despite the experimental discovery of the residual entropy of ice Ih in the 1930's [1], highly accurate measurements have yet to be made in experiments. The calculation started from Pauling in the 1930's [2]. As a recent calculation, there are results [3,4] by multicanonical simulations [5]. In this work, we aim to drastically improve the accuracy in large scale and complex systems.

The entropy is proportional to a logarithm of the density of states. In order to obtain accurate density of states, we proposed a new method [6] to combine the multicanonical replica-exchange method [7] and replica-exchange Wang-Landau method [8]. The residual entropy is defined by

$$S_0 = k_{\mathrm{B}} \log W \ ,$$

and our latest result is: [9]

$$W = 1.507480 \ \pm 0.000036.$$

We have also developed a two-dimensional replica-exchange method in grand canonical ensemble and studied a Lennard-Jones system [10]. In this simulation, a two-dimensional random walk in temperature and chemical potential is realized. The gas-liquid phase transition was studied where a first-order phase transition curve ends at a second-order phase transition point. After a single simulation run, we could obtain free energy surface and number density as functions of temperature and chemical potential. The latter is shown in Fig. 1.

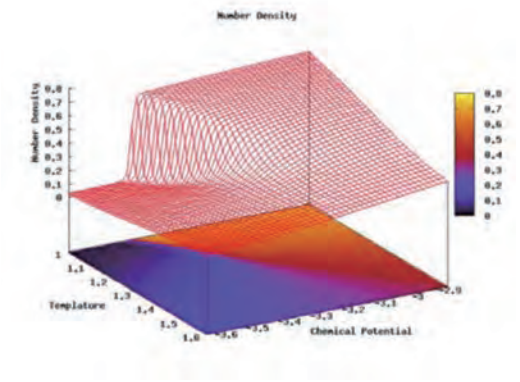

Fig. 1. Number density of a Lennard-Jones system as a function of temperature and chemical potential.

We are now studying the details of the phase transitions in this system using the two-dimensional replica-exchange method that we developed.

References

[1] J. D. Bernal and R. H. Fowler: J. Chem. Phys. **1** (1933) 515.

[2] L. Pauling, J. Am. Chem. Soc. **57** (1935) 2680.

[3] B. A. Berg, C. Muguruma, and Y. Okamoto, Phys. Rev. B **75** (2007) 092202.

[4] B. A. Berg, C. Muguruma, and Y. Okamoto, Mol. Sim. **38** (2012) 856.

[5] B. A. Berg and T. Neuhaus, Phys. Rev. Lett. **68** (1992) 9.

[6] T. Hayashi and Y. Okamoto, arXiv:1901.01430v1 (2019).

[7] Y. Sugita and Y. Okamoto, Chem. Phys. Lett. **329** (2000) 261.

[8] T. Vogel, Y. W. Li, T. Wüst and D. P. Landau, Phys. Rev. Lett. **110** (2013) 210603.

[9] T. Hayashi, C. Muguruma, and Y. Okaoto, in preparation.

[10] D. Matsubara and Y. Okamoto, in preparation.

Semiclassical dynamics of quantum spin systems

Takashi MORI
Riken CEMS, Wako 351-0198, Japan

I have studied the semiclassical dynamics of quantum spin systems with long-range interactions [1] using massive parallel computer simulations. In recent years, nonequilibrium dynamics of isolated quantum systems have extensively been studied. It has been observed that some isolated systems exhibit the phenomenon of *prethermalization*, that is the relaxation toward a quasi-stationary state before reaching true thermal equilibrium.

Prethermalization occurs due to several reasons. If the system is close to integrability, prethermalization occurs because of the presence of many quasi-conserved quantities. Here, quasi-conserved quantities are referred to as quantities that look conserved in short-time scales but relax in a longer timescale. It is known that prethermalization occurs in some quantum spin systems with long-range interactions. The mechanism of prethermalization in long-range interacting systems has not been understood.

I have clarified the mechanism of prethermalization in long-range interacting systems. I have proved that long-range interacting systems possess a family of quasi-conserved quantities, which explains prethermalization phenomena.

When long-range interaction potential decays as $1/r^\alpha$, where r is the distance between two spins and α satisfies $0 \leq \alpha < d$ with the spatial dimension d, the previous study reported that prethermalization occurs for $\alpha \leq d/2$ but not for $d/2 < \alpha < d$ [2]. However, I theoretically argued that prethermalization in general occurs for any $\alpha \in [0, d)$. The reason why prethermalization does not occur for $d/2 < \alpha < d$ in the previous work [2] is due to the speciality of the model considered. The model in Ref. [2] becomes completely integrable in the classical limit, while I argued that prethermalization should occur for any $\alpha \in [0, d)$ when the model becomes chaotic in the classical limit, which is more generic situation.

In order to support this theoretical prediction, I computed nonequilibrium dynamics of quantum spin systems with long-range interactions by using the method of truncated Wigner approximation, which is a kind of semiclassical approximations of the quantum dynamics. I consider the transverse-field Ising model with long-range interactions, which becomes chaotic in the classical limit. When there is no transverse field, the model becomes identical to the one studied in Ref. [2], and its classical limit leads to a completely integrable system.

As a result, I have found that numerical calculations support the theoretical prediction. Prethermalization occurs for any $\alpha \in [0, d)$ when a non-zero transverse field is applied.

References

[1] T. Mori, J. Phys. A **52**, 054001 (2019)

[2] M. Kastner, Phys. Rev. Lett. **106**, 130601 (2011)

Molecular Dynamics Simulation of Ferroelectrics Using a Shell Model IV

T. Hashimoto
Research Center for Computational Design of Advanced Functional Materials (CD-FMat), National Institute of Advanced Industrial Science and Technology (AIST), Tsukuba Central 2, 1-1-1 Umezono, Tsukuba, Ibaraki 305-8568, Japan

We have studied the structure of amorphous $BaTiO_3$. Amorphous $BaTiO_3$ can be formed by sputtering or molecular beam epitaxy (MBE) onto a substrate. The amorphous perovskites are assumed to have random networks of local bonding units (LBUs). By X-ray absorption fine-structure (XAFS) spectroscopy, the LBU in the amorphous phase was shown to be TiO_6[1]. The extended X-ray absorption fine structure (EXAFS) experiments show the evidence for the edge or face-sharing LBU linkages for amorphous $SrTiO_3$[2]. However, the LBU linkage is not well understood for amorphous $BaTiO_3$ because of the proximity of the Ba L_3 edge to the Ti K edge[1, 2], and it is only expected to be similar to that for amorphous $SrTiO_3$. To the author's knowledge, theoretical studies on the structure of amorphous $BaTiO_3$ are not done except for a classical MD simulations, but the LBU for amorphous $BaTiO_3$ is predicted to be TiO_4[3].

We used the isotropic shell model developed by Tinte *et al*[4]. In the shell model, each atom is composed of a core and a shell. The intra-atomic core-shell interaction is expressed by $V(r) = c_2 r^2/2 + c_4 r^4/24$, where r is the core-shell distance and c_2 and c_4 are parameters. The inter-atomic interaction is through the Coulomb interaction and the Buckingham type shell-shell interaction $V(r) = A\exp(-r/\rho) - C/r^6$, where r is the inter-atomic shell-shell distance and A, ρ, and C are parameters. The cutoff length for the non-bonded interactions were 10.0 Å. The computations were carried out in constant temperature and constant pressure (NPT) ensembles using the code developed by us. The pressure and the temperature were controlled by the Parrinello-Rahman method and the massive Nose-Hoover chain method, respectively. The externally applied pressure was set to 0 Pa.

In this study, the LBU in amorphous $BaTiO_3$ was mainly TiO_6, whitch is in agreement with the XAFS study[1]. The nearest Ti-Ti distance in the amorphous phase was about 1 Å shorter than that in the crystalline phase, and it had a trimodal distribution. It was shown that the trimodal distribution corresponds to apex, edge, and face-sharing LBUs, as expected experimentally for amorphous $SrTiO_3$[2].

References

[1] A. I. Frenkel, Y. Feldman, V. Lyahovitskaya, E. Wachtel, and I. Lubomirsky: Phys. Rev. B **71** (2005) 024116.

[2] A. I. Frenkel, D. Ehre, V. Lyahovitskaya, L. Kanner, E. Wachtel, and I. Lubomirsky: Phys. Rev. Lett. **99** (2007) 215502.

[3] P. P. Phule, P. A. Deymier, and S. H. Risbud: J. Mater. Res. **5** (1990) 1104.

[4] S. Tinte *et al.*: J. Phys.: Condens. Matter **16** (2004) 3495.

Randomness Effects on Spin-Peierls System

Chitoshi YASUDA and Shouta MIYARA
Department of Physics and Earth Sciences, Faculty of Science, University of the Ryukyus, Okinawa 903-0213, Japan

Since the quasi-one-dimensional (quasi-1D) inorganic compound $CuGeO_3$ was synthesized, randomness effects of the spin-Peierls (SP) system have attracted considerable attention. When nonmagnetic impurities are doped in the SP compound, an antiferromagnetic long-range order (AFLRO) is induced. The mechanism is understood by a cluster of magnetic moments induced near an impurity, which is called an 'effective spin'. By substituting nonmagnetic atoms for magnetic atoms, effective spins are induced near the nonmagnetic atoms. Since the effective spins interact through a sea of spin-singlet pairs, the AFLRO is induced. However, Cu nuclear quadrupole resonance (NQR) data contradictory to this interpretation was reported for $CuGe_{1-x}Si_xO_3$: the effective spins are not induced near diluted sites [1]. We need to take the lattice degrees of freedom into account in order to investigate positions of the effective spins.

In preceding projects, we investigated an $S = 1/2$ two-dimensional (2D) antiferromagnetic Heisenberg model composed by the intrachain interaction J coupled to the lattice distortion $\Delta_{i,j}$ and the interchain interaction J' using the quantum Monte Carlo (QMC) simulation with the continuous-imaginary-time loop algorithm [2]. Since this QMC simulation is suitable to parallel computing, we mainly performed parallel computing with the Message Passing Interface. As the result, we found that it is difficult to induce effective spins near diluted sites for large elastic constants, small interchain interactions, and large concentrations of dilution [3]. Furthermore, we estimated the dependence of the staggered magnetization on the concentration of site dilution at zero temperature assuming the situation obtained by the NQR measurements, and found that the AFLRO is induced at low concentrations of dilution [4]. We needed huge-scale numerical simulations for large size $N = 64 \times 64$ and extreme-low temperature $T = 0.0001J$.

In the previous works, we assume that the lattice distortions of the nondiluted chain are not affected by dilution and that they are expressed by those of the nondiluted system. For the quasi-1D magnet $CuGeO_3$, where the strength of the interchain interaction has been suggested to be $J' \sim 0.1$, this assumption seems to be reasonable. In the system with the large interchain interaction, however, the effect would be non-negligible.

In this project, we examine numerical methods to search self-consistently the lattice distortions of the nondiluted chains in the 2D system. In this method, the lattice distortions are optimized with the Lagrange multiplier method under the constraint $\sum_i \Delta_{i,j} = 0$ for all chains. Although the numerical convergence could be confirmed by repeating the calculations for several tens of times in the 1D system, we need large-scale time up to convergence in the 2D system. Therefore, the application of the Wolff algorithm for a calculation of the lattice distortion is under consideration.

References

[1] J. Kikuchi, *et al.*: Phys. Rev. Lett. **88**, 037603 (2002).

[2] S. Todo and K. Kato, Phys. Rev. Lett. **87**, 047203 (2001).

[3] C. Yasuda and S. Miyara: J. Phys. Soc. Jpn. **87**, 014704 (2018).

[4] S. Miyara and C. Yasuda: J. Phys. Soc. Jpn. **87**, 104702 (2018).

Quantitative computation of the dissociation rate of a protein-ligand complex using a manifold-learning technique

Takashi YOSHIDOME

Department of Applied Physics,

Tohoku University, 6-6-05, Aoba, Aramaki, Aoba-ku, Sendai 980-8579

The dissociation rate of a protein-ligand complex can be computed with a Markov state model (MSM) [1]. The model is constructed through the following steps: (i) Classify conformations into states; (ii) Calculate the transition probabilities between the states, and; (iii) Compute observables. We have previously demonstrated that an accurate computation of an observable is possible when a manifold-learning technique is employed for classification [2].

Toward applications of our MSM construction protocol to the computation of the dissociation rate, we first investigated a protocol for automatic determination of the number of states from the results of manifold-learning technique [3]. Trajectory of protein folding/unfolding of a coarse-grained molecular dynamics (MD) simulation was used. We found that automatic determination of the number of states is possible with the silhouette score.

Next, we moved on to construction of the MSMs of the processes of protein unfolding and ligand binding with all-atom MD simulations. After sampling trajectories of the processes, classification into states was performed. We have successfully found the transition state from the trajectories. However, more trajectories were required for quantitative computation of the transition probabilities toward the calculation of the dissociation rate.

The calculations were performed using the L4cpu, L2fat, and F18acc in the system B, and L4cpu in the system C. The programs AMBER16 [4] and CafeMol3.0 [5] were used for the MDs. We used our custom-made programs for constructing the MSMs.

References

[1] B.E. Husic and V.S. Pande, J. Am. Chem. Soc., **140**, 2386 (2018).

[2] R. Ito and T. Yoshidome, Chem. Phys. Lett., **691**, 22 (2018).

[3] R. Ito and T. Yoshidome, J. Phys. Soc. Jpn., **87**, 114802 (2018).

[4] D.A. Case, *et al.*, AMBER 2016, University of California, San Francisco (2016).

[5] H. Kenzaki, *et al.*, J. Chem. Theory and Comput., **7**, 1979 (2011).

Effect of interface on the dynamics of water confined in mesoporous silica

Tomoko MIZUGUCHI[1], Katsumi HAGITA[2], and Susumu FUJIWARA[1]

[1]*Faculty of Materials Science and Engineering, Kyoto Institute of Technology, Matsugasaki, Sakyo-ku, Kyoto 606-8585*
[2]*Department of Applied Physics, National Defense Academy, 1-10-20, Hashirimizu, Yokosuka, Kanagawa 239-8686*

Many studies have been done on water in confinement by both theoretical and experimental techniques and revealed that the properties of confined water may strongly differ from that of bulk water. It is clearly important to properly evaluate the influence of confinement on water, however, water behavior on amorphous surface is much more difficult to predict than that on crystalline surface because the topology of amorphous surface is ill-defined at the atomic level. We thus performed molecular dynamics (MD) simulations of confined water in nanoporous silica using the reactive force field (ReaxFF) [1] and examined the influence of amorphous surface on the physical properties of water. Specifically, the hydrogen bond (H-bond) dynamics was analyzed.

ReaxFF allows us to incorporate bond breakage and formation, which are particularly important on interface, in MD simulations with a lower computational cost than quantum-mechanics-level calculations. We used the ReaxFF parameter sets developed by Yeon and van Duin in 2015 to simulate hydrolysis reaxtions at silica/water interface [2]. All simulations were conducted in the NPT ensemble (T = 300 K and P = 1 atm) using the Nosé-Hoover thermostat and barostat with LAMMPS pre-installed in the supercomputer of ISSP. The ReaxFF MD simulations were carried out with a time step of 0.25 fs through the USER-REAXC package of LAMMPS. It is found that, in ReaxFF calculations using LAMMPS, FlatMPI parallelization is about twice as fast as than MPI/OpenMP Hybrid parallelization.

To investigate the structure and dynamics of water in the inhomogeneous system, we divided the cylindrical pore into hollow coaxial cylinders and calculated the physical quantities in each thin layer as a function of the radial distance from the pore central axis R. Figure 1 shows the average number of H-bonds per oxygen atom $\langle n_{\mathrm{HB}} \rangle$ and the first breakage time of H-bond τ_{on} as a function of R. The approximate location of the pore wall is also displayed, which is defined as the average location of the innermost Si atoms. τ_{on} is calculated using the following equation,

$$\tau_{\mathrm{on}} = \int_0^\infty t P_{\mathrm{on}}(t) dt, \qquad (1)$$

where $P_{\mathrm{on}}(t)$ is defined as the distribution of time from the formation of a H-bond to its destruction [3]. The H-bonds at 8 Å $< R <$ 11 Å have a longer lifetime, although $\langle n_{\mathrm{HB}} \rangle$ does not change from that in the pore center. It is because the H-bonds at 8 Å $< R <$ 11 Å include silanol (Si-OH) on the silica surface. Namely, the H-bonds including silanols are long-lived and lead to slower diffusion of water (not shown) near the surface.

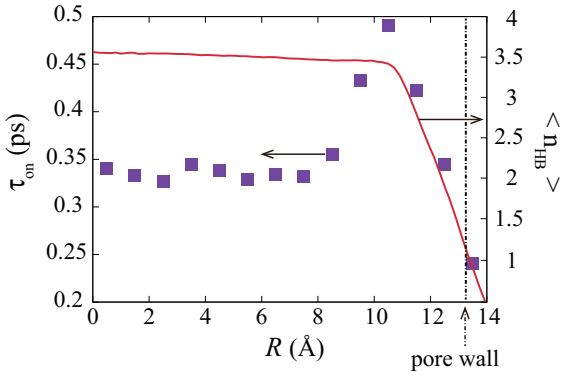

Figure 1: Average number of H-bonds per oxygen atom $\langle n_{\mathrm{HB}} \rangle$ (red solid line, right axis) and first breakage time of H-bond τ_{on} (filled square, left axis) as a function of the radial distance from the pore central axis R. $\langle n_{\mathrm{HB}} \rangle$ The approximate location of the pore wall is also displayed as a dash-dotted line.

References

[1] A. C. T. van Duin, S. Dasgupta, F. Lorant, and W. A. Goddard III: J. Phys. Chem. A **105** (2001) 9396.

[2] J. Yeon and A. C. T. van Duin: J. Phys. Chem. C **120** (2016) 305.

[3] Y. Tamai, H. Tanaka, K. Nakanishi. Macromolecules **29** (1996) 6761.

Numerical study of the off-diagonal ETH in disordered quantum spin chain.

Eiki Iyoda
Department of Physics, Tokai University
Kitakaname, Hiratsuka-shi, Kanagawa 259-1292

Thermalization in isolated quantum many-body systems recently attracts attention, and a plausible mechanism of thermalization is the eigenstate thermalization hypothesis (ETH) [1]. The ETH states that all the energy eigenstates in the microcanonical (MC) energy shell have thermal properties, i.e., the expectation value of an observable $\hat{O}$ approximately equals the MC average:

$$O_{ii} := \langle E_i|\hat{O}|E_i\rangle \simeq \langle \hat{O}\rangle_{\mathrm{MC}}, \tag{1}$$

which is also referred to as the diagonal ETH, because it is written with the diagonal elements. In the same manner, the off-diagonal version of the ETH has been also investigated [2]. The off-diagonal ETH states that

$$O_{ij} := \langle E_i|\hat{O}|E_j\rangle \simeq 0. \tag{2}$$

In this study, we have investigated the (off-)diagonal ETH in disordered quantum spin chains, which exhibit many-body localization transition [3] between the ergodic and the nonerdogic phases. In the disordered phase, the diagonal ETH is not true.

We have numerically investigated the ETHs by using the numerically exact diagonalization. As the indicator of the diagonal ETH, we adopt r defined in Ref. [3]. For the off-diagonal ETH, we calculate the following quantity

$$\Delta := \frac{1}{D(D-1)}\sum_{i\neq j}|O_{ij}|, \tag{3}$$

where D is the dimension of the Hilbert space of the energy shell. The summation is taken over the energy shell. We also calculate the statistical distribution of $|O_{ij}|$.

The Hamiltonian is $1d$ quantum XXZ spin chain with disordered magnetic field.

$$H := \sum_i (S_{\mathrm{x},i}S_{\mathrm{x},i+1} + S_{\mathrm{y},i}S_{\mathrm{y},i+1} + S_{\mathrm{z},i}S_{\mathrm{z},i+1}) + \sum_i h_i S_{\mathrm{z},i}, \tag{4}$$

where h_i is sampled uniformly from $[-h, h]$. We consider a very simple observable $\hat{O} = S_{\mathrm{z},1}$.

Fig. 1 shows h-dependence of r. When h is small, r is small, implying that the diagonal ETH is true. As h becomes larger, r becomes large. This implies that the diagonal ETH is false.

Fig. 2 shows h-dependence of Δ. As h becomes larger, Δ becomes smaller. This implies that the off-diagonal ETH is true in the non-ergodic phase. However, we think that this interpretation is not appropriate. The result is inconsistent with the result of the diagonal ETH. This discrepancy is due to the statistical distribution of $|O_{ij}|$.

Fig. 3 shows h-dependence of $|O_{ij}|$. In the ergodic phase with the weaker disorder, The median, upper quartile, and lower quartile decrease in h, probably because the participation entropy in the non-ergodic phase is small [3]. Thus, most of the energy eigenstates do not contribute to Δ. We consider that the maximum value of $|O_{ij}|$ should characterize the MBL transition of the off-diagonal ETH. The reason why the median and quartiles decrease is that most of the elements $|O_{ij}|$ are much

smaller than ones expected from the random matrix theory.

In this report, we have shown the results for the very simple observable. We also calculate other local observables, and they show similar behavior (not shown). Though the off-diagonal elements for other disorder realizations also show similar behavior, we should analyze systematically and quantitatively with more samples. Investigating non-local observables and other models, which exhibit another phase transition, are future issues.

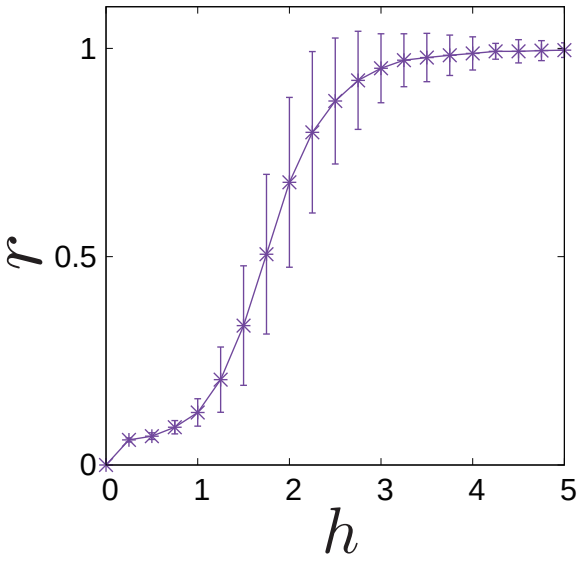

Figure 1: Disorder h-dependence of the diagonal-ETH indicator r. The number of samples is 200.

References

[1] M. Rigol, V. Dunjko, and M. Olshanii, Nature **452**, 854 (2008).

[2] R. Mondaini and M Rigol, Phys. Rev. E **96**, 012157 (2017).

[3] D. J. Luitz, N. Laflorencie, and F. Alet, Phys. Rev. B **91**, 081103 (2015).

[4] H. Kim, T. N. Ikeda, and D. A. Huse, Phys. Rev. E **90**, 052105 (2014).

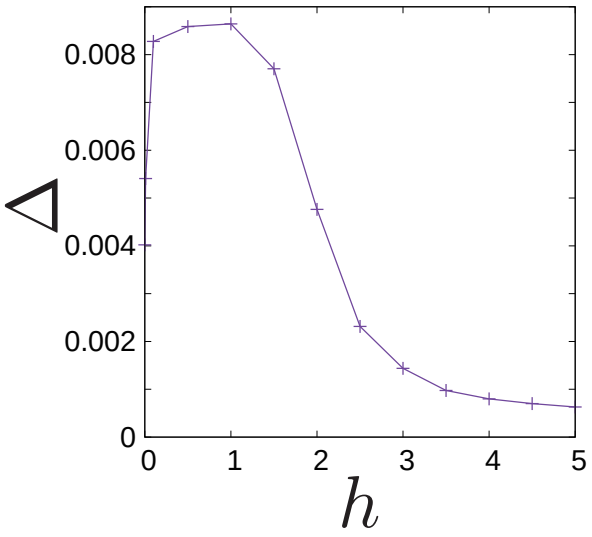

Figure 2: Disorder h-dependence of the off-diagonal-ETH indicator Δ. with single disorder realization.

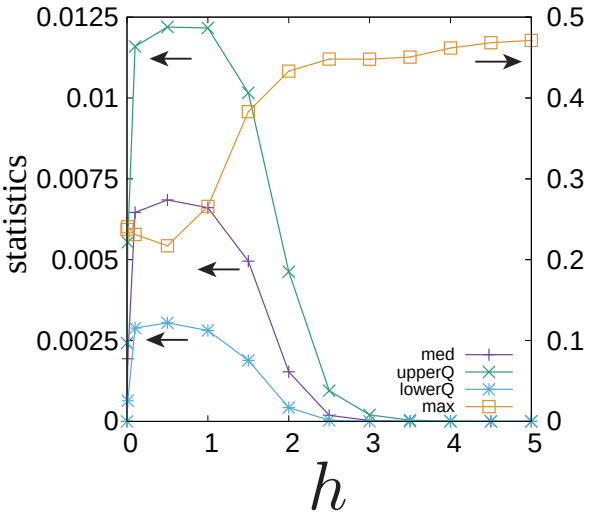

Figure 3: Disorder h-dependence of the median, upper quartile, lower quartile and maximum values of $|O_{ij}|$'s with single disorder realization.

Spinglass transitions in frustrated vector spin models

Hajime YOSHINO
Cybermedia Center, Osaka University
1-32 Machikaneyama, Toyonaka, Osaka 560-0043
(Dated: April 26th,2019)

Possibility of spinglass transitions induced by purely geometrical frustration without quenched disorder has been a long standing issue in the field of frustrated magnets. A prominent candidate [1] is the frustrated antiferromagnet on the pyrochlore lattice such as $Y_2M_2O_7$. Recently we found theoretically [2] that spinglass transitions without quenched disorder occur in a family of exactly solvable vectorial spin models in a large dimensional limit.

In the present project we analyzed static and dynamics properties of an original theoretical model [3] developed for the pyrochlore system performing Monte Carlo simulations. Our model is motivated by experiments which suggest relvance of lattice distortions: we consider classical Heisenberg spins on the vertices of the pyrochlore lattice which deforms dynamically. The lattice distortion induces changes of the magnetic coupling. Contrary to the conventional view point, we do *not* assume static, quenched distortion but allow *dynamic* distortions.

In the figure below we display some of our key findings. We found both the a) lattice and b) spin degrees of freedom exhibit critical slowing down approaching a critical temperature. The non-linear susceptibility c) become negatively large increasing the system size around the critical temperature. On the other hand, the static structure factors d) of the lattice and spin degrees of freedom exhibit no qualitative changes passing the critical temperature. These observations strongly suggest existence of a 2nd order spinglass transition where both the spins and lattice distortions collectively freeze at the same critical temperature.

Our simulations are performed on system B (2,000 points, 24000 node hours, jobclasses: B18acc, F18acc, L18acc). The program code was paralellized within nodes by openmp.

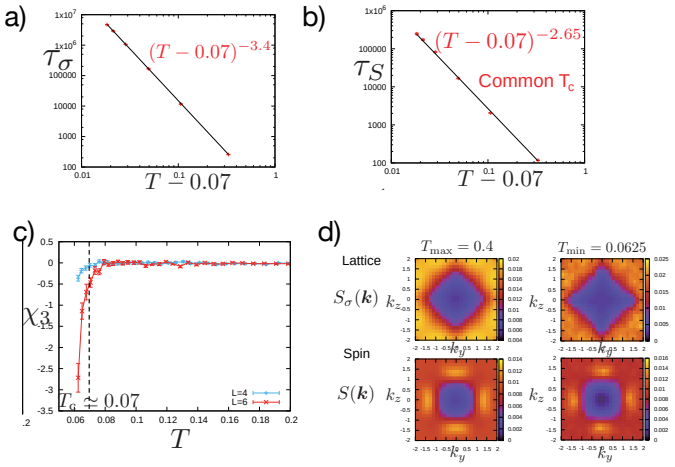

FIG. 1. Results of Monte Carlo simulations. a) and b): relaxation times of the spin and lattice auto-correlation functions. c): the non-linear susceptibility evaluated through the fluctuation formula. d): the static structure factors of the spin and lattice distortions.

[1] M. J. P. Ginsgras, et. al. PRL **78** 947 (1997).
[2] Hajime Yoshino, Disorder-free spin glass transitions and jamming in exactly solvable mean-field models, SciPost Physics, 4(6), 040 (2018).
[3] Kota Mitsumoto, Chisa Hotta, and Hajime Yoshino, in preparation.

Magnetic excitation and spin transport in frustrated quantum spin chain

Hiroaki ONISHI
Advanced Science Research Center, Japan Atomic Energy Agency
Tokai, Ibaraki 319-1195

In a spin-1/2 J_1-J_2 Heisenberg chain with ferromagnetic J_1 and antiferromagnetic J_2 in a magnetic field, there occurs a spin nematic liquid ground state, which is also spin-density-wave quasi-long-ranged. We have studied spin and quadrupole excitation spectra and found that low-energy excitations are governed by bound magnon pairs [1]. Thus we expect that magnon pairs would carry spin current.

To gain an insight into the spin transport property mediated by magnon pairs, we study the spin Drude weight [2]. We perform exact diagonalization with up to 24 sites to obtain all eigenenergies and eigenvectors and evaluate thermal expectation values. Utilizing the total magnetization and the momentum for block-diagonalization, the maximum dimension is 112720, accessible thanks to MPI simulations with ScaLAPACK on the system B of the ISSP supercomputer.

In Fig. 1(a), the temperature dependence of the spin Drude weight at zero magnetic field is presented. Note that data of $N = 4n$ sites and those of $N = 4n + 2$ sites show different behavior, since the system is regarded as two J_2 chains connected by J_1, and each J_2 chain includes even sites for $N = 4n$ and odd sites for $N = 4n + 2$. For $N = 4n$, the spin Drude weight decreases with N at high temperatures, while it increases with N at low temperatures. A crossover temperature separating these two regions seems to approach zero temperature with N. This is suggestive of vanishing spin Drude weight, i.e., diffusive spin transport.

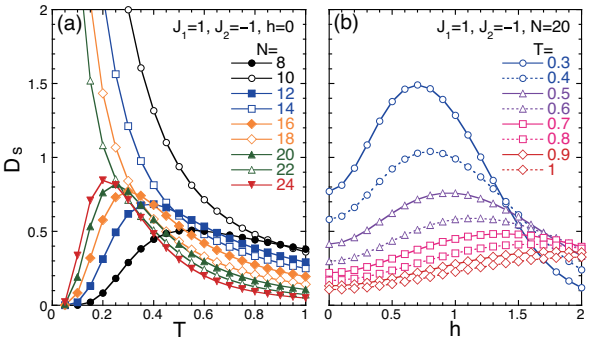

Figure 1: (a) Temperature and (b) magnetic field dependencies of spin Drude weight.

In Fig. 1(b), we show the dependence on the magnetic field at various temperatures. With increasing the magnetic field, the spin Drude weight is enhanced, while it is suppressed after showing a peak. The peak structure is more clearly seen at lower temperatures. Note that the ground state should have contribution to observables at low temperatures. In this sense, the enhancement of the spin Drude weight at low temperatures is regarded as a precursory phenomenon of the formation of magnon pairs at zero temperature, suggesting that magnon pairs would contribute to the spin transport.

References

[1] H. Onishi, J. Phys. Soc. Jpn. **84**, 083702 (2015); J. Phys.: Conf. Ser. **592**, 012109 (2015); Physica B **536**, 346 (2018).

[2] H. Onishi, J. Magn. Magn. Mater. **479**, 88 (2019).

Analysis on Structuring and Dynamics of Ionic Liquid Forming Electric Double Layer at Electrode Interfaces

Ken-ichi FUKUI

Department of Materials Engineering Science, Graduate School of Engineering Science, Osaka University, Machikaneyama, Toyonaka, Osaka 560-8531

Ionic liquids (ILs) are promising electrolytes for electrochemical devices such as secondary battery, capacitor, electric double layer (EDL)-FET, etc., due to their high chemical stability with negligible vaporization. Structuring and dynamics of the interfacial IL faced to charged graphite electrodes were analyzed by molecular dynamics (MD) calculations [1].

The MD simulations were performed with AMBER 11. The graphite substrate consisted of unit cells of linear dimensions 83.0×72.1 ×30.2 Å^3, respectively. Around 800 BMIM-TFSI ion pairs (46000 atoms) were sandwiched between the substrates and a vacuum layer (> 4 nm) (Fig. 1). The systems were equilibrated at a constant volume for 100 ps, followed by a constant volume simulation for 5 ns with fixing all of the substrate atoms. The MD simulations were performed at 300, 350, 400, and 450 K.

Fig. 2 shows the side view of the first-layer ions (z < 6.5 Å) and the total atom number density profiles as a function of the surface charge. The total atom number density profile of the BMIM cation (blue) at pzc (center) indicates a single peak (z = 3.5 Å) with shoulders, whose intensity increases with the negative potential and decrease with the positive potential without changing the overall shape. In contrast, the profile of the TFSI anion (red) at pzc (center) has three peaks at 3.0, 4.0, and 5.5 Å, and its potential dependence is more complicated at negative potential compared to the BMIM cation. These changes reflect a significant difference in the ionic arrangement on the graphite between the checkerboard type at the positive potential and the bilayer type at the negative potential and strongly affect the mobility of interfacial ions.

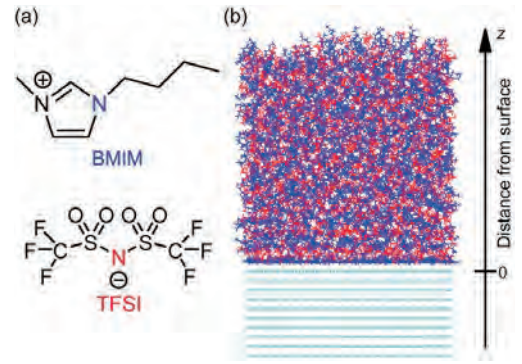

Fig. 1: (a) Ionic liquid (BMIM-TFSI) and (b) a MD snapshot for graphite the interface. BMIM cations and TFSI anions are represented by blue and red colors, respectively.

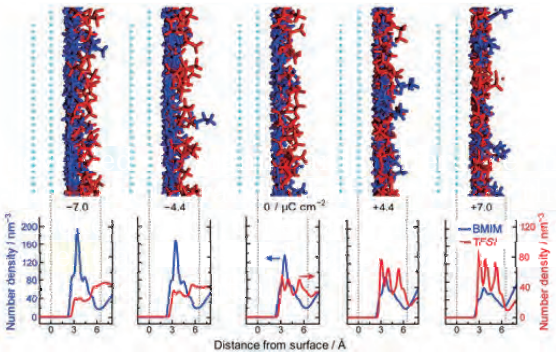

Fig. 2: (top) Side-view snapshots of the first layer ions (z < 6.5 Å) and (bottom) the total atom number density profiles for the indicated charge density of on the graphite electrode. BMIM cations and TFSI anions are represented by blue and red colors, respectively. Each cyan-colored dot represents a carbon atom in the graphite substrate.

Reference

[1] H. Miyamoto, Y. Yokota, A. Imanishi, K. Inagaki, Y. Morikawa, K. Fukui, *Phys. Chem. Chem. Phys.* **20**, 19408 (2018)

Transferability of machine learning forces to temperature and pressure

Ryo TAMURA
International Center for Materials Nanoarchitectonics,
National Institute for Materials Science,
1-1 Namiki, Tsukuba, Ibaraki, 305-0044

Data-driven techniques are becoming more and more valuable in materials science[1, 2, 3]. One of the important issues in this trend is to predict atomic forces by machine learning (ML). If we can develop a method to predict ML forces having almost the same accuracy as density functional theory (DFT) calculations, the cost of force calculations in molecular dynamics (MD) simulations will be much lower. As a result, we can perform prolonged MD simulations of large systems with DFT-level accuracy, and understanding of materials properties would be deepened.

In our study, we trained a machine-learning model for the Si and Ge single-component systems in order to directly predict the atomic forces at a wide range of temperatures and pressures in the liquid state[4, 5]. Gaussian process regression is adopted as the machine learning technique to predict atomic forces, and we use atomic fingerprints that express the local structure around the target atom. The training and test data are generated by MD simulations based on DFT using a linear-scaling method using the CONQUEST code[6].

We first clarified the accuracy of the ML model when both training and test data were sampled from the DFT-MD simulations at the same temperature. We found that the accuracy becomes the lowest around the phase boundary between the solid and liquid states. However, even in the liquid state, the relative error is smaller than 6.5% for the Si system and 5.2% for the Ge system. ML models with such accuracy are useful for performing MD simulations to calculate the physical properties. Figure 1 shows the prediction results for the Si system at 1200 K (solid state) and 9000 K (liquid state).

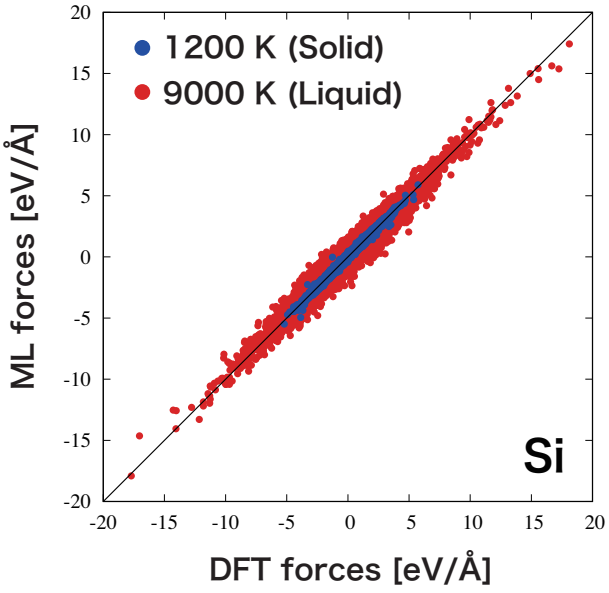

Figure 1: Parity plot of DFT forces versus ML forces for the Si single-component systems.

Next, we investigated the transferability of ML models trained in the liquid state to temperature and pressure. We demonstrated that, if the training is performed at a high temperature and if the volume change is not so large, the transferability of ML forces in the liquid state is sufficiently high, whereas its transfer-

ability to the solid state is very low. Thus, in the liquid state, the ML model using training data generated by the DFT-MD simulations under specific conditions, such as at a high temperature with a standard volume, can be used to accurately predict forces under various conditions without additional or further DFT-MD simulations.

References

[1] K. Shiba, R. Tamura, T. Sugiyama, Y. Kameyama, K. Koda, E. Sakon, K. Minami, H. T. Ngo, G. Imamura, K. Tsuda, and G. Yoshikawa, ACS Sensors **3**, 1592 (2018).

[2] M. Sumita, X. Yang, S. Ishihara, R. Tamura, and K. Tsuda, ACS Central Science **4**, 1126 (2018).

[3] K. Terayama, R. Tamura, Y. Nose, H. Hiramatsu, H. Hosono, Y. Okuno, and K. Tsuda, Phys. Rev. Matererials **3**, 033802 (2019).

[4] T. Suzuki, R. Tamura, and T. Miyazaki, Int. J. Quantum Chem. **117**, 33 (2017).

[5] R. Tamura, J. Lin, and T. Miyazaki, J. Phys. Soc. Jpn. **88**, 044601 (2019).

[6] http://www.order-n.org.

Schmidt-number dependence of phase-separation dynamics of colloidal suspensions

Michio Tateno and Hajime Tanaka
Department of Fundamental Engineering, Institute of Industrial Science, University of Tokyo
4-6-1 Komaba, Meguro-ku, Tokyo 153-8505

Colloidal suspensions are a mixture of large colloidal particles and small solvent molecules, between which there is a huge gap in the characteristic time scales of the motion. It is known that the Schmidt number, $S_c = \nu/D$, is a dimensionless parameter that characterizes the difference between the momentum and material diffusion, where ν is the kinetic viscosity of the solvent and D is the thermal diffusion constant of a free isolated colloid. In typical colloidal systems, these two diffusion coefficients differ by many orders of magnitude (for example, $S_c \sim 10^6$, for μm-size colloids suspended in water at room temperature), and this condition ($S_c \gg 1$) is widely assumed in the physical laws associated with the dynamics of colloids, such as the Stokes-Einstein relation. For such a large Schmidt number, numerically accessing the colloidal dynamics, such as collective colloidal motion, self assembly dynamics, and rheological behavior, starting from molecular-level dynamics, is almost impossible with current computational power. Indeed, in most of simulation studies, the Schmidt number has been set to modest values ($S_c < 10$) [1].

The main purpose of this project is to clarify the Schmidt number dependence on colloidal dynamics, with which we aim to provide a guidance on the minimum S_c that we need to reproduce real colloidal dynamics. In this project, we used a hydrodynamic simulation model, fluid particle dynamics (FPD) method [3, 4], which is based on direct computation of the Navier-Stokes equation. We have shown that this FPD method combined with fluctuating hydrodynamics at $S_c = 8$ can well reproduce the Brownian motion of a free isolated colloid while satisfiying statistical mechanical consistency between colloids and solvent [4]. Below we focus on phase-separation dynamics of colloidal suspensions, which may be regarded as a typical example of nonequilibrium phenomena of colloidal matter.

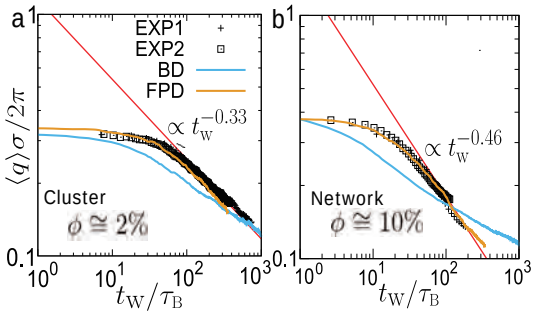

Figure 1: Time evolution of the characteristic wave number $\langle q(t) \rangle$ for two different volume fractions $\phi \simeq 2$ % (a) and 10 % (b). Here we compare two experiments and two simulations: EXP1 (black cross), EXP2 (black square), BD (blue curve) and FPD (brown curve). In FPD simulation, we set the Schmidt number as $S_c = 8$.

We first show the time evolution of the characteristic wave number $\langle q(t) \rangle$, which is approximately inversely proportional to the characteristic domain size of colloidal aggregates. Panel a and b in Fig. 1 corresponds to the results at the colloidal volume fractions of 2% and 10%, where isolated clusters and space-spanning network structure of the colloid-rich

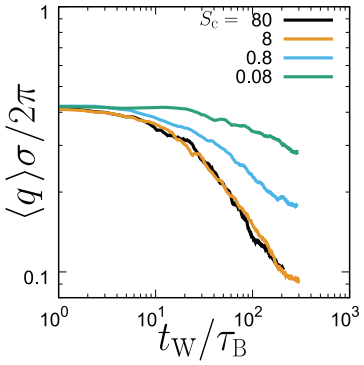

Figure 2: The temporal change of the characteristic wave number $\langle q \rangle$ during phase separation at $\phi \simeq 10$ % for four different Schmidt numbers.

phase are observed respectively. To evaluate the validity of the simulation results, here we compare them to experimental results obtained by three-dimensional (3D) confocal microscopy observations (black cross and black square). In the figure, we can cleary see that results obatined by the FPD simulation with $S_c = 8$ almost perfectly reproduce the experimental results (EXP1 and EXP2: see Ref. [5] on the detail of experiments). BD in Fig. 1 corresponds to simulation results by Brownian dynamics without hydrodynamic interactions, and obviously fails to reproduce the experimental results. These results clearly indicate the fundamental importance of many-body hydrodynamic interactions in colloidal phase separation.

Next we check under what condition the agreement in the time development of $\langle q \rangle$ during phase separation between EXP and FPD can be attained. In Fig. 2, we show the temporal change of the characteristic wave number $\langle q \rangle$ at $\phi \simeq 10\%$ for four different Schmidt numbers: $S_c = 0.08, 0.8, 8, 80$. We can clearly see that $\langle q \rangle$ is almost identical when the Schmidt number satisfies $S_c \geq 8$.

Here we consider why we can see such a good agreement even with a rather moderate Schmidt number $S_c \sim 10$. The key time scale is the characteristic time required for the momentum of the solvent to diffuse over a characteristic distance l_c from a particle, which is given by $\tau_\nu(l_c) \cong l_c^2/\nu$. Denoting the colloid diameter as σ and the Brownian time as $\tau_B = (\frac{\sigma}{2})^2/6D$, then $\tau_\nu/\tau_B \cong 24(l_c/\sigma)^2 S_c^{-1}$. This means that how far the momentum diffuses away within the time scale of τ_B depends on the value of S_c. For $S_c \sim 10$ and $\tau_\nu/\tau_B \sim 1$, for example, we obtain $l_c/\sigma \sim 1$, implying that a flow field around a particle is established by momentum diffusion at least up to a distance of about the particle diameter from that particle. This indicates that, for $S_c \sim 10$, our method can properly describe near-field many-body hydrodynamic interactions, which is expected to play a dominant role in the aggregation process of colloids undergoing Brownian motion.

In summary, we study the Schmidt number dependence of phase separation dynamics of colloidal suspensions, and found that our hydrodynamic simulation model (FPD method) with a moderate Schmidt number (i.e., $S_c \sim 10$) is able to precisely reproduce experimental results observed by confocal microscopy. Our result provides a guidance on the parameter setting required for proper hydrodynamic simulations of colloidal suspensions.

References

[1] F. B. Usabiaga, X. Xie, R. Delgado-Buscalioni and A. Donev : J. Chem. Phys. **139** (2013) 214113

[2] A. Furukawa and H. Tanaka: Phys. Rev. Lett. **104**, (2010) 245702.

[3] H. Tanaka and T. Araki: Phys. Rev. Lett. **85**, (1999) 1338

[4] A. Furukawa, M. Tateno and H. Tanaka: Soft Matter **14** (2018) 3738

[5] M. Tateno and H. Tanaka: npj Computational Materials **5** (2019) 40

Numerical study of collective motion transition of crowding cells with anisotropic shape.

Katsuyoshi Matsushita
Depertment of Biological Science, Osaka University
Machikaneyama 1-1, Toyonaka, Osaka 560-0043

Collective motion of cells is a fundamental phenomenon for development of organisms, wound healing, and immune response [1]. This motion usually be driven by pseudepod formation and is associated by the elongation of the cell shape due to the pseudepods. Therefore, the cell shape is correlated to the cell motion. The clarification of the correlation effects is an important issue for the understanding of physical mechanisms of these collective motion.

Even in crowding environments in organism bodys, these cells move with with this elongation. The elongation is expected to induce another correlation between motion and shape because the cell shape affects the excluded volume interaction and subsequently the interaction affects the motion. This composite effect is not clear today. To get insight into the composite effect on collective motion in crowding cells, we tried to model this situation and numerically investigated the shape dependence on the collective motion on the model.

For this purpose, we employed the Cellular Potts model and its Kinetic Monte Carlo simulation [2]. This model have used to appropriately represent the motion of cells through flexible shape changes in tissues, which is expected for collective motions under cell crowding in organism bodys [3]. Furthermore, this model can easily express the excluded volume of cells as a surface free energy. These properties help us to express the above crowding cells with collective motion.

We further constructed model elongated cells with correlating its motion by using the cell model with the spatial polarization in F-actin density [4]. We simulated the cells with elongation and showed that the elongation of the model cells stabilize their collective motion. This result implies the steric interaction effect due to the elngated excluded volume between cells. Namely, the steric interaction stabilizes the nematic ordering of the elongated cell shape and also thereby aligns cell motion in the elongation direction of cells.

In contrast, when the elongation due to F-actin is weaken and the cell shape exhibits isotoropy, the collective motion is destabilized. This is because the stabilization effect of steric interaction in cell shape is absent in the isotropic cell. In this case, the cells collectively exhibits large fluctuation in their motion and the direction of motion frequently changes in time advance. This result implies the function of the cell elongation for stabilization of the collective motion in organism bodys.

References

[1] C. J. Weijer: J. Cell Sci. 122 (2015) 3215.

[2] F. Graner and J. A. Glazier: Phys. Rev. Lett. 69 (1992) 2013.

[3] A. J. Kabla, J. R. Soc. Interface 9 (2012) 3268; K. Matsushita: Physical Review E 95 (2017) 032415.

[4] K. Matsushita: Proc Sympo. Simul. Traffic flow 23 (2017) 37.

Computer-simulated eight-beam and 18-beam X-ray pinhole topographs based on the Ewald-Laue dynamical theory and FFT

Kouhei OKITSU

Institute of Engineering Innovation, School of Engineering,

The University of Tokyo, 2-11-16 Yayoi Bunkyo-ku Tokyo 113-8656

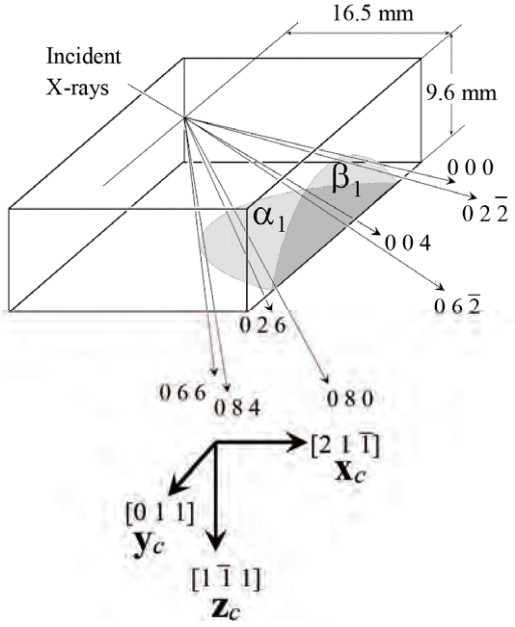

Fig. 1 Schematic drawing of the geometry of the eight-beam pinhole topographs [1].

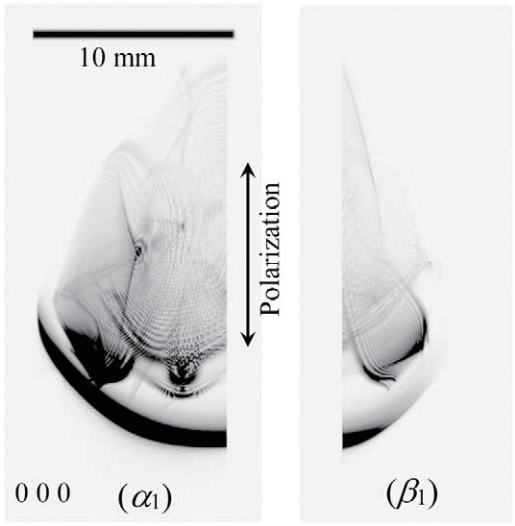

Fig. 2 Pinhole topograph of 0 0 0 forward-diffracted X-rays computer-simulated separately for α_1 and β_1 of Fig. 1. (α_1) and (β_1) were linked to obtain Fig. 3 [S_v(E-L)] [1].

Experimentally obtained and computer simulated eight-beam and 18-beam pinhole topographs were compared and agreed with each other.

In the eight-beam case, the experimental setup used when taking the topographs and assumed in the computer simulation is as shown in Fig. 1. (α_1) and (β_1) in Fig. 2 were computer-simulated pinhole topographs. These were separately calculated under the assumptions of [1 -1 1]-oriented silicon crystal with a thickness of 9.6 mm, and of [2 1 -1]-oriented one with a thickness of 16.5 mm, respectively. Figs. 2 (α_1) and 2 (β_1) were obtained by fast Fourier-transforming the amplitude of forward-diffracted or transmitted-reflected X-rays calculated based on the Ewald-Laue dynamical diffraction theory. This method (E-L FFT simulation) was reported by Kohn and Khikhlukha (2016) and Kohn (2017) for a symmetric six-beam case for the first time. However, the present eight-beam case is an asymmetric case for a silicon crystal whose shape is not single planar. Figs. 2 (α_1) and 2 (β_1) were linked to obtain Fig. 3 [S_v(E-L)] that are in excellent agreement with Fig. 3 [E_v] experimentally obtained.

On the other hand, experimentally obtained 18-

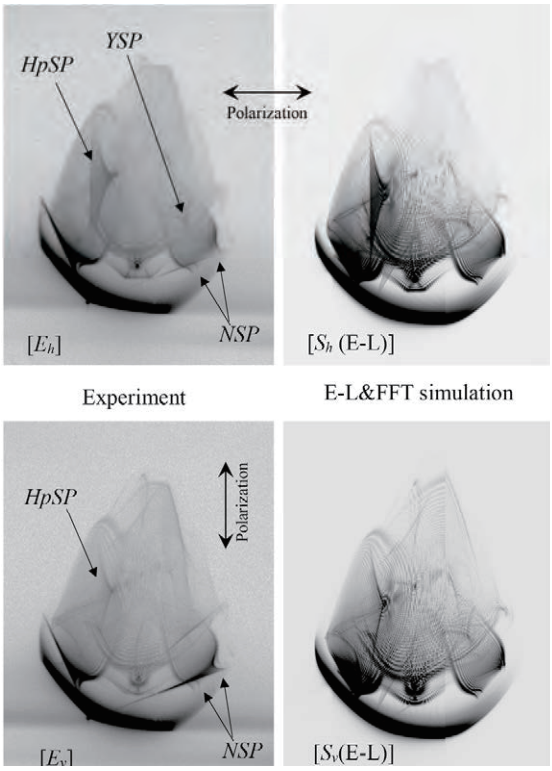

Fig. 3 [E_x] and [S_x(E-L)] (x is h or v; polarization state of the incident X-rays) are experimentally obtained and computer-simulated topographs [1].

beam pinhole topographs as shown in Fig. 4 (a) were also in good agreement with Fig. 4 (b). In this 18-beam case, reciprocal lattice nodes giving the Bragg reflections for inner six images and outer 12 ones do not exist on a circle in reciprocal space (non-circular case).

From the agreement between the experimentally obtained pinhole topographs and those obtained with the computer simulation, it has been revealed that the E-L FFT simulation is effective even when the crystal has a complex shape and/or the reciprocal lattice nodes simultaneously giving the Bragg reflections do not ride on a single circle in reciprocal space. This situation is the case for multiple reflection (widely known as the Renninger effect) in crystal structure analysis in general.

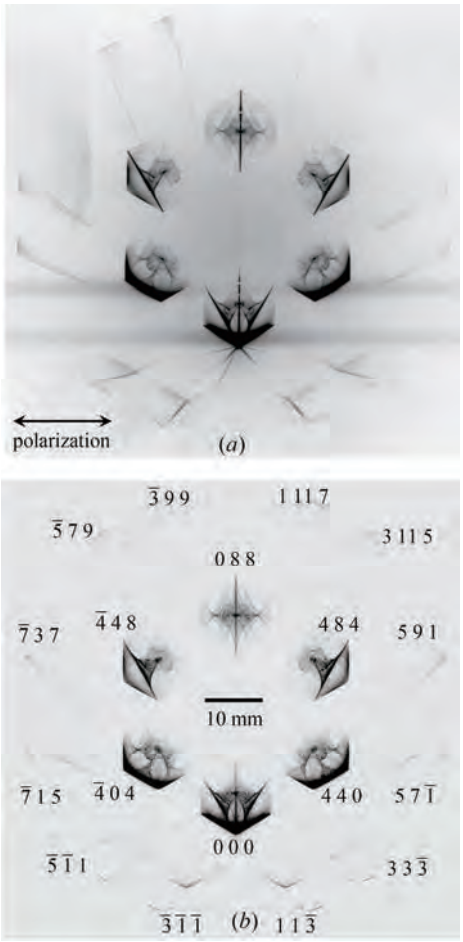

Fig. 4 (a) and (b) are experimentally obtained and computer-simulated 18-beam pinhole topographs [2].

The present author has a hypothesis that too large R factor for macro molecules is caused by multiple reflection and bankruptcy of the two-beam approximation that has been used for over 100 years. The present author has prepared to verify this hypothesis concerning the too large R factor of macro molecule crystals by estimating it with multiple-beam approximation in place of the conventional two-beam approximation.

References

[1] K. Okitsu, Y. Imai, Y. Yoda and Y. Ueji: *Acta Cryst.* **A75** (2019) In Press in Advanced Section.

[2] K. Okitsu, Y. Imai, and Y. Yoda: *Acta Cryst.* **A75** (2019) In Press in Advanced Section.

Calculation of ordered structures and their optical properties of soft materials

Jun-ichi FUKUDA

Department of Physics, Kyushu University, Motooka 744, Nishi-ku, Fukuoka 819-0395

We have made use of the supercomputer facility of ISSP in part to investigate particularly the ordered structures of a chiral liquid crystal under strong spatial confinement between two parallel plates. Last year we showed that such a thin system of a chiral liquid crystal exhibits various exotic ordered structures [1], including a hexagonal lattice of half-Skyrmions (a swirl-like structure of orientational order without singularities at the center) and a thin slice of bulk three-dimensional structure known as cholesteric blue phase. We also calculated their microscope images in excellent agreement with experimental ones.

This year, based on the solutions of the Maxwell equations for light wave utilized for the construction of numerical microscope images, we constructed numerical Kossel diagrams exhibited by the above-mentioned ordered structures [2]. Kossel diagrams are made up of straight or elliptic lines (Kossel lines) visualizing the directions of strong reflections of monochromatic light incident onto the sample from different directions within a certain solid angle. Kossel diagrams are commonly used to investigate the symmetry of bulk crystal structures exhibiting strong Bragg reflections. How Kossel diagrams should be interpreted for a thin system was not clear. We compared numerical Kossel diagrams again with experimental ones, and they showed good agreement with each other on the locations and intensities of Kossel lines. We further showed that Kossel lines of a thin system should be attributed not to Bragg reflections but the coupling between different guided modes through the periodic structure of the system. The locations of the Kossel lines deduced from the above theoretical argument are in perfect agreement with those of numerical Kossel lines. We demonstrated that Kossel diagrams are useful not only for the determination of bulk crystal symmetry but also for the investigation of the structural properties of a thin system.

References

[1] A. Nych, J. Fukuda, U. Ognysta, S. Žumer and I Muševič, Nature Phys. **13**, 1215 (2017).

[2] J. Fukuda, A. Nych, U. Ognysta, S. Žumer and I Muševič, Scientific Reports **8**, 17234 (2018).

Coherent Control of Nonadiabatic Wavepacket Dynamics of Electron-phonon-photon Systems

Kunio ISHIDA

Department of Electrical and Electronic Engineering, School of Engineering, Utsunomiya University, 7-1-2, Yoto, Utsunomiya, Tochigi 321-8585

Recent experiments on diamond showed the possibility of phonon-mediated coherence between qubits via Raman scattering processes[1]. In this case, entanglement between electrons, phonons, and photons plays an important role, which means that fully quantized theory of interaction between irradiated light and materials is necessary to reveal and/or design the control methods for them.

In order to study the quantum dynamics of those systems, we numerically solved the time-dependent Schödinger equation for electron-phonon-photon systems described by the Hamiltonian[2]:

$$\mathcal{H} = \omega a^{\dagger}a + \sum_{i=1}^{n} \Omega_i {c_i}^{\dagger} c_i + \{\mu(a^{\dagger} + a) + \varepsilon\}\frac{\sigma_z + 1}{2} + \left\{\sum_{i=1}^{n} \nu_i({c_i}^{\dagger} + c_i) + \lambda\right\}\sigma_x,$$

where n is the number of photon modes, and a and c_i denote the annihilation operators of phonons and the photons of the i-th mode, respectively. σ_i corresponds to the Pauli matrices which operate on the electronic states denoted by $|g\rangle$ ground state) and $|e\rangle$ excited state). ω and Ω_i are the angular frequencies of phonon and the i-th mode photon, while ν and μ_i give the strength of the electron-phonon coupling and the dipole interaction, respectively. λ is the nonadiabatic coupling between electronic states, and ε is the energy difference between $|g\rangle$ and $|e\rangle$. The initial state of the i-th mode photon is a coherent state parameterized by α_i. Since not only the phonon mode but also three photon modes are quantized, the dimension of the Hilbert space of electron-phonon-photon systems is as large as 10^8. Hence, numerical calculations require a lot of computational resources, and hybrid parallelization is made on the source code for the System B.

As an example of coherent dynamics of the system, we show the calculated results of control by external light field, we show that the relative phase between photons affects the created phonon states. Figure 1 shows the number of phonons $N_n(t) = \langle\Phi(t)|a^{\dagger}a|\Phi(t)\rangle$ for $\Delta\phi = -\pi, -\frac{\pi}{2}, 0, \frac{\pi}{2}$ and π, where $\Delta\phi$ denotes the phase difference between Stokes/anti-Stokes mode and the pump mode, i.e., $\alpha_2 = |\alpha_2|e^{i\Delta\phi}$ and $\alpha_3 = |\alpha_3|e^{-i\Delta\phi}$. Since the wavepacket

trajectory varies with $\Delta\phi$, different phonon states are created in the material, which shows that the number of phonons is able to be modified by $\Delta\phi$.

We have been studied the dynamical properties of a single electron-phonon system so far, and these results will be a basis to study various types of non-classical correlations between noninteracting systems mediated by incident light, e.g., creation of phonon entanglement in spatially separated diamond crystals[3].

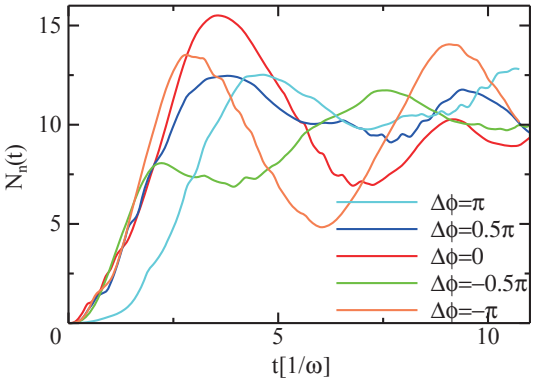

Fig.1 The average number of phonons $N_n(t)$ for $\alpha_1 = 5, \alpha_2 = \alpha_3 = 3.16, \lambda = 1.5$ with different values of $\Delta\phi$.

References

[1] D. G. England, *et al*., Phys. Rev. Lett. **117**, 073603 2016).

[2] K. Ishida, Eur. Phys. J. D, doi: 10.1140/epjd/e2019-09485-5.

[3] K. C. Lee, *et al*., Science **334**, 1253 2011).

Transport properties of the classical antiferromagnetic Heisenberg model on the triangular lattice

Kazushi AOYAMA
Department of Earth and Space Science, Graduate School of Science, Osaka University
Machikaneyama-cho, Toyonaka-shi, Osaka 560-0043

The ground state of the nearest neighbor(NN) antiferromagnetic Heisenberg model on the triangular lattice is the non-collinear 120° Neel state, so that the order parameter space has the $SO(3)$ symmetry. On the two-dimensional lattice, a point defect, namely, a vortex excitation, in the SO(3) manifold is characterized by the topological number of $\mathbf{Z}_2$. In contrast to a conventional vortex having an integer topological number $\mathbf{Z}$, less is known about how the $\mathbf{Z}_2$ vortices affect magnetic properties of the system. In this work, we investigate transport properties of the triangular-lattice Heisenberg model, putting emphasis on the role of the $\mathbf{Z}_2$-vortex excitation.

The spin Hamiltonian of the present system is given by

$$\mathcal{H} = -J \sum_{\langle i,j \rangle} \mathbf{S}_i \cdot \mathbf{S}_j \qquad (1)$$

where $\mathbf{S}_i$ is a classical Heisenberg spin at a lattice site i. From the Hamiltonian (1), one can derive the semiclassical equation of motion for spins as follows,

$$\frac{d\mathbf{S}_i}{dt} = \Big(-J \sum_{j \in N(i)} \mathbf{S}_j \Big) \times \mathbf{S}_i, \qquad (2)$$

where $N(i)$ denotes all the NN sites of i. Since Eq. (2) is a classical analogue of the Heisenberg equation for the spin operator, all the static and dynamical properties intrinsic to the Hamiltonian (1) could be described by the combined use of Eqs. (1) and (2).

Within the linear response theory, the conductivities of the spin current $\mathbf{J}_s$ and the thermal current $\mathbf{J}_{th}$ can be obtained by evaluating the thermal average of the time correlations of $\mathbf{J}_s$ and $\mathbf{J}_{th}$ which are respectively given by

$$\begin{aligned} \mathbf{J}_s &= \frac{J}{2} \sum_{\langle i,j \rangle} (\mathbf{r}_i - \mathbf{r}_j)(\mathbf{S}_i \times \mathbf{S}_j)^z, \\ \mathbf{J}_{th} &= \frac{J^2}{2} \sum_{\langle i,j,l \rangle} \mathbf{r}_l \, \mathbf{S}_l \cdot (\mathbf{S}_i \times \mathbf{S}_j) \end{aligned} \qquad (3)$$

with $\mathbf{r}_i$ being the position of a site i.

Starting from temperature-dependent initial spin configurations generated by Monte Carlo (MC) simulations, we numerically integrate Eq. (2) to obtain the time correlations of $\mathbf{J}_s$ and $\mathbf{J}_{th}$. In this work, we perform long-time integration typically up to $t/|J| = 100 - 800$ with time step $\delta t/|J| = 0.01$ and the thermal average is taken as the average of 2000-4000 initial spin configurations which are picked up every 1000 MC sweeps after 10^5 MC sweeps for thermalization. Here, in our MC simulations with linear system size L, one MC sweep consists of 1 Heatbath sweep and successive 10-30 over-relaxation sweeps. Most of the calculation is done by using the facilities of the Supercomputer Center, ISSP, the University of Tokyo.

It is found by performing the above calculations for $L = 24 - 768$ that the longitudinal spin conductivity is significantly enhanced at the $\mathbf{Z}_2$-vortex transition temperature T_v, while the thermal conductivity does not exhibit any clear anomaly near T_v.

Molecular simulation of colloidal suspensions

Takamichi TERAO

Department of Electrical, Electronic, and Computer Engineering,

Gifu University, Yanagido 1-1, Gifu, 501-1193

The self-assembly of colloidal particles is a fundamental topic in material science, and diverse colloidal composites are applied in various industries. The industrial applications include photonic crystals with bandgaps that prevent the propagation of light within a certain frequency range. Polymer–nanoparticle composites, also known as spherical polymer brushes, are a typical example of a soft colloidal system. Spherical polymer brushes contain an inner core particle that cannot overlap another core particle.

Recently, spherical dendritic brushes, which have many dendrons grafted onto the spherical surface of a core particle, have been investigated. By virtue of the stronger entropic repulsion between dendrons in the spherical than in the linear configuration, spherical polymer brushes improve the colloidal stability and their structural formation has roused great interest.

We have examined the self-assembly of colloidal particles with spherical dendritic brushes. The effective interaction between these particles was studied in Monte Carlo simulations of the Kremer–Grest model (Fig.1). Results confirmed the transferability of the effective potential at different temperatures. Using the potential of mean force obtained from Monte Carlo simulations, the structural formation of the system was studied in a three-dimensional system. The system is a crystalline state in the intermediate density range and exhibits re-entrant melting at much higher densities. Based on generalized local bond order analysis, a refined numerical method has been proposed for analyzing the structural formation of colloidal particles in three-dimensional systems [1].

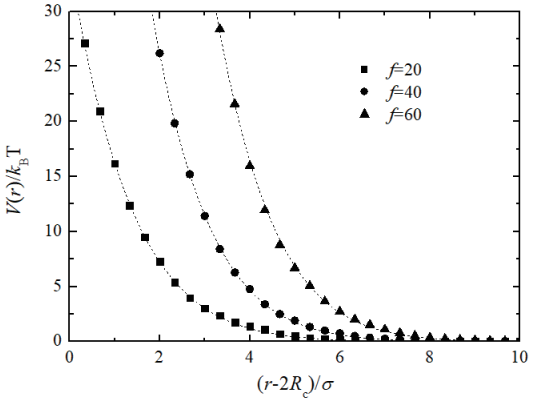

Fig. 1: Effective potential between a pair of spherical dendritic polymer brushes.

References

[1] R. Mizuno, K. Okumura, J. Oguri, and T. Terao: Mol. Simul. **45** (2019) 743.

Ground-State Phase Diagram of an Anisotropic $S=1$ Ferromagnetic-Antiferromagnetic Bond-Alternating Chain

Takashi Tonegawa

Professor Emeritus, Kobe Univ. and Visiting Professor, Osaka Prefecture Univ.

This report aims at exploring the ground-state phase diagram of an anisotropic $S=1$ ferromagnetic-antiferromagnetic bond-alternating chain by using mainly numerical methods. We express the Hamiltonian which describes this system as

$$\mathcal{H} = \sum\nolimits_j \{h^{\rm F}_{2j-1,2j} + h^{\rm AF}_{2j,2j+1} + D_2 (S^z_j)^2\}, \quad (1)$$

$$h^{\rm F}_{j,j'} = -J_{\rm F}(S^x_j S^x_{j'} + S^y_j S^y_{j'} + \Delta_{\rm F} S^z_j S^z_{j'}), \quad (2)$$

$$h^{\rm AF}_{j,j'} = J_{\rm AF}(S^x_j S^x_{j'} + S^y_j S^y_{j'} + \Delta_{\rm AF} S^z_j S^z_{j'}). \quad (3)$$

Here, S^μ_j ($\mu = x,\ y,\ z$) is the μ-component of the spin-1 operator $\vec{S}_j$ acting on the jth site; $J_{\rm F}(>0.0)$ and $J_{\rm AF}(\geq 0.0)$ denote, respectively, the magnitudes of exchange intereraction constants for the ferromagnetic and antiferromagnetic bonds; $\Delta_{\rm F}$ and $\Delta_{\rm AF}$ are, respectively, the parameters representing the XXZ-type anisotropies of the former and latter interactions.

Our motivation for treating this system is as follows. As we will concretely discuss in the next paragraph, this system can be mapped onto an anisotropic spin-2 chain, when $J_{\rm F}$ is sufficiently larger than $J_{\rm AF}$. In the ground-state phase diagram of the latter system, on the other hand, the intermediate-D (ID) phase, which is a typical example of the symmetry protected topological (SPT) phase received recently much attention, appears [1-8]. Thus, we are interested in how the ID phase appears in the ground-state phase diagram of the present anisotropic $S=1$ ferromagnetic-antiferromagnetic bond-alternating chain.

Discussing the mapping of the present anisotropic $S=1$ ferromagnetic-antiferromagnetic bond-alternating chain onto the anisotropic spin-2 chain, we perform lowest perturbation calculations by taking the unperturbed Hamiltonian as $\mathcal{H}_0 = -J_{\rm F}\sum_j \vec{S}_{2j-1}\cdot\vec{S}_{2j}$. Then, straightforward calculations lead to the result,

$$\tilde{\mathcal{H}} = \tilde{J}_{\rm AF}\sum\nolimits_j \left(T^x_j T^x_{j+1} + T^y_j T^y_{j+1} + \Delta_{\rm AF} T^z_j T^z_{j+1}\right) + \sum\nolimits_j \left\{\tilde{D}_2 \left(T^z_j\right)^2 + \tilde{D}_4 \left(T^z_j\right)^4\right\}, \quad (4)$$

where T^μ_j is the μ-component of the spin-2 operator $\vec{T}_j$ at the jth site, and $\tilde{J}_{\rm AF} = J_{\rm AF}/4$, $\tilde{D}_2 = \{7D_2 - 2J_{\rm F}(\Delta_F - 1)\}/6$, $\tilde{D}_4 = -D_2/6$. It is noted that these results are valid when $J_{\rm F} \gg J_{\rm AF} > 0.0$, $J_{\rm F} \gg |D_2|$, and $\Delta_{\rm F} \sim 1.0$.

There exist five interaction parameters, $J_{\rm F}$, $J_{\rm AF}$, $\Delta_{\rm F}$, $\Delta_{\rm AF}$, and D_2 in our Hamiltonian $\mathcal{H}$. Since we are much interested in the ID phase, we choose the values of these parameters under the condition that this phase appears as widely as possible when we perform the numerical calculations of the phase diagram. It is now known that in the ground-state phase diagram of the anisotropic spin-2 chain governed by $\tilde{\mathcal{H}}$, positive values of $\tilde{D}_4$ stabilize the ID phase [6,7]. Thus, referring to the above results of the perturbation calculations, we fix our attention upon the case where $J_{\rm F} = 1.0$ ($J_{\rm F}$ is the unit of energy), $\Delta_{\rm F} = 0.8$, and $D_2 = -1/30$, and numerically determine the phase diagram on the $J_{\rm AF}$ versus $\Delta_{\rm AF}$ plane. Note that the above values of $\Delta_{\rm F}$ and D_2 give $\tilde{D}_2 = 1/36$ and $\tilde{D}_4 = 1/180$, if we respectively use the above equations for $\tilde{D}_2$ and $\tilde{D}_4$.

Figure 1 shows our final result for the ground-state phase diagram on the $J_{\rm AF}$ versus $\Delta_{\rm AF}$ plane, which has been determined by using a variety of numerical methods based on the exact diagonalization calculation. This phase diagram consists of six phases, which are the $XY1$, large-D (LD), ID, Haldane (H), spin-1 singlet dimer (SD), and Néel (N) phases. Among these, the LD, H, and SD phases are the trivial phases, and the ID phase is the SPT phase. Interestingly, the former three are smoothly connected without any quantum phase transitions between the LD and H phases and between the H and SD phases, and therefore they belong to the same phase. It is also emphasized that the ID phase appears in a wider region compared with the case of the phase diagram of the anisotropic spin-2 chain for $\tilde{D}_4 = 0.0$ [2-5].

We now briefly discuss how to estimate numerically the phase boundary lines in the phase diagram shown in Fig. 1. We denote, respectively, by $E^{\rm P}_0(L,M)$ and $E^{\rm P}_1(L,M)$, the lowest and second-lowest energy eigenvalues of the Hamiltonian $\mathcal{H}$ under the periodic boundary condition within the subspace characterized by N and M, where $N(=4,\ 8,\ 12,\ 16)$ is the total number of spins in the system and $M(=0,\ \pm1,\ \cdots,\ \pm N)$ is the total magnetiza-

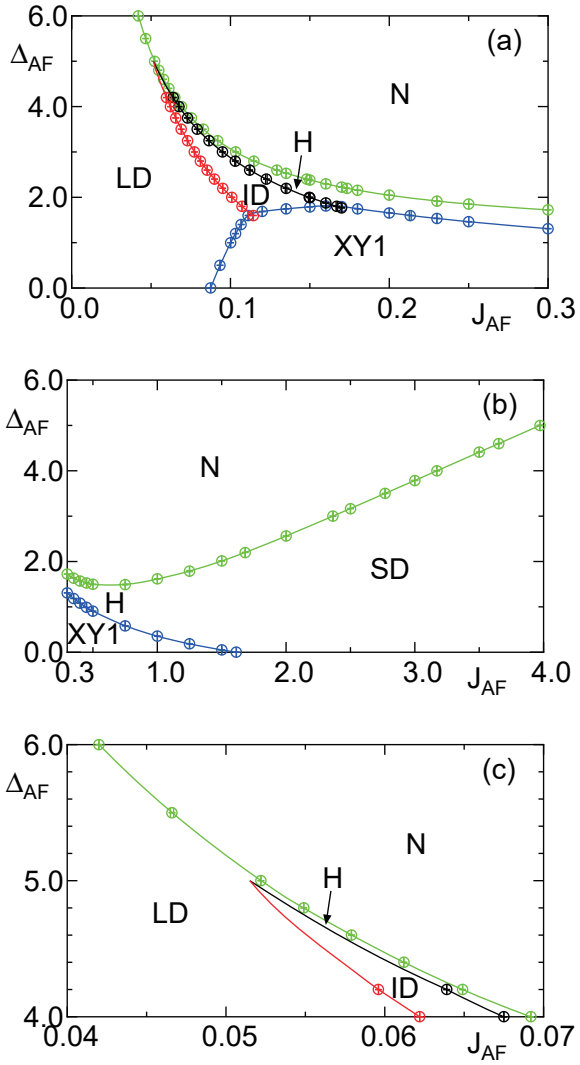

Figure 1: The ground-state phase diagram on the $J_{\rm AF}$ versus $\Delta_{\rm AF}$ plane for $J_{\rm F}=1.0$, $\Delta_{\rm F}=0.8$, and $D_2=-1/30$, obtained in the present work; (a) $0.0\le J_{\rm AF}\le 0.3$, (b) $0.3\le J_{\rm AF}\le 4.0$, in (c) part of (a) is enlarged.

tion. We also denote by $E_0^{\rm T}(L,M,P)$ the lowest energy eigenvalue of $\mathcal{H}$ under the twisted boundary condition within the subspace characterized by N, M, and P, where $P(=+1,\,-1)$ is the eigenvalue of the space inversion operator with respect to the twisted bond. We numerically calculate these energies by means of the exact-diagonalization method. In the following way, we evaluate the finite-size critical values of $J_{\rm AF}$ (or $\Delta_{\rm AF}$) for various values of $\Delta_{\rm AF}$ (or $J_{\rm AF}$) for each phase transition. Then, the phase boundary line for the transition is obtained by connecting the results for the $N\to\infty$ extrapolation of the finite-size critical values.

Firstly, the phase transition between the LD and ID phases and that between the ID and H phases are of the Gaussian type. Therefore, as is well established, the phase boundary lines can be accurately estimated by Kitazawa's level spectroscopy (LS) method [9]. That is to say, we numerically solve the equation,

$$E_0^{\rm T}(N,0,+1)=E_0^{\rm T}(N,0,-1) \qquad (5)$$

to calculate the finite-size critical values. It is noted that, at the $N\to\infty$ limit, $E_0^{\rm T}(N,0,+1)>E_0^{\rm T}(N,0,-1)$ in the ID phase and $E_0^{\rm T}(N,0,+1)<E_0^{\rm T}(N,0,-1)$ in the LD and H phases.

Secondly, the phase transitions between one of the LD, ID, ID, and SD phases and the $XY1$ phase are the Berezinskii-Kosterlitz-Thouless type. Then, the phase boundary line can be accurately estimated by the method developed by Nomura and Kitazawa [10]. Thus, we solve the following equation to calculate the finite-size critical values:

$$E_0^{\rm P}(N,2)=E_0^{\rm T}(N,0,P)\,, \qquad (6)$$

where $P=-1$ or $P=+1$ depending upon whether the transitions are associated with the ID phase or with the LD, ID, and SD phases.

Lastly, since the phase transitions between one of the LD, H, SD phases and the N phase are the 2D Ising-type transition, the phase boundary line between these two phases can be estimated by the phenomenological renormalization group method [11]. Then, the finite-size critical values for this transition are calculated by solving the equation,

$$N\,\Delta_{00}^{\rm P}(L,0)=(N+4)\,\Delta_{00}^{\rm P}(L+4,0)\,, \qquad (7)$$

where $\Delta_{00}^{\rm P}(L,0)=E_1^{\rm P}(L,0)-E_0^{\rm P}(L,0)$.

This work has been done in collaboration with K. Okamoto, M. Kaburagi, and T. Sakai.

[1] M. Oshikawa, J. Phys.: Condens. Matter **4**, 7469 (1992).
[2] T. Tonegawa, K. Okamoto, H. Nakano, T. Sakai, K. Nomura, and M. Kaburagi, J. Phys. Soc. Jpn. **80**, 043001 (2011).
[3] K. Okamoto, T. Tonegawa, H. Nakano, T. Sakai, K. Nomura, and M. Kaburagi, J. Phys. Conf. Ser. **302**, 012014 (2011).
[4] K. Okamoto, T. Tonegawa, H. Nakano, T. Sakai, K. Nomura, and M. Kaburagi, J. Phys. Conf. Ser. **320**, 012018 (2011).
[5] Y.-C. Tzeng, Phys. Rev. B **86**, 024403 (2012).
[6] J. A. Kjäll, M. P. Zaletel, R. S. K. Mong, J. H. Bardarson, and F. Pollmann, Phys. Rev. B **87**, 215106 (2013).
[7] K. Okamoto, T. Tonegawa, T. Sakai, and M. Kaburagi, JPS Conf. Proc. **3**, 014022 (2014).
[8] K. Okamoto, T. Tonegawa, and T. Sakai, J. Phys. Soc. Jpn. **85**, 063704 (2016).
[9] A. Kitazawa, J. Phys. A **30**, L285 (1997).
[10] K. Nomura A. and Kitazawa, J. Phys. A **31**, 7341 (1998).
[11] M. P. Nightingale: Physica A **83** (1976) 561.

Study on quantum annealing from a viewpoint of statistical mechanics

Shu TANAKA

Green Computing Systems Research Organization,

Waseda University, Waseda-cho, Shinjuku, Tokyo 162-0042

Quantum annealing is a promising calculation technique to perform combinatorial optimization [1,2]. We studied two topics on quantum annealing toward the construction of high-performance quantum annealing.

The first one is the quantum annealing on singular value decomposition. Hashizume et al. considered the adiabatic limit of the quantum annealing on the singular value decomposition [3]. Based on the previous study by Hashizume et al. [3], we studied dynamical properties of quantum annealing on singular value decomposition of random matrices. We investigated the performance of quantum annealing on the singular value decomposition up to five singular values depending on the energy gap at $t=0$ (initial state), the annealing time, and the selection of bases [4].

The second one is the quantum annealing on the Wajnflasz-Pick model which is a generalization of the Ising model [5]. In the model, the first-order quantum phase transition point is passed when we consider a usual quantum annealing using the time-dependent transverse field. It is known that a bottleneck of quantum annealing is the first-order quantum phase transition. We constructed a method to avoid the bottleneck by introducing a transverse *interaction* type quantum fluctuation [5].

References

[1] T. Kadowaki and H. Nishimori: Phys. Rev. E **58** (1998) 5355.

[2] S. Tanaka, R. Tamura, and B. K. Chakrabarti: “Quantum Spin Glasses, Annealing and Computation” Cambridge University Press, (2017).

[3] Y. Hashizume, T. Koizumi, K. Akiyama, T. Nakajima, S. Okamura, and M. Suzuki: Phys. Rev. E **92** (2015) 023302.

[4] Y. Hashizume, S. Tanaka, and R. Tamura: in preparation.

[5] Y. Seki, S. Tanaka, and S. Kawabata: J. Phys. Soc. Jpn. **88** (2019) 054006.

Transport properties of one-dimensional interacting electron systems by a quantum Monte Carlo method

Takeo KATO

Institute for Solid State Physics,

The University of Tokyo, Kashiwa-no-ha, Kashiwa, Chiba 277-8581

Effect of Coulomb interaction on electronic transport via nanoscale devices has been one of important problems in mesoscopic physics. It is still a challenging problem to evaluate electronic conductance in the presence of Coulomb interaction, in particular, at finite temperatures. In the present project, we considered interacting electron systems on a finite-size one-dimensional lattice, and tried to calculate a conductance in the one-body scattering problem by the quantum Monte Carlo method.

We first formulated the conductance by using the linear response theory, in which the current-current correlation function is related with the conductance [1,2]. Then, we considered the spinless Fermion chain with nearest-neighbor repulsive interaction with a local impurity one-body potential. Since this model is effectively described by the Tomonaga-Luttinger model [3], the model is convenient for consistency check of our formulation.

We employed the stochastic series expansion (SSE) method, which is one kind of the quantum Monte Carlo, to evaluate the current-current correlation function. On the supercomputer (system B), we have used simple parallelization method in the Monte Carlo sampling. We checked that the numerical results reproduce the conductance of the noninteracting electron systems, which is purely determined by the reflection probability. Furthermore, the numerical results show that the conductance is reduced from the one expected from the bare transmission probability. This behavior is consistent with the theory based on the Tomonaga-Luttinger model [3].

In order to obtain the conductance in more realistic situations, we need larger SSE simulations, which are left for the future important problem as well as improvement of our naive formulation based on the linear response theory.

References

[1] N. Shimada, Master Thesis (The University of Tokyo, 2018).

[2] N. Shimada and T. Kato, in preparation.

[3] C. L. Kane and M. P. A. Fisher, Phys. Rev. Lett. **68**, 1220 (1992)

Fast Algorithm for Generating Random Bit Strings

Hiroshi Watanabe
Institute for Solid State Physics, University of Tokyo
Kashiwa-no-ha, Kashiwa, Chiba 277–8581

Suppose we want to generate a bit string with length N in which each bit is set with arbitrary probability p. If we adopt the simple algorithm, which repeats check for each bit, we need to generate N random numbers. However, we can reduce the number of random number generations by adopting more sophisticated algorithms [1, 2]. We proposed three algorithm, the Binomial-Shuffle (BS), the Poisson-OR (PO), and the finite-digit algorithms.

The Binomial-Shuffle algorithm is an algorithm that first calculates how many bits are set and then shuffles them. Adopting Walker's alias method and Floyd's sampling method, it is possible to generate a random bit string with $pN+1$ random number generations. The Poisson-OR algorithm generates k bit strings with one of the bits is set randomly and takes the logical OR of them. This is a special case of the algorithm proposed by Todo and Suwa [3]. The average number of the random number generations is $-N\log(1-p)+1$. The finite digit method is effective when the probability p can be represented by a finite digit in the binary notation. When the probability p can be expressed by n digits in the binary notation, we can generate a random bit string with that probability by generating n bit strings in which each bit is set with a probability 1/2 and properly taking the logical operations. Therefore, the finite-digit algorithm with n digits involves the random number generates n times.

We constructed a hybrid algorithm, i.e., which first generates a bit string with probability $\tilde{p}$ close to p with the finite digit algorithm and corrects the difference $\tilde{p}-p$ by the Binomial-Shuffle or Poisson-OR algorithms. The expected number of random numbers generated to generate a string in which each bit is set with arbitrary probability is at most 7 for the 32-bit case and 8 for 64-bit case. Employing the developed algorithm, we applied the multispin coding technique to the one-dimensional bond-directed percolation and obtained a factor of 14 speed-up.

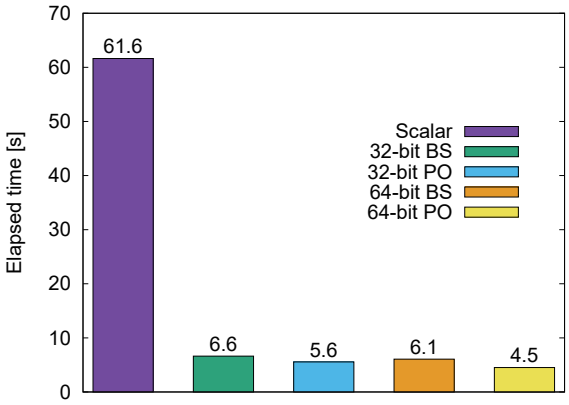

Figure 1: Multi-spin coding of the directed-percolation. Times required for the simulations with 32768 steps and 1000 independent samples with L = 32768.

References

[1] H. Watanabe, S. Morita, S. Todo, and N. Kawashima, J. Phys. Soc. Jpn. 88, 024004 (2019)

[2] `https://github.com/kaityo256/rbs`

[3] S. Todo and H. Suwa, J. Phys.: Conf. Ser. 473, 012013 (2013).

Dynamics of structure formation in charged colloids

Kyohei Takae and Hajime Tanaka
Institute of Industrial Science, University of Tokyo
4-6-1 Komaba, Meguro-ku, Tokyo 153-8505, Japan

We investigate non-equilibrium dynamics in charged colloidal suspensions. In numerical simulations of colloidal suspensions, an efficient computational methods called Fluid-Particle-Dynamics (FPD) method is often applied to study hydrodynamic effects in structure formation kinetics and responses to external field. In previous studies of charged colloidal solutions, it is assumed that the surface charge of the colloids are constant both in space and time. However, it is widely recognized that the surface charge becomes inhomogeneous under heterogeneous environment such as colloidal solutions in binary solvents and solutions under external fields. The surface charge also varies in time under nonequilibrium conditions. In these cases, surface charges relaxes to satisfy electrochemical equilibrium at the surface. This effect is called *charge regulation*, and is of great interest in chemistry and biology. We construct theoretical framework of electrohydrodynamics in colloidal solutions with charge regulation and thermodynamic consistency. By performing numerical simulations, we show application of our method to electrostatic and electrokinetic problems, where charge regulation plays an important role. We examine cluster formation of colloid particles where a significant reduction of the electrostatic repulsion between colloids results in the extra stabilization of clusters with a more compact shape. We also a dynamical problem, that is, single colloid particle under an external field. The surface charge of the colloid becomes highly heterogeneous under a strong electric field due to the deformation of the counterion cloud, resulting in the enhancement of electrokinetic mobility. We also examine collective dynamics of charged colloids under external electric field, where they form crystalline ordering in quiescent state.Under strong electric field, particles undergo collective vibration along the field direction, and eventually the crystals melt into disordered state. This is essentially caused by hydrodynamic interaction among the particles. To see this, we also examine the same calculation but neglecting hydrodynamic interaction by solving Brownian limit of our model, where we find no instability, clearly indicating that the instability is due to the electrohydrodynamic coupling. By these examples, we show not only the importance of considering charge-regulation effects in the self-organization of charged systems but also the applicability of our simulation method to more complex problems of charged soft matter systems.

References

[1] K. Takae and H. Tanaka: Soft Matter **14** (2018) 4711.

Calculation of higher-order moments by higher-order tensor renormalization group method

Satoshi MORITA

Institute for Solid State Physics,

The University of Tokyo, Kashiwa-no-ha, Kashiwa, Chiba 277-8581

Tensor networks (TN) are powerful tools for quantum and classical many-body problems. The tensor renormalization group method (TRG) provides an efficient contraction scheme based on coarse-graining TNs. The higher-order tensor renormalization group method (HOTRG) is one of the few TN methods applicable to higher-dimensional systems [1].

We propose a calculation method for higher-order moments of physical quantities based on HOTRG [2]. In TN methods, there are two ways of calculating an expectation value of a physical quantity like the magnetization. One method is numerical differentiation of the free energy with respect to the external field. The other is introduction of the impurity. However, both the methods have some difficulty in calculation of higher-order moments, which are important for analysis of critical phenomena. To resolve this problem, we introduce a coarse-grained tensor which represents summation of all configurations of multiple impurities and derive its update rule based on the systematic summation scheme. We showed that a jump of the Binder ratio precisely determines the transition temperature in the two-dimensional Potts model. The finite-size scaling analysis provides critical exponents and distinguishes the weakly first-order and continuous phase transitions.

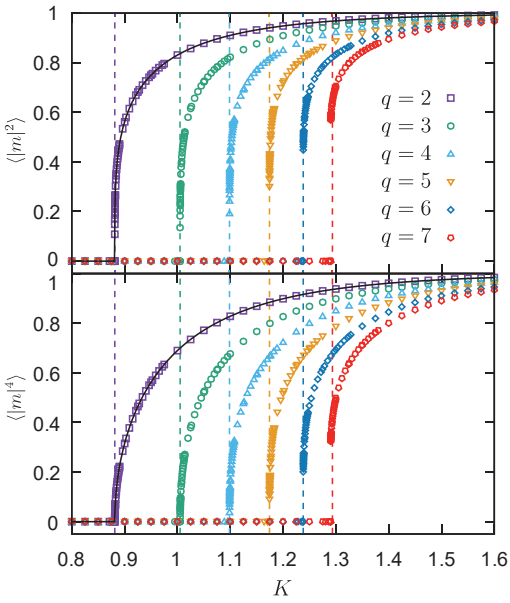

Fig. 1: The 2nd- and 4th-order moments of the magnetization of the q-state Potts model on a $2^{20} \times 2^{20}$ square lattice by HOTRG with $\chi = 48$.

References

[1] Z. Y. Xie, et al., Phys. Rev. B **86**, 045139 (2012)

[2] S. Morita and N. Kawashima, Comput. Phys. Commun, **236**, 65-71 (2019)

Compression behavior and inhomogeneous structure of silica glass in its intermediate state in structural transformations

Daisuke WAKABAYASHI[1] and Fuyuki SHIMOJO[2]

[1]*Photon Factory, Institute of Materials Structure Science, High Energy Accelerator Research Organization (KEK), Tsukuba 305-0801*

[2]*Department of Physics, Kumamoto University, Kumamoto 860-8555*

Silica glass is well known as an archetypal oxide glass and its compression behavior has attracted considerable attention in various fields of physical sciences. Recent small-angle X-ray scattering measurements have revealed the subnanometer-scale inhomogeneity appears in silica glass during the pressure-induced structural transformations [1].

To reveal the detailed structure of subnanometer-scale inhomogeneity, we have to conduct large-scale molecular-dynamics (MD) simulations with a system of ~10,000 atoms. We have confirmed that ab-initio methods can simulate the compression behavior of silica glass accurately [2]. On the basis of the results of ab-initio calculations, we fitted the potential with a machine-learning technique (ANN potential) and applied it for the calculations with an extended system.

To obtain the data for fitting ANN potentials, we conducted ab-initio calculations. The configurations of six-coordinated or densified four-coordinated glasses (corresponding to high-pressure phases of silica glass) were prepared by gradually cooling silica melt from 4,000 K at high pressures, and then the decompression and recompression processes were calculated. There is remarkable agreement between the densities on decompression and recompression. This suggests not only that six-coordinated and densified four-coordinated glasses behave in an elastic manner as a single phase but also that glass in the intermediate state seems to behave like a single phase, which agrees with our model.

We tested the MD simulations with a system of about 30,000 atoms using the ANN potential determined from the data at 40 GPa. The calculations at high temperatures can be made without numerical divergence by setting an appropriate time step. Large-scale simulations of decompression process will be carried out in the near future.

References

[1] T. Sato, N. Funamori, D. Wakabayashi, K. Nishida, and T. Kikegawa: Phys. Rev. B **98** (2018) 144111.

[2] E. Ryuo, D. Wakabayashi, A. Koura, and F. Shimojo: Phys. Rev. B **96** (2017) 05420.

Application of Eigenstate Thermalization Hypothesis to Non-equilibrium steady states

Tatsuhiko SHIRAI
Green Computing Systems Research Organization, Waseda University
Waseda-chou, Shinjuku-ku, Tokyo 162-0042

We have studied steady states of quantum many-body systems in a weak contact with out-of-equilibrium environment [1]. It is found that Gibbs state at a certain effective temperature can describe the steady state in some open quantum systems in spite of the violation of the detailed balance condition. The argument of the realization of the Gibbs state is based on the validity of the perturbation theory on weak system-environment coupling and the eigenstate thermalization hypothesis (ETH).

As for the weak coupling peturbation theory, it is known that the convergence radius of the perturbation series quickly shrinks to zero with the system size in generic open quantum systems [2]. Nevertheless, our numerical calculation of some spin systems suggest that the leading-order perturbative solution well describes the steady state in the thermodynamic limit provided that there is no current of a conserved quantitity in the bulk. This implies that the perturbative expansition is a kind of an asymptotic expansion. Furthemore, it also turns out that the perturbation theory completely fails when there is current in the bulk. We demonstrate the failure of the perturbation theory in a Bose-Hubbard model coupled to environments with different chemical potentials at each end.

As for the ETH, it is recognized as an important property of the Hamiltonian that explains the approach to themal equilibrium in isolated quantum system [3, 4]. With this property, if a density matrix is diagonalized in the basis of energy eigenstates and has a subextensive energy fluctuation, the state is indistinguishable from the Gibbs state at a certain effective temperature as far as we observe local quantities. We argued that in an open quantum system, the leading-order perturbative solution meets the above condition. Therefore, by combining the ETH with the perturbation theory, we can conclude that the steady state is described by the Gibbs state irrespective of the detailed balance condition.

In numerical simulations, we solve a quantum master equation called the Lindblad equation, which describes a time evolution of open quantum systems. Based on the symmetry of the time-evoluation operator of the Lindblad equation, we divide the density matrix into some sectors. We assign the matrix elements in each sector to each core, and perform a parallel simulation using openMPI.

References

[1] T. Shirai, and T. Mori: arXiv:1812.09713.

[2] H. C. F. Lemos, and T. Prosen: Phys. Rev. E **95** (2017) 042137.

[3] M. Rigol, V. Dunjko, and M. Olshanii: Nature **452** (2008) 854.

[4] T. Mori, T. N. Ikeda, and E. Kaminishi, and M. Ueda: J. Phys. B **51** (2018) 112001.

Structural Change of Electrolyte Solution in Nanospaces

Md Sharif Khan and Tomonori Ohba

Graduate School of Science,

Chiba University, 1-33 Yayoi, Inage, Chiba 263-8522

Massive parallel computer simulation has been used to elucidate the structural properties of the organic and aqueous electrolytes confined in the different carbon nanospaces. In nanospaces, molecules show unique properties by changing their structure and dynamics and have the potential applications in future technologies and industries [1]. Electrolytes in nanospaces play an important role in various fields including electrochemistry, biochemistry, biotechnology, and ion channel technology [2]. Various electrolytes such as aqueous electrolytes and organic electrolytes (OEs) have been utilized for their own advantages, however, the performance of those electrolytes can be extensively influenced due to the change of dynamics and structure in nanospaces [3]. The comprehensive understandings of the electrolyte structure and dynamics in the nanospaces are crucial to improve these technologies and develop efficient new technologies. We have been employed fully atomistic simulations to study the behavior of different electrolyte salts and different organic solvents in slit and cylindrical carbon nanopores, to reveal the structure and storage mechanism. Organic solvents with different properties were selected: ethylene carbonate (EC), propylene carbonate (PC) and ethyl methyl carbonate (EMC). We demonstrate, due to the one-dimensional confinement in CNTs there are much fewer ions inserted into the nanotubes than the amount inserted into slit carbon nanopores. Further, linear like structure EMC solvent shows higher performance owing to high cation accessibility rather than cyclic solvents EC and PC **(Fig. 1)** [4].

In addition, we have evaluated the structure

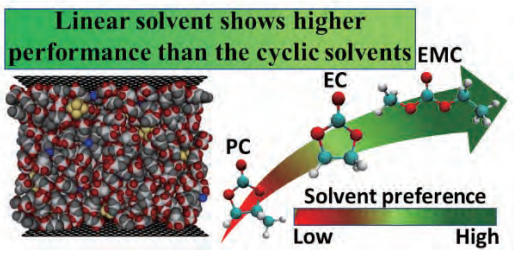

Fig. 1. Organic solvents effect on Na ion storage

of water, NaCl and LiCl aqueous solutions inside the carbon nanotubes with diameter 1 and 2 nm were evaluated by using molecular dynamics simulations and benchmarked the simulation outcomes by X-ray diffraction [5]. The intermolecular distances in aqueous solutions were decreased from that in water system in carbon nanotubes with 1 nm pore, while longer than those in carbon nanotubes with 2 nm pore. Significant hydration formation was observed in 2 nm carbon nanotubes since the elongated nearest neighbor distances were observed. Ions play the dominant role in the anomalous structure in extremely narrow carbon nanotubes.

References

[1] T. Ohba, K. Ideta, K. Hata, S. Yoon, J. Miyawaki: ChemPhysChem. **17** (2016) 3409.

[2] D. A. Newsome, D. S. Sholl: Nano Lett. **6** (2006) 2150.

[3] M. S. P. Sansom, P. C. Biggin: Nature ***414***, (2001) 156.

[4] A. Karatrantos, S. Khan, T. Ohba, Q. Cai: Phys. Chem. Chem. Phys. *20*, (2018) 6307.

[5] S. M. Khan, S. Faraezi, Y. Oya, K. Hata, T. Ohba: Adsorption in press.

Nonequilibrium phase transition and slow dynamics in the dense hard sphere systems

Masaharu ISOBE
Nagoya Institute of Technology
Gokiso-cho, Showa-ku, Nagoya, 466-8555

As one of the simplest model, the hard disk/sphere systems have been investigated in the field of both equilibrium and non-equilibrium statistical physics. In this project, we investigated non-equilibrium phenomena in the hard disk/sphere model system with modern algorithms, especially for Event-Chain Monte Carlo(ECMC) [1] and Event-Driven Molecular Dynamics(EDMD) [2], where we propose the "Hybrid Scheme", namely, ECMC for equilibration and EDMD for calculation of dynamical properties [3, 4].

Physical origin of facilitation in athermal molecular systems on approaching glass transition:

On approaching glass transition, the viscosity of the supercooled liquid would be increased rapidly. It often behaves as solid with disorder structure within an experimental timescale. One of the challenging issues is to understand whether the essential properties of glass forming materials is fundamentally thermodynamic or dynamic in origin. However, the microscopic origin of structural (so-called α) slow relaxation in deeply supercooled liquids at an atomic scale has remained elusive due to the limitation of both electron microscopy experiment and computer simulation. Although many theoretical models have been discussed, one of a perspective that favors a dynamic origin is called Dynamic Facilitation (DF) theory [5, 6, 7]. DF theory was known to explain a wide range of empirically observed dynamical features of thermal supercooled liquids and glasses. Recently, we devoted to investigating the applicability of DF theory to athermal systems, i.e., systems of hard particles where the relevant control parameter is pressure rather than temperature, under "supercompressed" conditions. By employing novel efficient algorithms [1, 2, 3], it was possible to find true equilibrium states and generate the phase diagram of a binary mixture of hard spheres. The novel methodologies allowed studying in detail the equilibrium dynamics of high-density systems. The slow relaxation at these conditions is consistent with the predictions of DF theory generalized to systems controlled by pressure rather than temperature. In such athermal molecular systems under "super-compressed" conditions — where what is facilitated is the ability of the constituent particles to structurally relax — giving rise to correlated and cooperative dynamics, in a manner predicted by theory [8]. In collaboration with the experimental group in Hong Kong, we resolve in detail that colloidal particles undergo a transition from collective "creeping" to the string-like "hopping" motion on approaching the glass transition, and the structural relaxation of the supercooled glass is just caused by string-like escape hopping motion. Furthermore, such a string-like motion has an ultra-high returning hopping probability which is proved to be the leading contribution to the kinetic arrest for slow relaxation. These results are also confirmed by extensive molecular dynamics simulation and show an evidence of the scenario of

DF theory [9].

References

[1] E. P. Bernard, W. Krauth, and D. B. Wilson: Phys. Rev. E **80** (2009) 056704.

[2] M. Isobe: Int. J. Mod. Phys. C **10** (1999) 1281.

[3] M. Isobe: Mol. Sim. **42** (2016) 1317.

[4] M. Isobe: "Advances in the Comutational Sciences — Proceedings of the Symposium in Honor of Dr Berni Alder's 90th Birthday", edited by Eric Shwegler, Brenda M. Rubenstein, and Stephen B. Libby, World Scientific, **Chapter 6** (2017) 83.

[5] D. Chandler and J. P. Garrahan: Annu. Rev. Phys. Chem. **61** (2010) 191.

[6] L. O. Hedges, R. L. Jack, J. P. Garrahan and D. Chandler: Science **323** (2009) 1309.

[7] A. S. Keys, L. O. Hedges, J. P. Garrahan, S. C. Glotzer, and D. Chandler, Phys. Rev. X, **1** (2011) 021013.

[8] M. Isobe, A. S. Keys, D. Chandler, and J. P. Garrahan: Phys. Rev. Lett. **117** (2016) 145701.

[9] C.-T. Yip, M. Isobe et al.: in preparation.

phase field simulation for amoeboid cells

Nen SAITO
Graduate School of Science, The University of Tokyo
7-3-1 Hongo, Bunkyo-ku, Tokyo 113-8656, Japan

Biological systems show variety of dynamic changes in morphology. Specifically in single cell morphodynamics, large deformations, such as membrane internalization (endocytosis) and externalization (exocytosis), occurs constitutively and spontaneously. In such morphological changes, geometry of membrane is not simple and the geometry itself deforms in time, which is quite different from theory of pattern formation via reaction-diffusion equation on a flat surface. How such shapes dynamics emerges in a self-organized manner is an important question not only for cell biology but also for physics.

To address dynamics in morphology of cell, we focus on macropinocytosis. Macropinocytosis is clathrin-independent endocytosis and allows internalization of large volume of extracellular fluid, as is illustrated in Fig1(a). Dictyostelium discoideum and tumor cells show constitutive macropinocytosis for uptake of nutrients from extracellular fluid. With help of recent advance of microscopy for 3D observation, macropinocytosis has been considered to be driven by self-organizing pattern of actin polymerization on the membrane. However, it remains still unknown how macropinositosis cup structure (see Fig1(a)) forms, how it closes and what chemical reactions make it possible.

From theoretical perspective, we introduce a mathematical model based on 3D phase-field method, which enables reaction-diffusion process on the membrane and large membrane deformation simultaneously. Phase field method has been wildly applied for numerical tracking of interface motions such as crystal growth, phase separation, and also 2-dimensional dynamics of amoeba cell [1]. The proposed model with the help of GPU successfully describes a spontaneous large invagination of cell membrane (see Fig1(b)), which is resemble to actual macropinocytosis observed in several experiments. Simulation results indicate that simple reaction-diffusion process on the cell membrane lead to drastic membrane deformation, which results in an engulfment of extracellular fluid [2]. We will continue to perform simulations with different parameters, and to analyze the results.

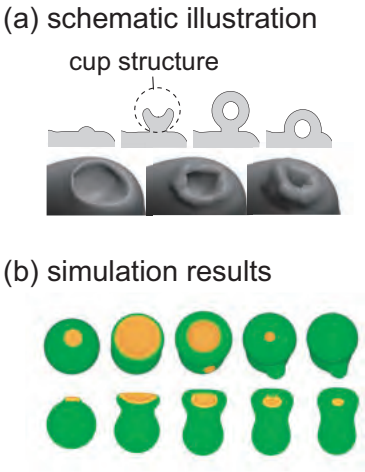

Figure 1: macropinocytosis

References

[1] D. Taniguchi, et al. Proc. Natl. Acad. Sci. U.S.A. 110(13), 5016 (2013) R. Kubo: J. Phys. Soc. Jpn. **12** (1957) 570.

[2] N. Saito and S. Sawai in preparation

Constructing the database of exited states for desigining photosynthetic pigments to absorb the longer wavelength radiation

Yu Komatsu
NINS Astrobiology Center, National Institutes of Natural Sciences
NINS National Astronomical Observatory, National Institutes of Natural Sciences
2-21-1 Osawa, Mitaka, Tokyo, 181-8588

Molecules absorbing longer wavelength radiation is gathering attention in varieties of research fields, e.g.) bioimaging and dye sensitized solar cell. In addition, in order to detect traces of photosynthesis from planets outside our solar system, it has been significant to learn limitations of photosynthesis from the red molecules or pigments. Here, starting with natural photosynthetic pigments, the database of excited states of pigments are being constructed for these applications. As an attempt through the construction of the database, the effect of the central metal of the pigments is examined. Bacteriochlorophyll *b* is a natural photosynthetic pigment which has the reddest absorption band. Like the other chlorophyll-type pigments, it has a tetrapyrrole-ring, which includes a central metal ion as Mg. With the tetrapyrrol, possessing metal ions has a significant benefit to adopt to changing environments and to have various functions.

Here, to focus on the ring, the effect of the central metal in bacteriochlorophyllide *b* (M-Bchl *b*) was investigated at DFT level. With CAM-B3LYP/Def2tzvp//B3LYP-D3/6-31G(d), the excited and ground states of M-Bchls *b* were estimated; M=2H, Mg, Ca, Ni, Zn, Sr, Pd, Cd, Pt, Hg and Pb. For M=Mg, 2H and Zn, the estimated energies in the first excited states are 757.03, 722.66, 737.46 nm, respectively. The energy for M=Pb is 771.60 nm as the longest wavelength absorption, while that for M=Pt is 698.24 nm as the lowest (73.36 nm difference). Moreover, elec-

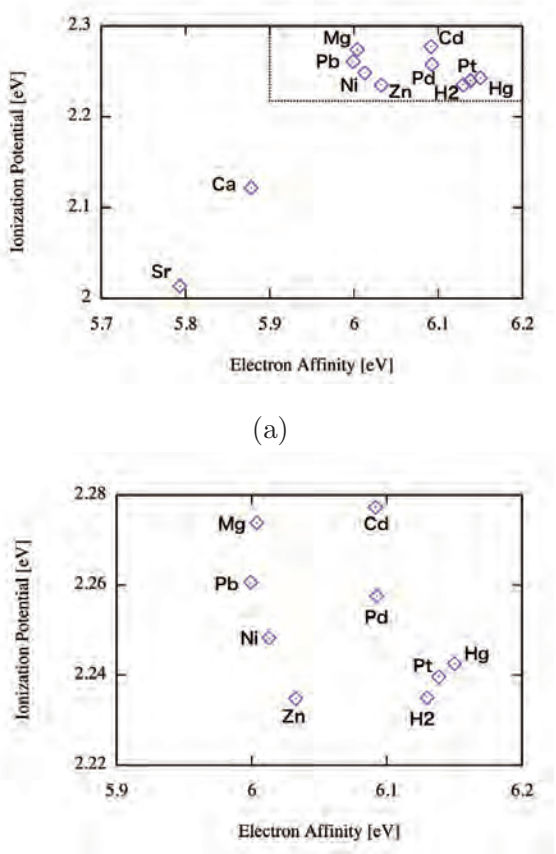

(a)

(b)

Figure 1: (a) Electron affinities and Ionization potentials for M-Bchl *b*. (b) The enlarged figure from the top right part of (a).

tron affinities and ionization potentials for M-Bchls *b* are shown in the Figure 1. The pigments for M=Ca and Sr do not seem to be alternative to original because of being apart from the others and their large atomic radius.

With the supercomputer in ISSP, NWChem 6.6 was used to make the model selection, including functionals and basis functions. The main calculations were performed with the supercomputer in NAOJ.

Realization and Manipulation of Topological States by Nanostructures

Toshikaze Kariyado

International Center for Materials Nanoarchitectonics,

National Institute for Materials Science, Namiki, Tsukuba, Ibaraki 305-0044

The main focus of this project was on (i) orbital magnetism in topological semimetals, and (ii) electronic states of graphene with nanostructure, where the supercomputing resources are required mainly for ab-initio simulations and model construction on top of that, and occasionally for massive parallelization in k-point sampling in computation of response functions.

For (i) orbital magnetism in topological semimetals, a Dirac material Sr_3PbO is analyzed as a typical example. After a little consideration, it turned out that some minor details of the band structure details of the band structure may have sizable effects on the magnetic susceptibility. Then, we first construct a model reflects features of the first-principle band structure using the maximally localized Wannier function method. By optimizing the number of relevant orbitals, we could successfully construct an improved model comparing with the previous work [1]. Using the improved model, the magnetic susceptibility is calculated using the Green's function based formula. In order to capture the contribution from Dirac electrons, or band singularities, a fine mesh is required for the k-point sampling. For this, we applied massive parallelization on the k-point sampling for numerical efficiency. The obtained results show fairly good agreement with experiments.

For (ii) graphene with nanostructure, we explored possible topological states in graphene nanomesh. We have established that by changing the hole alignment in nanomesh, the topological character can be tuned [2]. The topological characterization was done through the interface states, and also through the inspection of the irreducible representation of the relevant bands derived through the first-principles calculation.

References

[1] T. Kariyado and M. Ogata, J. Phys. Soc. Jpn. **81** (2012) 064701.

[2] T. Kariyado, Y.-C. Jiang, H. Yang, and X. Hu, Phys. Rev. B **98** (2018) 195416.

Quantitative Analysis of the Influence of Pulley Effect on the Strain-Hardening of Slide-Ring Gels.

Koichi Mayumi[1], Yusuke Yasuda[1], Masatoshi Toda[2], Hideaki Yokoyama[1], Hiroshi Morita[2], and Kohzo Ito[1]

[1] *Dept. of Advanced Materials Science, Graduate School of Frontier Sciences, the University of Tokyo, 5-1-5 Kashiwa-noha, Kashiwa, Chiba 277-8561.* [2]*National Institute of Advanced Industrial Science and Technology (AIST), 1-1-1, Umezono, Tsukuba, Ibaraki 305-8568.*

Slide-ring (SR) gel is a kind of supramolecular polymer network that does not have direct cross-links between polymer chains, but topological constraint by figure-of-8 shaped cross-linking molecules between them. [1] The unique feature of SR gel is that it has large deformability and toughness. [2]

The molecular origin of this deformability has been explained by a hypothesis, "pulley effect" [1]. In SR gels, movable cross-links act like pulleys and prevent stress-concentration on short chains in the networks. However this hypothesis has not been verified, because the visualization of the cross-linking points is experimentally difficult.

In the previous project, we fabricated a coarse-grained model of SR gels and conducted a uni-axial deformation simulation by means of molecular dynamics simulation technique, and succeeded in visualizing the pulley effect (Fig. 1(b).), and unexpected orientations of figure-of-eight cross-links (Fig. 1(a).), suggesting there is another mechanism contributing to stress relaxation of SR gels under deformation. (Fig. 1(c).)

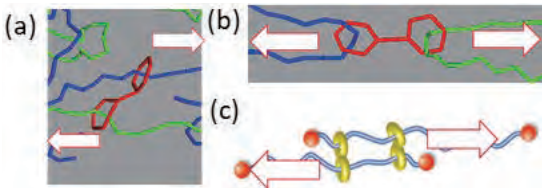

Fig. 1. (a) Unexpected orientation of figure-of-eight crosslinks (b) the orientation expected from pulley effect (c) the stress relaxation mechanism considered from orientation (a)

In this project, we visualized stress distribution in SR gels under deformation and analyzed local stress applied to the cross-links and polymer chains separately. Based on the results, we discuss which orientation of the cross-links shown in Fig.1 is dominant in SR gels.

We fabricated coarse-grained models of SR gel and fixed-crosslinking (FC) gel with the same crosslinking density using beads-spring model [3]. 20,000 and 35,000 beads system was used

for FC and SR gel, respectively. For simulation, we conducted Langevin dynamics equilibration simulation for $1.0 \times 10^7\ \tau$. Then we tried elongation simulation at an elongation speed of $4.37 \times 10^{-4}\ \sigma/\tau$ up to maximum elongation ratio $\lambda = 11$. The molecular dynamics simulations were performed using COGNAC engine in OCTA system, and LAMMPS.

Fig.2 shows stress distribution of FC and SR gels under large deformation. The chains loading more than $70\epsilon/\sigma$ force are colored in red, shown in Fig. 2. In FC gels, fully-stretched chains are percolated from end to the other end at a starch ratio of $\lambda = 5.5$. On the other hand, there is almost no fully stretched chain in SR gels at a stretch ratio of $\lambda = 7$, indicating that there is a stress relaxation mechanism owing to the effect of slidable cross-links in SR gels.

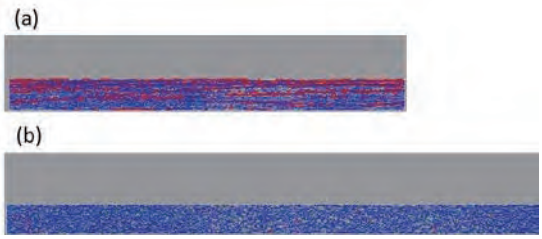

Fig. 2. Visualization of stretched bond by coloring the bonds loading force over $70\epsilon/\sigma$ in red for (a) FC gel at $\lambda = 5.5$ and (b) SR gel at $\lambda = 7$.

Next, Fig. 3 shows the stretch ratio dependence of loaded forces on cross-linking points and main chains in FC and SR gels. From Fig. 3(a), the averaged force loaded on both the main chains and cross-linking points increases with stretch ratio λ. The force loaded on the cross-linking points are larger than that on the main chains, suggesting the stress concentration at cross-linking point occurs under deformation in FC gels. Differently in the case of SR gels, only the stress on axial chains increases with deformation. Conversely, the stress on cross-linking points in SR gels hardly increases. If pulley effect was the main stress-relaxation mechanism of SR gels, stress would concentrate on both the cross-linking points and main chains in the same way as FC gels. Thus, these results suggest that the major molecular origin of the stress relaxation in SR gels is not the pulley effect (Fig. 1(a)), but the unexpected orientation of the cross-links perpendicular to deformation (Fig. 1(b)).

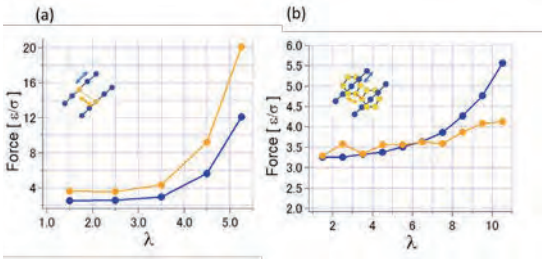

Fig. 3. Averaged forces loaded on crosslinking bond (yellow) and main chain (blue) for (a) FC gels and (b) SR gels.

References

[1] Y. Okumura, and K. Ito: *Adv. Mater.* **13** (2001) 485.

[2] K. Ito: *Polym. J.* **39** (2007) 489

[3] K. Kremer, G. S. Grest: *J. Chem. Phys.* **92** (1990) 5057.

Numerical study of vortices in ferromagnetic superconductor

Hirokazu TSUNETSUGU

The Institute for Solid State Physics,

The University of Tokyo, Kashiwa-no-ha, Kashiwa, Chiba 277-8581

This project has targeted a numerical study on the effects of domain structure on spatial configuration of supercurrent and vortices in ferromagnetic superconductors. A few uranium-based compounds exhibit a superconducting transition within their ferromagnetic phase, and two orders coexist. This is a very interesting system in that two different types of spontaneous symmetry breaking correlate. Domain walls of magnetic structure and vortices of superconducting current are two types of topological defects in ferromagnetic superconductors, but their interplays and correlations have not been well understood yet.

The possibility of self-induced vortex lattice has been pointed out as a distinguishing characteristic of ferromagnetic superconductors. We planned two stages of numerical investigation into this topic. The first stage employs a phenomenological Ginzburg-Landau model, and the second stage proceeds to target a microscopic tight-binding model of electrons with ferromagnetic electron-electron interactions. These interactions are treated by local mean-field approximation that converts the Hamiltonian into a Bogoliubov-de Gennes model. In these analyses, superconducting order parameters as well as electrons couple to magnetic field, which follows Maxwell's equations and are generated by electric currents.

Magnetic field is represented by vector potential, and this vector potential attaches the Peierls phase to electron hopping amplitudes in the microscopic model in the second stage. We plan to introduce ferromagnetic order and domain structure by a proper setting of their corresponding local order parameters.

We investigated the system with torus geometry and magnetic domain extends along its circumference direction, and found emergent supercurrent flowing parallel to the domain wall. We also found that the current direction depends on whether the magnetic domain wall is either Ising or Bloch type.

A big challenge in computations is the search of self-consistent solutions of the Bogoliubov-de Gennes and Maxwell equations. This is needed for understanding self-induced vortices in the microscopic level, and it is interesting to examine the difference in the local electronic structure between near and far from a vortex core.

Estimation of the density of states using Maximum entropy method and Sparse modeling

Yasuhiro H. MATSUDA

Institute for Solid State Physics,

The University of Tokyo, Kashiwa-no-ha, Kashiwa, Chiba 277-8581

We have studied a Shastry-Sutherland antiferromagnet $SrCu_2(BO_3)_2$[1] using massive parallel computer simulations. We have used a numerical solver HPhi[2] for calculation by thermal pure quantum states[3].

For obtaining field dependence of magnetic entropy, several calculations have been done with various fields. The calculation by thermal pure quantum states have reproduced substantially the magneto-caloric effect measurements on $SrCu_2(BO_3)_2$ (Fig. 1).

References

[1] Y. H. Matsuda *et al.*,: Phys. Rev. Lett. **111** (2013) 137204.

[2] M. Kawamura *et al.*,, Comp. Phys. Commun. **217** (2017) 180.

[3] S. Sugiura and A. Shimizu, Phys. Rev. Lett. 108 (2012) 240401.

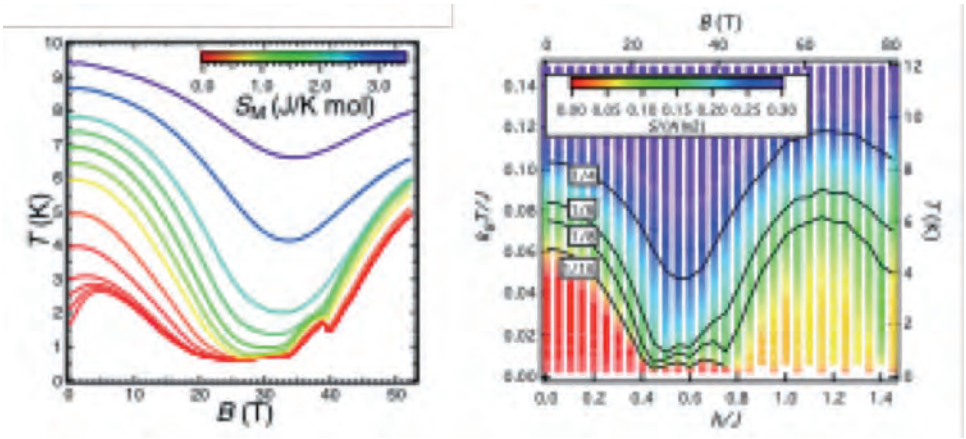

Fig.1 (Left) Temperature variation of $SrCu_2(BO_3)_2$ with various initial temperature due to Magneto-caloric effects. The colors of the lines show the magnetic entropy.
(Right) Color map of magnetic entropy of Shastry-Sutherland lattice system.

Theoretical studies on kagome antiferromagnets and related systems

Yoshiyuki Fukumoto
Department of Physics, Faculty of Science and Technology, Tokyo University of Science
2641 Yamazaki, Noda, Chiba 278-8510

We made, in this year, finite-temperature calculations of the spin-1/2 spherical kagome cluster and exact-diagonalization calculations for the orthogonal dimer system.

In the study of the spherical kagome cluster, taking Dzyaloshinskii-Moriya (DM) interactions into account, we study effects of thermal fluctuations on the magnetization process and magnetic field effects on the specific heat. The usage of the supercomputer is vital to carry out the present calculations, because (i) the dimension of the Hilbert space amounts to $2^{30} \simeq 10^9$ for our model with thirty spins and DM interactions and (ii) the present calculation contains two sampling procedures concerned with initial vectors of thermal pure quantum states and magnetic-field directions. Several years ago, we calculated specific heat under magnetic fields for spherical kagome cluster without DM interactions [1]. Recently, Kihara *et al.* made an experimental study on the low-temperature specific heat of a spherical kagome material $\{W_{72}V_{30}\}$ [2]. They reported that the total number of singlet states below the first triplet excitation is consistent with the theoretical result [1], but the curves of specific heat are different from each other qualitatively. In particular, the experimental specific heats show no magnetic-field dependence, although the theoretical specific heats depend on it. The DM interactions are expected to affect specific heat at low temperatures. However, the present calculations indicates that the DM interactions can not resolve the discrepancy between the theory and experiment. Thus, we have to explore other mechanisms.

As for the orthogonal dimer system, recently, Nakano *et al.* used the exact diagonalization method to find a new phase in the ground state phase diagram [3]. The main purpose of the present study is to clarify the nature of this new phase. In the present calculation, we consider extended models with (a) plaquette structures, (b) dimer structure, or (c) Ising-type anisotropy to study the adiabatic connection between the new phase and each of limits in (a)-(c). These extended models were used in series expansion studies [4, 5]. The first series expansion study, for the extended model of (a), suggested the existence of the plaquette phase [4]. A successive series expansion study reported that the ground state energy via the plaquette expansion is higher that via the dimer expansion [5]. However, it is not clear what these series expansion results mean. We hope the present exact-diagonalization study to shed light on this issue.

References

[1] N. Kunisada *et al.*, PTEP 2014, 41I01 (2014).
[2] T. Kihara *et al.*, PRB 99, 064430 (2019).
[3] H. Nakano *et al.*, JPSJ 87, 123702 (2018).
[4] A. Koga *et al.*, PRL 84, 4461 (2000).
[5] W. Zheng *et al.*, PRB 65, 014408 (2001).

Theoretical study for superconductivity in multilayer cuprates with two-particle self-consistent approach

Kazutaka NISHIGUCHI
Graduate School of Engineering Science, Osaka University,
Toyonaka, Osaka 560-8531
Graduate School of Science, Technology, and Innovation, Kobe University,
Nada-ku, Kobe 657-8501

In this report, the main result of "Theoretical study for superconductivity in multilayer cuprates with two-particle self-consistent approach" in 2018 fiscal year with using the supercomputer at ISSP is presented.

Superconductivity arising from layer differentiation in multilayer cuprates [1]

One salient feature in cuprate superconductors is that, if we look at representative homologous series, e.g., Hg-based multi-layer cuprates $HgBa_2Ca_{n-1}Cu_nO_{2n+2+\delta}$ [called Hg-12$(n-1)n$], where n is the number of CuO_2 layers within a unit cell and δ is the doping, the superconducting (SC) transition temperature T_c becomes the highest for multi-layer cases, which possess the highest T_c ($\simeq$ 135 K for Hg-1223) to date at ambient pressure. The CuO_2 plane can be described by the Hubbard model with on-site Coulomb repulsion along with electron hopping, where a competition between the itinerancy and localization of electrons takes place due to electron correlations. If we look more closely at the n-layer cuprates, T_c systematically depends on n for each homologous series: T_c increases for $1 \leq n \leq 3$ and decreases slightly and saturates for $n \geq 3$. To explain the superconductivity and other electronic properties, several pictures for the multi-layer superconductor have been theoretically proposed so far.

Recently, we have studied normal properties (carrier concentrations and magnetism) of OP and IP by investigating the three-layer Hubbard model as an effective model for Hg-1223, where we have employed the two-particle self-consistent (TPSC) approach for multi-layer systems [2]. When we applied this to the trilayer system, we first found that the concentration of hole carriers tends to be larger in OP than in IP with increasing on-site Coulomb repulsion, which is an electron correlation effect. Then the AF instability in the IP is shown to be always larger than in the OP. These results are consistent with the NMR results on the antiferromagnetism and carrier concentrations in OP and IP mentioned above. In particular, the many-body charge transfer between the OP and IP can be called a *self-doping effect*.

These have motivated us here to investigate the superconductivity itself in the multi-layer cuprates. Thus the present paper theoretically identifies the factors governing superconductivity in multi-layer cuprates with a three-layer Hubbard model in the TPSC approach. By solving the linearized Eliashberg equation for the gap function in a matrix form to examine the role of OP and IP, we shall show for the trilayer strongly correlated system that OPs dominate in the $d_{x^2-y^2}$-wave superconductivity, while IP dominates in the antiferromagnetism. This is caused by electron correlations because the crucial factor for the differentiated doping rates between OPs and IP, i.e. the self-doping effect, takes place in intermediate and strong correlation regimes.

Physically, the self-doping makes the strengths

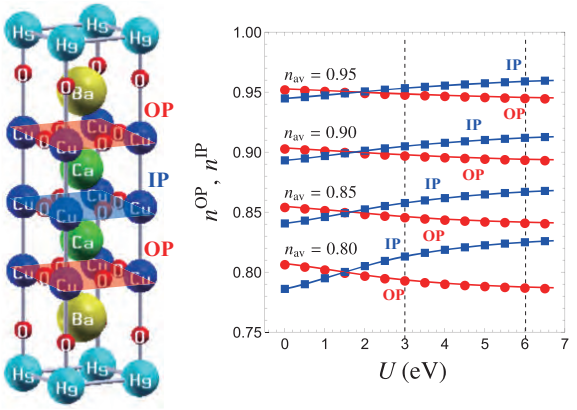

Figure 1: (Left) Crystal structure of Hg-1223 with two OPs and one IP in an unit cell. (Right) TPSC result for the layer fillings in the OP and IP, respectively, against the on-site Hubbard interaction U for various values of the average filling $n_{\rm av}$ = 0.95-0.80.

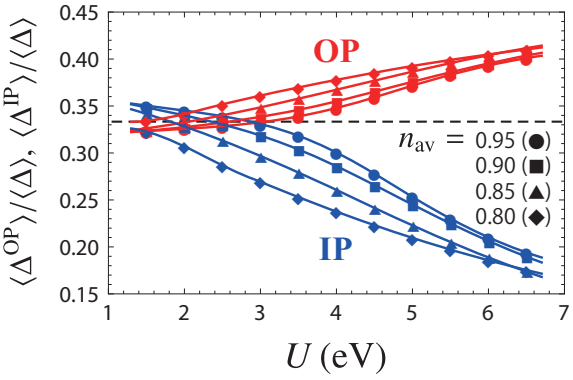

Figure 2: Weights of the OP and IP gap functions, $\langle\Delta^{\rm OP}\rangle/\langle\Delta\rangle$ (red symbols) and $\langle\Delta^{\rm IP}\rangle/\langle\Delta\rangle$ (blue), against the on-site Hubbard interaction U for various values of the average filling $n_{\rm av}$ = 0.95–0.80. The black horizontal line marks 1/3.

of electron correlation different between OP and IP: the AF spin fluctuations in the IP are stronger than in the OP due to the layer filling closer to half-filling in the IP, while the quasiparticle density of states (DOS) is reduced for the same reason around the antinodal regions in the IP, suppressing the $d_{x^2-y^2}$-wave superconductivity. We also show that, although the off-diagonal (inter-layer) elements in the gap function matrix are tiny, the inter-layer pair scattering processes are actually at work in enhancing $T_{\rm c}$ by comparing the results when these processes are turned on and off. We further reveal that the trilayer system has higher $T_{\rm c}$ than the single-layer system in the weak and intermediate correlation regimes due to the differentiation between OP and IP in a regime of the on-site Hubbard interaction U that includes those estimated for the cuprates. The present results are qualitatively consistent with NMR experiments in multi-layer cuprates superconductors.

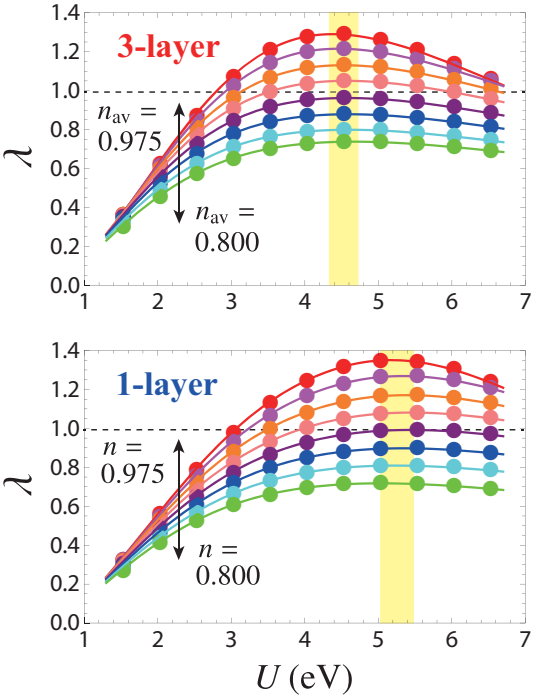

Figure 3: Eigenvalue λ of the linearized Eliashberg equation against the Hubbard interaction U for three-layer and single-layer Hubbard models for various values of the average filling $n_{\rm (av)}$ = 0.800–0.975. Peak positions are marked with a yellow shading in each panel.

References

[1] K. Nishiguchi, S. Teranishi, K. Kusakabe, and H. Aoki: Phys. Rev. B **98** 174508 (2018).

[2] K. Nishiguchi, S. Teranishi, and K. Kusakabe: J. Phys. Soc. Jpn. **86** 184707 (2017).

Numerical Study of One Dimensional Frustrated Quantum Spin Systems

Kazuo HIDA
Professor Emeritus, Division of Material Science, Graduate School of Science and Engineering Saitama, Saitama 338-8570

1 Model

We investigate the ground state phases of spin-1 distorted diamond chains described by the following Hamiltonian:

$$\mathcal{H}_{\rm B} = \sum_{l=1}^{N}\Big[(1+\delta)\boldsymbol{S}_l\boldsymbol{\tau}_l^{(1)} + (1+\delta)\boldsymbol{\tau}_l^{(1)}\boldsymbol{S}_{l+1} + (1-\delta)\boldsymbol{S}_l\boldsymbol{\tau}_l^{(2)} + (1-\delta)\boldsymbol{\tau}_l^{(2)}\boldsymbol{S}_{l+1} + \lambda\boldsymbol{\tau}_l^{(1)}\boldsymbol{\tau}_l^{(2)}\Big], \quad (1)$$

where $\boldsymbol{S}_l$, $\boldsymbol{\tau}_l^{(1)}$, $\boldsymbol{\tau}_l^{(2)}$ are spin-1 operators. The lattice structure is depicted in Fig. 1.

The overall ground state phase diagram is discussed in the activity report of last year. Also, the undistorted case is discussed in detail in ref. [1]. These works show that this model has a nonmangetic ground state in the appropriate range of parameters. In the present work, we show that this phase consists of at least two topologically distinct phases based on analytical and numerical calculations.

2 Weak distortion regime ($\delta \simeq 0$)

In the absence of distortion, the ground state for $1.0727 \lesssim \lambda \lesssim 2.5773$ is a Haldane phase[1]. The ground state remains in the Haldane phase for weak distortion, since nondegenerate gapped states are generally robust against weak distortions. This phase is a symmetry protected topological phase with half-integer edge spins.

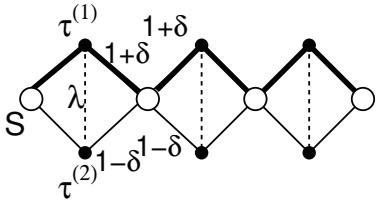

Figure 1: Structure of the distorted diamond chain (1).

3 Strong distortion regime ($\delta \simeq 1$)

For $\delta = 1$ and $\lambda = 0$, the whole system is decomposed into two parts. One is a single spin-1 chain of length $2N$ consisting of $\boldsymbol{S}_l$ and $\boldsymbol{\tau}_l^{(1)}$ with exchange constant $2J$ described by the Hamiltonian

$$\mathcal{H}_0 = \sum_{i=1}^{2N} 2J\boldsymbol{\sigma}_l\boldsymbol{\sigma}_{l+1}, \quad (2)$$

where $\boldsymbol{\sigma}_{2l} = \boldsymbol{\tau}_l^{(1)}$ and $\boldsymbol{\sigma}_{2l+1} = \boldsymbol{S}_l$. The ground state of the Hamiltonian (2) is a Haldane state. The remaining part is N isolated spins $\boldsymbol{\tau}_l^{(2)}$.

For small $1-\delta$ and λ, the spins $\boldsymbol{\tau}_l^{(2)}$ interact with each other mediated by the fluctuation in the chain (2). We estimate the effective interaction $J_{\rm eff}$ using eigenvalues and eigenvectors of the finite length spin-1 chains (2) with $2N = 8, 10$ and 12 obtained by numerical diagonalization. After the extrapolation to $N \to \infty$, we find that $J_{\rm eff}$ is positive for

$$0.594 \gtrsim \frac{1-\delta}{\lambda} \gtrsim 0.416. \quad (3)$$

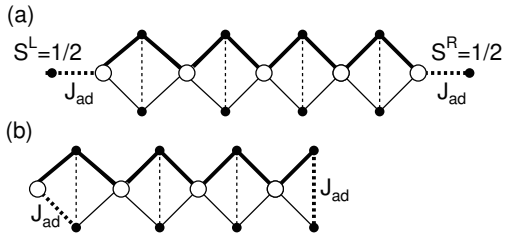

Figure 2: Structures of the distorted diamond chains used for the calculation of the energy gaps (a) $\Delta_{\rm H}$ and (b) $\Delta_{\rm DH}$ in the nonmagnetic phase.

Hence, the ground state of the chain consisting of spins $\boldsymbol{\tau}_l^{(2)}$ is a nonmagnetic Haldane state in the region (3). As a whole diamond chain, this corresponds to a double Haldane state[2, 3] that consists of two coupled chains each with Haldane ground state. This ground state is topologically trivial.

4 Numerical calculation

To distinguish these two phases, we carry out the finite size DMRG calculation to estimate the energy gap with structures H and DH depicted in the Figs. 2(a) and (b), respectively. Then, the energy gap $\Delta_{\rm H}$ in the Haldane phase should be finite for the structure H, and the energy gap $\Delta_{\rm DH}$ in the double Haldane phase should be finite for the structure DH.

The numerical results for $\delta = 0.5$ and 0.6 are shown in Fig. 3(a) and (b), respectively. We set the edge coupling $J_{\rm ad} = 1$. In the nonmagnetic phase, the scaled gaps $N_{\rm s}\Delta_{\rm H}$ and $N_{\rm s}\Delta_{\rm DH}$ are shown for several values of $N_{\rm s}$ by open symbols where the $N_{\rm s}$ is the number of spins including the additional spins. In the ferrimagnetic phases, the spontaneous magnetization per spin m is plotted for $N_{\rm s} = 72$.

For $\delta = 0.5$, the whole nonmagnetic phase belongs to the Haldane phase, since the scaled gap $N_{\rm s}\Delta_{\rm H}$ increases with the system size as shown in Fig. 3(a). On the other hand, for $\delta = 0.6$, the whole nonmagnetic phase belongs to the double Haldane phase, since the scaled gap $N_{\rm s}\Delta_{\rm DH}$ increases with the system size as shown in Fig. 3(b).

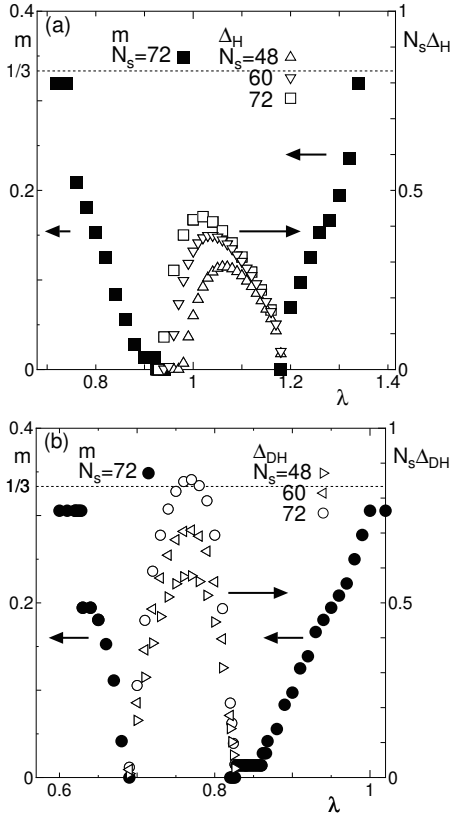

Figure 3: Spontaneous magnetization m, scaled energy gaps $N_{\rm s}\Delta_{\rm H}$ and $N_{\rm s}\Delta_{\rm DH}$ for (a) $\delta = 0.5$ and (b) $\delta = 0.6$.

References

[1] K. Hida and K. Takano: J. Phys. Soc. Jpn. **86**, 033707 (2017).

[2] T. Hikihara, J. Phys. Soc. Jpn. **71** 319 (2002) and references therein.

[3] A. K. Kolezhuk and U. Schollwöck, Phys. Rev. B **65**, 100401 (2002) and references therein.

Theory of multiple spin density waves and magnetic skyrmions in frustrated itinerant magnets

Takashi UCHIDA
Hokkaido University of Science
4-1, 7-15, Maeda, Teine-ku, Sapporo 006-8585

Magnetic skyrmions are topologically stable vortex-like magnetic structures with the spin directions distributing in all directions. Typically, the magnetic skyrmions emerge as 3Q multiple helical spin density waves in the Dzyaloshinskii-Moriya (DM) interaction driven systems under magnetic field. Recently, frustrated systems without the DM interaction have been found to reveal magnetic skyrmions [1, 2]. In order to explore theoretically the possibility of magnetic skyrmions in the frustrated itinerant systems without the DM interactions, we have applied the molecular spin dynamics (MSD) method [3] to the triangular-lattice single-band Hubbard model.

The MSD method is based on the functional integral method for the spin fluctuation theories and the isothermal molecular dynamics method. The method allows us to find automatically the magnetic structure of a large system with thousands of atoms in a unit cell at finite temperatures. Starting from the Hamiltonian expressed in terms of the locally rotated coordinates and by adopting the static approximation to the functional integral technique, the MSD method reduces to the generalized Hartree-Fock approximation at the ground state.

In the numerical calculations the most time-consuming process is the magnetic force calculation at each time step, where the local electronic structures are calculated in real space by means of the recursion method. We have adopted the automatic parallel calculation scheme and found it to be effective in saving both computing time and CPU resources.

We have performed the magnetic structure calculations on the supercell with $n \times n$ ($n = 20, 40$) triangular lattice, which is embedded in a large cluster consisting of 3×3 supercells, each of which are connected by the periodic boundary condition. Under zero magnetic field and the fixed value of the temperature $T/t = 0.001$, we have changed the Coulomb interaction strength U/t and the electron number n. For $n = 0.80 \sim 1.10$, the 120°-structure based complex magnetic structures were found. Of these, the main components for $U/t = 5$ and $n = 0.95$, $U/t = 6 \sim 8$ and $n = 0.95 \sim 1.05$, $U/t = 9$ and $n = 0.95$, $U/t = 10$ and $n = 1.05$ were found to be 3Q states, where the three Q vectors are directed along the axes of the triangular lattice. Although the skyrmion-like features can be seen in these 3Q states, the skyrmion lattice was not detected in the present results. In order to investigate the possibility of realizing the skyrmion lattice, the magnetic structure calculations near the ferromagnetic boundary ($n \sim 1.3$) are now in progress.

References

[1] T. Okubo, S. Chung, and H. Kawamura: Phys. Rev. Lett. **108** (2012) 017206

[2] Y. kakehashi, D. Koja, T. Olonbayar, and H. Miyagi: J. Phys. Soc. Jpn. **87** (2018) 094712.

[3] Y. Kakehashi, S. Akbar, and N. Kimura: Phys. Rev. B**57** (1998) 8354.

3.5 SCCMS Projects

First-Principles Phase Field Mapping I

Kaoru Ohno

Department of Physics, Faculty of Engineering Science,

Yokohama National University, Tokiwadai, Hodogaya-ku, Yokohama 240-8501

To perform, for example, accurate mapping of first-principles results to phase field models, it would be necessary to perform accurate and reliable first-principles calculations. To analyze XPS spectra, the so-called ΔSCF method using MRDCI, CCSD, and other quantum chemistry approaches is applicable for isolated molecules, but the ΔSCF method using density functional theory (DFT) is generally not applicable to this problem in particular for crystals. So, relying on quasiparticle theory for a deep core hole, we performed GW calculation for XPS spectra of crystals using TOMBO [1]. The result is listed in Figure 1. On the other hand, a photoabsorbed excited state can be constructed by adding one electron to the second empty level of a cationic state. The neutral ground state is constructed by adding one electron to the first empty level of a cationic state. Then, the photoabsorption energy can be evaluated as a difference between these two energy gains in the two processes of adding an electron to a cationic state that can be simultaneously obtained by applying the GW(Γ) method to a cationic system without solving the Bethe-Salpeter equation. We called this method the GW(Γ) method without the Bethe-Salpeter equation. We succeeded in reproducing the experimental photoabsorption energy within the 0.1 eV accuracy by applying the self-consistent GWΓ method of TOMBO to several cationic systems as shown in Figure 2 [2].

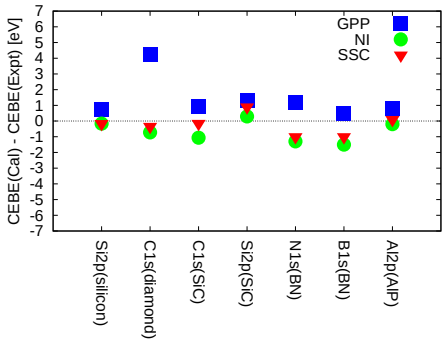

Fig. 1 Core electron binding energy (CEBE) difference between GW and experimental data.

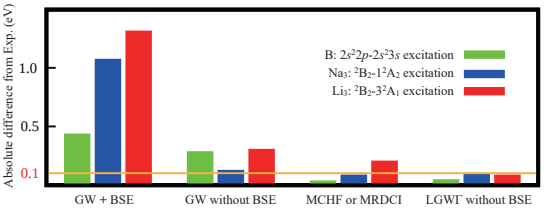

Fig. 2 Absolute difference of calculated photoabsorption energies from experimental data.

References

[1] Tsubasa Aoki and Kaoru Ohno, J. Phys.: Condensed Mat. (Letter, open access) **30**, 21LT01 (2018).

[2] Tomoharu Isobe, Riichi Kuwahara, and Kaoru Ohno, Phys. Rev. A **97**, 060502(R);1-6 (2018).

First-Principles Phase Field Mapping II

Kaoru Ohno

Department of Physics, Faculty of Engineering Science,

Yokohama National University, Tokiwadai, Hodogaya-ku, Yokohama 240-8501

Theoretical understanding of microstructure is very important in predicting the durability and performance of alloys. For this purpose, phase field models have been widely used to simulate the time evolution of microstructures and various properties. However, the results strongly depend on the input parameters, which are mostly empirical. Therefore, we propose a new and simple method to determine the input parameters purely from first principles. We developed first-principles phase field model by using cluster expansion theory and potential renormalization theory [1] together and succeeded in obtained an excellent result for Ni-Al alloy systems [2]. Our results clearly distinguish the local composition of alloys in accord with the experimental phase diagram (Fig 1). We have also succeeded in predicting the time evolution of microstructures of Ni-Al alloys at different compositions at 1300K.

References

[1] Y. Misumi, S. Masatsuji, R. Sahara, S. Ishii, and K. Ohno, J. Chem. Phys. **128**, 234702 (2008).

[2] S. Bhattacharyya, R. Sahara and K. Ohno, in submission to Nature Communications.

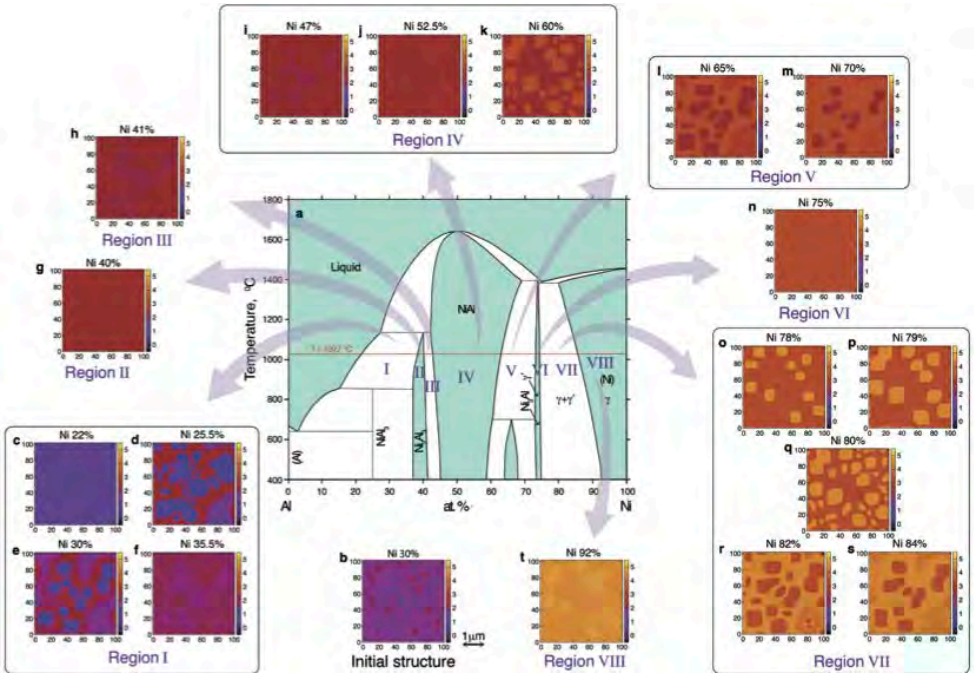

Fig. 1 Microstructures of NiAl alloys obtained by the first-principles phase field model

Electrochemical reaction on a platinum surface

OSAMU SUGINO

Institute for Solid State Physics,

The University of Tokyo, Kashiwa-no-ha, Kashiwa, Chiba 277-8581

The fuel-cell reactions can be recognized as a transfer of proton onto the reaction intermediates, O_2, O_2H, OH, H and O, adsorbed on the surface or a direct transfer onto the surface, but there still remain controversies even on the well-defined Pt(111) surface. While, the conventional approaches like density functional theory (DFT) within the generalized gradient approximation (GGA) for the exchange-correlation (xc) of electrons is not accurate enough to reveal all the details. In this context, we applied the random phase approximation (RPA) to investigate the H adsorption [1]. The calculated adsorption energy is 290 meV in consistent with experimentally estimated value $\leq$270 meV at full coverage condition although the GGA provides a value larger than RPA by 100 meV without the van der Waals (vdW) correction and a value larger by 30-40 meV with the correction. The most stable adsorption site is the fcc site although the top site is less stable only by 23 meV being comparable to the thermal energy at room temperature. The small difference in the adsorption energy indicates that H at the fcc site, H_{fcc}, coexists with H_{atop}, which explains why signal from the top site is measured experimentally, although GGA predicts predominance of H_{fcc}. The difference between RPA and GGA can be traced back to overestimation of the GGA on the lattice constant of Pt; interestingly, the relative adsorption energy, $\Delta E_{\mathrm{ads}} \equiv E_{\mathrm{ads}}(\mathrm{H_{fcc}}) - E_{\mathrm{ads}}(\mathrm{H_{atop}})$, happens to be similar between RPA and GGA when using a common lattice constant. Importantly, H_{fcc} is more stable than H_{atop} in RPA because the quantum confinement effect is much larger for H_{atop}: Within the classical approximation, H_{fcc} is less stable. The reversed order of stability suggests different proton transfer mechanism to occur between the quantum and classical systems; this may explain why the reaction efficiency is different between hydrogen and deuterium as observed experimentally. Further, our subsequent and preliminary simulations have shown that the solvent effect yields rather minor effect on the adsorption energies and the coverage effect is also minor; however, the adsorbed H can easily hop among fcc, hcp, and top sites when simulated at room temperature at a 2/3 coverage condition. The result suggests

incorrectness of the old picture that H_{fcc} plays a role as a spectator in the hydrogen evolution/oxidation reaction as if forming a stable hydrated structure. The result suggests a new picture, instead, that there is large fluctuation in the hydrogen density profile and fluctuation is associated with the enhancement of the reaction: Further investigation is admittedly needed to confirm this picture, which is remained as a target of the next-year project.

References

[1] L. Yan, Y. Sun, Y. Yamamoto, S. Kasamatsu, I. Hamada, and O. Sugino: J. Chem. Phys. **149** (2018) 167402.

Large-scale molecular simulation of two-dimensional glass-forming liquid

Hayato SHIBA
Institute for Materials Research, Tohoku University
2-1-1 Katahira, Aoba-ku, Sendai 980-8577

Recently, large-scale molecular dynamics simulation by the present author a and colloidal experiments have revealed that a two-dimensional (2D) liquid supercooled toward the glass transition exhibits long-wavelength phonon fluctuations that has been overlooked in the literature on glasses. These phonon fluctuations are stabilized by the rigidities emerging with decreasing temperatures, in a manner similar to those in 2D crystalline solids. Furthermore, its structural relaxation turns out to be similar between two and three dimensions, if structural changes in terms of neighbor switching is properly taken into account in considering the relaxation.

For this year, we have numerically investigated the the mechanism of the slowdown in the dynamics of a 2D supercooled liquid at a high number density $N/V = 1.2$, where the pairwise interactions are defined by a modified Kob-Andersen parameters Up to 4096000 particles are simulated using our original simulation codes optimally parallelized for the ISSP system. First, by investigating the diffusivity in the long-time limit, we have clarified that not only the long-wavelength phonons but also long-wavelength hydrodynamic flow affects the transport behavior in the present 2D liquid, causing logarithmically divergent diffusivity D in the long-time limit. We have carried out an explicit calculation of the velocity autocorrelation function a relatively high temperature $T = 1.0$ It exhibits coming and going between positive and negative correlations, and finally, in a system with millions of particles, pure hydrodynamic correlation turns out to emerge in the long-time limit.

We have also investigated the relaxation times τ_α, $\tau_{\rm R}$, and $\tau_{\rm B}$ defined as decay times of the following three relaxation functions: (a) The standard intermediate scattering function (ISF), density correlation defined on the basis of particle displacements, where fluctuations on the scale of particle sizes are considered. (b) Another ISF, representing local density fluctuation, defined on the basis of relative displacements between neighboring particles, and (c) The decay in the number of neighboring particles (*i.e.* imaginary "bonds"). We have compared these time scales with the stress relaxation in terms of the autocorrelation function $G(t) = (V/k_{\rm B}T)\langle\sigma_{xy}(t)\sigma_{xy}(0)\rangle$ with $\sigma_{xy}(t)$ the shear component of the stress tensor. In usual (three-dimensional) supercooled liquid, a proportionality $\tau_\alpha \sim \eta/T$ usually hold, but this relation breaks down in the 2D glass-forming liquids. Instead, an alternative proportionality $\tau_{\rm R} \sim \eta/T$ is found to hold by our careful calculation. This result suggests that the local density fluctuation governs divergence of viscosity with vitrification, behind elastic and hydrodynamic anomalies taking at long-wavelengths in 2D liquids.

References

[1] H. Shiba, T. Kawasaki, and K. Kim: in preparation.

Study of many-body correlation effects on spin relaxation rate in quantum dots

Kazuyoshi Yoshimi and Takeo Kato
Institute for Solid State Physics, University of Tokyo
Kashiwa-no-ha, Kashiwa, Chiba 277-8581

Quantum dot systems have been studied for long time to realize quantum devices utilizing microscopic quantum levels in analogy of the atoms. Using this property, it is utilized in a wide range of applications, such as quantum computer elements, optical non-linear switching, fluorescent probes in living organisms and solar cells. For these applications, the spin relaxation rate is one of the important parameters, which can be evaluated from accurate evaluation of the electronic state, which incorporate the effects of electron correlation, spin-orbit interaction, and electron-phonon coupling.

The calculation of spin relaxation rate is performed on a model with the confined-harmonic potential, electron-electron and spin-orbit interactions using the Fermi's golden rule[1]. Recently, we have developed a spin relaxation rate analysis tool for quantum dot systems using the quantum lattice model solver $\mathcal{H}\Phi$[2]. In this report, we introduce the tool through the actual calculation.

The Hamiltonian under the magnetic field B is given by[1]

$$\mathcal{H} = \mathcal{H}_0 + \mathcal{H}_{ee} + \mathcal{H}^R_{so} + \mathcal{H}^D_{so}. \quad (1)$$

Here, $\mathcal{H}_0 = \sum_i (\boldsymbol{P}_i^2/2m^* + (m^*\omega_0^2/2)r_i^2 + g\mu_B B\sigma_i^z/2)$ is the non-interaction part of the Hamiltonian, where $\boldsymbol{P}_i = -i\hbar\nabla_i + (e/c)\boldsymbol{A}_i$ with $\boldsymbol{A}_i = (B/2)(-y_i, x_i, 0)$ stands for the electron momentum, $\boldsymbol{r}_i$ is the position vector, and σ_i^l is the $l(= x, y, z)$-component of the Pauli spin matrices at i-th particle, respectively. m^* is the effective mass, ω_0 is the eigenfrequency of the confined-harmonic potential, g is the Lande's g factor, μ_B is the Bohr magneton and B is the magnetic field. $\mathcal{H}_{ee} = (e^2/2\kappa)\sum_{i\neq j} r_{ij}^{-1}$ is the electron-electron interaction part of the Hamiltonian, where κ is the static relative dielectric constant and r_{ij} is the distance between i-th and j-th particles. $\mathcal{H}^R_{so} = \sum_i(\alpha/\hbar)(P_i^y\sigma_i^z - P_i^x\sigma_i^y)$ and $\mathcal{H}^D_{so} = \sum_i(\beta/\hbar)(P_i^y\sigma_i^y - P_i^x\sigma_i^x)$ are the Rashba- and Dresselhaus-type spin orbit interactions part of the Hamiltonian with coupling constants α and β, respectively.

The spin relaxation rate is obtained by

$$\Gamma = \frac{2\pi}{\hbar}\sum_{\boldsymbol{q},\lambda}|M_{\boldsymbol{q},\lambda}|^2|\langle f|e^{i\boldsymbol{q}\cdot\boldsymbol{r}}|i\rangle|^2\delta(\epsilon_f - \epsilon_i - \hbar\omega_{\boldsymbol{q},\lambda}), \quad (2)$$

where $M_{\boldsymbol{q},\lambda}$ is the scattering matrix element, $\omega_{\boldsymbol{q},\lambda}$ is the phonon energy spectrum of branch λ and momentum $\boldsymbol{q}$, respectively. $\epsilon_{i(f)}$ is the energy at the initial (final) state. In our calculation, we use the long wavelength approximation $|M_{\boldsymbol{q},\lambda}|^2 \sim M_\lambda(\tilde{q})^2 g_\lambda(\theta,\phi)$. The three types of electron-acoustic phonon scatterings are considered. One is the scattering due to the deformation potential, $M_\lambda(\tilde{q})^2 = (\hbar\Xi^2/2DVv_{sl}l)\tilde{q}_l$, $g_{sl}(\theta,\phi) = 1$, where D is the crystal density, Ξ is the acoustic deformation potential constant, v_{sl} is the sound speed for longitudinal phonon mode, l is the magnetic length and $\tilde{q} = ql$ is the dimensionless parameter. The second is the scatterings due to the piezoelectric field for the longitudinal phonon mode, $M_{pl}(\tilde{q})^2 = (32\pi^2\hbar e^2 e_{14}^2 l/\kappa^2 DVv_{sl})/\bar{q}_l$, $g_{pl}(\theta,\phi) = 9\sin^4\theta\cos^2\theta\sin^2\phi\cos^2\phi$, where

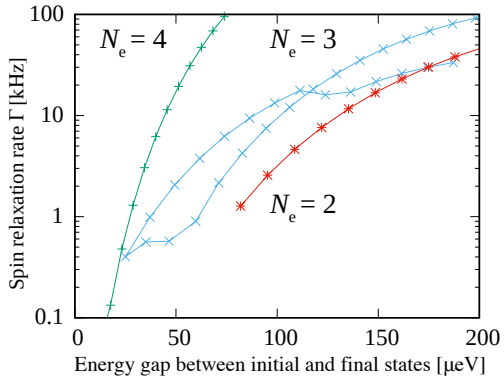

Figure 1: The energy-gap between initial and final states dependency of the spin-relaxation rates from the high spin state to the low spin state at $N_e = 2, 3, 4$.

e_{14} is the piezoelectric constant. The other is the piezoelectric field for the transverse phonon mode, $M_{pt}(\tilde{q})^2 = (32\pi^2\hbar e^2 e_{14}^2 l/\kappa^2 DV v_{st})/\tilde{q}_l$, $g_{pl}(\theta,\phi) = \sin^2\theta\cos^2\theta + \sin^4\theta\cos^2\phi\sin^2\phi - 9\sin^4\theta\cos^2\theta\sin^2\phi\cos^2\phi$, where v_{st} is the sound speeds for transversal phonon mode.

To analyze the quantum dot system, we first consider the eigenstates of the one-body part Hamiltonian. By mapping the basis of $\mathcal{H}_{ee}$ into these states and using the configuration interaction method, we obtain the eigenstates of $\mathcal{H}$ using numerical exact diagonalization method. In this calculation, we consider the 28 basis. The parameters are set as follows; $\hbar\omega_0 = 2.65$ [meV], $m^* = 0.067, \kappa\epsilon_0 = 12.9, g = -0.28, \alpha = 0$, $\beta = 25$ [meVÅ], $D = 5.31\times10^3$ [kg/m^3], $v_{sl} = 4.72\times10^3$ [m/s], $v_{st} = 3.34\times10^3$ [m/s], $e_{14} = 1.41\times10^9$ [V/m], $\Xi = 8.6$ [eV]. The magnetic field B is varied from 1.5 to 2.5[T]. In Fig. 1, the spin relaxation rates from the high spin state to the low spin state at the electron number $N_e = 2, 3, 4$ are shown. We found that the energy-gap dependence of spin relaxation rates shows the similar behavior of the experiments, i.e. the spin relaxation rates become large with increasing N_e in the small energy-gap region[3].

Finally, parallelization performance using GPGPU calculation is briefly described. Since $\mathcal{H}_{ee}$ is mapped into the basis of the one-body part of the Hamiltonian, the total numbers of the Coulomb interactions becomes about $(2N_s)^4$, where N_s is the total number of considered basis. When the electron number is a few, the Hilbert space becomes small and thus the parallelization about interaction terms is efficient. For comparison, we calculated the ground state on the 28 basis Hubbard model at 5 electrons by the hybrid parallelization with 72 processes and 12 threads (MPI+OpenMP) and 2 GPUs (MPI+GPGPU), respectively. We found that the latter calculation becomes 4 times faster than the former calculation. Thus, the GPGPU implementation is expected to be useful for searching the suitable parameters in the quantum dot systems. Our tools are still under development and thus not yet released. However, we plan to release it as free-software after some improvements.

Acknowledgement: We thank A. Oiwa, H. Kiyama, and T. Misawa for fruitful discussions. This work was supported by support service of program portability to General Purpose Graphics Processing Unit. Numerical calculations were mainly performed at the Supercomputer Center, Institute for Solid State Physics, University of Tokyo.

References

[1] M. Rontani, C. Cavazzoni, D. Bellucci et al., J. Chem. Phys. 124 124102 (2006); J. I. Climente, A. Bertoni, G. Goldoni et al. Phys. Rev. B 76 085305 (2007).

[2] M. Kawamura, K. Yoshimi, T. Misawa, Y. Yamaji, S. Todo, N. Kawashima, Com. Phys. Comm. **217**, 180 (2017).

[3] H. Kiyama and A. Oiwa (Private communication).

Unified Photonic-Electronic Devices

Kazuhiro YABANA

Center for Computational Sciences,

University of Tsukuba, Tsukuba 305-8577

We develop a first-principles computational method to investigate electron dynamics induced by ultrashort laser pulses based on time-dependent density functional theory (TDDFT) in real time. We develop the code SALMON (Scalable Ab-initio Light-Matter simulator for Optics and Nanoscience) and make it open to the public at our website, http://salmon-tddft.jp. The code paper of SALMON has been published recently [1].

SALMON has been developed so that it runs efficiently in supercomputers with various kinds of professors. To make a comparison of performance with the processor Xeon Gold 6148 of Skylate-SP architecture equipped in System C, we use the System C to obtain the performance data. SALMON has already been optimized for many-core processors such as Knights Landing Xeon Phi 7250 that is equipped in Oakforest-PACS at JCAHPC. Since Skylate-SP architecture is quite close to the many-core, we confirmed that the present version of SALMON runs efficiently at System C without further efforts, with performance about 40% relative to the theoretical one.

As a new feature of SALMON, we have developed a theory and computational method to describe interaction of strong and ultrashort pulsed light with thin materials, from atomic monolayer to thick films. The method solves the time-dependent Kohn-Sham equation and the Maxwell equations using a common spatial grid. We have also developed a two-dimensional (2D) theory describing optical responses of thin materials in TDDFT, without the elaborate coupling with Maxwell equations. It was found that the latter 2D theory is justified for films of thickness less than 5nm for Si nano-films through the comparison with the former elaborate calculation.

References

[1] M. Noda, S.A. Sato, Y. Hirokawa, M. Uemoto, T. Takeuchi, S. Yamada, A. Yamada, Y Shinohara, M. Yamaguchi, K. Iida, I. Floss, T. Otobe, K.-M. Lee, K. Ishimura, T. Boku, G.F. Bertsch, K. Nobusada, K. Yabana, “SALMON: Scalable Ab-initio Light–Matter simulator for Optics and Nanoscience”, Comp. Phys. Comm. 235, 356 (2019).

Ring Decomposition of Tensors[1]

Naoki KAWASHIMA
Institute for Solid State Physics, University of Tokyo
Kashiwa-no-ha, Kashiwa, Chiba 277-8581

While the tensor-network-based methods for renormalization group (TNRG) are similar to the Migdal-Kadanoff RG in essense, they generally provides much more accurate and, more importantly, systematic and controllable series of approximations. Theoretically, the approximation made there becomes infinitly accurate as we increase the bond-dimension, the control parameter of the methods. However, in practice, it is not so easy. One of the main sources of difficulty is the contributions from short-range correlations. While there are a few proposals for removing these undesirable contributions, separation of such contribution from the fixed-point tensors is usually a non-linear optimization problem and, therefore, may take a long time to find the optimal solution. Meanwhile, the tensor-ring decomposition of tensors plays a key role in various applications of tensor network representation in physics as well as in other fields. In most heuristic algorithms for the tensor-ring decomposition, one encounters the problem of local-minima trapping. This is essentially the same problem as we encounter in the TNRG. Particularly, the minima related to the topological structure in the correlation are hard to escape. Therefore, identification of the correlation structure, somewhat analogous to finding matching ends of entangled strings, is the task of central importance. We propose [1] a method for solving this problem.

For a bench-mark test, we consider a corner-double-line (CDL) tensor. The CDL tensor appears typically in the TNRG as a part of renormalized tensors. It represents the short-range component of the correlations. Specifically, we consider the 3rd-order CDL that consists of three 9-dimensional outher indices and three 3-dimensional inner indices as illustrated in the inset of the figure. We apply our method for varying dimensions for the inner indices, and compare the results with the alternating-least-square method. The contrast is very clear.

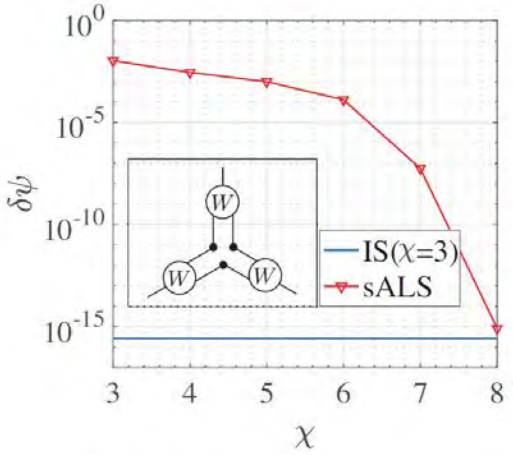

Figure 1: The comparison of the approximation errors $\delta\psi$ obtained by the present method and a heuristic method (sALS) as a function of the bond dimension χ. The target tensors are a third-order corner-double-line tensor with the dimension of the inner bonds fixed to be 3. (Adopted from [1])

[1] This report is based on Hyun-Yong Lee and Naoki Kawashima (arXiv:1807.03862).

Simulation of organic-inorganic interfaces

Shuji OGATA
Nagoya Institute of Technology
Gokiso-cho, Showa-ku, Nagoya 466-8555, Japan

In the fiscal year of 2018, we have addressed two subjects using our, hybrid quantum-classical (QM-CL) simulation code and classical MD code.

Subject 1: Chemical Reactions Involved in Moisture-Induced Weakening of Adhesion Between Aluminum and Epoxy Resin [1]. Using the hybrid QM-CL simulation method, we have successfully reproduced the adhesion strengths between surface-oxidized Al and bisphenol-A (bisA) resin at a comparative magnitude to the experimental values. For the DFT calculation of the QM region, the divide-and-conquer- type real-space grid code (DC-RGDFT) is used with the PBE-GGA xc-potential and the norm-conserving pseudopotentials. We divide the QM region with the buffer Al atoms and set the grid points with size h = 0.2911 Å to represent the eigenfunctions and potentials; finer grid points are auxiliarily set around C and O atoms. The h corresponds to the cutoff energy 3.81 $(\pi/\mathrm{h(Å)})^2$ = 443 eV in the plane-wave representation. The nine-point finite difference method is adopted to calculate their derivatives.

As the water content in the contact region has increased (case A < case B < case C), the calculated adhesion strength has decreased in the ordering of case B > case A > case C. In cases A and B, where a liquid layer has not been formed in the contact region, we have found that some of the OH groups of the bisA molecules reacted with surface Al atoms. In case C, the surface Al atoms have been well saturated by OH and H_2O molecules and the liquid layer in the contact region has been alkaline. Some of the bisA ether groups have been broken due to the alkaline environment.

We compare cases A-C in the present study with the experimental conditions. In case A, the surface oxide had no H atom; therefore, it was reactive with the bisA OH group. In case B, all the H_2O molecules in the contact region reacted with the surface oxide. The surface oxide in case B still reacted with the bisA OH group. An alkaline (free OH-rich) liquid layer was formed in case C. Under experimental conditions, the theoretical alkaline liquid layer may become neutralized through other environmental factors unaccounted for by the computation, e.g., the experimental deformation speed is much slower than the present value and hence free OH may diffuse to environment. Therefore, the experimentally dry conditions correspond best to either case B or intermediate between cases B and C. The wet condition corresponds to case C.

Subject 2: Novel Calculation Scheme for the Work of Adhesion between a Liquid and Polymer-Grafted Substrates [2]. A method to calculate the work of adhesion appropriate for the interface between a liquid and a polymer-grafted solid surface was developed herein by using two novel ideas. First, spherically symmetric potentials were introduced to separate the liquid molecules from the solid surface according to its shape. Second, a parameter update scheme for the potentials was defined so that sharp variations in the free energy gradient are suppressed when the liquid molecules are separated gradually from the solid surface. The proposed method was applied at the interface between water and a gold substrate modified by poly(ethylene oxide).

References

[1] S. Ogata and M. Uranagase, J. Phys. Chem. C **122** (2018) 17748-17755.
[2] M. Uranagase, S. Ogata, et al., J, Phys. Chem. Phys. **148** (2018) 064703-1-9..

Conversion and storage of energy−fuel cells and secondary batteries: Research and development of fundamental technologies of battery simulators.

Susumu OKAZAKI
Department of Materials Chmistry, Nagoya University
Furo-cho, Chikusa-ku, Nagoya 464-8603

The goal of our project is to develop the basic technology of the whole battery simulator. One of the key techniques is molecular-level design of polymer membranes controlling transportation of protons and ions across the membrane with proper stiffness resistant to mechanical deformation under external stress. Such membranes are widely applicable to the fuel cells used in the industrial products.

On the system B and C, we performed fully atomistic molecular dynamics (MD) calculations of hydrated perfluorosulfonic acid (PFSA) ionomers composed of a hydrophobic polytetrafluoroethylene backbone with hydrophilic side chains terminated by sulfonic acid[1], as a model of proton exchange polymer electrolyte membrane of fuel cells. On the basis of these atomistic MD calculations, we constructed a predictive coarse-grained (CG) model for the structure and morphology of PFSA membranes[2]. A series of molecular dynamics simulations of PFSA ionomers with different side chain (SC) length explored the effect of SC length on the morphology and mechanical properties of the PFSA membrane[3]. To realize a tensile test of polymer materials, microscopic expression of the pressure tensor using the fast multipole method (FMM) with periodic boundary conditions are derived[4].

These results will contribute to the development of higher performance fuel−cells and secondary batteries and to the realization of the entire battery simulator in the near future.

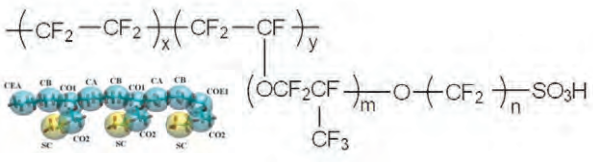

Figure 1: Molecular structure of perfluorosulfonic acid (PFSA) ionomers. Inserted figure is the CG model of PFSA ionomers[2].

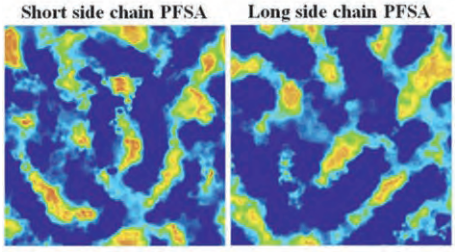

Figure 2: Number density maps of sulfonic acid groups, water, and hydronium ions at one cut plane for PFSA ionomers with different side chain length[3].

References

[1] A. T. Kuo, W. Shinoda, S. Okazaki : J. Phys. Chem. C **120** (2016) 25832.

[2] A. T. Kuo, S. Okazaki, W. Shinoda : J. Chem. Phys. **147** (2017) 094904.

[3] A. T. Kuo, K. Takeuchi, A. Tanaka, S. Urata, S. Okazaki, and W. Shinoda : Polymer **146** (2018) 53.

[4] N. Yoshii, Y. Andoh, S. Okazaki : J. Comput. Chem. **39** (2018) 1192.

Development of an excited-state theory based on many-body Green's functions and fragment molecular orbital method

Takatoshi Fujita
Institute for Molecular Science
Myodaiji, Okazaki, Aichi 444-8585

Predicting charge-transfer (CT) excited states across the donor/acceptor interface is essential for understanding the charge photogeneration process in an organic solar cell. However, the first-principles computations of the CT states in an organic/organic interface remain challenging, because both electron correlation and polarizable environmental effects must be taken into account. The GW many-body Green's function theory [1] can offer an accurate and practical scheme to explore electronic states in condensed matter. The quasiparticle energy directly corresponds to a charged excitation energy, such as an ionization potential or an electron affinity. The neutral excitation energy can also be computed in combination with the Bethe-Salpeter equation (BSE). Although the recent developments of the computational algorithm have enabled a GW calculation for a system over 100 atoms, it is still difficult to treat very large system over 1,000 atoms.

To extend the applicability of GW to larger and more complex systems, we have been developing the large-scale GW method based on the fragment molecular orbital (FMO) method [2]. The total polarization function is approximated as the sum of intrafragment polarization functions that are calculated from fragment molecular orbitals in the FMO method. The combined GW and COHSEX approximations is employed to calculate self-energies, in which the dynamically-screened Coulomb potential is explicitly evaluated for a target fragment, while the statistically-screened Coulomb potential of the entire system is evaluated at the COHSEX level. Based on the fragment-based implementation, we have performed a large-scale GW calculation for an organic/organic interface system over 2,000 atoms. We have highlighted the effects of the environmental polarization effects on the CT states. The FMO-based formalism can be applied to any disordered or heterogeneous molecular aggregates for the accurate evaluation of charged excitations and also provides a starting point for the optical excitations within the BSE. In combination with the fragment-based excited-state theory [3, 4], the delocalized excited states can also be treated.

References

[1] L. Hedin, Phys. Rev. **139** (1965) A796.

[2] T. Fujita, Y. Noguchi, Phys. Rev. B **98** (2018) 205140.

[3] T. Fujita, Y. Mochizuki, J. Phys. Chem. A **11** (2018) 3886.

[4] T. Fujita, A. M. Khorshed, T. Hoshi, **20** (2018) 26443.

First-principles materials design by multi-scale simulation

Tetsuya FUKUSHIMA
Institute for NanoScience Design, Osaka University, Osaka 560-8531, Japan
Institute for Datability Science, Osaka University, Osaka 565-0871, Japan

A "scale-bridging" (multi-scale) simulation technique, combining the Korringa-Kohn-Rostoker (KKR) Green's function method and model approaches, was developed this year. On the basis of the "scale-bridging" simulation technique and massively parallel computing, we designed new functional dilute magnetic semiconductors (DMSs), such as Fe-based DMSs [1] and Eu-based DMSs [2]. Here, we introduce the materials design of the Fe-based DMS systems.

Fe-based DMSs have recently been attracting much attention. In particular, in Fe-doped III-V semiconductors, the substitutional Fe atoms are expected to exist as a neutral state (Fe^{3+}), in which case they will not provide extrinsic carriers for the system. Thus, the conduction carriers are not provided by the doped Fe impurities but instead are supplied from the conduction or valence bands. Since the effect of impurity scattering is small, the coherence length is increased. This provides the possibility of realizing new functionalities, such as low power consumption and high-speed operation, due to the quantization of the electronic structures. It is also noteworthy that both n- and p-type DMS systems can be fabricated easily since the carrier characteristics can be controlled independently of the Fe impurities.

We have elucidated the effects of n- and p-type doping and of the Fe distribution on the magnetic properties of DMSs and have investigated the possibility of high $T_{\rm C}$. For this purpose, we have demonstrated the control of the magnetic exchange coupling constants (J_{ij}), chemical pair interactions (V_{ij}), and T_C in (Ga,Fe)Sb and (In,Fe)Sb by changing the carrier characteristics (i.e., chemical potential), using first-principles electronic structure calculations. J_{ij} is calculated by the Liechtenstein's formula:

$$J_{ij} = \frac{1}{4\pi}\mathrm{Im}\int^{E_{\rm F}} dE\ \mathrm{Tr}_L\{\Delta_i T_{\uparrow}^{ij}\Delta_j T_{\downarrow}^{ij}\}, \quad (1)$$

where $\Delta_i = t_{i\uparrow}^{-1} - t_{i\downarrow}^{-1}$, with $t_{i\uparrow(\downarrow)}$ being the atomic t-matrix of the magnetic impurities at site i for spin up (down) state. $T_{\uparrow(\downarrow)}^{ij}$ is scattering path operator between site i and j for spin up (down) state. Tr_L is the trace over the orbital variables. We calculate V_{ij} by the generalized perturbation method expressed as

$$V_{ij} = -\frac{1}{\pi}\mathrm{Im}\int^{E_{\rm F}} dE\ \mathrm{Tr}_L\{\Delta T_{\uparrow}^{ij}\Delta T_{\downarrow}^{ij}\}, \quad (2)$$

where $\Delta = t_{\rm A}^{-1} - t_{\rm B}^{-1}$, with $t_{\rm A(B)}^{-1}$ being the atomic t-matrix of the A(B) atom. The Liechtenstein's formula and generalized perturbation method make it possible to calculate Fermi level dependence of J_{ij} and V_{ij} by replacing the Fermi level $E_{\rm F}$ with a variable energy. Finally, $T_{\rm C}$ is estimated by the random phase approximation, which is based on the Tyablikov decoupling method.

The results from our KKR Green's function calculations clearly indicate that isoelectronic Fe dopants induce antiferromagnetic interactions due to the superexchange mechanism in both GaSb and InSb. By considering artificial changes in the Fermi level, we

have found that the magnetic exchange coupling constants in these systems exhibit universal behavior. Antiferromagnetic-ferromagnetic transitions occur for both n- and p-type doping, and this behavior can be well understood in terms of the Alexander-Anderson-Moriya mechanism. The Fermi level dependence of the chemical pair interactions also shows characteristic features, which can be reasonably explained by magnetic frustration and the nature of the covalent bond. Our multi-scale simulations show that finite values of T_{C} are realized in n- and p-type regions. For p-type doping, the spinodal nano-decomposition caused by annealing drastically enhances T_{C}. However, for n-type doping, the initial phases have higher T_{C} values than the final phases. Based on the results of our calculations, we propose that high values of T_{C} may be realized and that the magnetic states of (Ga, Fe)Sb and (In, Fe)Sb may be manipulated by controlling the gate voltage, chemical doping, and annealing process. Such features will be very important for next-generation semiconductor spintronics.

References

[1] H. Shinya, T. Fukushima, A. Masago, K. Sato, and H. Katayama-Yoshida, J. Appl. Phys. **124** (2018) 103962.

[2] A. Masago, H. Shinya, T. Fukushima, K. Sato, and H. Katayama-Yoshida, Phys. Rev. B **98** (2018) 214426.

Electron Theory on Sodium Secondary-Battery Materials

Hiroki KOTAKA[1], Motoyuki HAMAGUCHI[2], Hiroyoshi MOMIDA[1,2], Tamio OGUCHI[1,2]
[1]*ESICB, Kyoto University, Katsuragoryo, Kyoto, Kyoto 615-8245*
[2]*ISIR, Osaka University, Mihogaoka, Ibaraki, Osaka 567-0047*

Microscopic mechanism of charge/discharge reactions in several battery systems is studied by first-principles calculations to explore new sodium secondary batteries. In this year, we focus on Na/SnS and Li/Li$_x$$MTiO_4$ (M=V, Mn, Fe, Co, and Ni) systems.

Tin compounds are known as high-capacity materials in charge/discharge reactions and have advantages in price and safety for practical applications, being considered as a good candidate for the anode materials of sodium secondary battery.[1, 2] We investigate the electronic mechanism in discharge reactions in Na/SnS system. From experimental works, several stages are involved in conversion reactions starting from SnS. We clarify the possible reaction route considering the intermediate process of the discharge reaction, and theoretically obtain the reaction formulae of the Na/SnS battery systems. In SnS cathode, Na_4SnS_4, Sn, and Na_2S are generated as intermediate products. In addition, generated Sn and newly introduced Na may react to form several alloy phases as $NaSn_5$→$NaSn_2$→$NaSn$→Na_9Sn_4→$Na_{15}Sn_4$.
This multi-stage discharge reaction may explain discharge voltage-capacity curve measured by Kitajou *et al.*[3] To identify possible phases in the discharge reaction, calculated x-ray absorption spectroscopy (XAS) spectra for SnS and Na_2S are compared with experimental ones.[3] In order to accurately calculate the excitation energy, we perform the transition probability including the core hole effect. By the comparison of XAS spectrum, the intermediate phases Na_2S and Na_4SnS_4 are confirmed. The reaction products Na_2S and Na_4SnS_4 can precipitate in the SnS electrodes during the discharge process and the electrode is recovered to be SnS again after charging.

The so-called cation-disordered rock-salt materials including Li_2MnTiO_4 have attracted much attention because of a possible candidate for high-voltage and high-capacity cathode materials of Li-ion batteries. In this rock-salt-based oxides, high stability to O dissociation is highly expected because of the rigid and dense atomic structure. Recently, it has been experimentally reported that the battery performance such as capacity can be significantly improved by optimizing the Li composition ratio as to be $Li_{2+2x}Mn_{1-x}Ti_{1-x}O_4$ with the best value of $x \sim 0.2$. In this study, we perform the first-principles calculations for $Li_{2+2x}Mn_{1-x}Ti_{1-x}O_4$ models with several Li excess amount of x ranging from 0 to 0.5. Effects of x on the theoretical voltage-capacity profiles are compared with the experimental results. From the calculations, it is found that a two-stage process associated with Mn+Ti and Mn+O redox reactions take place depending on the Li concentration especially in the early and late discharge process, respectively.

References

[1] J. W. Wang *et al.*, Nano Lett. **12**, 5897 (2012).

[2] C. J. Pelliccione *et al.*, J. Phys. Chem. C **120**, 5331 (2016).

[3] A. Kitajou and S. Okada, private communications.

Development of permanent magnet materials

Takashi MIYAKE
CD-FMat, AIST
Umezono, Tsukuba, Ibaraki 305-8568

High performance permanent magnets require high saturation magnetization and high coercivity. The RFe$_{12}$-type compounds (R=rare-earth) having the ThMn$_{12}$ structure are potential main phase of high performance magnets, because they have high saturation magnetization and strong magnetoctystalline anisotropy for proper choice of R. The former comes from high Fe content, whereas the R element is essential for the latter. However, RFe$_{12}$ are thermodynamically unstable. We have studied stability of RFe$_{12}$ for a series of R element by means of density functional theory in the generalized gradient approximation. The R-4f electrons are treated as open-core states. Figure 1 shows the formation energy of RFe$_{12}$ relative to R_2Fe$_{17}$ and α-Fe [1]. We found that the stability is sensitive to the choice of R element. There is strong correlation between the atomic radius of the R element and the stability. The formation energy shows a minimum for R=Dy. It was reported recently that Sm(Fe,Co)$_{12}$ has excellent intrinsic magnetic properties. The present result indicates that partial substitution of Sm with e.g. Gd, Y and Zr would enhance the stability of the compound. We also calculated spin dispersion of Sm(Fe,Co)$_{12}$ from first-principles [2]. We found that the spin-wave dispersion of SmFe$_{12}$ is highly anisotropic around the Γ point. It is shown that the spin waves propagate more easily in the a^*-direction than in the c^*-direction. The spin-wave stiffness is enhanced by Co-doping.

We have been developing computational scheme for magnetization reversal using spin model for Nd$_2$Fe$_{14}$B. This year, we have developed a computational scheme for evaluating exchange stiffness constant by connecting analyses with two different scales of length, namely, Monte Carlo method for an atomistic spin model and Landau-Lifshitz-Gilbert equation for a continuous model. We found that the magnitude and temperature dependence of the exchange stiffness depends on the orientation in the crystal [3].

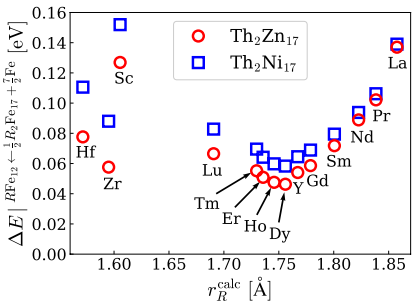

Figure 1: Formation energy of RFe$_{12}$ relative to R_2Fe$_{17}$ and α-Fe.

References

[1] Y. Harashima et al.: J. Appl. Phys. **124** (2018) 163902.

[2] T. Fukazawa et al.: J. Magn. Magn. Mater. **469** (2019) 296.

[3] Y. Toga et al.: Phys. Rev. B **98** (2018) 054418.

First-principles calculations of interface magnetic properties at magnetic materials

Yoshihiro GOHDA
Department of Materials Science and Engineering, Tokyo Institute of Technology
J1-3, Nagatsuta-cho 4259, Midori-ku, Yokohama 226-8502, Japan

Magnetic materials such as permanent magnets, multiferroic materials [1–3], and magnetic refrigerants are not only important in practical applications but also of significant interest fundamentally in the sense of understanding of magnetism due to electron-electron interaction. In such materials, effects of interfaces are significant: the coercivity of permanent magnets comes from interfaces in microstructures; a practical magnitude of multiferroicity is achievable only using the interface effects. However, our understanding of interface effects in magnetic materials is far from being complete. Furthermore, in the viewpoint of large scale computations, first-principles calculations of interfaces are challenging, because they are typically performed with large supercells.

In this project, first-principles studies were performed to understand magnetic materials, in particular permanent magnets [4–8] and multiferroic materials [3, 9]. First, on the basis of first-principles melt-quench molecular dynamics simulations by the OpenMX code [10], we performed structural analyses using graph theory for amorphous Nd-Fe alloys, a relevant subphase in Nd-Fe-B permanent magnets [5]. With improving the implementation of the Liechtenstein method in the OpenMX code, we also examined the exchange-coupling constants between two atoms in the Nd-Fe amorphous phase. We obtained strong composition dependence of the Curie temperature.

We also investigated the interface multiferroicity [3, 9]. The magnetoelectric coupling in a ferromagnetic/multiferroic interface, bcc-Fe/$BiFeO_3$(001), is significantly large [3]. We further clarified that the interface-magnetic anisotropy governs the direction of the bcc-Fe magnetization through the exchange coupling within bcc Fe. As for ferromagnetic/ferroelectric interfaces [9], we succeeded in enlarging interface magnetoelectric couplings by modifying the stacking of atomically controlled ferromagnetic thin-film heterostructures with Heusler alloys.

[1] T. Taniyama, J. Phys.: Condens. Matter **27**, 504001 (2015).

[2] C.-G. Duan, S. S. Jaswal, and E. Y. Tsymbal, Phys. Rev. Lett. **97**, 047201 (2006).

[3] K. Fujita and Y. Gohda, Phys. Rev. Appl. **11**, 024006 (2019).

[4] Y. Tatetsu, S. Tsuneyuki, and Y. Gohda, Mater. **4**, 388 (2018).

[5] A. Terasawa and Y. Gohda, J. Chem. Phys. **149**, 154502 (2018).

[6] Y. Tatetsu, Y. Harashima, T. Miyake, and Y. Gohda, Phys. Rev. Mater. **2**, 074410 (2018).

[7] N. Tsuji, H. Okazaki, W. Ueno, Y. Kotani, D. Billington, A. Yasui, S. Kawaguchi, K. Sugimoto, K. Toyoki, T. Fukagawa, T. Nishiuchi, Y. Gohda, S. Hirosawa, K. Hono, and T. Nakamura, Acta Mater. **154**, 25 (2018).

[8] Y. Gohda, Y. Tatetsu, and S. Tsuneyuki, Mater. Trans. **59**, 332 (2018).

[9] Y. Hamazaki and Y. Gohda, in preparation.

[10] T. Ozaki, Phys. Rev. B. **67**, 155108 (2003).

Multiscale simulations on complex multiphase flows

Yohei MORII, Takahiro MURASHIMA and Toshihiro KAWAKATSU

Department of Physics, Tohoku University, Sendai 980-8578

Multiphase flows, such as cavitation flows, flows in clouds, are complex flows where multiscale domain structures generated by phase coexistence play an important role in determining the macroscopic properties of the flow. Here, the main problem arises from the fact that the microscopic state at any point of the flow changes often in an unpredictable manner. This is due to the inhomogeneity of the flow, where a simple constitutive equation cannot be applied.

To solve such a problem, we develop Multi-Scale Simulation Platform for complex flows (MSSP), where microscopic simulators (MicS) such as molecular dynamics simulators are embedded in each point of the macroscopic flow (See Fig.1). We adopt Smoothed Particle Hydrodynamics (SPH) simulation technique, where the macroscopc flow is described by many hydrodynamic particles. In the MSSP, each hydrodynamic particle has one MicS as a representative of its microscopic state. We performed a benchmark simulation of MSSP on a macroscopic flow passing a cylindrical obstacle with use of Newtonian constitutive equation or Maxwell's constitutive equation as MicS. The results are shown in Fig.2. We also obtain quantitatively similar results to those in Fig.2 by using a set of many dumbbells as MicS. Simulation results show that the non-Markovian nature of viscoelastic fluid.

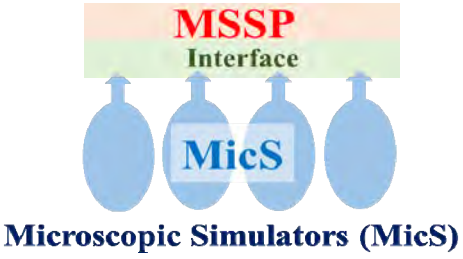

Fig. 1: Concept viscoelastic fluid.

As the correlation between MicS's arises only through the SPH level, the calculations of the time evolution of MicS's can be performed independently, which guarantees a high performance of parallelization calculation of MSSP.

Acknowledgements

This research was supported by MEXT, Japan as "Exploratory Challenge on Post-K computer" (Challenge of Basic Science – Exploring Extremes through Multi-Physics and Multi-Scale Simulations).

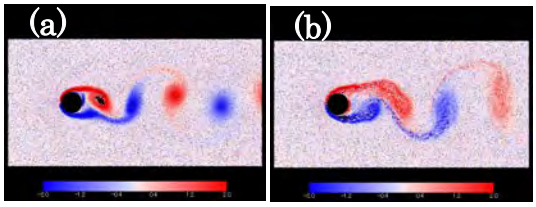

Fig. 2: (a) Newtonian fluid and (b)

Computational study of hydrous minerals using the path integral molecular dynamics method II

Tsutomu Kawatsu, and Toshiaki Iitaka

Computational engineering application unit, R&D group, Head office for information system and cybersecurity, Riken, 2-1 Hirosawa, Wako, Saitama 351-0198

We calculated thermodynamical structures of ice VIII-VII-X models [1] which was similar to the high-pressured hydrous mineral, δ-AlOOH [2,3] that we have calculated in last-year project. The δ-AlOOH has hydrogen bonds between polyhedrons of aluminium oxides, which symmetrize in high-pressured condition and asymmetrize in low pressure. The extremely high-pressured ices, ice X has symmetrized hydrogen bonds and relatively lower pressured ice VIII has asymmetrized ones. The ice VII is then a disordered intermediate state.

We used ab initio path integral molecular dynamics (AI-PIMD) method [4] with the parallel PIMD code [5] linked with parallel electronic structure calculation code, Quantum Espresso (QE) [6]. The AI-PIMD calculations in present study constructed in thirty-two parallel QE processes for the same number of connected replicas with single-node parallel of the QE process in system B. We then took 100,000 NPT sampling steps after 10,000 equilibrium steps for each trajectory and each pressure condition in every 10 GPa from 10 to 140 GPa. The temperature was set to 300 K. We used a minimum cell including two water molecules. The k-points was x3x3x3 and the energy cut off was 100. Ry.

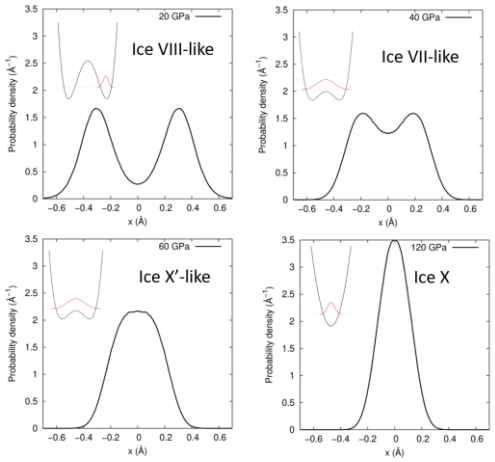

Fig. 1. Computed hydrogen-atom distributions between hydrogen-bonded water molecules in high pressures. The illustration in each graph is the overview of the potential and wave function of the hydrogen atom.

Figure 1 shows the computed distributions of the hydrogen atoms projected to the oxygen-oxygen axis using AI-PIMD method. These calculations represented the ice phases of VII, VIII, and X depending on the pressure. Using these structural distributions, we calculated quantum kinetic energy of the hydrogen and oxygen atoms. The kinetic energy of the hydrogen atom strongly depends on the phase of

the ice while that of the oxygen atom only depends on the pressure itself. On the other hand, δ-AlOOH has little different view. Instead of the hydrogen atom, the quantum kinetic energy of both the hydrogen and oxygen atoms are affected by the phase transition because the order of Al-O bonds can be changed with O-H bonds even though the oxygen atom is 16 times heavier than the hydrogen atom.

References

[1] E. Sugimura, T. Iitaka, K. Hirose, K. Kawamura, N. Sata, Y. Ohishi: Phys. Rev. B **77** (2008) 214103.

[2] A. Suzuki, E. Ohtani, T. Kamada: Phys. Chem. Minerals **27** (2000) 689.

[3] A. Sano-Fukukawa, H. Kagi, T. Nagai, S. Nakano, S. Fukura, D. Ushijima, R. Iizuka, E. Ohtani, T. Yagi: Am. Mineral. **94** (2009) 1255.

[4] G. J. Martyna, A. Hughes, M. Tuckerman: J. Chem. Phys. **110** (1999) 3275.

[5] S. Ruiz-Barragan, K. Ishimura, M. Shiga: Chem. Phys. Lett., **646** (2016) 130.

[6] P. Giannozzi *et al.*: J.Phys.: Condens. Matter 21 (2009) 395502.

Structure study of ε-solid oxygen using ab initio molecular dynamics

Tsutomu Kawatsu, Le The Anh, and Toshiaki Iitaka

Computational engineering application unit, R&D group, Head office for information system and cybersecurity, Riken, 2-1 Hirosawa, Wako, Saitama 351-0198

This study is a part of preliminary study for "structure study of silicate melts using linear scaling ab initio molecular dynamics." The silicate melts are an important component of the earth science, which is often called as "magma" if it is on the surface area of the earth. The magma is made in the deep earth and it forms various minerals depending the temperature and pressure. To calculate the silicate melts we have to optimize the computational methods which can describe the both crystal and molecular systems and calculate large system size, because the melts has a lot of non-bonding interactions and non-periodic structure. To investigating the methods, we have chosen solid-oxygen model which has both conditions of the crystal and molecule and measured by our corroborators [1]. It is the molecular crystal in lower pressure and loses the molecular character in high pressure. We have investigated the density functional method for the solid oxygen [2], and in present study, we run ab initio molecular dynamics (AI-MD) calculation for investigating the thermal effect onto the structure of the solid oxygen using the PIMD program [3] linked with parallel electronic structure calculation code, Quantum Espresso (QE) [4]. We performed AI-MD calculations for the epsilon phase of the solid oxygen in various temperatures and computational conditions with four-node parallel calculations in system B. We took 100,000 steps of NVT samplings after 10,000 equilibrium steps for each trajectory with 20 GPa volume. We used a minimum cell including eight oxygen molecules and PBE density functional with PAW method. The k-points was x5x3x2, and the energy cut off was 100. Ry.

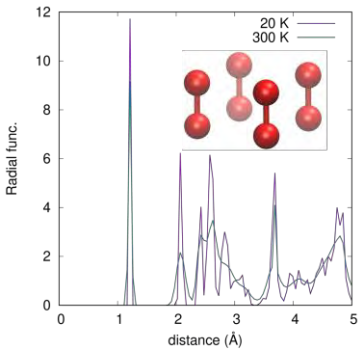

Fig. 1. Computed radial distribution function of the oxygen atoms in the ε-solid oxygen. The figure in graph is a single unit cell of the ε-oxygen.

Figure 1 shows the computed radial distribution function the ε-solid oxygen in 20 K and 300 K. The first peak is intra-molecular

distance and the second and fourth peaks are neighboring molecular distances in the unit cell. The four oxygen molecules construct a square unit and the third peak comes from the distance of next square units. Comparing 20 K and 300 K results, the position of peaks does not change while these peaks broaden. The thermal effect may conserve the structure in room temperature although we should also check the NPT sampling.

References

[1] H. Fukui et al. unpublished.

[2] L. The Anh et al. submitted.

[3] S. Ruiz-Barragan, K. Ishimura, M. Shiga: Chem. Phys. Lett., **646** (2016) 130.

[4] P. Giannozzi *et al.*: J.Phys.: Condens. Matter 21 (2009) 395502.

3.6 Software Advancement Projects, GPGPU Implementation, and Workshop Support

Development of first principles electronic-structure calculation software by combining effective-model derivation code RESPACK and model-analysis codes $\mathcal{H}\Phi$ and mVMC

Kazuma NAKAMURA[1], Kazuyoshi YOSHIMI[2], Mitsuaki KAWAMURA[2], Takahiro MISAWA[2], Yuichi MOTOYAMA[2] Taisuke OZAKI[2]
[1]*Department of Basic science, Kyushu Institute of Technology, Kitakyushu, 804-8550*,
[2]*Institute for Solid State Physics, University of Tokyo, Kashiwa, 277-8581*

As Project for advancement of software usability in materials science at the fiscal year of 2018, we have released a new version of the software RESPACK [1] for many-body perturbation calculation and effective low-energy model derivation. RESPACK is possible to derive parameters for the effective low-energy model from first principles. The new version includes *ab initio* GW calculation and utility tool such as transfer analysis and interfaces to model-analysis solvers mVMC [2] and $\mathcal{H}\Phi$ [3]. Users can now automatically obtain the model-analysis-software inputs via RESPACK.

RESPACK consists of five programs:

- Wannier function calculation (`wannier`)
- Dielectric function calculation (`chiqw`)
- Electronic interaction calculation for direct and exchange integrals (`calc_w3d`, `calc_j3d`),
- *Ab initio* GW calculation (`calc_gw`),
- Utility code for transfer analysis (`transfer_analysis`)

These programs are run under the following inputs:

- Input file for RESPACK calculation (`input.in`)
- Band-calculation outputs contained in a directory `dir-wfn`

RESPACK supports *ab initio* band calculation codes using norm conserving pseudopotentials plus plane wave basis set, and officially supports xTAPP [4] and Quantum ESPRESSO [5] packages. Automatic generation scripts which convert results of the band calculation to inputs for RESPACK is prepared for xTAPP and Quantum ESPRESSO codes. An input file for specifying RESPACK calculation conditions is designed pursuing simplicity and is given in a namelist format. It supports OpenMP/MPI and can be used in both laboratory-computer environment and System B at ISSP, the University of Tokyo. RESPACK has a wide application including simple metals, semiconductors, $3d/4d$ transition-metal compounds, organic and aromatic compounds, etc. In this report, we present an *ab initio* calculation of the excitation spectrum of an impurity system using three software: xTAPP, RESPACK, and $\mathcal{H}\Phi$.

Figure 1(a) is the atomic geometry of the impurity system of ruby (Al_2O_3:Cr), and the panel (b) is our calculated band structure, where we see two impurity bands near the Fermi level due to the Cr impurity. Blue dotted curves are the Wannier interpolated band

obtained from `wannier` program. We also performed `chiqw`, `calc_w3d`, and `calc_j3d` and calculated effective interactions.

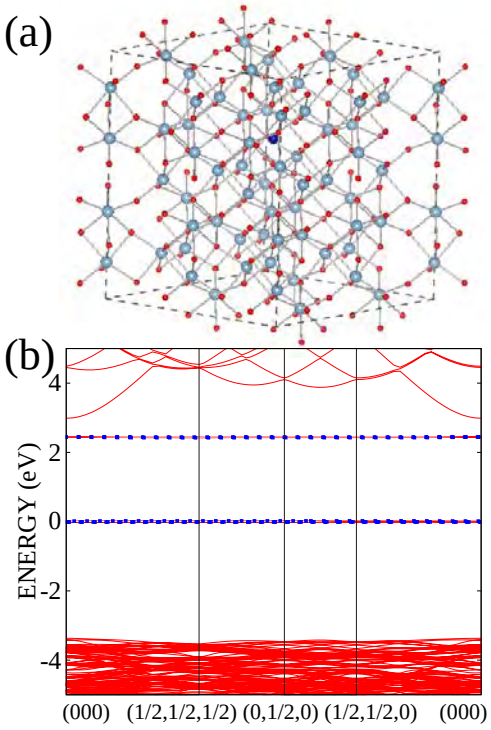

Figure 1: (a) Atomic geometry for impurity sistem: $Al_{47}CrO_{72}$ (2×2×1 supercell). (b) Calculated xTAPP band structure with 5×5×5 k-point sampling and 100-Ry cutoff.

When the RESPACK job (`wannier, chiqw, calc_w3d, calc_j3d`) is executed, a directory `dir-mvmc` is generated under the calculation directory, and the files necessary for model-analysis softwares mVMC and $\mathcal{H}\Phi$ are output. Using these data and a standard-mode input for mVMC and $\mathcal{H}\Phi$, all inputs of the model calculations are automatically generated under the following command:

```
HPhi -s stan.in (or vmc.out -s stan.in)
```

Here, `HPhi` and `vmc.out` are execution files of $\mathcal{H}\Phi$ and mVMC, respectively, and `stan.in` is an input file for standard mode. This interface code has the lattice conversion function; when the user moves from *ab initio* calculation to model one, the lattice adopted at the *ab initio* calculation can be flexibly changed. Also, the code has an option for avoiding the Hartree-term double count; user can adjust one-body correction $\Delta_{i\mathbf{0}}$ by optional parameter α,

$$\begin{aligned}\Delta_{i\mathbf{0}} &= \alpha U_{i\mathbf{0},i\mathbf{0}} D^{\mathrm{KS}}_{i\mathbf{0},i\mathbf{0}} \\ &+ \sum_{\mathbf{R}\neq\mathbf{0}} \sum_{k} D^{\mathrm{KS}}_{k\mathbf{0},k\mathbf{0}} \Big(U_{i\mathbf{0},k\mathbf{R}} - (1-\alpha) J_{i\mathbf{0},k\mathbf{R}} \Big),\end{aligned} \tag{1}$$

where U, J, and D are the direct integral, exchange integrals, and density matrix with the Kohn-Sham orbital, respectively.

Table 1 shows our calculated excitation energy diagram of the impurity model. The excitation energy depends on α in Eq. (1), and the results correcting of the Hartree-term double counting reasonably reproduce the experimental result.

Table 1: Calculated energy diagram of impurity model from RESPACK. The unit is eV. Values of the ground state (GS) are the total energy.

Expt	Theory		
-	$\Delta_{i\mathbf{0}}=0$	$\alpha=0.5$	$\alpha=1$
GS(^4A)	47.9(^4A)	5.60(^4A)	−3.04(^4A)
1.79(^2E)	1.67(^2E)	1.61(^2E)	1.62(^2E)
1.87(^2T)	1.78(^2T)	1.73(^2T)	1.84(^2T)
2.23(^4T)	2.29(^4T)	1.79(^4E)	2.32(^2A)
2.62(^2T)	2.46(^4T)	2.23(^4T)	2.56(^4T)
3.10(^4T)	2.69(^2T)	2.60(^4A)	2.78(^4T)

For code developments of RESPACK, we thank to Yoshihide Yoshimoto, Yoshiro Nohara, Yusuke Nomura, Terumasa Tadano, and Maxime Charlebois.

References

[1] https://sites.google.com/view/kazuma7k6r

[2] https://github.com/issp-center-dev/mVMC

[3] http://issp-center-dev.github.io/HPhi/index.html

[4] http://xtapp.cp.is.s.u-tokyo.ac.jp/

[5] http://www.quantum-espresso.org/

DSQSS - A PIMC-based quantum lattice model solver [1]

Naoki KAWASHIMA
Institute for Solid State Physics, University of Tokyo
Kashiwa-no-ha, Kashiwa, Chiba 277-8581

Among many numerical solutions to the quantum many-body problems on lattices, the path-integral Monte Carlo method (PIMC) has probably the most broad range of applicability [1]. By using PIMC, we can calculate the thermal expectation values of observables of interest with no systematic error for larger systems than can be handled by exact methods. The method works in arbitrary dimension at finite temperature as long as the system is free from the sign problem. The Monte Carlo method generally suffers from the slow convergence near the critical point ('critical slowing down'). For discrete space problems, several update methods, e.g., the loop algorithm and the directed-loop algorithm (DLA), have been developed to overcome the critical slowing down. These methods have been extended for massive parallelization for modern supercomputers.

While the loop-type update algorithms are quite powerful in selected problems, the worm-type update algorithm, the DLA included, are more frexible in various applications. Representative examples are boson systems and, equivalently, antiferromagnets with uniform magnetic field. In spite of these broad range of applicability, very few DLA-based open-source software has been available for parallel computation. Therefore, we proposed to develop one in the ISSP software-development/improvement project, to make it easier for non-experts to run DLA simulation on pararell machines without much effort.

Specifically, We are developing a PIMC program package for quantum lattice problems, which we call DSQSS (Discrete Space Quantum Systems Solver). Since DSQSS adopts the DLA for update scheme, it can update configurations effectively even under a symmetry-breaking field, DSQSS supports arbitrary Hamiltonians and lattices while it comes with additional tools to make it easier to define standard Hamiltonians and lattices. For example, models such as XXZ model defined on hypercubic lattice are pre-defined in DSQSS. As a result, in many cases of interest, users can perform QMC calculation by providing only a small amount of information (typically a few ten lines of text file) to define the condition of the simulation precisely. DSQSS also offers the parallelized multi worm algorithm for massively parallel calculation.

[1] This report is based on collaboration of Y. Motoyama (ISSP), K. Yoshimi (ISSP), A. Masaki-Kato (Hitachi Ltd.), N. K., and T. Kato (ISSP).

[2] The software website is
https://github.com/issp-center-dev/dsqss

GPGPU implementation of divide-and-conquer density-functional tight-binding molecular dynamics

Takeshi Yoshikawa[1], and Hiromi Nakai[1-3]

[1]*Waseda Research Institute for Science and Engineering, Waseda University, Okubo, Shinjuku-ku, Tokyo 169-8555*

[2]*School of Advanced Science and Engineering, Waseda University, Okubo, Shinjuku-ku, Tokyo 169-8555*

[3]*ESICB, Kyoto University, Kyotodaigaku-Katsura, Nishigyoku, Kyoto 615-8520*

Many biochemical systems, including rhodopsin in vertebrate eyes and photoactive yellow protein in purple bacteria, exhibit photo activity. After photon absorption, a photoactive protein converts the light energy into chemical energy or a signal with conformational changes such as proton and electron transfers. Although hydrogen atoms and/or protons play important roles in protein function, it is difficult to identify their position experimentally due to spatial resolution restrictions. Quantum mechanical molecular dynamics (QM-MD) simulations is a powerful tool for the analysis of geometric and electronic structures. One of the challenges in QM-MD simulations is the applicability to large systems on account of high computational demands with respect to the system size. In our group, divide-and-conquer density-functional tight-binding (DC-DFTB) [1] has been developed to reduce the computational cost and shown to perform reasonably well for many large systems.

In this study, the Graphical processing units (GPU) code for DC-based DFTB methods is implemented to enable long-time QM-MD simulation for support service of GPGPU implementation. The GPU code is heterogynous algorithm on CPU and GPU architectures. The construction of Hamiltonian and evaluation of the derivative terms is accelerated on GPU. The diagonalization of Hamiltonian is performed on CPU. Table 1 shows the wall-clock times for DC-DFTB calculations of water cluster $500H_2O$. The heterogynous algorithm achieves 2.46-fold and 3.43-fold speedups for construction of Hamiltonian and evaluation of derivative term, respectively.

Table 1. Wall-clock times for DC-DFTB calculations of water cluster $500H_2O$.

	CPU	GPU
Construction of Hamiltonian	11.3	4.6
Evaluation of derivative term	16.7	4.9

References

[1] H. Nishizawa, Y. Nishimura, M. Kobayshi, S. Irle, H. Nakai, J. Comput. Chem. **37** (2016) 1983.

Report of CCMS hands-on sessions in the 2018 fiscal year

Takahiro Misawa
Institute for Solid State Physics, University of Tokyo
Kashiwa-no-ha, Kashiwa, Chiba 277-8581

In the 2018 fiscal year, center for computational materials science (CCMS) in institute for solid state physics (ISSP) held five hands-on sessions by using supercomputer (sekirei) of ISSP. A list of the hands-on sessions is shown in table 1. In this report, we briefly summarize the hands-on sessions.

DCore is a tool for performing quantum many-body simulations based on the dynamical mean-filed theory (DMFT). Development of DCore was supported by "Project for advancement of software usability in materials science"(PASMS) [1] in the 2017 fiscal year. Hiroshi Shinaoka and co-developers explained the basics of the DMFT and gave a tutorial on DCore [2, 3].

MateriApps LIVE! is a Debian Live Linux system that contains OS, editors, several materials science application software packages. Synge Todo explained how to install and used MateriApps LIVE! [4, 5] and explained how to use several software packages included in MateriApps LIVE!.

xTAPP is a first-principles plane-wave pseudo-potential code. In the hands-on session in xTAPP [6, 7], Yoshihide Yoshimoto and Kanako Yoshizawa explained the basic usages of xTAPP and how to use it in sekirei.

$\mathcal{H}\Phi$ is an exact diagonalization package and its development was supported by PASMS in the 2015 and 2017 fiscal years. Youhei Yamaji and co-developers explained the how to use HΦ [8, 9] and recently implemented functions such as the real-time evolution.

RESPACK is a first-principles calculation software package for evaluating the interaction parameters of materials and its development was partially supported by PASMS in the 2018 fiscal year. Kazuma Nakamura explained the details of RESPACK [10, 11] and how to use it.

Date	Software	Main lecturer
Jul. 30	DCore	H. Shinaoka
Aug. 28	MateriApps LIVE!	S. Todo
Oct. 19	xTAPP	Y. Yoshimoto
Dec. 12	$\mathcal{H}\Phi$	Y. Yamaji
Mar. 1	RESPACK	K. Nakamura

Table 1: List of software packages used in CCMS hands-on sessions.

References

[1] http://www.issp.u-tokyo.ac.jp/supercom/softwaredev

[2] https://ma.issp.u-tokyo.ac.jp/en/app/1004

[3] https://ccms.issp.u-tokyo.ac.jp/event/570

[4] https://ma.issp.u-tokyo.ac.jp/en/app/275

[5] https://ccms.issp.u-tokyo.ac.jp/event/653

[6] https://ma.issp.u-tokyo.ac.jp/en/app/741

[7] https://ccms.issp.u-tokyo.ac.jp/event/697

[8] https://ma.issp.u-tokyo.ac.jp/en/app/367

[9] https://ccms.issp.u-tokyo.ac.jp/event/1101

[10] https://ma.issp.u-tokyo.ac.jp/en/app/772

[11] https://ccms.issp.u-tokyo.ac.jp/event/1331

Supercomputer course of Computational Materials Design (CMD®) workshop

Masaaki GESHI[1], Yoshitada MORIKAWA[2], Tomoya ONO[3]

[1]*Institute for NanoScience Design,*
Osaka University, Machikaneyama, Toyonaka, Osaka 560-8531

[2]*Department of Precision Science and Technology,*
Osaka University, Yamada-oka, Suita, Osaka 565-0871

[3]*Center for Computational Science,*
University of Tsukuba, Tenno-dai, Tsukuba, Ibaraki 305-8577

The 33rd Computational Materials Design (CMD®) workshop (CMD33) has been held from September 3 to September 7 and the 34th CMD® workshop (CMD34) has been done from February 18 to February 22 at Graduate School of Engineering Science, Osaka University. In this workshop we have the supercomputer course to train up human resources to advance researches by using system B supercomputer of ISSP, the University of Tokyo.

In CMD33 nine participants took the supercomputer course and got a tutorial on STATE-Senri developed by Y. Morikawa. After explaining how to use the supercomputer of ISSP and explaining how to use STATE-Senri, calculation models on each research subject of the participants were built and their calculations were carried out. Concrete themes were molecular adsorption on solid surfaces, chemical reactions at electrode interfaces, adsorption and diffusion of atoms on graphene, electronic structures of oxides for ion batteries and so on. The participants performed the calculations and examined the results.

In CMD34 thirteen participants took the supercomputer course and four participants used the supercomputer of ISSP. They got a tutorial on RSPACE developed by T. Ono. After describing the calculation method of electronic states and electron conduction property using RSPACE, exercises published in the manual were carried out. Then, electronic state calculations were carried out on a plurality of molecular systems, and the electronic density distribution was visualized. Finally, the atomic structure optimization of the system in which molecules are sandwiched between metal electrodes was carried out, and the calculation of electron conduction properties of molecules was analyzed.

4 PUBLICATION LIST

Example:

LASTNAME, Firstname [project class; # points (B), # points (C)] (Page #)

— *Project title*

1. First paper
   Names of Authors, etc.
2. Second paper
   ...

□ ISSP Joint Research Projects

AKAGI, Kazuto [C class; 4000 (B), 0 (C)] (105)

— *Topological Analysis and Order Parameter of the System*

1. Local chemical ordering within the incubation period as a trigger for nanocrystallization of a highly supercooled Ti-based liquid
   Z. Wang, C. L. Chen, S. V. Ketov, K. Akagi, A. A. Tsarkov, Y. Ikuhara and D. V. Louzguine-Luzgin: Materials and Design **156** (2018) 504-513.

AKAI, Hisazumi [B class; 1300 (B), 50 (C)] (139,140)

— *Stability and magnetic properties of rare earth mixed crystal magnet materials*

1. First-principles study of spin-wave dispersion in $Sm(Fe_{1-x}Co)_{12}$
   T. Fukazawa, H. Akai. Y. Harashima, and T. Miyake : J. Magn, Magn. Mater. **469**, 296 (2019).
2. Ab initio Study of High-field NMR Shift of ^{59}Co in the Ferromagnetic Heusler Alloy C_2TiGa
   H. Nishihara, H. Akai, K. Sato, T. Kanomata, M. Geshi, T. Sakon, and T. Wada: J. Phys. Soc. Jpn. **88**, 034712 (2019).

AKASHI, Ryosuke [C class; 6500 (B), 0 (C)] (70)

— *First-principles quantitative approach to the interplay of charge and spin fluctuations in superconductors*

AOYAMA, Kazushi [B class; 1300 (B), 90 (C)] (282)

— *Theoretical study of dynamical spin correlations in Heisenberg antiferromagnets on the triangular lattice*

— *Transport properties of the classical antiferromagnetic Heisenberg model in two dimension*

1. Spin ordering induced by lattice distortions in classical Heisenberg antiferromagnets on the breathing pyrochlore lattice
   K. Aoyama and H. Kawamura: Phys. Rev. B **99** (2019) 144406.

ARAI, Munehito [C class; 5000 (B), 0 (C)] ()

— *Theoretical analysis and design of proteins for industrial and pharmaceutical applications*

ARAIDAI, Masaaki [C class; 2500 (B), 800 (C)] (117)

— *First-principles study on two-dimensional crystals of germanium*

ASANO, Yuta [C,E class; 22000 (B), 3300 (C)] (205)

— *A Molecular Dynamics Study of the Cavitation*

— *Molecular Dynamics Simulation of a Karman-Vortex Cavitation*

1. Polymer effects on Karman vortex: Molecular dynamics study

Y. Asano, H. Watanabe, and H. Noguchi: J. Chem. Phys. **148**,(2018) 144901.

BUI, PHO VAN [C class; 4000 (B), 1300 (C)] (88)
— *Study on removal mechanism in catalyst referred etching of single crystalline SiC with pure water*

1. Catalyzed Chemical Polishing of SiO2 Glasses in Pure Water
   D. Toh, P.V. Bui, A. Isohashi, N. Kidadi. S. Matsuyama, Y. Sano, Y. Morikawa, K. Yamauchi: Rev. Sci. Instru. **90** (2019) accepted
2. High-efficiency SiC polishing using a thin film catalyst in pure water
   P.V. Bui, D. Toh, S. Matsuyama, Y. Sano, K. Yamauchi: euspen's 19th Internation Conference and Exhibition (2019)

EGAMI, Yoshiyuki [C class; 3500 (B), 350 (C)] (107)
— *Development of a time-dependent electron-transport simulator and its application to atomic-layered materials*

1. Efficient calculation of the self-energy matrices for electron-transport simulations
   Y. Egami, S. Tsukamoto and T. Ono: submitted to Phys. Rev. B.

FUCHIZAKI, Kazuhiro [C class; 4500 (B), 0 (C)] (252)
— *Phase equilibria and polyamorphism*

1. Liquid–Gas Spinodal of the Modified Lennard-Jones Fluid
   K. Fuchizaki and K. Watanabe: J. Phys. Soc. Jpn. **87** (2018) 114006.
2. Pressure-induced local symmetry breaking upon liquid–liquid transition of GeI_4 and SnI_4
   K. Fuchizaki, T. Sakagami, and H. Iwayama: J. Chem. Phys. **150** (2019) 114501.
3. A polymerization scenario of the liquid–liquid transition of GeI_4
   K. Fuchizaki, H. Naruta, and T. Sakagami: J. Phys.: Condens. Matter **31** (2019) 225101.

FUJIMOTO, Yoshitaka [C class; 2000 (B), 0 (C)] (128)
— *First-principles study of electronic properties of graphene layers*

1. Gas adsorption effects on the stabilities, electronic structures and scanning tunneling microscopy of graphene monolayers doped with B or N
   Y. Fujimoto and S. Saito: Jpn. J. Appl. Phys. **58**, 015005 (2019).
2. STM visualization of carbon impurities in sandwich structures consisting of hexagonal boron nitride and graphene
   T. Haga, Y. Fujimoto, and S. Saito: Jpn. J. Appl. Phys., Accepted.
3. Electronic structures and scanning tunneling microscopy images of graphene/carbon-doped hexagonal boron nitride heterostructures
   T. Haga, Y. Fujimoto, and S. Saito: Phys. Rev. B, submitted.
4. Design and Analysis of Carbon-Based Nanomaterials for Removal of Environmental Contaminants
   Y. Fujimoto: Nanotechnology for Sustainable Water Remediation (Wiley-Scrivener Publishers 2018) Chapter 9, p.277.

FUJISHIRO, Hiroki [C class; 1500 (B), 0 (C)] (137)
— *Strained Band-Structure Engineering for Antimonide-Based Terahertz Transistors*

FUKUDA, Jun-ichi [B class; 1500 (B), 0 (C)] (279)
— *Calculation of ordered structures and their optical properties of soft materials*

1. Liquid-crystalline half-Skyrmion lattice spotted by Kossel diagrams
   J. Fukuda, A. Nych, U. Ognysta, S. Žumer and I. Muševič: Scientific Reports **8** (2018) 17234.
2. Theoretical study on optical properties of liquid crystalline Skyrmion lattice
   J. Fukuda and S. Žumer: Proc. SPIE **10941** (2019) 1094108.

FUKUI, Ken-ichi [C class; 2000 (B), 0 (C)] (271)
— *Analysis on Structuring and Dynamics of Ionic Liquid Forming Electric Double Layer at Electrode Interfaces*

1. Microscopic properties of ionic liquid / organic semiconductor interfaces revealed by molecular

dynamics simulations
Y. Yokota, H. Miyamoto, A. Imanishi, J. Takeya, K. Inagaki, Y. Morikawa, and K. Fukui: Phys. Chem. Chem. Phys. **20** (2018) 13075.

2. Potential dependent changes of structural and dynamical properties of 1-butyl-3-methylimidazolium bis(trifluoromethanesulfonyl)imide on graphite electrode revealed by molecular dynamics simulation
H. Miyamoto, Y. Yokota, A. Imanishi, K. Inagaki, Y. Morikawa, K. Fukui: Phys. Chem. Chem. Phys.**20** (2018) 19408.

FUKUMOTO, Yoshiyuki [B class; 500 (B), 0 (C)] (305)
— *Theoretical studies on kagome antiferromagnets and related systems*

1. Impact of Dzyaloshinsky-Moriya Interactions and Tilts of the g Tensors on the Magnetization Process of a Spherical Kagomé Cluster in $\{W_{72}V_{30}\}$
Y.Fukumoto, Y. Yokoyama, and H. Nakano: J. Phys. Soc. Jpn. 87, 124710, 2018
2. Canonical-Ensemble Calculations of the Magnetic Susceptibility for a Spin-1/2 Spherical Kagome Cluster With DzyaloshinskiiMoriya Interactions by Using Microcanonical Thermal Pure Quantum States
K. Inoue, Y. Maeda, H. Nakano, Y. Fukumoto: IEEE TRANSACTIONS ON MAGNETICS 55, 2019

GESHI, Masaaki [C class; 3500 (B), 700 (C)] (100)
— *Development of new structural search method and search for new functional materials*

GOHDA, Yoshihiro [C class; 4500 (B), 800 (C)] (87)
— *Rashba effects in surface-Bi nanostructures*

1. First-principles study of magnetoelectric coupling at Fe/$BiFeO_3$(001) interfaces
K. Fujita and Y. Gohda: Phys. Rev. Appl. **11**, 024006 (2019).
2. First-principles prediction of one-dimensional giant Rashba splittings in Bi-adsorbed In atomic chains
T. Tanaka and Y. Gohda: Phys. Rev. B **98**, 241409(R) (2018).
3. First-principles study on substitution effects in Nd_2(Fe, X)$_{14}$B
Y. Tatetsu, S. Tsuneyuki, and Y. Gohda: Mater. **4**, 388 (2018).
4. Hidden order in amorphous structures: extraction of nearest neighbor networks of amorphous Nd-Fe alloys with Gabriel graph analyses
A. Terasawa and Y. Gohda: J. Chem. Phys. **149**, 154502 (2018).
5. Role of typical elements in $Nd_2Fe_{14}X$ (X=B, C, N, O, F)
Y. Tatetsu, Y. Harashima, T. Miyake, and Y. Gohda: Phys. Rev. Mater. **2**, 074410 (2018).

HAGITA, Katsumi [C class; 3500 (B), 700 (C)] (254)
— *Coarse grained MD simulation for fracture and reinforcement of polymer materials*

1. Super resolution for asymmetric resolution of FIB-SEM 3D imaging of silica nanoparticles in SBR
K. Hagita, T. Higuchi and H. Jinnai: Scientific reports, 8 (2018) 5877.
2. Molecular dynamics simulations of cross-linked phenolic resins using a united-atom model
A. Izumi, Y. Shudo, K. Hagita and M. Shibayama: Macromolecular Theory and Simulations, 27 (2018) 1700103.
3. Two-dimensional scattering patterns of polymers in elongated polymer networks and composites
K. Hagita: Polymer, 147 (2018) 247-259.
4. Diffusion Behavior of Methanol Molecules Confined in Cross-Linked Phenolic Resins Studied Using Neutron Scattering and Molecular Dynamics Simulations
Y. Shudo, A. Izumi, K. Hagita, T. Yamada, K. Shibata and M. Shibayama: Macromolecules, 51 (2018) 6334-6343.
5. Multipoint segmental repulsive potential for entangled polymer simulations with dissipative particle dynamics
N. Iwaoka, K. Hagita and H. Takano: J. Chem. Phys., 149 (2018) 114901.
6. Two-dimensional scattering patterns and stress-strain relation of elongated clay nano composite

gels: Molecular dynamics simulation analysis
K. Hagita, Y. Shudo and M. Shibayama: Polymer, 154 (2018) 62-79.

7. Thinning Approximation for Calculating Two-Dimensional Scattering Patterns in Dissipative Particle Dynamics Simulations under Shear Flow
K. Hagita, T. Murashima and N. Iwaoka: Polymers, 10 (2018) 1224.
8. Structure formation of a quenched single polyethylene chain with different force fields in united atom molecular dynamics simulations
K. Hagita, S. Fujiwara and N. Iwaoka: AIP Advances, 8 (2018) 115108.
9. Molecular Dynamics Studies on Pressure-Induced Structural Change of Poly(4-methyl-1-pentene) Melts
K. Hagita and Y. Senda: J. Phys. Soc. Jpn., 87 (2018) 114803.
10. Elongational viscosity of weakly entangled polymer melt via coarse-grained molecular dynamics simulation
T. Murashima, K. Hagita and T. Kawakatsu: J. Soc. Rheol. Jpn. (Nihon Reoroji Gakkaishi), 46 (2018) 207-220.
11. Effect of diameter distribution on two-dimensional scattering patterns of a rubber model filled with carbon black and silica NPs
K. Hagita: Polymer, 160 (2019) 65-72.
12. Scattering Patterns and Stress-Strain Relations on Phase-separated ABA Block Copolymers under Uniaxial Elongating Simulations
K. Hagita, T. Tominaga, K. Akutagawa and H. Jinnai: Soft Matter, 15 (2019) 926-936.
13. Study of Commodity VR for Computational Material Sciences
K. Hagita, S. Matsumoto and K. Ohta: ACS Omega, 4 (2019) 3990-3999.
14. An Accelerated United-Atom Molecular Dynamics Simulation on the Fast Crystallization of Ring Polyethylene Melts
K. Hagita, S. Fujiwara and N. Iwaoka: J. Chem. Phys., 4 (2019) 3990-3999.
15. Two-dimensional scattering patterns of coarse-grained molecular dynamics model of filled polymer gels during uniaxial expansion
K. Hagita: Polymer, 166 (2019) 155-168.
16. Applications of aesthetic pentagon-shaped stereo tiling employing pentagraphene carbon - star walls and embossment design
K. Hagita, Y. Kawazoe and M. Ogino: AIP Advances, 9 (2019) 035001.
17. Nanovoids in Uniaxially Elongated Polymer Network Filled with Polydisperse Nanoparticles via Coarse-Grained Molecular Dynamics Simulation and Two-Dimensional Scattering Patterns
K. Hagita: Polymer, (2019) in press.

HAGIWARA, Satoshi [B class; 700 (B), 90 (C)] (149)
— *First-principles study on positron states in d0 ferromagnetics and at solid surfaces*

HAMADA, Ikutaro [C class; 4500 (B), 800 (C)] (86)
— *van der Waals density functional study of molecular adsorption on metal surfaces*

HAMAMOTO, Yuji [C class; 2000 (B), 0 (C)] (126)
— *van der Waals density functional study of organic-metal interfaces*

HARADA, KENJI [C class; 5000 (B), 0 (C)] (248)
— *Numerical study of phase transition in non-equilibrium systems*

1. Entropy governed by the absorbing state of directed percolation
Kenji Harada and Naoki Kawashima, arXiv:1902.10479.

HASHIMOTO, Tamotsu [C class; 3000 (B), 0 (C)] (262)
— *Molecular dynamics simulation of ferroelectrics using a shell model IV*

1. Structure of Amorphous $BaTiO_3$ by Molecular Dynamics Simulations Using a Shell Model
T. Hashimoto and H. Moriwake: submitted.

HASHMI, Arqum [C class; 1500 (B), 0 (C)] ()
— *Spin-valley polarization & quantum anomalous Hall conductivity in Transition metal dichalcogenides*

HATANO, Naomichi [B class; 0 (B), 90 (C)] ()
— *Fractality of the Anderson localization with binary randomness*

HATSUGAI, Yasuhiro [C class; 4000 (B), 750 (C)] (249)
— *Numerical studies of topological phases and bulk-edge correspondence*

1. Weyl points of mechanical diamond
   Y. Takahashi, T. Kariyado and Y. Hatsugai: Phys. Rev. B 99, 024102 (2019).
2. Z_N Berry Phases in Symmetry Protected Topological Phases
   Toshikaze Kariyado, Takahiro Morimoto, and Yasuhiro Hatsugai: Phys. Rev. Lett. 120, 247203 (1-5) (2018).
3. Fractional Quantum Hall Effect in n = 0 Landau Band of Graphene with Chern Number Matrix
   K. Kudo and Y. Hatsugai: J. Phys. Soc. Jpn. 87, 063701 (1-5) (2018).
4. Many-Body Chern Number without Integration
   Koji Kudo, Haruki Watanabe, Toshikaze Kariyado, and Yasuhiro Hatsugai: Phys. Rev. Lett. 122, 146601 (1-5) (2019), (Editors' Suggestion).
5. Phase diagram of a disordered higher-order topological insulator: A machine learning study
   H. Araki, T. Mizoguchi and Y. Hatsugai: Phys. Rev. B 99, 085406 (1-8) (2018).
6. Symmetry-protected exceptional rings in two-dimensional correlated systems with chiral symmetry
   Tsuneya Yoshida, Robert Peters, Norio Kawakami, and Yasuhiro Hatsugai: Phys. Rev. B 99, 121101(R)(1-5) (2019).

HATTORI, Ken [C class; 3000 (B), 650 (C)] (110)
— *Atomic structure and electronic states for Si surfaces with adsorbates*

HAYAMI, Satoru [C class; 6000 (B), 0 (C)] (183)
— *Effect of magnetic anisotropy on skyrmion crystal in the Kondo lattice model*

1. Néel- and Bloch-Type Magnetic Vortices in Rashba Metals
   S. Hayami and Y. Motome: Phys. Rev. Lett. **121**, 137202 (2018).
2. Classification of atomic-scale multipoles under crystallographic point groups and application to linear response tensors
   S. Hayami, M. Yatsushiro, Y. Yanagi, and H. Kusunose: Phys. Rev. B **98** (2018) 165110.
3. Effect of magnetic anisotropy on Skyrmions with a high topological number in itinerant magnets
   S. Hayami and Y. Motome: Phys. Rev. B **99**, 094420 (2019).
4. Multiple-Q Magnetic States in Spin-Orbit Coupled Metals
   S. Hayami and Y. Motome: IEEE Trans. Magn. **55**, 1500107 (2018).

HIDA, Kazuo [B class; 300 (B), 90 (C)] (308)
— *Numerical Study of One Dimensional Frustrated Quantum Spin Systems*

HIGUCHI, Yuji [C class; 4500 (B), 0 (C)] (251)
— *Assembly process and mechanical properties of crystalline polymers by large-scale coarse-grained molecular dynamics simulation*

HINOKIHARA, Taichi [C class; 4000 (B), 0 (C)] (258)
— *Construction of coarse-graining spin model and analysis of the coercivity*

HINUMA, Yoyo [B class; 600 (B), 80 (C)] (154)
— *Calculation of oxide surface properties for catalyst informatics*

1. Density Functional Theory Calculations of Oxygen Vacancy Formation and Subsequent Molecular Adsorption on Oxide Surfaces
   Y. Hinuma, T. Toyao, T. Kamachi, Z. Maeno, S. Takakusagi, S. Furukawa, I. Takigawa, and K. Shimizu: J. Phys. Chem. C, **122** (2018) 29435.

2. Effects of composition, crystal structure, and surface orientation on band alignment of divalent metal oxides: A first-principles study
   Y. Hinuma, Y. Kumagai, and I. Tanaka, F Oba: Phys. Rev. Mater., **2** (2018) 124603.
3. Temperature coefficient of redox potential of LixFePO4
   Y. Fukuzumi, Y. Hinuma, and Y. Moritomo: AIP Advances, **8** (2018) 065021.

HIRATSUKA, Masaki [B class; 1300 (B), 170 (C)] ()
— *ab initio calculations to determine the phase equilibrium conditions of TBAB semiclathrate hydrates*
— *ab initio molecular dynamics study on the vibrational spectra of semi-clathrate hydrates*

HIYAMA, Miyabi [B class; 600 (B), 80 (C)] (153)
— *Elucidation of electronic states for caged compounds in aqueous solution*

HOSHI, Takeo [C class; 5000 (B), 850 (C)] (80)
— *Large-scale device-material research by massively parallel electronic structure calculation and data-driven science*

1. Solution of the k-th eigenvalue problem in large-scale electronic structure calculations
   Dongjin Lee, Takeo Hoshi, Tomohiro Sogabe, Yuto Miyatake, Shao-Liang Zhang, submitted; Preprint (arXiv.1710.05134)

HOSHINO, Shintaro [C class; 2500 (B), 0 (C)] (192)
— *Numerical approach to unconventional electronic orderings in strongly correlated systems*

1. Spontaneously orbital selective superconductivity in a three-orbital Hubbard model
   K. Ishigaki, J. Nasu, A. Koga, S. Hoshino and P. Werner: Phys. Rev. 98, 235120 (2018)a
2. Staggered ordered phases in the three-orbital Hubbard model
   K. Ishigaki, J. Nasu, A. Koga, S. Hoshino and P. Werner: Phys. Rev. 99, 085131 (2019)a
3. Unconventional orbital ordering and emergent dimensional reduction in fulleride superconductors
   S. Hoshino, P. Werner and R. Arita, arXiv:1902.09053 (2019)
4. Nature of superconducting fluctuation in photo-excited systems
   R. Iwazaki, N. Tsuji and S. Hoshino, arXiv:1904.05820 (2019)
5. Unconventional full-gap superconductivity in Kondo lattice with semi-metallic conduction bands
   S. Iimura, M. Hirayama and S. Hoshino, arXiv:1904.06240 (2019)

HOTTA, Chisa [D class; 2000 (B), 0 (C)] (195)
— *Study on the bond random transverse Ising model*

HOTTA, Takashi [C class; 5500 (B), 0 (C)] (187)
— *Multi-channel Kondo Effect in Rare-Earth Systems*

1. Impurity Effects in Nodal Extended s- and Nodeless d-Wave Superconductors: Gap Symmetry of BiS_2-Based Layered Superconductors
   Akihiro Ichikawa and Takashi Hotta, J. Phys. Soc. Jpn. **87**, 114706 (2018).
2. Microscopic Theory of Γ_3 Quadrupole Ordering in Pr Compounds on the Basis of a j-j Coupling Scheme
   Ryosuke Yamamura and Takashi Hotta, J. Phys. Soc. Jpn. **88**, 034715 (2019).

HUKUSHIMA, Koji [C class; 6500 (B), 0 (C)] (228)
— *Data-driven science for material science*
— *Statistical-mechanical study for chiral magnets*

1. Phase transitions in quantum annealing of an NP-hard problem detected by fidelity susceptibility
   J Takahashi, K Hukushima: Journal of Statistical Mechanics: Theory and Experiment (2019) 043102a
2. Solid-liquid transition of skyrmions in a two-dimensional chiral magnet
   Y Nishikawa, K Hukushima, W Krauth: Physical Review B **99** (2019) 064435/1-10
3. Power-law decay in the nonadiabatic photodissociation dynamics of alkali halides due to quantum wavepacket interference

Y Mizuno, K Hukushima: J. Chem. Phys. **149** (2018) 174313/1-6

4. Data-driven diagnosis for compressed sensing with cross validation
   Y Nakanishi-Ohno, K Hukushima: Physical Review E **98** (2018) 052120/1-6

IGARASHI, Ryo [C class; 500 (B), 150 (C)] ()

— *Full diagonalization using low-rank approximation to Hamiltonian matrices and its application to quantum spin models*

IKEDA, Hiroaki [B class; 1100 (B), 70 (C)] (142)

— *Development of the first-principles approach and analysis of superconductivity*

— *Electronic structure and superconductivity based on a first-principles approach*

IKUHARA, Yuichi [C class; 6000 (B), 0 (C)] (79)

— *Ab initio study on atomic and electronic structure of functional materials*

— *Atomic structure and properties of functional materials*

1. Ceramic phases with one-dimensional long-range order
   D. Yin, C. Chen, M. Saito, K. Inoue, Y. Ikuhara: Nat. Mat. **18** (2019) 19-23.
2. Atomic-scale valence state distribution inside ultrafine CeO_2 nanocubes and its size dependence
   X. Hao, A. Yoko, C. Chen, K. Inoue, M. Saito, G. Seong, S. Takami, T. Adschiri, Y. Ikuhara: SMALL **14** (2018) 1802915.

IMADA, Masatoshi [D,E class; 52000 (B), 6700 (C)] (168,171)

— *Highly accurate analysis of an effective Hamiltonian for high Tc cuprates by the many-variable variational Monte Carlo method combined with tensor network*

— *Mechanism of pseudogap and superconductivity with low-energy fermionic excitations in high-Tc cuprates*

— *Study on frustrated quantum spin systems using machine-learning solvers*

1. Competition among various charge-inhomogeneous states and d-wave superconducting state in Hubbard models on square lattices
   Kota Ido, Takahiro Ohgoe, and Masatoshi Imada: Phys. Rev. B **97** (2018) 045138.
2. Quantum spin liquid signatures in Kitaev-like frustrated magnets
   Matthias Gohlke, Gideon Wachtel, Youhei Yamaji, Frank Pollmann, and Yong Baek Kim: Phys. Rev. B **97**, (2018) 075126.
3. Ab initio effective Hamiltonians for cuprate superconductors
   Motoaki Hirayama, Youhei Yamaji, Takahiro Misawa, and Masatoshi Imada: Phys. Rev. B. **98** (2018) 134501.
4. Direct connection between Mott insulators and d-wave high-temperature superconductors revealed by continuous evolution of self-energy poles
   Shiro Sakai, Marcello Civelli, and Masatoshi Imada : Phys. Rev. B.**98** (2018) 195109
5. Stripe and superconducting order competing in the Hubbard model on a square lattice studied by a combined variational Monte Carlo and tensor network method
   Andrew S. Darmawan, Yusuke Nomura, Youhei Yamaji, and Masatoshi Imada: Phys. Rev. B 98,**98** (2018) 205132.
6. Resummation of diagrammatic series with zero convergence radius for strongly correlated fermions
   Riccardo Rossi, Takahiro Ohgoe, Kris Van Houcke, and Felix Werner: Phys. Rev. Lett. **121** (2018) 130405.
7. Contact and Momentum distribution of the Unitary Fermi Gas
   Riccardo Rossi, Takahiro Ohgoe, Kris Van Houcke, and Felix Werner: Phys. Rev. Lett. **121** (2018) 130406.
8. mVMC-Open-source software for many-variable variational Monte Carlo method
   Takahiro Misawa, Satoshi Morita, Kazuyoshi Yoshimi, Mitsuaki Kawamura, Yuichi Motoyama, Kota Ido, Takahiro Ohgoe, Masatoshi Imada, Takeo Kato: Compt. Phys. Commun.,**235** (2019) 447.
9. Excitons and Dark Fermions as Origins of Mott Gap, Pseudogap and Superconductivity in Cuprate Superconductors — General Idea and Basic Concept Based on Gap Physics

Takafumi J. Suzuki, Masatoshi Imada: J. Phys. Soc. Jpn. **88** (2019) 024701.

INAGAKI, Kouji [C class; 4000 (B), 400 (C)] (166)
— *First-principles meta-dynamics analysis of Catalyst Referred Etching method -Analysis of surface roughness formed by etching-*

1. Platinum-catalyzed hydrolysis etching of SiC in water: A density functional theory study
   P. V. Bui, D. Toh, A. Isohashi, S. Matsuyama, K. Inagaki, Y. Sano, K. Yamauchi, and Y. Morikawa: Jpn. J. Appl. Phys. **57** (2018) 055703.

INAOKA, Takeshi [C class; 500 (B), 150 (C)] (155)
— *Search and realization of novel electronic properties of solid surfaces and interfaces and of small particles*

1. Vibration-induced structures in scanning tunneling microscope light emission spectra of Ni(110)-(2x1)O
   Y. Uehara, T. Inaoka, T. Nishio, and S. Katano: J. Appl. Phys. **123** (2018) 224302 (8 pages).

ISHIBASHI, Shoji [C class; 4000 (B), 0 (C)] (104)
— *Prediction of properties of organic ferroelectrics and piezoelectrics by first-principles calculation*

1. Computational findings of metastable ferroelectric phases of squaric acid
   S. Ishibashi, S. Horiuchi, and R. Kumai: **97** (2018) 184102.

ISHIDA, Kunio [B class; 1300 (B), 90 (C)] (280)
— *Ultrafast nonadiabatic dynamics of electron-phonon-photon system*
— *Ultrafast nonadiabatic dynamics of electron-phonon-photon systems*

1. Interplay of electron-phonon nonadiabaticity and Raman scattering in the wavepacket dynamics of electron-phonon-photon systems
   Kunio Ishida: Eur. Phys. J. D, doi:10.1140/epjd/e2019-09485-5

ISHIHARA, Sumio [B class; 1600 (B), 0 (C)] (196)
— *Complexed quantum dynamics in strongly interacting systems*
— *Opto-spintronics in correlated magnets*

1. Photocontrol of magnetic structure in an itinerant magnet
   Atsushi Ono and Sumio Ishihara: Phys. Rev. B **98**, 214408 (2018).
2. Photoinduced topological spin texture in a metallic ferromagnet
   Atsushi Ono and Sumio Ishihara: J. Phys. Soc. Jpn. **88**, 023703 (2019).
3. Photoinduced collective mode, inhomogeneity, and melting in a charge-order system
   Hitoshi Seo, Yasuhiro Tanaka, and Sumio Ishihara: Phys. Rev. B **98**, 235150 (2018).
4. Quantum Paramagnet Near Spin-State Transition
   K. Tomiyasu, N. Ito, R. Okazaki, Y. Takahashi, M. Onodera, K. Iwasa, T. Nojima, T. Aoyama, K. Ohgushi, Y. Ishikawa, T. Kamiyama, S. Ohira-Kawamura, M. Kofu, and S. Ishihara: Advanced Quantum Technologies, 1800057 (2018).
5. Probing ultrafast spin-relaxation and precession dynamics in a cuprate Mott insulator with seven-femtosecond optical pulses
   T. Miyamoto, Y. Matsui, T. Terashige, T. Morimoto, N. Sono, H. Yada, S. Ishihara, Y. Watanabe, S. Adachi, T. Ito, K. Oka, A. Sawa, and H. Okamoto: Nature Communications **9**, 3948 (2018).

ISHII, Fumiyuki [C class; 13500 (B), 0 (C)] (27)
— *First-principles study of spin conversion materials*
— *First-principles study of topological thermoelectric materials*

1. Clear variation of spin splitting by changing electron distribution at non-magnetic metal/Bi_2O_3 interfaces
   H. Tsai, S. Karube, K. Kondou, N. Yamaguchi, F. Ishii, Y. Otani: Sci. Rep. **8** (2018) 5564.
2. Strong Rashba effect in the localized impurity states of halogen-doped monolayer $PtSe_2$
   M. A. U. Absor, I. Santoso, Harsojo, K. Abraha, H. Kotaka, F. Ishii, and M. Saito: Phys. Rev. B **97**, (2018) 205138.

3. First-principles study on thermoelectric properties of half-Heusler compounds CoMSb(M=Sc, Ti, V, Cr, and Mn)
   S. Minami, F. Ishii, Y. P. Mizuta, and M. Saito: Appl. Phys. Lett. **113** (2018) 032403.
4. First-principles Study of Rashba Spin Splitting at Strained SrTiO3(001) Surfaces
   N. Yamaguchi and F. Ishii: e-J. Surf. Sci. Nanotechnol. **16** (2018) 360.
5. Implementation of Generalized Bloch Theorem Using Linear Combination of Pseudo-Atomic Orbitals
   T. B. Prayitno and F. Ishii: J. Phys. Soc. Jpn. **87** (2018) 114709.
6. Large Anomalous Nernst Coefficient in an oxide Skyrmion Crystal Chern Insulator
   Y. P. Mizuta, H. Sawahata, and F. Ishii: Phys. Rev. B **98** (2018) 205125.
7. Electric field dependence of topological edge states in one-bilayer Bi(111) : A first-principles study
   H. Sawahata, N. Yamaguchi, H. Kotaka, and F. Ishii : e-J. Surf. Sci. Nanotechnol. **16** (2018) 427.
8. Anisotropic thermoelectric effect on phosphorene and bismuthene: first-principles calculations based on nonequilibrium Green's function theory
   Y. Tanaka, M. Saito, and F. Ishii: Jpn. J. App. Phys. **57** (2018) 125201.
9. First-principles design of the spinel iridate Ir_2O_4 for high-temperature quantum spin ice
   S. Onoda and F. Ishii: Phys. Rev. Lett. **122** (2019) 067201.
10. Doping-induced persistent spin helix with a large spin splitting in monolayer SnSe
    M.A.U. Absor and F. Ishii: Phys. Rev. B. **99** (2019) 075136.
11. First-principles Study of Spin-wave Excitations of 3d Transition Metals with Linear Combination of Pseudo-atomic Orbitals
    T.B. Prayitno and F. Ishii: J. Phys. Soc. Jpn. **88** (2019) 054701.

ISHIZUKA, Ryosuke [E class; 12000 (B), 1950 (C)] ()
— *Seeking of catalytic reaction with the MD/order-N DFT self-consistent scheme*

ISOBE, Masaharu [B class; 700 (B), 0 (C)] (295)
— *Nonequilibrium phase transition and slow dynamics in the dense hard sphere systems*
1. 粉体乱流ーマクロとミクロをつなぐ架け橋へ
   礒部雅晴，齊藤国靖：日本物理学会誌, **73** (2018) 469-474.

IYODA, Eiki [C class; 2500 (B), 0 (C)] (267)
— *Numerical study of eigenstate thermalization hypothesis in phase transition*

JESCHKE, Harald [C class; 6500 (B), 0 (C)] (226)
— *Doping effect on electronic structure and superconductivity in two-dimensional layered materials*
— *Effects of pressure in iron chalcogenide superconductors*
1. Two-dome superconductivity in FeS induced by a Lifshitz transition
   M. Shimizu, N. Takemori, D. Guterding, H. O. Jeschke: Phys. Rev. Lett. **121**, 137001 (2018)
2. Quantum and classical phases of the pyrochlore Heisenberg model with competing interactions
   Y. Iqbal, T. Mller, P. Ghosh, M. J. P. Gingras, H. O. Jeschke, S. Rachel, J. Reuther, R. Thomale: Phys. Rev. X **9**, 011005 (2019)

KAGESHIMA, Hiroyuki [C class; 1500 (B), 0 (C)] (136)
— *Study on physical properties of structural elementary excitations of semiconductor surfaces and interfaces*
1. Oxygen concentration dependence of silicon oxide dynamical properties
   Yuji Yajima, Kenji Shiraishi, Tetsuo Endoh, and Hiroyuki Kageshima: Jpn. J. Appl. Phys. **57** (2018) 06KD01.
2. First-principles Study on Charged Vacancies in MoS_2
   S. Urasaki and H. Kageshima, Jpn. J. Appl. Phys. **57** (2018) 125202.

KAMACHI, Takashi [B class; 600 (B), 80 (C)] ()
— *Database construction for activation and reaction of small molecules on solid surfaces*

KARIYADO, Toshikaze [B class; 600 (B), 90 (C)] (300)

— Realization and Manipulation of Topological States by Nanostructures

1. Z_N Berry Phases in Symmetry Protected Topological Phases
   T. Kariyado, T. Morimoto, and Y. Hatsugai: Phys. Rev. Lett. **120** (2018) 247202.
2. Counterpropagating topological interface states in graphene patchwork structures with regular arrays of nanoholes
   T. Kariyado, Y.-C. Jiang, H. Yang, and X. Hu: Phys. Rev. B **98** (2018) 195416.
3. Weyl points of mechanical diamond
   Y. Takahashi, T. Kariyado, and Y. Hatsugai: Phys. Rev. B **99** (2019) 024102.

KASAMATSU, Shusuke [C class; 6000 (B), 950 (C)] (69)

— Development of Structure/Property Prediction Framework Based on Replica Exchange Method Combined with Ab Initio Calculations

1. Direct coupling of first-principles calculations with replica exchange Monte Carlo sampling of ion disorder in solids
   S. Kasamatsu and O. Sugino: J. Phys.: Condens. Matter **31** (2019) 085901.

KATO, Takeo [D class; 1000 (B), 0 (C)] (287)

— Transport properties of one-dimensional interacting electron systems by a quantum Monte Carlo method

KAWAKAMI, Norio [C class; 11500 (B), 1900 (C)] (177)

— Study of magnetism, topological phase formation, and response to external fields in strongly correlated quantum systems

— Study of response to external fields and topological phenomena in strongly correlated quantum systems

1. Quantum oscillations in strongly correlated topological Kondo insulators
   Robert Peters, Tsuneya Yoshida, and Norio Kawakami: arXiv:1901.05099
2. Impact of the Rashba Spin Orbit Coupling on f-electron Materials
   Yoshihiro Michishita and Robert Peters: arXiv:1812.10888
3. Interplay between charge, magnetic, and superconducting order in a Kondo lattice with attractive Hubbard interaction
   Benedikt Lechtenberg, Robert Peters, and Norio Kawakami: Phys. Rev. B **98** (2018) 195111.
4. Breakdown of topological Thouless pumping in the strongly interacting regime
   Masaya Nakagawa, Tsuneya Yoshida, Robert Peters, and Norio Kawakami: Phys. Rev. B **98** (2018) 115147.
5. Magnetic states in a three-dimensional topological Kondo insulator
   Robert Peters, Tsuneya Yoshida, and Norio Kawakami: Phys. Rev. B **98** (2018) 075104.
6. Non-Hermitian perspective of the band structure in heavy-fermion systems
   Tsuneya Yoshida, Robert Peters, and Norio Kawakami: Phys. Rev. B **98** (2018) 035141.
7. Topological properties of magnetically ordered heavy-fermion systems in the presence of mirror symmetry
   Kazuhiro Kimura, Tsuneya Yoshida, and Norio Kawakami: J. Phys. Soc. Jpn. **87** (2018) 084705.
8. Reduction of topological Z classification in cold-atom systems
   Tsuneya Yoshida, Ippei Danshita, Robert Peters, and Norio Kawakami: Phys. Rev. Lett. **121** (2018) 025301.
9. Equilibrium and real-time properties of the spin correlation function in the two-impurity Kondo model
   Benedikt Lechtenberg and Frithjof B. Anders: Phys. Rev. B **98** (2018) 035109.
10. Chaotic-integrable transition in the Sachdev-Ye-Kitaev model
    Antonio M. Garcia-Garcia, Bruno Loureiro, Aurelio Romero-Bermudez, and Masaki Tezuka: Phys. Rev. Lett **120** (2018) 241603.

KAWAMURA, Hikaru [B,C,E class; 24000 (B), 0 (C)] (207,208)
— *Novel order in frustrated magnets*
— *Numerical simulations on statistical models of earthquakes*

1. Slow-slip phenomena represented by the one-dimensional Burridge-Knopoff model of earthquakes
   H. Kawamura, M. Yamamoto and Y. Ueda: J. Phys. Soc. Jpn. **87**, (2018) 053001.
2. Randomness-induced quantum spin liquid behavior in the $s = 1/2$ random $J_1 - J_2$ Heisenberg antiferromagnet on the square lattice
   K. Uematsu and H. Kawamura: Phys. Rev. B **98**, (2018) 134427.
3. Nature of the high-speed rupture of the two-dimensional Burridge-Knopoff model of earthquakes
   H. Kawamura, K. Yoshimura, and S. Kakui: Phil. Trans. R. Soc. A **377** (2018) 20170391.
4. Spin ordering induced by lattice distortions in classical Heisenberg antiferromagnets on the breathing pyrochlore lattice
   K. Aoyama and H. Kawamura: Phys. Rev. B **99**, (2019) 1444062.

KAWASHIMA, Naoki [E class; 46000 (B), 6000 (C)] (204,337)
— *Tensornetwork Method and Its Application to Non-Magnetic States*

1. A series of magnon crystals appearing under ultrahigh magnetic fields in a kagome antiferromagnet
   R. Okuma, D. Nakamura, T. Okubo, A. Miyake, A. Matsuo, K. Kindo, M. Tokunaga, N. Kawashima, S. Takeyama and Z. Hiroi: Nature Communications **10**, 1229/1-7 (2019).
2. Calculation of higher-order moments by higher-order tensor renormalization group
   Satoshi Morita, Naoki Kawashima: Computer Physics Communications **236**, 65-71 (2019)
3. Detecting signals of weakly first-order phase transitions in two-dimensional Potts models
   Shumpei Iino, Satoshi Morita, Anders W. Sandvik, and Naoki Kawashima: J. Phys. Soc. Jpn. **88**, 034006/1-8 (2019).
4. Spin-one bilinear-biquadratic model on a star lattice
   Hyun-Yong Lee, and Naoki Kawashima: Phys. Rev. B **97**, 205123/1-7 (2018).
5. Spin Thermal Hall Conductivity of a Kagome Antiferromagnet
   Hayato Doki, Masatoshi Akazawa, Hyun-Yong Lee, Jung Hoon Han, Kaori Sugii, Masaaki Shimozawa, Naoki Kawashima, Migaku Oda, Hiroyuki Yoshida, and Minoru Yamashita: Phys. Rev. Lett. **121**, 097203/1-4 (2018).
6. Fast algorithm for generating random bit strings and multispin coding for directed percolation
   Hiroshi Watanabe, Satoshi Morita, Synge Todo, and Naoki Kawashima: J. Phys. Soc. Jpn. **88**, 024004 (2019).

KITA, Takafumi [C class; 5500 (B), 0 (C)] (242,244)
— *Analysis of many-body effects in Bose-Einstein condensate*
— *Microscopic calculation of the flux-flow Hall effect baed on the augmented quasiclassical equations*

1. Charging in a Superconducting Vortex Due to the Three Force Terms in Augmented Eilenberger Equations
   Hikaru Ueki, Marie Ohuchi, and Takafumi Kita: J. Phys. Soc. Jpn. **87** (2018) 044704.
2. A Variational Approach to Many-Body Problems Incorporating Many-Body Effects at Finite Temperature
   Akimitsu Kirikoshi, Wataru Kohno, and Takafumi Kita: J. Phys. Soc. Jpn., in press.

KITAO, Akio [C class; 5500 (B), 900 (C)] (235)
— *Efficient sampling simulation of the soft modes significantly contribute to protein properties*

1. Dissociation Process of a MDM2/p53 Complex Investigated by Parallel Cascade Selection Molecular Dynamics and the Markov State Model
   D.P. Duy and A. Kitao: J. Phys. Chem. B, **123** (2019) 2469.
2. Refining evERdock: Improved selection of good protein-protein complex models achieved by MD optimization and use of multiple conformations
   A. Shinobu, K. Takemura, N. Matubayasi, and A Kitao: J. Chem. Phys., **149** (2018) 195101.
3. Similarities and Differences between Thymine (6–4) Thymine/Cytosine DNA Lesion Repairs by Photolyases
   H.M. Dokainish and A. Kitao: J. Phys. Chem. B, **122** (2018) 8537.

4. ColDock: Concentrated Ligand Docking with All-Atom Molecular Dynamics Simulation
K. Takemura, C. Sato, and A. Kitao: J. Phys. Chem. B, **122** (2018) 7191.

KOBAYASHI, Katsuyoshi [B class; 400 (B), 50 (C)] (163)
— *Study on electronic properties in new nanoscale surfaces and interfaces*

KOBAYASHI, Nobuhiko [C class; 4500 (B), 800 (C)] (84)
— *First-principles study of quantum transport in nanostructures*

1. Theory of electron transport at the atomistic level
N. Kobayashi, H. Ishii, K. Hirose: Jpn. J. Appl. Phys. 57, 08NA01 (2018).
2. Computational Study on Atomic Structures, Electronic Properties, and Chemical Reactions at Surfaces and Interfaces and in Biomaterials
Y. Takano, N. Kobayashi, Y. Morikawa: J. Phys. Soc. Jpn. 87, 061013 (2018).
3. Quantitative mobility evaluation of organic semiconductors using quantum dynamics based on density functional theory
H. Ishii, J. Inoue, N. Kobayashi, K. Hirose: Phys. Rev. B 98, 235422 (2018).
4. Surface Structure of Organic Semiconductor [n]Phenacene Single Crystals
Y. Wakabayashi, M. Nakamura, K. Sasaki, T. Maeda, Y. Kishi, H. Ishii, N. Kobayashi, S. Yanagisawa, Y. Shimo, Y. Kubozono: J. Am. Chem. Soc. 140, 14046 (2018).
5. Operando Direct Observation of Charge Accumulation and the Correlation with Performance Deterioration in PTB7 Polymer Solar Cells
T. Kubodera, M. Yabusaki, V. Rachmat, Y. Cho, T. Yamanari, Y. Yoshida, N. Kobayashi, K. Marumoto: ACS Appl. Mater. Interfaces 10, 26434 (2018).
6. Theory of Electrical Conduction
N. Kobayashi, H. Ishii, K. Hirose: 3D Local Structure and Functionality Design of Materials eds H. Daimon, Y. C. Sasaki (World Scientific, 2018) p133.

KOGA, Akihisa [C class; 8000 (B), 1450 (C)] (180)
— *Competition between superconductivity and orbital order emerging in strongly correlated electron systems*
— *Stability of magnetic phases in strongly correlated electron systems with various electron filling*

1. Quantum and classical behavior of spin-S Kitaev models in an anisotropic limit
T. Minakawa, J. Nasu, and A. Koga, Phys. Rev. B 99, 104408/1-8 (2019)
2. Staggered ordered phases in the three-orbital Hubbard model
K. Ishigaki, J. Nasu, A. Koga, S. Hoshino, and P. Werner, Phys. Rev. B 99, 085131/1-11 (2019)
3. Symmetry breaking states in the half-filled two-orbital Hubbard model with crystalline electric field
K. Ishigaki, J. Nasu, and A. Koga, J. Phys. Soc. Jpn. 88, 024702/1-5 (2019)
4. Spontaneously orbital-selective superconductivity in a three-orbital Hubbard model
K. Ishigaki, J. Nasu, A. Koga, S. Hoshino, and P. Werner, Phys. Rev. B 98, 235120/1-7 (2018)
5. Incipient and well-developed entropy plateaus in spin-S Kitaev models
J. Oitmaa, A. Koga, and R. R. P. Singh, Phys. Rev. B 98, 214404/1-6 (2018)
6. Successive Majorana Topological Transitions Driven by a Magnetic Field in the Kitaev Model
J. Nasu, Y. Kato, Y. Kamiya, and Y. Motome, Phys. Rev. B 98, 060416/1-6 (2018)
7. Majorana quantization and half-integer thermal quantum Hall effect in a Kitaev spin liquid
Y. Kasahara, T. Ohnishi, Y. Mizukami, O. Tanaka, Sixiao Ma, K. Sugii, N. Kurita, H. Tanaka, J. Nasu, Y. Motome, T. Shibauchi, and Y. Matsuda, Nature 559, 227-231 (2018)
8. Unusual Thermal Hall Effect in a Kitaev Spin Liquid Candidate α-RuCl3
Y. Kasahara, K. Sugii, T. Ohnishi, M. Shimozawa, M. Yamashita, N. Kurita, H. Tanaka, J. Nasu, Y. Motome, T. Shibauchi, and Y. Matsuda, Phys. Rev. Lett. 120, 217205/1-6 (2018)
9. Magnetoelectric Effect in a Spin-State Transition System
M. Naka, E. Mizoguchi, J. Nasu, and S. Ishihara, J. Phys. Soc. Jpn. 87, 063709/1-5 (2018)
10. Ground-state and thermodynamic properties of an S=1 Kitaev model
A. Koga, H. Tomishige, and J. Nasu, J. Phys. Soc. Jpn. 87, 063703 (2018)

KOMATSU, Yu [B class; 600 (B), 90 (C)] (298)
— *Constructing the database of exited states for desigining photosynthetic pigments to absorb the longer wavelength radiation*

KOURA, Akihide [C class; 4000 (B), 0 (C)] (103)
— *Ab initio molecular dynamics study of static structure of glasses*
1. Peculiar atomic dynamics in liquid GeTe with asymmetrical bonding: Observation by inelastic x-ray scattering
   M. Inui, A. Koura, Y. Kajihara, S. Hosokawa, A. Chiba, K. Kimura, F. Shimojo, S. Tsutsui, and A. Q. R. Baron: Phys. Rev. B **97**, (2018) 174203.
2. Static Structure of Liquid GeSe Under Pressure: *Ab Initio* Molecular Dynamics Simulations
   A. Koura and F. Shimojo: Phys. Status Solidi B **255** (2018) 1800103.
3. Electronic structures and impurity cluster features in Mg-Zn-Y alloys with a synchronized long-period stacking ordered phase
   S. Hosokawa, K. Maruyama, K. Kobayashi, J. R. Stellhorn, B. Paulus, A. Koura, F. Shimojo, T. Tsumuraya, M. Yamasaki, Y. Kawamura, S. Yoshioka, and H. Sato: J. Alloys Compd. **762** (2018) 797.

KUNISADA, Yuji [C class; 10500 (B), 0 (C)] (55)
— *Reduction of Rare Metals in Formic Acid Decomposition Catalysts and Oxygen Storage Materials*
1. Sr Substitution Effects on Atomic and Local Electronic Structure of $Ca_2AlMnO_{5+\delta}$
   Y. Kunisada, G. Saito, K. Hayami, T. Nomura, N. Sakaguchi: Surf. Inter. Anal. **51** (2019) 65.
2. Interaction of Localized Surface Plasmons of a Silver Nanosphere Dimer Embedded in a Uniform Medium: STEM-EELS and DDA Simulation
   N. Sakaguchi, S. Matsumoto, Y. Kunisada, M. Ueda: J. Phys. Chem. C **123** (2019) 6735.

KUROKI, Kazuhiko [C class; 11500 (B), 1800 (C)] (179)
— *First principles and model study of electron correlation and superconductivity in multiband systems*
— *Numerical study on unconventional superconductivity in bilayer strongly correlated systems*
1. Effective interaction for vanadium oxyhydrides $Sr_{n+1}V_nO_{2n+1}H_n$ ($n = 1$ and $n \to \infty$): A constrained-RPA study
   M. Ochi, K. Kuroki: Phys. Rev. B. **99** (2019) 155143.

KUSAKABE, Koichi [C class; 3000 (B), 0 (C)] (124)
— *Theoretical analysis of dynamical effects of nanographene*
1. Edge States Caused by Shift of Dirac Points at the Armchair Edge of Distorted nanographene
   K. Kusakabe, K. Nishiguchi, S. Teranishi, Y. Wicaksono: J. Phys. Soc. Jpn. **87** (2018) 084716.
2. Tunable induced magnetic moment and in-planeconductance of graphene in Ni/Graphene/Ni nano spin-valve like structure: a first principles study
   Y. Wicaksono, S. Teranishi, K. Nishiguchi, K. Kusakabe: CARBON **143** (2018) 828.
3. Supercondictivity arising from layer- differen- tiation in multi-layer cuprates with inter-layer effects
   K. Nishiguchi, S. Teranishi, K. Kusakabe, H. Aoki: Phys. Rev. B **98** (2018) 174508.
4. Material-dependent screening of Coulomb interaction in single-layer cuprates
   S. Teranishi, K. Nishiguchi, K. Kusakabe: J. Phys. Soc. Jpn. **87** (2018) 114701.
5. ナノグラファイトの構造と電子状態の関係：トポロジカル物性の予測
   草部浩一: ニューダイヤモンド **35** (2018) 38.

MACHIDA, Manabu [B class; 600 (B), 0 (C)] ()
— *Optical properties of random media*

MAKINO, Takayuki [B,C class; 1000 (B), 420 (C)] (138)
— *Study on electronic structures in Yb2O3 crystals*
— *Study on optical transition and density of states in Yb2O3*
1. Temperature Dependent Localization Dynamics of Excitons in MgZnO Alloyed Semiconductor
   Md. Sherajul Islam, Md. Soyaeb Hasan, E. Kobayashi, T. Makino: Physica B 558, 127 (2019)

MAO, Wei [C class; 4000 (B), 750 (C)] ()
— *First-principles calculation of microscopic behaviors of hydrogen in metal oxides for tritium permeation barrier*

MASAKI-KATO, Akiko [C class; 6000 (B), 950 (C)] ()
— *Study of excitation dynamics of Heisenberg models*

MATSUDA, Yasuhiro [B class; 500 (B), 70 (C)] (304)
— *Estimation of the density of states using Maximum entropy method and Sparse modeling*

MATSUKAWA, Hiroshi [C class; 2000 (B), 550 (C)] ()
— *Physics of Friction*

MATSUMOTO, Munehisa [C class; 11000 (B), 1350 (C)] (233)
— *Bridging space-time scales via coarse grained Green's function and reverse Monte Carlo between microscopic electronic structure and macroscopic observation*
— *Integration of ab initio data of microscopic electronic structure and experimental data of mesoscopic domain structure for ferromagnetic f-d intermetallics*

1. First-principles calculations of the magnetocrystalline anisotropy of the prototype 2:17 cell boundary phase $Y(Co_{1-x-y}Fe_xCu_y)_5$
   Christopher E. Patrick, Munehisa Matsumoto, Julie B. Staunton: Journal of Magnetism and Magnetic Materials 477 (2019) 147.
2. Calculated Curie temperatures for rare-earth permanent magnets: *ab initio* inspection on localized magnetic moments in *d*-electron ferromagnetism
   preprint (arXiv: 1812.04842)
3. Site preference of dopant elements in $Nd_2Fe_{14}B$
   Munehisa Matsumoto: preprint (arXiv: 1812.10945)
4. Navigating the trends in the proximity to magnetic quantum critical point and superconductivity for Ce-based heavy-fermion compounds
   Munehisa Matsumoto: preprint (arXiv: 1812.11502)
5. Optimal uni-axial ferromagnetism in (La,Ce)2Fe14B for permanent magnets
   Munehisa Matsumoto, Masaaki Ito, Noritsugu Sakuma, Masao Yano, Tetsuya Shoji, Hisazumi Akai: preprint (arXiv: 1901.10119)
6. Anisotropic ferromagnetism and structure stability in $4f$-$3d$ intermetallics: *ab initio* structure optimization and magnetic anisotropy for RCo_5 (R=Ce, La, and Y)
   Munehisa Matsumoto: preprint (arXiv: 1901.11498)
7. Electronic Structure Calculations of $CeRh_3B_2$
   Shotaro Doi and Munehisa Matsumoto: preprint (arXiv: 1903.08480)

MATSUNAKA, Daisuke [B class; 600 (B), 0 (C)] (158)
— *First-principles Study of Defects of Magnesium Alloys*

1. EAM ポテンシャルにおける異種原子間相互作用の検討
   小細浩輔, 藤岡芳弥, 吉川創, 松中大介: 計算工学講演論文集, **24** (2019) A-03-04.
2. Molecular Dynamics Simulation on Defect Nucleation from Pre-existing I1 Stacking Fault in Magnesium
   S. Yoshikawa and D. Matsunaka: to be submitted.

MATSUSHITA, Katsuyoshi [C class; 1000 (B), 600 (C)] (276)
— *Numerical Analysis of Instability in Motion of Crowding Cellular Tissue*
— *Numerical study of collective motion transition of crowding cells with anisotropic shape.*

1. Katsuyoshi Matsushita, Emergence of collective propulsion through cell-cell adhesion
   Physical Review E: 97 (2018) 042413
2. Cell Migration driven by Receptor Density Polarity of Cell-Matrix Adhesion
   Katsuyoshi Matsushita, Kazuya Horibe, Naoya Kamamoto and Koichi Fujimoto, Proceedings of

the Symposium on Simulation of Traffic Flow 24, (2018) 5

MAYUMI, Koichi [B class; 600 (B), 80 (C)] (301)
— *Study on Dynamics of Ring and Axial Molecules of Slide-Ring Gel Under Deformation*

1. Sliding Dynamics of Ring on Polymer in Rotaxane: a Coarse-Grained Molecular Dynamics Simulation Study.
   Y. Yasuda, M. Toda, K. Mayumi, H. Yokoyama, H. Morita, and K. Ito: accepted.
2. Molecular Dynamics of Polyrotaxane in Solution Investigated by Quasi-Elastic Neutron Scattering and Molecular Dynamics Simulation: Sliding Motion of Rings on Polymer.
   Y. Yasuda, Y. Hidaka, K. Mayumi, T. Yamada, K. Fujimoto, S. Okazaki, H. Yokoyama, and K. Ito, submitted.

MISAWA, Masaaki [B class; 700 (B), 0 (C)] (150)
— *Molecular dynamics study on pressure-induced transformation of silicates*

MISAWA, Takahiro [E class; 14500 (B), 2500 (C)] (15)
— *Superconductivity and quantum spin liquid in multi-orbital systems with inverted Hund's rule coupling*

1. Ab initio effective Hamiltonians for cuprate superconductors
   Motoaki Hirayama, Youhei Yamaji, Takahiro Misawa, and Masatoshi Imada: Phys. Rev. B **98**, 134501 (2018).
2. mVMC - Open-source software for many-variable variational Monte Carlo method
   Takahiro Misawa, Satoshi Morita, Kazuyoshi Yoshimi, Mitsuaki Kawamura, Yuichi Motoyama, Kota Ido, Takahiro Ohgore, Masatoshi Imada, and Takeo Kato :Comput. Phys. Commun. **235**, 447 (2019).

MIYASHITA, Seiji [C class; 6000 (B), 950 (C)] (223)
— *Manipulation of quantum state by external fields*

1. Optical bistability in a low-photon-density regime
   Tatsuhiko Shirai, Synge Todo, Hans de Raedt, and Seiji Miyashita:Phys. Rev. A **98**, 043802 (2018).
2. Mechanism for subgap optical conductivity in honeycomb Kitaev materials
   A. Bolens, H. Katsura, M. Ogata, and S. Miyashita:Phys. Rev. B**97**, 161108 (R), (1-5) (2018)
3. Exploration of the effects of dipole-dipole interactions in $Nd_2Fe_{14}B$ thin films based on a stochastic cutoff method with a novel efficient algorithm,
   T. Hinokihara, M. Nishino, Y. Toga, and S. Miyashita:Phys. Rev. B**97**, 104427(1-8) (2018)
4. Anisotropy of exchange stiffness based on atomic-scale magnetic properties in the rare-earth permanent magnet $Nd_2Fe_{14}B$
   Yuta Toga, Masamichi Nishino, Seiji Miyashita, Takashi Miyake, and Akimasa Sakuma: Phys. Rev. B**98**, 054418 (2018).

MIZUGUCHI, Tomoko [C class; 2500 (B), 0 (C)] (265)
— *Effect of interface on the dynamics of water confined in mesoporous silica*

1. Hydrogen bond analysis of confined water in mesoporous silica using the reactive force field
   T. Mizuguchi, K. Hagita, S. Fujiwara and T. Yamada: submitted to Mol. Sim.

MIZUKAMI, Wataru [C class; 2000 (B), 0 (C)] (125)
— *Exploration of surface reactions on model real catalyst*

MOMIDA, Hiroyoshi [C class; 3000 (B), 500 (C)] (113)
— *Theoretical design of energy harvesting and storage device materials by first-principles calculations*

1. First-Principles Study on Cathode Properties of Li_2MTiO_4 (M = V, Cr, Mn, Fe, Co, and Ni) with Oxygen Deficiencies for Li-Ion Batteries
   M. Hamaguchi, H. Momida, and T. Oguchi, J. Phys. Soc. Jpn. **87**, 044805 (2018).
2. Elucidation of Discharge Mechanism and Evaluation of Na-Ion Battery Performance of Tin Sulfide (SnS) Electrode by using First-Principles Calculation

H. Kotaka, H. Momida, A. Kitajou, S. Okada, and T. Oguchi, J. Comput. Chem. Jpn. **18**, 78 (2019).

3. First-Principles Study of Na-Ion Battery Performance and Reaction Mechanism of Tin Sulfide as Negative Electrode
   H. Kotaka, H. Momida, A. Kitajou, S. Okada, and T. Oguchi, Chem. Rec. (2019) in press.

MORI, Takashi [C class; 3000 (B), 0 (C)] (261)
— *Semiclassical dynamics of quantum spin systems*

1. Prethermalization in the transverse-field Ising chain with long-range interactions
   T. Mori: J. Phys. A **52**, 054001 (2019).

MORIKAWA, Yoshitada [C class; 2500 (B), 900 (C)] (114)
— *First-principles Thermodynamics and Statistical Mechanics Simulations of Catalytic Reactions at Solid Surfaces*

1. A New Pentacene Polymorph Induced by Interaction with a Bi(0001) Substrate
   T. Shirasawa, S. Yanagisawa, S. Hatada, W. Voegeli, Y. Morikawa, and T. Takahashi: J. Phys. Chem. C **122** (2018) 6240.
2. Platinum-catalyzed hydrolysis etching of SiC in water: A density functional theory study
   P. V. Bui, D. Toh, A. Isohashi, S. Matsuyama, K. Inagaki, Y. Sano, K. Yamauchi, and Y. Morikawa: Jpn. J. Appl. Phys. **57** (2018) 055703.
3. Computational Study on Atomic Structures, Electronic Properties, and Chemical Reactions at Surfaces and Interfaces and in Biomaterials
   Y. Takano, N. Kobayashi, and Y. Morikawa: J. Phys. Soc. Jpn. **87** (2018) 061013.
4. Hydrogen-bond Induced Nitric Oxide Dissociation on Cu(110)
   T. N. Pham, M. Sugiyama, F. Muttaqien, S. E. M. Putra, K. Inagaki, D. N. Son, Y. Hamamoto, I. Hamada, and Y. Morikawa: J. Phys. Chem. C **122** (2018) 11814.
5. Enhancement of CO_2 adsorption on oxygen-functionalized epitaxial graphene surface under near-ambient conditions
   S. Yamamoto, K. Takeuchi, Y. Hamamoto, R. Liu, Y. Shiozawa, T. Koitaya, T. Someya, K. Tashima , H. Fukidome, K. Mukai, S. Yoshimoto, M. Suemitsu, Y. Morikawa, J. Yoshinobu, and I. Matsuda: Phys. Chem. Chem. Phys. **20** (2018)19532.
6. Diffusion mechanism of Na ionpolaron complex in potential cathode materials $NaVOPO_4$ and $VOPO_4$ for rechargeable sodium-ion batteries
   H. D. Luong, T. D. Pham, Y. Morikawa, Y. Shibutani, and V. A. Dinh: Phys. Chem. Chem. Phys., **20** (2018) 23625.
7. Effects of Surface Termination and Layer Thickness on Electronic Structures of $LaNiO_3$ Thin Films
   H. D. Nguyen, B. T. Cong, and Y. Morikawa: J. Phys. Soc. Jpn. **87** (2018) 114704.
8. First-principles study of polar, nonpolar, and semipolar GaN surfaces during oxide vapor phase epitaxy growth
   T. Kawamura*, A. Kitamoto, M. Imade, M. Yoshimura, Y. Mori, Y. Morikawa, Y. Kangawa, K. Kakimoto, and T. Akiyama: Jpn. J. Appl. Phys. **57** (2018) 115504.
9. Platinum Single-atom Adsorption on Graphene: A Density Functional Theory Study
   S. A. Wella, Y. Hamamoto, Suprijadi, Y. Morikawa, and I. Hamada: Nanoscale Adv. **1** (2019) 1165.
10. Experimental and Computational Studies on Ruthenium(II) Bis-diimine Complexes of N,N'-Chelate Ligand: The Origin of the Change in the Absorption Spectra upon Oxidation and Reduction
    S. S. Tan, S. Yanagisawa, K. Inagaki, M. B. Kassim and Y. Morikawa: Phys. Chem. Chem. Phys. **21** (2019) 7973.
11. Van der Waals Density Functional Study of Formic Acid Adsorption and Decomposition on Cu(111)
    S. E. M. Putra, F. Muttaqien, Y. Hamamoto, K. Inagaki, I. Hamada, and Y. Morikawa: J. Chem. Phys. **150** (2019) 154707.

MORIMOTO, Kenichi [C class; 2000 (B), 0 (C)] ()
— *RANS-LES Hybrid Analysis of Turbulent Heat Transfer*

MORITA, Satoshi [B class; 700 (B), 90 (C)] (290)
— *Quantum many-body problem solver with tensor network methods*

1. Calculation of higher-order moments by higher-order tensor renormalization group
   S. Morita and N. Kawashima: Comput. Phys. Commun. **236**, 6571 (2019).
2. Detecting signals of weakly first-order phase transitions in two-dimensional Potts models
   S. Iino, S. Morita, N. Kawashima, and A. W. Sandvik: J. Phys. Soc. Jpn. **88**, 034006 (2019).
3. Fast Algorithm for Generating Random Bit Strings and Multispin Coding for Directed Percolation
   H. Watanabe, S. Morita, S. Todo, and N. Kawashima: J. Phys. Soc. Jpn. **80**, 024004 (2019).

MOTOME, Yukitoshi [C,D class; 16000 (B), 1950 (C)] (173)
— *Dynamics of Majorana particles in Kitaev spin liquids in a magnetic field*
— *Numerical study on novel quantum phenomena in spin-orbit coupled materials*
— *Numerical study on quantum magnetism in spin-orbit coupled materials*

1. Unusual Thermal Hall Effect in a Kitaev Spin Liquid Candidate α-$RuCl_3$
   Y. Kasahara, K. Sugii, T. Ohnishi, M. Shimozawa, M. Yamashita, N. Kurita, H. Tanaka, J. Nasu, Y. Motome, T. Shibauchi, and Y. Matsuda: Phys. Rev. Lett. **120** (2018) 217205.
2. Nonreciprocal spin Seebeck effect in antiferromagnets
   R. Takashima, Y. Shiomi, and Y. Motome: Phys. Rev. B **98** (2018) 020401(R).
3. Majorana quantization and half-integer thermal quantum Hall effect in a Kitaev spin liquid
   Y. Kasahara, T. Ohnishi, Y. Mizukami, O. Tanaka, Sixiao Ma, K. Sugii, N. Kurita, H. Tanaka, J. Nasu, Y. Motome, T. Shibauchi, and Y. Matsuda: Nature **559** (2018) 227.
4. Successive Majorana topological transitions driven by a magnetic field in the Kitaev model
   J. Nasu, Y. Kato, Y. Kamiya, and Y. Motome: Phys. Rev. B **98** (2018) 060416(R).
5. Néel and Bloch-Type Magnetic Vortices in Rashba Metals
   S. Hayami and Y. Motome: Phys. Rev. Lett. **121** (2018) 137202.
6. Magnetic structural unit with convex geometry: A building block hosting an exchange-striction-driven magnetoelectric coupling
   K. Kimura, Y. Kato, K. Yamauchi, A. Miyake, M. Tokunaga, A. Matsuo, K. Kindo, M. Akaki, M. Hagiwara, S. Kimura, M. Toyoda, Y. Motome, and T. Kimura: Phys. Rev. Materials **2** (2018) 104415.
7. Multiple-Q magnetic orders in Rashba-Dresselhaus metals
   K. N. Okada, Y. Kato, and Y. Motome: Phys. Rev. B **98** (2018) 224406.
8. Band crossings in honeycomb-layered transition metal compounds
   Y. Sugita and Y. Motome: Phys. Rev. B **99** (2019) 041101(R).
9. Magnetoelectric behavior from cluster multipoles in square cupolas: Study of $Sr(TiO)Cu_4(PO_4)_4$ in comparison with Ba and Pb isostructurals
   Y. Kato, K. Kimura, A. Miyake, M. Tokunaga, A. Matsuo, K. Kindo, M. Akaki, M. Hagiwara, S. Kimura, T. Kimura, and Y. Motome: Phys. Rev. B **99** (2019) 024415.
10. Effect of magnetic anisotropy on skyrmions with a high topological number in itinerant magnets
    S. Hayami and Y. Motome: Phys. Rev. B **99** (2019) 094420.
11. Antiferromagnetic Kitaev Interaction in f-Electron Based Honeycomb Magnets
    S.-H. Jang, R. Sano, Y. Kato, and Y. Motome: preprint (arXiv:1807.01443), submitted to Phys. Rev. B.
12. Magnetoelectric effect in band insulator-ferromagnet heterostructures
    K. N. Okada, Y. Kato, and, Y. Motome: preprint (arXiv:1902.04204), accepted for the publication in Phys. Rev. B.
13. Spin-current diode with a monoaxial chiral magnet
    S. Okumura, H. Ishizuka, Y. Kato, J. Ohe, and Y. Motome: preprint (arXiv:1903.12358), submitted to Appl. Phys. Lett.

MOTOYAMA, Yuichi [B class; 800 (B), 100 (C)] (199)
— *Drawing phase diagram from many-variable variational wave functions with machine learning*

MURASHIMA, Takahiro [E class; 20000 (B), 3000 (C)] (209)
— *Numerical analysis of non-equilibrium dynamics of polymeric liquid*

1. Elongational Viscosity of Weakly Entangled Polymer Melt via Coarse-Grained Molecular Dynamics Simulation
   T. Murashima, K. Hagita, T. Kawakatsu: J. Soc. Rheol. Jpn. **46** (2018) 207.
2. Coupling Finite Element Method with Large Scale Atomic/Molecular Massively Parallel Simulator (LAMMPS) for Hierarchical Multiscale Simulations
   T. Murashima, S. Urata, S. Li: arXiv:1902.09171, submitted to EPJB.

NADA, Hiroki [B,C class; 4000 (B), 90 (C)] (256,257)
— *Analysis of Formation Mechanism of Calcium Phosphate Crystal by Large-Scale Molecular Dynamics Simulation Combined with Metadynamics Method*
— *Large-Scale Molecular Dynamics Simulation Study on the Crystallization Mechanism of Water Including Air Molecules*

1. A New Methodology for Evaluating the Structural Similarity Between Different Phases Using a Dimensionality Reduction Technique
   H. Nada: ACS Omega, **3** (2018) 5789.
2. Computer Simulations: Essential Tools for Crystal Growth Studies
   H. Nada: Crystals, **8** (2018) 314.
3. Shock Growth of Ice Crystals Near Equilibrium Melting Pressure Under Dynamic Compression
   Y.-J. Kim, Y.-H. Lee, S. Lee, H. Nada and G. W. Lee: Proc. Natl. Acad. Sci. U.S.A., in press.
4. Anisotropy in Stable Conformations of Hydroxylate Ions Between the 001 and 110 Planes of TiO_2 Rutile Crystals for Glycolate, Lactate, and 2-Hydroxybutyrate Ions Studied by Metadynamics Method
   H. Nada, M. Kobayashi and M. Kakihana: submitted to ACS Omega.

NAKAHARA, Akio [B class; 700 (B), 90 (C)] ()
— *Numerical simulation for memory effect in paste of flow and vibration*

NAKAMURA, Kazuma [C class; 4500 (B), 0 (C)] (96,335)
— *Ab initio derivation of effective low-energy model for excitonic insulator Ta2NiSe5*
— *Development of ab initio many-body perturbation calculation software RESPACK*

1. Hydrostatic pressure effects on superconducting transition of nanostructured niobium highly strained by high-pressure torsion
   M. Mito, Y. Kitamura, T. Tajiri, K. Nakamura, R. Shiraishi, K. Ogata, H. Deguchi, T. Yamaguchi, N. Takeshita, T. Nishizaki, K. Edalati, Z. Horita: J. Appl. Phys. **125**, (2019) 125901.

NAKANO, Hiroki [C class; 4500 (B), 1100 (C)] (240)
— *Numerical study on low-energy states of quantum spin systems*

1. Impact of Dzyaloshinskii-Moriya Interactions and Tilts of g Tensors on the Magnetization of a Spherical Kagome Cluster in $\{W_{72}V_{30}\}$
   Y. Fukumoto, Y. Yokoyama, and H. Nakano: J. Phys. Soc. Jpn. **87** (2018) 124710(1-6)
2. Third Boundary of the Shastry-Sutherland Model by Numerical Diagonalization
   H. Nakano and T. Sakai: J. Phys. Soc. Jpn. **87** (2018) 123702(1-5)
3. Precise Estimation of the $S = 2$ Haldane Gap by Numerical Diagonalization
   H. Nakano and T. Sakai: J. Phys. Soc. Jpn. **87** (2018) 105002(1-2)
4. Numerical-Diagonalization Study of Magnetization Process of Frustrated Spin-1/2 Heisenberg Antiferromagnets in Two Dimensions: – Triangular- and Kagome-Lattice Antiferromagnets–
   H. Nakano and T. Sakai: J. Phys. Soc. Jpn. **87** (2018) 063706(1-5)
5. Metamagnetic jump in the spin-1/2 antiferromagnetic Heisenberg model on the square kagome lattice
   Y. Hasegawa, H. Nakano, and T. Sakai: Phys. Rev. B **98** (2018) 014404(1-9)
6. Ground state with nonzero spontaneous magnetization of the two-dimensional spin-1/2 Heisenberg antiferromagnet with frustration

T. Sakai and H. Nakano: AIP Adv. **8** (2018) 101408(1-5)

7. Gapless spin excitations in the S=1/2 Kagome- and triangular-lattice Heisenberg antiferromagnets
   T. Sakai and H. Nakano: Physica B **536** (2018) 85-88
8. Spontaneous Magnetization of the Spin-1/2 Heisenberg Antiferromagnet on the Triangular Lattice with a Distortion
   A. Shimada, T. Sakai, H. Nakano, and K. Yoshimura: J. Phys.: Conf. Series **969** (2018) 012126(1-6)
9. Quantum Spin Fluid Behaviors of the Kagome- and Triangular-Lattice Antiferromagnets
   T. Sakai and H. Nakano: J. Phys.: Conf. Series **969** (2018) 012127(1-6)

NAKAYAMA, Takashi [C class; 5500 (B), 950 (C)] (73)

— First-principles study of ionization and diffusion of metal atoms at metal/solid interfaces in electric fields: toward semiconductor and organic substrates

1. Physics of Fermi-Level "Unpinning" at Metal/Ge Interfaces; First-Principles View
   T. Nakayama, T. Nishimoto: ECS Transactions **86** (2018) 291.
2. Structural and Charging Stability of Metal Nanodot Memory in SiO2; First-Principles Study
   T. Nakayama, S. Yamazaki, Y. Shiraishi: ECS Transactions **86** (2018) 69.
3. Metal-atom penetration and diffusion in organic solids: difference between sigma- and pai- orbital molecular systems
   S. Watanabe, T. Nakayama: Jpn. J. Appl. Phys. (2019) in press.

NISHIDATE, Kazume [C class; 1500 (B), 0 (C)] (135)

— Density functional calculations of the catalytic site of fuel cell and photocatalyst

1. Oxygen reduction reaction of FeN_4 center embedded in graphene and carbon nanotube: Density functional calculations
   S. Aoyama, J. Kaiwa, P. Chantngarm, S. Tanibayashi, H. Saito, M. Hasegawa, and K. Nishidate: AIP Advances **8** (2018) 115113.

NISHIGUCHI, Kazutaka [B class; 500 (B), 0 (C)] (306)

— Theoretical study for superconductivity in multilayer cuprates with two-particle self-consistent approach

1. Superconductivity arising from layer differentiation in multilayer cuprates
   K. Nishiguchi, S. Teranishi, K. Kusakabe, and H. Aoki: Phys. Rev. B **98** (2018) 174508.

NOGUCHI, Hiroshi [C class; 13000 (B), 1900 (C)] (210)

— structure formation of biomembranes

1. Angular-momentum conservation in discretization of the Navier-Stokes equation for viscous fluids
   H. Noguchi: Phys. Rev. E **99**, 023307 (2019).
2. Limiting shapes of confined lipid vesicles
   B. Kavčič, A. Sakashita, H. Noguchi, and P. Ziherl: Soft Matter **15**, 602 (2019).

NOGUCHI, Yoshifumi [C class; 6000 (B), 950 (C)] (68)

— XPS simulation using self-consistent GW method

1. Optical properties of six isomers of three dimensionally delocalized π-conjugated carbon nanocage
   Y. Noguchi, D. Hirose, and O. Sugino: Eur. Phys. J. B **91** (2018) 125.a

NOMURA, Yusuke [C class; 10500 (B), 1700 (C)] (185)

— Development of machine-learning solvers for Hamiltonians with electron-phonon interactions

— Implementation and application of multi-orbital TRILEX -a new method to bridge weak-coupling and strong coupling methods-

1. Stripe and superconducting order competing in the Hubbard model on a square lattice studied by a combined variational Monte Carlo and tensor network method
   Andrew S. Darmawan, Yusuke Nomura, Youhei Yamaji, and Masatoshi Imada: Phys. Rev. B **98** (2018) 205132.
2. Constructing exact representations of quantum many-body systems with deep neural networks

Giuseppe Carleo, Yusuke Nomura, and Masatoshi Imada: Nat. Commun. **9** (2018) 5322.

NUGRAHA, Ahmad Ridwan Tresna [B class; 200 (B), 30 (C)] (164)
— *Coherent phonon spectroscopy of atomic layer materials*

OBATA, Masao [C class; 3000 (B), 300 (C)] (116)
— *Analysis on atomic and magnetic structure in magnetic molecular complex, crystal and interface and investigation of electron correlation effect*
— *Analysis on atomic structure in magnetic molecular complex, crystal and interface using spin dependent van der Waals density functional and investigation of electron correlation effect*

1. Implementation of Magnetic Dipole Interaction in the Planewave-Basis Approach for Slab Systems
   T. Oda and M. Obata: J. Phys. Soc. Jpn. **87** (2018) 064803.
2. A Comprehensive Study of Sign Change in Electric Field Control Perpendicular Magnetic Anisotropy Energy at Fe/MgO Interface: First Principles Calculation
   I. Pardede, T. Kanagawa, N. Ikhsan, I. Murata, D. Yoshikawa, M. Obata, and T. Oda: IEEE Transactions on Magnetics **55**, (2018) 1700104.
3. Investigation of magnetic dipole-dipole interaction using magnetic density on solid oxygen based on first-principles approach
   M. Obata, M. Christivana, and T. Oda: AIP Advances **8** (2018) 101419.
4. Shape Magnetic Anisotropy From Spin Density in Nanoscal Slab Systems
   T. Oda, I. Pardede, T. Kanagawa, N. Ikhsan, D. Yoshikawa, and M. Obata: IEEE Transactions on Magnetics **55**, (2018) 1300104.
5. Noncollinear magnetic structure with spin-dependent van der Waals density functional approach: β-phase solid oxygen
   M. Christivana, M. Obata, and T. Oda: submitted to J. Phys. Soc. Jpn.

ODA, Masato [C class; 2500 (B), 600 (C)] (119)
— *Modulation of phonon modes originate from impurities in GaN*

1. Investigation of the electronphonon interactions around Ga vacancies in GaN and their role in the first stage of defect reactions
   M. Oda: Jpn. J. Appl. Phys., in press

ODA, Tatsuki [E class; 28500 (B), 4650 (C)] (46,48)
— *Analyses on atomic, magnetic, and electronic structures in high-performance spintronics materials*
— *Analyses on magnetic and electronic structures in high-performance spintronics materials*

1. Implementation of magnetic dipole interaction in the planewave-basis approach for slab systems
   Tatsuki Oda and Masao Obata: Journal of the Physical Society of Japan, 87, 064803 (2018)
2. A comprehensive Study of Sign Change in Electric Field Control Perpendicular Magnetic Anisotropy Energy at Fe/MgO Interface: First Principles Calculation
   Indra Pardede, Tomosato Kanagawa, Nurul Ikhsan, Itsuki Murata, Daiki Yoshikawa, Masao Obata, and Tatsuki Oda: IEEE Transactions on Magnetics, 55, 1700104 (2018)
3. Ab Initio study of martensitic transition in Ni2MnGa
   T. Koubský, P. Sedlák, H. Seiner, Jaroslava Fojtíková, Masao Obata, Tatsuki Oda, and Ladislav Kalvoda: ACTA PHYSICA POLONICA A, 134, 804 (2018)
4. Shape Magnetic Anisotropy from Spin Density in Nanoscale Slab Systems
   Tatsuki Oda, Indra Pardede, Tomosato Kanagawa, Nurul Ikhsan, Daiki Yoshikawa, and Masao Obata: IEEE Transactions on Magnetics, 55, 1300104 (2018)
5. Perpendicular and in-plane magnetic anisotropies in Cr-buffered Fe(x)/MgO interface from first-principles approach
   Nurul Ikhsan, Tomosato Kanagawa, Indra Pardede, Daiki Yoshikawa, and Tatsuki Oda: The Science Reports of Kanazawa University, 62, 23 (2018)
6. Fermi level smearing effect in the perpendicular interface Fe/MgO magnetic anisotropy
   Nurul Ikhsan, Indra Pardede, Tomosato Kanagawa, Daiki Yoshikawa, and Tatsuki Oda: The Science Reports of Kanazawa University, 62, 37 (2018)
7. Investigation of magnetic dipole-dipole interaction using magnetic density on solid oxygen based

on first-principles approach
Masao Obata, Mega Christivana, and Tatsuki Oda: AIP Advances, 8, 101419 (2018)

8. Noncollinear magnetic structure with spin-dependent van der Waals density functional approach: β-phase solid oxygen
Mega Christivana, Masao Obata, and Tatsuki Oda: submitted for publication, (2018)
9. Large nonvolatile control of magnetic anisotropy in CoPt/ZnO magnetic tunnel junctions
Muftah Al-Mahdawi, Mohamed Belmoubarik, Masao Obata, Daiki Yoshikawa, Hideyuki Sato, Tomohiro Nozaki, Tatsuki Oda, Masashi Sahashi: submitted for publication, (2018)

OHBA, Tomonori [B class; 700 (B), 0 (C)] (293)
— *Organic Electrolyte Solution in Nanospaces*

1. Anomalous changes of intermolecular distance in aqueous electrolytes in narrow pores of carbon nanotubes
S. M. Khan, S. Faraezi, Y. Oya, K. Hata, T. Ohba: Adsorption, in press.
2. Phase Transition of $S = 1/2$ Heisenberg Antiferomagnet
A. Karatrantos, S. Khan, T. Ohba, Q. Cai: Phys. Chem. Chem. Phys. **20** (2018) 6307.

OHGOE, Takahiro [C class; 10500 (B), 1700 (C)] (239)
— *Development of the diagrammatic Monte Carlo method and its application to cold Fermi gases*
— *Highly accurate numerical analysis of Tan's contact of two-component cold Fermi gases*

1. Diagrammatic Monte Carlo algorithm for the resonant Fermi gas
K. Van Houcke, F. Werner, T. Ohgoe, N.V. Prokof'ev and B. V. Svistunov: Phys. Rev. B **99** (2019) 035140.
2. Contact and Momentum distribution of the Unitary Fermi Gas
R. Rossi, T. Ohgoe, E. Kozik, N. Prokof'ev, B. Svistunov, K. Van Houcke, and F. Werner: Phys. Rev. Lett. **121** (2018) 130406.
3. Resummation of diagrammatic series with zero convergence radius for strongly correlated fermions
R. Rossi, T. Ohgoe, K. Van Houcke, and F. Werner: Phys. Rev. Lett. **121** (2018) 130405.

OHMURA, Satoshi [C class; 3000 (B), 0 (C)] (123)
— *Effects of light elements on transport properties of liquid Fe alloy under ultrahigh pressure condition : ab initio molecular-dynamics simulations*

1. Structural change in liquid sulphur from chain polymeric liquid to atomic simple liquid under high pressure
S Ohmura and F Shimojo: Journal of Physics: Condensed Matter **31** (2019) 215101.
2. Selective reduction mechanism of graphene oxide driven by photon mode versus thermal mode
Hada Masaki, Miyata Kiyoshi, Ohmura Satoshi, Arashida Yusuke, Ichiyanagi Kohei, Katayama Ikufumi, Suzuki Takayuki, Chen Wang, Mizote Shota, Sawa Takayoshi, Yokoya Takayoshi, Seki Toshio, Matsuo Jiro, Tokunaga Tomoharu, Itoh Chihiro, Tsuruta Kenji, Fukaya Ryo, Nozawa Shunsuke, Adachi Shin-ichi, Takeda Jun, Onda Ken, Koshihara Shin-ya, Hayashi Yasuhiko Nishina Yuta: ACS Nano under review

OHNISHI, Masato [C class; 3500 (B), 750 (C)] (98)
— *Analysis of Thermoelectric Properties of Clathrate Compounds with Ab Initio Calculations*

1. Perspective: Towards ultimate impedance of phonon transport by nanostructure interface
Masato Ohnishi, Junichiro Shiomi: APL Materials, 7, 013102 (2019).

OHSAWA, Kazuhito [C class; 1000 (B), 0 (C)] (144)
— *Study of interaction between radiation damage and interstitial atom*

OHTO, Tatsuhiko [C,D class; 9000 (B), 0 (C)] (59,60,61)
— *Ab initio molecular dynamics simulation of doped-graphene/water interfaces*
— *First-principles molecular dynamics simulation of the interface between water and a supramolecular self-assembled monolayer*
— *Interaction between osmolytes in water revealed by ab initio molecular dynamics simulation*

1. Chemical dopants on edge of holey graphene accelerate electrochemical hydrogen evolution reaction
   Akichika Kumatani, Chiho Miura, Hirotaka Kuramochi, Tatsuhiko Ohto, Mitsuru Wakisaka, Yuki Nagata, Hiroki Ida, Yasufumi Takahashi, Kailong Hu, Samuel Jeong, Jun-ichi Fujita, Tomokazu Matsue, Yoshikazu Ito: Adv. Sci. in press.
2. Boosting Electrochemical Water Splitting via Ternary NiMoCo Hybrid Nanowire Arrays
   Kailong Hu, Mingxing Wu, Satoshi Hinokuma, Tatsuhiko Ohto, Mitsuru Wakisaka, Jun-ichi Fujita, and Yoshikazu Ito: J. Mater. Chem. A 7, 2156 (2019)
3. Structure and Dynamics of Water at the Water-Air Interface Using First Principles Molecular Dynamics Simulations within Generalized Gradient Approximation
   Tatsuhiko Ohto, Mayank Dodia, Sho Imoto, and Yuki Nagata: J. Chem. Theory Comput. 15, 595 (2019)
4. Orientational Distribution of Free O-H Groups of Interfacial Water Is Exponential
   Shumei Sun, Fujie Tang, Sho Imoto, Daniel R. Moberg, Tatsuhiko Ohto, Francesco Paesani, Mischa Bonn, Ellen H. G. Backus, and Yuki Nagata: Phys. Rev. Lett. 121, 246101 (2018)
5. Single-molecule rectifiers based on voltage-dependent deformation of molecular orbitals in carbazole oligomers
   Ryo Yamada, Ken Albrecht, Tatsuhiko Ohto, Keigo Minode, Kimihisa Yamamoto, and Hirokazu Tada: Nanoscale 10, 19818 (2018)
6. Large Hydrogen Bond Mismatch between TMAO and Urea Promotes Their Hydrophobic Association
   Wen Jun Xie, Seoncheol Cha, Tatsuhiko Ohto, Wataru Mizukami, Yuezhi Mao, Manfred Wagner, Mischa Bonn, Johannes Hunger, and Yuki Nagata: Chem 4, 2615 (2018)
7. Graphene Layer Encapsulation of Non-Noble Metal Nanoparticles as Acid-Stable Hydrogen Evolution Catalysts
   Kailong Hu, Tatsuhiko Ohto, Linghan Chen, Jiuhui Han, Mitsuru Wakisaka, Yuki Nagata, Junichi Fujita, and Yoshikazu Ito: ACS Energy Letters 3, 1539 (2018)
8. Structure and Dynamics of Water at Water-Graphene and Water-Hexagonal Boron Nitride Sheet Interfaces Revealed by Ab Initio Sum-Frequency Generation Spectroscopy
   Tatsuhiko Ohto, Hirokazu Tada, and Yuki Nagata: Phys. Chem. Chem. Phys. 20, 12979 (2018)
9. Aggregation-Induced Emission Enhancement from Disilane-Bridged Donor–Acceptor–Donor Luminogens Based on the Triarylamine Functionality
   Tsukasa Usuki, Masaki Shimada, Yoshinori Yamanoi, Tatsuhiko Ohto, Hirokazu Tada, Hidetaka Kasai, Eiji Nishibori, Hiroshi Nishihara: ACS Appl. Mater. Interfaces, 10, 12164 (2018)
10. Cooperation between holey graphene and NiMo alloy for hydrogen evolution in an acidic electrolyte
    Yoshikazu Ito, Tatsuhiko Ohto, Daisuke Hojo, Mitsuru Wakisaka, Yuki Nagata, Linghan Chen, Kailong Hu, Masahiko Izumi, Jun-ichi Fujita, and Tadafumi Adschiri ACS Catal. 8, 3579 (2018)

OHTSUKI, Tomi [C class; 5500 (B), 900 (C)] (232)
— *Scaling theories of random topological and non topological systems*

1. Unconventional Scaling Theory in Disorder-Driven Quantum Phase Transition
   X. Luo, T. Ohtsuki, R. Shindou: Physical Review B **98**, 020201 (2018)
2. Critical Exponent of the Anderson Transition Using Massively Parallel Supercomputing
   K. Slevin, T. Ohtsuki: Journal of the Physical Society of Japan **87**, 094703 (2018)
3. Topological Matter in the Absence of Translational Invariance
   Advanced Topological Insulators, 109-157, Wiley online (2019)

OKADA, Susumu [B class; 600 (B), 80 (C)] ()
— *Physical properties of nanoscale carbon materials under an external electric field*

OKAMOTO, Yuko [E class; 3000 (B), 0 (C)] (259)
— *Study on complex systems by generalized-ensemble algorithms*

OKITSU, Kouhei [C class; 1500 (B), 0 (C)] (277)
— *Study on 'cubic algorithm' for solving n-beam Takagi-Taupin equation*

1. Experimentally obtained and computer-simulated X-ray asymmetric eight-beam pinhole topographs for a silicon crystal
   K. Okitsu, Y. Imai, Y. Yoda and Y. Ueji: Acta Cryst. **A75** (2019) In Press in Advansed Section.
2. Experimentally obtained and computer-simulated X-ray non-coplanar 18-beam pinhole topographs for a silicon crystal
   K. Okitsu, Y. Imai and Y. Yoda: Acta Cryst. **A75** (2019) In Press in Advansed Section.

OKUBO, Tatsuya [C class; 1500 (B), 0 (C)] ()
— *Theoretical and experimental investigation on phase selectivity in zeolite syntheses*

OKUBO, Tsuyoshi [C class; 5500 (B), 900 (C)] (230)
— *Novel phases in honeycomb lattice Kitaev materials*

1. Field-enhanced quantum fluctuation in an $S = \frac{1}{2}$ frustrated square lattice
   H. Yamaguchi, Y. Sasaki, T. Okubo, M. Yoshida, T. Kida, M. Hagiwara, Y. Kono, S. Kittaka, T. Sakakibara, M. Takigawa, Y. Iwasaki and Y. Hosokoshi: Phys. Rev. B **98** (2018) 094402.
2. A series of magnon crystals appearing under ultrahigh magnetic fields in a kagom antiferromagnet
   R. Okuma, D. Nakamura, T. Okubo, A. Miyake, A. Matsuo, K. Kindo, M. Tokunaga, N. Kawashima, S. Takeyama and Z. Hiroi: Nat. Commun. **10** (2019) 1229.
3. Gapless Kitaev Spin Liquid to Classical String Gas through Tensor Networks
   H.-Y. Lee, R. Kaneko, T. Okubo and N. Kawashima: arXiv:1901.05786.
4. Multiple–q states of the J_1–J_2 classical honeycomb-lattice Heisenberg antiferromagnet under magnetic fields
   T. Shimokawa, T. Okubo and H. Kawamura: arXiv:1902.01582.

OKUMURA, Hisashi [C class; 6500 (B), 0 (C)] (224)
— *Oligomerization process of full-length amyloid-beta peptides studied by molecular dynamics simulations*

1. Effects of a hydrophilic/hydrophobic interface on amyloid-β- peptides studied by molecular dynamics simulations and NMR experiments
   S. G. Itoh, M. Yagi-Utsumi, K. Kato, and H. Okumura: J. Phys. Chem. B **123** (2019) 160.
2. Cavity closure of 2-hydroxypropyl-β- cyclodextrin: Replica exchange molecular dynamics simulations
   K. Kerdpol, J. Kicuntod, P. Wolschann, S. Mori, C. Rungnim, M. Kunaseth, H. Okumura, N. Kungwan, and T. Rungrotmongkol: Polymers **11** (2019) 145.
3. Conformational properties of an artificial GM1 glycan cluster based on a metal-ligand complex
   Y. Tachi, Y. Okamoto, and H. Okumura: J. Chem. Phys. **149** (2018) 135101.

ONISHI, Hiroaki [C class; 2000 (B), 0 (C)] (270)
— *Magnetic excitation and spin transport in frustrated quantum spin chain*

1. Dynamical quadrupole structure factor of ferromagnetic frustrated chain
   H. Onishi, Physica B 536, 346-349 (2018).
2. Magnetic excitations and transport properties in frustrated ferromagnetic chain
   H. Onishi, J. Magn. Magn. Mater. 479, 88-90 (2019).

ONO, Tomoya [C class; 9000 (B), 1350 (C)] (56)
— *Development of first-principles electronic-structure and transport calculation method based on real-space finite-difference approach*

1. Complex band structure calculations based on the overbridging boundary matching method without using Green's functions
   S. Tsukamoto, T. Ono, S. Iwase, and S. Blügel: Phys. Rev. B **98** (2018) 195422.
2. Contour integral method for obtaining the self-energy matrices of electrodes in electron transport calculations
   S. Iwase, Y. Futamura, A. Imakura, T. Sakurai, S. Tsukamoto, and T. Ono: Phys. Rev. B, **97** (2018) 195449.

3. First-principles study on leakage current caused by oxygen vacancies at $HfO_2/SiO_2/Si$ interface
   K. Takagi and T. Ono: Jpn. J. Appl. Phys. **57** (2018) 066501.
4. DFT calculation for oxidation reaction of SiC(0001)
   T. Ono: Materials Science Forum, accepted.

ONO, Yoshiaki [C class; 4000 (B), 750 (C)] (189)
— *First-principles calculation and dynamical mean-field theory for superconductivity in multi-band systems*

1. FFLO Superconductivity Mediated by Excitonic Fluctuation in Semimetallic Ta_2NiSe_5
   Takemi Yamada, Kaoru Domon, Yoshiaki Ono: J. Phys. Soc. Jpn., in press

OSHIKAWA, Masaki [B class; 800 (B), 0 (C)] ()
— *Numerical study of many-body polarization and quantum dynamics*

OSHIYAMA, Atsushi [E class; 34500 (B), 5250 (C)] (44)
— *Mechanisms of Semiconductor Interface Formation and its Electronic Properties based on Quantum Theory*

1. Structural stability and energy levels of carbon-related defects in amorphous SiO_2 and its interface with SiC
   Y.-i. Matsushita and A. Oshiyama: Jpn. J. Appl. Phys. **57** (2018) 125701
2. Microscopic mechanism of carbon annihilation upon SiC oxidation due to phosphorous treatment: Density functional calculations combined with ion mass spectrometry
   T. Kobayashi, Y.-i. Matsushita, T. Okuda, T. Kimoto and A. Oshiyama: Appl. Phys. Exp. **11** (2018) 121301
3. Reaction Pathway of Surface-Catalyzed Ammonia Decomposition and Nitrogen Incorporation in Epitaxial Growth of Gallium Nitride
   K. M. Bui, J.-I. Iwata, Y. Kangawa, K. Shiraishi, Y. Shigeta, and A. Oshiyama: J. Phys. Chem. C **122** (2018)
4. First-Principle Study of Ammonia Decomposition and Nitrogen Incorporation on the GaN Surface in Metal Organic Vapor Phase Epitaxy
   K. M. Bui, J.-I. Iwata, Y. Kangawa, K. Shiraishi, Y. Shigeta, and A. Oshiyama: J. Cryst. Growth **507** (2019)
5. Structural determination of phosphosilicate glass based on first-principles molecular dynamics calculation
   T. Kobayashi, Y.-i. Matsushita, T. Kimoto and A. Oshiyama: Jpn. J. Appl. Phys. **58** (2019) 011001

OTOMO, Junichiro [B,D class; 1000 (B), 570 (C)] (130)
— *Analysis of ion conduction in materials of proton-conducting solid electrolyte*
— *Theoretical analysis of catalytic surface reaction with proton conductors*

OZEKI, Yukiyasu [C class; 8500 (B), 0 (C)] (221)
— *Study on topological phase transitions by dynamical scaling analysis*
— *Study on topological phase transitions by dynamical scaling analysis II*

1. Dynamical scaling analysis of phase transition and critical properties for the RP^2 model in two dimensions
   Y. Ozeki, A. Matsuda and Y. Echinaka: Phys. Rev E **99** (2019) 012116

RAEBIGER, Hannes [B class; 700 (B), 0 (C)] ()
— *Theory of self-organized nano-structures for electronic devices*

SAITO, Mineo [C class; 8500 (B), 0 (C)] (64)
— *First-principles calculation for muon and positron experiments of wide gap semiconductors*

1. Anisotropic thermoelectric effect on phosphorene and bismuthene: first-principles calculations based on nonequilibrium Green's function theory

Yuto Tanaka, Mineo Saito and Fumiyuki Ishii: J. J. Appl. Phys. **57** (2018) 125201.

2. Electronic band structures of group-V two-dimensional materials
   Nuning Anugrah Putri Namari and Mineo Saito: J. J. Appl. Phys., accepted for publication.

SAITO, Nen [B class; 600 (B), 90 (C)] (297)
— *phase field simulation for amoeboid cells*

SAKAGUCHI, Norihito [C class; 4000 (B), 0 (C)] (102)
— *Reduction of Rare Metals in Fuel Cell Catalysts and Hydrogen Permeable Membrane*

1. Enhanced hydrogen permeability of hafnium nitride nanocrystalline membranes by interfacial hydridic conduction
   青木芳尚，倉千晴，國貞雄治，朱春宇，幅崎浩樹: クリーンエネルギー **27** (2018) 44.
2. Adsorption and Diffusion Properties of a Single Iron Atom on Light-Element-Doped Graphene
   S. Hasegawa, Y. Kunisada, N. Sakaguchi: e-J. Surf. Sci. Nanotech. **16** (2018) 193.
3. Combustion synthesis of AlN doped with carbon and oxygen
   G. Saito, Y. Kunisada, T. Watanabe, X. Yi, T. Nomura, N. Sakaguchi, T. Akiyama: J. Am. Ceram. Soc. **102** (2019) 524.
4. Hydrogen isotope absorption in unary oxides and nitrides with anion vacancies and substitution
   T. Watanabe, Y. Kunisada, N. Sakaguchi: ChemPhysChem in press.
5. グラフェン上での金属原子吸着状態の理論的研究
   長谷川瞬，國貞雄治，坂口紀史: 表面と真空 印刷中
6. Exploration of Long-Life Pt/Heteroatom-Doped Graphene Catalysts in Hydrogen Atmosphere
   S. Hasegawa, Y. Kunisada, N. Sakaguchi: ACS Omega **4** (2019) 6573.

SAKAI, Toru [C class; 8500 (B), 1500 (C)] (218,219)
— *Numerical Diagonalization Study on the Quantum Spin Liquid in Frustrated Spin Systems*
— *Numerical Study on Quantum Phase Transitions of the Spin Tubes*

1. Spin-1/2 Triangular-Lattice Heisenberg Antiferromagnet with $\sqrt{3}\times\sqrt{3}$-Type Distortion -Behavior around the Boundaries of the Intermediate Phse-
   A. Shimada, H. Nakano, T. Saka and K. Yoshimura: J. Phys. Soc. Jpn. 87 (2018) 034706.
2. The Spin-1/2 Heisenberg Antiferromagnet on a Triangular-Lattice with $\sqrt{3}\times\sqrt{3}$-Type Distortion -Magnetization Process and Magnetic Susceptibility-
   A. Shimada, H. Nakano, T. Saka and K. Yoshimurai: J. Jpn. Soc. Powder Powder Metallurgy 65 (2018) 3.
3. Quantum Spin Fluid Behaviors of the Kagome- and Triangular-Lattice Antiferromagnets
   T. Sakai and H. Nakano: J. Phys.: Conf. Ser. 969 (2018) 012127/1-6
4. Spontaneous Magnetization of the Spin-1/2 Heisenberg Antiferromagnet on the Triangular Lattice with a Distortion
   A. Shimada, T. Sakai, H. Nakano and K. Yoshimurai: J. Phys.: Conf. Ser. 969 (2018) 012126/1-6
5. Gapless Spin Excitations in the $S = 1/2$ Kagome- and Triangular-Lattice Heisenberg Antiferromagnets
   T. Sakai and H. Nakano: Physica B 536 (2018) 85-88
6. Numerical Diagonalization Study of Magnetization Process of Frustrated Spin-1/2 Heisenberg Antiferromagnets in Two Dimensions -Triangular- and Kagome-Lattice Antiferromagnets-
   H. Nakano and T. Sakai: J. Phys. Soc. Jpn. 87 (2018) 063706/1-5
7. Precise Estimation of the $S = 2$ Haldane Gap by Numerical Diagonalization
   H. Nakano and T. Sakai: J. Phys. Soc. Jpn. 87 (2018) 105002/1-2
8. Ground-State Phase Diagram of an Anisotropic $S = 1/2$ Ladder with Different Interactions
   T. Tonegawa, T. Hikihara, K. Okamoto, S. C. Furuya and T. Sakai: J. Phys. Soc. Jpn. 87 (2018) 104002/1-11
9. Third Boundary of the Shastry-Sutherland Model by Numerical Diagonalization
   H. Nakano and T. Sakai: J. Phys. Soc. Jpn. 87 (2018), 123702/1-5
10. Ground state with nonzero spontaneous magnetization of the two-dimensional spin-1/2 Heisenberg antiferromagnet with frustration
    T. Sakai and H. Nakano: AIP ADVANCES 8 (2018) 101408/1-5

11. Metamagnetic jump in the spin-1/2 antiferromagnetic Heisenberg model on the square kagome lattice
    Y. Hasegawa, H. Nakano and T. Sakai: Phys. Rev. B 98 (2018) 014404/1-9
12. Analysis of Rashba Effect on Au(111) Model Surface
    M. Fujiwara, N. Shima, K. Makoshi and T. Sakai: J. Phys. Soc. Jpn. 88 (2019), 034604/1-5
13. From kagome strip to kagome lattice: Realizations of frustrated $S = 1/2$ antiferromagnets in Ti(III) fluorides
    H. O. Jeschke, H. Nakano and T. Sakai: Phys. Rev. B 99 (2019) 140410(R)/1-6

SAKAKIBARA, Hirofumi [B class; 800 (B), 100 (C)] (147)
— *Development of the determination technique of model parameters based on the accurate ab-initio quantum simulation*

SAKURAGI, Shunsuke [C class; 1000 (B), 0 (C)] (143)
— *Development and control of surface and interface spin texture by band engineering using quantum-well state*

1. Change in magnetization of ferromagnetic Pd(001) ultrathin films induced by the strain effect of $BaTiO_3$
   Yusuke Ban, Katsuyoshi Komatsu, Shunsuke Sakuragi, Tomoyasu Taniyama, Hiroyuki Kageshima, and Tetsuya Sato: Appl. Phys. Lett. **112** (2018) 142409.
2. Spontaneous distortion via the appearance of ferromagnetism in Pd ultrathin films: Observation of an inverse mechanism for the Stoner criterion
   Shunsuke Sakuragi, Hiroo Tajiri, Hiroyuki Kageshima, and Tetsuya Sato: Phys. Rev. B **97** (2018) 214421.
3. Switching of magnetism via modifying phase shift of quantum-well states by tailoring the interface electronic structure
   Shunsuke Sakuragi, Hiroyuki Kageshima, and Tetsuya Sato: submitted to Phys. Rev. B

SASAKI, Takehiko [C class; 1500 (B), 0 (C)] (133)
— *Reaction processes of polyalcohols in high temperature water by First Principles Calculations*

1. Understanding Competition of Polyalcohol Dehydration Reactions in Hot Water
   Y. L. Chang, T. Sasaki, J. Ribas Ariño, M. Machida, M. Shiga: J. Phys. Chem. B **123** (2019) 1662.

SATO, Tetsuya [C class; 3000 (B), 0 (C)] (122)
— *Magnetic properties of Fe/Pd(001) bilayer affected by quantum-well states in Pd layer*

1. Spontaneous distortion via the appearance of ferromagnetism in Pd ultrathin films: Observation of an inverse mechanism for the Stoner criterion
   SAKURAGI Syunsuke: Phys. Rev. B **97**, 214421 (2018).

SAYYAD, Sharareh [B,E class; 8600 (B), 1930 (C)] ()
— *Nonequilibrium investigation of high temperature superconductors*
— *Numerical study of d-wave superconductors in equilibrium*

SEKINE, Yasushi [C class; 4000 (B), 0 (C)] (101)
— *Elucidation of the surface of supported metal catalyst in an electric field*

1. The important role of N2H formation energy for low-temperature ammonia syntheis in an electric field
   K. Murakami, Y. Tanaka, R. Sakai, K. Toko, K. Ito, A. Ishikawa, T. Higo, T. Yabe, S. Ogo, M. Ikeda, H. Tsuneki, H. Nakai, Y. Sekine : Catal. Today, in press.

SHIGETA, Yasuteru [C class; 6000 (B), 950 (C)] (67)
— *Analyses on self-organization processes using dissimilarity sampling*

1. Programmed Dynamical Ordering in Self-organization Processes of Nano-cube: A Molecular Dynamics Study

R. Harada, T. Mashiko, M. Tachikawa, S. Hiraoka, Y. Shigeta: Phys. Chem. Chem. Phys. **20** (2018) 9115.

2. Coulomb and CH-π interactions in (6-4) photolyaseDNA complex dominate DNA binding and repair abilities
   Y. Terai, R. Sato, T. Yumiba, R. Harada, K. Shimizu, T. Toga, T. Ishikawa-Fujiwara, T. Todo, S. Iwai, Y. Shigeta, J. Yamamoto: Nucl. Acid. Res., **46** (2018) 6761.
3. How low-resolution data can predict conformational changes of a protein: a molecular dynamics study
   R. Harada,Y. Shigeta: Phys. Chem. Chem. Phys. **20** (2018) 17790.
4. On-the-Fly Specifications of Reaction Coordinates in Parallel Cascade Selection Molecular Dynamics Accelerate Conformational Transitions of Proteins
   R. Harada, TY. Shigeta: J. Chem. Theor. Comput. **14** (2018) 3332.

SHIMADA, Toshihiro [B class; 700 (B), 0 (C)] (152)
— *Formation mechanism and electronic structures of novel two dimensional materials and nanotubes - BCN and MX2 systems*

1. Single crystal growth, structural analysis and electronic band structure of anitrogen-containing polyacene Benzo[i]benzo[6',7']quinoxalino[2',3':9,10]phenanthro[4,5-abc]phenazine
   Nobuhiko Sakai, Takahiro Tamura, Takashi Yanase, Taro Nagahama, Toshihiro Shimada: Jpn. J. Appl. Phys.**58** (2019) SBBG08.
2. Search for new nitrogen-doped carbon materials by compressing molecular crystals
   Ichiro Yamane, Takashi Yanase, Taro Nagahama,Toshihiro Shimada: Jpn. J. Appl. Phys.**58** (2019) SBBG13.

SHIMAMURA, Kohei [C class; 2500 (B), 600 (C)] (118)
— *Ab initio molecular dynamics simulation of sustained chemical reaction processes in deep-sea hydrothermal vents*

1. *Ab Initio* Molecular Dynamics Study of Prebiotic Production Processes of Organic Compounds at Meteorite Impacts on Ocean
   K. Shimamura, F. Shimojo, A. Nakano, and S. Tanaka: J. Comp. Chem. **40** (2019) 349.

SHIMOJO, Fuyuki [C class; 5000 (B), 0 (C)] (92)
— *First-Principles Molecular-Dynamics Study of Structural and Electronic Properties of Covalent Liquids and Glass under Pressure*

1. Electronic Structure of Titania Nanosheets with Vacancies Based on Nonadiabatic Quantum Molecular Dynamics Simulations
   Y. Uchida, M. Hara, A. Funatsu, and F. Shimojo: Phys. Status Solidi B **255**, 1700689 (2018).
2. Electronic structures and impurity cluster features in Mg-Zn-Y alloys with a synchronized long-period stacking ordered phase
   S. Hosokawa, K. Maruyama, K. Kobayashi, J. R. Stellhorn, B. Paulus, A. Koura, F. Shimojo, T. Tsumuraya, M. Yamasaki, Y. Kawamura, S. Yoshioka, and H. Sato: J. Alloys Compd. **762**, 797 (2018).
3. Photo-induced lattice contraction in layered materials
   H. Kumazoe, A. Krishnamoorthy, L. Bassman, R. K. Kalia, A. Nakano, F. Shimojo, and P. Vashishta: J. Phys.: Condens. Matter **30**, 32LT02 (2018).
4. Static structure of liquid GeSe under pressure: *ab initio* molecular dynamics simulations
   A. Koura and F. Shimojo: Phys. Status Solidi B **255**, 1800103 (2018).

SHIMOKAWA, Tokuro [C class; 5000 (B), 900 (C)] (237)
— *Multiple-Q states of the frustrated Heisenberg model on the honeycomb lattice*

1. Ripple state in the frustrated honeycomb-lattice antiferromagnet
   T. Shimokawa and H. Kawamura: submitted to Phys. Rev. Lett.
2. Multiple-q states of the J1-J2 classical honeycomb-lattice Heisenberg antiferromagnet under magnetic fields
   T. Shimokawa, T. Okubo and H. Kawamura: submitted to Phys. Rev. B

SHINAOKA, Hiroshi [C class; 1500 (B), 800 (C)] (193)
— *Dynamical mean-field calculations of strongly correlated transition metal compounds*

SHINODA, Wataru [E class; 13000 (B), 1750 (C)] (35)
— *Molecular basis analysis of Soft Materials using All-Atom and Coarse-Grained Molecular Dynamics Simulations*

1. SPICA Force Field for Lipid Membranes: Domain Formation Induced by Cholesterol.
   Sangjae Seo and Wataru Shinoda: Journal of Chemical Theory and Computation, 15, 762-774 (2019).
2. Free energy analysis of membrane pore formation process in the presence of multiple melittin peptides
   Yusuke Miyazaki, Susumu Okazaki, Wataru Shinoda: BBA-Biomembranes, DOI:10.1016/j.bbamem.2019.03.002
3. Exploring the effect of pendent side chain length on the structural and mechanical properties of hydrated perfluorosulfonic acid polymer membranes by molecular dynamics simulation
   An-Tsung Kuo, Kotono Takeuchi, Atsushi Tanaka, Shingo Urata, Susumu Okazaki, Wataru Shinoda: Polymer, 146, 53-62 (2018).
4. Molecular mechanism of material deformation and failure in butadiene rubber: Insight from all-atom molecular dynamics simulation using a bond breaking potential model
   Rajdeep S. Payal, Kazushi Fujimoto, Changwoon Jang, Wataru Shinoda, Yuki Takei, Hiroshi Shima, Katsuhiko Tsunoda, Susumu Okazaki: Polymer, 170, 113-119 (2019).

SHINOHARA, Yasushi [C,D class; 5000 (B), 650 (C)] (108)
— *First-principles calculations for nonlinear light absorption of insulators*
— *Relaxation effect on high-order harmonic generation from crystalline solids*

1. Polarization-Resolved Study of High Harmonics from Bulk Semiconductors
   K. Kaneshima, Y. Shinohara, K. Takeuchi, N. Ishii, K. Imasaka, T. Kaji, S. Ashihara, K.L. Ishikawa, and J. Itatani: Phys. Rev. Lett. 120 (2018) 243903.
2. High-order harmonic generation from hybrid organicinorganic perovskites thin films
   Hideki Hirori, Peiyu Xia, Yasushi Shinohara, Tomohito Otobe, Yasuyuki Sanari, Hirokazu Tahara, Nobuhisa Ishi, Jiro Itatani, Kenichi L. Ishikawa, Tomoko Aharen, Masashi Ozaki, Atsushi Wakamiya, Yoshihiko Kanemitsu: APL Materials 7, 041107 (2019)

SHIOMI, Junichiro [B,C class; 12600 (B), 1000 (C)] (211,213,214)
— *Control of phonon and electron transport properties using mechanical strain*
— *Screening for Thermal Functional Materials using Materials Informatics*
— *Understanding Mechanical and Thermal Properties of Sustainable Materials through Molecular Simulations*

1. Ultranarrow-Band Wavelength-Selective Thermal Emission with Aperiodic Multilayered Metamaterials Designed by Bayesian Optimization
   A. Sakurai, K. Yada, T. Simomura, S. Ju, M. Kashiwagi, H. Okada, T. Nagao, K. Tsuda, and J. Shiomi: ACS Central Science 5, 319, (2019).
2. Materials Informatics for Heat Transfer: Recent Progresses and Perspectives
   S. Ju, J. Shiomi: Nanoscale and Microscale Thermophysical Engineering 23, 157 (2019).
3. Parametric Model to Analyze the Components of the Thermal Conductivity of a Cellulose-Nanofibril Aerogel
   M. Obori, D. Suh, S. Yamasaki, T. Kodama, T. Saito, A. Isogai, J. Shiomi: Phys. Rev. Appl. 11 (2019) 024044.
4. Corrrection to Thermal Boundary Conductance Across Heteroepitaxial ZnO/GaN Interfaces: Assessment of the Phonon Gas Model
   John Gaskins, George Kotsonis, Ashutosh Giri, Shenghong Ju, Andrew Rohskopf, Yekan Wang, Tingyu Bai, Edward Sachet, Christopher Shelton, Zeyu Liu, Zhe Cheng, Brian Foley, Samuel Graham, Tengfei Luo, Asegun Henry, Mark S. Goorsky, Junichiro Shiomi, Jon-Paul Maria, and Patrick E. Hopkins: Nano Lett., 19, 14081408 (2019).
5. High-working-pressure Sputtering of ZnO for Stable and Efficient Perovskite Solar Cells

Abhishek Thote, Il Jeon, Hao-Sheng Lin, Sergei Manzhos, Takafumi Nakagawa, Donguk Suh, Junho Hwang, Makoto Kashiwagi, Junichiro Shiomi, Shigeo Maruyama, Daiguji Hirofumi, Yutaka Matsuo: ACS Applied Electronic Materials, 1, 389396 (2019).

6. Quantifying phonon particle and wave transport in nanostructures–The unexpectedly strong particle effect in silicon nanophononic metamaterial with cross junction
   Dengke Ma, Anuj Arora, Shichen Deng, Junichiro Shiomi, Nuo Yang: Materials Today Physics, 8, 56-61 (2019).
7. Tuning phonon transport spectrum for better thermoelectric materials
   Takuma Hori, Junichiro Shiomi: Science and Technology of Advanced Materials, 20, 10-25 (2018).
8. Akhiezer mechanism limits coherent heat conduction in phononic crystals
   Yuxuan Liao, Takuma Shiga, Makoto Kashiwagi, and Junichiro Shiomi: Physical Review B 98, 134307 (2018).
9. Thermal boundary conductance across heteroepitaxial ZnO/GaN interfaces: Failures of the phonon gas model
   John Gaskins, George Kotsonis, Ashutosh Giri, Shenghong Ju, Andrew Rohskopf, Yekan Wang, Tingyu Bai, Edward Sachet, Christopher Shelton, Zeyu Liu, Zhe Cheng, Brian Foley, Samuel Graham, Tengfei Luo, Asegun Henry, Mark S. Goorsky, Junichiro Shiomi, Jon-Paul Maria, and Patrick E. Hopkins: Nano letters, 18, 7469-7477 (2018).
10. Modulating temperature dependence of thermal conductivity by nanostructuring
    Takuma Shiga, Junichiro Shiomi: Japanese Journal of Applied Physics, 57, 120312 (2018).
11. Thermal phonon engineering by tailored nanostructures
    Masahiro Nomura, Junichiro Shiomi, Takuma Shiga, and Roman Anufriev: Japanese Journal of Applied Physics 57, 080101 (2018).
12. Revisiting PbTe to identify how thermal conductivity is really limited
    Shenghong Ju, Takuma Shiga, Lei Feng and Junichiro Shiomi: Phys. Rev. B 97, 184305 (2018).
13. Modelling heat conduction in nanoporous silicon with geometry distributions
    Makoto Kashiwagi, Yuta Sudo, Takuma Shiga, and Junichiro Shiomi: Physical Review Applied, 10, 044018 (2018).

SHIRAI, Tatsuhiko [B class; 700 (B), 0 (C)] (292)

— *Application of Eigenstate Thermalization Hypothesis to Non-equilibrium steady states*

1. Optical bistability in a low-photon-density regime
   T. Shirai, S. Todo, H. de Raedt and S. Miyashita: Pays. Rev. A **98** (2018) 043802.
2. Thermalization in Open Many-Body Systems Based on Eigenstate Thermalization Hypothesis
   T. Shirai and T. Mori: submitted to Phys. Rev. Lett.

SHIRAISHI, Kenji [C class; 6000 (B), 950 (C)] ()

— *Multiphysics Simulation of MOVPE Growth of Nitride Semiconductor Based on Unification of First Principles Calculations and Fluid Dynamics*

SHUDO, Ken-ichi [B class; 600 (B), 0 (C)] (157)

— *Chemical doping of nano-structured PbS*

1. Electronic states of 3D aromatic molecules on Au(111) surfaces: adsorption of carboranethiol
   Takuto Aoki, Yuta Nakahama, Tadao Ikeda, Masako Shindo, Masanobu Uchiyama, and Ken-ichi Shudo: Journal of Materials Science, *in press* (2019).
2. Chemical synthesis and band gap control of Ga2O3:Co nanocrystals
   Kohki Mukai , Akira Tsuno, Ken-ichi Shudo, and Hiroyuki Otani: Japanese Journal of Applied Physics **58**, SBBK05 (2019).
3. Core electron topologies in chemical compounds: case study of carbon vs. silicon
   Daisuke Yoshida, Hannes Raebiger, Ken-ichi Shudo, and Koichi Ohno: Angewandte Chemie Int. Ed. **57**, 7012–7018 (2018).

SUGINO, Osamu [E class; 13000 (B), 2350 (C)] (50)

— *Functional property of electrodes*

1. Direct coupling of first-principles calculations with replica exchange Monte Carlo sampling of ion

disorder in solids
Shusuke Kasamatsu and Osamu Sugino, J. Phys. Cond. Mat., 31. 085901 (2019).
2. Hydrogen adsorption on Pt (111) revisited from random phase approximation
Lei Yan, Yang Sun, Yoshiyuki Yamamoto, Shusuke Kasamatsu, Ikutaro Hamada, and Osamu Sugino, J. Chem. Phys. 149, 164702 (2018).
3. First-principles investigation of polarization and ion conduction mechanisms in hydroxyapatite
Shusuke Kasamatsu and Osamu Sugino, Phys. Chem. Chem. Phys. 20 8744 (2018).

SUZUKI, Takafumi [C class; 8500 (B), 1600 (C)] (216)
— *Dynamical properties of honeycomb-lattice Kitaev-Heisenberg models in magnetic fields*
— *Ramman spectra in the effective models for honeycomb-lattice magnet $RuCl_3$*
1. Effective model with strong Kitaev interactions for α-$RuCl_3$
Takafumi Suzuki and Sei-ichiro Suga: Phys. Rev. B **97** (2018) 134424.
2. Thermal properties of spin-S Kitaev-Heisenberg model on a honeycomb lattice
Takafumi Suzuki and Youhei Yamaji: Physica B **536** (2018) 637-639.
3. Field dependence of THz spectra of effective models for α-$RuCl_3$
Takafumi Suzuki and Sei-ichiro Suga: AIP Advances **8** (2018) 101414.
4. Quantized $\Delta S = 2$ Excitation Spectra by Confinement in an $S = 1$ Spin Chain
Takafumi Suzuki and Sei-ichiro Suga: Accepted in J. Phys. Soc. Jpn.

SUZUKI, Tatsuo [C class; 2000 (B), 550 (C)] ()
— *Theoretical search for high-efficient monolayer water-splitting photocatalysts II*

SUZUKI, Yuji [C class; 8500 (B), 0 (C)] (62)
— *Development of High-performance Polymer Electret*
1. 量子化学計算を用いた高性能アモルファスフッ素ポリマー・エレクトレットの開発
S. Kim, K.Suzuki, and Y. Suzuki: 日本機械学会熱工学コンファレンス 2018, 富山, 2018 年 10 月 20 日-10 月 21 日, D126.
2. Development of A High-performance Amorphous Fluorinated Polymer Electret Based on Quantum Chemical Analysis
18th Int. Conf. on Micro and Nanotechnology for Power Generation and Energy Conversion Applications (PowerMEMS 2018), Daytona Beach, T4B-01, (2018)
3. 量子化学計算を用いた高電子親和力官能基を持つ アモルファスフッ素ポリマーエレクトレットの開発
応用物理学会春季学術講演会，東京，2019 年 3 月 9 日-12 日, 11p-W242-2

TAKAE, Kyohei [B class; 800 (B), 0 (C)] (289)
— *Dynamics of structure formation in charged colloids*
1. Hydrodynamic simulations of charge-regulation effects in colloidal suspensions
K. Takae and H. Tanaka: Soft Matter **14** (2018) 4711.
2. Self-organization into ferro- and antiferroelectric crystals via the interplay between particle shape and dipolar interaction
K. Takae and H. Tanaka: Proc. Natl. Acad. Sci. **115** (2018) 9917.

TAKETSUGU, Tetsuya [C class; 3500 (B), 700 (C)] (99)
— *Ab initio study on the structure and functions of nanomaterials*
1. Low-lying Excited States of hqxcH and Zn-hqxc Complex: Toward Understanding Intramolecular Proton Transfer Emission
M. Ebina, Y. Kondo, T. Iwasa, T. Taketsugu: Inorg. Chem., **58**, (2019) 4686-4698.
2. Photoluminescence Properties of [Core+exo]-Type Au6 Clusters: Insights into the Effect of Ligand Environments on the Excitation Dynamics
Y. Shichibu, M. Zhang, T. Iwasa, Y. Ono, T. Taketsugu, S. Omagari, T. Nakanishi, Y. Hasegawa, K. Konishi: J. Phys. Chem. C, **123**, (2019) 6934-6939.
3. Ammonia-rich combustion and ammonia combustive decomposition properties of various supported catalysts

S. Hinokuma, K. Araki, T. Iwasa, S. Kiritoshi, Y. Kawabata, T. Taketsugu, and M. Machida: Catal. Commun., **123**, (2019) 64-68.

4. Combined Automated Reaction Pathway Searches and Sparse Modeling Analysis for Catalytic Properties of Lowest Energy Twins of Cu_13
   T. Iwasa, T. Sato, M. Takagi, M. Gao, A. Lyalin, M. Kobayashi, K. Shimizu, S. Maeda, T. Taketsugu: J. Phys. Chem. A, **123**, (2019) 210-217.
5. 金・銀・銅クラスターの安定構造，異性化反応経路，および NO 解離反応経路の探索とその電子物性
   近藤有輔，高原里奈，毛利広野，高木牧人，前田理，岩佐豪, 武次徹也: J. Comput. Chem. Jpn., **18**, (2019) 64-69.
6. First principles calculations toward understanding SERS of 2,2′ -bipyridyl adsorbed on Au, Ag and Au-Ag alloy
   M. Takenaka, Y. Hashimoto, T. Iwasa, T. Taketsugu, G. Seniutinas, A. Balčytis, S. Juodkazise, Y. Nishijima: J. Comput. Chem., **40**, (2019) 925-932.
7. Supported binary CuOx − Pt catalysts with high activity and thermal stability for the combustion of NH3 as a carbon-free energy source
   S. Kiritoshi, T. Iwasa, K. Araki, Y. Kawabata, T. Taketsugu, S. Hinokuma, and M. Machida: RSC Advances, **8**, (2018) 41491-41498.
8. Spiral Eu(III) Coordination Polymers with Circularly Polarized Luminescence
   Y. Hasegawa, Y. Miura, Y. Kitagawa, S. Wada, T. Nakanishi, K. Fushimi, T.Seki, H. Ito, T. Iwasa, T. Taketsugu, M. Gon, K. Tanaka, Y. Chujo, S. Hattori, M. Karasawa, and K. Ishii: Chem. Commun., **54**, (2018) 10695-10697.
9. Insights into Geometries, Stabilities, Electronic Structures, Reactivity Descriptors, and Magnetic Properties of Bimetallic NimCun-m (m = 1, 2; n = 3-13) Clusters: Comparison with Pure Copper Clusters
   R. K. Singh, T. Iwasa, and T. Taketsugu: J. Comput. Chem., **39**,(2018) 1878-1889 .

TAMURA, Ryo [C class; 1500 (B), 400 (C)] (272)

— Development of effective model estimation method by machine learning for multiple input measured data

1. Functional nanoparticles-coated nanomechanical sensor arrays for machine learning-based quantitative odor analysis
   K. Shiba, R. Tamura, T. Sugiyama, Y. Kameyama, K. Koda, E. Sakon, K. Minami, H. T. Ngo, G. Imamura, K. Tsuda, and G. Yoshikawa: ACS Sensors **3** (2018) 1592.
2. Hunting for organic molecules with artificial intelligence: Molecules optimized for desired excitation energies
   M. Sumita, X. Yang, S. Ishihara, R. Tamura, and K. Tsuda: ACS Central Science **4** (2018) 1126.
3. Machine learning forces trained by Gaussian process in liquid states: Transferability to temperature and pressure
   R. Tamura, J. Lin, and T. Miyazaki: Journal of the Physical Society of Japan **88** (2019) 044601.
4. Efficient construction method for phase diagrams using uncertainty sampling
   K. Terayama, R. Tamura, Y. Nose, H. Hiramatsu, H. Hosono, Y. Okuno, and K. Tsuda: Physical Review Materials **3** (2019) 033802.
5. Quantum Phase Transition in Fully-Connected Quantum Wajnflasz–Pick Model
   Y. Seki, S. Tanaka and S. Kawabata: J. Phys. Soc. Jpn. **88** (2019) 054006.
6. Application of Ising Machines and a Software Development for Ising Machines
   K. Tanahashi, S. Takayanagi, T. Motohashi and S. Tanaka: J. Phys. Soc. Jpn., in press.
7. A Fully-Connected Ising Model Embedding Method and Its Evaluation for CMOS Annealing Machines
   D. Oku, K. Terada, M. Hayashi, M. Yamaoka, S. Tanaka and N. Togawa: IEICE Transactions in press.
8. Li-ion conductive Li3PO4-Li3BO3-Li2SO4 mixture: Prevision through density functional molecular dynamics and machine learning
   M. Sumita, R. Tamura, K. Homma, C. Kaneta, and K. Tsuda: Bulletin of the Chemical Society of Japan in press.
9. Expanding the horizon of automated metamaterials discovery via quantum annealing

K. Kitai, J. Guo, S. Ju, S. Tanaka, K. Tsuda, J. Shiomi and R. Tamura: submitted.

TANAKA, Hajime [B class; 1700 (B), 0 (C)] (274)
— *Hydrodynamic effects on crystal nucleation in a hard-sphere colloidal system*
— *Schmidt number dependence on dynamics in colloidal suspensions*

1. Numerical prediction of colloidal phase separation by direct computation of Navier-Stokes equation
   Michio Tateno and Hajime Tanaka: npj Computational Materials **5** (2019) 40
2. Physical foundation of the fluid particle dynamics method for colloid dynamics simulation
   Akira Furukawa, Michio Tateno and Hajime Tanaka: Soft Matter **14** (2018) 3738

TANAKA, Shu [C class; 1000 (B), 200 (C)] (286)
— *Study on quantum annealing from a viewpoint of statistical mechanics*

1. Quantum Phase Transition in Fully-Connected Quantum Wajnflasz–Pick Model
   Y. Seki, S. Tanaka and S. Kawabata: J. Phys. Soc. Jpn. **88** (2019) 054006.
2. Application of Ising Machines and a Software Development for Ising Machines
   K. Tanahashi, S. Takayanagi, T. Motohashi and S. Tanaka: J. Phys. Soc. Jpn., in press.
3. A Fully-Connected Ising Model Embedding Method and Its Evaluation for CMOS Annealing Machines
   D. Oku, K. Terada, M. Hayashi, M. Yamaoka, S. Tanaka and N. Togawa: IEICE Transactions in press.
4. Expanding the horizon of automated metamaterials discovery via quantum annealing
   K. Kitai, J. Guo, S. Ju, S. Tanaka, K. Tsuda, J. Shiomi and R. Tamura: submitted.
5. Functional nanoparticles-coated nanomechanical sensor arrays for machine learning-based quantitative odor analysis
   K. Shiba, R. Tamura, T. Sugiyama, Y. Kameyama, K. Koda, E. Sakon, K. Minami, H. T. Ngo, G. Imamura, K. Tsuda, and G. Yoshikawa: ACS Sensors **3** (2018) 1592.
6. Hunting for organic molecules with artificial intelligence: Molecules optimized for desired excitation energies
   M. Sumita, X. Yang, S. Ishihara, R. Tamura, and K. Tsuda: ACS Central Science **4** (2018) 1126.
7. Machine learning forces trained by Gaussian process in liquid states: Transferability to temperature and pressure
   R. Tamura, J. Lin, and T. Miyazaki: Journal of the Physical Society of Japan **88** (2019) 044601.
8. Efficient construction method for phase diagrams using uncertainty sampling
   K. Terayama, R. Tamura, Y. Nose, H. Hiramatsu, H. Hosono, Y. Okuno, and K. Tsuda: Physical Review Materials **3** (2019) 033802.
9. Li-ion conductive Li_3PO_4-Li_3BO_3-Li_2SO_4 mixture: Prevision through density functional molecular dynamics and machine learning
   M. Sumita, R. Tamura, K. Homma, C. Kaneta, and K. Tsuda: Bulletin of the Chemical Society of Japan in press.

TATENO, Masaru [C class; 4000 (B), 0 (C)] ()
— *Molecular dynamics free energy calculations of functional mechanisms of biological macromolecular complex systems*

TATETSU, Yasutomi [C class; 4000 (B), 800 (C)] (95)
— *First-principles calculations of a search for subphases and large-scale calculations for the grain boundaries of Nd-Fe-B magnets*

1. First-principles study on substitution effects in $Nd_2(Fe, X)_{14}B$
   Y. Tatetsu, S. Tsuneyuki, and Y. Gohda: Materialia, 4, 388-394 (2018).
2. Dynamic interface formation in magnetic thin film heterostructures
   S. Nakashima, T. Miyamachi, Y. Tatetsu, Y. Takahashi, Y. Takagi, Y. Gohda, T. Yokoyama, and F. Komori: Advanced Functional Materials, 29, 1804594 (2018).
3. Role of typical elements in $Nd_2Fe_{14}X$ (X = B, C, N, O, F)
   Yasutomi Tatetsu, Yosuke Harashima, Takashi Miyake, and Yoshihiro Gohda: Physical Review Materials 2, 0744100-1 − 0744100-9 (9) (2018).

TATEYAMA, Yoshitaka [C class; 4500 (B), 950 (C)] (82)

— *DFT sampling studies on interfacial properties of batteries and catalysts*

1. A General Representation Scheme for Crystalline Solids based on Voronoi-Tessellation Real Feature Values and Atomic Property Data
   R. Jalem, M. Nakayama, Y. Noda, T. Le, I. Takeuchi, Y. Tateyama, H. Yamazaki: Sci. Tech. Adv. Mater. **19** (2018) 231-242.
2. First-Principles Microkinetic Analysis of NO + CO Reactions on Rh(111) Surface toward Understanding NOx Reduction Pathways
   A. Ishikawa, Y. Tateyama: J. Phys. Chem. C **122** (2018) 17378-17388.
3. Liquid electrolyte informatics using an exhaustive search with linear regression
   K. Sodeyama, Y. Igarashi, T. Nakayama, Y. Tateyama, M. Okada: Phys. Chem. Chem. Phys. **20** (2018) 22585-22591.
4. Dynamical Solvent Effects on the Charge and Reactivity of Ceria-Supported Pt Nanoclusters
   L. Szabova, M. F. Camellone, F. N. Ribeiro, V. Matolin, Y. Tateyama, S. Fabris: J. Phys. Chem. C **122** (2018) 27507-27515.
5. Structures, Electronic States, and Reactions at Interfaces between LiNi0.5Mn1.5O4 Cathode and Ethylene Carbonate Electrolyte: A First-Principles Study
   Y. Okuno, K. Ushirogata, K. Sodeyama, G. Shukri, Y. Tateyama: J. Phys. Chem. C **123** (2019) 2267-2277.
6. Oxygen Redox Promoted by Na Excess and Covalency in Hexagonal and Monoclinic Na2-xRuO3 Polymorphs
   M. H. N. Assadi, M. Okubo, A. Yamada, Y. Tateyama: J. Electrochem. Soc. **166** (2019) A5343-A5348.

TERAO, Takamichi [B class; 1100 (B), 150 (C)] (283)

— *Molecular simulation of colloidal suspensions*

1. Generalised local bond order parameter analysis: application to colloidal particles with dendritic polymer brushes
   R. Mizuno, K. Okumura, J. Oguri, and T. Terao: Mol. Simul. **45** (2019) 743. .

TERASAWA, Asako [B,C class; 4200 (B), 650 (C)] (93)

— *First principles calculations and development of graph analysis method for magnetic alloys and amorphous grain boundary phases in permanent magnets*

— *First principles calculations and mathematical analyses of amorphous magnetic alloys and amorphous grain boundary phases in permanent magnets*

1. Hidden order in amorphous structures: Extraction of nearest neighbor networks of amorphous NdFe alloys with Gabriel graph analyses
   A. Terasawa and Y. Gohda, J. Chem. Phys., **149**, 154502, (2018).

TODO, Synge [C class; 5500 (B), 900 (C)] (229)

— *Topological Order and Quantum Dynamics in Quantum Many-body Systems*

1. Crystal structure prediction supported by incomplete experimental data
   N. Tsujimoto, D. Adachi, R. Akashi, S. Todo, S. Tsuneyuki, Phys. Rev. Materials 2, 053801 (7pp) (2018)
2. Optical bistability in a low-photon-density regime
   T. Shirai, S. Todo, H. de Raedt, S. Miyashita, Phys. Rev. A 98, 043802 (13pp) (2018)
3. ZN Berry phase and symmetry protected topological phases of SU(N) antiferromagnetic Heisenberg chain
   Y. Motoyama, S. Todo, , Phys. Rev. B 98, 195127 (6pp) (2018)
4. Localized mode and nonergodicity of a harmonic oscillator chain
   F. Ishikawa, S. Todo, Phys. Rev. E 98, 062140 (8pp) (2018)
5. Parallel loop cluster quantum Monte Carlo simulation of quantum magnets based on global union-find graph algorithm
   S. Todo, H. Matsuo, H. Shitara, Comp. Phys. Comm. 239, 84-93 (2019)

6. Fast algorithm for generating random bit strings and multispin coding for directed percolation
   H. Watanabe, S. Morita, S. Todo, N. Kawashima, J. Phys. Soc. Jpn. 88, 024004 (8pp) (2019)
7. Search for Common Minima in Joint Optimization of Multiple Cost Functions
   D. Adachi, N. Tsujimoto, R. Akashi, S. Todo, S. Tsuneyuki, to appear in Comp. Phys. Comm.

TOHYAMA, Takami [C class; 4500 (B), 850 (C)] (246)
— *Dynamical DMRG study of spin dynamics in frustrated quantum spin systems*

1. Magnetic phase diagram of a frustrated spin ladder
   T. Sugimoto, M. Mori, T. Tohyama, and S. Maekawa: Phys. Rev. B **97**, (2018) 144424.
2. Dynamical density matrix renormalization group study of spin and charge excitations in the four-leg t-t'-J ladder
   T. Tohyama, M. Mori, and S. Sota: Phys. Rev. B **97**, (2018) 235137.
3. Ground state phase diagram of the Kitaev-Heisenberg model on a honeycomb-triangular lattice
   M. Kishimoto, K. Morita, Y. Matsubayashi, S. Sota, S. Yunoki, and T. Tohyama: Phys. Rev. B **98**, (2018) 054411.
4. Ground-state phase diagram of the Kitaev-Heisenberg model on a kagome lattice
   K. Morita, M. Kishimoto, and T. Tohyama: Phys. Rev. B **98**, (2018) 134437.
5. Syntheses and first-principles calculations of the pseudobrookite compound $AlTi_2O_5$
   T. Tohyama, R. Ogura, K. Yoshinaga, S. Naito, N. Miyakawa, and E. Kaneshita: J. Phys. Chem. Solids **127**, (2019) 035121.
6. Magnetization plateau and supersolid phases in the spin-1/2 antiferromagnetic Heisenberg model on a tetragonally distorted fcc lattice
   K. Morita and T. Tohyama: Phys. Rev. B **99**, (2019) 144417.

TOKIWA, Hiroaki [C class; 3500 (B), 0 (C)] (112)
— *Theoretical Study of Industrial Enzyme and Drug Target Protein using the Forth Revolution*

1. Development of analysis toolkit to visualize interaction energies generated by fragment molecular orbital calculations
   Takaki Tokiwa, Shogo Nakano, Yuta Yamamoto, Takeshi Ishikawa, Sohei Ito, Vladimir Sladek, Kaori Fukuzawa, Yuji Mochizuki, Hiroaki Tokiwa, Fuminori Misaizu, and Yasuteru Shigeta: J. Chem. Info. Model (DOI:10.1021/acs.jcim.8b00649) 59(1), 25-30 (2018)
2. Protein residue networks from energetic and geometric data: Are they identical?
   Vladimir Sladek, Hiroaki Tokiwa, Hitoshi Shimano, Yasuteru Shigeta: J. Chem. Theor. Comp. (DOI: 10.1021/acs.jctc.8b00733) 14(12), 6623-6631 (2018)
3. Dual conformation of the ligand induces the partial agonistic activity of retinoid X receptor α (RXR α)
   Yurina Miyashita, Nobutaka Numoto, Sundaram Arulmozhiraja, Shogo Nakano, Naoya Matsuo, Kanade Shimizu, Osamu Shibahara, Michiko Fujiwara, Hiroki Kakuta, Sohei Ito, Teikichi Ikura, Nobutoshi Ito, Hiroaki Tokiwa: FEBS Lett. (DOI: 10.1002/1873-3468.13301) 593(2), 242-250 (2018)
4. Benchmark analysis of native and artificial NAD^+-dependent enzymes generated by a sequence based design method with or without phylogenetic data
   Shogo Nakano, Tomoharu Motoyama, Yurina Miyashita, Yuki Ishizuka, Naoya Matsuo, Hiroaki Tokiwa, Suguru Shinoda, Yasuhisa Asano, and Sohei Ito: Biochem. (DOI: 10.1021/acs.biochem.8b00339) 57(26), 3722-3732 (2018)
5. Molecular association model of PPARα and its new specific and efficient ligand, pemafibrate: Structural basis for SPPARMα
   Yuta Yamamoto, Kenta Takei, Sundaram Arulmozhiraja, Vladimir Sladek, Naoya Matsuo, Songiee Han, Takashi Matsuzaka, Motohiro Sekiya, Takaki Tokiwa, Mitsuo Shoji, Yasuteru Shigeta, Yoshimi Nakagawa, Hiroaki Tokiwa,Hitoshi Shiman: Biochem. Biophys. Res. Comm. (DOI: 10.1016/j.bbrc.2018.03.135) 499(2), 239-245 (2018)
6. Total Synthesis of Termicalcicolanone A via Organocatalysis and Regioselective Claisen Rearrangement
   Saki Ito, Taiki Kitamura, Sundaram Arulmozhiraja, Kei Manabe, Hiroaki Tokiwa, and Yumiko Suzuki: Org. Lett.(DOI: 10.1021/acs.orglett.9b00731) 21(8), 2777-2781 (2019)

7. 25S-Adamantyl-23-yne-26,27-dinor-1α,25-dihydroxyvitamin D_3: Synthesis, Tissue Selective Biological Activities, and X-ray Crystal Structural Analysis of Its Vitamin D Receptor Complex
   Rocio Otero, Michiyasu Ishizawa, Nobutaka Numoto, Teikichi Ikura, Nobutoshi Ito, Hiroaki Tokiwa, Antonio Mourin, Makoto Makishima, and Sachiko Yamada: J. Med. Chem. (DOI: 10.1021/acs.jmedchem.8b00427) 61(15), 6658-6673 (2018).
8. 3-(Triflyloxy)benzynes Enable the Regiocontrolled Cycloaddition of Cyclic Ureas to Synthesize 1,4-Benzodiazepine Derivatives
   Hideki Kaneko, Takashi Ikawa, Yuta Yamamoto, Sundaram Arulmozhiraja, Hiroaki Tokiwa, Shuji Akai: Syn. Lett. (DOI: 10.1055/s-0036-1591924) 29(07), 943-948 (2018).

TONEGAWA, Takashi [B class; 1200 (B), 0 (C)] (284)
— *Numerical Study of the One-Dimensional Quantum Spin Systems with Spatial Structures*

1. Ground-State Phase Diagram of an Anisotropic $S = 1/2$ Ladder with Different Leg Interactions
   T. Tonegawa, T. Hikihara, K. Okamoto, S. C. Furuya, and T. Sakai: J. Phys. Soc. Jpn. **87**, 104002 (2018)

TOYAO, Takashi [B class; 500 (B), 70 (C)] (159)
— *Calculation of catalyst electronic structures for catalyst informatics*

TOYODA, Masayuki [B class; 700 (B), 0 (C)] (151)
— *Theoretical Study on Magnetoelectric Effects of Localized Spin Systems in Quadrupole Alignemnt*

1. A-cation control of magnetoelectric quadrupole order in $A(\mathrm{TiO})\mathrm{Cu}_4(\mathrm{PO}_4)_4$ (A = Ba, Sr, and Pb)
   K. Kimura, M. Toyoda, P. Babkevich, K. Yamauchi, M. Sera, V. Nassif, H. M. Rønnow, and T. Kimura: Physical Review B, 97, 134418 (2018)

TSUMURAYA, Takao [C class; 500 (B), 0 (C)] (161)
— *First-principles study on the formation mechanism of long-period stacking ordered structure in Fe based shape memory alloys and Mg alloys*

TSUNETSUGU, Hirokazu [B class; 600 (B), 0 (C)] (303)
— *Numerical study of vortices in ferromagnetic superconductor*

TSUNEYUKI, Shinji [C class; 7000 (B), 1000 (C)] (65)
— *Development and application of first-principles simulation methods: from structure prediction to superconductivity*

1. First-principles study on substitution effects in $\mathrm{Nd}_2(\mathrm{Fe, X})_{14}\mathrm{B}$
   Y. Tatetsu, S. Tsuneyuki and Y. Gohda: Materialia **4** (2018) 388.
2. First-principles study of phonon anharmonicity and negative thermal expansion in ScF_3
   Y. Oba, T. Tadano, R. Akashi and S. Tsuneyuki: Phys. Rev. Materials **3** (2019) 033601.
3. Ab initio prediction of structural phase-transition temperature of SrTiO_3 from finite-temperature phonon calculation
   T. Tadano and S. Tsuneyuki: J. Ceram. Soc. Jpn., in press.
4. Crystal structure prediction supported by incomplete experimental data
   N. Tsujimoto, D. Adachi, R. Akashi, S. Todo and S. Tsuneyuki: Phys. Rev. Materials **2** (2018) 053801.
5. Neural-network Kohn-Sham exchangecorrelation potential and its out-of-training transferability
   R. Nagai, R. Akashi, S. Sasaki and S. Tsuneyuki: J. Chem. Phys. **148** (2018) 241737.
6. Ferromagnetism above 1000 K in highly cation-ordered double-perovskite insulator $\mathrm{Sr}_3\mathrm{OsO}_6$
   Y.K. Wakabayashi, Y. Krockenberger, N. Tsujimoto, T. Boykin, S. Tsuneyuki, Y. Taniyasu and H. Yamamoto: Nat. Commun. **10** (2019) 535.
7. Search for common minima in joint optimization of multiple cost functions
   D. Adachi, N. Tsujimoto, R. Akashi, S. Todo and S. Tsuneyuki: Comp. Phys. Commun., in press.

TSURUTA, Kenji [C class; 1500 (B), 0 (C)] (132)
— *Ab-initio Metaheuristics for Functional Design of Nanocarbon*

1. Metaheuristic Ab-initio Optimum Search for Doping Effects in Nanocarbons
   Kenji Tsuruta, Keiichi Mitani, Md. Abdullah Al Asad, Yuta Nishina, Kazuma Gotoh, and Atsushi Ishikawa: Materials Science Forum

UCHIDA, Takashi [B class; 300 (B), 80 (C)] (310)
— *Theory of multiple spin density waves and magnetic skyrmions in frustrated itinerant magnets*

UDAGAWA, Masafumi [C,D class; 11500 (B), 450 (C)] (215)
— *Dynamics of fractional excitations in quantum spin liquid*
— *Gauge charge picture of spin liquids: Structure formation and magnetic correlation*

1. Vison-Majorana complex zero-energy resonance in Kitaev's spin liquid
   Masafumi Udagawa: Physical Review B **98**, 220404(R)-1-5
2. Spectrum of itinerant fractional excitations in quantum spin ice
   Masafumi Udagawa, Roderich Moessner: Phys. Rev. Lett. **122** (2019) 117201
3. Magnetic clustering, half-moons, and shadow pinch points as signals of a proximate Coulomb phase in frustrated Heisenberg magnets
   Tomonari Mizoguchi, Ludovic D. C. Jaubert, Roderich Moessner, Masafumi Udagawa: Phys. Rev. B **98** (2018) 144446

WAKABAYASHI, Daisuke [B class; 700 (B), 0 (C)] (291)
— *Compression behavior and inhomogeneous structure of silica glass in its intermediate state in structural transformations*

WATANABE, Hiroshi [B class; 800 (B), 100 (C)] (288)
— *Data compression for molecular dynamics simulation on the basis of multiresolution analysis*

1. Fast algorithm for generating random bit strings and multispin coding for directed percolation
   H. Watanabe, S. Morita, S. Todo, and N. Kawashima, J. Phys. Soc. Jpn. **88**, 024004 (2019)

WATANABE, Hiroshi [B class; 600 (B), 0 (C)] (201)
— *Novel phenomena induced by intradimer charge degree of freedom in molecular conductors*

1. Mechanism of superconductivity and electron-hole doping asymmetry in κ-type molecular conductors
   H. Watanabe, H. Seo, and S. Yunoki: submitted, arXiv: 1811.09035.

WATANABE, Kazuyuki [C class; 10000 (B), 1750 (C)] (53)
— *First-Principles Study of Excited Electron, Positron and Atom Dynamics and Optical Responses of Nanostructures*

1. Electron scattering in time-dependent density functional theory
   L. Lacombe, Y. Suzuki, K. Watanabe, and N. T. Maitra, The European Physical Journal B **91**, 96 (2018).
2. Secondary-electron emission from multi-layer graphene: time-dependent first-principles study
   Y. Ueda, Y. Suzuki, and K. Watanabe, Appl. Phys. Express **11**, 105101 (2018).
3. Time-Dependent Multicomponent Density Functional Theory for Coupled Electron-Positron Dynamics
   Y. Suzuki, S. Hagiwara and K. Watanabe, Phys. Rev. Lett. **121**, 133001 (2018).
4. Thermal effects on laser-assisted field evaporation from a Si surface: A real-time first-principles study
   K. Uchida, Y. Suzuki, and K. Watanabe, submitted.

WATANABE, Satoshi [C class; 12000 (B), 1850 (C)] (51)
— *Theoretical Analyses on Various Properties Concerning Nanodevices*

1. CO-tip manipulation using repulsive interactions
   N. K. M. Nazriq, E. Minamitani, and T. K. Yamada: Nanotechnology **29** (2018) 495701.

2. Inelastic electron tunneling spectroscopy by STM of phonons at solid surfaces and interfaces
   E. Minamitani, N. Takagi, R. Arafune, T. Frederiksen, T. Komeda, H. Ueba, and S. Watanabe: Prog. Surf. Sci. **93** (2018) 131.
3. Phonon Angular Momentum Induced by the Temperature Gradient
   M. Hamada, E. Minamitani, M. Hirayama, S. Murakami: Phys. Rev. Lett. 121 (2018) 175301.
4. 固体表面を舞台とした電子フォノン相互作用の研究
   南谷英美: 固体物理 **53** (2018) 609.
5. 電子相関とスピン軌道相互作用が生み出す吸着分子の新奇な磁性
   南谷英美, 高木紀明: 日本物理学会誌 **73** (2018) 690.
6. ニューラルネットワークを用いたアモルファス物質中の原子拡散の研究
   安藤康伸, 李文文 and 渡邉 聡: 固体物理 **53** (2018) 389.
7. A Comparative Study on the Diffusion Behaviors of Metal and Oxygen Ions in Metal-Oxide Based Resistance Switches via Ab Initio Molecular Dynamics Simulations
   B. Xiao, X.-F. Yu, and S. Watanabe: ACS Appl. Electronic Mater., in press.
8. Moisture Effect on the Diffusion Behaviors of Cu ions in $Cu/Ta_2O_5/Pt$ and $Cu/SiO_2/Pt$ Resistance Switches: A First-Principle Study
   B. Xiao and S. Watanabe: submitted to Sci. Technol. Adv. Mater.
9. Mechanically tunable spontaneous vertical charge redistribution in few-layer WTe_2
   Z. Ni, E. Minamitani, K. Kawahara, R. Arafune, C.-L. Lin, N. Takagi, and S. Watanabe: submitted to ACS Nano
10. First-principles study of Li-ion distribution at γ-Li_3PO_4/metal interfaces
    K. Shimizu, W. Liu, W. Li, S. Kasamatsu, Y. Ando, E. Minamitani, and S. Watanabe: submitted to Phys. Rev. Mater.

YAMADA, Atsuo [C class; 5500 (B), 900 (C)] (75)
— *First-principles investigations of battery materials*

1. Redox-Driven Spin Transition ina Layered Battery Cathode Material
   E. Watanabe, W. Zhao, A. Sugahara, B.Mortemard de Boisse, L. Lander, D. Asakura, Y.Okamoto, T. Mizokawa, M. Okubo and A.Yamada: Chem. Mater. **31** (2019) 2358.
2. Combined Theoretical and Experimental Studies of Sodium Battery Materials
   E. Watanabe, S. Chung, S. Nishimura, Y.Yamada, M. Okubo and A. Yamada: Chem. Rec. **19** (2019)1.

YAMADA, Atsushi [C class; 2500 (B), 600 (C)] (191)
— *Superconductivity and magnetic properties of the Hubbard model*

YAMAGUCHI, Shu [C class; 5000 (B), 0 (C)] (90)
— *Bronsted Acidity on Oxide Surface Induced by Neutralization of Lewis Acid Sites by Molecules*

YAMAJI, Youhei [E class; 12000 (B), 2250 (C)] (175)
— *Numerical studies on fractional excitations in strongly correlated electron systems*

1. Path to stable quantum spin liquids in spin-orbit coupled correlated materials
   Andrei Catuneanu, Youhei Yamaji, Gideon Wachtel, Yong Baek Kim, and Hae-Young Kee: npj Quantum Materials **3** (2018) 23.
2. Ab initio effective Hamiltonians for cuprate superconductors
   Motoaki Hirayama, Youhei Yamaji, Takahiro Misawa, and Masatoshi Imada: Phys. Rev. B **98** (2018) 134501.
3. Classical and quantum spin dynamics of the honeycomb Γ model
   Anjana M. Samarakoon, Gideon Wachtel, Youhei Yamaji, D. A. Tennant, Cristian D. Batista, and Yong Baek Kim: Phys. Rev. B **98** (2018) 045121.
4. Stripe and superconducting order competing in the Hubbard model on a square lattice studied by a combined variational Monte Carlo and tensor network method
   Andrew S. Darmawan, Yusuke Nomura, Youhei Yamaji, and Masatoshi Imada: Phys. Rev. B **98** (2018) 205132.

YAMAMOTO, Norifumi [B class; 800 (B), 100 (C)] (146)
— *Theoretical Study on the Aggregation-Induced Emission*

YAMASHITA, Koichi [C class; 6000 (B), 0 (C)] (77)
— *Large scale ab initio calculations on the fundamental processes of solar energy convergence devices and on designing principles for new materials*

1. Investigations on the charge transfer mechanism at donor/acceptor interfaces in quest of descriptors of organic solar cell performance
   A. Muraoka, M. Fujii, K. Mishima, H. Matsunaga, H. Benten, H. Ohkita, S. Ito and K. Yamashita: Phys. Chem. Chem. Phys. **20** (2018) 1219312199.
2. Halogen in materials design: Revealing the nature of hydrogen bonding and other non-covalent interactions in the polymorphic transformations of methylammonium lead tribromide perovskite
   A. Varadwaj, P. R. Varadwaj, H. M. Marques and K. Yamashita: Mater. Today Chem. **9** (2018) 116.
3. *cis*-1 Isomers of tethered bismethano[70]fullerene as electron acceptors in organic photovoltaics
   T. Umeyama, S. Takahara, S. Shibata, K. Igarashi, T. Higashino, K. Mishima, K. Yamashita and H. Imahori: RSC Adv. **8** (2018) 1831618326.
4. Influence of the aggregate state on band structure and optical properties of C60 computed with different methods
   A. Pal, S. Arabnejad, K. Yamashita and S. Manzhos: J. Chem. Phys. **148** (2018) 204301.
5. Palladium‐ Catalyzed Intramolecular CH Arylation versus 1,5-Palladium Migration: A Theoretical Investigation
   N. Misawa, T. Tsuda, R. Shintani, K. Yamashita and K. Nozaki: Chem. Asian J. **13** (2018) 25662572.
6. Revealing the Cooperative Chemistry of the Organic Cation in the Methylammonium Lead Triiodide Perovskite Semiconductor System
   A. Varadwaj, P. R. Varadwaj and K. Yamashita: ChemistrySelect **3** (2018) 72697282.
7. Two-dimensional optical excitations in the mixed-valence $Cs_2Au_2I_6$ fully inorganic double perovskite
   G. Giorgi, K. Yamashita and M. Palummo: J. Mater. Chem. C **6** (2018) 1019710201.
8. Anion-Substitution-Induced Non-Rigid Variation of Band Structure in $SrNbO_{3-x}N_x$ $(0 \leq x \leq 1)$ Epitaxial Thin Films
   D. Oka, Y. Hirose, M. Kaneko, S. Nakao, T. Fukumura, K. Yamashita and T. Hasegawa: ACS Appl. Mater. Interfaces **10** (2018) 3500835015.
9. Can Combined Electrostatic and Polarization Effects Alone Explain the F···F Negative-Negative Bonding in Simple Fluoro-Substituted Benzene Derivatives? A First-Principles Perspective
   P. R. Varadwaj, A. Varadwaj, H. M. Marques and K. Yamashita: Computation **6** (2018) 51.
10. Nature of the Electronic and Optical Excitations of RuddlesdenPopper Hybrid OrganicInorganic Perovskites: The Role of the Many-Body Interactions
    G. Giorgi, K. Yamashita and M. Palummo: J. Phys. Chem. Lett. **9** (2018) 58915896.
11. Halogen in materials design: Chloroammonium lead triiodide perovskite ($ClNH_3PbI_3$) a dynamical bandgap semiconductor in 3D for photovoltaics
    P. R. Varadwaj, A. Varadwaj, H. M. Marques and K. Yamashita: J. Comput. Chem. **39** (2018) 19021912.
12. Probing the nature of the Co(III) ion in corrins: The reactions of aquacyano-5-seco-cobyrinic acid heptamethyl ester with anionic ligands
    M. Nowakowska, S. M. Chemaly, A. L. Rousseau, P. P. Govender, P. R. Varadwaj, A. Varadwaj, K. Yamashita and H. M. Marques: Inorg. Chim. Acta **484** (2018) 402413.
13. Epitaxy of $(GaN)_{1-x}(ZnO)_x$ Solid-Solution Thin Films with Widely Tunable Chemical Composition and Strong Visible Absorption
    C. Yang, Y. Hirose, T. Wakasugi, N. Kashiwa, H. Kawai, K. Yamashita and T. Hasegawa: Phys. Rev. Applied **10** (2018) 44001.
14. A Theoretical study on the charge and discharge states of Na- ion battery cathode material, $Na_{1+x}FePO_4F$
    C. Shinagawa, Y. Morikawa, S. Nishimura, H. Ushiyama, A. Yamada and K. Yamashita: J.

Comput. Chem **40** (2019) 237246.
15. Molecular QTAIM Topology Is Sensitive to Relativistic Corrections
J. S. M. Anderson, J. I. Rodriguez, P. W. Ayers, D. E. Trujillo-Gonzalez, A. W. Goetz, J. Autschbach, F. L. Castillo-Alvarado and K. Yamashita: Chem. Eur. J. **25** (2019) 25382544.
16. Significance of hydrogen bonding and other noncovalent interactions in determining octahedral tilting in the $CH_3NH_3PbI_3$ hybrid organic-inorganic halide perovskite solar cell semiconductor
P. Varadwaj, A. Varadwaj, H. M. Marques and K. Yamashita: Sci. Rep. **9** (2019) 50.
17. Regression model for stabilization energies associated with anion ordering in perovskite-type oxynitrides
M. Kaneko, M. Fujii, T. Hisatomi, K. Yamashita, K. Domen: J. Energy Chem. **36** (2019) 714.
18. Effect of Nuclear Motion on Charge Transport in Fullerenes: A Combined Density Functional Tight BindingDensity Functional Theory Investigation
S. Arabnejad, A. Pal, K. Yamashita and S. Manzhos: Front. Energy Res. **7** (2019) 3.
19. Li and Na Interaction with Ti_2C-MXene: A First-Principles Calculation
S. Kurahashi, S. Arabnejad, H. Ushiyama and K. Yamashita: J. Comput. Chem. Jpn. **18** (2019) 8494.
20. First-principles study on visible light absorption of defected $SrNbO_3$
M. Kaneko, K. Mishima and K. Yamashita: J. Photochem. Photobiol. A: Chem. **375** (2019) 175180.

YAMASHITA, Tomoki [C class; 3000 (B), 850 (C)] (106)
— *Developments of new materials using materials informatics*

1. Fine-grained optimization method for crystal structure prediction
K.Terayama, T. Yamashita, T. Oguchi, and K. Tsuda, npj Comput. Mater. **4**, 32 (2018).

YAMAUCHI, Kunihiko [C class; 6000 (B), 0 (C)] (76)
— *First-Principles DFT Calculations for Topological Matter*

1. Ultrathin Bismuth Film on 1T-TaS_2: Structural Transition and Charge- Density-Wave Proximity Effect
Keiko Yamada, Seigo Souma, Kunihiko Yamauchi, Natsumi Shimamura, Katsuaki Sugawara, Chi Xuan Trang, Tamio Oguchi, Keiji Ueno, Takashi Takahashi, and Takafumi Sato: Nano Lett. **18** (2018) 3235.
2. *A*-cation control of magnetoelectric quadrupole order in $A(TiO)Cu_4(PO_4)_4$ (A =Ba, Sr, and Pb)
K. Kimura, M. Toyoda, P. Babkevich, K. Yamauchi, M. Sera, V. Nassif, H. M. Rønnow, and T. Kimura: Phys. Rev. B **97** (2018) 2268.
3. Ultrathin Bismuth Film on High-Temperature Cuprate Superconductor $Bi_2Sr_2CaCu_2O_{8+\delta}$ as a Candidate of a Topological Superconductor
Natsumi Shimamura, Katsuaki Sugawara, Sukrit Sucharitakul, Seigo Souma, Katsuya Iwaya, Kosuke Nakayama, Chi Xuan Trang, Kunihiko Yamauchi, Tamio Oguchi, Kazutaka Kudo, Takashi Noji, Yoji Koike, Takashi Takahashi, Tetsuo Hanaguri, and Takafumi Sato: ACS Nano **12** (2018) 10977.
4. Magnetic structural unit with convex geometry: A building block hosting an exchange-striction-driven magnetoelectric coupling
Kenta Kimura, Yasuyuki Kato, Kunihiko Yamauchi, Atsushi Miyake, Masashi Tokunaga, Akira Matsuo, Koichi Kindo, Mitsuru Akaki, Masayuki Hagiwara, Shojiro Kimura, Masayuki Toyoda, Yukitoshi Motome, and Tsuyoshi Kimura: Phys. Rev. Mater. **2** (2018) 10415.

YANAGISAWA, Susumu [C class; 3000 (B), 0 (C)] (120)
— *First-principles band structure calculation of organic crystals at finite-temperature*
— *Search for adsorption geometry of an organic molecular layer on a metal surface with the first-principles molecular dynamics*

1. Impact of the molecular quadrupole moment on ionization energy and electron affinity of organic thin films: Experimental determination of electrostatic potential and electronic polarization energies
K. Yamada, S. Yanagisawa, T. Koganezawa, K. Mase, N. Sato, and H. Yoshida: Phys. Rev. B

97 (2018) 245206.
2. Surface Structure of Organic Semiconductor [n]Phenacene Single Crystals
Y. Wakabayashi, M. Nakamura, K. Sasaki, T. Maeda, Y. Kishi, H. Ishii, N. Kobayashi, S. Yanagisawa, Y. Shimo, and Y. Kubozono: J. Am. Chem. Soc. **140** (2018) 14046.
3. Nano-scale first-principles electronic structure simulations of materials relevant to organic electronics
S. Yanagisawa and I. Hamada: A Chapter in Theoretical Chemistry for Advanced Nanomaterials - Functional Analysis by Computation and Experiment edited by Taku Onishi (Springer Nature, 2019)

YANAGISAWA, Takashi [B class; 800 (B), 130 (C)] (198)
— *Optimization variational Monte Carlo study of strongly correlated electron systems*
— *Study of strongly correlated electron systems based on optimization Monte Carlo method and first-principles calculations*

1. Possibility of flat-band ferromagnetism in hole doped pyrochlore oxide $Sn_2Nb_2O_7$ and $Sn_2Ta_2O_7$
I. Hase, T. Yanagisawa, Y. Aiura, K. Kawashima: Physical Review Letters 120 (2018) 196401.
2. Antiferromagnetism, Superconductivity and phase diagram in the two-dimensional Hubbard model
T. Yanagisawa: J. Phys. Soc. Jpn. 88 (2019) 054702.a
3. Optimized wave function by kinetic renormalization effect in strongly correlated region of the three-band Hubbard model
T. Yanagisawa, M. Miyazaki, I. Hase and K. Yamaji: J. Phys. Conf.Ser. 1054 (2018) 012017.a
4. Electronic structure of novel binary superconductor $SrGe_2$
I. Hase, T. Yanagisawa, A. Iyo, H. Eisaki, Y. Yoshida and K. Kawashima: J. Phys. Conf. Series 1054 (2018) 012004.
5. The Competition between CDW and the superconducting state in valence skip compounds
I. Hase, T. Yanagisawa and K. Kawashima: Communications in Computational Physics 23 (2018) 773.
6. Crossover induced electron pairing and superconductivity by kinetic renormalization in correlated electron systems
T. Yanagisawa, M. Miyazaki, K. Yamaji: Condensed Matter 3 (2018) 26.a
7. Massless and quantized modes of kinks in the phase space of superconductors
T. Yanagisawa: Phys. Lett. A382 (2018) 3483.
8. Renormalization group analysis of the hyperbolic sine-Gordon model
T. Yanagisawa: Prog. Theor. Exp. Phys. 2019 (2019) 023A01.
9. Antiferromagnetism, Superconductivity and phase diagram in the three-band model of hig temperature superconductors
T. Yanagisawa: J. Phys. Conf. Ser. (2019) in press.a
10. Green's functions of Nambu-Goldstone and Higgs modes in superconductors
T. Yanagisawa: J. Supercond. Novel Magne. 2018 (2018) 4983 on line.

YASUDA, Chitoshi [C class; 2500 (B), 300 (C)] (263)
— *Randomness Effects on Spin-Peierls System*

1. Antiferromagnetic Long-Range Order for $S = 1/2$ Two-Dimensional Site-Diluted Heisenberg Model Coupled to Lattice Degree of Freedom
S. Miyara and C. Yasuda: J. Phys. Soc. Jpn. **87** (2018) 104702.
2. Ground-state properties of spin-1/2 Heisenberg antiferromagnets with frustration on the diamond-like-decorated square and triangular lattices
Y. Hirose, S. Miura, C. Yasuda, and Y. Fukumoto: AIP Advances **8** (2018) 101427.

YASUOKA, Kenji [C class; 9500 (B), 0 (C)] (58)
— *Study on the Temperature Induced Stability of Defects on Rutile TiO2(110) Surfaces*
— *The Effect of Defect Density on O_2 Absorption Reactions on Rutile TiO_2(110) Surfaces*

YOKO, Akira [B class; 500 (B), 0 (C)] (160)
— *Structural study on surface reconstruction and solvent effects of nanoparticles*

1. Impact of Surface Energy on the Formation of Composite Metal Oxide Nanoparticles
   A. Yoko, N. Umezawa, T. Ohno, and Y. Oshima: J. Phys. Chem. C **122**, 24350-24358 (2018).

YOSHIDA, Tsuneya [C class; 7000 (B), 0 (C)] (181)
— *Anomalous phenomena induced for correlated topological systems*
— *Non-Hermitian properties induced by strong correlations*

1. Symmetry-protected exceptional rings in two-dimensional correlated systems with chiral symmetry
   Tsuneya Yoshida, Robert Peters, Norio Kawakami, and Yasuhiro Hatsugai: Phys. Rev. B 99, (2019) 121101(R)
2. Breakdown of topological Thouless pumping in the strongly interacting regime
   Masaya Nakagawa, Tsuneya Yoshida, Robert Peters, and Norio Kawakami: Phys. Rev. B 98, (2018) 115147
3. Magnetic states in a three-dimensional topological Kondo insulator
   Robert Peters, Tsuneya Yoshida, and Norio Kawakami: Phys. Rev. B 98, (2018) 075104
4. Non-Hermitian perspective of the band structure in heavy-fermion systems
   Tsuneya Yoshida, Robert Peters, and Norio Kawakami: Phys. Rev. B 98, (2018) 035141
5. Topological Properties of Magnetically Ordered Heavy-Fermion Systems in the Presence of Mirror Symmetry
   Kazuhiro Kimura Tsuneya Yoshida, and Norio Kawakami: J. Phys. Soc. Jpn. 87, (2018) 084705
6. Reduction of Topological Z Classification in Cold-Atom Systems
   Tsuneya Yoshida, Ippei Danshita, Robert Peters, and Norio Kawakami: Phys. Rev. Lett. 121, (2018) 025301

YOSHIDOME, Takashi [C class; 2000 (B), 700 (C)] (264)
— *Quantitative computation of the dissociation rate of a protein-ligand complex using a manifold-learning technique*

1. An Automatic Classification of Molecular Dynamics Simulation Data into States, and Its Application to the Construction of a Markov State Model
   R. Ito and T. Yoshidome: J. Phys. Soc. Jpn. **87** (2018) 114802.

YOSHINO, Hajime [C class; 2000 (B), 0 (C)] (269)
— *Spinglass transitions in frustrated vector spin models*

□ SCCMS Projects

FUJITA, Takatoshi [3000 (B), 0 (C)] (323)
— *Development of an excited-state theory based on many-body Green's functions and fragment molecular orbital method*

1. Development of the fragment-based COHSEX method for large and complex molecular systems
   T. Fujita, Y. Noguchi, Phys. Rev. B **98** (2018) 205140.
2. Thousand-atom ab initio calculations of excited states at organic/organic interfaces: toward first-principles investigations of charge photogeneration
   T. Fujita, A. M, Khorshed, T. Hoshi, Phys. Chem. Chem. Phys. **20** (2018) 26443.

FUKUSHIMA, Tetsuya [5000 (B), 500 (C)] (324)
— *First-principles materials design by multi-scale simulation*

1. Anomalous Hall conductivity and electronic structures of Si-substituted Mn2CoAl epitaxial films
   K. Arima, F. Kuroda, S. Yamada, T. Fukushima, T. Oguchi, and K. Hamaya: Phys. Rev. B **97** (2018) 054427.
2. First-principles prediction of the control of magnetic properties in Fe-doped GaSb and InSb
   H. Shinya, T. Fukushima, A. Masago, K. Sato, and H. Katayama-Yoshida: J. Appl. Phys. **124** (2018) 103962.
3. Magnetism of Eu-doped GaN modulations by spinodal nanodecomposition
   A. Masago, H. Shinya, T. Fukushima, K. Sato, and H. Katayama-Yoshida: Phys. Rev. B **98** (2018) 214426.
4. Magnetic and transport properties of equiatomic quaternary Heusler CoFeVSi epitaxial films
   S. Yamada, S. Kobayashi, F. Kuroda, K. Kudo, S. Abo, T. Fukushima, T. Oguchi, and K. Hamaya: Phys. Rev. Materials **2** (2018) 124403.

GOHDA, Yoshihiro [5000 (B), 500 (C)] (328)
— *First-principles calculations of interface magnetic properties at magnetic materials*

1. First-principles study of magnetoelectric coupling at Fe/$BiFeO_3$(001)interfaces
   K. Fujita and Y. Gohda: Phys. Rev. Appl. **11**, 024006 (2019).
2. First-principles prediction of one-dimensional giant Rashba splittings in Bi adsorbed In atomic chains
   T. Tanaka and Y. Gohda: Phys. Rev. B **98**, 241409(R) (2018).
3. First-principles study on substitution effects in Nd_2(Fe, X)$_{14}$B
   Y. Tatetsu, S. Tsuneyuki, and Y. Gohda: Mater. **4**, 388 (2018).
4. Hidden order in amorphous structures: extraction of nearest neighbor networks of amorphous Nd-Fe alloys with Gabriel graph analyses
   A. Terasawa and Y. Gohda:J. Chem. Phys. **149**, 154502 (2018).
5. Role of typical elements in $Nd_2Fe_{14}X$ (X=B, C, N, O, F)
   Y. Tatetsu, Y. Harashima, T. Miyake, and Y. Gohda: Phys. Rev. Mater. **2**, 074410 (2018).

HOSHI, Takeo [5000 (B), 500 (C)] (80)
— *Large-scale device-material research by massively parallel electronic structure calculation and data-driven science*

1. Solution of the k-th eigenvalue problem in large-scale electronic structure calculations
   Dongjin Lee, Takeo Hoshi, Tomohiro Sogabe, Yuto Miyatake, Shao-Liang Zhang, submitted; Preprint (arXiv.1710.05134)

IITAKA, Toshiaki [20000 (B), 100 (C)] (330,332)
— *Computational study of hydrous minerals using the path integral molecular dynamics method II*
— *Structure study of silicate melts using linear scaling ab initio molecular dynamics*

IMADA, Masatoshi [20000 (B), 2000 (C)] (168,171)

— *Emergent Phenomena from Combined Strong Electron Correlation and Electron-Phonon Coupling*

— *Applications of highly accurate lattice model solvers with tensor network and machine learning for mechanisms of superconductivity*

1. Competition among various charge-inhomogeneous states and d-wave superconducting state in Hubbard models on square lattices
   Kota Ido, Takahiro Ohgoe, and Masatoshi Imada: Phys. Rev. B **97** (2018) 045138.
2. Quantum spin liquid signatures in Kitaev-like frustrated magnets
   Matthias Gohlke, Gideon Wachtel, Youhei Yamaji, Frank Pollmann, and Yong Baek Kim: Phys. Rev. B **97**, (2018) 075126.
3. Ab initio effective Hamiltonians for cuprate superconductors
   Motoaki Hirayama, Youhei Yamaji, Takahiro Misawa, and Masatoshi Imada: Phys. Rev. B. **98** (2018) 134501.
4. Direct connection between Mott insulators and d-wave high-temperature superconductors revealed by continuous evolution of self-energy poles
   Shiro Sakai, Marcello Civelli, and Masatoshi Imada : Phys. Rev. B.**98** (2018) 195109
5. Stripe and superconducting order competing in the Hubbard model on a square lattice studied by a combined variational Monte Carlo and tensor network method
   Andrew S. Darmawan, Yusuke Nomura, Youhei Yamaji, and Masatoshi Imada: Phys. Rev. B 98,**98** (2018) 205132.
6. Resummation of diagrammatic series with zero convergence radius for strongly correlated fermions
   Riccardo Rossi, Takahiro Ohgoe, Kris Van Houcke, and Felix Werner: Phys. Rev. Lett. **121** (2018) 130405.
7. Contact and Momentum distribution of the Unitary Fermi Gas
   Riccardo Rossi, Takahiro Ohgoe, Kris Van Houcke, and Felix Werner: Phys. Rev. Lett. **121** (2018) 130406.
8. mVMC-Open-source software for many-variable variational Monte Carlo method
   Takahiro Misawa, Satoshi Morita, Kazuyoshi Yoshimi, Mitsuaki Kawamura, Yuichi Motoyama, Kota Ido, Takahiro Ohgoe, Masatoshi Imada, Takeo Kato: Compt. Phys. Commun.,**235** (2019) 447.
9. Excitons and Dark Fermions as Origins of Mott Gap, Pseudogap and Superconductivity in Cuprate Superconductors — General Idea and Basic Concept Based on Gap Physics
   Takafumi J. Suzuki, Masatoshi Imada: J. Phys. Soc. Jpn. **88** (2019) 024701.

KAWAKATSU, Toshihiro [10000 (B), 1000 (C)] (329)

— *Multiscale simulations on complex multiphase flows*

1. Supercomputer System at ISSP
   T.Murashima, K. Hagita and T.Kawakatsu: J. Soc. Rheol. Jpn. **46** (2018) 207-220.

KAWASHIMA, Naoki [20000 (B), 2000 (C)] (320)

— *Application of Tensor Network Methods to Condensed Matter Physics*

— *Tensor Network Method and Its Application to Condensed Matter Physics*

1. A series of magnon crystals appearing under ultrahigh magnetic fields in a kagome antiferromagnet
   R. Okuma, D. Nakamura, T. Okubo, A. Miyake, A. Matsuo, K. Kindo, M. Tokunaga, N. Kawashima, S. Takeyama and Z. Hiroi: Nature Communications **10**, 1229/1-7 (2019).
2. Calculation of higher-order moments by higher-order tensor renormalization group
   Satoshi Morita, Naoki Kawashima: Computer Physics Communications **236**, 65-71 (2019)
3. Detecting signals of weakly first-order phase transitions in two-dimensional Potts models
   Shumpei Iino, Satoshi Morita, Anders W. Sandvik, and Naoki Kawashima: J. Phys. Soc. Jpn. **88**, 034006/1-8 (2019).
4. Spin-one bilinear-biquadratic model on a star lattice
   Hyun-Yong Lee, and Naoki Kawashima: Phys. Rev. B **97**, 205123/1-7 (2018).
5. Spin Thermal Hall Conductivity of a Kagome Antiferromagnet
   Hayato Doki, Masatoshi Akazawa, Hyun-Yong Lee, Jung Hoon Han, Kaori Sugii, Masaaki Shimozawa, Naoki Kawashima, Migaku Oda, Hiroyuki Yoshida, and Minoru Yamashita: Phys. Rev.

Lett. **121**, 097203/1-4 (2018).

6. Fast algorithm for generating random bit strings and multispin coding for directed percolation
Hiroshi Watanabe, Satoshi Morita, Synge Todo, and Naoki Kawashima: J. Phys. Soc. Jpn. **88**, 024004 (2019).

KOHYAMA, Masanori [20000 (B), 2000 (C)] (312,313)

— *First-Principles Phase Field Mapping*

1. Accurate quasiparticle calculation of x-ray photoelectron spectra of solids
T. Aoki and K. Ohno: J. Phys.: Condensed Mat. **30** (2018) 21LT01.
2. GW($\Gamma\Theta$) method without the Bethe-Salpeter equation for photoabsorption energies of spin-polarized systems
T. Isobe, R. Kuwahara, and K. Ohno: Phys. Rev. A **97**, (2018) 060502(R).
3. A first-principles phase field method for quantitatively predicting multi-composition phase separation without thermodynamic empirical parameter
Swastibrata Bhattacharyya, Ryoji Sahara, and K. Ohno: in submission to Nature Communications.

MISAWA, Takahiro [10000 (B), 1000 (C)] (15)

— *Spin Hall magnetization switching in topological Dirac semimetal*

— *Study of correlated quantum many-body systems using RESPACK*

1. Ab initio effective Hamiltonians for cuprate superconductors
Motoaki Hirayama, Youhei Yamaji, Takahiro Misawa, and Masatoshi Imada: Phys. Rev. B **98**, 134501 (2018).
2. mVMC - Open-source software for many-variable variational Monte Carlo method
Takahiro Misawa, Satoshi Morita, Kazuyoshi Yoshimi, Mitsuaki Kawamura, Yuichi Motoyama, Kota Ido, Takahiro Ohgore, Masatoshi Imada, and Takeo Kato :Comput. Phys. Commun. **235**, 447 (2019).

MIYAKE, Takashi [2500 (B), 0 (C)] (326)

— *Development of permanent magnet materials*

1. First-principles study of spin-wave dispersion in $Sm(Fe_{1-x}Co_x)_{12}$
Taro Fukazawa, Hisazumi Akai, Yosuke Harashima and Takashi Miyake: J. Mag. Mag. Mater. **469** (2019) 296.
2. Effect of R-site substitution and pressure on stability of RFe_{12}: A first-principles study
Yosuke Harashima, Taro Fukazawa, Hiori Kino, and Takashi Miyake: J. Appl. Phys. **124** (2018) 163902.
3. Anisotropy of exchange stiffness based on atomic-scale magnetic properties in rare-earth permanent magnet $Nd_2Fe_{14}B$
Yuta Toga, Masamichi Nishino, Seiji Miyashita, Takashi Miyake and Akimasa Sakuma: Phys. Rev. B **98** (2018) 054418.
4. Important descriptors and descriptor groups of Curie temperatures of rare-earth transition-metal binary alloys
Hieu-Chi Dam, Viet Cuong Nguyen, Tien Lam Pham, Anh Tuan Nguyen, Kiyoyuki Terakura, Takashi Miyake, and Hiori Kino: J. Phys. Soc. Jpn. **87** (2018) 113801.
5. Leaning structure-property relationship in crystalline materials: A study of lanthanide-transition metal alloys
Tien-Lam Pham, Duong-Nguyen Nguyen, Van Doan Nguyen, Hiori Kino, Takashi Miyake, and Hieu Chi Dam: J. Chem. Phys. **148** (2018) 204106.

MORITA, Akihiro [5000 (B), 0 (C)] ()

— *Molecular simulation of ion transport and desolvation at electrode interface*

NOGUCHI, Hiroshi [10000 (B), 1000 (C)] (205)

— *Molecular Dynamics Simulation of Complex Fluids*

1. Polymer effects on Karman vortex: Molecular dynamics study

Y. Asano, H. Watanabe, and H. Noguchi: J. Chem. Phys. **148**,(2018) 144901.

OGATA, Shuji [5000 (B), 0 (C)] (321)
— *Simulation of organic-inorganic interfaces*

1. Unveiling the Chemical Reactions Involved in Moisture-Induced Weakening of Adhesion between Aluminum and Epoxy Resin
   S. Ogata and M. Uranagase: J. Phys. Chem. C (2018) 122 17748-17755.
2. E cient scheme for calculating work of adhesion between a liquid and polymer-grafted substrate
   M. Uranagase, S. Ogata, K. Tanaka, H. Mori, and S. Tajima: J. Chem. Phys. **148** (2018) 064703/1-9.

OGUCHI, Tamio [5000 (B), 0 (C)] (326)
— *Electron Theory on Sodium Secondary-Battery Materials*

1. First-Principles Study on Cathode Properties of Li_2MTiO_4 (M = V, Cr, Mn, Fe, Co, and Ni) with Oxygen Deficiencies for Li-ion Batteries
   M. Hamaguchi, H. Momida, and T. Oguchi, J. Phys. Soc. Jpn. **87**, 044805 (2018).
2. Elucidation of discharge mechanism and evaluation of Na-ion battery performance of tin sulfide (SnS) electrode by using first-principles calculation
   H. Kotaka, H. Momida, A. Kitajou, S. Okada, and T. Oguchi, J. Comput. Chem. Jpn. **18**, 78 (2019).
3. First-Principles Study of Na-Ion Battery Performance and Reaction Mechanism of Tin Sulfide as Negative Electrode
   H. Kotaka, H. Momida, A. Kitajou, S. Okada, and T. Oguchi, Chem. Rec. **19**, 811 (2019).

OKAZAKI, Susumu [10000 (B), 1000 (C)] (322)
— *Conversion and storage of energy - Fuel cells and secondary batteries: Research and development of fundamental technologies of battery simulators*

1. Exploring the Effect of Pendent Side Chain Length on the Structural and Mechanical Properties of Hydrated Perfluorosulfonic Acid Polymer Membranes by Molecular Dynamics Simulation
   A. Kuo, K. Takeuchi, A. Tanaka, S. Urata, S. Okazaki, and W. Shinoda: Polymer,146, 53-62 (2018)
2. Molecular Mechanism of Material Deformation and Failure in Butadiene Rubber: Insight from All-Atom Molecular Dynamics Simulation Using a Bond Breaking Potential Model
   R. S. Payal, K. Fujimoto, C. Jang, W. Shinoda, Y. Takei, H. Shima, K. Tsunoda, and S. Okazaki: Polymer, 170, 113-119 (2019)
3. Difference in molecular mechanisms governing changes in membrane properties of phospholipid bilayers induced by addition of nonionic and zwitterionic surfactants
   Y. Andoh, S. Kitou, S. Okazaki: J. Mol. Liquids, 271, 933-941(2018)

OSHIYAMA, Atsushi [10000 (B), 1000 (C)] (44)
— *Exploration of new-functionality and high-performance semiconductor devices*

1. Structural stability and energy levels of carbon-related defects in amorphous SiO_2 and its interface with SiC
   Y.-i. Matsushita and A. Oshiyama: Jpn. J. Appl. Phys. **57** (2018) 125701
2. Microscopic mechanism of carbon annihilation upon SiC oxidation due to phosphorous treatment: Density functional calculations combined with ion mass spectrometry
   T. Kobayashi, Y.-i. Matsushita, T. Okuda, T. Kimoto and A. Oshiyama: Appl. Phys. Exp. **11** (2018) 121301
3. Reaction Pathway of Surface-Catalyzed Ammonia Decomposition and Nitrogen Incorporation in Epitaxial Growth of Gallium Nitride
   K. M. Bui, J.-I. Iwata, Y. Kangawa, K. Shiraishi, Y. Shigeta, and A. Oshiyama: J. Phys. Chem. C **122** (2018)
4. First-Principle Study of Ammonia Decomposition and Nitrogen Incorporation on the GaN Surface in Metal Organic Vapor Phase Epitaxy
   K. M. Bui, J.-I. Iwata, Y. Kangawa, K. Shiraishi, Y. Shigeta, and A. Oshiyama: J. Cryst. Growth

507 (2019)
5. Structural determination of phosphosilicate glass based on first-principles molecular dynamics calculation
T. Kobayashi, Y.-i. Matsushita, T. Kimoto and A. Oshiyama: Jpn. J. Appl. Phys. **58** (2019) 011001

SAITO, Susumu [5000 (B), 500 (C)] ()
— *Materials design using B, C, and N for next-generation device*

SHIBA, Hayato [10000 (B), 1000 (C)] (316)
— *Molecular dynamics simulation of the hierarchical dynamics and functional dynamics of electrolyte liquids*
— *Numerical simulations of universal features of slow glassy dynamics from molecular liquids to electrolytes*

1. Molecular dynamics study of mesophase transitions upon annealing of imidazolium-based ionic liquids with long-alkyl chains
H. Peng, M. Kubo, and H. Shiba: Phys. Chem. Chem. Phys. 9796-9805 (2018).

SUGINO, Osamu [10000 (B), 1000 (C)] (314)
— *Priority project 5 – energy conversion (chemical energy)*

1. Direct coupling of first-principles calculations with replica exchange Monte Carlo sampling of ion disorder in solids
Shusuke Kasamatsu and Osamu Sugino, J. Phys. Cond. Mat., 31. 085901 (2019).
2. Hydrogen adsorption on Pt (111) revisited from random phase approximation
Lei Yan, Yang Sun, Yoshiyuki Yamamoto, Shusuke Kasamatsu, Ikutaro Hamada, and Osamu Sugino, J. Chem. Phys. 149, 164702 (2018).
3. First-principles investigation of polarization and ion conduction mechanisms in hydroxyapatite
Shusuke Kasamatsu and Osamu Sugino, Phys. Chem. Chem. Phys. 20 8744 (2018).

TAKETSUGU, Tetsuya [10000 (B), 1000 (C)] (99)
— *Ab initio study on abundant nano-catalysts free from precious metals*
— *Ab initio study toward abundant element nanocatalysts with less precious metals*

1. Low-lying Excited States of hqxcH and Zn-hqxc Complex: Toward Understanding Intramolecular Proton Transfer Emission
M. Ebina, Y. Kondo, T. Iwasa, T. Taketsugu: Inorg. Chem., **58**, (2019) 4686-4698.
2. Photoluminescence Properties of [Core+exo]-Type Au6 Clusters: Insights into the Effect of Ligand Environments on the Excitation Dynamics
Y. Shichibu, M. Zhang, T. Iwasa, Y. Ono, T. Taketsugu, S. Omagari, T. Nakanishi, Y. Hasegawa, K. Konishi: J. Phys. Chem. C, **123**, (2019) 6934-6939.
3. Ammonia-rich combustion and ammonia combustive decomposition properties of various supported catalysts
S. Hinokuma, K. Araki, T. Iwasa, S. Kiritoshi, Y. Kawabata, T. Taketsugu, and M. Machida: Catal. Commun., **123**, (2019) 64-68.
4. Combined Automated Reaction Pathway Searches and Sparse Modeling Analysis for Catalytic Properties of Lowest Energy Twins of Cu_13
T. Iwasa, T. Sato, M. Takagi, M. Gao, A. Lyalin, M. Kobayashi, K. Shimizu, S. Maeda, T. Taketsugu: J. Phys. Chem. A, **123**, (2019) 210-217.
5. 金・銀・銅クラスターの安定構造，異性化反応経路，および NO 解離反応経路の探索とその電子物性
近藤有輔，高原里奈，毛利広野，高木牧人，前田理，岩佐豪, 武次徹也: J. Comput. Chem. Jpn., **18**, (2019) 64-69.
6. First principles calculations toward understanding SERS of 2,2′ -bipyridyl adsorbed on Au, Ag and Au-Ag alloy
M. Takenaka, Y. Hashimoto, T. Iwasa, T. Taketsugu, G. Seniutinas, A. Balčytis, S. Juodkazise, Y. Nishijima: J. Comput. Chem., **40**, (2019) 925-932.
7. Supported binary CuOx − Pt catalysts with high activity and thermal stability for the combustion

of NH3 as a carbon-free energy source
S. Kiritoshi, T. Iwasa, K. Araki, Y. Kawabata, T. Taketsugu, S. Hinokuma, and M. Machida: RSC Advances, **8**, (2018) 41491-41498.

8. Spiral Eu(III) Coordination Polymers with Circularly Polarized Luminescence
Y. Hasegawa, Y. Miura, Y. Kitagawa, S. Wada, T. Nakanishi, K. Fushimi, T.Seki, H. Ito, T. Iwasa, T. Taketsugu, M. Gon, K. Tanaka, Y. Chujo, S. Hattori, M. Karasawa, and K. Ishii: Chem. Commun., **54**, (2018) 10695-10697.
9. Insights into Geometries, Stabilities, Electronic Structures, Reactivity Descriptors, and Magnetic Properties of Bimetallic NimCun-m (m = 1, 2; n = 3-13) Clusters: Comparison with Pure Copper Clusters
R. K. Singh, T. Iwasa, and T. Taketsugu: J. Comput. Chem., **39**,(2018) 1878-1889 .

TOHYAMA, Takami [5000 (B), 0 (C)] (246)
— *Cooperation Research with Big Experimental Facilities*

1. Magnetic phase diagram of a frustrated spin ladder
T. Sugimoto, M. Mori, T. Tohyama, and S. Maekawa: Phys. Rev. B **97**, (2018) 144424.
2. Dynamical density matrix renormalization group study of spin and charge excitations in the four-leg t-t'-J ladder
T. Tohyama, M. Mori, and S. Sota: Phys. Rev. B **97**, (2018) 235137.
3. Ground state phase diagram of the Kitaev-Heisenberg model on a honeycomb-triangular lattice
M. Kishimoto, K. Morita, Y. Matsubayashi, S. Sota, S. Yunoki, and T. Tohyama: Phys. Rev. B **98**, (2018) 054411.
4. Ground-state phase diagram of the Kitaev-Heisenberg model on a kagome lattice
K. Morita, M. Kishimoto, and T. Tohyama: Phys. Rev. B **98**, (2018) 134437.
5. Syntheses and first-principles calculations of the pseudobrookite compound $AlTi_2O_5$
T. Tohyama, R. Ogura, K. Yoshinaga, S. Naito, N. Miyakawa, and E. Kaneshita: J. Phys. Chem. Solids **127**, (2019) 035121.
6. Magnetization plateau and supersolid phases in the spin-1/2 antiferromagnetic Heisenberg model on a tetragonally distorted fcc lattice
K. Morita and T. Tohyama: Phys. Rev. B **99**, (2019) 144417.

YABANA, Kazuhiro [15000 (B), 1500 (C)] (319)
— *Dynamics in nano-interface excited by high-intensity pulsed light*
— *Unified Photonic-Electronic Devices*

1. 電子動力学シミュレーションコードのメニーコアプロセッサと GPU における性能比較
廣川祐太, 朴泰祐, 植本光治, 佐藤駿丞, 矢花一浩, 情報処理学会研究報告 2018-HPC-163, 1-11
2. SALMON: Scalable Ab-initio LightMatter simulator for Optics and Nanoscience
M. Noda, S.A. Sato, Y. Hirokawa, M. Uemoto, T. Takeuchi, S. Yamada, A. Yamada, Y Shinohara, M. Yamaguchi, K. Iida, I. Floss, T. Otobe, K.-M. Lee, K. Ishimura, T. Boku, G.F. Bertsch, K. Nobusada, K. Yabana, Comp. Phys. Comm. 235, 356 (2019)

YAMADA, Atsuo [5000 (B), 500 (C)] (75)
— *Theoretical design of electrode materials with oxygen redox activity*

1. Redox-Driven Spin Transition ina Layered Battery Cathode Material
E. Watanabe, W. Zhao, A. Sugahara, B.Mortemard de Boisse, L. Lander, D. Asakura, Y.Okamoto, T. Mizokawa, M. Okubo and A.Yamada: Chem. Mater. **31** (2019) 2358.
2. Combined Theoretical and Experimental Studies of Sodium Battery Materials
E. Watanabe, S. Chung, S. Nishimura, Y.Yamada, M. Okubo and A. Yamada: Chem. Rec. **19** (2019)1.

YOSHIMI, Kazuyoshi [10000 (B), 1000 (C)] (317)
— *Study of many-body correlation effects on spin relaxation rate in quantum dots*
— *Study of spatial anisotropy potential effects on spin relaxation rate in quantum dots*

□ Doctor Theses

1. **HIROKAWA, Yuta**
   Co-design of the ab-initio electron dynamics simulation in advanced high performance computer systems (in Japanese)
   University of Tsukuba, 2018-09

2. **IMOTO, Fumihiro**
   Development of Orbital-Free Density Functional Theory with Machine Learning and its Applications
   the University of Tokyo, 2019-03

3. **INOMOTO, Fumihiro**
   Development of Orbital-Free Density Functional Theory with Machine Learning and its Applications
   the University of Tokyo, 2019-03

4. **KAWASAKI, Airi**
   Geminal theory for strongly correlated few-body systems
   the University of Tokyo, 2019-03

5. **KIM, Seonwoo**
   Development of A High-performance Fluorinated Polymer Electret based on Quantum Chemical Analysisa
   the University of Tokyo, 2019-03

6. **KUMAZOE, Hiroyuki**
   Non-adiabatic ab initio molecular dynamics study of structural and dynamic properties of two-dimensional transition metal dichalcogenides
   Kumamoto University, 2019-03

7. **MIYARA, Shouta**
   Study of Dilution Effects in the Two-Dimensional Antiferromagnetic Heisenberg Model Coupled to the Lattice Degree of Freedom
   University of the Ryukyus, 2019-03

8. **NURUL, Ikhsan**
   Development of first principles approach on the magnetic anisotropy in Fe/MgO interfaces
   Kanazawa University, 2018-09

9. **ONO, Atsushi**
   Theory of Photoinduced Ultrafast Spin Dynamics
   Tohoku University, 2019-03

10. **PRAYITNO, Teguh Budi**
    First-principles Study on Spin Spiral using Linear Combination of Pseudo Atomic Orbitals
    Kanazawa University, 2018-09

11. **SATO, Ryuhei**
    The Research on the Basicity and Proton Conductivity on Hydrated Zrironia
    the University of Tokyo, 2018-09

12. **SUGITA, Yusuke**
Theoretical study of spin-orbit coupled systems with honeycomb-layered structures
the University of Tokyo, 2019-03

13. **TAMURA, Takahiro**
Development and Exploration of New Materials Related with Carbon and Boron Nitride
Hokkaido University, 2018-09

14. **TANAKA, Yuta**
Effect of the electronic entropy on structural change and ablation of metals by an ultrashort laser pulse
the University of Tokyo, 2019-03

15. **TATENO, Michio**
Phase ordering dynamics of colloidal suspensions
the University of Tokyo, 2019-03

16. **TSUJIMOTO, Naoto**
Data assimilation for crystal structure prediction: Construction and implementation of the algorithm and its application
the University of Tokyo, 2019-03

17. **UEDA, Yoshihiro**
Secondary electron emission from nanographene studied by time-dependent density functional theory
The Tokyo University of Science, 2019-03

18. **YAMAMURA, Ryosuke**
Microscopic Theory of Γ_3 Quadrupole Ordering in Pr Compounds on the Basis of a j-j Coupling Scheme
Tokyo Metropolitan University, 2019-03

19. **YOSHITAKE, Junki**
Spin dynamics at finite temperatures in the Kitaev model
the University of Tokyo, 2019-03

□ Master Theses

1. **AKAI, Satoshi**
   First-principles calculation of doping properties in Pb-perovskite halide semiconductors
   Chiba University, 2019-03

2. **CHANG, Yong Lik**
   Elucidation of Reaction Mechanism of Polyalcohol Dehydration in High Temperature Water with Metadynamics
   the University of Tokyo, 2019-03

3. **CHRISTIVANA, Mega**
   First-Principles Calculation on Crystal Structure and Magnetism in β-phase Solid Oxygen
   Kanazawa University, 2018-09

4. **FUJIMOTO, Jun**
   First-principles Study on the Isotope Effect in Hydrocarbons Adsorbed on Noble Metal Surfaces
   Osaka University, 2019-03

5. **FPUTRA, Septia Eka Marsha**
   Theoretical Study of Formic Acid (HCOOH)) on the Cu(111) Surface: Single Molecule and Polymeric Structures
   Osaka University, 2018-09

6. **HASEGAWA, Miki**
   Analysis on the Catalytic Effect of Pt for Etching of Ga at Stepped and Kinked GaN(0001) Surfaces
   Osaka University, 2019-03

7. **HIZUME, Yuma**
   Theoretical study on the effect of spin-fluctuation in superconductivity in iron under high pressure
   the University of Tokyo, 2019-03

8. **IWAHASHI, Daichi**
   Analysis of Cu ion migration in amorphous Ta_2O_5 using neural network potentials
   the University of Tokyo, 2019-03

9. **KANEHIRA, Shinichi**
   Development of descriptor for crystal structure prediction using deep learning
   Osaka University, 2019-03

10. **KANG, Gun-Woo**
    Construction of neural network potentials to analyze ion migration in non-stoichiometric amorphous TaO_x
    the University of Tokyo, 2019-03

11. **KIMURA, Kazuhiro**
    Topological magnetic phases protected by crystalline symmetry in heavy fermion systems
    Kyoto University, 2019-03

12. **KIRIKOSHI, Akimitsu**
    Construction of a Variational Approach for Incorporating Many-Body Effects Self-Consistently in Bose–Einstein Condensed Phase at Finite Temperature
    Hokkaido University, 2019-03

13. **KITAGUCHI, Tomohiro**
First-principles analysis on magnetic properties of systems consisting of transition metal dichalcogenides and adsorbed magnetic metal atoms
the University of Tokyo, 2019-03

14. **KURODA, Yuki**
Hybridization Effects of Molecular Orbitals on Valence Band of Organic Semiconductors
University of Tsukuba, 2019-03

15. **MICHISHITA, Yoshihiro**
The impacts of Rashba spin-orbit coupling, non-hermiticity and periodic laser driving on f-electron materials
Kyoto University, 2019-03

16. **MOCHIHARA, Kosuke**
Magnetic properties of Fe/Pd(001) bilayer affected by quantum-well states formed in Pd layer
Keio University, 2019-03

17. **MORIYA, Tomotaka**
Construction of high-dimensional neural network potentials to analyze Li ion migration in Li_3PO_4 under applied electric fields
the University of Tokyo, 2019-03

18. **MURATA, Itsuki**
Implementation and extension of the band-unfolding method in supercell electronic structure calculation
Kanazawa University, 2019-03

19. **NAGASAWA, Riki**
Defect formation at metal/semiconductor interfaces in electric field: first-principles study
Chiba University, 2019-03

20. **NAITO, Tomoya**
Density functional theory with finite-light-speed correction
the University of Tokyo, 2019-03

21. **NAKAMURA, Kengo**
Research of Kondo effect in two-orbital Anderson model using numerical renormalization group method
Tokyo Metropolitan University, 2019-03

22. **NAKANISHI, Ken M.**
Quantum-classical hybrid algorithm for estimating excited energies of quantum many-body systems
the University of Tokyo, 2019-03

23. **NAKAYAMA, Takafumi**
Evaluation of Optical Activity of Chiral Perylene Derivative (Chiral-PTCDI) Using Classical Molecular Dynamics and Machine Learning Techniques
Osaka University, 2019-03

24. **NISHIMOTO, Toshiki**
Origin of Fermi-level depinning at metal/Ge interfaces: first-principles study
Chiba University, 2019-03

25. **OGURA, Masayoshi**
Development of neural network potentials for calculations of thermal conductivity
the University of Tokyo, 2019-03

26. **ONO, Takanori**
Coarse grained molecular dynamics study of PEGylated lipid effect on physical properties of lipid membranes
Nagoya University, 2019-03

27. **SUGITA, Megumi**
First-principles study of noble metal surfaces and noble metal/oxides interfaces
Kanazawa University, 2019-03

28. **SUZUKI, Motoi**
Event-chain path-integral Monte Carlo and its application to novel quantum phase of Bosons
the University of Tokyo, 2019-03

29. **TAKEDA, Kazuki**
Evaluation of the Structural Stability and Magnetism of Co-doped Anatase TiO_2
Osaka University, 2019-03

30. **TAKEUCHI, Kotono**
Molecular dynamics study on hydrogen permeability for polymer electrolyte membranes
Nagoya University, 2019-03

31. **TAMURA, Miyu**
Multi-dimensional free energy analysis on membrane permeation of ionizable drug
Nagoya University, 2019-03

32. **TANAKA, Yuto**
Anisotropic thermoelectric effect on phosphorene and bismuthene: first-principles calculations based on nonequilibrium Green's function theory
Kanazawa University, 2019-03

33. **WATANABE, Shunta**
First-principles calculation of metal-atom penetration into organic molecular solids
Chiba University, 2019-03

34. **WAZA, Kazunori**
Femtosecond Time-Resolved Spectroscopy in YO Epitaxial Films
University of Fukui, 2019-03

35. **YAJIMA, Yuji**
Study of Dynamical Properties of Silicon Oxide based on First-principles Molecular Dynamics
Shimane University, 2019-03

36. **YAMAGUCHI, Satoshi**
First-principles calculations and experimental consideration of ferromagnetism in Pt(100) ultra thin films
Keio University, 2019-03

37. **YOSHIDA, Hidetaka**
Description of the interaction between magnetic molecules using the DFT+U method
the University of Tokyo, 2019-03